THE DUCTILITY OF COUPLED SHEAR WALLS

A thesis presented for

the degree of Doctor of Philosophy

in Civil Engineering

in the University of Canterbury

Christchurch, New Zealand

by

A.R. Santhakumar

1974

ERRATA

Page X — Replace references 2 and 3 by:
2. Fintel, M., "Ductile Shear Walls in Earthquake Resistant Multistorey Buildings", Proceedings ACI Journal Vol. 71, No. 6, June 1974, pp. 296-305.
3. "Preliminary Report - The Behaviour of Reinforced Concrete Structures in the Caracas, Venezuela Earthquake of July 29, 1967", Portland Cement Association, Skokie, 1967, 51pp.

Page XIV — Delete last line.

Page 18 — In last column of Table 2.1 replace "1296, 1008 and 720" by 1440, 720 and 576 respectively.

Page 19 — 2nd paragraph, line 8 after 14") add: ", i.e. the dimensions of the fictitious rectangular wall section are 18'-0" by 14" ".

Page 21 — 5th paragraph, line 4, replace "ε_q" by "q".

Page 24 — Paragraph (a) replace "0.60" by "0.50".

Page 28 — Line 11 add: "and the number of storeys varying between 6 and 25 ."

Page 31 — At top of Fig. 2.13(b) replace "0.75" by "75"

Page 33 — Fig. 2.15 on vertical axis replace c/H by H/c.

Page 39 — Line 20 delete "of a shear wall" and replace by "of the example structure (the models used in the tests)".

Page 66 — At end add: "The conclusions refer to structures in which the thicknesses of the coupling beams and the walls are of the same order".

Page 69 — Add to Eq. (3.2b): " or $\phi f_{yst} A_{st} \frac{l_s}{s}$ whichever is less." and add to Eq. 3.2 "or $\geq \frac{2 \rho f_{ym} (d-d')d}{\phi f_{yst} l_s^2}$ "

Page 70 — In title of Fig. 3.1(d) replace "distbution" by "distribution".

Page 80 — Paragraph 1, line 3 replace "θ_A" by "θ_E" .

Page 106 — The dashed lines refer to conventionally reinforced beams and full lines refer to diagonally reinforced beams.

Page 108 — Section 3.5.1. (iv) line 3, replace "true" by "probable".

Page 109 — Section 3.5.2 (a) line 1, replace "Flexureal" by "Flexural".

Page 111 — Line 5, after M_u add "(positive moment refers to compression on the left side of the section illustrated in Fig. 3.19)".

Page 113 — Add at end of paragraph (iv) "Because the deflections in both walls are essentially the same the curvature in the tension wall is limited and this may delay its failure."

Page 122 — Add footnote to Table 3.1. "The values of ϕ_y and ϕ_u correspond to two particular loading histories i.e. (d) and (e)."

Page 130 — In Fig. 3.25. The top arrowed line marked (1) in the third diagram of the top row to extend to unit distance.

Page 131 — Line 5 from bottom and remainder of the sentence to be replaced by "the closest to the curves obtained for the compression wall but both quantities reduce to below this value at the critical base area of the tension wall."

Page 143 — Line 3 from bottom replace "shown" by "assumed".

Page 146 — Add after line 6 "The term wall refers to one wall of the structure, while the term shear wall means the entire coupled shear wall structure."

Page 158 — Line 5 from bottom, add "Fig. 4.11 shows the idealised situation with infinitely rigid coupling beams, which implies that no compression occurs in the tension wall."

Page 184 — Add new paragraph: (h) For positive loading the jacks and load cells were situated as in Fig. 5.9.b. For reversed (negative) loading both jacks and load cells were placed at the opposite side of the specimen so that the applied forces were introduced as shown by broken arrows in Fig. 5.5.

Page 187 — Add in line 2 after "Appendix B", "The accuracy of the theodolite readings are discussed on page 240."

Page 258 — At bottom of Fig. 6.23 add behind "(inches)", $\times 10^{-2}$.

Page 300 — In line 2 from bottom, delete "estimated".

Page 344 — Last line of paragraph 8.1, insert after "load", "and greater energy absorption capacity".

ABSTRACT

In this project the strength and behaviour of coupled shear walls subjected to seismic type of lateral load are examined.

The sensitivity of shear wall response to changes in relative stiffnesses of beams and walls, and the effects of cracking are studied. Using a finite difference approximation the application of laminar analysis is extended to coupled walls with variation in properties of beams and walls with height, different boundary conditions, different pattern of loading and two or more rows of openings.

Theoretical approaches are suggested for the estimation of strength and post-cracking stiffnesses of beams and walls. Using these approaches, with the aid of finite difference approximation of the laminar technique, the history of the shear wall's behaviour is followed by an incremental non-linear elasto-plastic analysis which exposes the ductility requirements of beam and wall hinges and reveals the sequence of their yielding.

Two quarter full size seven storey reinforced concrete coupled shear wall models, with differently reinforced coupling beams, have been tested under static reversed cyclic loading to simulate seismic effects. The experiments revealed that carefully designed and detailed shear walls can possess adequate ductility to give the desirable protection against catastrophic ground shaking. The shear wall model with diagonally reinforced beams exhibited superior stiffness, ductility and energy dissipation characteristics.

Finally, the significant findings of this investigation have been translated into design recommendations for coupled shear wall structures.

ACKNOWLEDGEMENTS

To Dr. T. Paulay I express my grateful thanks. Without his continual help, guidance and encouragement, this project would not have been possible.

I acknowledge with thanks the assistance received from Professor H.J. Hopkins, Head of the Department of Civil Engineering.

I am thankful to Mr. H.T. Watson, for his technical assistance, Mr. A. G. Foot for preparation of the mould, Mr. J.G.C. Van Dyk and Mr. G.P. Balantine for the help rendered during the preparation of the models and during testing, Mr. H. Patterson for his excellent photographic work, Mr. R.P. Hall for setting up the theodolites,and many others in the Department of Civil Engineering. My very special thanks go to Mr. J.N. Byers who not only made the elaborate testing frames but also took the responsibility of coordinating the various aspects of the experiment. The reliability of the results is largely due to his conscientious effort.

I am indebted to Mrs. A. Watt for her arduous task of typing the script.

My thanks are extended to the University Grants Committee for the Commonwealth Scholarship offered to me, and for providing financial assistance to build the test frames. The generosity of Certified Concrete Limited for donating the concrete is acknowledged.

I wish to thank my parents for their encouragement and understanding during this project. Finally, my deep gratitude goes to my wife, Vanaja, who not only traced numerous diagrams, but who has been so forebearing.

TABLE OF CONTENTS

REFERENCES

1. - "Recommended lateral force requirements and commentary", Seismologic Committee, Structural Engineers' Association of California (SEAOC) 1968
2. Veletsos, A.S., and Newmark, N.M., "Effect of inelastic behaviour on the response of simple systems to earthquake motions", Proceedings, Second World Conference on Earthquake Engineering, Tokyo, 1960, Vol. II, pp.895-912.
3. Penzien, J., "Elastic-plastic response of idealized multi-storey structures subjected to a strong motion earthquake", Proceedings, Second World Conference on Earthquake Engineering, Tokyo, 1960, Vol. II, pp.739-760.
4. Paulay, T., "Coupling beams of reinforced concrete shear walls", Proceedings, Structural Division, ASCE, Vol. 97, No. ST3, March 1971, pp.843-862.
5. Paulay, T., "Simulated seismic loading of spandrel beams", Proceedings, Structural Division, ASCE, Vol. 97, No. ST9, Sept. 1971, pp.2407-2419.
6. Binney, J.R., "Diagonally reinforced coupling beams", M.E. Report, University of Canterbury, Christchurch, New Zealand, Feb. 1972.
7. Paulay, T., "An elasto-plastic analysis of coupled shear walls", Proceedings, ACI Journal, Vol. 67, 1970, pp.915-922.
8. Chitty, L., "On the cantilever composed of a number of parallel beams interconnected by cross bars", The London, Edinburgh and Dublin Philosophical Magazine and Journal of Science, Vol. 38, Oct. 1947, pp. 685-699.
9. Beck, H., "Ein neues Berechnungsverfahren fuer gegliederte Scheiben, dargestellt am Beispiel der Vierendeeltraegers", Der Bauingenieur, Vol. 31, Heft 12, 1956, pp. 463-443.

10. Beck, H., "Ein Beitrag zur Berechnung regelmaessig gegliederter Scheiben", Ingenieur-Archiv, Vol. XXVI, 1958.

11. Rosman, R., "Beitrag zur statischen Berechnung waagrecht belasteter Querwaende bei Hochbauten", Der Bauingenieur, Part I, Vol. 35, Heft 4, 1960, pp. 133-136, Part II, Vol. 37, Heft 1, 1962, pp. 24-26, Part III, Vol. 37, Heft 8, pp. 303-308.

12. Beck, H., A discussion of Reference 11 Der Bauingenieur, Vol. 35, Heft 12, 1960, pp. 481-482.

13. Beck, H., "Contribution to the analysis of coupled shear walls", Proceedings, ACI Journal, Vol. 59, Aug. 1962, pp. 1055-1069.

14. Coull, A., and Choudhury, J.R., "Stresses and deflections in coupled shear walls", Proceedings, ACI Journal, Vol. 64, Feb. 1967, pp. 65-72.

15. Coull, A. and Choudhury, J.R., "Analysis of coupled shear walls", Proceedings, ACI Journal, Vol. 64, Sept. 1967, pp. 587-593.

16. Magnus, D., "Pierced shear walls", Concrete and Constructional Engineering, Vol. LX, Part I, No. 3, March 1965, pp. 89-98, Part II, No. 4, April 1965, pp. 127-137, Part III, No. 5, May 1965, pp. 177-185.

17. Ericksson, O. and Malmstrom, P.E., "Analysis of wind bracing walls in multistorey housing", Ingenioren - international edition, Vol. 5, 1961, pp. 115-124.

18. Rosman, R., "Approximate analysis of shear walls subject to lateral loads", Proceedings, ACI Journal, Vol. 61, June 1964, pp. 717-732.

19. Rosman, R., "An approximate method of analysis of walls of multistorey buildings", Civil Engineering and Public Works Review, Vol. 59, Jan. 1964, pp. 67-69.

20. Rosman, R., "Die statische Berechnung von Hochhauswaender mit Oeffnungsreihen", Bauingenieur Praxis, Heft 65, Wilhelm Ernst and Sohn, Berlin, 1965.

21. Rosman, R., "Zahlentafeln für die Schnittkrafte von Windscheiben mit Öffnungsreihen, Bauingenieur Praxis, Heft 66, Wilhelm Ernst and Sohn, Berlin, 1965.

22. Rosman, R., "Gegliederte Windscheiben mit Stufenartig Veränderlichen Querschnittswerten", Bauingenieur Praxis, Heft 67, Wilhelm Ernst and Sohn, Berlin 1967.

23. Coull, A. and Puri, R.D., "Analysis of coupled shear walls of variable thickness", Building Science, Vol. 2, Pergamon Press, 1967, pp. 181-188.

24. Traum, E.E., "Multistorey pierced shear walls of variable cross-section", Symposium on Tall Buildings with Particular Reference to Shear Wall Structures", University of Southampton, April 1966, Oxford, Pergamon Press, 1967, pp. 181-206.

25. Burns, R.J., "An approximate method of analysing coupled shear walls subject to triangular loading", Proceedings, Third World Conference on Earthquake Engineering, 1965, New Zealand, Vol. III, pp. IV-123-140.

26. Barnard, P.R. and Schwaighofer, J., "The interaction of shear walls connected solely through slabs", Symposium on tall buildings with particular reference to shear wall structures", University of Southampton, April 1966, Oxford, Pergamon Press, 1967, pp. 157-173.

27. Batchelor, W.G., "Solution of shear wall problems using the Galerkin form of the Ritz process", Cement and Concrete Association Report No. DC 36/66, London, 1966.

28. Soane, A.J.M., "The analysis of interconnected shear walls by Analogue Computation", Symposium on tall buildings with particular reference to shear wall structures, University of Southampton, April 1966, Oxford, Pergamon Press, 1967, pp.207-222.

29. Coull, A. and Puri, R.D., "Analysis of pierced shear walls", Proceedings, Structural Division, ASCE, Vol. 94, No. ST1, Jan. 1968, pp. 71-82.

30. Rosman, R., "Pierced shear walls subject to gravity loads", Concrete, Vol. 2, June 1968, pp. 252-258.

31. Schwaighofer, J., "Door openings in shear walls", Proceedings, ACI Journal, Vol. 64, Nov. 1967, pp. 730-734.

32. Schultz, M., "Analysis of reinforced concrete walls with openings", The Indian Concrete Journal, Vol. 35, Nov. 1961, pp. 432-433.

33. Michael, D., "Coupled plane shear walls of tapered thickness", Proceedings, Institution of Civil Engineers, London, Vol. 40, Aug. 1968, pp. 511-518.

34. Thadani, B.N., "Analysis of shear wall structures", The Indian Concrete Journal, Vol. 40, March 1966, pp. 97-102.

35. Naumann, W. and Walter, H., "Bericht zur Statischen Berechnung Waagrecht Belasteter Querwande bei Hachbauten", Der Bauingenieur, Vol. 36, Heft 8, 1961, pp. 311-313.

36. Zbirohowski-Koscia, K., "Estimated wind stresses in cross walls with large openings", Civil Engineering and Public Works Review, Vol. 53, Part I, June 1958, pp. 675-678, Part II, July 1958, pp. 795-797.

37. Jordaan, I.J. and Loov, R.E., "Coupled walls subjected to discontinuous distributed loads", Proceedings, Structural Division, ASCE, Vol. 98, No. ST7, July 1972, pp. 1675-1680.

38. Tso, W.K. and Chan, H.B., "Dynamic analysis of plane coupled shear walls", Proceedings, Engineering Mechanics Division, ASCE, Vol. 97, No. EM1, Feb. 1971, pp. 33-48.

39. Coull, A., "Stiffening of coupled shear walls against foundation movement", The Structural Engineer, The Journal of the Institution of Structural Engineers, Vol. 52, No. 1, Jan. 1974, pp. 23-26.

40. Rosman, R., "Analysis of symmetric shear wall structures", Response of multistorey concrete structures to lateral forces, ACI publication, SP-36, Paper SP36-11, 1973, pp. 225-240.

41. Coull, A., "Distribution of shear forcein coupled shear wall structures", Response of multistorey concrete structures to lateral forces", ACI Publication SP-36, Paper SP36-10, 1973, pp. 217-224.

42. MacLeod, I.A., "Shear wall-frame interaction - A design aid with commentary", Special Publication, Portland Cement Association, April 1971, pp. 31-43.

43. Tso, W.K. and Chan, P.C., "Flexible foundation effect on coupled shear walls", Proceedings, ACI Journal, Vol. 69, Nov. 1972, pp. 678-683.

44. Cardan, B., "Concrete shear walls combined with rigid frames in multistorey buildings", Proceedings, ACI Journal, Vol. 58, Sept. 1961, pp. 299-316.

45. Michael, D., "The effect of local wall deformations on the elastic interaction of cross walls coupled by beams", Symposium on tall buildings with particular reference to shear wall structures, University of Southampton, April 1966, Oxford, Pergamon Press, 1967, pp. 253-272.

46. Smith, B.S., "Modified beam method for analysis of symmetrical interconnected shear walls", Proceedings ACI Journal, Vol. 67, Dec. 1970, pp. 977-980.

47. Kratky, R.J. and Puri, S.P.S., A discussion of reference 46, Proceedings, ACI Journal, Vol. 68, June 1971, p.472.

48. Schwaighofer, J. and Microys, H.F., "Analysis of shear walls using standard computer programmes", Proceedings, ACI Journal, Vol. 66, Dec. 1969, pp. 1005-1007.

49. Qadeer, A. and Smith, B.S., "The bending stiffness of slabs connecting shear walls", Proceedings, ACI Journal, Vol. 66, June 1969, pp. 464-473.

50. Hrennikoff, A.P., "Solutions of problems of elasticity by frame-work method", Journal of Applied Mechanics, Vol. 8, A146, 1941.

51. McHenry, D., "A lattice analogy for the solution of plane stress

51. McHenry, D., "A lattice analogy for the solution of plane stress problem", Journal of the Institution of Civil Engineers, London, Vol. 21, No. 2, 1943-44.

52. McCormic, C.W., "Plane stress analysis", Proceedings, Structural Division, ASCE, Vol. 89, No. ST4, Aug. 1963, pp. 37-54.

53. Grinter, L.E., "Statistical state of stress by grid analysis", Numerical Method of Analysis in Engineering, The MacMillan Company, 1949.

54. Alwood, R., "Triangles versus quadrilaterals", Proceedings of International Conference on the use of computers in Structural Engineering, University of Newcastle upon Tyne, England, 1966.

55. Tocher, J.L. and Hartz, B.J.,"Higher orderfinite element for plane stress", Proceedings, Engineering Mechanics Division, ASCE, Vol. 93, No. EM4, Aug. 1967, pp. 149-171.

56. MacLeod, I.A., "New rectangular finite element for shear wall analysis", Proceedings, Structural Division, ASCE, Vol. 95, No. ST3, March 1969, pp. 349-410.

57. Cerny, L., "Column-supported shear walls with openings", Proceedings of the International Conference on Planning and Design of Tall Buildings , Lehigh University, Bethlehem, Vol. 5, 1972, pp. 633-640.

58. Weaver, W., and Oakberg, R.G., "Analysis of frames with shear walls by finite-element methods", Proceedings of the Symposium on Application of Finite Element Methods in Civil Engineering, Vanderbilt University, Nashville, Tennessee, Nov. 1969, pp.567-600.

59. Girijavallabhan, C.V., "Analysis of shear walls by finite element method", Proceedings of the Symposium on Application of Finite Element Methods in Civil Engineering, Vanderbilt University, Nashville, Tennessee, Nov. 1969, pp. 631-641.

60. Zienkiewicz, O. and Cheung, Y.K., "The finite element method in structural and continuum mechanics", McGraw-Hill Book Company, London, 1967.

61. Winokur, A. and Gluck, J., "Ultimate strength anaylsis of coupled shear walls", Proceedings, ACI Journal, Vol. 65, Dec. 1968, pp. 1029-1036.

62. Gluck, J., "Elasto-plastic analysis of coupled shear walls", Proceedings, Structural Division, ASCE, Vol. 99, No. ST8, Aug. 1973, pp. 1743-1760.

63. Gormack, P.J., "Non-linear finite element analysis of shear walls and two dimensional reinforced concrete structures", M.E. Report, University of Canterbury, Christchurch, New Zealand, Feb. 1974, pp. 80-92.

64. Branzan, I., "Berechnung von Stahlbetonscheiben mit einer Öffnungsreihe in plastischen Bereich", Die Bautechnik, Vol. 46, Dec. 1969, pp. 415-418.

65. Beekhuis, W.J., "An experimental study of squat shear walls", M.E. Report, University of Canterbury, Christchurch, New Zealand, Feb. 1971, 132pp.

66. Paparoni, M., and Holoma, S., "A model study of coupling beams for the Parque Central Buildings - Caracus, Venezuela", Caracus, April 1971 (Private communication).

67 - "Estudos Estructurais Dos Edificios de Parque Central", Laboratorio Nacional de Engenharia Civil, Ensaios Sismicos de Paredes Transversais, Lisboa, Jan. 1971 (Private communication).

68. Luisoni, C.J., Somenson, H.M., and Ungaro, M.A., "Verification Experimental de un Calculo Plastico y otro Elastico de una pared de corte", XIV Jornadas Sudamericanas de Ingenieria Estructural y IV Simpsio Panamericano de Estructuras, Buenos Aires, Argentina, Oct. 1970, Vol. 5, pp. 230-286.

69. Tomii, M., "State of the art report No. 4 - Shear wall", Proceedings of the International Conference on Planning and Design of Tall Buildings, Lehigh University, Bethlehem. Vol. 3, 1972, pp. 57-75.

70. Tomii, M. and Takeuchi, M., "The relationship between the deformed angle and the shearing force ratio (0.80 ~ 1.00) with regard to 200 shear walls", Transactions of the Architectural Institute of Japan, No. 153, Nov. 1968. (In Japanese).

71. Tomii, M., and Miyata, S., "Study on shearing resistance of quake resisting walls having various openings", Transactions of the Architectural Institute of Japan, Part I and II, No. 66, Oct. 1960, Part III, No. 67, Feb. 1961, Part IV, No. 68, June 1961. (In Japanese).

72. Ban, S., "Experimental study on the seismic resistance of walls with opening", Transactions of the Architectural Institute of Japan, No. 30, Sept. 1943. (In Japanese).

73. Hisatoku, T. and Matano, H., "Aseismic analysis of the tall building structure with coupled shear wall", Proceedings of the Fifth World Conference on Earthquake Engineering, Rome, 1973, Session 5D:Earthquake-Resistant Design - Paper 251.

74. Paulay, T., "The coupling of shear walls", Ph.D. Thesis, University of Canterbury, Christchurch, New Zealand, 1969, 222pp.

75. - New Zealand standard model building by-law, Basic design loads", NZSS 1900 Chapter 8, 1965, New Zealand Standards Institute, Wellington, New Zealand, 39pp.

76. Park, R. and Paulay, T., "Ultimate strength design of reinforced concrete structures", Chapter 12, University of Canterbury, Christchurch, New Zealand, 1969, pp.284-285.

77. Paulay, T., "Reinforced concrete shear walls", New Zealand engineering, Vol. 24, No. 10, Oct. 1969, pp.315-321.

78. MacLeod, I.A., "Lateral stiffness of shear walls with openings", Symposium on Tall Buildings With Particular Reference to Shear Wall Structures, University of Southampton, April, 1966, Oxford, Pergamon Press, 1967, pp.223-252.

79. "Response of buildings to lateral forces", ACI Committee 442, ACI Journal, Vol. 68, No. 2, Feb. 1971, pp.81-106.

80. Gere, J.M., "Moment distribution", University Series in Civil Engineering and Applied Mechanics, D. Van Nostrand Company, Chapter 6, Section 6.6, pp.229-244.

81. Bhatt, P., "Effect of beam-shear wall junction deformations on flexibility of the connecting beams", Building Science, Vol. 8, 1973, pp.149-151.

82. ACI Standard 318-71, Building Code Requirements for Reinforced Concrete (ACI 318-71), American Concrete Institute, Detroit, 78pp.

83. Branson, D.E., "Design procedures for computing deflections", Proceedings ACI Journal, Vol. 65, No. 9, Sept. 1968, pp.730-742.

84. Umemura, H. and Aoyama, H., "Evaluation of inelastic seismic deflections of reinforced concrete frames based on the tests of members", Proceedings, Fourth World Conference on Earthquake Engineering, Santiago, Chile, Vol. 1, B.2, pp.92-107.

85. Kordina, K., A discussion on "Cracking and crack control", International Conference on Planning and Design of Tall Buildings, ASCE-IABSE International Conference Preprints Vol. D.S. Aug. 1972, pp.748-749.

86. Ishidahoman, J.I., "Elasto-plastic behaviour of reinforced concrete coupled shear walls", M.E. Report, University of Canterbury, Christchurch, New Zealand, Feb. 1971, 115pp.

87. Hognestad, E., Hanson, N.W. and McHenry, D., "Concrete stress distribution in ultimate strength design", Proceedings, ACI Journal, Vol. 27, No. 4, Dec. 1955.

88. "Effects of steel strength and reinforcement ratio on the mode of failure of reinforced concrete beams", ACI Committee 439, ACI Journal, Vol. 66, No. 3, March 1969.

89. Blume, J.A. Newmark, N.M. and Corning, L.H., "Design of multistorey reinforced concrete buildings for earthquake motions", Portland Cement Association, Chicago, 1961, 318pp.

90. Baker, A.L.L. and Amarakone, A.M.N., "Inelastic frame analysis", Proceedings of the International Symposium on Flexural Mechanics of Reinforced Concrete, ASCE-ACI, Miami, Nov. 1964.

91. Baker, A.L.L., "Ultimate load theory applied to the design of reinforced and prestressed concrete frames", Concrete publication, London, 1956.

92. Soliman, M.T.M. and Yu, C.W., "The flexural stress strain relationship of concrete confined by rectangular transverse reinforcement", Magazine of Concrete Research, No. 61, Dec. 1967.

93. MacGregor, J.G., "Stability of reinforced concrete building frames", International Conference on Planning and Design of Tall Buildings, ASCE-IABSE International Conference Preprints Vol. III-23, Aug. 1972, pp.19-35.

94. Steinbrugge, K.V. and Flores, R.A., "The Chilean earthquake of May 1960. A structural engineering viewpoint", Bulletin of the Seismological Society of America, Vol. 53, No. 2, Feb. 1963, pp.225-307.

95. Berg, V.B. and Stratta, J.L., "Anchorage and the Alaska earthquake of March 27, 1964", American Iron and Steel Institute, New York, 1964.

96. Bertero, V.V., "Ductility and seismic response", Discussion - International Conference on Planning and Design of Tall Buildings, Preprints, Vol. DS, Section TC6, Earthquake Loading and Response Criteria - D6, pp.271-277.

NOTATIONS

Areas and their Properties

A	area of cross section
A_h	area of the horizontal reinforcement
A_s	area of the flexural steel in one face of a beam or area of the steel in one diagonal of a diagonally reinforced coupling beam
A_v	area of one stirrup
A_1, A_2, A_3	areas of wall 1 , wall 2 , wall 3
I	moment of inertia
I_b	moment of inertia of coupling beams
I_{eff}	effective moment of inertia with allowance for cracking
I_F	moment of inertia of a fictitious shear wall without flanges
I_g	gross moment of inertia
I_o	sum of moment of inertia of the walls of coupled shear walls
I_t	moment of inertia of cracked transformed section
I_x	reduced moment of inertia of coupling beam allowing for flexural shear and flexible joint deformations

Bending Moments

M_{cr}	the cracking moment
M_{d1}, M_{d2}	reliable moment capacities of walls
M_o	total external cantilever moment
M_{o1} , M_{o2}	overstrength moment capacities of walls
M_p	moments generated by the separation forces
M_{p1} , M_{p2}	probable moment capacities of walls
M_u	ultimate moment
M_{u1} , M_{u2}	ideal ultimate moment capacities for wall 1 and wall 2 respectively taking axial load into account

M_{10} , M_{20} moments induced by external load only in walls 1 and 2

M_1 , M_2 , M_3 bending moments in wall 1, wall 2 and wall 3

Displacements

d_a differential displacement of coupled shear walls owing to axial forces

Δ deflection at the centre loading pin of the model

Δ_A end deflection of the model

Δ_E deflection associated with beam elongation

Δew top floor deflection because of elastic wall curvatures

Δ_F deflection associated with flexural action in conventional beams

Δfb deflection due to yielding of flexural steel at anchorages

ΔH elongation of coupling beams

Δpw top floor deflection because of plastic rotation at base

Δ_s top floor deflection of shear wall

Δ_V relative vertical deflection of the ends of coupling beam associated with truss action in conventional beams

Δ_1 diagonal elongation along the tension chord of diagonally reinforced coupling beams

Δ_2 diagonal contraction along compression chord of diagonally reinforced coupling beams

y lateral deflection of shear wall

Energy

E_A actual energy absorbed in structure

E_{Aw} energy absorbed in the wall flexural steel

E_{Ab} energy absorbed by beam diagonal steel

E_o theoretical energy absorbed assuming bilinear load-deformation relationship

Forces

C	force in compression diagonal
C_u	ultimate force in compression diagonal of diagonally reinforced beam
P	point load at top of shear wall
P_u	ultimate shear across coupling beams or ultimate axial forces in tension or compression wall
P_u^*	theoretical ultimate load on models
$p(x)$, $p(\xi)$	laminar separation forces
P_1, P_2, P_3	static loads on shear wall model
Q_b	shear force in a coupling beam
q_n	laminar shear force at node n
$q(x)$, $q(\xi)$	laminar shear force
q_u	ultimate laminar shear
R	base reaction
T	axial force at any level of a wall or force in the tension chord of the diagonally reinforced beam
T_A , T_B	total force generated in shear wall with two rows of openings due to accumulation of laminar shear in span A and span B
T_n	axial force generated in shear walls at node n
T_t	tension force in top flexural bar of conventionally reinforced beam
T_u	ultimate force in tension diagonal in diagonally reinforced beam or ultimate axial force at base of the walls
V	applied shear
V_b	base shear for shear wall
V_c	shear resisted by concrete
V_p	base shear force for prototype shear wall
V_s	shear resisted by stirrups
V_u	ultimate shear force
V_{up}	ultimate shear force for the prototype wall
V_p^*	theoretical ultimate load on prototype shear wall

V_1 , V_2	base shear forces for wall 1 and wall 2
W	total triangular load on structure
W_1	total uniformly distributed load on structure
W_1 , W_2	prestressing forces simulating dead load
W_d	dead load on coupled shear wall structure
W_m	weight of model

Linear Dimensions

b	width of a rectangular beam
c	depth of neutral axis from compression face
d	effective depth of a beam
D_a	average depth of compression strut in coupling beam
D_A , D_B	overall depths of beams of shear wall with two rows of openings
d'	cover to centroid of reinforcement
H	total height of shear wall structure
h	floor height
h_o	distance between nodal points in finite difference approximation
l_A , l_B	distances between centroidal axes of walls of a coupled shear wall with two rows of openings
L_{pc} , L_{pt}	lengths of plastic hinges for compression and tension walls respectively.
l_s	clear span of coupling beam
l_{SA} , l_{SB}	distance between the inner faces of walls of a coupled shear wall with two rows of openings
l_1 , l_2	distance from axis of coupled shear wall structure to centroidal axis of wall 1 and wall 2 respectively
l_{1A} , l_{2A}	distances of wall centroidal axes from the centre line of coupling system in span A
l_{1B} , l_{2B}	distances of wall centroidal axes from the centre line of coupling system in span B
l'	length of diagonal steel between ends of a diagonally reinforced beam
l'_d	development length of flexural steel in anchorages
s	stirrup spacing
p	pitch of square spiral

Parameters, Factors and Coefficients

C	geometric factor used in laminar analysis
e	strain limit
h_e	damping constant
J_a	modulus of flexibility of a joint
F_r	rotational flexibility of foundation
F_s	vertical displacement flexibility of foundation
K_F	stiffness of a fictitious shear wall with infinitely rigid coupling beams
K_S	stiffness of shear wall model
$K_{\theta 1}$, $K_{\theta 2}$	rotational stiffness of foundation under wall 1 and wall 2 respectively
K_θ	$= K_{\theta 1} + K_{\theta 2}$
$K_{\delta 1}$, $K_{\delta 2}$	vertical displacement stiffness of foundation under wall 1 and wall 2 respectively
K_δ	equivalent vertical displacement stiffness of the foundation
α	geometric parameter used in laminar analysis
α_y	reduction factor to account for loss of flexural rigidity due to cracking in coupling beams
β	a geometric parameter
ρ_{max}	maximum permissible steel content
ρ''	ratio of volume of binding steel to volume of concrete bound
ρ^*	equivalent steel content in one diagonal of a diagonally reinforced beam
ξ	distance factor (x/H)
ν	Poisson's ratio or ratio of beam span to the length of stirrups
ν_1	ratio of beam length to internal lever arm
η	ratio of steel force carried by web reinforcement to load on coupling beam
ϵ	strain at a point
ϵ_I	moment of inertia ratio I_o/I_F

ϵ_K	stiffness ratio K_S/K_F
ϵ_q	laminar shear factor
ϵ_T	axial force factor
ϵ_Δ	top floor deflection factor
φ	capacity reduction factor
φ_y	yield curvature
φ_{yc} , φ_{yt}	yield curvature at base of compression and tension walls respectively
μ	ductility
μ_b	beam ductility
μ_s	section ductility
μ_o	the overall displacement ductility
μ_w	wall ductility

Rotations

θ	rotation of base reference line
θ_a	rotation owing to arch action in coupling beams
θ_b	rotation of coupling beam or total laminar rotation
θ_{bp}	plastic rotation of beam
θ_{by}	elastic limit rotation of beam
θ_C	rotation owing to contraction of compression chord in diagonally reinforced beams
θ_F	rotation owing to flexural action in conventional beams
θ_E	rotations owing to deformation of steel in anchorages
θ_l	beam rotation owing to elongation of flexural reinforcement
θ_m	flexural rotation of coupling beam
θ_{pc} , θ_{pt}	plastic rotation at base of compression and tension walls respectively
θ_T	rotation owing to elongation of tension chord in diagonally reinforced beams

θ_{uc} , θ_{ut}	ultimate rotations at base of compression and tension walls respectively.
θ_{V}	rotation owing to truss action in coupling beams
θ_{W}	rotation of a wall
θ_{wp}	plastic rotation of wall
θ_{wy}	elastic limit wall rotation
θ_{wyc}	compression wall yield rotation
θ_{z}	rotation of wall at the node z
θ_{wyt}	tension wall yield rotation

Stresses

E	Young's modulus
E_b	Young's modulus of the coupling beam
E_w	Young's modulus of the wall
f_c	concrete compression stress
f'_c	cylinder strength of concrete
f'_{cu}	cube strength of concrete
f_u	ultimate strength of steel
f_y	yield strength of steel
f_{ym}	yield strength of flexural steel in conventionally reinforced beams
f_{yst}	yield strength of stirrup steel
G	shear modulus of the coupling beam

CHAPTER ONE

INTRODUCTION

1.1 SHEAR WALL STRUCTURES

In high rise buildings, shear walls provide the required rigidity for lateral loads resulting from wind and earthquake effects. Walls designed for earthquakes should satisfy the requirements of ductility, energy absorption, damping characteristics and damage control in addition to the primary requisites of strength and stiffness. Windows, doors and service ducts require that these shear walls are pierced by a number of openings. In regular coupled shear walls these openings are in a vertical row. The coupling consists of a number of spandrel beams which connect the walls. Though coupled shear walls have been accepted to provide the required rigidity to minimize non-structural damage during moderate seismic disturbances, there has been a certain amount of distrust[1] with respect to their ductility and energy absorption properties. Only in exceptional cases will it be possible to resist the earthquake generated inertia forces within the elastic range of behaviour. In the case of catastrophic earthquakes, it is generally accepted that energy dissipation, involving considerable excursions into the post-elastic range, will have to be relied upon.

The response of coupled shear walls in the elastic range has been predicted by various methods. Many of these methods are applicable for regular structures with uniform member properties. As coupled shear walls are expected to perform satisfactorily also during large earthquakes, methods which account for the inelastic actions are necessary to assess post-elastic behaviour. Previous studies which examined the behaviour of coupled shear walls in the elastic and elasto-plastic range are reported in Section 1.3.

1.2 CRITICAL ASPECTS OF COUPLED SHEAR WALL BEHAVIOUR

There are three areas in two coupled shear walls in which critical conditions may arise during a strong seismic disturbance. These areas are shown in Fig. 1.1.

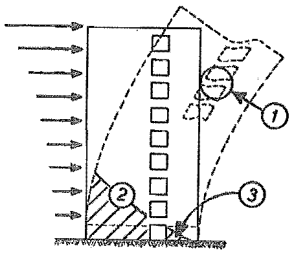

(1) Coupling beams.

(2) Tension wall.

(3) Compression wall.

FIG. 1.1 TYPICAL LATERALLY LOADED COUPLED SHEAR WALLS

1.2.1 Coupling Beams (Area (1))

The damage suffered by the coupling beams during known earthquakes[2,3] and the experiments carried out by Paulay[4] show that these beams, conventionally designed for shear and flexure with stirrups and horizontal flexural reinforcement respectively, cannot sustain the flexural yield load when subjected to high intensity cyclic loading. These experiments revealed that shear deformation greatly overshadowed flexural ones. Even when the stirrup reinforcement provided was in excess of that required for the maximum possible shear force, which would develop when the flexural steel yields, it has been found that after a few cycles, causing alternate yielding in the top and bottom flexural reinforcement, the beam may fail in sliding shear. When the flexural steel yields at the face of the wall nearly the whole of the shear force is transferred across the concrete in the compression zone. However, this concrete has cracked during previous loading cycles and its frictional shear resistance diminishes rapidly as a result of repeated opening and closing of the cracks. This shows that even a drastic increase of

stirrup steel cannot improve the behaviour as sliding shear may occur between the two adjacent stirrups. Such a sliding shear failure in coupling beams cannot be considered as a satisfactory mode of failure for the purposes of seismic resistance. Moreover, sliding shear means a considerable loss of strength.

The concern for the inadequate ductility of coupling beams led to the investigation of a different arrangement of reinforcement. Paulay[5] developed the concept of diagonally reinforced beams. It was observed[6] that with careful arrangement and detailing of reinforcement, greatly increased ductility could be attained in these beams. Theoretical studies[7] indicated that the ductilities attained experimentally for the diagonally reinforced beams are adequate when compared with the ductilities imposed on a shear wall during severe seismic disturbances.

1.2.2 Tension Wall (Area (2))

The shear strength of one of the walls may be seriously affected by axial tension generated by the earthquake induced overturning moments. It is important to realise that under these conditions, the contribution of the concrete to shear strength becomes negligible.

1.2.3 Compression Wall (Area (3))

The axial compression generated by the earthquake induced forces and by gravity load on the structure may limit the ductility attainable in the compression wall. Apart from this, construction joints in shear walls (shown with broken lines in Fig. 1.1) may become the weakest link in the chain of resistance.

1.3 PREVIOUS INVESTIGATIONS

This survey is limited to investigations related to the behaviour of reinforced concrete coupled shear walls subjected to static loading and is divided into the following three parts:

(1) Elastic analyses.

(2) Elasto-plastic analyses.

(3) Experimental investigations.

1.3.1 Elastic Analyses

The following three approaches have been used in the analyses of coupled shear walls:

(a) Laminar analysis.

(b) Frame analysis.

(c) Finite element analysis.

(a) Laminar analysis: This approach, by which the statically indeterminate problem of coupled shear walls is reduced to a relatively simple analysis, originates from Chitty[8]. Beck, in his first publication[9] deals with wall panels containing one or more rows of openings. The Vierendeel girder is one example in which he replaced the individual columns by an equivalent laminar system, similar to that used by Chitty[8]. In 1959, Beck[10] extended his laminar analysis of Vierendeel girders so as to allow for significant axial deformations in coupled shear walls and the shear deformation of the deep coupling beams in symmetrical structures. In 1960 appeared the first publication[11] of Rosman. Making use of the laminar system and strain energy considerations, he established the fundamental Eulerian differential equation of the problem. He chose the solution in terms of the axial force in the walls and expressed this by trignometric series. In this approach he neither allowed for shear deformation nor considered the separation forces exerted by the spandrel beams. In a discussion of Rosman's paper, Beck[12] pointed out the similarity to his mathematical model with that used by Rosman and proposed the complete solution by giving expressions for the laminar separation forces and the singular separation force at the topmost lamina.

Since then, in a number of published papers, the method has been further developed. (See references 13 to 43). The problems

considered in these publications are: the number of rows of openings, different types of loading, different foundation conditions and certain variation in properties with height. A list of the investigations which may be considered to have application in the design of the coupled shear wall has been tabulated by MacLeod[42]. This table shows the different aspects considered by these studies.

(b) Frame analysis: Cardan[44] rightly suggested that a general matrix analysis, which allows for all the significant deformations in a coupled shear wall structure, can be programmed for a computer. It has been pointed out by MacLeod[42] that the plane frame programme when used to solve coupled shear walls should consider the effect of finite joints. The effect of flexibility of the joint between the beam and the wall has been investigated by Michael[45]. Smith[46], Kratky and Puri[47], Schwaighofer and Microys[48] and Qadeer and Smith[49] suggest various methods by which a standard computer programme for the analysis of a frame could be modified and used also for coupled shear walls.

(c) Finite Element analysis: Both finite and frame-work elements have been used in the elastic analysis of coupled shear walls. Frame-work elements are line elements loaded axially and in bending, whereas finite elements are two dimensional which connect more than two nodes. Hrennikoff[50], McHenry[51], McCormick[52] and Grinter[53] have used different types of frame-work elements in their analyses. Different shapes of finite elements have been used by Alwood[54], Tocher and Hartz[55], MacLeod[56], Cerny[57], Weaver and Oakberg[58] and Girijavallabhan[59]. The method is now well established and documented[60].

1.3.2 Elasto-Plastic Analysis

In 1968 Winokur and Gluck[61] proposed a design method based on a collapse mechanism and suggested procedures by which simplicity in the analysis and economy in reinforcement may be achieved. Paulay[7] used the laminar analysis to assess the post-cracking "elastic" behaviour of coupled shear walls and suggested a step by step procedure for evaluating

the post-elastic performance of the structure. In his recent work, Gluck[62] has proposed a solution for the overall ductility of the shear wall when plastic hinges develop at the ends of the beams only over part of the height. For this case, charts for the determination of overall ductility factor, and the associated rotational ductility of the coupling beams, have been presented. Gormack[63] investigated the behaviour of the coupled shear wall by using a non linear iterative elasto plastic finite element analysis.

1.3.3 Experimental Investigations

A number of elastic model studies compare the results of the elastic analysis with model behaviour. The results of these investigations have limited application in predicting the behaviour of reinforced concrete coupled shear walls and hence these are not reported here.

The first known experiment with a large scale reinforced concrete coupled shear wall model was reported from Rumania[64]. These models were studied under monotonic loading. Apart from the experimental investigations of Paulay[4,5], Binney[6] and Beekhuis[65], reinforced concrete model studies of coupling beams using certain unconventional types of reinforcement have been undertaken by Paparoni[66] et al. Reinforced concrete model studies of the Parque Central Building[67] reveal that the behaviour of connecting beams is not completely independent from the whole shear wall behaviour. Luisoni et al[68] show that good agreement is obtained with experimental evidence when simple theoretical assumptions are made in the analysis, incorporating elasto-plastic criteria. In a state of the art report, during the international conference on planning and design of tall buildings held at Lehigh University, Bethlehem, Tomii[69] has summarised the findings of a number of Japanese investigations[70,71,72] on shear walls with openings. The results of these investigations have been used[69] to arrive at empirical coefficients for the prediction of the behaviour of shear walls with various sizes of openings. Recently Hisatoku and Matano[73] have investigated the behaviour of a 1/20 scale model of an 18-storey coupled shear wall

structure. The model was made of reinforced mortar. The test result agreed with the behaviour of the model predicted by a finite-element analysis.

1.4 THE SCOPE OF THIS PROJECT

The behaviour of tall rectangular cantilever shear walls and those of the coupling beams indicate that with careful arrangement and detailing of reinforcement large ductilities could be achieved. The primary aim of this project was to examine the ductile behaviour of reinforced concrete coupled shear walls when the coupling beams and the walls are designed and detailed accordingly.

Based on the elastic analysis, the sensitivity of shear wall response to changes in relative stiffness of the coupling beams and walls and to the effects of cracking are studied. Using a finite difference approximation the application of the laminar analysis is extended to coupled shear walls with variation in properties of beams and walls with height, different boundary conditions, different pattern of external lateral load and two or more rows of openings.

The strength and stiffness properties of the coupling beams and coupled walls are assessed based on theoretical considerations. The elastic and elasto-plastic responses of the critical sections of the tension and compression walls to static loading are determined, using the load-moment-curvature relationships.

The load-moment-curvature relationship and the finite difference approximation of the laminar technique are used in a non-linear elasto-plastic analysis, in which the history of the shear wall's behaviour is followed, through stages of incremental loading, till the ultimate load is reached and the desired overall ductility is attained. This analysis exposes the ductility demand of the coupling beams and the critical wall sections during their various stages of plastification.

In two quarter full size seven storey reinforced concrete coupled shear wall models the various effects of differently reinforced coupling beams upon the overall behaviour were studied. The models were tested by subjecting them to static cyclic reversed loading, to simulate earthquake effects. The results of these tests are presented. Wherever applicable the results, obtained during the experiment, are compared with those predicted by the theoretical study mentioned in the preceding paragraph.

These tests have shown that carefully designed and detailed coupled shear walls can possess all the qualities required to give the highest degree of protection against nonstructural damage during moderate earthquakes while assuring survival in the case of catastrophic seismic disturbances on account of their ductility.

Finally, the most important findings are translated into design recommendations for coupled shear walls.

CHAPTER TWO

THE ELASTIC ANALYSIS OF COUPLED SHEAR WALLS

2.1 INTRODUCTION

A brief review of elastic laminar analysis as applied to shear walls is presented. Based on this analysis, the sensitivity of the shear wall's response to changes in the relative stiffnesses of the coupling beams and the walls are examined. The influence of cracking upon the static quantities is studied, based on an approximate analysis, which allows for a reduction of the stiffnesses of the cracked components.

The use of finite element analysis and the frame analysis, as applied to the solution of the coupled shear walls, are discussed.

The laminar analysis is modified to handle specified variations of the properties of the beams and walls, by a finite difference approximation. This analysis is then extended to shear walls with two or more rows of openings. Numerical examples demonstrate the application of the proposed analyses.

2.2 THE LAMINAR ANALYSIS

The coupled shear wall, to be considered here, consists of the two walls connected by the coupling beams at each floor level as indicated in Fig. 2.1.a. For the purpose of analysis the beams are replaced by a set of infinitisimal elastic laminae. This replacement enables the statically highly indeterminate problem to be reduced to the solution of a single, second order, ordinary differential equation. The mathematical model, depicted in Fig. 2.1.b. simulates well the real structure when the number of storeys is large.

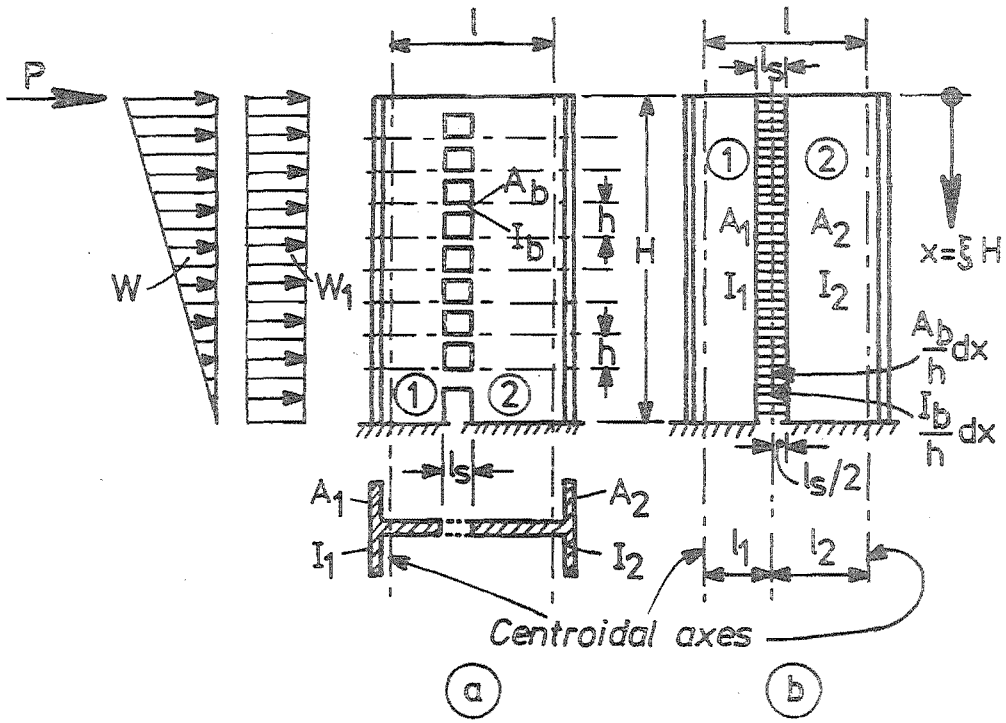

FIG. 2.1 A PROTOTYPE COUPLED SHEAR WALL STRUCTURE AND ITS MATHEMATICAL MODEL

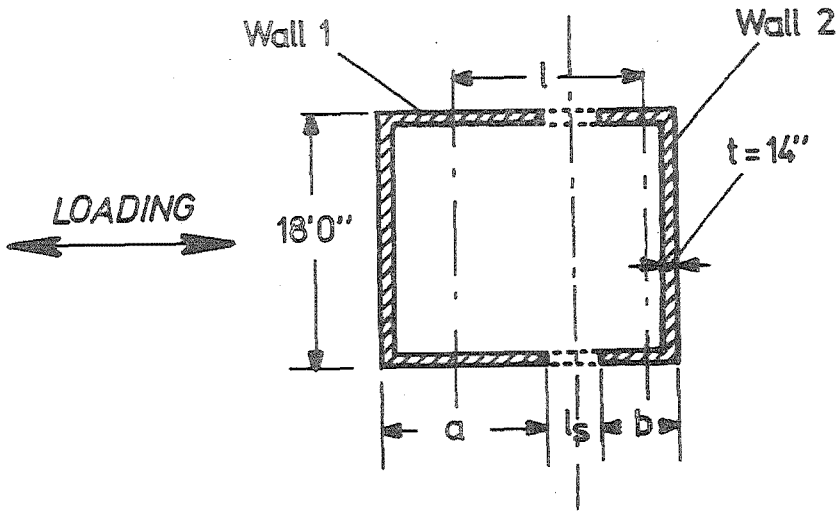

FIG. 2.2 SHEAR WALL DIMENSIONS

2.2.1 Assumptions

In addition to homogeneity, isotropy and linear elasticity, the following assumptions are made:

(a) The floor heights are uniform so that the coupling beams are equally spaced.

(b) The coupling beams are of the same size, with the exception of the top-most beam, the stiffness of which is one half of that of the others.

(c) The properties of the walls do not vary with the height.

(d) The axial deformation of the beams and the shear deformation of the walls are neglected.

(e) The stiffness of the walls is very large compared to that of the coupling beams. Thus, the slopes of these walls are locally unaffected by the discrete beams. Consequently, at any level, the slopes and deflections of the two walls are the same. This implies that each coupling beam has a point of contraflexure at its mid-span.

(f) The external load can be expressed as a continuous function of the distance measured from the top of the structure.

2.2.2 The Differential Equation

In order to set up the basic equation of the problem the coupled shear wall structure is cut along the centres of the connecting laminae (see Fig. 2.1.b). The displacements at the cut end of the lamina due to actions on the walls, and due to the laminar shear force, are expressed and combined. Based on the conditions of equilibrium and compatibility, the following relationship between the external moment, M_o, axial force in the wall, T_x, and the laminar shear force, q_x, at any level is abtained [74].

$$\frac{1}{EI_o}\int_x^H M_o dx - \frac{l^2}{EI_o}\int_x^H T_x\,dx - \frac{1}{E}\left(\frac{1}{A_1}+\frac{1}{A_2}\right)\int_x^H T_x dx - \frac{hl_s^3}{12EI_x}q_x = 0 \qquad \ldots (2.1)$$

where $I_x = \dfrac{I_b}{1 + \dfrac{12EI_b f}{GA_b l_s^2}}$, ... (2.1a)

the reduced moment of inertia of the coupling beam to allow for the shear deformation

A_b = area of the beam

I_b = moment of inertia of the beam

f = form factor to account for the non-uniformity of shear stress distribution

G = the modulus of rigidity

I_o , A_1 , A_2, l , l_s are the geometrical properties of the shear wall as defined in Fig. 2.1.

Combining the common terms and differentiating these with respect to x , the differential equation of axial force in the walls is obtained[74].

$$\frac{d^2T_x}{dx^2} - \alpha^2 T_x = - \gamma M_o \qquad \text{... (2.2)}$$

where T_x is the axial force in the wall at x

and $$\alpha^2 = \left(\frac{1}{A_1} + \frac{1}{A_2} + \frac{l^2}{I_o}\right) \left(\frac{12\ I_x}{hl_s^3}\right) \qquad \text{... (2.3)}$$

and $$\gamma = \frac{12l\ I_x}{I_o h l_s^3} \qquad \text{... (2.4)}$$

The solution for the differential equation yields the axial force, T_x thus

$$T_x = A \sinh\alpha x + B \cosh\alpha x + T_{px} \qquad \text{... (2.5)}$$

where $$T_{px} = \frac{\gamma}{\alpha^2} \left\{ M_o + \frac{d^2M_o}{\alpha^2 dx^2} + \frac{d^4M_o}{\alpha^4 dx^4} + \ldots\ldots\ldots \right\}$$

... (2.6)

is the particular integral. The integration constants A and B are obtained from the known boundary conditions.

2.2.3 External Load

Three load patterns which commonly represent equivalent seismic loads are considered, as shown in Fig. 2.1

(a) A single point load, P , applied at the top of the shear wall.

(b) A distributed linearly varying load, W , acting with maximum intensity at the top of the structure.

(c) A uniformly distributed load, W_1 .

The bending moment at any level due to these loads is

$$M_o = WH\left(\xi^2 - \frac{\xi^3}{3}\right) + PH\xi + W_1 H \frac{\xi^2}{2} \qquad .. (2.7)$$

where $\xi = \frac{x}{H}$ so that $0 < \xi < 1$

2.2.4 Boundary Conditions

Only two boundary conditions are considered.

(a) Each wall, acting as a cantilever, is fully fixed at its base, hence (i) when $x = 0$, $T = 0$ ... (2.8)

and (ii) when $x = H$, $q = 0$, i.e. $\frac{dT}{dx} = 0$ ... (2.9)

(b) The walls are restrained at the base and are also provided with a rigid diaphragm at the top so that

(i) when $x = 0$, $q = 0$, i.e. $\frac{dT}{dx} = 0$ ... (2.10)

and (ii) when $x = H$, $q = 0$, i.e. $\frac{dT}{dx} = 0$ ... (2.11)

2.2.5 Internal Actions and the Deflections

Substituting the appropriate values of the moment (Eq. (2.7)), its derivatives in the particular integral (Eq.(2.6)), and applying the boundary conditions (Eqs. (2.8) to (2.11)) the unknown axial force T (Eq. (2.5)) is obtained. All other internal actions and deflections are derived based on the well known principles of structural mechanics

as indicated below:

(a) Shear wall fully restrained at the base

The axial force is obtained as:

$$T(\xi) = \frac{\gamma W H^3}{\beta^2}\left[\left(\frac{2}{\beta^2}+\frac{\rho'}{\beta^2}\right)\tanh\beta \sinh\beta\xi + \frac{\sinh\beta\xi}{\beta\cosh\beta}\left(\frac{2}{\beta^2}-1-\rho'-\rho\right)\right.$$

$$\left. - \cosh\beta\xi\left(\frac{2}{\beta^2}+\frac{\rho'}{\beta^2}\right) + \left(\xi^2 - \frac{\xi^3}{3} + \rho\xi + \rho'\frac{\xi^2}{2}\right) + \frac{1}{\beta^2}\left(2 - 2\xi + \rho'\right)\right] \quad \ldots (2.12)$$

where $\beta = \alpha H$, $\rho = \frac{P}{W}$ and $\rho' = \frac{W_1}{W}$

The load ratios ρ and ρ' are assumed to remain constant throughout the load history.

The axial force is the accumulation of laminar shear $q(\xi)$. Hence the laminar shear $q(\xi) = \left(\frac{dT(\xi)}{d\xi}\right).\left(\frac{1}{H}\right)$

On substitution of $T(\xi)$ from Eq. (2.12)

$$q(\xi) = \frac{\gamma W H^3}{\beta^2}\left(\frac{1}{H\beta}\right)\left[(2+\rho')\tanh\beta\cosh\beta\xi + \frac{\cosh\beta\xi}{\cosh\beta}\left(\frac{2}{\beta}-\beta-\rho'\beta-\rho\beta\right)\right.$$

$$\left. - (2+\rho')\sinh\beta\xi + 2\beta\xi - \beta\xi^2 + \beta\rho + \beta\rho'\xi - \frac{2}{\beta}\right] \quad \ldots (2.13)$$

The shearing force $V_{p(x)}$ generated by the separation forces[74,12] $p(x)$ is

$$V_{p(x)} = \frac{dM_p}{dx} = C\frac{dT_x}{dx} = C\,q_x$$

$$\text{where } C = \frac{I_1 l_2 - I_2 l_1}{I_o} \quad \ldots (2.14)$$

$$\text{Thus, } p(x) = \frac{dV_p}{dx} = C\frac{dq_x}{dx}$$

On substitution of $q(\xi)$ from Eq. (2.13), the separation force is

$$p(\xi) = \gamma WHC \left[\frac{2+\rho'}{\beta^2} \tanh\beta \sinh\beta\xi + \frac{\sinh\beta\xi}{\beta\cosh\beta\xi}\left(\frac{2}{\beta^2} - 1 - \rho' - \rho\right) \right.$$

$$\left. - \cosh\beta\xi \left(\frac{2+\rho'}{\beta^2}\right) + \frac{2}{\beta^2} - 2\frac{\xi}{\beta^2} + \frac{\rho'}{\beta^2} \right] \quad \ldots (2.15)$$

The lateral deflection of shear wall is computed using the relationship

$$EI_o \frac{d^2y}{dx^2} = M_o - 1T_x$$

whence $$y(\xi) = \frac{WH^3}{EI_o}\left\{\frac{1}{60}\left(\frac{\gamma l}{\alpha^2} - 1\right)\left[\xi^5 - 5\xi^4 + 15\xi - 11 - 10\rho\left(\xi^3 - 3\xi + 2\right)\right.\right.$$

$$\left. + \left(10\xi - 2.5\xi^4 - 7.5\right)\rho'\right] - \frac{\gamma l}{\alpha^2\beta^4\cosh\beta}\left[\left(\sinh\beta\xi - \sinh\beta\right)\right.$$

$$\left(2\sinh\beta + \frac{2}{\beta} - \beta - \beta\rho - \beta\rho' + \rho'\sinh\beta\right) - \cosh\beta\,(2+\rho')$$

$$\left(\cosh\beta\xi - \cosh\beta\right) - \frac{\beta^2\cosh\beta}{3}\left(\xi^3 - 3\xi^2 - 1.5\xi^2\rho' + 1.5\rho'\right.$$

$$\left.\left. + 3(\xi - 1)\left(\frac{2}{\beta^2} - \rho\right) + 2\right)\right]\right\} \quad \ldots (2.16)$$

(b) Walls with rigid diaphragm at the top

When the two walls are restrained at the base and provided with a rigid diaphragm at the top the various internal actions from consideration of Eqs. (2.10) and (2.11) become as follows

$$T(\xi) = \frac{\gamma WH^3}{\beta^2}\left[\left(\frac{2}{\beta^3} - \frac{\rho}{\beta}\right)\left(\sinh\beta\xi + \frac{\cosh\beta\xi}{\sinh\beta} - \frac{\cosh\beta\xi}{\tanh\beta}\right) - \left(\frac{1}{\beta} + \frac{\rho'}{\beta}\right)\frac{\cosh\beta\xi}{\sinh\beta}\right.$$

$$\left. - \frac{\xi^3}{3} + \xi^2 + \frac{2}{\beta^2}(1 - \xi) + \rho\xi + \rho'\frac{\xi^2}{2} + \frac{\rho'}{\beta^2}\right] \quad \ldots (2.17)$$

$$q(\xi) = \frac{\gamma WH^2}{\beta}\left[\left(\frac{2}{\beta^3} - \frac{\rho}{\beta}\right)\left(\cosh\beta\xi + \frac{\sinh\beta\xi}{\sinh\beta} - \frac{\sinh\beta\xi}{\tanh\beta}\right) - \left(\frac{1}{\beta} + \frac{\rho'}{\beta}\right)\left(\frac{\sinh\beta\xi}{\sinh\beta}\right)\right.$$

$$\left. + \frac{1}{\beta}\left(2\xi - \xi^2 - \frac{2}{\beta^2} + \rho + \rho'\xi\right)\right] \quad \ldots (2.18)$$

$$p(\xi) = \gamma WCH \left[\left(\frac{2}{\beta^3} - \frac{\rho}{\beta}\right) \left(\sinh\beta\xi + \frac{\cosh\beta\xi}{\sinh\beta} - \frac{\cosh\beta\xi}{\tanh\beta}\right) - \left(\frac{1}{\beta} + \frac{\rho'}{\beta}\right) \frac{\cosh\beta\xi}{\sinh\beta} \right.$$

$$\left. + \frac{1}{\beta^2} \left(2 - 2\xi + \rho'\right) \right] \qquad \ldots (2.19)$$

$$y(\xi) = \frac{WH^3}{EI_o} \left\{ \left(\frac{\gamma l}{\alpha^2} - 1\right) \frac{1}{60} \left[\xi^5 - 5\xi^4 + 15\xi - 11 - 10\left(\xi^3 - 3\xi + 2\right)\rho \right.\right.$$

$$\left. - \left(2.5\xi^4 - 10\xi + 7.5\right) \rho' \right] - \frac{\gamma l}{\alpha^2\beta^4} \left[\left(\frac{2}{\beta} - \beta\rho\right) \left(\sinh\beta\xi - \sinh\beta \right.\right.$$

$$\left. + \beta - \beta\xi\right) - \left(\frac{2}{\beta} - \rho\beta\right) \left(\frac{\cosh\beta\xi - \cosh\beta}{\sinh\beta}\right) \left(\cosh\beta - 1\right) - \left(\beta - \beta\rho'\right)$$

$$\left. \left(\frac{\cosh\beta\xi - \cosh\beta}{\sinh\beta}\right) - \frac{\beta^2}{3} \left(\xi^3 - 3\xi^2 + 2 - 1.5\rho'\xi^2 + 1.5\rho'\right) \right] \right\}$$

$$\ldots (2.20)$$

The moments in wall 1 and wall 2 are obtained as

$$M_1 = \frac{I_1}{I_o} \left[M_o - 1T_x \right] \qquad \ldots (2.21)$$

$$M_2 = \frac{I_2}{I_o} \left[M_o - 1T_x \right] \qquad \ldots (2.22)$$

Thus, $$M_o = M_1 + M_2 + 1T_x \qquad \ldots (2.23)$$

The above equations do not easily lend themselves to manual computations. The use of a computer programme is inevitable for speed and accuracy.

2.3 THE EFFECT OF SIGNIFICANT VARIABLES

To examine the sensitivity of the structure's response to the changes in the relative dimensions of the coupling beams and walls, the effect of the following variables upon the performance and efficiency of the coupling system was studied.

(a) The stiffness of the coupling beams

(b) Provision of a rigid diaphragm at the top of the structure

(c) Total stiffness of walls 1 and 2

(d) Ratio of the stiffness of wall 1 to the stiffness of wall 2

(e) Cracking in the beams and in the tension wall

(f) Flexible beam-wall junction.

For the purpose of this study the core of a 20-storey building, consisting of two channel shaped walls, was chosen. Fixed as well as variable dimensions of this core are shown in Fig. 2.2. The relevant dimensions of the chosen structure and details of equivalent lateral load considered are summarised below.

Constant data

Floor height, h = 11'-0" , Total height, H = 220'-0"

Number of storeys = 20. Wall thickness, t = 14"

Span of the coupling beams, l_s = 6'-0"

Triangular load, W = 600 kips.

Point load, P = 80 kips.

The load corresponds to the prototype seismic requirements of the New Zealand Building Code[75].

The properties of the walls

The dimensions a and b of the walls were varied from 6'-0" to 14'-0" in different combinations to reveal the effect of changing the wall dimensions on the significant design quantities.

The properties of the coupling beams

The dimensions of the beams were varied as indicated in Table 2.1.

Table 2.1 PROPERTIES OF BEAMS

NO.	ASPECT RATIO	DEPTH	WIDTH	AREA*
	D/l_s	D	B	A=2BD
		in.	in.	Sq.in.
1	0.83	60	12	1296
2	0.42	30	12	1008
3	0.33	24	12	720
4	0.25	18	12	432
5	0.08	6	24	288
Note: * area of two beams				

As and when necessary beams of depth varying from 0" ($D/l_s = 0$) to 6" ($D/l_s = 0.08$) and from 60" ($D/l_s = 0.83$) to 132" ($D/l_s = 1.83$) were also used to evaluate the effect of providing either a very flexible or a very stiff coupling system.

2.3.1 The Effect of the Variation of the Stiffness of the Coupling Beams

The effectiveness of the coupling between the two walls depends on the stiffness of the coupling beams. In these coupled walls the accumulation of the laminar shear generates axial tension in one wall and compression in the other. The axial force, T, generated in each wall produces the moment, lT, which is usually the major component resisting the external moment, M_o. (See Eq. (2.23)). A very stiff coupling system will lead to large axial forces and hence to an efficient structural action. With diminishing stiffnesses of the laminae the walls will tend to accept the load as cantilevers subjected to shear forces and large bending moments[76,77]. Moments M_1 and M_2 increase consequent to the decrease of the lT component.

In Fig. 2.3 the efficiency of coupling is evaluated in terms of the stiffness of the structure. For this purpose, the stiffness of the shear wall, k_S, is defined as the load in the previously defined pattern, required to produce unit deflection at the top of the structure. This stiffness is compared with the stiffness, k_F, of a fictitious wall with the same dimensions as the prototype structure but having an infinitely rigid coupling system. The efficiency of coupling for this fictitious structure is taken as unity. Thus, the efficiency of coupling of the prototype wall is expressed in terms of the stiffness ratio, $\epsilon_k = \frac{k_S}{k_F}$.

In Fig. 2.4, the efficiency of coupling as affected by different total wall stiffness of wall 1 and wall 2, is studied. For this purpose the total wall stiffness of wall 1 and wall 2 is represented by the moment of inertia ratio, ϵ_I, which is defined as the ratio of total moment of inertia, I_o, for the prototype shear wall shown in Fig. 2.1, to the total moment of inertia, I_F, of a fictitious wall which has the same dimensions for the webs of the channel shaped sections as the prototype structure but does not have flanges (i.e. a = b = 14"). The efficiency of coupling, ϵ_k, for the stiffest symmetrical shear wall section considered ($\epsilon_I = 150$), with infinitely rigid coupling beams, is taken as unity. The efficiency of coupling for different total stiffness of wall 1 and wall 2 is thus expressed in terms of the stiffness ratio $\epsilon_k = \frac{k_S \text{ for the prototype shear wall}}{k_F \text{ for the fictitious shear wall with } \epsilon_I = 150}$

An examination of Figs. 2.3 and 2.4 reveals that:

(a) Decreasing the stiffness of the beams decreases the efficiency of coupling as would be expected.

(b) The efficiency of coupling falls off rapidly when the stiffness of the beams, as measured by the aspect ratio, D/l_s of the coupling beams, falls below a certain value. For example the stiffness of a symmetrical coupled shear wall of given height increases 20 fold when

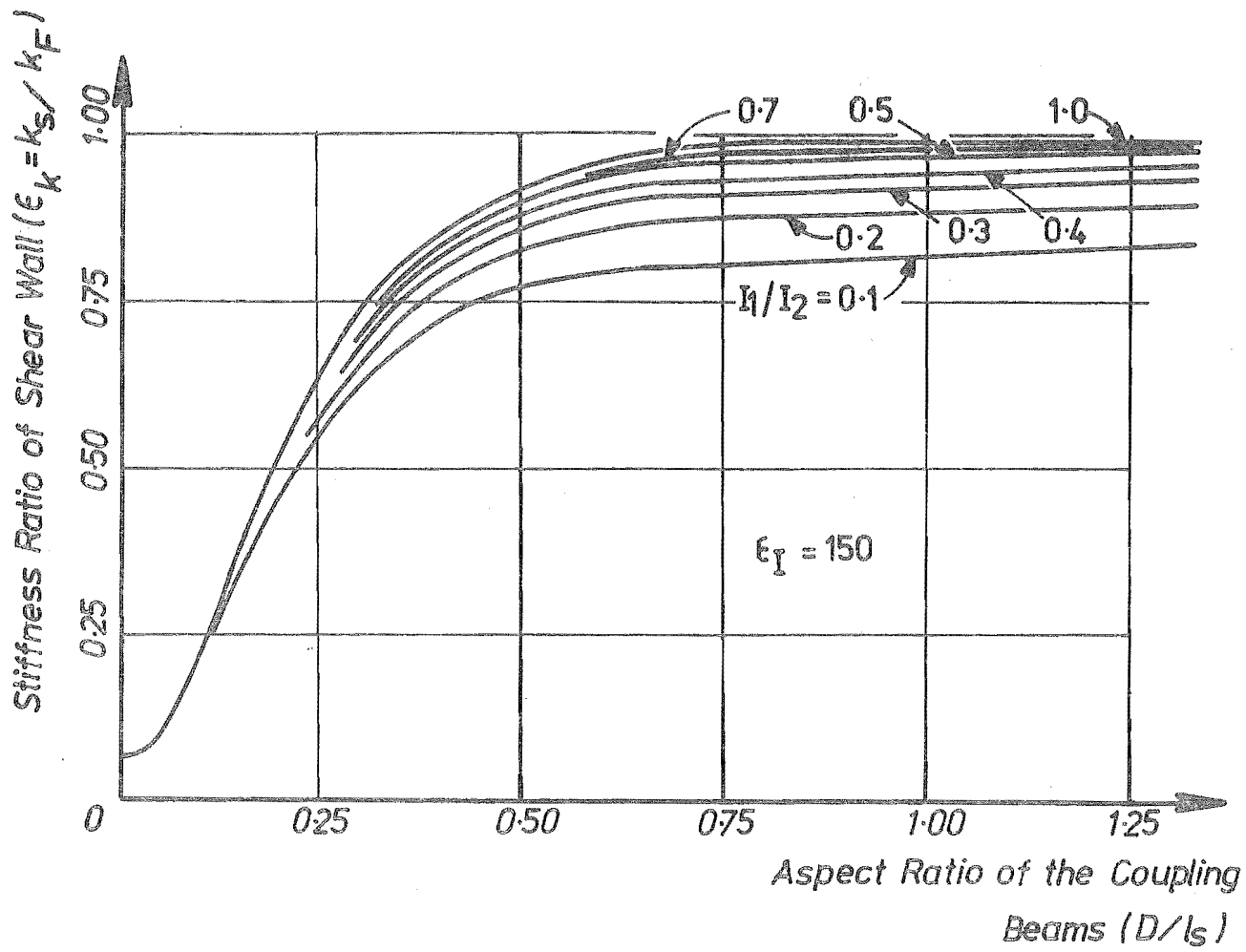

FIG. 2.3 THE STIFFNESS RATIO OF A SHEAR WALL AS AFFECTED BY THE STIFFNESS OF THE COUPLING BEAMS FOR DIFFERENT VALUES OF I_1/I_2

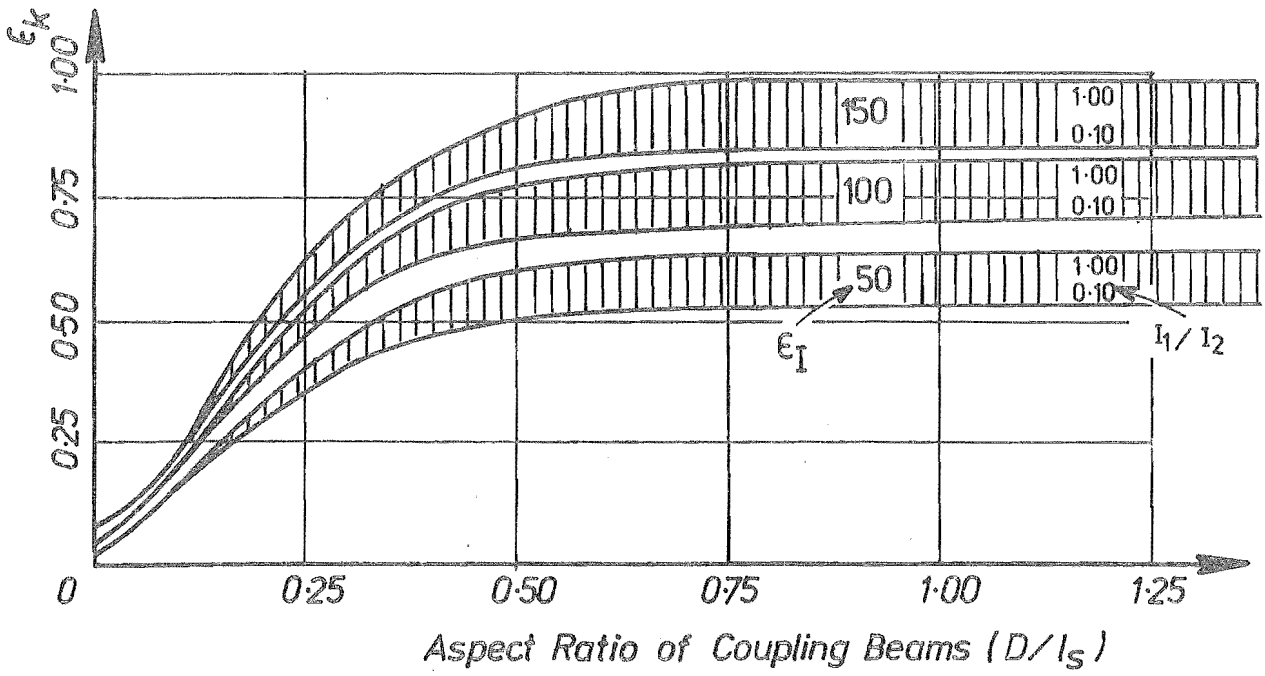

FIG. 2.4 THE STIFFNESS RATIO OF A SHEAR WALL AS AFFECTED BY THE STIFFNESS OF THE COUPLING BEAMS FOR DIFFERENT MOMENT OF INERTIA RATIO ϵ_I

the aspect ratio, D/l_s, of the coupling beams increases from zero to 0.33.

(c) The efficiency of coupling is not sensitive to changes in beam stiffness when the aspect ratio is larger than 0.75 (see Fig. 2.3).

(d) The stiffness of the shear wall increases with an increase in total stiffness of wall 1 and wall 2, as expressed by the moment of inertia ratio, ϵ_I, (See Figure 2.4).

(e) The stiffness of the coupled shear wall increases with the wall moment of inertia ratio, I_1/I_2, for a given total moment of inertia, I_0. However this increase is insignificant when I_1/I_2 is more than 0.5.

Hence, for efficient structural action, the designer could aim at selecting overall dimensions so that the aspect ratio of the coupling beam is larger than 0.33 and that the inertia ratio of the two walls (I_1/I_2) is more than 0.5.

In Fig. 2.5.a, the variation of laminar shear factor, ϵ_q, with the height of the shear wall for different beam aspect ratios is shown. The laminar shear factor is defined as the ratio of laminar shear, ϵ_q, of the prototype shear wall to the maximum laminar shear, q_F, of a fictitious shear wall with infinitely rigid coupling system. As expected the maximum laminar shear increases with increasing beam stiffness. As the depth of the coupling beam is reduced, the height at which the maximum laminar shear occurs, moves up. For very lightly coupled shear walls, the laminar shear is almost uniform.

In Fig. 2.6.a, the variation of axial force factor, ϵ_T, with height of the shear wall for different beam aspect ratios is shown. The axial force factor is defined as the ratio of axial force, T, of the prototype shear wall at any level to the maximum axial force, T_F, of a fictitious shear wall with infinitely rigid coupling system. As expected the axial force factor at the base of the walls also increases with beam stiffness.

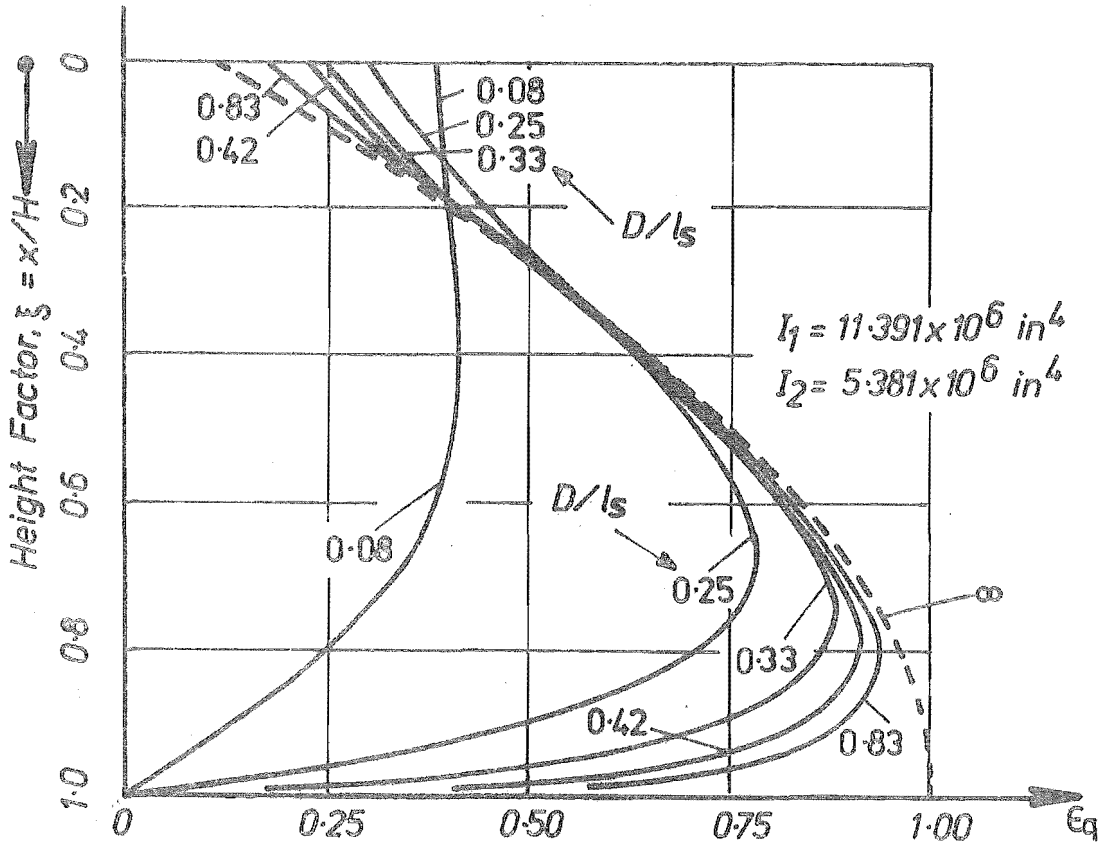

(a) Variation of laminar shear factor, ϵ_q, with height of the shear wall for different beam aspect ratios

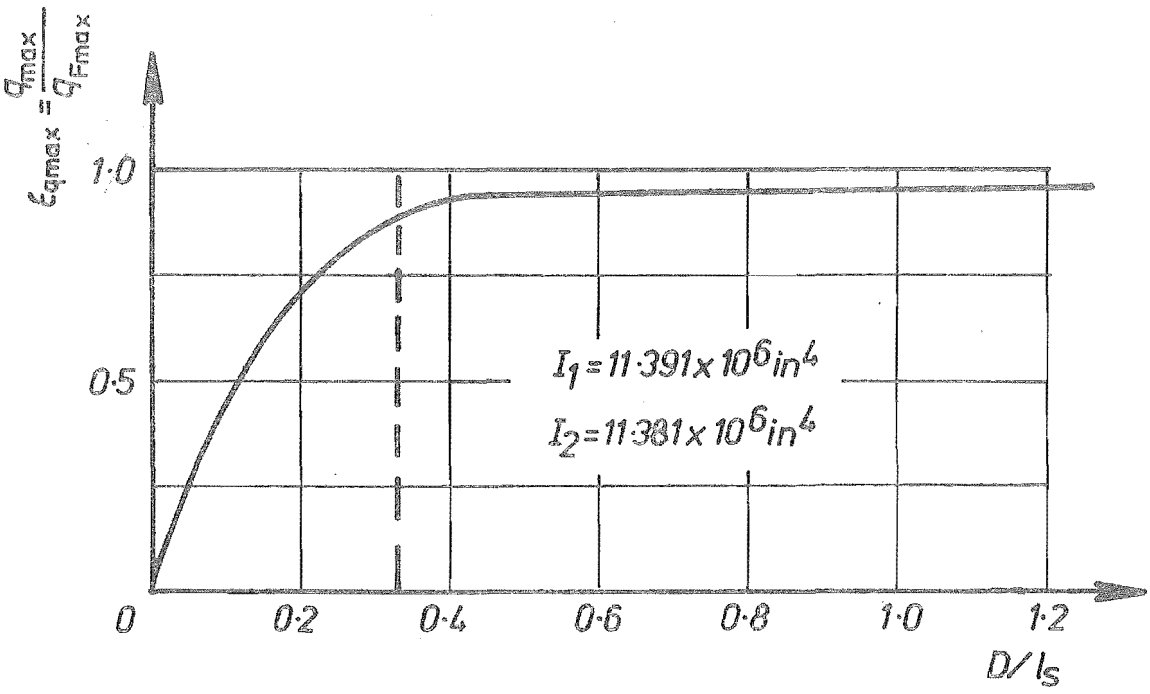

(b) Variation of maximum laminar shear factor, ϵ_q, for different beam aspect ratios

FIG. 2.5 THE EFFECT OF VARIATION OF BEAM STIFFNESS ON THE LAMINAR SHEAR FACTOR, ϵ_q

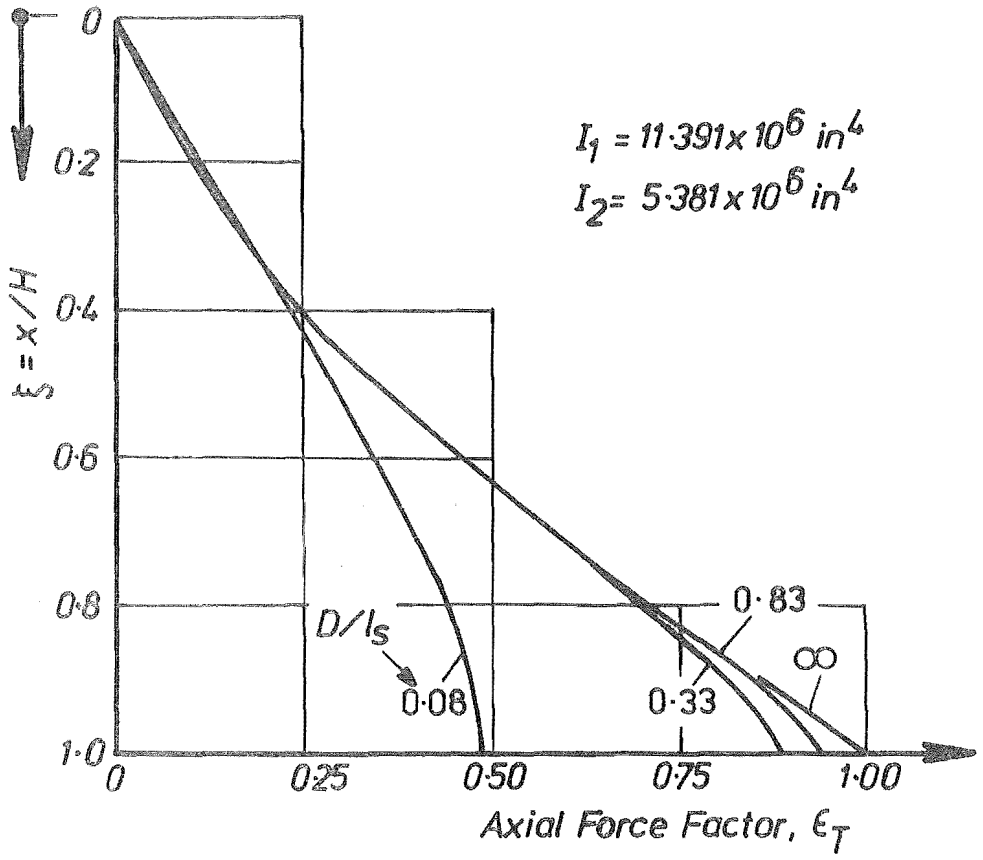

(a) Variation of axial force factor, ϵ_T, with height of the shear wall for different beam aspect ratios

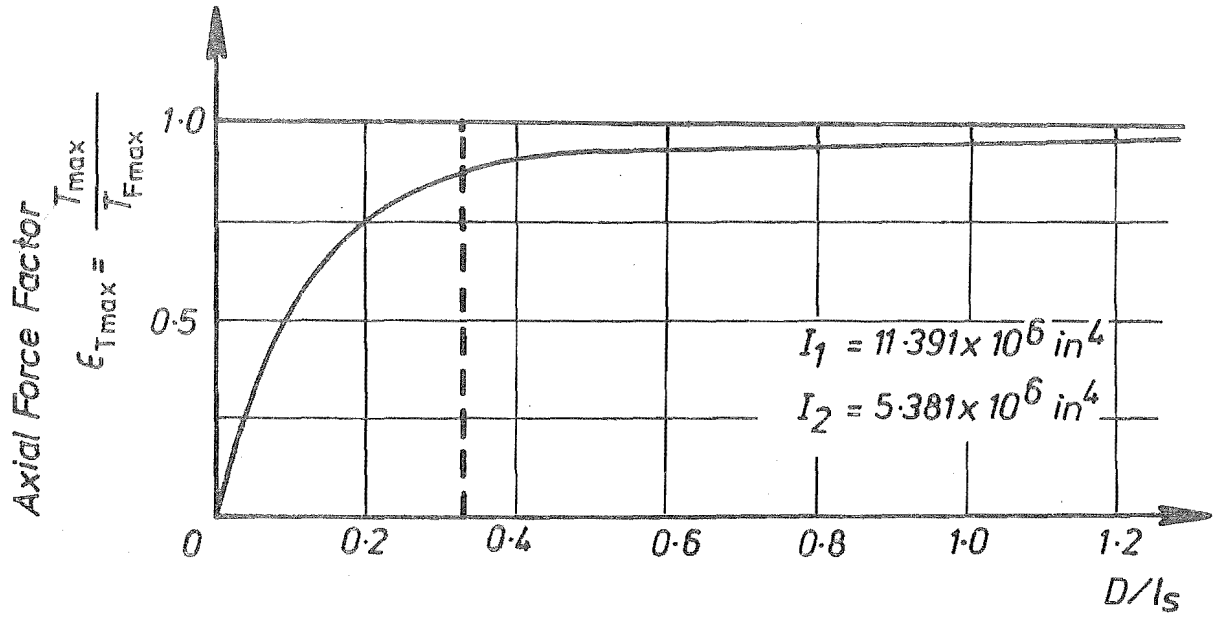

(b) Variation of maximum axial force factor, ϵ_T, for different beam aspect ratios

FIG. 2.6 THE EFFECT OF VARIATION OF BEAM STIFFNESS ON THE AXIAL FORCE FACTOR, ϵ_T

Figs. 2.5.b and 2.6.b show the sensitivity of maximum laminar shear factor, ϵ_q , and maximum axial force factor, ϵ_T , to the changes in beam aspect ratios respectively. For aspect ratios greater than 0.33 the variations of the maximum laminar shear factor and maximum axial force factor are insignificant.

In Figs. 2.7 and 2.8, the bending moment variation in wall 1 M_1 , and wall 2, M_2 , is plotted against the height of the structure in terms of total base moment, M_0 , due to lateral load. As expected both wall moment ratios M_1/M_0 and M_2/M_0 increase with decreasing beam stiffnesses. When the aspect ratio of the beam decreases, the axial force, T , decreases. This decreases the 1T component in Eq. (2.23). To resist the same external moment, M_0 , the wall moments M_1 and M_2 increases by 1 times the decrease of axial force, T . Thus, the wall moments are much more sensitive to changes in beam stiffness than other static quantities like the laminar shear, q , or axial force, T .

Fig. 2.9 shows the variation of the components of M_0 with height for different beam aspect ratios. In Fig. 2.10, the moments resisted by wall 1, wall 2 and the 1T component at the base of the shear wall for different beam aspect ratios are expressed in terms of the total external moment M_0 at the base. An examination of the Figs. 2.9 and 2.10 reveals that:

(a) For an aspect ratio greater than 0.60 the increase in the component 1T , consequent to an increase in the depth of the beams, is insignificant.

(b) An aspect ratio less than 0.33 requires the walls to accept a large proportion of the load as cantilevers. (Wall moments are doubled when the aspect ratio is reduced from 0.33 to 0.16.)

As expected deflections decrease with increasing beam stiffness of the coupled shear wall as shown in Fig. 2.11.a. In this figure, the deflection factor, ϵ_Δ , is plotted against the height of the structure for different beam aspect ratios. The deflection factor, ϵ_Δ , is the ratio of the deflection of the prototype shear wall to the top floor

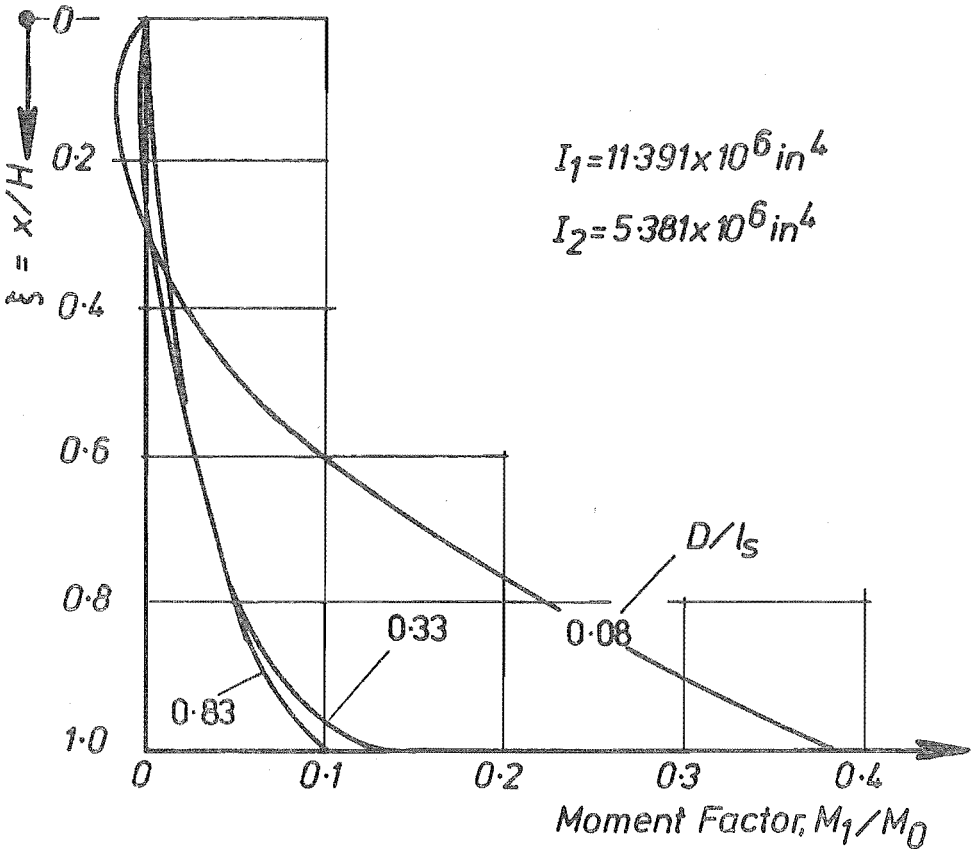

FIG. 2.7 VARIATION OF MOMENT FACTOR M_1/M_0 WITH HEIGHT OF THE SHEAR WALL FOR DIFFERENT BEAM ASPECT RATIOS

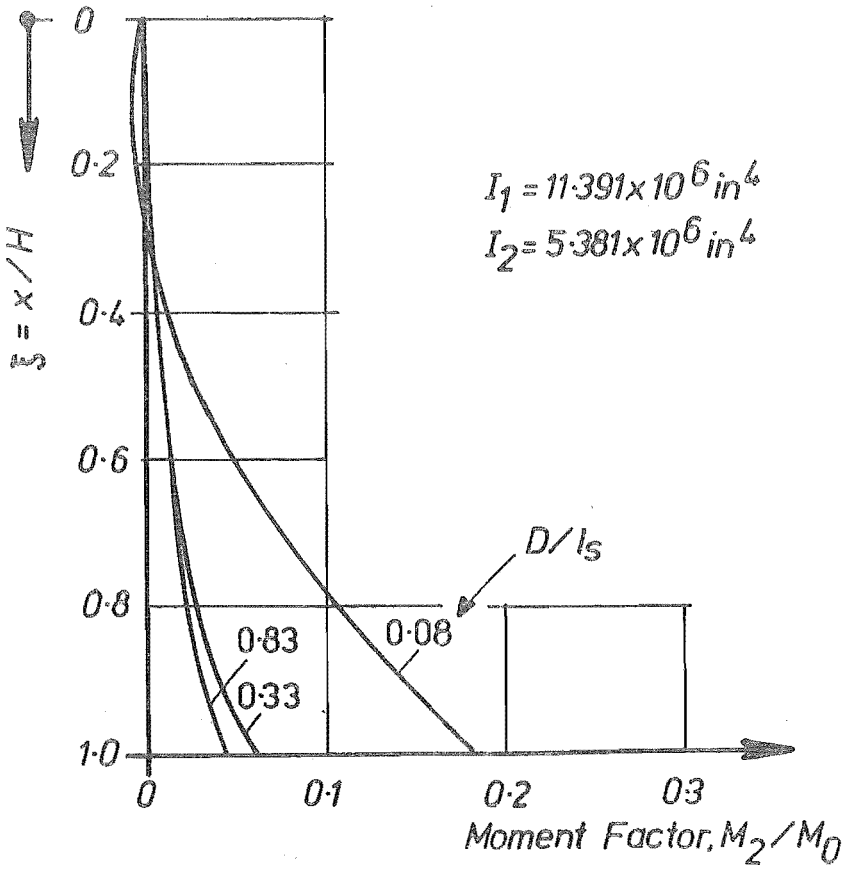

FIG. 2.8 VARIATION OF MOMENT FACTOR M_2/M_0 WITH HEIGHT OF THE SHEAR WALL FOR DIFFERENT BEAM ASPECT RATIOS

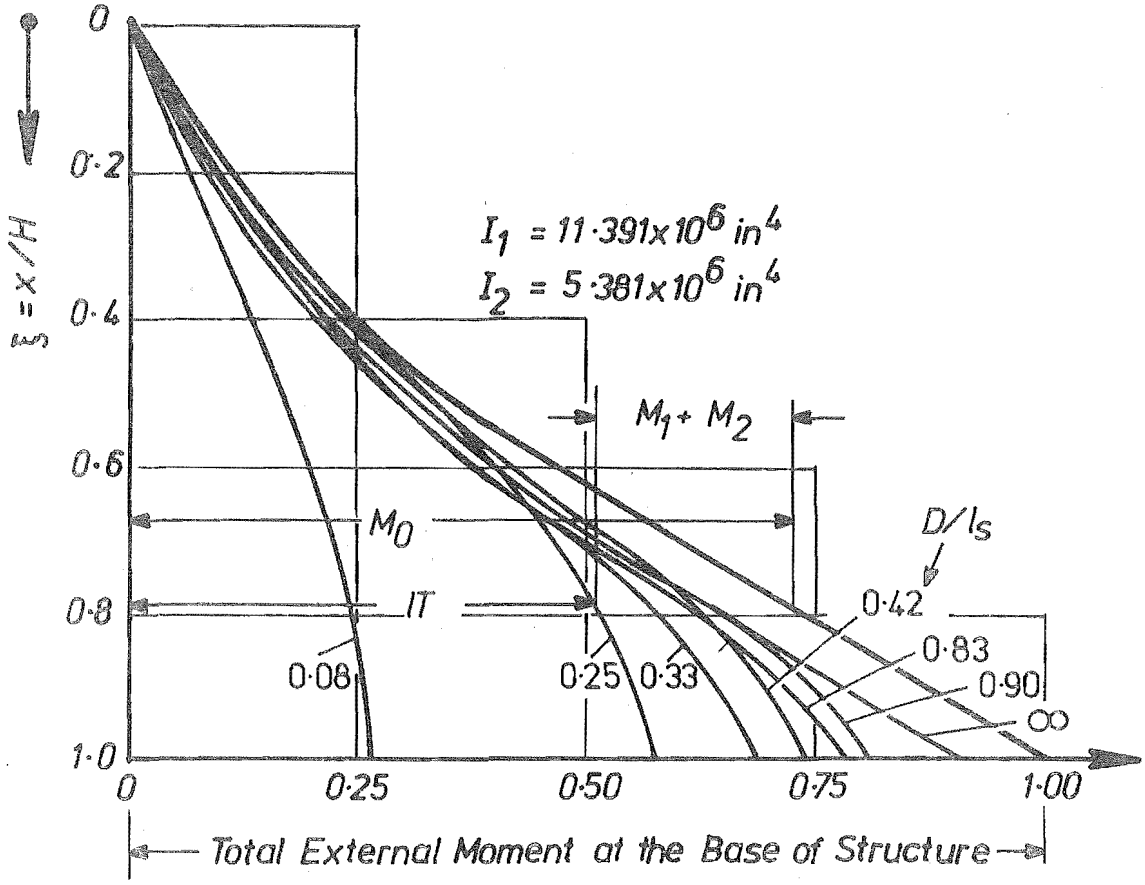

FIG. 2.9 VARIATION OF THE COMPONENT, IT , WITH HEIGHT FOR DIFFERENT BEAM ASPECT RATIOS

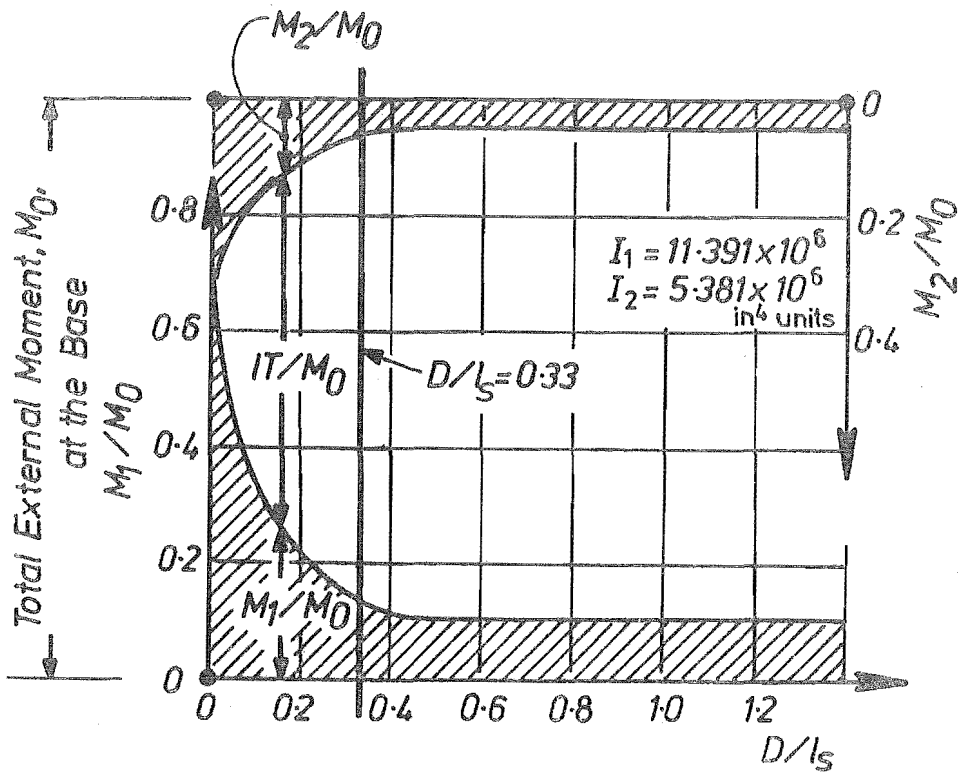

FIG. 2.10 VARIATION OF THE COMPONENTS OF THE EXTERNAL MOMENT, M_o, AT THE BASE OF THE SHEAR WALL FOR DIFFERENT BEAM ASPECT RATIOS

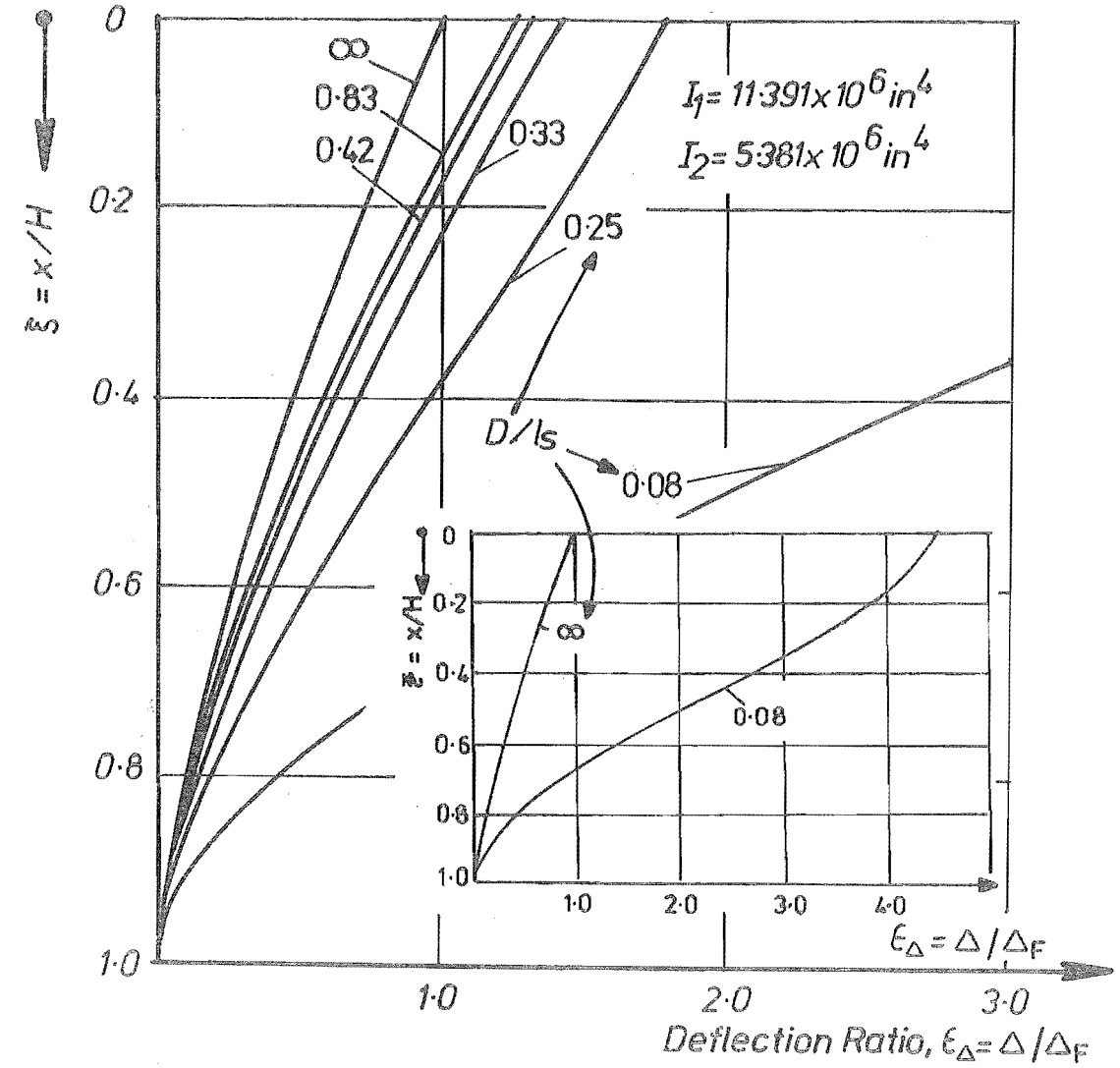

FIG. 2.11.(a) VARIATION OF DEFLECTION FACTOR, ϵ_Δ, WITH HEIGHT FOR DIFFERENT BEAM ASPECT RATIOS

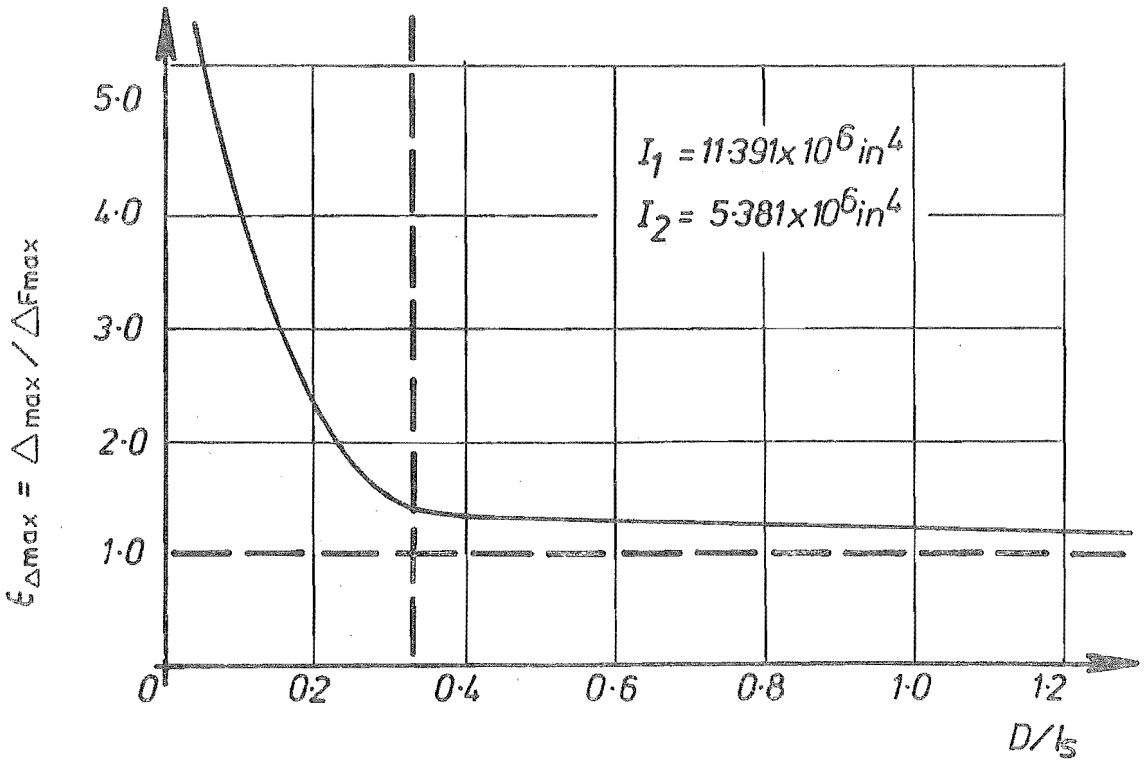

FIG. 2.11.(b) VARIATION OF MAXIMUM DEFLECTION FACTOR, $\epsilon_{\Delta max}$, FOR DIFFERENT BEAM ASPECT RATIOS

deflection of a fictitious shear wall with infinitely rigid coupling beams having the same wall dimensions as the prototype shear wall. Fig. 2.11.b shows the variation of the maximum deflection factor, $\epsilon_{\Delta\ max}$, for different beam aspect ratios. Figs. 2.11.a and 2.11.b show that for beam aspect ratios greater than 0.33 the variations in the top floor deflections, as expressed by the variations in the top floor deflection factor, ϵ_{Δ}, are insignificant.

Thus both from the consideration of stiffness and efficient structural action, the designer should aim at selecting the overall dimension of the coupling beam so that its aspect ratio is larger than 0.33 for the shear walls in which $35 \times 10^6 > I_o > 50 \times 10^3$ in^4 units.

2.3.2 The Effect of Variation of Total Stiffness of Wall 1 and Wall 2

The magnitude of the laminar shear, q, has a bearing on the design of coupling beams as well as the walls. Fig. 2.12.a shows the variation of laminar shear factor, ϵ_q, for different beam aspect ratios with respect to the total moment of inertia of wall 1 and wall 2 for a particular I_1/I_2 ratio. The laminar shear factor, ϵ_q, is the ratio of maximum laminar shear, q_{max}, in the prototype shear wall to the maximum laminar shear, $q_{F\ max}$, of a fictitious shear wall with a = b = 14" (see Fig. 2.2) and with infinitely rigid coupling beams. It is seen from Fig. 2.12.a that increasing $\epsilon_I = \frac{I_o}{I_F}$ decreases the laminar shear. I_o and I_F are the sum of the moment of inertias of walls 1 and 2 of the prototype and fictitious (a = b = 14") shear walls respectively. This is to be expected as an increase in stiffness of the walls will relieve the coupling beams. However, for coupling beams with aspect ratios greater than 0.25 the moment of inertia ratio, ϵ_I, does not significantly affect the laminar shear.

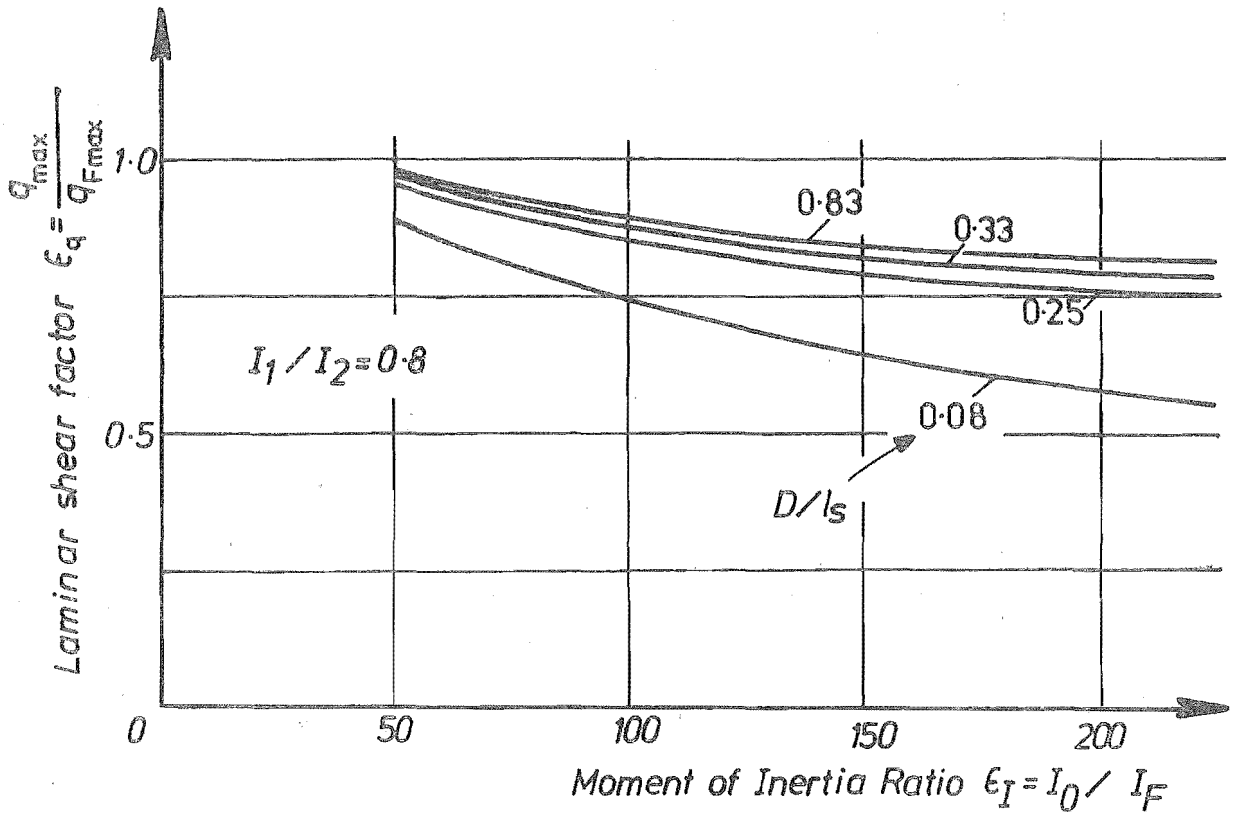

FIG. 2.12(a) VARIATION OF LAMINAR SHEAR FACTOR, ϵ_q, FOR DIFFERENT BEAM ASPECT RATIOS WITH RESPECT TO TOTAL MOMENT OF INERTIA FACTOR, ϵ_I

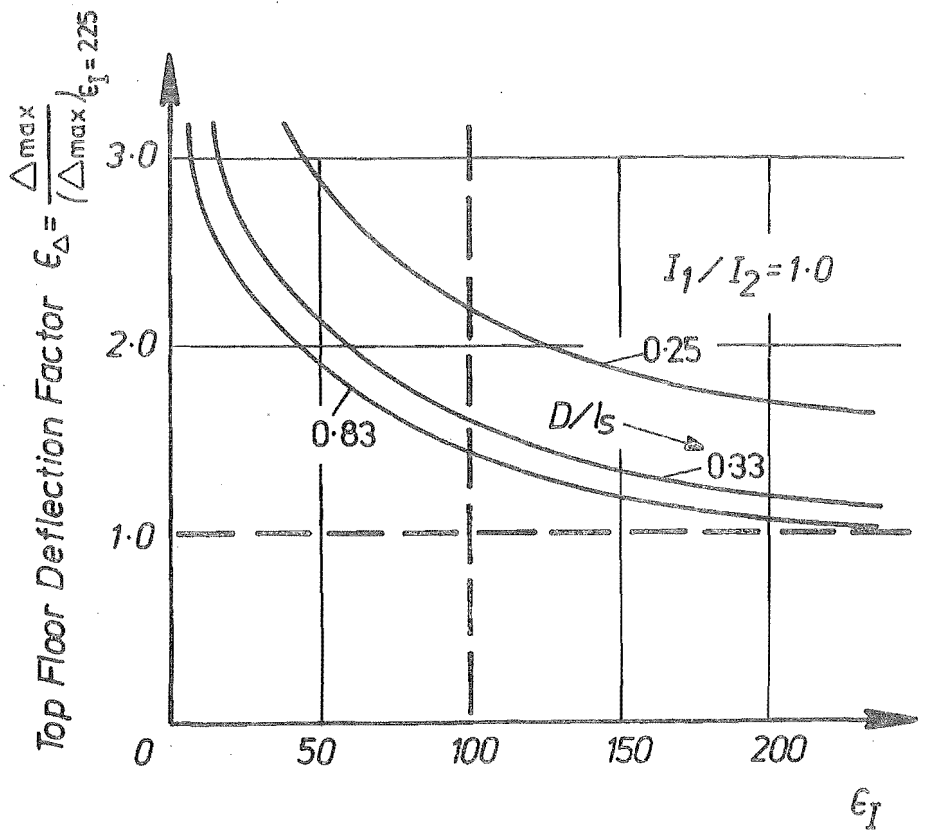

FIG. 2.12(b) VARIATION OF TOP FLOOR DEFLECTION FACTOR, ϵ_Δ, FOR DIFFERENT BEAM ASPECT RATIOS WITH RESPECT TO THE TOTAL MOMENT OF INERTIA FACTOR, ϵ_I

Fig. 2.12.b shows the variation of top floor deflection factor, ϵ_{Δ}, for different ϵ_I values of the shear wall for a particular I_1/I_2 ratio of the walls. As expected deflections decrease with increasing wall stiffness. However, above $\epsilon_I = 100$ the decrease in deflection consequent to an increase in ϵ_I value is insignificant.

2.3.3 The Effect of Variation of Wall Stiffness Ratio I_1/I_2

The variation of laminar shear factor, ϵ_q, for different beam aspect ratios with respect to the wall stiffness ratio, I_1/I_2, for a particular value of I_o is shown in Fig. 2.13.a. It is seen that the laminar shear factor, ϵ_q, does not appreciably vary with the relative stiffnesses of wall 1 and wall 2 for any aspect ratio.

Fig. 2.13.b shows the variation of top floor deflection factor, ϵ_{Δ}, for different I_1/I_2 ratios for a particular value of I_o. The deflections decrease with increasing I_1/I_2 ratios. However, this decrease is insignificant for $I_1/I_2 > 0.25$. Hence, the variation of I_1/I_2 for a constant I_o does not significantly affect either the stiffness of the structure or the efficiency of the coupling when $I_1/I_2 > 0.25$.

2.3.4 The Effect of Variation of the Parameter 'αH'

Several dimensionless parameters have been used[14,15,42] to define the behaviour of a shear wall structure. The most useful of these is αH[42], α being the coefficient of the governing differential equation, Eq. (2.2). MacLeod[42] studied the overall stiffness of the structure with respect to variation of the parameter αH. This study was based on the analysis made for shear walls with a constant overall aspect ratio $H/C = 3.15$, where C is a dimension defined in Fig. 2.15. The results of this analysis revealed[42] that

(1) For $\alpha H > 8$ the increase of deflections with αH are not large

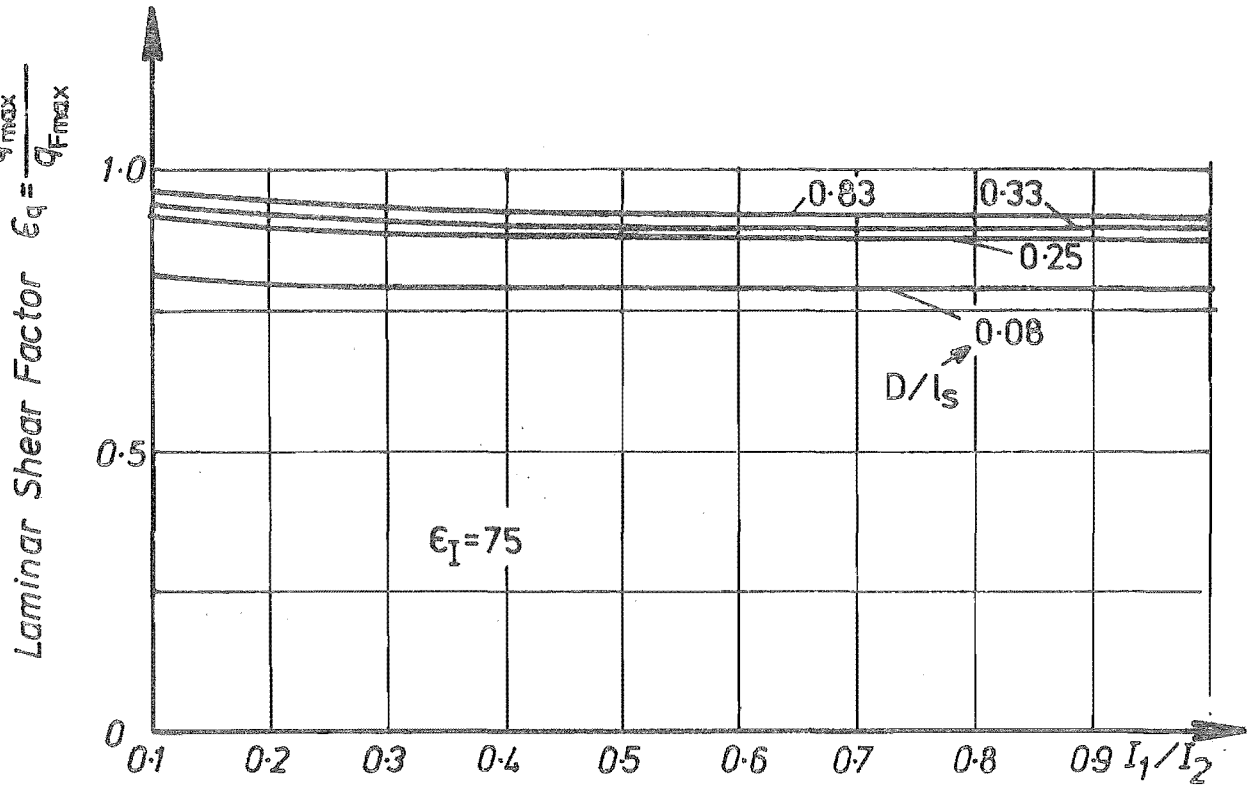

FIG. 2.13(a) THE VARIATION OF LAMINAR SHEAR FACTOR, ϵ_q, FOR DIFFERENT BEAM ASPECT RATIOS WITH RESPECT TO THE MOMENT OF INERTIA FACTOR, I_1/I_2

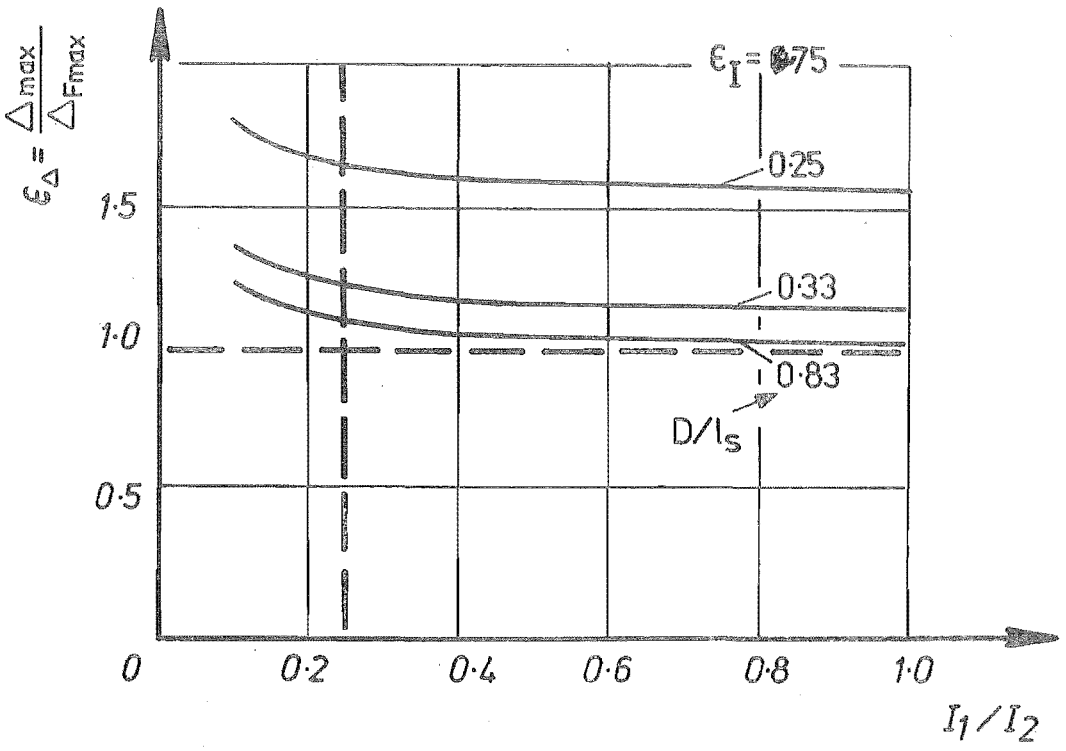

FIG. 2.13(b) VARIATION OF TOP FLOOR DEFLECTION FACTOR, ϵ_Δ, FOR FOR DIFFERENT BEAM ASPECT RATIOS WITH RESPECT TO WALL MOMENTS OF INERTIA RATIO, I_1/I_2

(2) For $\alpha H < 4$ a small variation in the value of αH could produce a significant change in deflection.

These findings are assembled in the form of a behaviour table[42,78]. (See Table 2.2)

TABLE 2.2 BEHAVIOUR OF COUPLED SHEAR WALLS

αH	Behaviour
> 8	Close to that of a wall without openings
4 - 8	Transition
0 - 4	Behaviour approaches that of a frame

Though the above study is useful in determining the stiffness of a structure, it does not depict the influence of the efficiency of coupling on shear wall behaviour. For this purpose the variation of axial force, T, at the base and the deflection, Δ, at the top floor, with the parameter, αH, for shear walls with various overall aspect ratios, H/C, subjected to the previously defined load pattern, were examined. The dimension, C, was chosen as fixed and H was varied. The variation of axial force factor, ϵ_T, and deflection factor, $\epsilon_{\Delta max}$, with αH for an overall aspect ratio $H/C = 2.00$ are shown in Figs. 2.14.a and b respectively. Reference may be made to Section 2.3.1 for the definition of ϵ_T and $\epsilon_{\Delta max}$

Limit a - Beyond this the behaviour is that of a shear wall with infinitely rigid coupling system. q_{max} occurs at location $0.90 \leq \xi \leq 1.00$

Limit b - Beyond this the maximum axial force, T_{max}, at the base of the shear wall is more than 95% of the maximum axial force developed by a shear wall with infinitely rigid coupling system. q_{max} occurs at location $0.8 \leq \xi \leq 1.00$

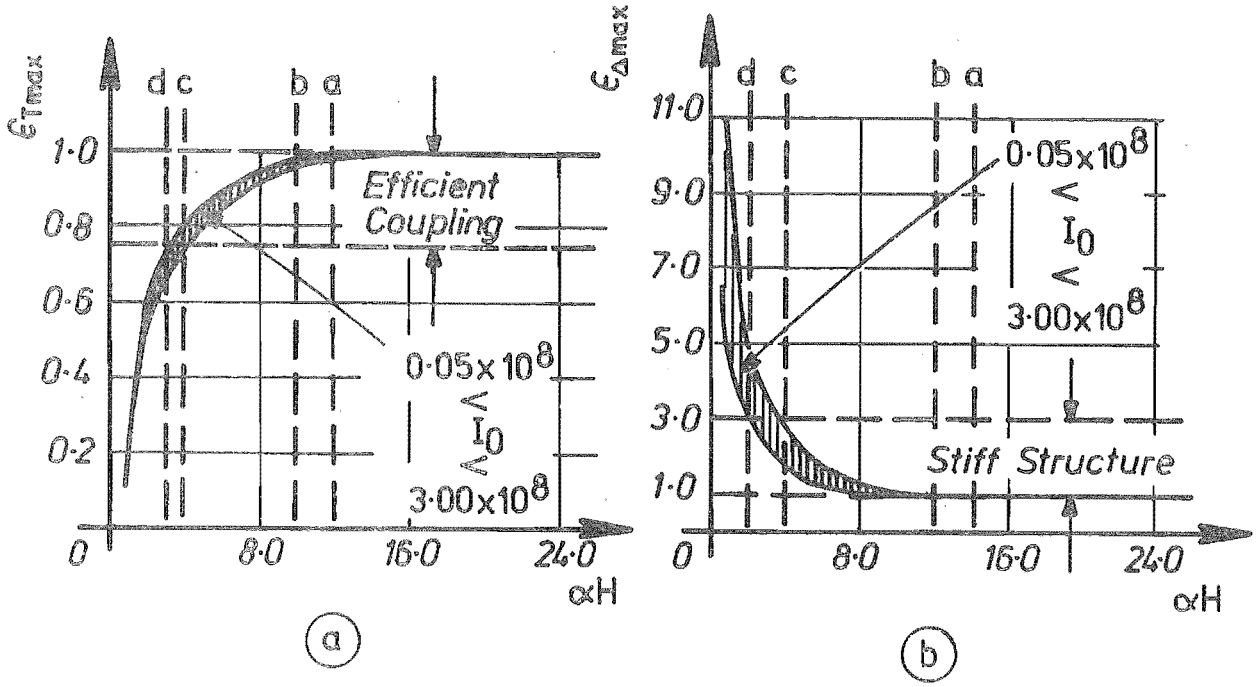

FIG. 2.14 VARIATION OF AXIAL FORCE FACTOR, ϵ_{Tmax}, AND TOP FLOOR DEFLECTION FACTOR, $\epsilon_{\Delta max}$, WITH PARAMETER αH

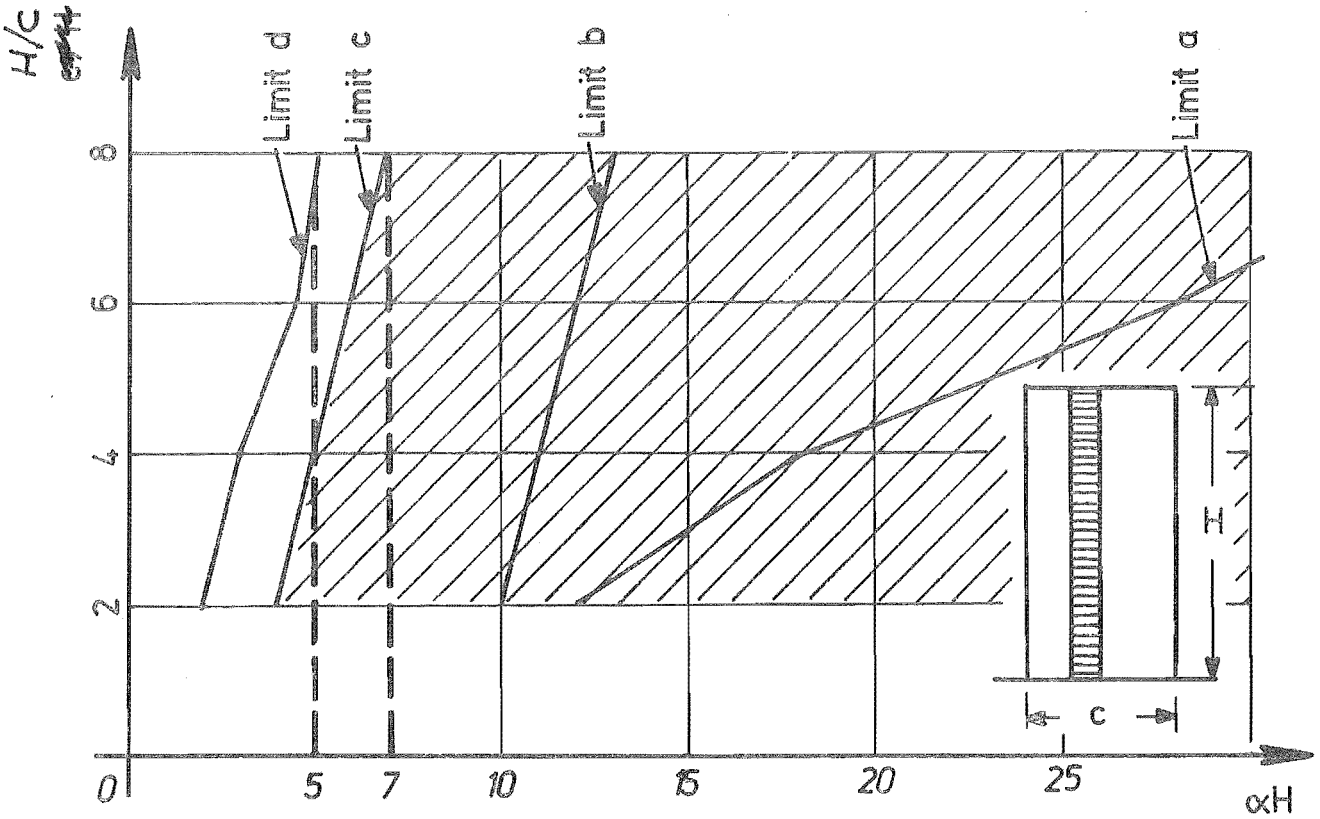

FIG. 2.15 THE VARIATION OF THE BEHAVIOUR LIMITS WHICH SIGNIFY THE THE EFFICIENCY OF COUPLING AND STIFFNESS OF THE SHEAR WALL, WITH PARAMETERS αH and H/C

Limit c - Beyond this the shear wall develops at the base more than 75% of the maximum axial force in a shear wall with an infinitely rigid coupling system. This range is arbitrarily defined as "efficient coupling". The top floor deflection is less than twice the top floor deflection of a shear wall with an infinitely rigid coupling system. q_{max} occurs at location $0.7 \leq \xi \leq 1.00$

Limit d - Beyond this the axial force at the base of the shear wall is more than 60% and the top floor deflection is less than three times the corresponding values for a shear wall with an Infinitely rigid coupling system. q_{max} occurs at $0.6 \leq \xi \leq 1.00$. Beyond this limit the axial deformation of the walls and shear deformation of the beams should be considered in the analysis. This range is arbitrarily assumed to result in a stiff structure.

For αH less than at limit d , the behaviour approaches that of two cantilevers subjected to shear forces and bending moments. The laminar analysis may introduce significant errors in short walls.

In Fig. 2.15 the above limits of αH are plotted against the overall aspect ratio H/C . The lower and upper bounds of the limits a to d correspond to the aspect ratio H/C = 2.00 and 8.00 respectively. The shaded area shows the combination of values of αH and H/C for which the coupling system is efficient. For values of αH and H/C which result in a point beyond limit d the structure is stiff. An examination of this figure shows that:

(i) Beyond $\alpha H = 7$, the coupling system is efficient.

(ii) Beyond $\alpha H = 5$, the structure is stiff.

2.3.5 The Effects of Cracking

The reinforced concrete shear wall could remain crack free only when the lateral load is very small. Therefore, theoretical elastic analyses or photo-elastic observations of the structure have limited

value in predicting the behaviour of the structure in earthquake prone countries. The cracking of concrete signifies that the reinforcement has commenced to contribute more effectively to the strength of the structure. This may significantly alter the behaviour of the coupled shear wall[7].

The coupling beams are subjected to flexure, in the presence of large shearing forces. In these beams, which are often deep members, the maximum flexural stress at the tension corner could be expected to be more than those predicted with linear strain variation across the section. Near the re-entrant corners, the concrete is in a biaxial state of stress. Moreover, stress concentrations occur. The onset of cracking in the beams could be expected at smaller loads than in shallow reinforced concrete beams. Owing to subsequent loading, the diagonal crack may develop and propagate from the tension corners. This may result in loss of laminar shear transfer and also in a reduction of the efficiency of coupling.

The cracking of the walls is likely to commence at the base. Consequently there is a loss of flexural rigidity over the affected height. This leads to increased flexural rotations. In one of the walls tension will promote the development of the cracks. In the other wall compressive stresses may delay the formation of the cracks. In the bottom storeys, where the stresses are critical, the formation and development of cracks are likely to be severe. Thus, the loss in stiffness due to cracking is likely to be more in the bottom storeys than in the top of the structure.

The foregoing discussion implies that the elastic laminar analysis may have limited application for certain reinforced concrete coupled shear wall structures. A more exact analysis which takes into account the varying stiffness of the walls and beams is possible and this is developed in Section 2.5. To study the effects of cracking, considering the gross section shown in Fig. 2.2, uniform properties have been

assumed for each of the three main components of the shear wall,(i.e. the tension wall, the compression wall, and the coupling beams) based on the procedure outlined by Paulay [74]. It was assumed that as a consequence of cracking

(i) The stiffness of all coupling beams was reduced by 70%

(ii) The tension wall lost 50% of its flexural stiffness, and 30% of its area.

The assumption that stiffnesses reduce over the full height of a structure may be crude but in the absence of the data regarding disposition of reinforcement, improved assumptions and approximations to simulate the exact variation of stiffness with height would seldom be warranted. The effects of cracking on a typical shear wall core may be evaluated by examining the effects of stiffness variation of beams in Figs. 2.5 to 2.11, and of walls in Figs. 2.12 and 2.13. A study of these figures reveals that the stiffness reduction of the beams and walls affects the behaviour of the shear wall as follows:

(i) Cracking of the beams reduces the stiffness of the coupling system. Herein, the effects of cracking are studied based on the assumption that it results in a 70% loss of stiffness of the beams. The effect of providing a beam whose moment of inertia is $0.3\ I_b$, where I_b is the gross moment of inertia of the beam, is the same as that of a beam with an equivalent depth, $D_{eq} = \sqrt[3]{0.3}\ D \approx 0.7D$. Hence the effects of cracking are the same as reducing the aspect ratio of the coupling beam to $0.7D/l_s$, where D and l_s are the depth and clear span of the coupling beam respectively. It was pointed out in Section 2.3.1 that for beam aspect ratios larger than 0.33 the static quantities are insensitive to changes in beam stiffness. The equivalent aspect ratio, D_{eq}/l_s, would be more than 0.33 for beam aspect ratios $D/l_s > 0.60$. Thus, it may be concluded that for beam aspect ratio $D/l_s > 0.60$ cracking has insignificant effects on static design quantities.

(ii) Cracking in wall 1 reduces the moments in wall 1 and increases the moments in wall 2. This is due to reduction in the proportion of the moment of inertia of wall 1 to the total moment of inertia, I_o. Cracking of wall 1 has the same effect as providing a less stiff wall. The effect of variation of wall stiffness on critical design quantities were studied in Section 2.3.2 and Section 2.3.3. During this study it was observed that the variation of the stiffness of the walls (total stiffness or relative stiffness expressed by I_o or I_1/I_2 ratio respectively) do not affect the shear transfer capacity of the beam when the beam aspect ratio $D/l_s > 0.25$. The equivalent aspect ratio of the cracked beam would be more than 0.25 when the beam aspect ratio $D/l_s > 0.36$. Thus it may be concluded that for beam aspect ratios more than 0.36, cracking of the walls has negligible effect on the efficiency of coupling.

(iii) Cracking of the wall reduces I_1 and hence it decreases the I_1/I_2 ratio. It was pointed out in Section 2.3.3 that the variation of I_1/I_2 for a constant I_o does not significantly affect either the stiffness of the structure or the efficiency of the coupling when $I_1/I_2 > 0.25$. The equivalent moment of inertia ratio would be more than 0.25 if $I_1/I_2 > 0.5$. Thus for shear walls with $I_1/I_2 > 0.50$ the effect of cracking of wall 1 on laminar shear and top floor deflection is insignificant.

2.3.6 The Effects of Flexible Beam-Wall Joints

It has been assumed in the laminar analysis that the walls are rigid compared to the coupling beams. The deformation of the coupling beams due to the semi-rigid nature of finite joint, shown in Fig. 2.16, is ignored. It is difficult to determine the rigidity of this finite joint. It would be stiffer than the coupling beam but not infinitely stiff. The finite joint acts as an end block to the beam restraining it at the junction of the wall against rotation. Herein, an attempt is made to study the sensitivity of the static quantities for changes in

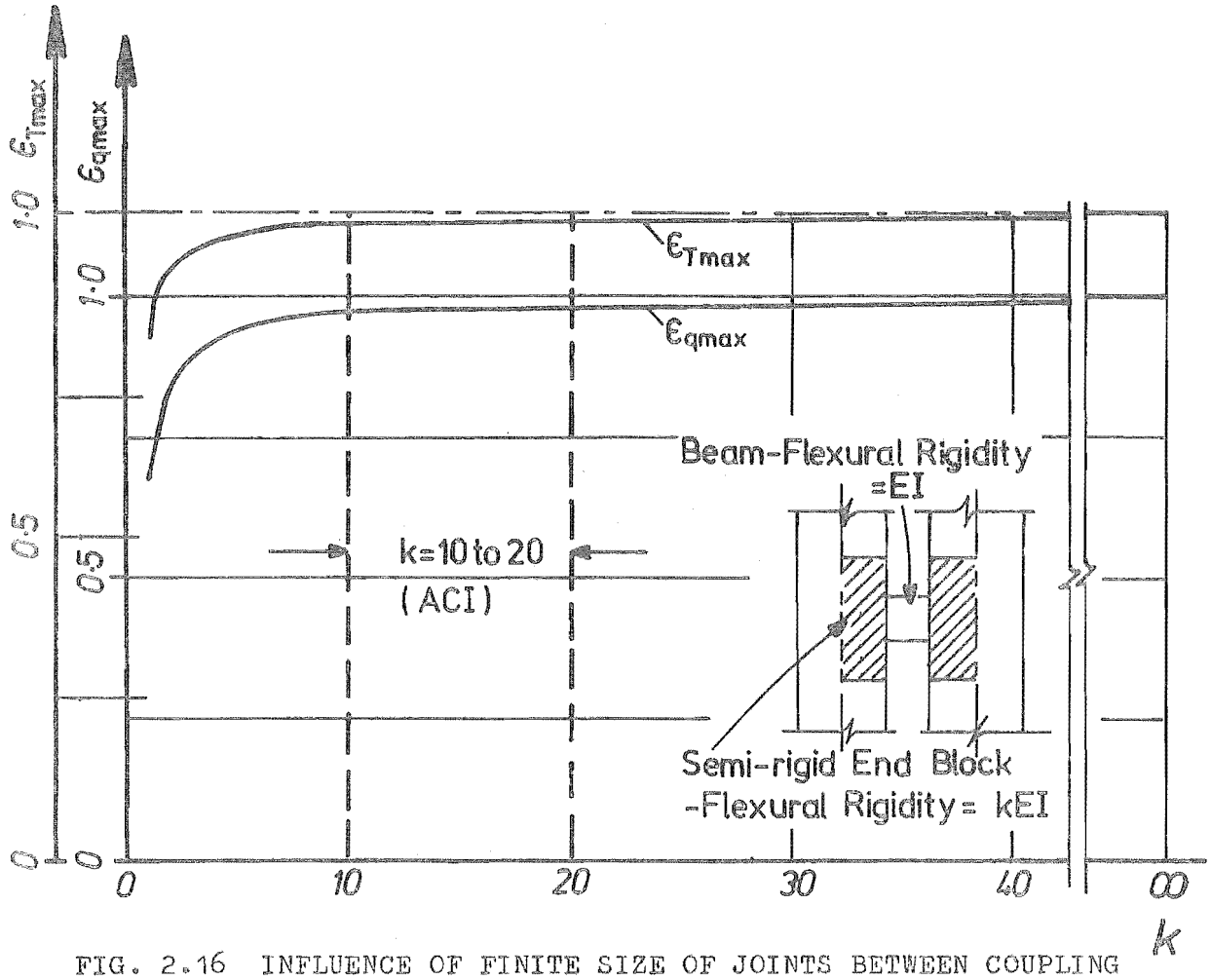

FIG. 2.16 INFLUENCE OF FINITE SIZE OF JOINTS BETWEEN COUPLING BEAM AND SHEAR WALL

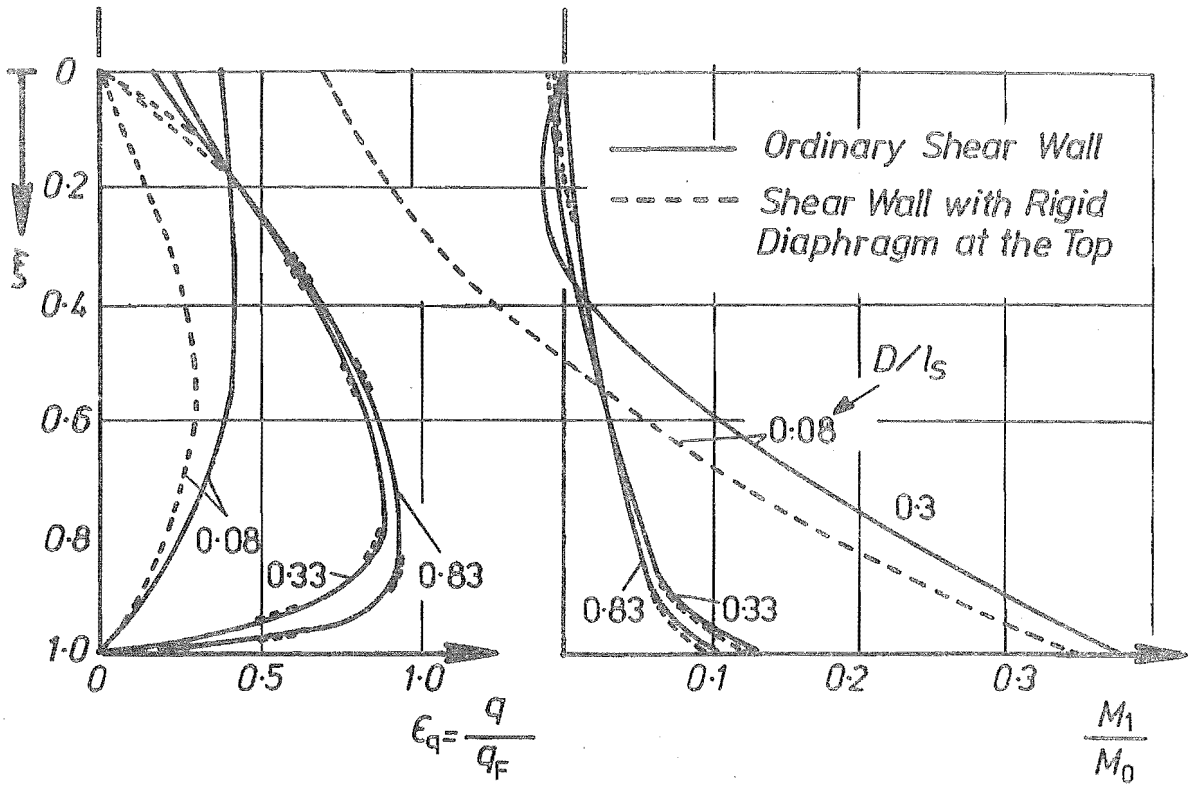

FIG. 2.17 COMPARISON OF ORDINARY SHEAR WALL AND SHEAR WALL WITH INFINITELY RIGID DIAPHRAGM AT THE TOP

the assumed values of rigidity for the finite joint. For this purpose the rigidity of the finite joint is expressed in terms of the rigidity factor, k, where

$$k = \frac{\text{flexural rigidity of the finite joint}}{\text{flexural rigidity of the beam}}$$

For the example structure, the critical design quantities were computed for various values of the rigidity factor, k, within the limits of $1 < k < \infty$. The plot in Fig. 2.16 shows the effect of flexible joints on the maximum laminar shear factor, ϵ_{qmax}, and maximum axial force factor, ϵ_{Tmax}. The maximum laminar shear factor, ϵ_{qmax}, is the ratio of the maximum laminar shear developed by the coupling beam having finite joints with rigidity factor, k, to the maximum laminar shear developed by a fictitious coupling beam having finite joints with rigidity factor $k = \infty$. Similarly, the maximum axial force factor, ϵ_{Tmax}, is the ratio of the maximum axial force developed in the walls of a coupled shear wall with coupling beams having finite joints with a rigidity factor k to the maximum axial force developed in a fictitious coupled shear wall having coupling beams with infinitely rigid finite joints. For comparison, the limits of end block rigidity suggested by the ACI Committee 442[79] are also shown. It can be seen that the error introduced in the elastic analysis of a shear wall with $k > 10$ is insignificant. However, cracking of the structure and consequent loss of bond forces which anchor the reinforcement of the coupling beams in the wall may more significantly alter the behaviour (stiffness) of the shear wall during post-elastic high intensity loading. This is discussed in Chapter 7 with reference to the post-elastic loading of Shear Wall B test specimen.

2.3.7 The Effect of a Rigid Diaphragm at the Top of the Two Walls

Infinitely rigid interconnection at the top arises in practical situations when a shear core extends above roof level and has no holes corresponding to those below. Fig. 2.17 compares the laminar shear

factor, ϵ_q , and bending moment ratio M_1/M_0 for a shear wall with infinitely rigid diaphragm at the top with that of a normal shear wall. For aspect ratios above 0.33, where the efficiency of coupling is good, there is very little difference in the maximum laminar shear and wall moments. However, for very lightly coupled shear walls there is a significant decrease in the laminar shear. Critical design quantities are hardly affected by the type of connection when coupling system is efficient.

2.4 OTHER METHODS OF ANALYSES

The use of the frame method and the finite element method in the analysis of a coupled shear wall is discussed briefly.

2.4.1 The Frame Method

Any plane frame computer programme is useful in the analysis of shear walls. However, to avoid significant errors the programme should consider

(a) finite joints (see Fig. 2.18)

(b) axial deformation of the walls

(c) shear deformation of the beams.

The inclusion of the above in the computer programme does not significantly affect the solution time. However,frame analyses, using stiffness matrix methods, was found to take three times as much time as the laminar analysis. (The time taken to analyse a 10-storey shear wall by the laminar method was 65 secs. on an IBM $360/44^{k}$ computer). A normal frame analysis also requires more input data compared to a laminar analysis.

The laminar analysis has been shown [42] to give significant errors in the following two cases.

(1) When the number of storeys is few

(2) When the stiffness of the walls approaches that of the beams.

These limitations do not apply to frame method. In particular, the

following variations can be accommodated without having to make simplifying assumptions as in laminar analysis:

(1) Different storey height

(2) Different foundation conditions

(3) Flexible Joints

(4) Variation in the properties along the height of the shear wall

(5) Second Order (P - Δ) effects.

2.4.2 The Finite Element Method

This involves division of the shear wall into a number of small elements. Force-displacement relationships of these elements are combined with equilibrium and compatibility conditions and the resulting equations are solved to obtain the unknown static quantities of the structure. For this, the use of a computer is indispensable. Elements commonly used in the shear wall analyses are shown in Fig. 2.19 [42,50,51,52,53,58,59]. Almost any shape of shear wall can be accommodated. The main disadvantages are:

(1) The analysis takes considerably more time than the laminar analysis. (448 sec for a 10-storey structure in the IBM 360/44^{k} computer)

(2) More input data is required compared with both the frame and laminar analysis

(3) There is no means of assessing the behaviour till the final results are obtained. In the laminar method the behaviour of the shear wall can be predicted using the parameter 'αH'.

2.5 THE FINITE DIFFERENCE METHOD

The application of the laminar analysis in its present form is restricted to shear walls which have uniform properties throughout the height for the beams and the walls. This idealised situation may not be realised even when the shear wall is uncracked. In tall shear

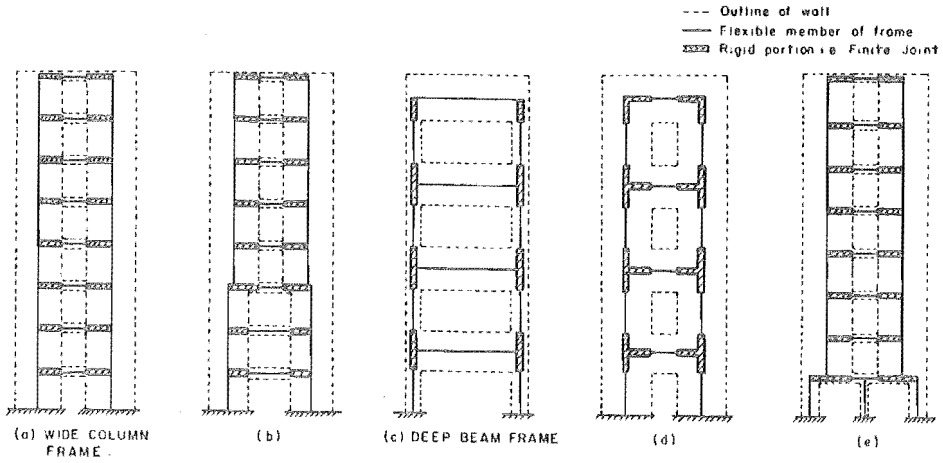

FIG. 2.18 FRAMES WITH FINITE JOINTS[42]

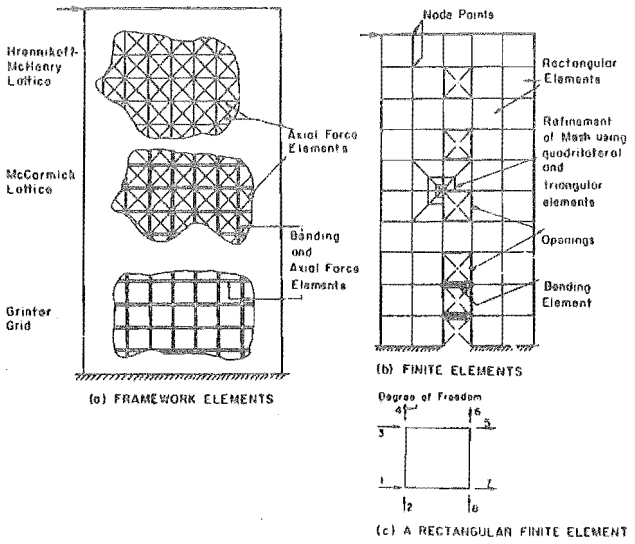

FIG. 2.19 VARIOUS TYPES OF ELEMENTS[42] USED IN THE ANALYSIS OF SHEAR WALLS

walls, the amount of steel in the beams may be varied so that the strength of the coupling system corresponds approximately with the elastic laminar shear distribution, as shown in Fig. 2.5. Though the laminar analysis has been extended [22, 23, 24, 25] to accommodate certain variations in the properties of the components with the height, these methods could not be used for a reinforced concrete shear wall in which the properties of the walls and beams vary considerably also due to cracking.

In the laminar analysis the compatibility of the deformations at the mid-points of the laminae led to the differential equation, (Eq. (2.4)). This, when solved in closed form, gave the unknown axial force, T . (Eq. (2.5)). In the laminar analysis several assumptions were made to enable a closed solution to be obtained. The differential equation of laminar action may be rearranged, incorporating variable properties for the walls and the coupling beams. This equation may then be transformed into a recurrence equation involving the unknown axial force at specified points (nodal points) as indicated in Fig. 2.20. These equations may then be solved by simple arithmetical means to obtain the unknown axial forces at these nodal points.

2.5.1 The Recurrence Equation

The equation, Eq. (2.4), which represents the compatibility of deformation at the mid-point of a lamina is modified to incorporate the variation in properties, thus

$$\int_x^H \frac{l_x M_o \, dx}{E_{wx} I_{ox}} - \int_x^H \frac{l_x^2 T_x \, dx}{E_{wx} I_{ox}} dx - \int_x^H \frac{1}{E_{wx}} \left(\frac{1}{A_{1x}} + \frac{1}{A_{2x}} \right) T_x dx$$

$$- \frac{h_x l_{sx}^3}{12 E_{bx} I_{Xx}} q_x = 0 \qquad \ldots (2.24)$$

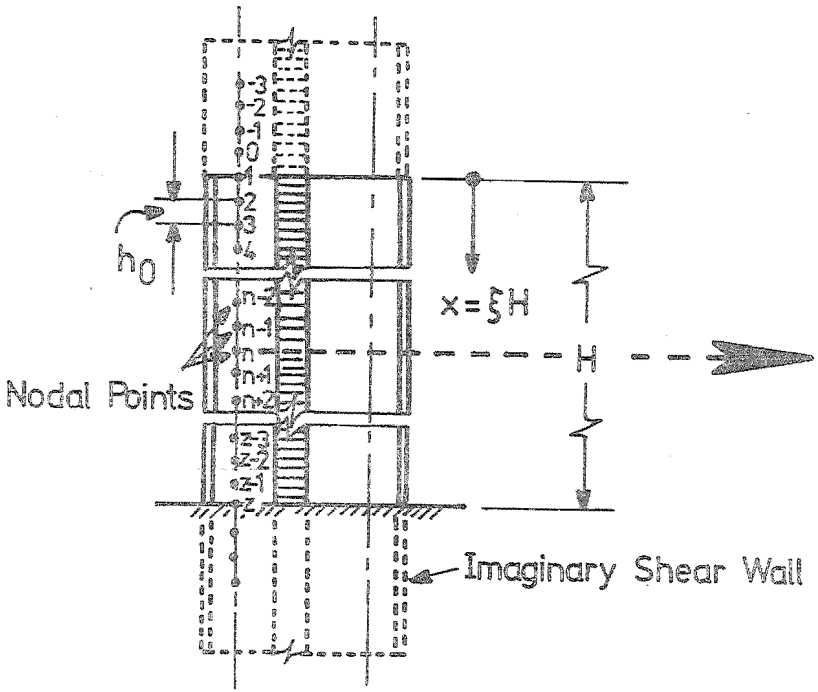

FIG. 2.20 MATHEMATICAL MODEL FOR THE FINITE DIFFERENCE METHOD OF SHEAR WALL ANALYSIS

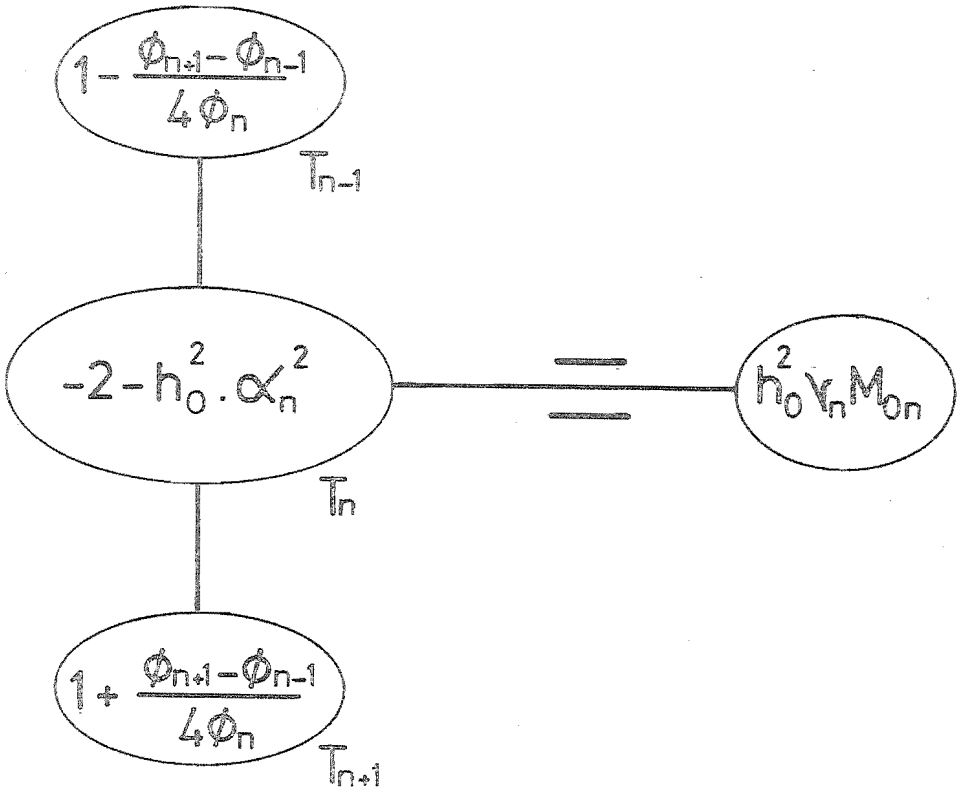

FIG. 2.21 FINITE DIFFERENCE OPERATOR FOR NODE 'n'

where E_{wx} = Youngs modulus of the wall at x from top

E_{bx} = Youngs modulus of the beam at x from top

A_{1x}, A_{2x}, I_{xx} , etc = dimensional properties of the beams and the walls which are variable. They refer to the corresponding properties at a distance x from top.

Differentiating the above equation with respect to x leads to

$$- \frac{M_o \, l_x}{E_{wx} \, I_{ox}} + \frac{1}{E_{wx}} \left(\frac{1}{A_{1x}} + \frac{1}{A_{2x}} + \frac{l_x^2}{I_{ox}} \right) T_x - \varphi \frac{dq_x}{dx} - q_x \frac{d\varphi}{dx} = 0 \qquad \ldots(2.25)$$

where $$\varphi = \frac{h \, l_{sx}^3}{12 E_{bx} I_{Xx}} \qquad \ldots(2.25a)$$

On dividing by φ and rearranging the terms, the above equation reduces to

$$\frac{d^2 T_x}{dx^2} + \left(\frac{\frac{d\varphi}{dx}}{\varphi} \right) \left(\frac{dT_x}{dx} \right) - \alpha^2 T_x = - \gamma \, M_o \qquad \ldots (2.26)$$

This is a differential equation involving the variables φ , α , γ , M_o and T with respect to x . All the above values except T are known at the nodal points. Reference may be made to Fig. 2.20 with respect to identification of the nodal points. Eq. (2.26) is transformed into the following recurrence equation involving the unknown axial forces at the discrete nodal points.

$$T_n - 1 \left[1 - \left(\frac{\varphi_{n+1} - \varphi_{n-1}}{4\varphi_n} \right) \right] + T_n \left[- 2 - h_o^2 \, \alpha_n^2 \right]$$

$$+ T_{n+1} \left[1 + \left(\frac{\varphi_{n+1} - \varphi_{n-1}}{4\varphi_n} \right) \right] = - h_o^2 \, \gamma_n \, M_{on} \qquad \ldots (2.27)$$

where h_o = distance between the nodal points. The subscripts denote the nodal point number for the variables.

In Fig. 2.21, this equation is shown as a difference operator for the nodal point n . The solution consists of:

(a) Applying the recurrence operator to all the nodal points (1 to z) to get z simultaneous linear algebraic equations.

(b) Transforming the boundary conditions into a difference form at the top and bottom of the shear wall and incorporating them in the above set of equations.

(c) Solving the equations to get the unknown axial forces at the z nodal points.

(d) Solving the other static quantities for the structure at these nodal points making use of the nodal axial forces.

2.5.2 Loading

Any type of load variation can be accommodated. The bending moment M_{on} is expressed in terms of the loads at the nodal points. For the general seismic loading shown in Fig. 2.1 using uniformly spaced nodal points

$$M_{on} = \frac{\rho WHn}{z} + \frac{\rho_1 WHn^2}{2z^2} + \frac{Wn^2H}{3z^3}\left(3z - n\right) \qquad \ldots (2.28)$$

where z = number of the nodal point at the base of the wall

n = number of the nodal point at which the bending moment is computed.

2.5.3 Boundary Conditions

The boundary conditions commonly encountered in practice are considered as follows:

(a) The boundary conditions at the top. (Fig. 2.22.a)

(i) Free at the top : At $n = 1$, $T_1 = 0$ ... (2.29)

(ii) With a rigid diaphragm at the top. (Fig. 2.22.b)

At $n = 1$, $\frac{dT}{dx} = 0$ since $q_1 = 0$ ... (2.30)

i.e. $\frac{T_2 - T_o}{2 h_o} = 0$

$$T_o = T_2 \qquad \ldots (2.31)$$

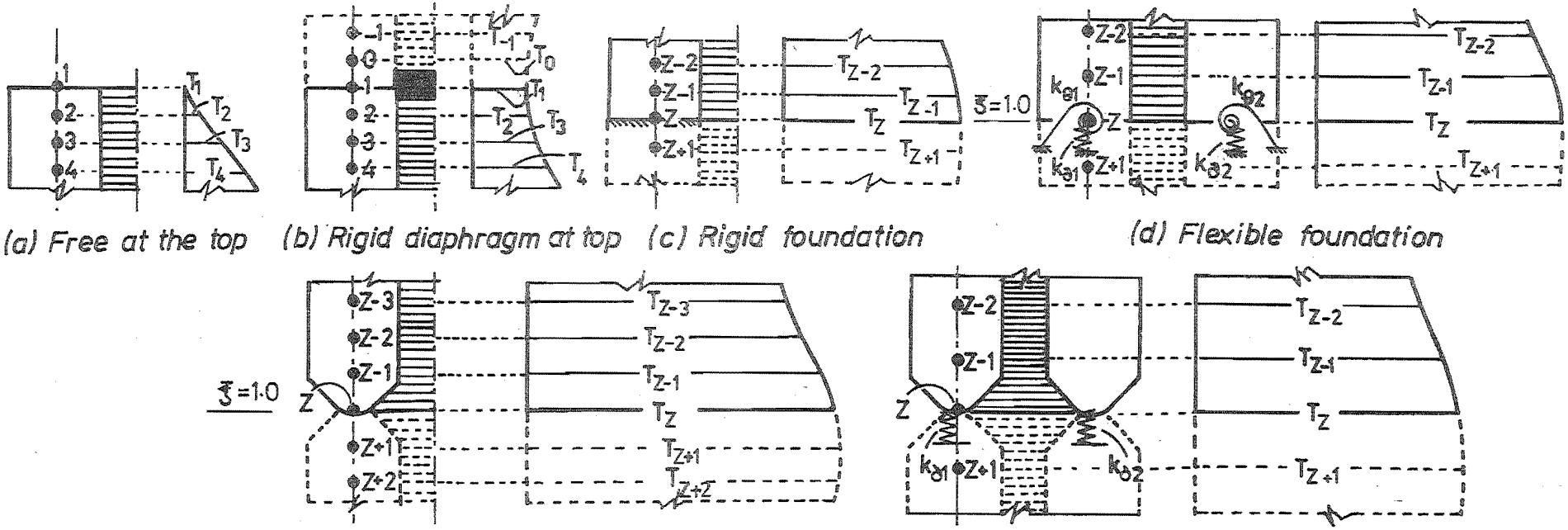

FIG. 2.22 THE BOUNDARY CONDITIONS FOR THE COUPLED SHEAR WALL IN THE FINITE DIFFERENCE FORM

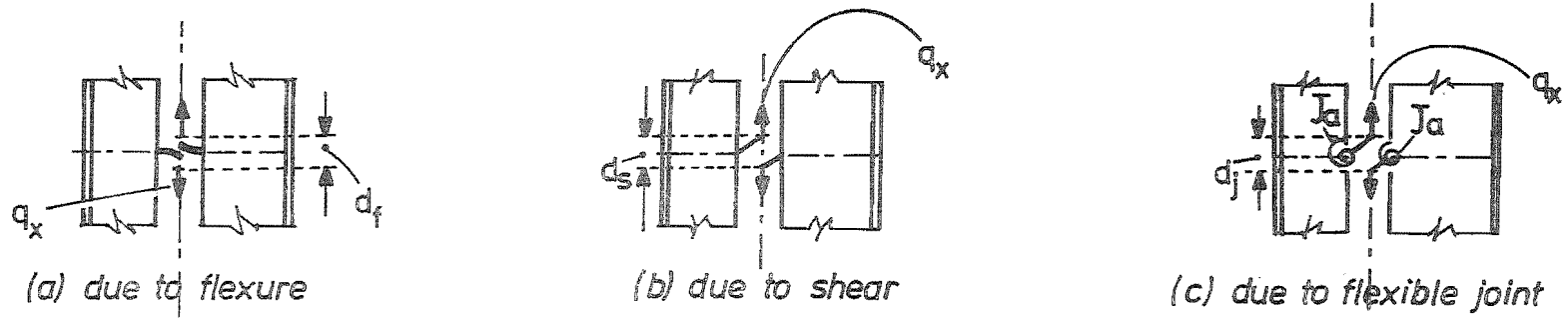

FIG. 2.23 THE DEFORMATIONS OF A TYPICAL LAMINA

(b) The boundary conditions at the base. (Fig. 2.22.c)

(i) Restrained at the base : At n = z , $\frac{dT}{dx} = 0$ since $q_z = 0$

$$\frac{T_{z+1} - T_{z-1}}{2 h_o} = 0$$

$$T_{z+1} = T_{z-1} \qquad \ldots (2.32)$$

(ii) Flexible foundation at the base. (Fig. 2.22.d)

The deformation due to the flexible foundation is incorporated into the deformation compatibility equation for the bottom most lamina thus

$$\int_x^H \frac{1 M_o dx}{E_w I_o} - \int_x^H \frac{1^2}{E_w I_o} T_x \, dx - \int_x^H \frac{1}{E_w} \left(\frac{1}{A_1} + \frac{1}{A_2} \right) T_x \, dx - \frac{h l_s^3}{12 E_b I_x} q_x - \Delta = 0 \qquad \ldots (2.33)$$

where Δ is the displacement due to foundation settlement. The first two terms of Eq. (2.33) represent 1 times the slope of the wall.

$$\text{i.e. } 1 \left(\frac{dy}{dx} \right) - \int_x^H \frac{1}{E_w} \left(\frac{1}{A_1} + \frac{1}{A_2} \right) T_x \, dx - \frac{h l_s^3}{12 E_b I_x} q_x - \Delta = 0 \qquad \ldots (2.34)$$

$$\text{At } x = H , \; 1 \left(\frac{dy}{dx} \right) - \varphi_z q_z - \Delta = 0 \qquad \ldots (2.35)$$

Mid points of the laminae are the points of contraflexure as per the assumptions made in the laminar analysis. The slopes of wall 1 and wall 2 at the foundation are the same.

The slope,

$$\left(\frac{dy}{dx} \right)_z = \theta_z = \frac{M_{1z}}{K_{\theta 1}} = \frac{M_{2z}}{K_{\theta 2}} = \frac{M_{1z} + M_{2z}}{K_{\theta 1} + K_{\theta 2}} = \frac{M_{oz} - 1 T_z}{K_\theta} \qquad \ldots (2.36)$$

where $K_\theta = K_{\theta 1} + K_{\theta 2}$ $\qquad \ldots (2.37)$

$K_{\theta 1}$, $K_{\theta 2}$ = the rotational stiffness of foundation under wall 1 and wall 2 respectively.

The vertical settlement is

$$\Delta = \frac{T_z}{K_{\delta 1}} + \frac{T_z}{K_{\delta 2}} = \frac{T_z}{K_\delta} \qquad \ldots (2.38)$$

where $$\frac{1}{K_\delta} = \frac{1}{K_{\delta 1}} + \frac{1}{K_{\delta 2}} \qquad \ldots (2.39)$$

$K_{\delta 1}$, $K_{\delta 2}$ = the vertical displacement stiffness under wall 1 and wall 2 respectively.

Using Eqs. (2.35) to (2.39), the boundary condition at z is written as

$$\left(\frac{dT}{dx}\right)_z = -\left(F_r + F_s\right) T_z + \frac{F_r}{l} M_o \qquad \ldots (2.40)$$

where $$F_r = \frac{l^2}{\varphi K_\theta} \qquad \ldots (2.41)$$

and $$F_s = \frac{1}{\varphi K_\delta} \qquad \ldots (2.42)$$

Eq. (2.40) is transformed into the finite difference form as follows:

$$\frac{T_{z+1} - T_{z-1}}{2h_o} = -\left(F_r + F_s\right) T_z + \frac{F_r}{l} M_o \qquad \ldots (2.43)$$

which leads to

$$T_{z+1} = T_{z-1} - 2h_o \left(F_r + F_s\right) T_z + 2h_o \frac{F_r}{l} M_o \qquad \ldots (2.44)$$

If F_r and F_s are both zeros, Eq. (2.44) reduces to the familiar boundary condition for fully rigid foundations in Eq. (2.32).

(iii) Hinged base (Fig. 2.22.d)

For this condition Eq. (2.34) reduces to

$$l\left(\frac{M_o - lT_x}{E_x I_o}\right) - \int_x^H \frac{1}{E_w}\left(\frac{1}{A_1} + \frac{1}{A_2}\right) T_x \, dx - \frac{hl_s^3}{12E_b T_x} q_x = 0 \qquad \ldots (2.45)$$

At $n = z$,

$$1\left(\frac{M_{oz} - 1T_z}{E_w I_{oz}}\right) - \varphi\left(\frac{T_{z+1} - T_{z-1}}{2h_o}\right) = 0 \qquad \ldots\ldots (2.46)$$

This reduces to

$$T_{z+1} = T_{z-1} + \frac{2h_o 1}{E_w I_{oz} \varphi}\left(M_{oz} - 1T_z\right) \qquad \ldots (2.47)$$

(iv) Hinged base on elastic foundation.(Fig. 2.22.e)

For this condition Eq. (2.34) reduces to

$$1\left(\frac{M_o - 1T_x}{E_w I_o}\right) - \int_x^H \frac{1}{E_w}\left(\frac{1}{A_1} + \frac{1}{A_2}\right) T_x \, dx - \frac{hl_s^3}{12E_b I_x} q_x - \Delta = 0 \qquad \ldots (2.48)$$

Combining this with Eqs. (2.38) and (2.39) at $x = H$,

$$T_{z+1} = T_{z-1} - 2h_o F_s T_z + \frac{2h_o 1}{\varphi E_w I_{oz}}\left(M_o - 1T_z\right) \qquad \ldots (2.49)$$

When $F_s = 0$ Eq. (2.49) reduces, because of the changed boundary condition for hinged foundation, to Eq. (2.47).

In practice these boundary conditions may occur in any combination. These can be incorporated into the algebraic equations obtained from applying the recurrence operator to the nodes, before solving for the unknown axial forces.

2.5.4 Flexible Beam-Wall Joints

The effect of flexible joints is incorporated into the laminar analysis by introducing a factor J_a to represent the joint modulus[80] in the expression for equivalent or reduced moment of inertia, I_x , of the coupling beam. The additional deflection due to the flexibility of the joint (see Fig. 2.23.c)

$$d_j = \frac{hl_s^2}{2 J_a} q_x \qquad \ldots (2.50)$$

Combining this with the deflections of the lamina due to flexure, d_f, and shear, d_s, shown in Fig. 2.23, gives the laminar deflection,

$$d_b = d_f + d_s + d_j = \frac{h l_s^3}{12 E_b I_b} \left\{ 1 + \frac{12 E_b I_b f}{G A l_s^2} + \frac{12 E_b I_b}{2 J_a I_s} \right\} q_x \quad \ldots (2.51)$$

The equivalent or reduced moment of inertia derived by Paulay[74] is modified as

$$I_x = \frac{I_b}{\left\{ 1 + \frac{12 E_b I_b f}{G A l_s^2} + \frac{6 E_b I_b}{J_a l_s} \right\}} \quad \ldots (2.52)$$

The value of J_a can either be assumed or obtained using the curves of Bhatt[81].

2.5.5 Computer Storage and Time

The total number of independent unknowns (T) for this problem is equal to the number of nodal points. All other unknowns like q, M_1, M_2, etc, are directly solved once these axial forces are found. As the nodal numbers follow a regular pattern, the input data for the shear wall at the nodal points are generated for the storeys in which there is no variation of the properties with height. This reduces the total input data. The bandwidth of the matrix formed by the coefficients of the simultaneous difference equations is only 3. This tri-banded form of the matrix is taken advantage of in reducing the storage requirement.

2.5.6 Shear Walls with Two or More Rows of Openings

The procedure as explained above is extended to analyse shear walls with two or more rows of openings. For each row of opening one compatibility equation for the deformation of the laminae is set up. These differential equations are coupled. A shear wall with two rows of openings is shown in Fig. 2.24. The coupled differential equations for span A and span B of this shear wall are:

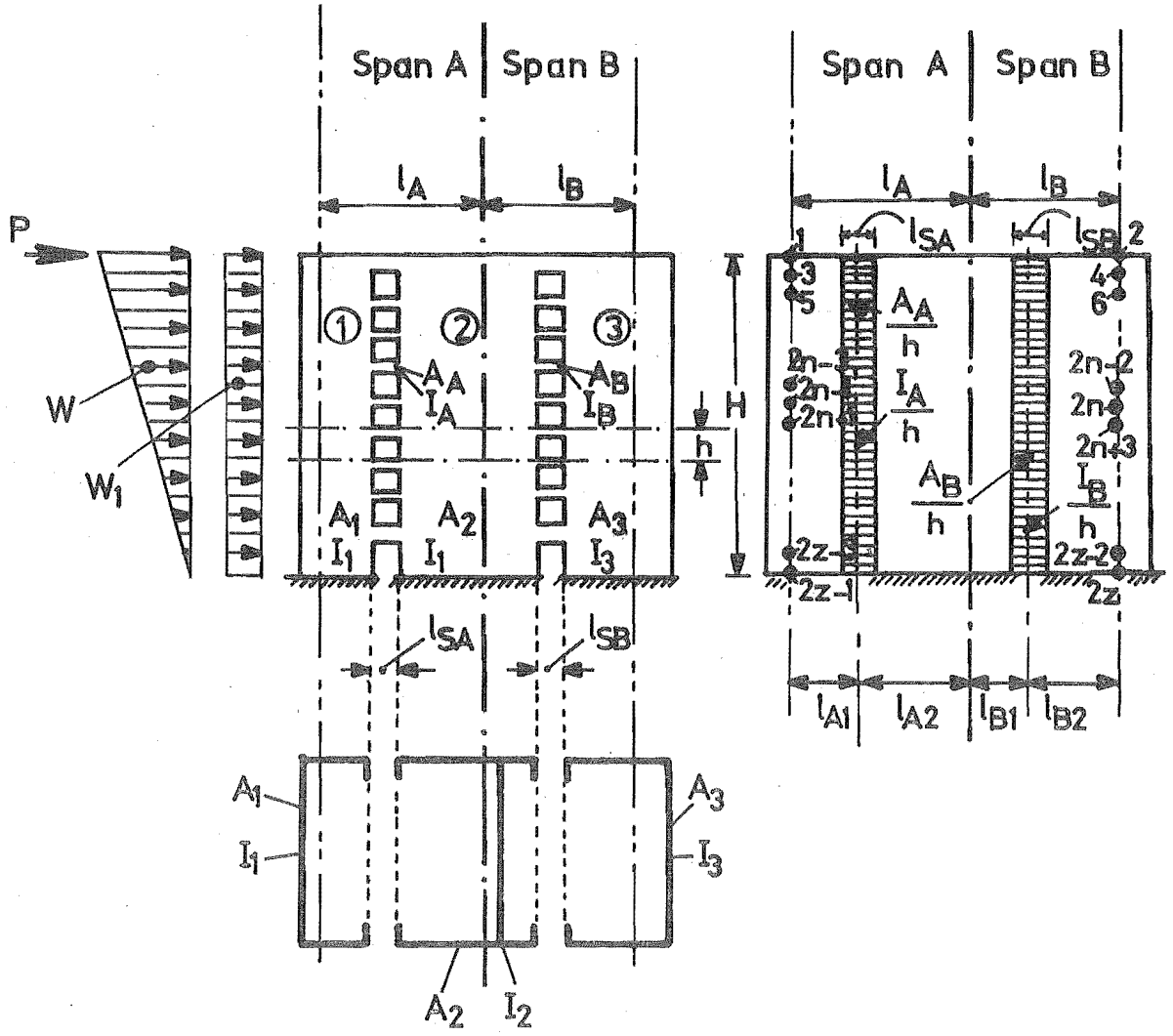

FIG. 2.24 A PROTOTYPE COUPLED SHEAR WALL STRUCTURE WITH TWO ROWS OF OPENINGS AND ITS MATHEMATICAL FINITE DIFFERENCE MODEL

$$\frac{d^2T_A}{dx^2} + \frac{d\varphi_A}{\varphi_A dx}\frac{dT_A}{dx} - \alpha_A^2 T_A - \psi^2 T_B = \gamma_A M_o \qquad \ldots (2.53)$$

and

$$\frac{d^2T_B}{dx^2} + \frac{d\varphi_B}{\varphi_B dx}\frac{dT_B}{dx} - \alpha_B^2 T_B - \psi^2 T_A = \gamma_B M_o \qquad \ldots (2.54)$$

where the parameter $\psi^2 = \frac{l_A l_B}{E_W I_o} - \frac{1}{E_W A_2}$ ... (2.55)

the axial force in wall (1) $T_A = \int_x^H q_{Ax}\, dx$ ... (2.56)

the axial force in wall (3) $T_B = \int_x^H q_{Bx}\, dx$ ... (2.57)

the parameters α_A , γ_A , φ_A and α_B , γ_B , φ_B are the values of α , γ , φ (Eq. (2.3), Eq. (2.4), Eq. (2.2b)) for the span A and span B respectively.

The recurrence equation for the nodal points $2n-1$ and $2n$ are:

$$\left\{ 1 - \frac{\varphi_{A(2n+1)} - \varphi_{A(2n-3)}}{4\,\varphi_{A(2n-1)}} \right\} T_{A(2n-3)} + \left(0\right) T_{B(2n-2)}$$

$$+ \left(h_o^2\, A_{(2n-1)} - 2\right) T_{A(2n-1)} + \left(h_o^2\, B_{(2n)}\right) T_{B(2n)}$$

$$+ \left\{ 1 + \frac{\varphi_{A(2n+1)} - \varphi_{A(2n-3)}}{4\,\varphi_{A(2n-1)}} \right\} T_{A(2n+1)} = h_o^2\, C_{(2n-1)} \qquad \ldots (2.58)$$

and

$$\left\{ 1 - \frac{\varphi_{B(2n+2)} - \varphi_{B(2n-2)}}{4\,\varphi_{B(2n)}} \right\} T_{B(2n-2)} + \left(h_o^2\, D_{(2n-1)} \right) T_{A(2n-1)}$$

$$+ \left(h_o^2\, E_{(2n)} - 2 \right) T_{B(2n)} + \left(0 \right) T_{A(2n+1)} + \left\{ 1 + \frac{\varphi_{B(2n+2)} - \varphi_{B(2n-2)}}{4\,\varphi_{B(2n)}} \right\}$$

$$T_{B(2n+2)} = h_o^2\, F_{(2n)} \qquad \ldots (2.59)$$

where the subscripts A and B correspond to the values for span A and span B respectively. The bracketed subscripts correspond to the nodal point number. Reference may be made to Fig. 2.24 with regard to identification of the nodal points.

$A_{(2n-1)} = -\alpha^2$ for the left hand span at (2n-1)

$B_{(2n)} = -\psi^2$ at (2n)

$C_{(2n-1)} = \gamma M_o$ for the left span at (2n-1)

$D_{(2n-1)} = -\psi^2$ at (2n-1)

$E_{(2n)} = -\alpha^2$ for the right span at (2n)

$F_{(2n)} = \gamma M_o$ for the right span at (2n)

The nodal numbers are odd for span A and even for span B. The recurrence equation in the operator form is shown in Fig. 2.25. The equations obtained by applying these operators to all the nodal points, together with the boundary conditions at the top and bottom of the walls give as many linear, algebraic, simultaneous equations as the unknown values of axial forces at the nodes. The other static quantities for the structure (q_A , q_B , etc) are again obtained using the principles of statics. The details regarding the loading, boundary conditions etc. are not included here as the steps involved are similar to those explained in the previous sections for the shear wall with a single row of openings.

Finally, the analyses presented above could be made use of to allow for the discrete nature of the coupling beams. For this, zero

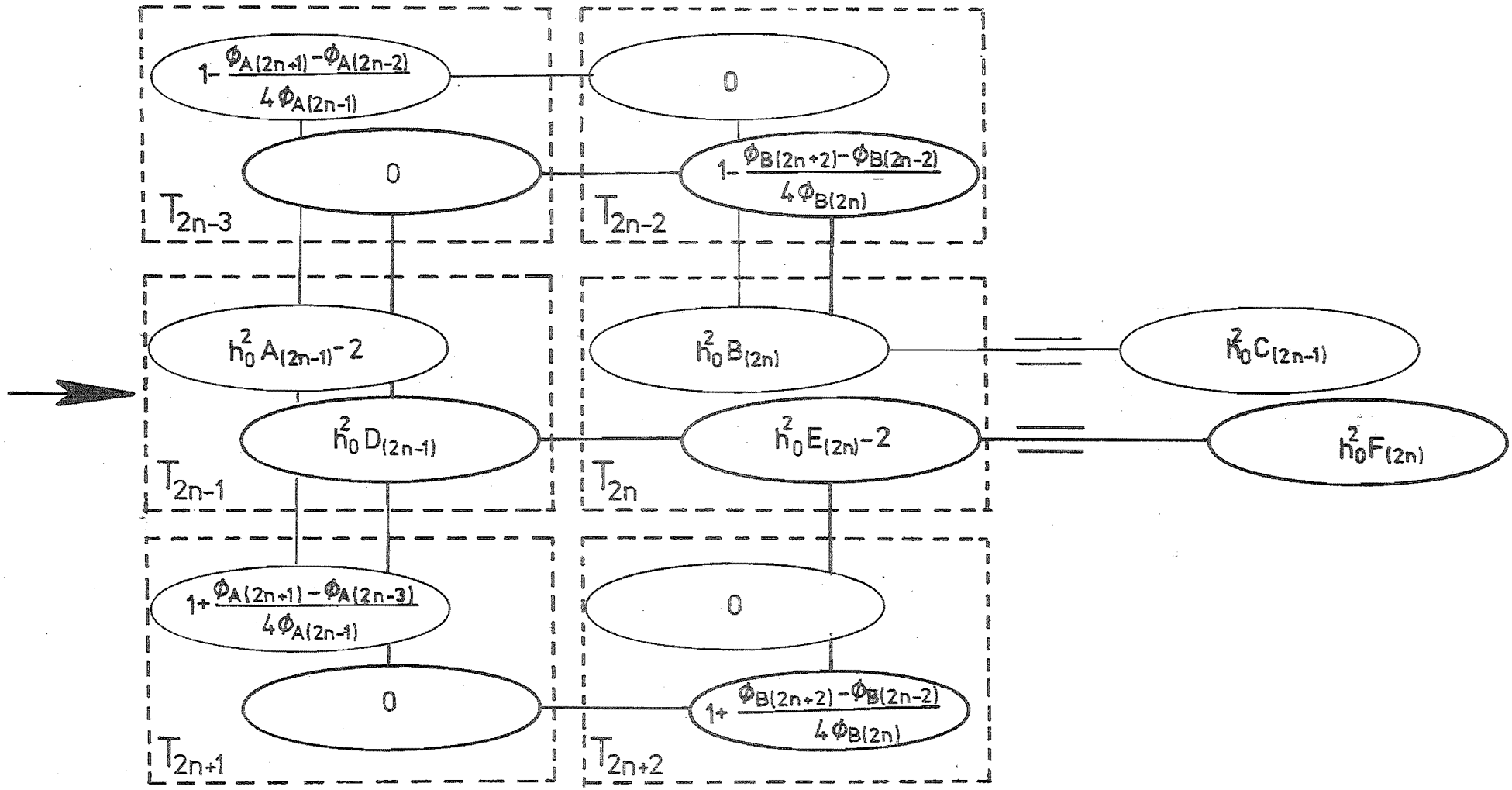

FIG. 2.25 THE FINITE DIFFERENCE OPERATOR FOR THE COUPLED DIFFERENTIAL EQUATION

beam properties may be assigned for the nodes associated with the openings and the relevant beam properties for the nodes associated with the beams. A sensitivity analysis was made to assess the order of errors introduced by this approximate method on the static design quantities. This was done by choosing different number of nodal points. The details of this analysis are not shown. The analysis showed that the order of errors introduced on critical design quantities is less than 5% provided that

(a) The number of storeys is more than 6

(b) The stiffness of the walls is comparable to the stiffness of the coupling beams, i.e. $\alpha H > 6$

(c) The distance between the nodal points is less than half the floor height, i.e. $h_o < 0.5h$.

2.6 NUMERICAL EXAMPLES

To illustrate the application of the finite difference method to the shear walls with varying properties two examples are considered. One is a coupled shear wall structure with a single row of openings and the other with two rows of openings. In these examples, the properties of the walls have been assumed to vary in each storey. It is unlikely that in a real structure variation of this nature would occur. These examples are used to illustrate the application of the finite difference method to a coupled shear wall structure. The examples were not intended to simulate the prototype structure. In the second example the properties of the coupling beams also vary with height. The results are also obtained using the laminar analysis, assuming uniform average properties, to estimate the errors involved due to this assumption. The final results, in both the examples, are compared with those obtained using a frame analysis.

2.6.1 Coupled Shear Wall with Single Row of Openings

A ten storey shear wall core is considered. Openings at each floor pierce the opposite walls of the box section. Reference may be made to Fig. 2.1 with respect to the notations. The properties of the structure and the loading are assembled in Table 2.3. The following three analyses were made.

Analysis A : The properties given in Table 2.3 were used. The shear wall was analysed by the conventional frame analysis which incorporates finite joints, axial deformation of walls and the shear deformation of beams.

Analysis B : The properties given in Table 2.3 were used. The shear wall was analysed using finite difference approximation given in Section 2.5.

Analysis C : Average uniform properties were assumed as follows: $A_1 = 4.55 \times 10^3$ in^2 , $A_2 = 4.65 \times 10^3$ in^2 , $I_1 = 5.25 \times 10^6$ in^4 , $I_2 = 6.75 \times 10^6$ in^4 , h = 105 in. instead of variable properties. The shear wall was analysed using laminar analysis given in Section 2.2.

The results are presented in Fig. 2.26. The diagrams show that:

(a) The number of nodal points was ample so that the errors introduced by the finite difference method, when compared with the results of the frame analysis, were negligible.

(b) For the example structure the assumption of average properties introduced errors which may be considered acceptable for design purposes. For significant quantities they are shown in Table 2.4.

The total computation times required to analyse this shear core by the above mentioned three analyses are: Analysis A - 189 sec., Analysis B - 85 sec., Analysis C - 65 sec. The number of nodal points used for Analysis B was 75 .

TABLE 2.3 PROPERTIES OF SHEAR WALL WITH A SINGLE ROW OF OPENINGS

FLOOR	WALL PROPERTIES				FLOOR HEIGHT
	A_1	A_2	I_1	I_2	h
	$\times 10^3 in^2$	$\times 10^3 in^2$	$\times 10^6 in^4$	$\times 10^6 in^4$	in
10th	3.55	3.65	3.90	4.50	90
9	3.75	3.85	4.20	5.00	105
8	3.95	4.05	4.50	5.55	105
7	4.15	4.25	4.80	6.00	105
6	4.35	4.45	5.10	6.50	105
5	4.55	4.65	5.40	7.00	105
4	4.75	4.85	5.70	7.50	105
3	4.95	5.05	6.00	8.00	105
2	5.35	5.45	6.30	8.50	120
1	5.55	5.65	6.60	9.00	120

Constant Data:

Total height of shear wall H = 1065 in.
Span l = 168.7 in., l_1 = 82.2 in., l_2 = 86.5 in.
Overall dimension of shear core: 15'-0" x 12'-0"
Beam properties: All beams are of same size and strength
Depth D = 24 in., Width B = 14 in.,
Span l_s = 38 in.
Young's modulus E = 5000 ksi.
Load: Total base shear = 340 kips.
Triangular load W = 300 kips.
Uniformly distributed load W_1 = 0 kips
Point load P = 40 kips.

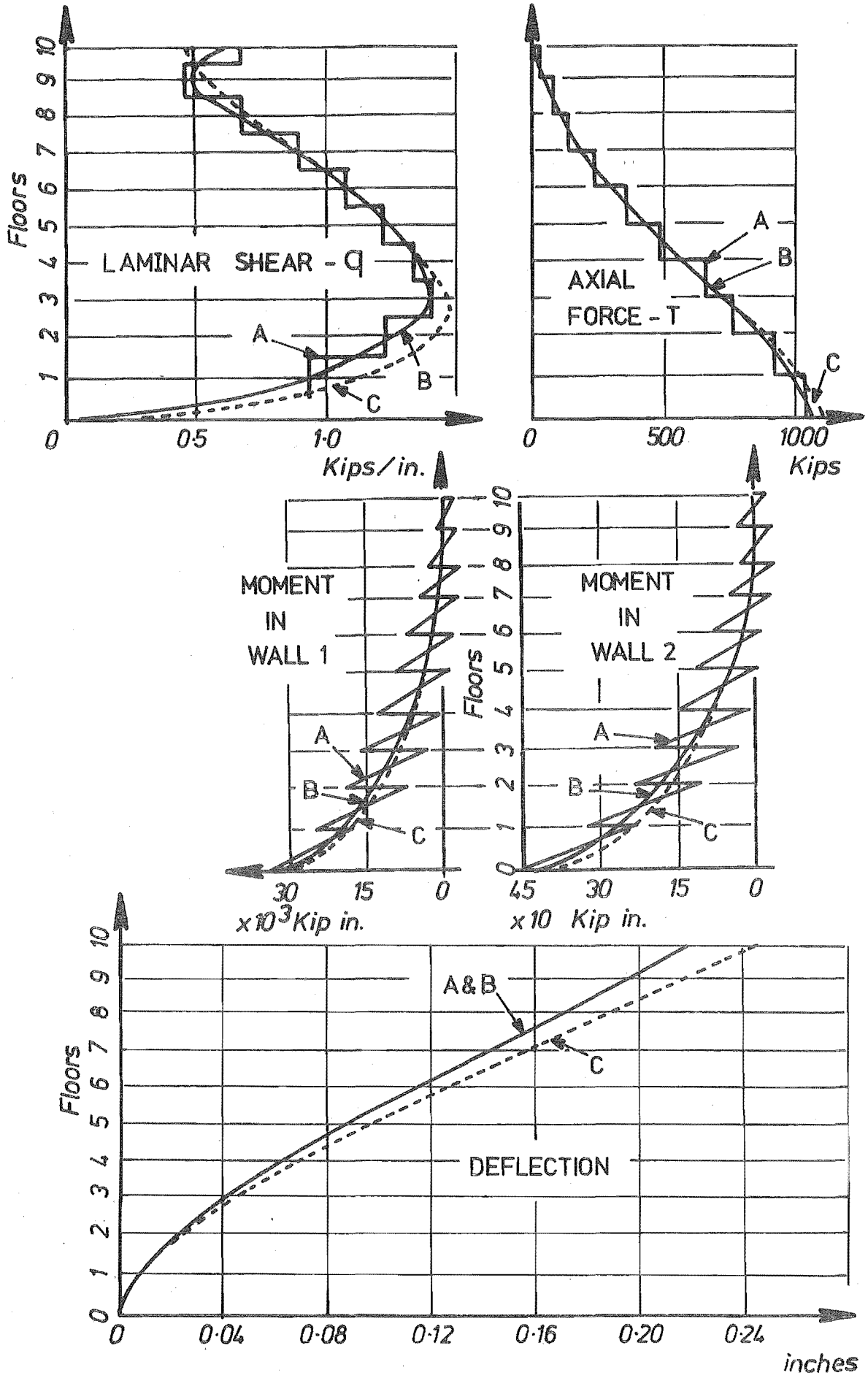

FIG. 2.26 RESULTS OF THE ANALYSIS OF A 10-STOREY COUPLED SHEAR WALL WITH SINGLE ROW OF OPENINGS

TABLE 2.4 COMPARISON OF ANALYSES FOR THE SHEAR WALL WITH SINGLE ROW OF OPENINGS

Significant response examined	Units	Analyses A and B	Analysis C	% Error
Shear in the critical beam Q_b	Kips	105 x 1.41 x 0.50 = 74.02	105 x 1.48 x 0.50 = 77.70	+ 4.97
Shear in the top beam Q_{bt}	Kips	45 x 0.68 x 0.50 = 15.30	45 x 0.46 x 0.50 = 10.70	- 30.00*
Axial force at the base T	Kips	1040	1100	+ 5.76
Wall moment 1 at the base M_1	Kip.in.	32.5×10^3	28×10^3	- 13.84
Wall moment 2 at the base M_2	Kip.in.	44.5×10^3	40×10^3	- 10.1
Deflection at the top Δ	In.	0.110	0.123	+ 11.81

* This is not critical in the design.

2.6.2 Coupled Shear Wall with Two Rows of Openings

A ten storey shear core combining two wells was considered. Openings at each floor pierce the opposite walls of the twin box section. Reference may be made to Fig. 2.24 with respect to dimension, shape and notation. The properties of the structure and the loading are assembled in Table 2.5. The following three analyses were considered.

Analysis A : The properties given in Table 2.5 were used. The shear wall was analysed as a conventional frame incorporating finite joints, axial deformations of the walls and the shear deformations of the beams.

Analysis B : The properties given in Table 2.5 were used. The shear wall was analysed using finite difference approximation as given in Section 2.5.6.

Analysis C : Average uniform properties were used as follows: $A_1 = 4.55 \times 10^3 in^2$, $A_2 = 4.65 \times 10^3 in^2$, $A_3 = 5.75 \times 10^3 in^2$, $I_1 = 5.25 \times 10^6 in^4$, $I_2 = 6.75 \times 10^6 in^4$, $I_3 = 9.75 \times 10^6 in^4$, $A_A = 874\ in^2$, $A_B = 1034\ in^2$, $h = 105$ in. For this case also the shear wall was analysed using finite difference approximation.

The results are presented in Fig. 2.27. The diagrams show that the differences between the results for the three analyses are negligible.

For the example structure with assumed average properties, the resulting errors are given in Table 2.6.

The total computer time required to analyse this twin shear core by the above mentioned three analyses are: Analysis A - 248 sec., Analysis B - 125 sec., Analysis C - 120 sec. The number of nodal points used for the analyses B and C was 100 .

TABLE 2.5 PROPERTIES OF THE TWIN CORE SHEAR WALL

FLOOR	WALL PROPERTIES						BEAM PROPERTIES		FLOOR HEIGHT
	A_1	A_2	A_3	I_1	I_2	I_3	A_A	A_B	h
	$\times 10^3 in^2$	$\times 10^3 in^2$	$\times 10^3 in^2$	$\times 10^6 in^4$	$\times 10^6 in^4$	$\times 10^6 in^4$	in^2	in^2	in
10th	3.55	3.65	4.75	3.90	4.50	7.50	794	998	90
9th	3.75	3.85	4.95	4.20	5.00	8.00	794	998	105
8th	3.95	4.05	5.15	4.50	5.50	8.50	794	998	105
7th	4.15	4.25	5.35	4.80	6.00	9.00	842	1055	105
6th	4.35	4.45	5.55	5.10	6.50	9.50	842	1055	105
5th	4.55	4.65	5.75	5.40	7.00	10.00	842	1055	105
4th	4.75	4.85	5.95	5.70	7.50	10.50	987	1240	105
3rd	4.95	5.05	6.15	6.00	8.00	11.00	987	1240	105
2nd	5.35	5.45	6.55	6.30	8.50	11.50	987	1240	120
1st	5.55	5.65	6.75	6.60	9.00	12.00	987	1240	120

Constant Data

Total height of shear wall H = 1065 , Overall dimension of shear cores = 22'-0" x 12'-0"
Span l_A = 168.7 in, l_{A1} = 82.2 in, l_{A2} = 86.5 in, Span l_B = 204.4 in, l_{B1} = 91.8 in., l_{b2} = 112.8 in.
Beam properties for span A : Beam depth D_A = 24.0,in, Width B_A = 14.0 in, Span l_{SA} = 38 in.
Beam properties for span B : Beam depth D_B^A = 30.0 in, Width B_B^A = 14.0 in, Span l_{SB} = 45 in.
Load: Total base shear = 550 Kips

Triangular load W = 400 Kips, Uniformly distributed load W_1 = 100 Kips, Point load P = 50 Kips.

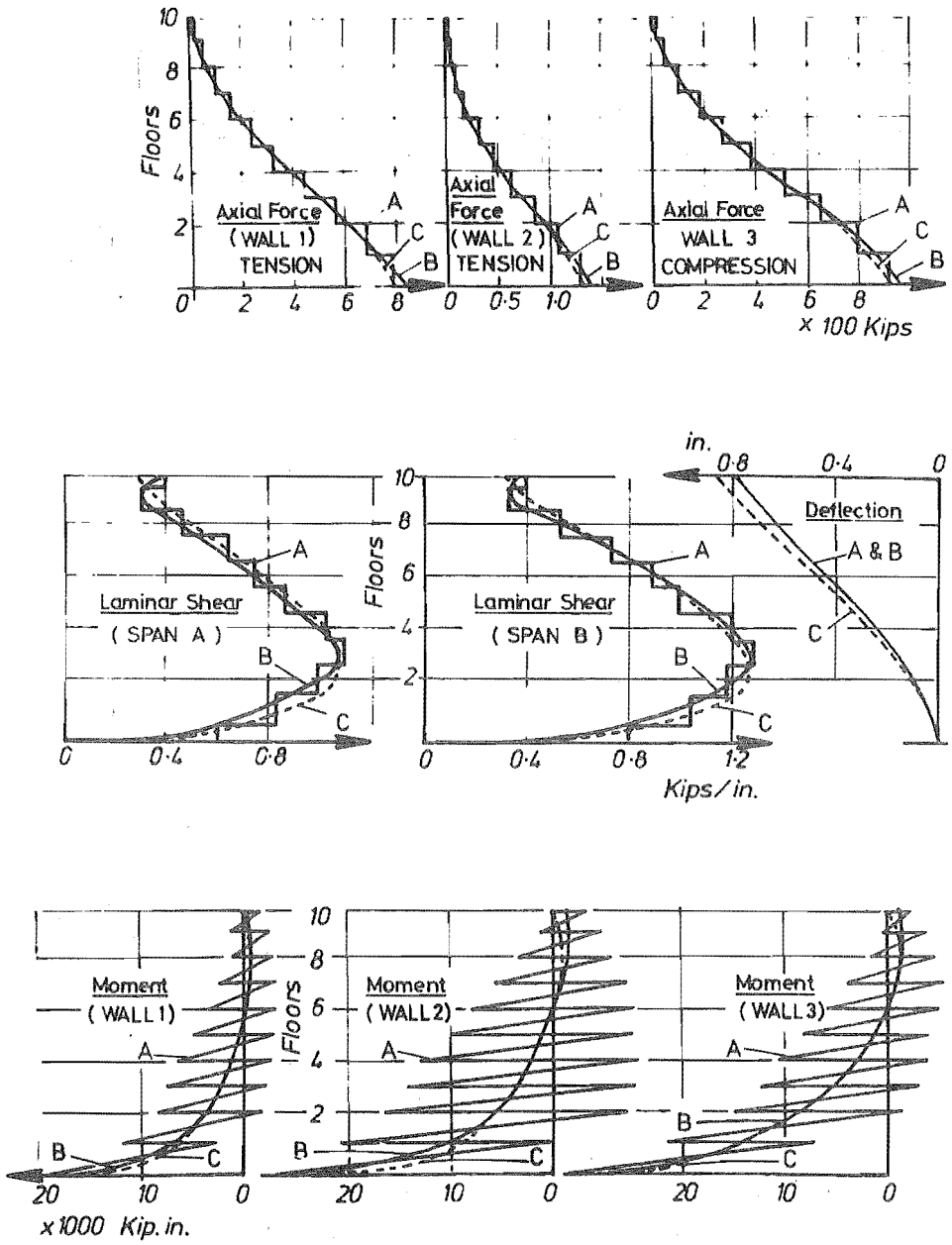

FIG. 2.27 RESULTS OF THE ANALYSIS OF A 10-STOREY COUPLED SHEAR WALL TWO ROWS OF OPENINGS

TABLE 2.6 COMPARISON OF ANALYSES FOR THE SHEAR WALL WITH TWO ROWS OF OPENINGS

Significant response examined	Units	Analyses A and B	Analysis C	% Error
Shear in the critical beam in the left span	Kips	105 x 1.09 x 0.5 = 57.20	105 x 1.06 x 0.5 55.60	- 2.82
Shear in the critical beam in the right span	Kips	105 x 1.28 x 0.5 = 67.20	105 x 1.23 x 0.5 64.60	- 3.87
Shear in the top beam in the left span	Kips	45 x 0.39 x 0.5 = 8.80	45 x 0.30 x 0.5 6.75	- 23.01*
Shear in the top beam in the right span	Kips	45 x 0.40 x 0.5 = 9.00	45 x 0.32 x 0.5 7.20	- 20.00*
Axial force				
in wall 1	Kips	782.0	786.0	+ 0.56
in wall 2	Kips	129.0	137.1	+ 0.08
in wall 3	Kips	-912.0	-923.1	- 0.01
Bending moment				
in wall 1	Kips	18,700	17,950	- 4.01
in wall 2	Kips	27,200	26,300	- 3.33
in wall 3	Kips	31,800	31,400	- 0.00
Deflection at the top	in.	0.080	0.088	+ 10.00

* These are not critical in design.

2.7 CONCLUSIONS

1. For an efficient coupling, the designer should aim at selecting the overall dimensions of the coupling beams so that the aspect ratio D/l_s is greater than 0.33. In the above range the following variables do not significantly affect the static quantities, i.e. laminar shear, axial force, and wall moments:

(a) Provision of rigid diaphragm at the top.

(b) Variation of relative stiffness of the walls.

(c) Variation of total stiffness of the walls.

2. It is preferable to choose the dimensions of the walls so that the wall moment of inertia ratio I_1/I_2 is greater than 0.50.

3. For an efficient shear wall structure the critical parameter, αH, should not be less than 7.

4. For beam aspect ratio, $D/l_s > 0.60$ cracking does not significantly affect the static design quantities.

5. The finite difference technique is a powerful method of analysis for structures in which properties vary with height. This analysis requires considerably less computer storage and time than the frame analysis. The following variables have been accommodated in the finite difference approximation to laminar analysis:

(a) Variation of properties of members with height.

(b) Variation in storey height.

(c) Various boundary conditions likely to be met with in practice.

(d) Shear walls with one or two rows of openings.

(e) Flexible beam-wall joints.

6. The order of error introduced to static design quantities due to the use of finite difference approximation is less than 5% provided that

(a) The number of storeys is more than 6

(b) The distance between the nodal points is less than

half the floor height, i.e. $h_o < 0.5h$

(c) The stiffness of the walls is comparable to the stiffness of the coupling system, i.e. $\alpha H > 6$.

CHAPTER THREE

THE PROPERTIES OF THE CRACKED COMPONENTS IN COUPLED SHEAR WALLS

3.1 INTRODUCTION

It was shown in the previous chapter that the coupling system plays an important part in the transfer of load to the foundations. The external lateral load generates flexure, shear and axial loads in the walls and bending in the presence of high shear stresses in the coupling beams. It is of considerable importance to assess the stiffness of these coupling beams in order to be able to predict their contribution to the resistance of the total external moment in the elastic range of behaviour.

Cracking in the walls is affected by the axial loads present. In one of the walls axial tension may encourage the development of cracks and consequent loss of stiffness. The loss of stiffness is more near the bottom floors. This is likely to affect the relative contribution of the walls to the resistance of the external load.

Herein, an attempt is made to assess the strength and the stiffness properties of the cracked components of the shear wall in order to predict more accurately their elastic and elasto-plastic response to high intensity loading

3.2 DIAGONALLY CRACKED BEAMS WITH CONVENTIONAL REINFORCEMENT

Spandrel beams reinforced with horizontal bars for flexure and with stirrups for shear will be defined as "conventionally reinforced coupling beams" or "conventional beams".

3.2.1 Ultimate Strength

A series of tests have been carried out by Paulay [4,74] to

investigate the behaviour of conventionally reinforced coupling beams. It was observed that only about 85% of the flexural strength, as predicted by conventional ultimate load analysis, can be expected to develop in beams with a span to depth ratio less than 1.5 .

By equating the maximum shear capacity, permitted by the ACI code[82] , to the flexural capacity Paulay[5] showed that

$$\frac{A_{s,max}}{bd} \leq \rho_{max} = \frac{4.71_s\sqrt{f'_c}}{(d-d')f_y} \qquad \ldots (3.1)$$

where l_s = clear span of the coupling beam

d = effective depth

d' = effective cover to the top steel

This shows that the flexural steel has to be limited to avoid a shear failure in accordance with the ACI code[82] requirements. However, Paulay[5] also found that with this shear stress intensity sliding shear failure will occur after a few cycles of reversed loading if yielding in the top and bottom flexural steel occurs. He recommended[5] that in order to minimise the danger of a sliding shear failure the flexural steel content, ρ_{max} , be limited so that

$$\rho_{max} \leq \frac{3\,l_s\sqrt{f'_c}}{(d-d')f_y} \qquad \ldots (3.1a)$$

The maximum shear in a coupling beam, when the capacity of the flexural reinforcement is attained, is approximately

$$V_{max} = \frac{2\,A_s\,f_{ym}(d-d')}{l_s} \qquad \ldots (3.2a)$$

where f_{ym} = yield strength of flexural steel.

The maximum dependable shear force that could be resisted by the stirrups provided is

$$V_{max} = \varphi f_{yst} A_{st} \frac{d}{s} \quad \ldots (3.2b)$$

where φ = capacity reduction factor

f_{yst} = yield strength of stirrup steel

A_{st} = area of stirrup steel

s = stirrup spacing

Equating Eqs. (3.2a) and (3.2b) the stirrup reinforcing content required to avoid a shear failure is

$$\rho_w \geq \frac{2\rho (d-d') f_{ym}}{\varphi l_s f_{yst}} \quad \ldots (3.2)$$

where $\rho_w = \frac{A_w}{bs}$, the web steel content.

3.2.2 Analytical Assessment of Deformations

In his earlier work Paulay[74] derived expressions for the deformation of these beams based on the observed mechanism of shear resistance. The model on which his analysis was based is shown in Fig. 3.1.a. The crack pattern for a typical beam tested by Paulay can be seen in the photograph reproduced in Fig. 3.1.h. The total beam rotation, θ, as defined in Fig. 3.6, was found by the superposition of distortions due to four separate actions as shown in Fig. 3.1.c,e, f and g. The total rotation was defined thus:

$$\theta = \theta_V + \theta_a + \theta_m + \theta_l \quad \ldots (3.3)$$

where the rotation owing to truss action (Fig. 3.1.c) is

$$\theta_V = \frac{\Delta_V}{l_s} \quad \ldots (3.3a)$$

the rotation owing to arch action (Fig. 3.1.e) is

$$\theta_a = \frac{\Delta_a}{l_s} \quad \ldots (3.3b)$$

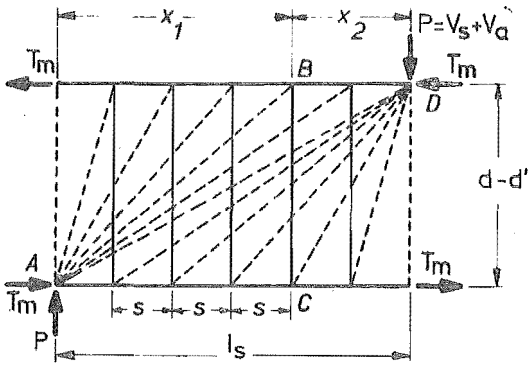

(a) The model truss

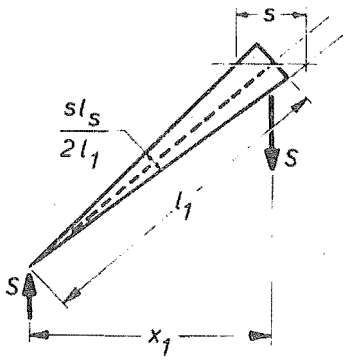

(b) Dimensions of a typical concrete strut

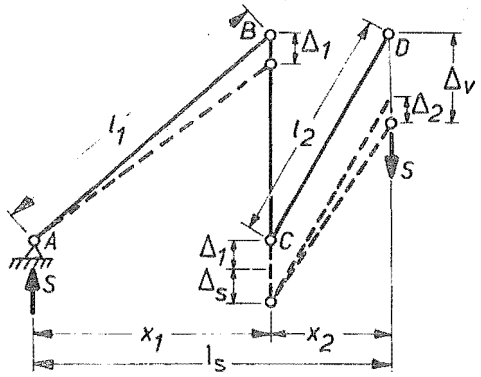

(c) Deformations along one linkage of the model truss

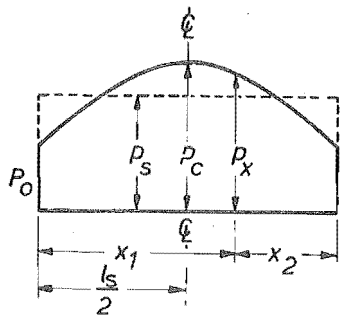

(d) Assumed distbution of stirrup forces

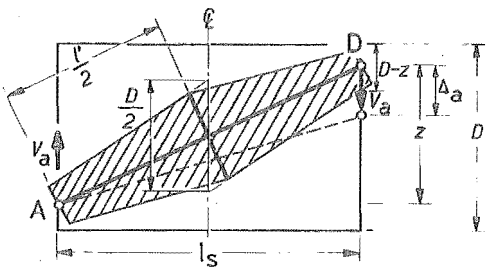

(e) The model arch

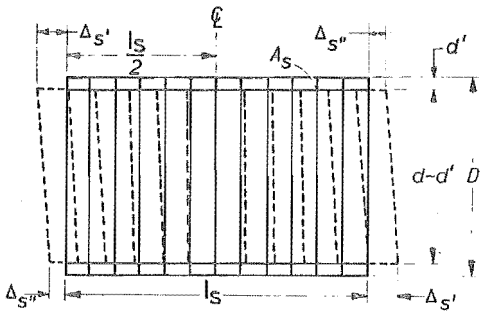

(f) Flexural rotation

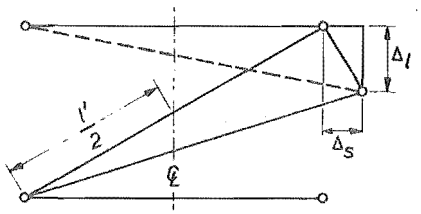

(g) Beam elongation

NOTE: FIG. 3.1.h The photograph of the crack pattern for a typical beam tested by Paulay is on page 266.

74

FIG. 3.1 PAULAY'S ANALYTICAL ASSESSMENT OF DEFORMATIONS OF THE CONVENTIONALLY REINFORCED COUPLING BEAMS

the rotation owing to flexural action (Fig. 3.1.f) is

$$\theta_m = \frac{\Delta'_s - \Delta''_s}{(d-d')} \qquad \ldots (3.3c)$$

the rotation owing to beam elongation (Fig. 3.1.g) is

$$\theta_l = \frac{\Delta_l}{l_s} \qquad \ldots (3.3d)$$

Superposition of rotations due to different actions is incorrect as it does not satisfy the requirements of compatibility. Moreover, Paulay did not consider the deformations in the end block region where the flexural steel is anchored. The arch action (see Fig. 3.1.e) is likely to be negligible when the stirrup steel approaches yielding, as a single potential diagonal failure crack forms between diagonally opposite corners (see Fig. 3.1.h). This crack would have to close if compression stresses are to be transferred along the diagonal AD of Fig. 3.1.e.

Fig. 3.2.a. shows the model which includes all the members whose deformations contribute to the rotation of conventional beams. The deformable members are shown in thin lines. For the purpose of analysis, the members shown in thick lines are assumed to be infinitely rigid, i.e., their contribution to the beam rotation is neglected. A development length, l'_d, for the flexural reinforcement, has been assumed on either side of the face of the wall. The deformation of this portion of flexural steel is also included in the analysis.

The distortion of the truss, shown in Fig. 3.2.a., results from the deformations of (a) the stirrups and diagonal concrete struts, (b) the top and bottom flexural bar and (c) the flexural steel in the end blocks.

(a) Distortions associated with the deformations of stirrups and diagonal concrete struts.

The shear force, P, shown in Fig. 3.2.a. is transmitted from one support to the other by stirrups, which together with the diagonal

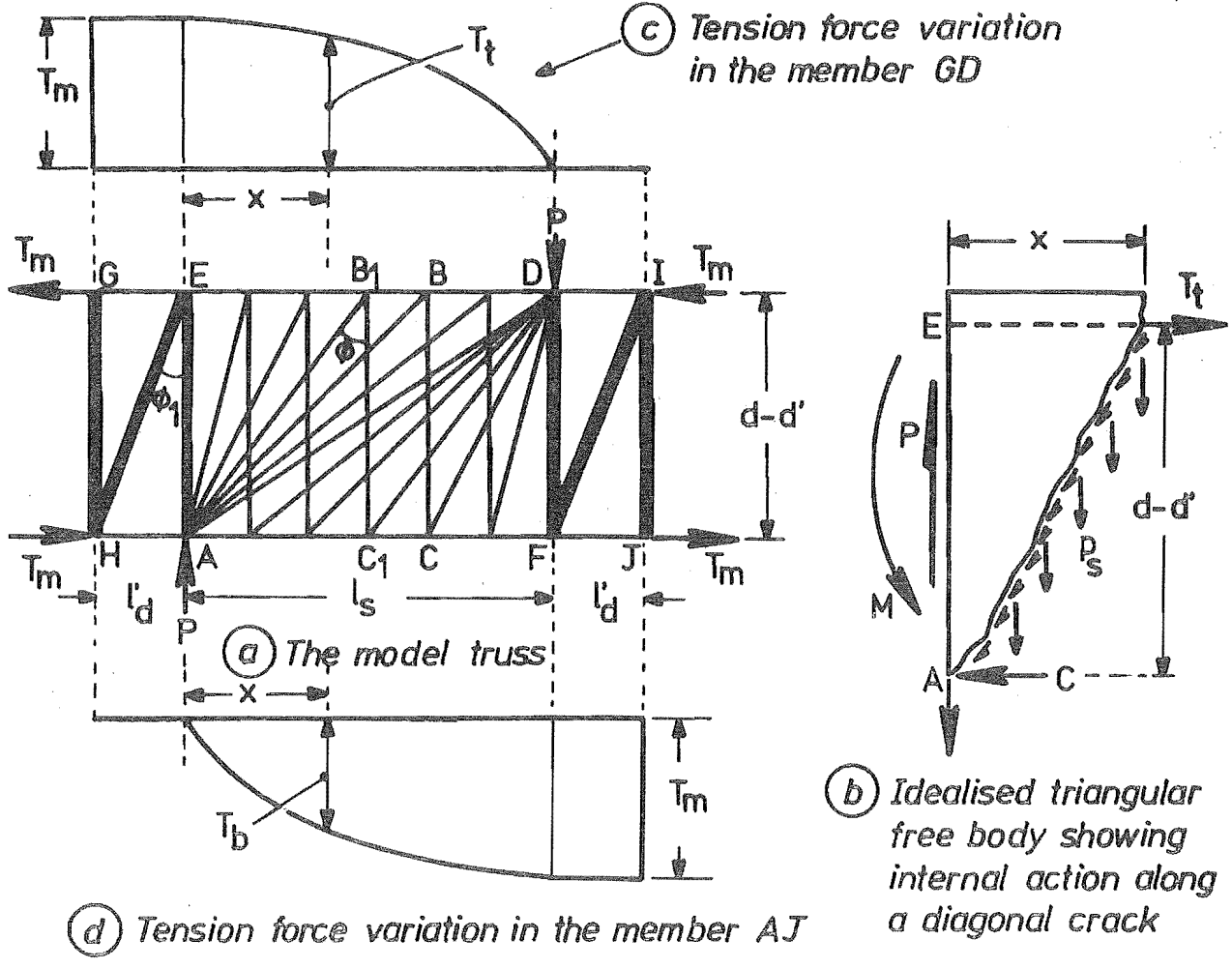

(c) Tension force variation in the member GD

(a) The model truss

(b) Idealised triangular free body showing internal action along a diagonal crack

(d) Tension force variation in the member AJ

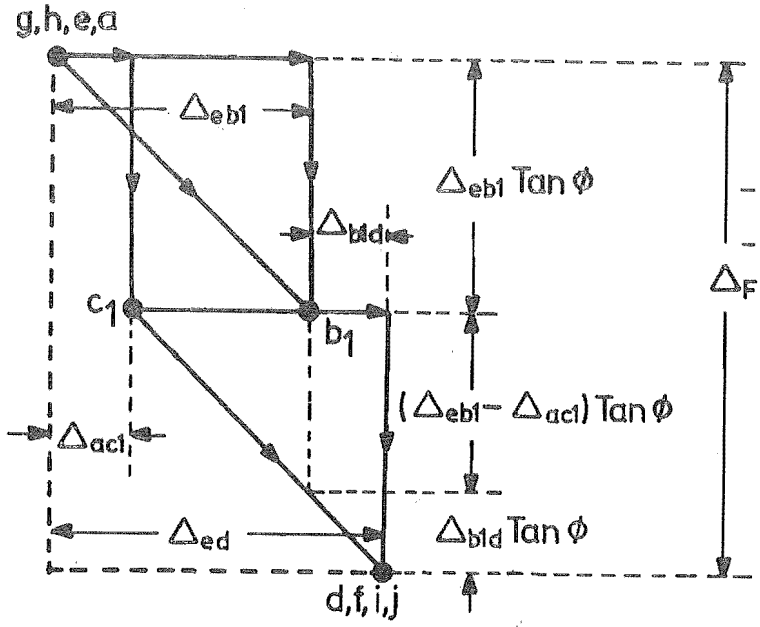

(e) Distortions associated with the elongation of members ED and AF

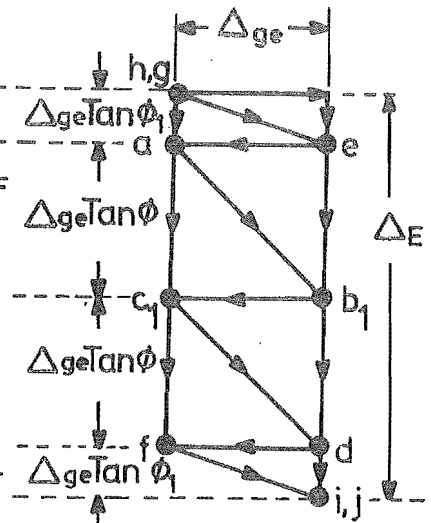

(f) Distortions associated with the elongation of members GE and FJ

FIG. 3.2 DISTORTIONS ASSOCIATED WITH THE ELONGATION OF TOP AND BOTTOM FLEXURAL BARS OF THE CONVENTIONALLY REINFORCED COUPLING BEAMS

concrete struts, form a truss. This shear may be transferred through as many paths across this statically indeterminate truss as there are stirrups. While considering the distortions associated with the deformations of stirrups and diagonal concrete struts, all other members (top and bottom flexural bars and the members in the end blocks) of the model truss are assumed to be infinitely rigid.

Paulay[74] determined the distortions of this indeterminate truss by examining the deformations of a typical linkage ABCD. This is shown in Fig. 3.1.c. For the purpose of analysis the dimensions of the diagonal concrete strut was assumed as shown in Fig. 3.1.b. The deformations resulting from one component force, S, for a particular linkage, ABCD, shown in Fig. 3.1.c., is

$$\Delta_V = \frac{2\,S\,(d-d')}{l_s\,b\,E_c}\left[\left(1+\frac{x_1^2}{(d-d')^2}\right)^2+\left(1+\frac{x_2^2}{(d-d')^2}\right)^2+\frac{1}{2n\rho_w}\right] \qquad \ldots (3.4)$$

The displacement compatibility require that the vertical displacement of all linkages at the right hand support be the same, i.e. Δ_V must be the same for all associated values of x_1 and x_2. For the purpose of this study Paulay[74] assumed a parabolic stirrup force distribution based on observed strain variation. This is shown in Fig. 3.1.d. From the compatibility of deformations of suitably chosen linkages, the factor, $\frac{p_c}{p_o}$, which represents the degree of non-uniformity of stirrup force variation, was found to be

$$\frac{p_c}{p_o} = \frac{1+(1+\nu^2)^2+\frac{1}{2n\rho_w}}{2\left(1+\frac{\nu^2}{4}\right)+\frac{1}{2n\rho_w}} \qquad \ldots (3.5)$$

where ν = the ratio $l_s/(d-d')$

n = the modular ratio E_s/E_c

Combining Eqs. (3.4) and (3.5), the vertical displacement, Δ_V, was obtained as

$$\Delta_V = \frac{6Pl_s\left[1 + (1+\nu^2)^2 + \frac{1}{2n\rho_w}\right]}{\nu\, b\, E_c \left(1 + 2\frac{p_c}{p_o}\right)} \qquad \ldots (3.6)$$

(b) Distortions associated with the elongation of the top and bottom flexural bars

By considering the equilibrium of the forces acting on the triangular portion of the beam shown in Fig. 3.2.b, the expression for tension force variation in the flexural steel of the conventional coupling beams obtained by Paulay can be approximated by

$$T_t = T_m \left[1 - \frac{x^2}{l_s^2}\right] \qquad \ldots (3.7)$$

where the maximum tension force at the support, $T_m = \frac{Pl_s}{2(d-d')}$ ... (3.7a)

The variation of this tension force, T_t, in the member GD and the tension force, T_b, in the member AJ are shown in Fig. 3.2.c. and Fig. 3.2.d. respectively.

The distortions associated with the elongation of the top and bottom flexural bars are shown in Fig. 3.2.e. The construction of this Williot diagram was based on the following two assumptions:

(1) Only the deformations of members ED and AF are considered. All other members of the model truss are assumed to be infinitely rigid.

(2) The displacement compatibility for the linkages has been considered while assessing the deformations of the stirrups and diagonal concrete struts. Hence, for the purpose of simplicity, only the linkage A, B, C, D, for which $\tan\Phi = \frac{l_s}{2(d-d')}$, is considered.

From Fig. 3.2.e, the vertical displacement, Δ_F, is seen to be

$$\Delta_F = \frac{l_s \Delta_{ed}}{2(d-d')} + \frac{l_s (\Delta_{eb} - \Delta_{ac})}{2(d-d')} \quad \ldots (3.8a)$$

in which $$\Delta_{ed} = \frac{1}{A_s E_s} \int_0^{l_s} T_t(x)\, dx \quad \ldots (3.8b)$$

and $$\Delta_{eb} - \Delta_{ac} = \frac{1}{A_s E_s} \left\{ \int_0^{l_s/2} T_t(x)\, dx - \int_0^{l_s/2} T_b(x)\, dx \right\} \quad \ldots (3.8c)$$

Substituting Eqs. (3.8b) and (3.8c) in Eq. (3.8a)

$$\Delta_F = \frac{Pl_s^3}{16A_s E_s (d-d')^2} + \frac{Pl_s^3}{4A_s E_s (d-d')^2} \quad \ldots (3.8d)$$

The first term is the vertical displacement caused by the differential elongation of the top and bottom bars, whereas the second term is the vertical displacement caused by the elongation of the bars.

(c) Distortions associated with the elongation of steel in the anchorages

The deformation of flexural steel anchored in the walls will also influence the distortions of the beam. The anchorage length, l_d', over which the deformation would be significant, is uncertain. For the purpose of this analysis this length is assumed to have an upper limit of $0.25l_s$ and a lower limit of zero. The force T_m at E (see Fig. 3.2.c) is assumed to be constant over the anchorage length l_d'. The force in the member DI is likely to be small and it is neglected.

The distortions associated with the elongation of bars in the anchorages is shown in Fig. 3.2.f. The construction of this Williot diagram is based on the assumptions similar to those made in connection with Fig. 3.2.e.

The vertical displacement at the right end relative to member GH is seen to be

$$\Delta_E = \frac{2\,\Delta_{ge}\,l'_d}{(d-d')} + \frac{2\,\Delta_{ge}\,l_s}{(d-d')} \qquad \ldots (3.9a)$$

in which $$\Delta_{ge} = \frac{T_m\,l'_d}{A_s E_s} \qquad \ldots (3.9b)$$

Therefore, the vertical displacement

$$\Delta_E = \frac{Pl_s\,l'_d\,(l'_d + l_s)}{A_s\,E_s(d-d')^2} \qquad \ldots (3.9c)$$

when $l'_d = 0$ $\qquad \Delta_E = 0$ $\qquad \ldots (3.9d)$

when $l'_d = 0.25l_s$ $\qquad \Delta_E = \frac{5}{16}\,\frac{Pl_s^3}{A_s E_s (d-d')^2}$ $\qquad \ldots (3.9e)$

(d) The total rotation of conventionally reinforced beams

The total rotation of the beam is

$$\theta = \theta_V + \theta_F + \theta_E \qquad \ldots (3.10)$$

where $\theta_V = \frac{\Delta_V}{l_s}$, the rotation associated with the deformations of the diagonal concrete struts and stirrups, obtained from Eq. (3.6)

$\theta_F = \frac{\Delta_F}{l_s}$, the rotation associated with the elongation of the top and bottom flexural bars, obtained from Eq. (3.8)

$\theta_E = \frac{\Delta_E}{l_s}$, the rotation associated with the elongation of the bars anchored in the end blocks, obtained from Eq. (3.9).

3.2.3 A Comparison of Computed Stiffnesses with the Experimental Evidence

In Fig. 3.3, a comparison of theoretical stiffnesses (Eq. (3.10)) of conventionally reinforced beams, and the stiffnesses observed by Paulay during his experimental investigations is presented. For

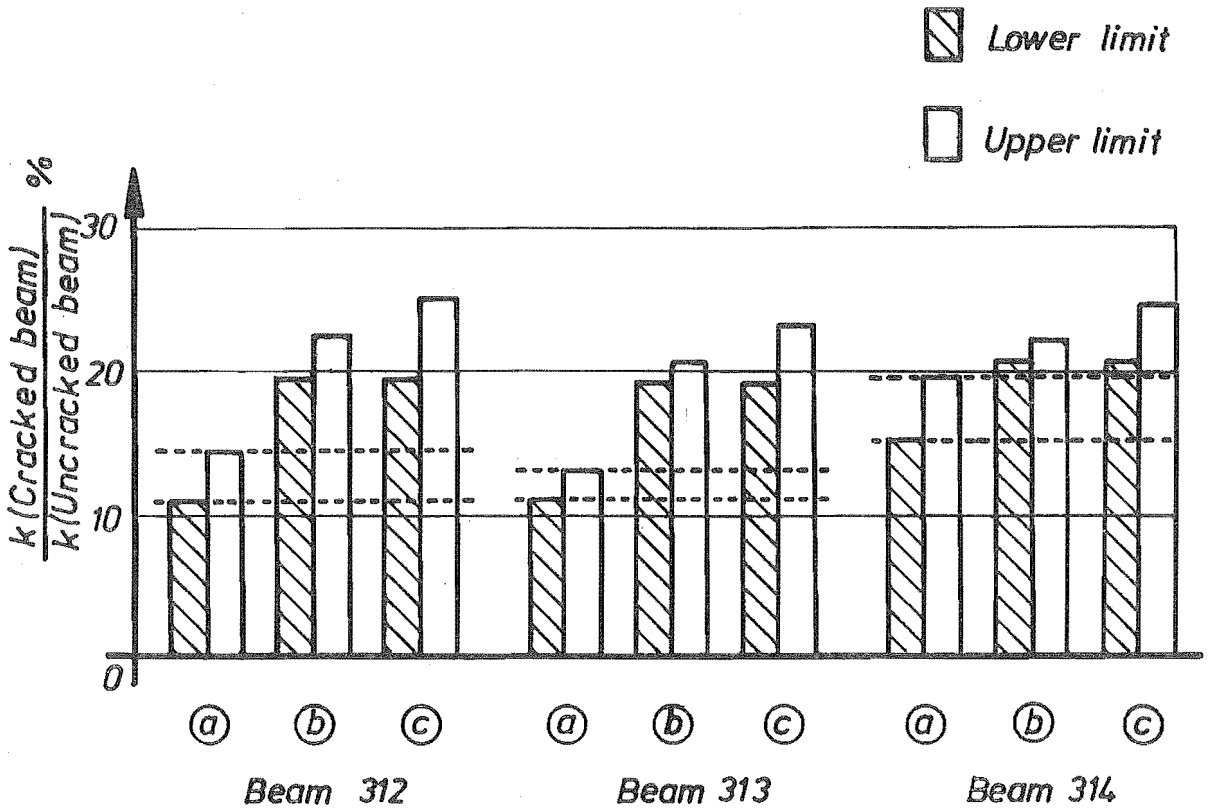

(a) Stiffnesses observed by Paulay during his experimental investigation also shown by broken lines.
(b) Theoretical stiffness based on Paulay's assessment.
(c) Theoretical stiffness based on Eq. (3.10).

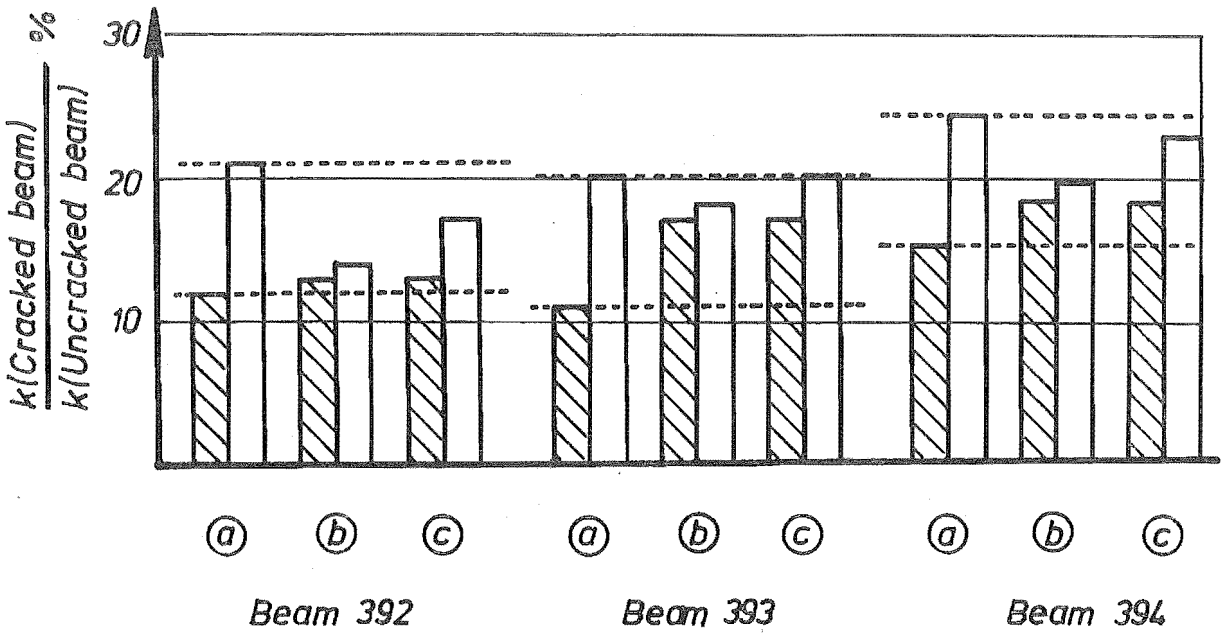

FIG. 3.3 A COMPARISON OF THEORETICAL AND OBSERVED STIFFNESSES

this purpose the stiffness, K, of the beam is defined as the load, P, required to cause unit rotation of the beam at both of its supports. The stiffness of each cracked beam is then expressed as a percentage of its computed stiffness in the uncracked state. To have an estimate of the error introduced by Paulay's assessment of rotations, the stiffness calculated from Eq. (3.3) is also shown in this figure.

For each, the theoretical and experimental stiffnesses, a lower and upper limit is indicated. In Paulay's assessment the lower limit corresponds with stiffnesses computed on the assumption that 30% of the total shear, P , is transmitted across AD (see Fig. 3.1.e) by arch action and the upper limit is based on the assumption that the force resisted by arch action is negligible. For the assessment based on Eq. (3.10), the lower limit corresponds with stiffnesses computed on the assumption that the development length, $l'_d = 0.25l_s$ and the upper limit is based on the assumption that the development length, $l'_d = 0$. The upper and lower limits for the experimentally determined stiffnesses, on the other hand, represent the highest and lowest values observed during cyclic loading. The broken lines in each figure show the range within which the observed stiffness varied.

Considering the approximations which formed the basis of the study presented in Section 3.2.2, it may be said that fair agreement exists between theory and observation. Paulay's analytical assessment of deformations also leads to approximately the same final stiffnesses. This is due to the compensating effect of the following two errors in Paulay's equations.

(i) The rotations were overestimated owing to the superposition of the deformations caused by different actions. This led to an underestimate of stiffness.

(ii) The rotations associated with the elongation of steel in the anchorages were not considered. This led to an overestimate of stiffness.

When the assumed development length $l'_d = 0.25l_s$, the errors associated with (i) and (ii) happened to be the same. Thus the lower limits of stiffnesses, computed with Paulay's assessment, and with Eq. (3.10), give identical values.

3.2.4 The Proportions of the Component Rotations

Eqs. (3.6), (3.8d), (3.9e) and (3.10) reveal that the geometry of the beam as well as the steel content contribute to the stiffness. To examine the influence of steel content on stiffness, the rotations θ_V , θ_F and θ_E have been modified. The relative proportions of these rotations were examined at the onset of yield during the assumed theoretical bilinear elasto-plastic behaviour. By substituting the total shear, P , at this limit, in terms of the steel area, A_s , and yield stress, f_y , in the above equations, the rotations θ_V , θ_F and θ_E are expressed in terms of the aspect ratio, $\frac{l_s}{d}$, and steel content, ρ , thus

$$\theta_V = \frac{12\,\rho\left(\frac{f_y}{E_s}\right)\left(\frac{d-d'}{d}\right)\left[1+\left(1+\nu^2\right)+\frac{1}{2n\rho_w}\right]}{\nu\left(\frac{l_s}{d}\right)^2\left(1+2\,\frac{p_c}{p_o}\right)} \qquad \ldots (3.11a)$$

$$\theta_F = \frac{\left(\frac{f_y}{E_s}\right)\left(\frac{l_s}{d}\right)}{8\left(\frac{d-d'}{d}\right)} + \frac{\left(\frac{f_y}{E_s}\right)\left(\frac{l_s}{d}\right)}{2\left(\frac{d-d'}{d}\right)} \qquad \ldots (3.11b)$$

$$\theta_E = \frac{2\left(\frac{f_y}{E_s}\right)\left(\frac{l'_d}{l_s}\right)\left(\frac{l'_d+l_s}{l_s}\right)\left(\frac{l_s}{d}\right)}{\left(\frac{d-d'}{d}\right)} \qquad \ldots (3.11c)$$

and $$\theta_y = \theta_V + \theta_F + \theta_E \qquad \ldots (3.11d)$$

It is seen that the rotation, θ_V, is dependent on steel content. However, the rotations θ_F and θ_E are independent of steel content.

The variations of the components of yield rotation (θ_V, θ_F and θ_E) for different steel contents, ρ, for an aspect ratio of $\frac{l_s}{D} = 1.00$ were computed. This was based on an assumed effective cover $d' = 0.1d$ and an assumed development length $l'_d = 0.25l_s$. For the purpose of computing the shear deformation, θ_V, it was assumed that sufficient quantity of web steel, ρ_w, as expressed by Eq. (3.2), was provided so that shear failure should not occur. The results of the analysis are shown in Fig. 3.4. The percentage of web steel content, ρ_w, required to prevent a premature shear failure, as per Eq. (3.2), is also shown in this figure. An examination of this figure shows that:

1. For the chosen aspect ratio, the shear deformation, θ_V, which is dependent on the steel content, ρ, is more than the sum of the rotations θ_F and θ_A which are independent of the steel provided, when $\rho \geq 0.75\%$.

2. The flexural capacity of the beam increases with the steel content, ρ. To avoid a shear failure increasing amounts of web steel are necessary. Eq. (3.2) shows that $\rho_w \approx 2\rho$ when the aspect ratio $\frac{l_s}{D} = 1.00$. The values of ρ_w plotted in the figure indicate this.

3.2.5 An Examination of the Methods of Assessing the Stiffnesses

The trend towards the use of higher strength concrete and steel and ultimate strength design has made the use of lighter members possible. This led to a number of investigations which aimed at predicting more accurately the deflections of reinforced

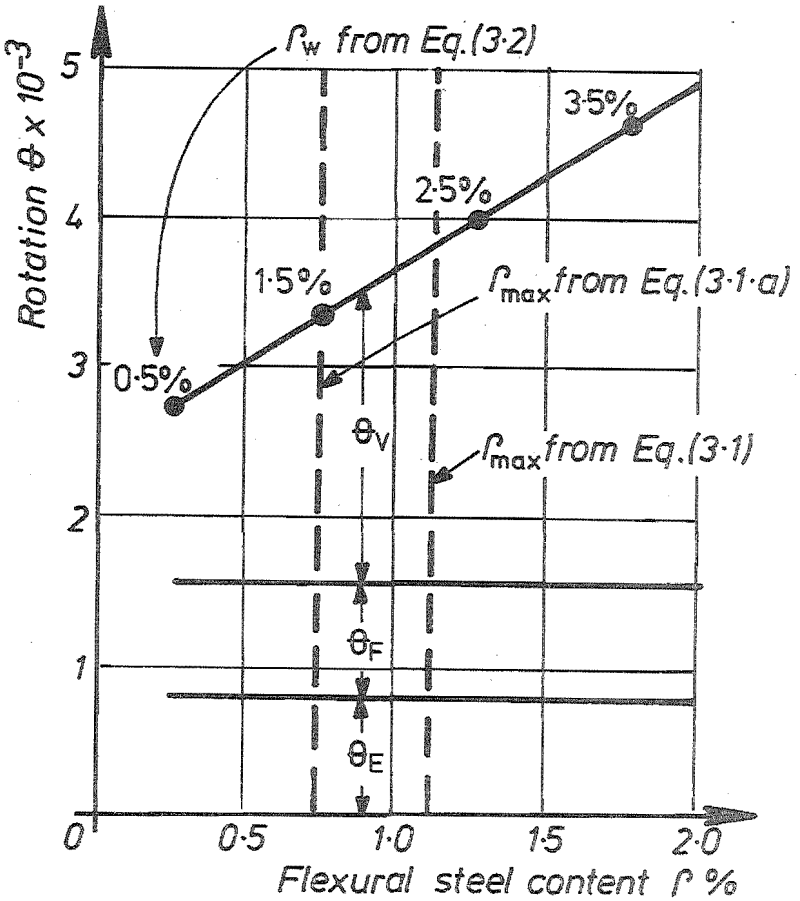

FIG. 3.4 VARIATION OF THE COMPONENTS OF YIELD ROTATIONS OF CONVENTIONALLY REINFORCED BEAMS FOR DIFFERENT PERCENTAGES OF STEEL FOR AN ASPECT RATIO l_s/D = 1.00, WITH AN ASSUMED DEVELOPMENT LENGTH, $l'_d = 0.25\ l_s$

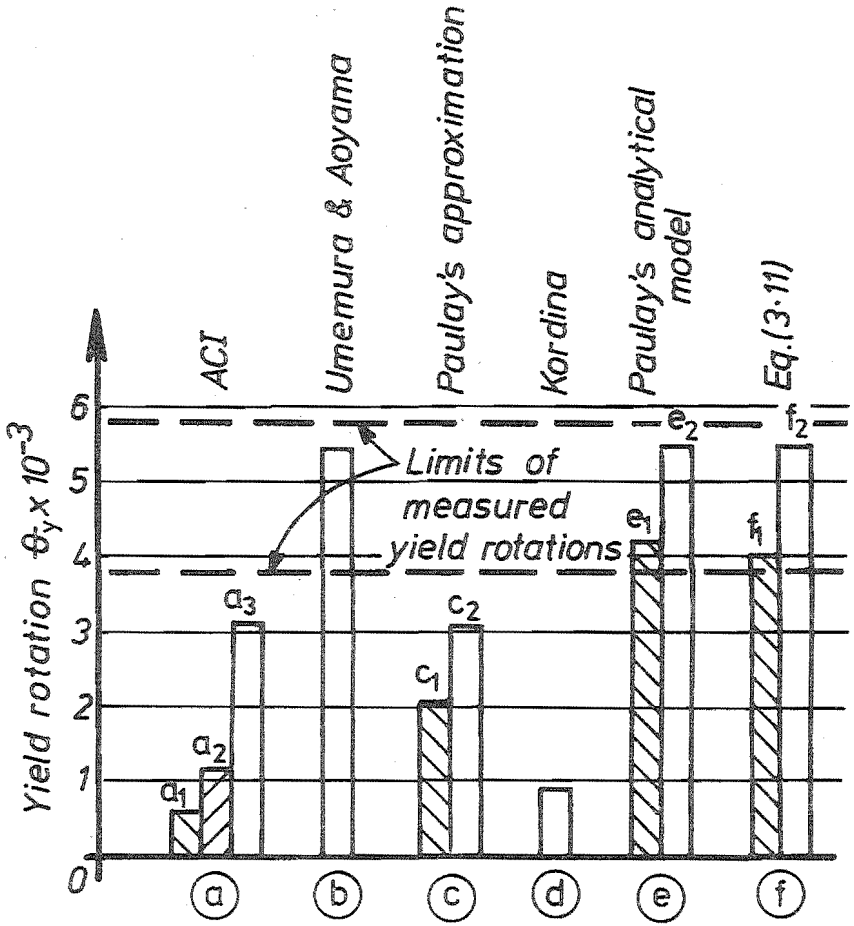

FIG. 3.5 COMPARISON OF YIELD ROTATION COMPUTED USING VARIOUS METHODS WITH THAT OBSERVED DURING TEST FOR THE COUPLING BEAMS USED IN SHEAR WALL A

concrete members. Only a few of these focussed attention on deep beams. Herein an attempt is made to compare the rotations computed, using various methods applicable to reinforced concrete members. The yield rotations of the coupling beam of the test model shear wall A are computed using these methods and also Eqs. (3.3) and (3.11). This is then compared with the yield rotations measured during cyclic loading*. The relevant particulars for these beams are as follows:

(i) The percentage of flexural steel content, ρ = 0.62

(ii) The percentage of stirrup steel content, ρ_w = 1.76

(iii) The aspect ratio, l_g/D = 1.25 .

A critical examination of the methods of assessing the stiffness of coupling beams in the cracked state is then made.

(a) <u>The method of estimation of deflection according to the ACI Code 318-71</u>[82]

For cracked beams it has been suggested that the deformation could be predicted using an equivalent moment of inertia as follows

$$I_{eq} = \left(\frac{M_{cr}}{M_{max}}\right)^3 I_g + \left[1 - \left(\frac{M_{cr}}{M_{max}}\right)^3\right] I_t \qquad \ldots (3.12)$$

where I_g = gross moment of inertia of the section ignoring steel

I_t = moment of inertia of the cracked transformed critical section

M_{cr} = $7.5\sqrt{f'_c}\, I_g/y_t$, the cracking moment

Y_t = distance from centroidal axis of gross section, neglecting the reinforcement, to the extreme fibre in tension

M_{max} = the maximum moment in member at the stage for which deflection is being computed.

---

* This is discussed in detail in Chapter 6.

This equation was proposed by Branson[83]. It is based on tests conducted on shallow reinforced concrete beams. An examination of Eq. (3.12) will reveal that this value of equivalent moment of inertia, I_{eq}, is between the limits of I_g and I_t. I_{eq} is expressed as the weighted sum of I_g and I_t, depending on the extent of cracking as expressed by the cube of the ratio of cracking moment to the maximum moment present in the span. Using I_g and I_t only would give lower and upper limits of the deformations respectively. I_{eq} from Eq. (3.12) gives the transition between the above two cases. To compare the range of values given by Eq. (3.12) rotations are computed based on I_g, I_{eq} and I_t for the example beam. These rotations are shown as a_1, a_2 and a_3 in Fig. 3.5. The upper and lower limits of the yield rotations measured during cyclic loading are shown with broken lines.

It is seen that using the ACI equations does not lead to a realistic assessment of stiffness as expected. In deep members shear deformations are significant. The ACI equation does not allow for stiffness reduction associated with shear deformation.

(b) A method proposed by Umemura and Aoyama[84]

When assessing the inelastic deflection of the reinforced concrete frames with infilled panels, Umemura and Aoyama[84] suggested a reduction factor of $\alpha_y = 0.35$ for the flexural rigidity, EI, and a reduction factor, $\beta_y = \frac{f_q}{0.004G}$, for the shear rigidity, AG, for approximately square panels. f_q in the reduction factor, β_y, represents the maximum shear stress present in the beam. These reduction factors are based on the results of the tests on reinforced concrete deep members. With their suggestion the reduced moment of inertia, I_x, in Eq. (2.1a) modifies to

$$I_x = \frac{\alpha_y I_g}{1 + \frac{12 \alpha_y E I_g f}{\beta_y G A l_s^2}} \qquad \ldots (3.13)$$

where I_g = the gross moment of inertia

f = form factor

Using a form factor, $f = 1.2$, the yield rotation of the beam, θ_y, was computed for the example beam and the result is shown in Fig. 3.5. The rotation computed as per this method is seen to lie between the upper and lower limits of the rotations observed during cyclic loading.

(c) Paulay's [4,74] approximation for cracked spandrel beams

When estimating the effects of cracking it has been suggested that a reduction of 70% to 80% can be made to the gross stiffness of coupling beams for obtaining their stiffness in the cracked state. The rotations so calculated for the example beam is shown in Fig. 3.5. It is seen that it overestimates the stiffnesses. The stiffness of the beam determined in this way could be used for the preliminary approximate analysis when the properties of the coupling beams (ρ and ρ_w) are not yet known.

(d) Kordina's [85] reduction factor method

Kordina suggests a reduction factor of $(0.6 + 10\rho)$ for assessing the stiffness of members in the cracked state. No effort has been made to include shear distortions in this reduction factor. Hence it is presumed that this is applicable to shallow members only. As expected the values resulting from Kordina's expression would give significant errors for deep members (see Fig. 3.5.)

(e) Paulay's analytical assessment (Eq. (3.3))

Fig. 3.5 also shows two limits of the rotations computed from Eq. (3.3). The lower limit, e_1, corresponds to the rotation computed based on the assumption that the force resisted by arch action is negligible. The upper limit, e_2, corresponds to the rotation computed based on the assumption that 30% of the total shear, P, is transmitted across AD (see Fig. 3.1.e) by arch action. It is seen that there is good correlation between the predicted and observed rotations.

(f) Yield rotation based on Eq. (3.11)

Fig. 3.5 shows two limits for the rotations computed from Eq. (3.11). The upper limit, f_2, and the lower limit, f_1, correspond to rotations that are computed based on the development lengths of $l'_d = 0.25l_s$ and $l'_d = 0$ respectively. As expected these rotations are of the same order as the rotations predicted by Paulay's assessment, Eq. (3.3). It is seen that there is good correlation between the predicted and observed rotations.

3.2.6 Post-elastic Performance of Conventionally Reinforced Beams

Paulay's[4,74] tests on conventionally reinforced beams revealed three distinct ranges of beam behaviour when they were subjected to a number of high intensity load reversals. In Fig. 3.6 the load-deformation curve for a typical coupling beam is reproduced. As no readings were recorded for these beams when unloaded a straight line was drawn between the last measured value of extension and that at no load. The three ranges are:

1. A "soft range" at very low load
2. A "steady range" at medium loads
3. A "plastic range" near ultimate load.

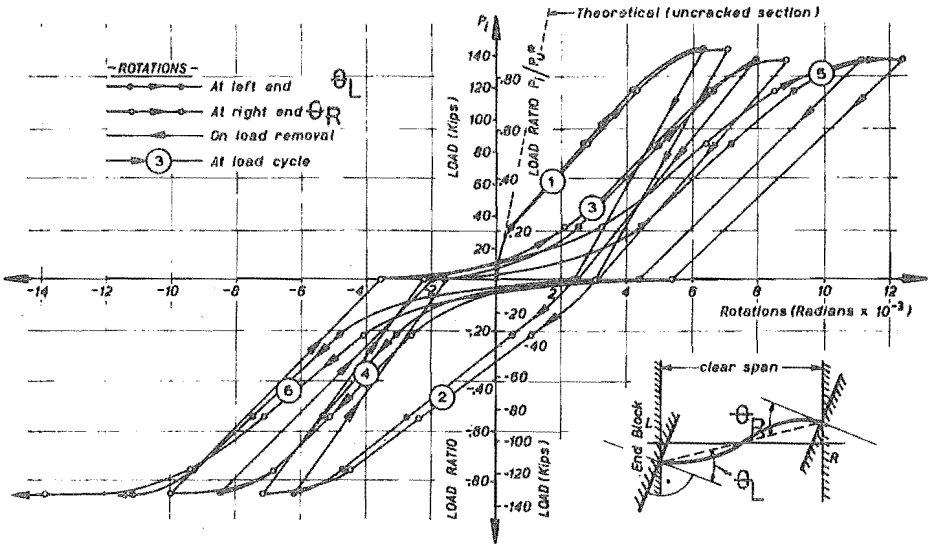

74

FIG. 3.6 A TYPICAL LOAD-ROTATION CURVE OBSERVED BY PAULAY FOR A CONVENTIONALLY REINFORCED COUPLING BEAM WITH AN ASPECT RATIO OF $l_s/D = 1.29$

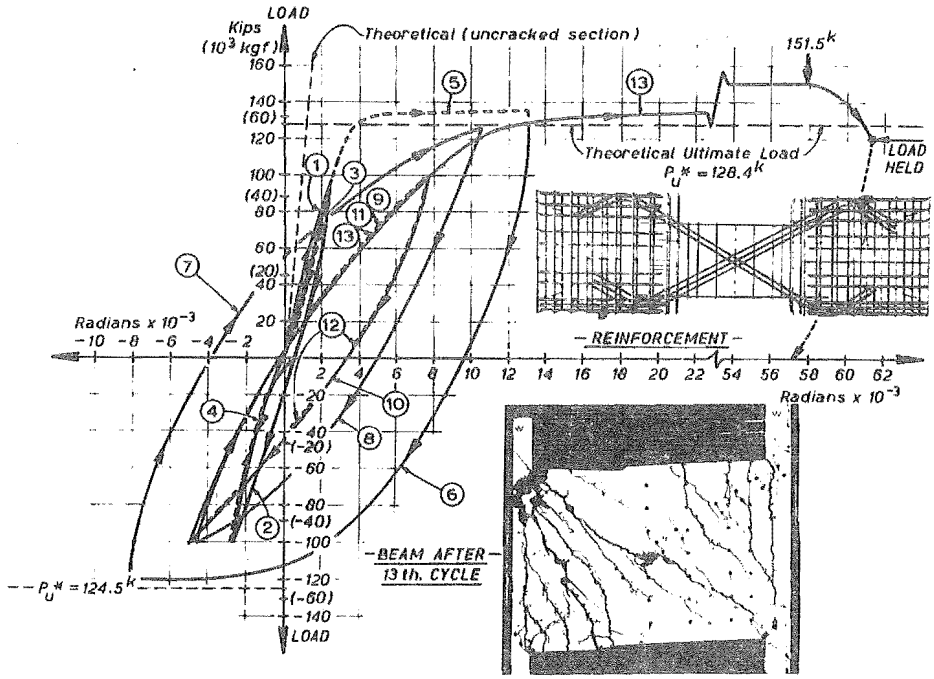

FIG. 3.7 A TYPICAL LOAD-ROTATION CURVE OBSERVED BY PAULAY FOR A DIAGONALLY REINFORCED BEAM OF ASPECT RATIO $l_s/D = 1.29$

The coupling beams possess equal amounts of top and bottom steel. Shallow beams with equal amounts of top and bottom steel are known to sustain large plastic rotations. However, in deep spandrel beams, a sliding shear failure will occur after a few cycles of reversed loading if,due to flexure,yielding in the top and bottom steel occurs. This is likely to restrict the ductility of these beams. Moreover, the shear force and the consequent diagonal cracking cause tension to develop in the top as well as in the bottom reinforcement. The "compression" reinforcement in these beams is subjected to tensile strains over the full span. Thus the relief with respect to ductility owing to the presence of the compression reinforcement cannot be expected. The bulk of the shear force must be transferred across the concrete compression zone of the beams into the walls. The concrete in these areas is subjected to cracking. During a number of load reversals these cracks open and close several times. The opening and closing of cracks in this zone may eventually lead to the deterioration of the compressive strength of the concrete. This is because the faces of the crack might not come into even contact due to slight relative displacement in the cracks. Because of the full depth cracking at this section, the whole shear force must be carried by the dowel action of the main reinforcement alone. The initial "softness" in stiffness, witnessed at low moments, as can be seen in Fig. 3.6, is due to these open cracks in the compression zone and the shear force being resisted mainly by the dowel forces. When the cracks close in the compression zone, as expected, an increase in stiffness is observed. Both the ineffectiveness of the compression reinforcement and the imminent danger of sliding shear failure, restrict the plastic rotational capacity of these coupling beams.

3.3 DIAGONALLY REINFORCED COUPLING BEAMS

The above findings led to a study of alternative solutions for an effective coupling beam. At this stage, the concept of diagonally reinforced coupling beams, as shown in Fig. 3.8, was developed by Paulay[5]. The philosophy behind this design is that the shear and moment on the coupling beam could be resisted by steel forces alone. This is provided by uniformly stressed diagonal reinforcement acting in compression along one diagonal and in tension along the other. The tests conducted by Paulay[5] and later by Binney[6] have revealed that these beams meet much more successfully the ductility demands indicated by the theoretical studies[74] provided that adequate lateral ties are provided to enable the compression diagonal to sustain the yield load without buckling.

3.3.1 Ultimate Strength

The ultimate strength of these beams may be derived from simple force equilibrium equations. With the notation used in Fig. 3.8 it is seen that

$$T_u = C_u = A_s f_y \qquad \ldots (3.14)$$

$$P_u = T_u \sin\alpha + C_u \sin\alpha$$

$$= 2\, T_u \sin\alpha \qquad \ldots (3.15)$$

The moment, M_u, at the junction of the beam and the face of the wall is

$$M_u = 0.5\, P_u\, l_s \qquad \ldots (3.16)$$

Therefore, the dependable shear strength and flexural strength are

$$P_u = \varphi\, 2\, A_s f_y \sin\alpha \qquad \ldots (3.17)$$

and

$$M_u = \varphi\, A_s f_y l_s \sin\alpha \qquad \ldots (3.18)$$

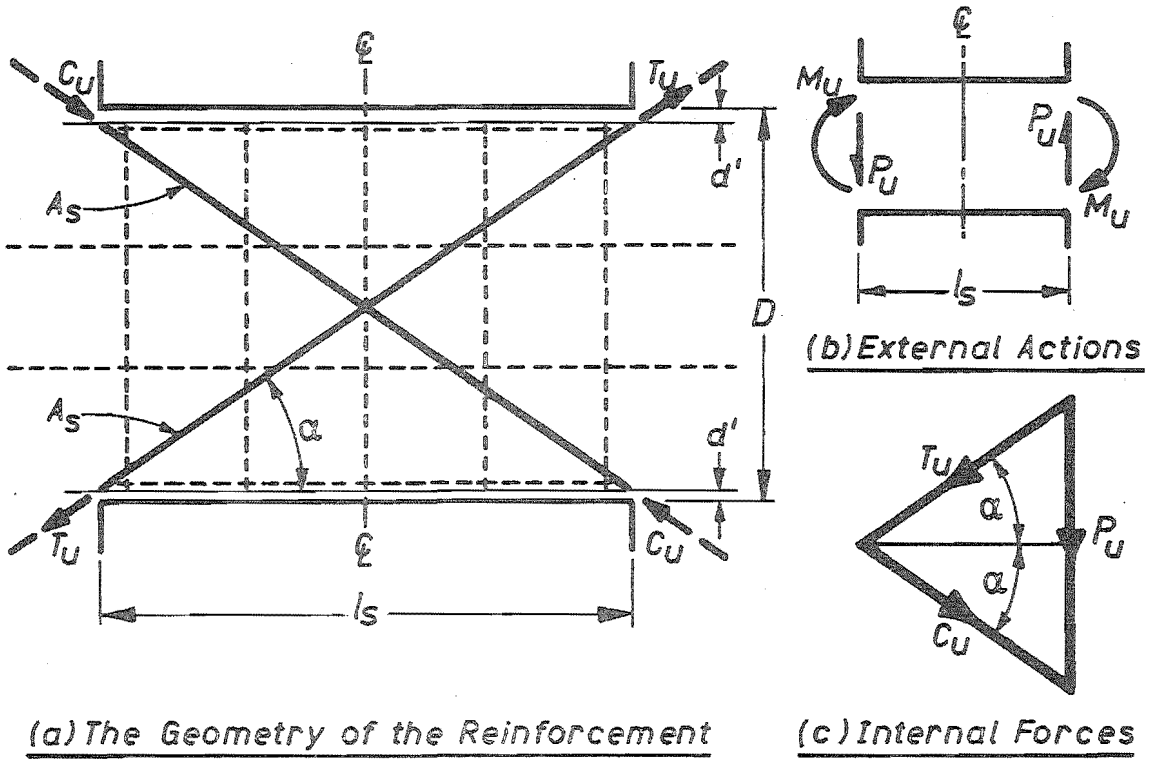

FIG. 3.8 MECHANISM OF LOAD RESISTANCE IN A DIAGONALLY REINFORCED COUPLING BEAM

respectively, where φ is the capacity reduction factor.

3.3.2 An Analytical Assessment of Deformations

In diagonally reinforced beams, the observed distribution of strains, reproduced in Fig. 3.9, are almost uniform[6]. This figure shows the strains along the diagonal steel during first high intensity loading. Therefore, the steel compression strains are very small as the concrete is still contributing. The observed strains indicate that the beam behaves like a truss. There are only negligible bond forces present between the tension steel and the surrounding concrete. The compression chord of the truss is a composite section consisting of steel and the surrounding concrete. The area of concrete which contributes to the resistance of the compression force is dependent upon the formation and development of cracks and so it cannot be clearly defined. The area in compression is likely to vary from a minimum value at the edge of the beam to a maximum value at the centre line of the beam. The strain variation of the steel in the compression chord, observed by Binney (see Fig. 3.9), also suggests this.

A typical diagonally reinforced coupling beam, with span l_s and depth D, is shown in Fig. 3.10.a. After cracking the beam forms a new mechanism. The tension force, T, is resisted by the steel, AD. The concrete is still effective in resisting compression. For the purpose of analysis the diagonal compression strut is approximated by the shaded area indicated in Fig. 3.10.a. Accordingly the mean area of the tapered diagonal strut is $\frac{l_s b}{4l'}(3D - 2Z)$ where the symbols can be identified from Fig. 3.10.a. The implications of this assumption are examined in Section 3.3.3.

The model on which this analytical assessment is based is shown in Fig. 3.10.b. The deformation of the steel, anchored in the end block of length l'_d on either side of the face of the wall, is also included in the analysis.

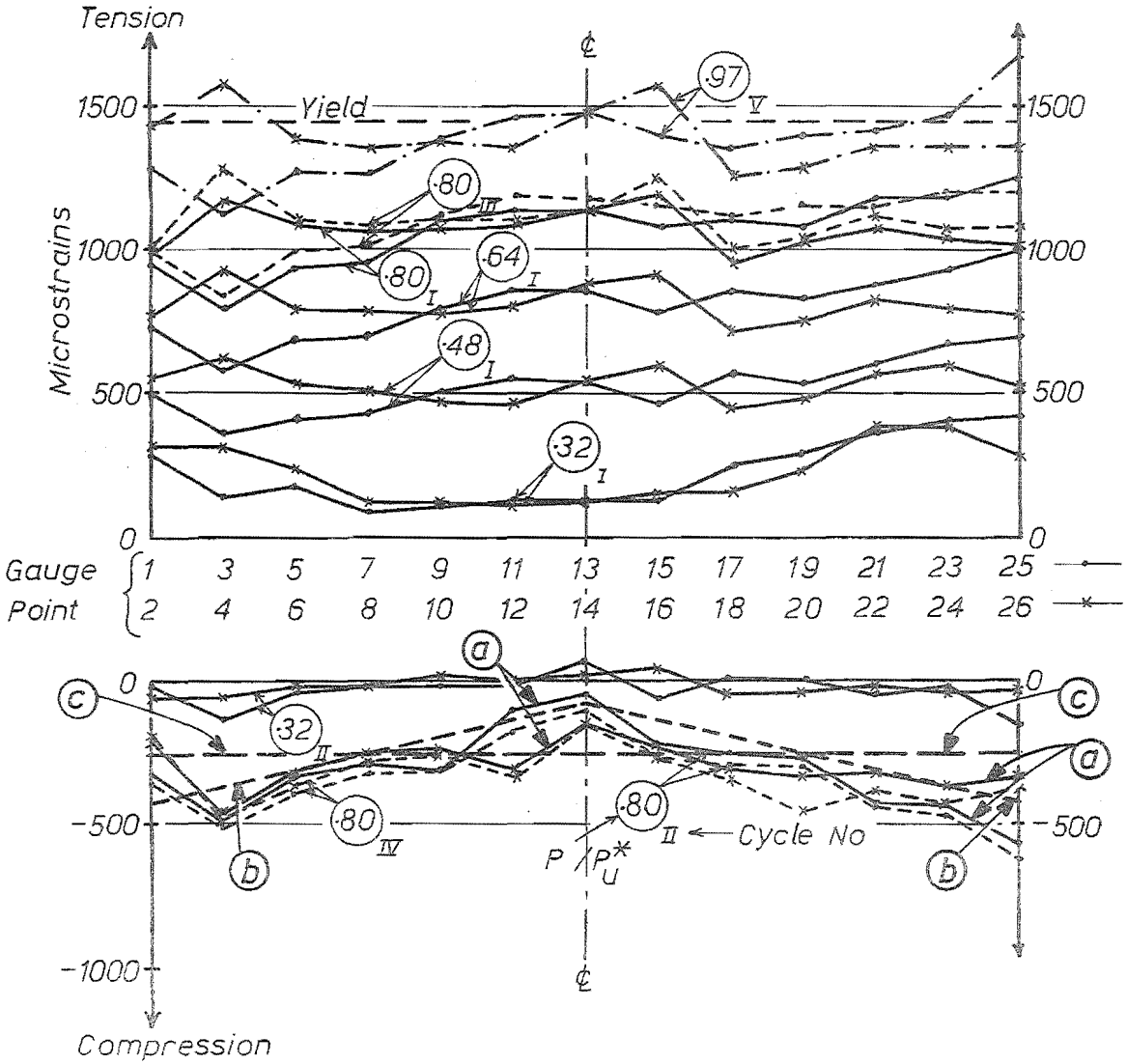

P_u^* = Theoretical ultimate shear

I,III = Cycle number

(a) = Typical strain variation for steel along the compression diagonal

(b) = Idealised straight line variation

(c) = Average strain

FIG. 3.9 THE DISTRIBUTION OF STEEL STRAINS IN A TYPICAL DIAGONALLY REINFORCED BEAM[6]

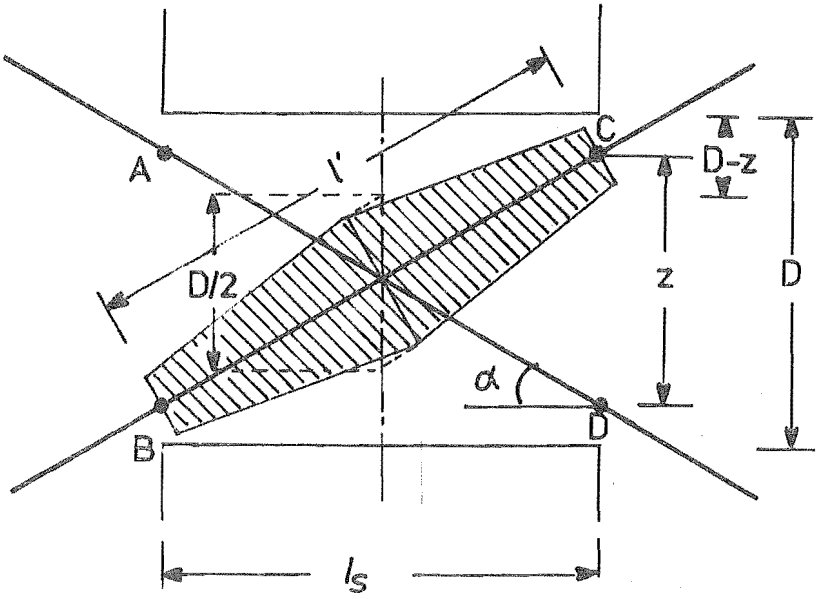

(a) A typical diagonally reinforced coupling beam showing the assumed dimensions of the diagonal concrete strut

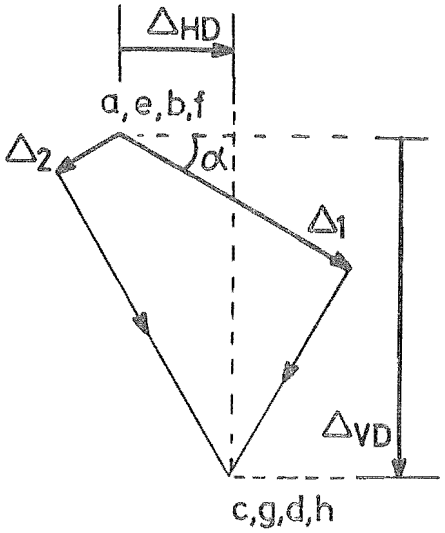

(c) The distortions associated with the deformations of diagonal members AD and BC

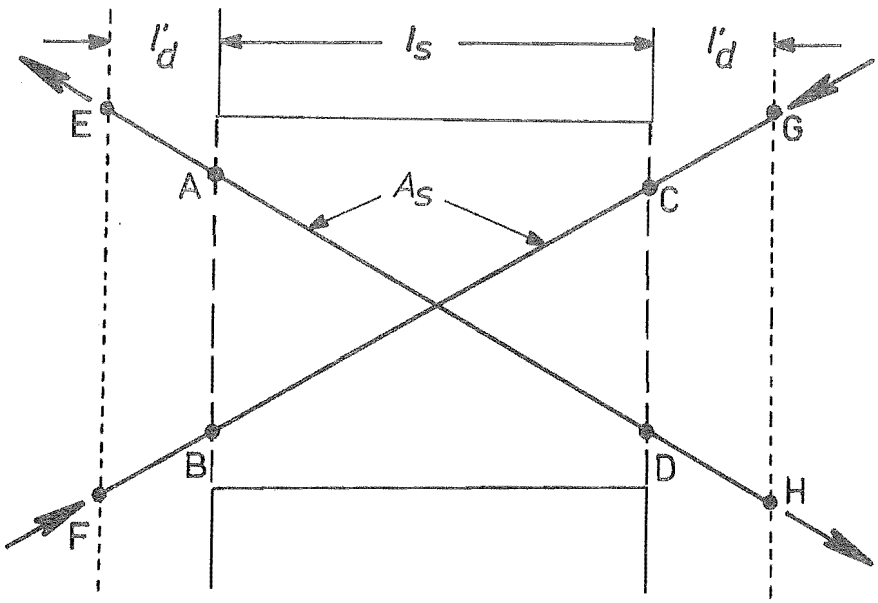

(b) The model truss

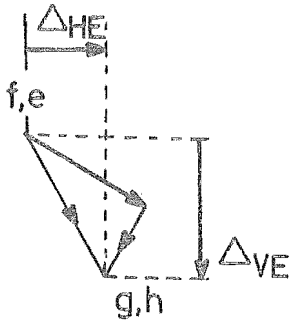

(d) The distortions associated with the deformation of steel in the anchorages

FIG. 3.10 ANALYTICAL ASSESSMENT OF DEFORMATIONS OF DIAGONALLY REINFORCED COUPLING BEAMS

The distortions of the truss, shown in Fig. 3.10.b, result from the deformations of:

(a) diagonal members AD and BC in the spandrel beams

(b) diagonal steel anchored in the end blocks of length l_d' (AE , DH , FB and CG).

(a) Distortions associated with the deformations of diagonal steel AB and CD

The rotations associated with the axial deformation of the diagonal steel AB and CD are shown in Fig. 3.10.c. Δ_2 is the diagonal contraction along BC. Δ_1 is the diagonal elongation along AD. From the geometry of this Williot diagram the net vertical displacement of C relative to A is

$$\Delta_{VD} = \frac{\Delta_1 + \Delta_2}{2\sin\alpha} \qquad \ldots (3.19)$$

where α is the inclination of the diagonal reinforcement to the axis of the beam.

With the notations used in Fig. 3.10, the vertical displacement associated with the deformations of the diagonal steel is expressed in terms of the steel content and the maximum shear across the beam as

$$\Delta_{VD} = \frac{Pl_s l'^2}{4Z^2 bd\rho^* nE_c} + \frac{Pl_s l'^4}{bl_s^2 Z^2(3D-2Z)E_c + 4Z^2(n-1)E_c\rho^* l'^2 bd} =$$

$$= \Delta_{VD1} + \Delta_{VD2} \qquad \ldots (3.20)$$

where P = maximum shear force across the beam

A_s = area of steel in one diagonal

$\rho^* = \frac{A_s}{bd} \cdot \frac{l_s}{l'}$, the equivalent steel content.

The first term, Δ_{VD1} , in the above expression corresponds to the deformation associated with the tension chord and the second term, Δ_{VD2} , corresponds to the deformation associated with the compression chord.

(b) Distortions associated with the deformation of steel in anchorages

The deformations of diagonal steel anchored in the walls will also influence the distortions of the beam. The end block length, l'_d, (see Fig. 3.10.b), in which the deformation of the anchored diagonal bars would be significant, is not exactly known. For the purpose of this analysis this length is again assumed to have an upper limit of $0.25l_s$ and a lower limit of zero. The same force, T, (see Fig. 3.10.b), as in the member AD is assumed to be present in the members EA and DH. The deformations of the compression members FB and CG are likely to be small and they are neglected. While considering the distortions associated with the deformation of the bars in the anchorages the diagonal bars AD and BC are assumed to be infinitely rigid. Fig. 3.10.d shows these distortions.

The vertical displacement, Δ_{VE}, at the right end relative to the left end, is seen to be

$$\Delta_{VE} = \frac{Pl'_d\, l'^2}{2z^2 bd\, \rho^*\, n\, E_c} \qquad \ldots (3.21)$$

when $l'_d = 0$, $\Delta_{VE} = 0$ ... (3.21a)

when $l'_d = 0.25l_s$, $\Delta_{VE} = \frac{Pl_s\, l'^2}{8z^2 bd\, \rho^*\, n\, E_c}$ ... (3.21b)

(c) The total rotation of diagonally reinforced beams

The total rotation of the beam is

$$\theta = \theta_T + \theta_C + \theta_E \qquad \ldots (3.22)$$

where $\theta_T = \frac{\Delta_{VD1}}{l_s}$, the rotation associated with the elongation of the tension chord, AD, obtained from Eq. (3.20).

$\theta_c = \frac{\Delta_{VD2}}{l_s}$, the rotation associated with the contraction of the compression chord, BC , obtained from Eq. (3.20)

$\theta_E = \frac{\Delta_{VE}}{l_s}$, the rotation associated with the deformation of steel in the anchorages, obtained from Eq. (3.21).

3.3.3 A Critical Examination of the Assumptions

a) It was assumed that the principal mode of load transfer and the associated distortions, when the beam is diagonally cracked, are due to tension and compression along the respective diagonals of the beam. However, secondary reinforcements (stirrups and horizontal bars) when provided may be responsible for resisting a portion of the ultimate load in a different fashion. The increase in stiffness associated with such secondary basketing reinforcements has not been included. When the secondary reinforcement is curtailed at the face of the wall the increase in stiffness is likely to be negligable.

b) It was assumed earlier that the average depth of the compression strut is

$$D_a = \frac{l_s}{41}, \quad (3D - 2Z) \qquad \ldots (3.22)$$

As pointed out earlier, the exact depth of compression strut is uncertain. The depth would be greater than the lateral dimension of the spirals, which are provided to prevent the main bars from buckling, and less than the overall depth, D . However, using the strain measurements, made on diagonally reinforced beams by Binney[6] the equivalent depth of concrete strut could be estimated.

The curve (a) in Fig. 3.9 shows the typical strain variation for the steel along the compression diagonal observed by Binney. For the purpose of analysis, this curve was idealised by the straight line, (b). The horizontal line (c) shows the average strain, ϵ'_s , in the compression diagonal. The average steel force in the compression diagonal is therefore

$$C' = A_s E_s \epsilon'_s \qquad \ldots (3.23a)$$

For equilibrium, the total force C in the compression chord must be equal to the tension force, T , along the tension chord.

Thus $$C = T = A_s f_y \qquad \ldots (3.23b)$$

Therefore, the force resisted by concrete, C_c , is

$$C_c = C - C' = A_s f_y - A_s E_s \epsilon'_s \qquad \ldots (3.23c)$$

For the composite action of the diagonal concrete strut, the strain in the concrete, ϵ'_c should be approximately equal to the strain in the compression steel ϵ'_s .

Thus $$C_c = A_c E_c \epsilon'_c = A_c E_c \epsilon'_s \qquad \ldots (3.23d)$$

Combining Eqs. (3.23c) and (3.23d) the average depth, D_a , of the concrete strut is

$$D_a = \frac{A_s f_y - A_s E_s \epsilon'_s}{b\, E_c \epsilon'_s} \qquad \ldots (3.23e)$$

Fig. 3.11 compares the depth of concrete strut for the three beams reported by Binney, using the observed strain variation and Eq. (3.23e), with the assumed depth calculated from Eq. (3.22). The shaded blocks show the assumed depths as per Eq. (3.22). The unshaded blocks show the depths computed from observed strain variations, as per Eq. (3.23e). It is seen that the assumed and computed depths are of the same order for beams 316 and 318.

To trace the sensitivity of yield rotation to the changes in the assumed depth, D_a , rotations were computed for the beam shown in Fig. 3.12.a. for various values of D_a , $(0 < D_a < D)$ with an assumed end block length, $l'_d = 0.25$. The curve (b) in Fig. 3.12.b. shows this. In the practical range $(0.1 < \frac{D_a}{D} < 1.00)$, it is seen that the assumption regarding the depth of the compression strut does not significantly affect the yield rotation.

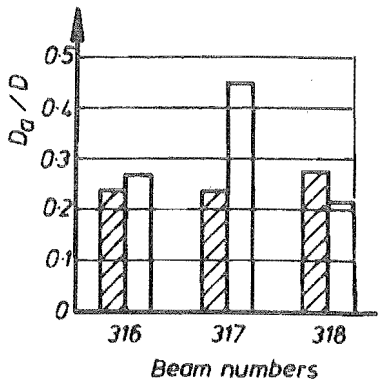

FIG. 3.11 COMPARISON OF DEPTH OF CONCRETE RESPONSIBLE FOR RESISTING COMPRESSION BASED ON OBSERVED STRAIN VARIATION WITH THAT ASSUMED IN THE ASSESSMENT OF DEFORMATIONS

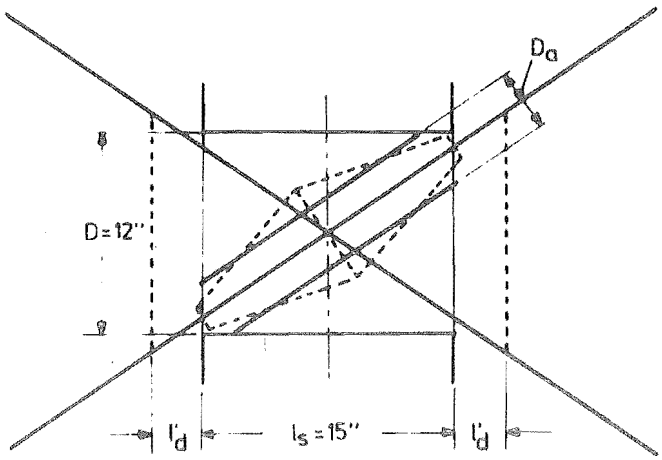

(a) The dimensions of the example coupling beam

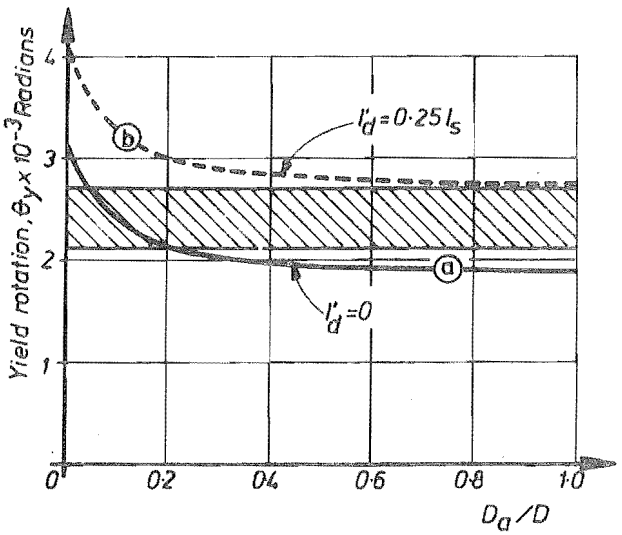

(b) The sensitivity of yield rotations with respect to the values of D_a and l'_d

FIG. 3.12 AN EXAMINATION OF THE YIELD ROTATION OF THE DIAGONALLY REINFORCED COUPLING BEAM AS AFFECTED BY THE AVERAGE EFFECTIVE DEPTH OF CONCRETE IN THE DIAGONAL COMPRESSION STRUT AND THE END BLOCK LENGTH, l'_d, OVER WHICH THE STRAINS ARE ASSUMED TO BE SIGNIFICANT

c) It was assumed that the steel anchored in the end block of length, l'_d , (see Fig. 3.10.b) will influence the distortions of the coupling beam. The upper and lower limits for this length were assumed as zero and $0.25l_s$. The variation of computed yield rotation for the example beam (see Fig. 3.12.a), for various assumed depths of compression strut, for $l'_d = 0.25l_s$ (curve(b)),and for $l'_d = 0$ (curve(a))are shown in Fig. 3.12.b. The theoretical values of rotation lie between the curves (a) and (b) depending on the depth of concrete, D_a , resisting compression, and the value of l'_d . It is seen that the rotations are sensitive to changes in the assumed values of l'_d . When $l'_d = 0.25l_s$ nearly 30% of the rotations are due to the deformation of steel in the anchorages.

The dimensions of the example beam are the same as those of the coupling beams used in the test specimen Shear Wall B* . The shaded band in Fig. 3.12.b. indicates the limits within which the rotations observed during cyclic loading lie. It is seen that this band lies between the curves (a) and (b) of Fig. 3.12.b. when $0 < l'_d < 0.25l_s$ and $0.2 < D_a/D < 1.0$.

3.3.4 The Proportions of Component Rotations in Diagonally Reinforced Beams

To examine the influence of the steel content on stiffness, the expressions for rotations θ_T , θ_C and θ_E have been modified. The relative proportions of these rotations were examined at the onset of yield during the assumed theoretical bilinear elasto-plastic behaviour. By substituting the total shear, P, at this limit,in terms of the steel area, A_s , and yield stress, f_y , in Eqs. (3.20), (3.21) and (3.22), the rotations are expressed in terms of the aspect ratio, $\frac{l_s}{D}$, and steel content, ρ^* as

---

* Details of this specimen are included in Chapter 5. The results of the test are presented in Chapter 7.

$$\theta_T = \frac{1}{2}\left(\frac{f_y}{nE_c}\right)\frac{1}{\sin\alpha\cos\alpha} \quad \ldots (3.24a)$$

$$\theta_C = \frac{2\rho^*\left(\frac{f_y}{E_c}\right)}{\cos^3\alpha\sin\alpha\left(\frac{3D-2Z}{d}\right) + 4(n-1)\rho^*\sin\alpha\cos\alpha} \quad \ldots (3.24b)$$

$$\theta_E = \frac{1}{4}\left(\frac{f_y}{nE_c}\right)\frac{1}{\sin\alpha\cos\alpha} \quad \text{when } l_d' = \frac{l_s}{4} \quad \ldots (3.24c)$$

$$\theta_E = 0 \quad \text{when } l_d' = 0 \quad \ldots (3.24d)$$

and $$\theta_y = \theta_T + \theta_C + \theta_E \quad \ldots (3.24e)$$

where θ_y = the yield rotation of the diagonally reinforced beam.

The variation of the components of rotation θ_T, θ_C and θ_E, are plotted against the steel content for an aspect ratio, $\frac{L}{D} = 1.00$ in Fig. 3.13. It is seen that

1. The rotations associated with the elongation of steel in the tension chord, θ_T, and the rotations associated with the deformation of steel in the anchorages, θ_E, do not depend on the steel content. These constitute the major portion of the total rotations.
2. The rotations associated with the contraction of compression chord is proportional to steel content. However, the rotation associated with the deformation of the compression strut is small compared to the total yield rotation, θ_y.
3. The rotations associated with the deformation of steel in the anchorages, θ_E, is approximately 25 to 35% of the total rotation when $l_d' = 0.25 l_s$.

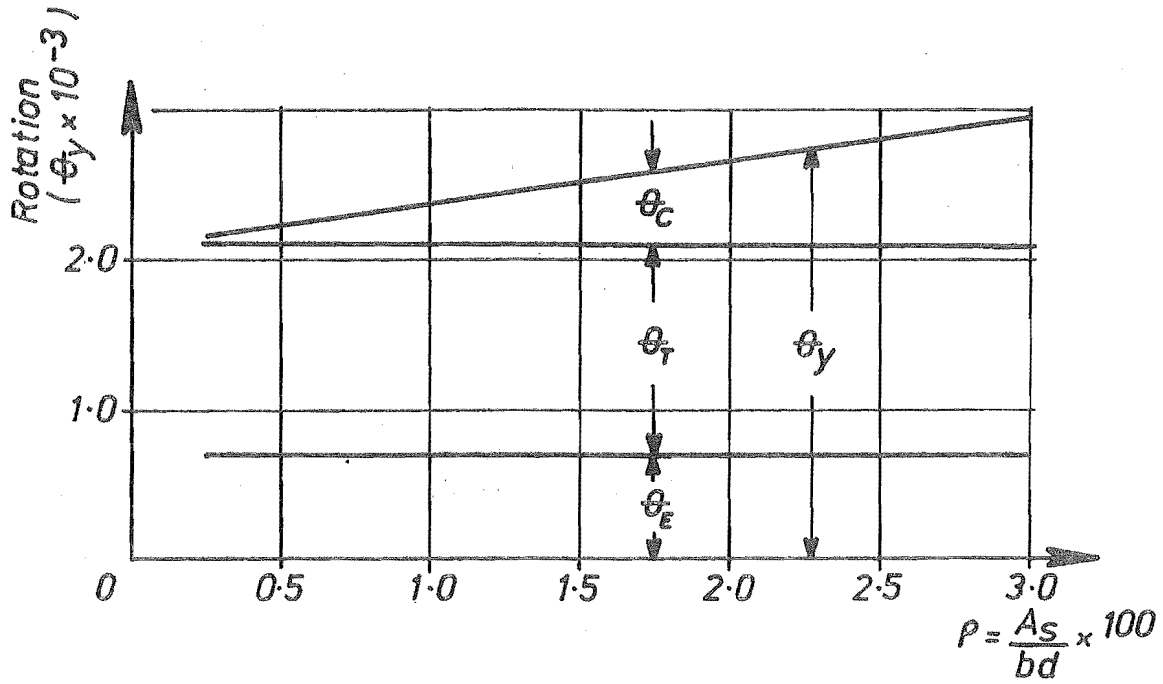

FIG. 3.13 VARIATION OF THE COMPONENTS OF YIELD ROTATION FOR DIFFERENT PERCENTAGES OF STEEL, ρ , FOR AN ASPECT RATIO l_s/D = 1.00 IN A DIAGONALLY REINFORCED COUPLING BEAM

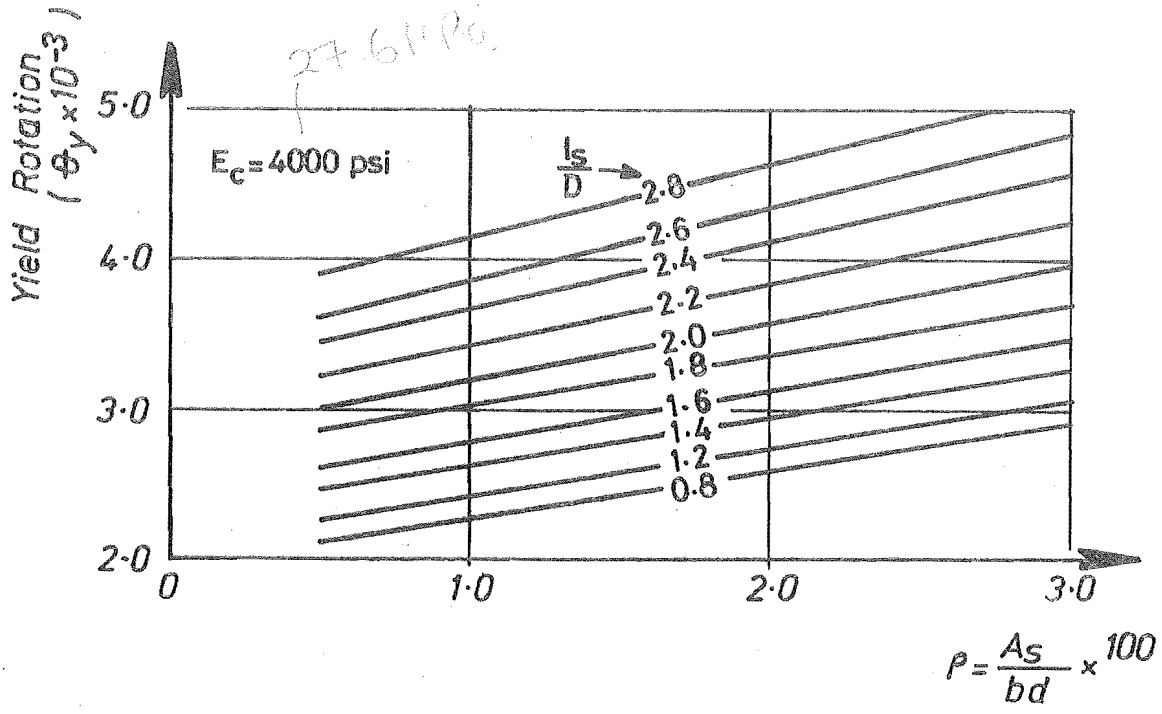

FIG. 3.14 DESIGN CHART FOR THE DETERMINATION OF YIELD ROTATION OF DIAGONALLY REINFORCED BEAMS

3.3.5 A Chart for the Determination of Yield Rotation

The yield rotation for the diagonally reinforced beam is plotted against the diagonal steel content for various aspect ratios of the beam in Fig. 3.14. This figure can be used as a design aid. The equivalent flexural rigidity EI_{eq} of the diagonally cracked beam is

$$EI_{eq} = \frac{P_u l^2}{12\theta_y} \qquad \ldots (3.25)$$

where θ_y = the yield rotation for the particular aspect ratio and steel content from Fig. 3.14.

P_u = theoretical ultimate shear as given by Eq. (3.17).

3.3.6 A Comparison of Computed Stiffnesses with the Experimental Evidence

Binney's report on diagonally reinforced beams includes Paulay's pilot test and the tests on two diagonally reinforced beams conducted by him. In Fig. 3.15, a comparison of stiffness of the diagonally reinforced beams, computed with Eq. (3.22) and the stiffness observed during test is made for the beams reported by Binney, and for the beams used in Shear Wall B test specimens. The stiffnesses are expressed in terms of the stiffness in the uncracked state.

For each, the theoretical and observed stiffnesses, a lower and upper limit is indicated. For the theoretical assessment the upper limit corresponds to the value computed with $l_d' = 0$ and the lower limit to the value computed with $l_d' = 0.25 l_s$. The two limits for the experimentally determined stiffnesses represent the highest and lowest values observed during cyclic loading. It is seen that, generally, there is good agreement between the values computed with Eq. (3.22) and those observed during test.

3.3.7 Post-elastic Performance of the Diagonally Reinforced Beams

A typical load rotation curve of a diagonally reinforced beam observed by Paulay[5] is shown in Fig. 3.6. This figure shows the

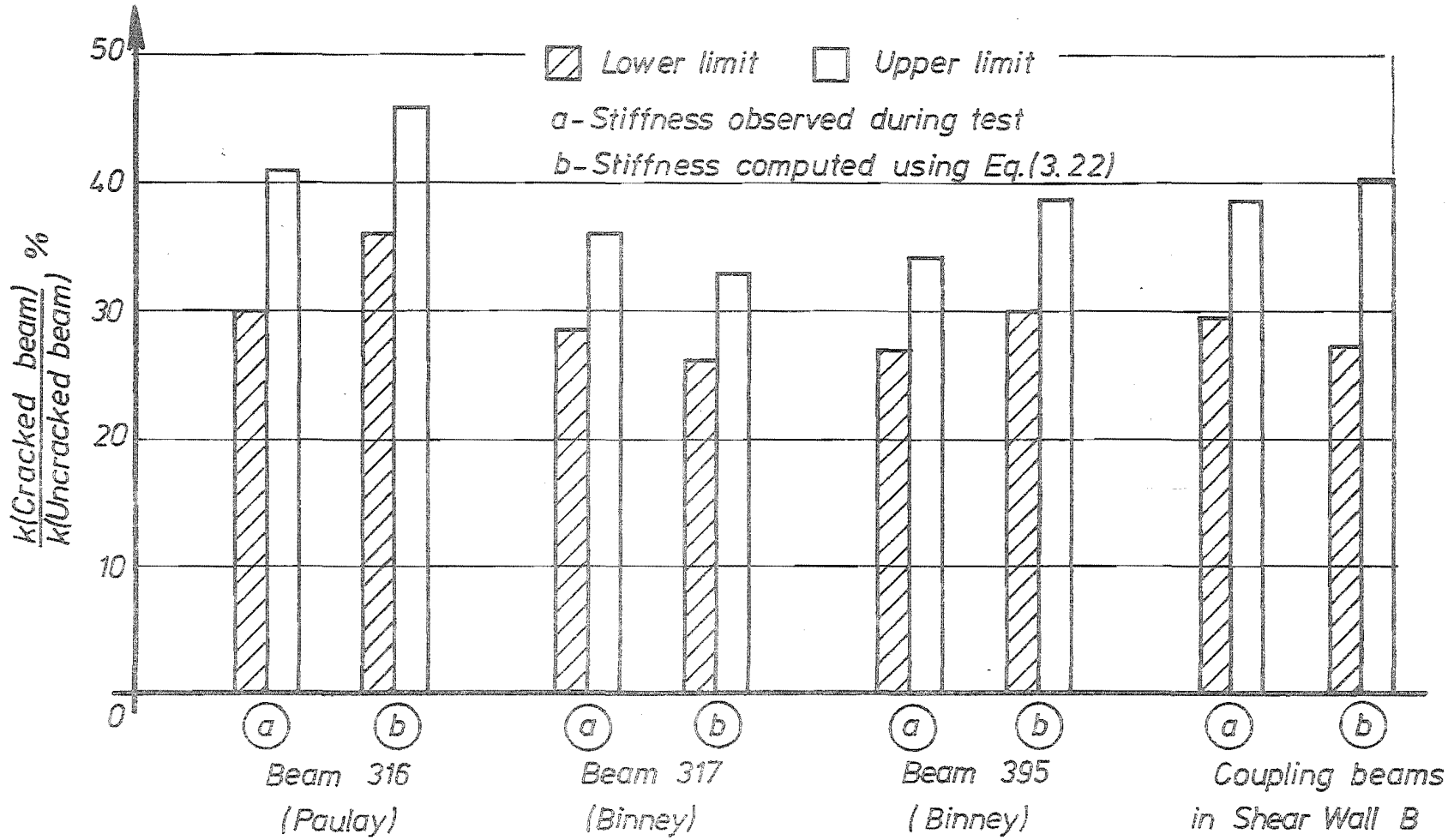

FIG. 3.15 COMPARISON OF THEORETICAL AND OBSERVED STIFFNESSES OF DIAGONALLY REINFORCED BEAMS

excellent energy absorption characteristics of the diagonally reinforced beams. The hysteresis loops of the diagonally reinforced beams bear the characteristics of a steel member. As expected, the soft range, witnessed in conventionally reinforced beams,is absent. Upon load reversal the compression diagonal was subjected to yield before cracks crossing it closed and before the concrete was engaged in the transfer of compression. The compression yielding and the Bauschinger effect associated with it can be seen in the loops. Thus the entire shear and flexure could be resisted by the steel forces alone.

3.4 A COMPARISON BETWEEN THE BEHAVIOUR OF THE TWO TYPES OF COUPLING BEAMS

3.4.1 Stiffness

Fig. 3.16 compares the theoretical rotations of the conventionally reinforced beams with diagonally reinforced beams for an aspect ratio of 1.00 for various percentages of steel. The rotations of the conventional beams are 1.4 to 2.0 times larger than the rotations of diagonally reinforced beams, depending upon the steel content. The increase in rotations for the conventionally reinforced beams is more for heavily reinforced beams (100% when p = 3.00). In the uncracked state it is reasonable to assume that both the conventionally reinforced beam and the diagonally reinforced beam of the same dimensions have approximately equal stiffnesses.

The conventionally reinforced beam exhibits a soft range at very low loads,during which its stiffness is very low, when it is subjected to a number of high intensity load reversals. This behaviour is undesirable for earthquake resistant design. The stiffness of diagonally reinforced beams increases till it reaches a steady range. The soft range of stiffness, associated with the shear deformation,is absent in the diagonally reinforced beam.

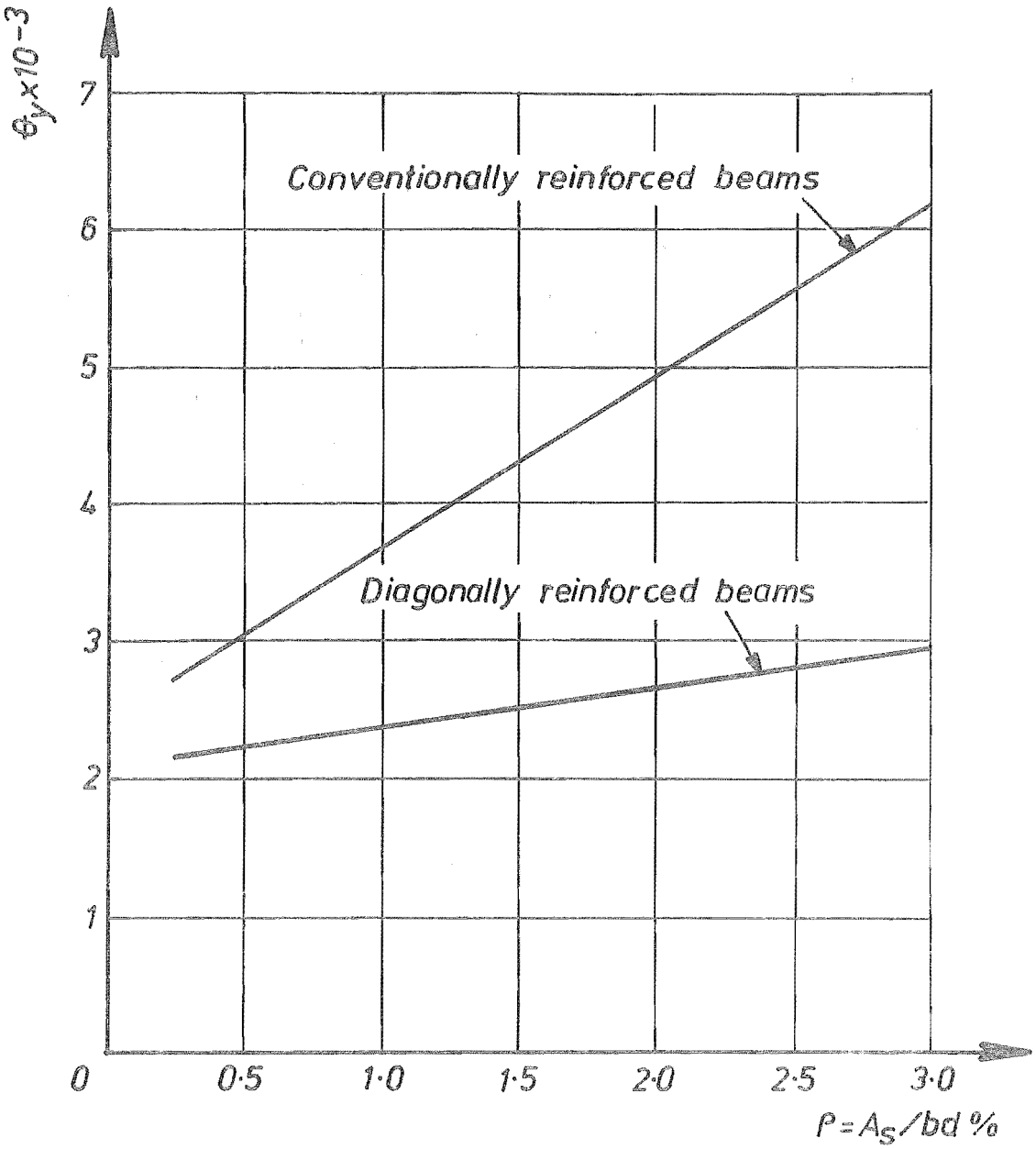

FIG. 3.16 A COMPARISON OF YIELD ROTATIONS FOR THE CONVENTIONALLY REINFORCED BEAMS AND THE DIAGONALLY REINFORCED BEAMS FOR THE SAME ASSUMED LENGTHS OF ANCHORAGE, $1'_d = 0.25l_s$

3.4.2 Ductility

For the purpose of comparing the ductility factor of conventional and diagonally reinforced beams, the ductility of a coupling beam is defined as the ratio of the rotation sustained at ultimate load to its yield rotation. The cummulative ductility attained by a beam is defined as the sum of the maximum ductilities attained at maximum load levels during each high intensity load reversal. The percentage of ultimate load plotted against the cumulative ductilities attained by the beams, tested by Paulay[5] and Binney[6], at maximum load levels for the various cycles are shown in Fig. 3.17. This has been reproduced from Binney's report[6]. The improvement in ductility characteristics of the diagonally reinforced beam could be clearly seen in this figure. It is also seen that the diagonally reinforced beams retain much longer their ability to transfer load at large ductilities.

3.4.3 Energy Absorption Characteristics

Fig. 3.18 shows the ratio of actual energy absorbed (area under the load-rotation curve) to the theoretical energy absorbed (area under the theoretical bilinear load-rotation curve), E_A/E_O, plotted against the cumulative post-elastic energy for the various cycles at the maximum E_A/E_O levels. This was used by Binney[6] to quantify the energy absorption characteristics of diagonally and conventionally reinforced beams. The superior energy absorption properties of the diagonally reinforced beams is again evident from this figure.

3.5 THE TENSION AND COMPRESSION WALLS

In a coupled shear wall structure one wall is subjected to tension and the other wall to compression in the presence of wall moments M_1 and M_2 respectively. The plastic hinges in the walls will develop at the base when the ultimate load is approached. While discussing the strength and deformation properties of these walls,

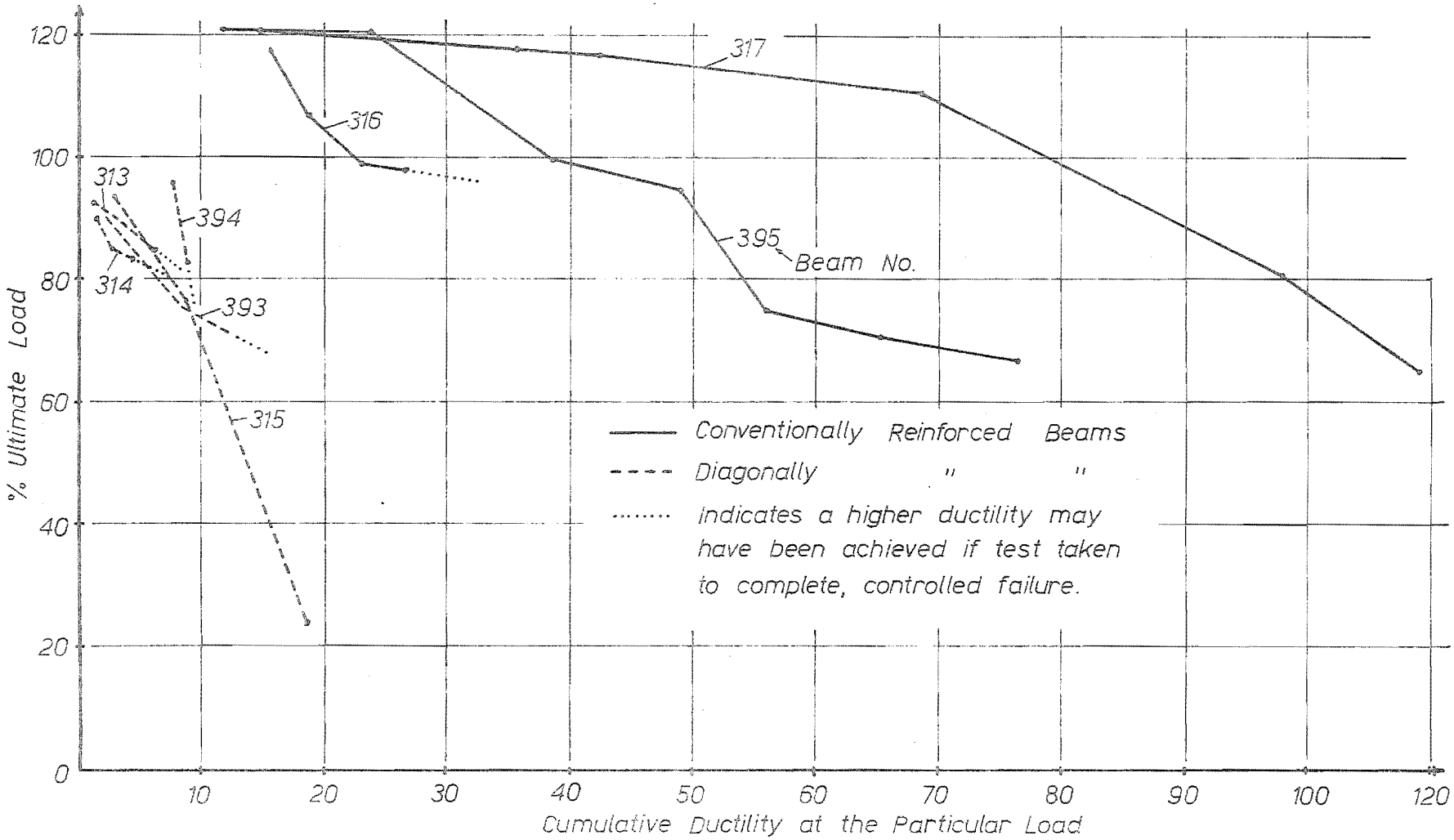

FIG. 3.17 CUMULATIVE DUCTILITIES AT THE PARTICULAR LOAD LEVELS FOR THE BEAMS TESTED BY PAULAY AND BINNEY[6]

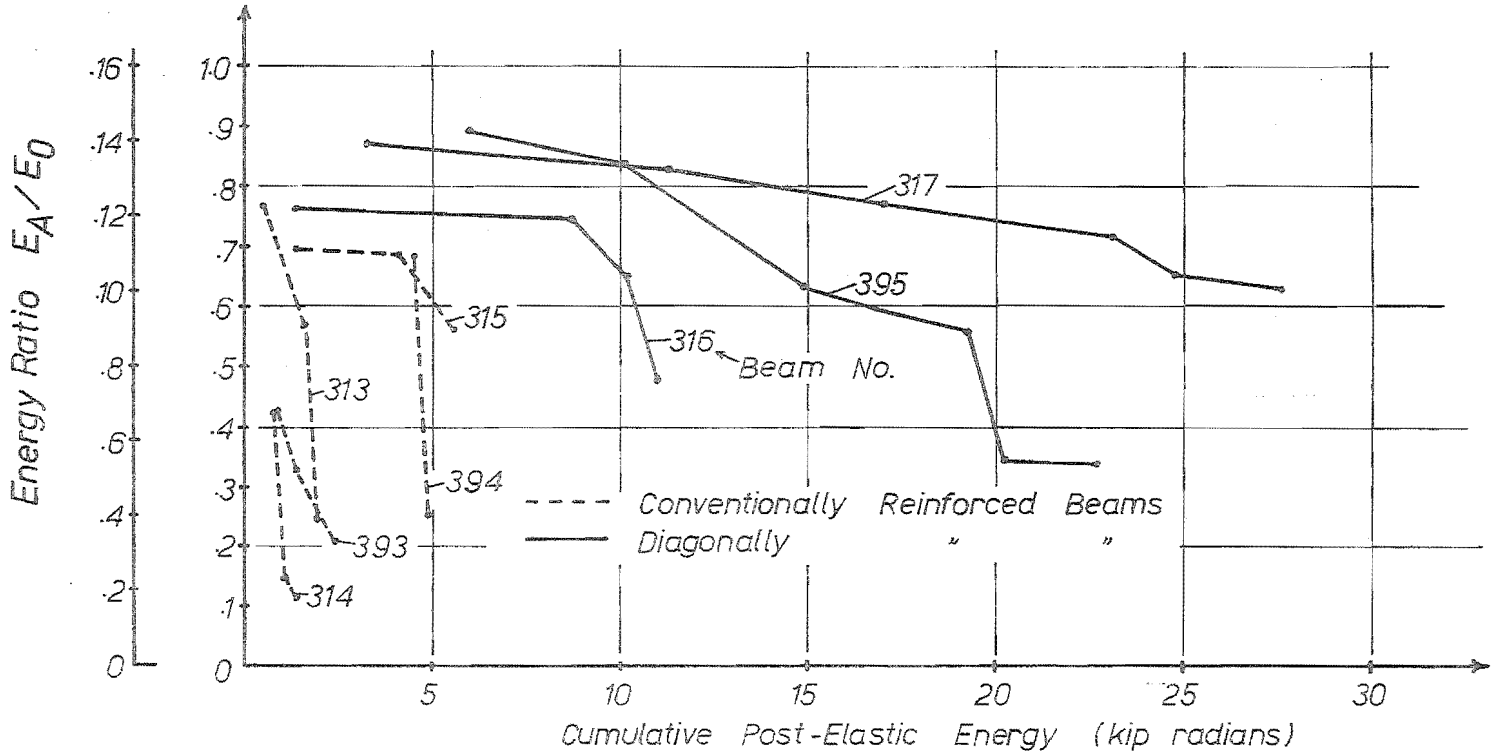

FIG. 3.18 CUMULATIVE POST-ELASTIC ENERGY AT A PARTICULAR VALUE OF E_A/E_O FOR THE BEAMS TESTED BY PAULAY AND BINNEY[6]

several terms have been introduced.

3.5.1 Definition of Terms Used

(i) Ideal moment capacities M_{u1} , M_{u2}

The subscripts 1 and 2 refer to tension and compression walls respectively. This is the section's theoretical moment capacity calculated from accepted first principles using specified minimum steel and concrete strengths.

(ii) Reliable moment capacities M_{d1} , M_{d2}

These are ideal capacities multiplied by the corresponding capacity reduction factors, i.e. $M_{d1} = \varphi_1 M_{u1}$ and $M_{d2} = \varphi_2 M_{u2}$ These are the moments to be relied upon in design.

(iii) Probable moment capacities M_{p1} , M_{p2}

This is the section's theoretical moment capacity calculated from expected mean material strengths.

(iv) Overstrength moment capacities M_{o1} , M_{o2}

This is the expected maximum moment capacity of a member. It makes allowance for true yield strength, for possible extra steel that may participate and for strain hardening. It can be considered as the upper bound of the member's strength in flexure.

(v) Notation used for shear capacities

The same subscripts as used in (i) to (iv) when used with the letter V instead of the letter M, refer to the corresponding shear capacities. For example V_{u1} and V_{u2} refer to the ideal shear capacities of the tension wall and the compression wall respectively.

(vi) Terms used to define the centroid of a section

(a) Geometric centroid (O). This refers to the centre of gravity of the gross area of the concrete section.

(b) Force centroid (F). This is the centroid of resistance of a section resulting from stresses induced when the steel and the concrete

are subjected to a predefined uniform strain, e . Thus the force centroid in tension is different from that in compression. For an unsymmetrical section the position of force centroid varies for different predefined uniform strains.

(c) Plastic centroid. This is the centroid of resistance of a section resulting from stresses produced when the steel and the concrete are subjected to a uniform theoretical ultimate strain of 0.003. Thus the plastic centroid is the same as the force centroid when the predefined uniform strain is 0.003.

3.5.2 The Ultimate Strength of the Walls

(a) Flexureal strength

The overall dimensions of the walls remain sensibly constant over the full height. In a few tall shear walls the thickness of the walls may be reduced in the upper storeys. The ultimate strength of these walls can be evaluated using the axial load-bending moment interaction relationship, similar to eccentrically loaded columns. As pointed out in Chapter 2, both the moments and the axial forces reduce in the upper storeys. Therefore, the flexural reinforcement could be curtailed in the upper storeys. For each wall, the sign of the axial force and moment changes whenever the load is reversed. Because more than one axial load-bending moment combination may have to be considered at various levels of the structure, to assess the strength of these walls, it may be advantageous to construct the appropriate interaction curves for the ultimate condition. With the aid of a small computer, this is a relatively easy task[86].

Fig. 3.19 shows the axial force-moment interaction for the four different sections used in the walls of the shear wall models* A and B at ultimate load. For the purpose of obtaining these interaction curves various locations, as shown in Fig. 3.20.b, were assumed for the neutral axis position for the section considered.

---

* The reinforcement details are given in Chapter 5.

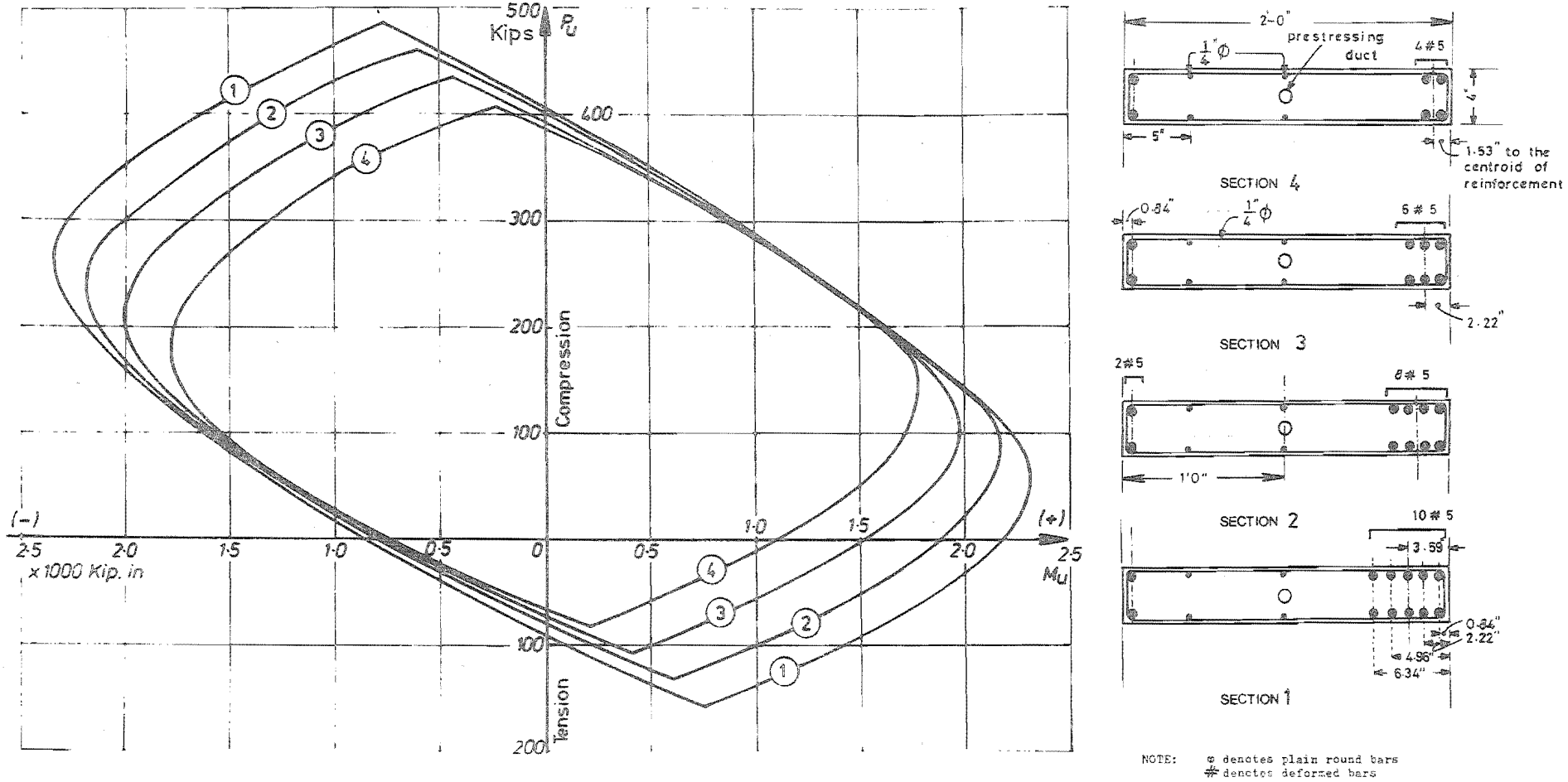

FIG. 3.19 INTERACTION CURVES FOR THE VARIOUS SECTIONS USED IN THE WALLS OF THE MODELS

Fig. 3.20.c and d show the stresses and the equivalent compressive stress block used in the analysis. The properties of this compressive stress block are those defined by Hognestad[87] et al. For each neutral axis position the combination of ultimate axial force P_u and ultimate moment M_u are computed based on the condition shown in Fig. 3.20.b. The moments are computed about the geometric centroid, O , so that the moments from the interaction diagrams could be directly related to the moments calculated using the finite difference approximation of the laminar analysis described in Chapter 2. Fig. 3.19 shows that the interaction diagrams are "displaced". When there is a uniform compressive strain, the ordinate for moment indicates a small negative value. This is because the moments are computed about the geometric centroid instead of the plastic centroid. These interaction diagrams are used to

(a) determine the ultimate nominal strengths M_{u1} and M_{u2} for the critical sections at the base, and

(b) determine the locations at which the flexural reinforcement in the walls may be curtailed in the upper storeys.

(b) Shear strength

In the design of the shear walls it is necessary to ensure that shear failure does not occur before the ductile type of failure, associated with yielding of flexural steel, could be achieved. The probable moment capacities, M_{p1} and M_{p2}, will be greater than the nominal moment capacities, M_{u1} and M_{u2}, calculated using the interaction curves. Indeed the failure moment is likely to be more than the probable moment capacities M_{p1} and M_{p2} owing to the following reasons:

(i) In the hard grade A432 (f_y = 60 ksi) steel, stresses may increase with an increase in yield strain above the designated yield point[88].

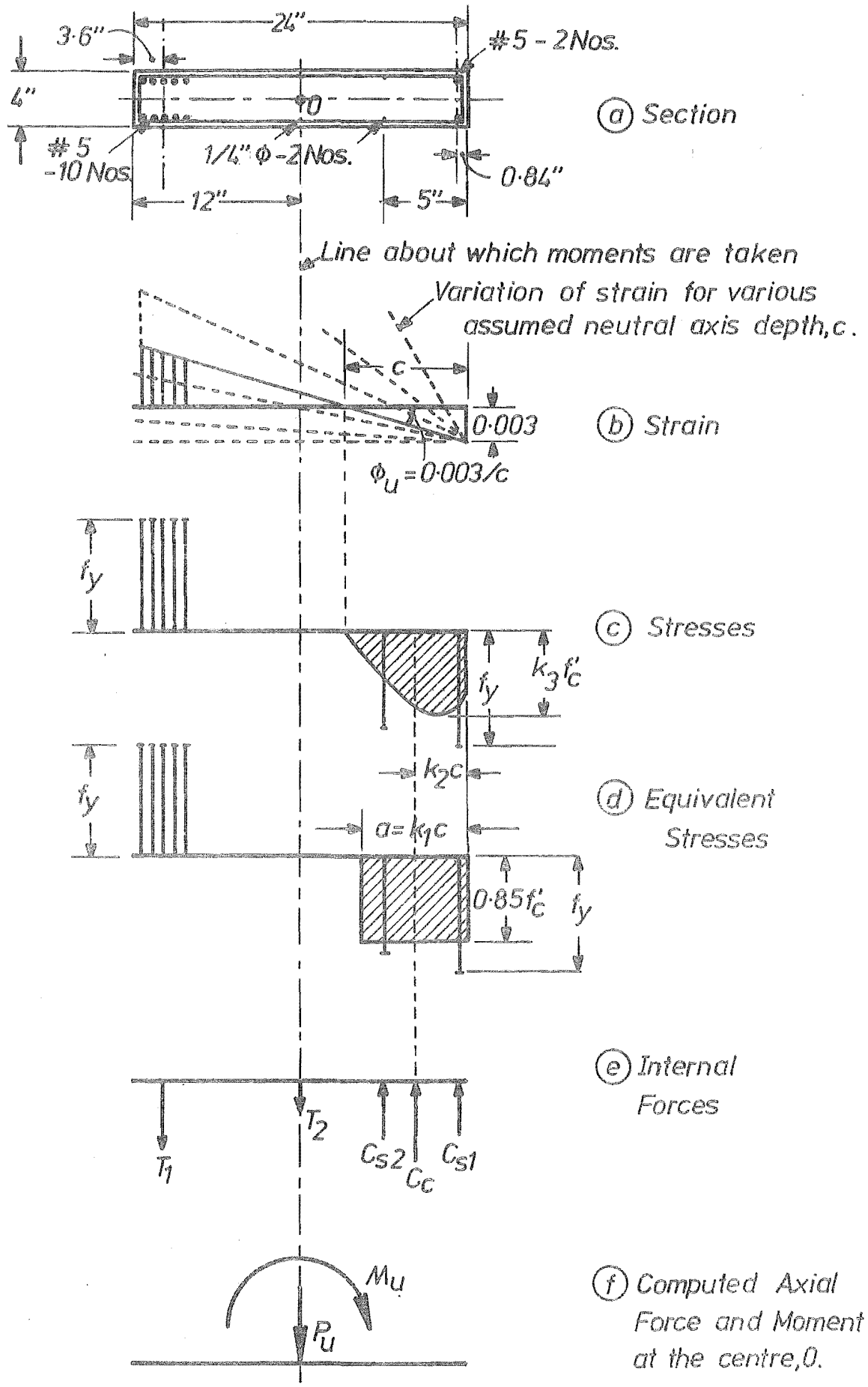

FIG. 3.20 TYPICAL SHEAR WALL SECTION SUBJECTED TO AXIAL LOAD AND BENDING MOMENT AT ULTIMATE LOAD

(ii) The steel provided in the critical coupling beam is likely to reach yield strain first. From the onset of this yield, the steel in the critical coupling beam is subjected to plastic deformation. In well designed shear walls, the walls reach ultimate load after the steel in most of the coupling beams reaches yield strain. When the walls reach ultimate load the steel strains in the beams in the critical region could be in the strain hardening range owing to very large yield deformations sustained by them. This leads to an increase in the value of the axial force, T_u, generated by the accumulation of coupling beam shears. This increases the ultimate moment capacity of the structure due to increase in the lT_u component. (See Eq. (2.23)).

(iii) Case studies of prototype shear wall structures indicate that the axial compression generated in the critical wall section is likely to be below balanced load. Therefore, the probable failure moment, M_{p2}, is likely to increase because of the increase in the axial compression force T_u. (See Fig. 3.19.)

(iv) The tension force, T_u, computed at the base of Wall 1 is relatively large. Wall 1 should resist this tension force and the wall moment, M_{1u}. Case studies of the prototype shear wall indicate that the depth of compressive stress block, c, required to develop this moment, M_{1u}, with an axial tension in the wall would be small compared to the total depth of the shear wall. The strain pattern associated with this small neutral axis depth may cause the strain in the tension steel, farthest from the neutral axis, to be in the strain hardening range when the ultimate load on the wall is reached.

For the walls to be able to attain the failure moments, without the danger of shear failure, the shear capacity of the tension and compression walls of the coupled shear wall need be based on over-strength moment capacities M_{o1} and M_{o2}. The reliable shear

capacity of the tension and compression walls should therefore be

$$V_{s1} = \frac{1}{\varphi_1 \varphi_s} \frac{M_{o1}}{M_{u1}} V_{u1} \quad \ldots(3.26)$$

$$V_{s2} = \frac{1}{\varphi_2 \varphi_s} \frac{M_{o2}}{M_{u2}} V_{u2} \quad \ldots(3.27)$$

where φ_1 is the capacity reduction factor for moment in tension walls

φ_2 is the capacity reduction factor for moment in compression walls

φ_s is the capacity reduction factor for shear.

In the above expressions the ideal moment capacities M_{u1} and M_{u2} are calculated using specified minimum concrete and steel strength properties. Multiplication of nominal strengths by factors ranging from 1.1 to 1.4 would make allowance for the factors listed earlier.

While providing stirrups to resist the shear it should be borne in mind that, under severe seismic induced loads, which would cause yielding in the walls, flexural and diagonal cracking and consequent loss of shear capacity of concrete would occur. It is doubtful whether under these conditions there would be any shear resistance provided by the concrete, especially in the tension wall. Thus, it is recommended that the contribution of concrete to shear resistance in the region of the plastic hinges be ignored. The horizontal stirrups provided should be able to supply the necessary reliable shear capacity computed using Eqs. (3.26) and (3.27).

3.5.3 Axial Load-Moment Curvature Relationships for the Wall Sections

The wall sections are subjected to flexure and axial load. The axial load influences the curvature and hence there is no unique moment-curvature relationship as in the case of members subjected to moments alone[89]. However, the value of the curvature is unique for

a particular combination of axial load and bending moment. Hence the curvature variation of a particular section depends on the axial load-moment history of the section, as the shear wall is loaded from zero load to its ultimate capacity.

In the previous section ultimate load moment interaction was computed based on the limiting maximum concrete strain $e_c = 0.003$. Blume[89] et al, have plotted the curvatures, ϕ_u, against the ultimate axial load, P_u, for various axial load-moment combinations at ultimate condition represented by the extreme concrete fibre reaching a strain of 0.003. A better understanding of the elastic and post-elastic deformations could be had if a continuous plot of curvature variation is made for the critical section. The theoretical axial load-moment history for this section is known from the elasto-plastic analysis of the shear wall*. When the shear wall is loaded from zero load to its theoretical ultimate load, the concrete strains in the critical sections increase from 0 to 0.003. The maximum steel strains increase from zero to beyond yield till the strain for that neutral axis depth, as shown in Fig. 3.20.b, is reached. The interaction diagrams in Fig. 3.19 show the combinations of load and moment at a strain limit of $e_c = 0.003$.

To trace the behaviour of the section from zero load to ultimate load a set of interaction diagrams for the critical section of the model walls, shown in Fig. 3.19, for various stipulated maximum concrete strains (0 to 0.003) and steel strains (0 to $\geq \frac{f_y}{E_s}$) are plotted. (Fig. 3.21.) The various neutral axis depths considered satisfied the following conditions:

1. maximum concrete strain $\leq e_c$
2. maximum steel strains $\leq e_{st}$
3. either the concrete strain was equal to e_c or the steel strain farthest from the neutral axis was equal to e_{st}.

---

* An incremental elasto-plastic analysis is proposed in Chapter 4.

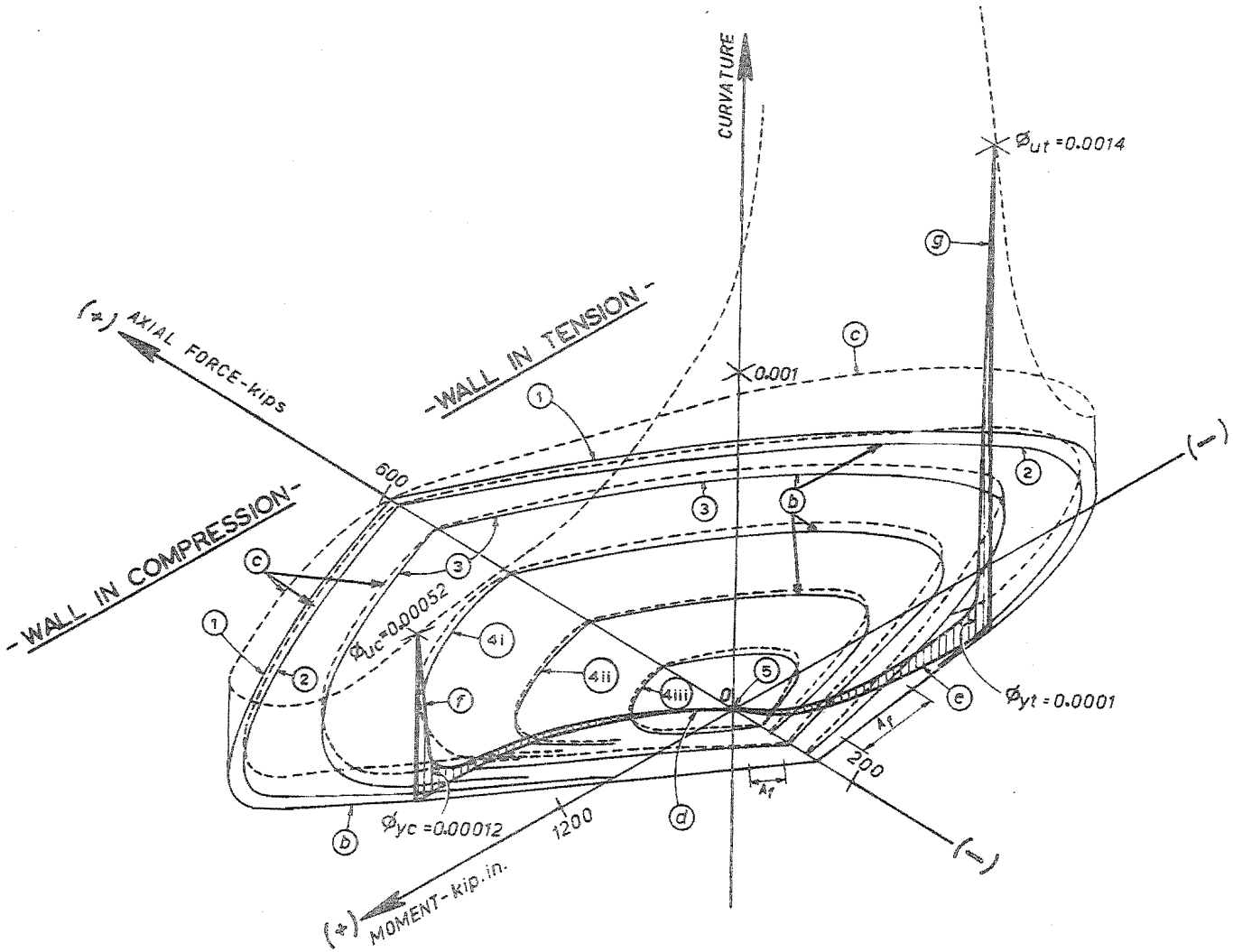

FIG. 3.21 VARIATION OF CURVATURE FOR THE CRITICAL SECTIONS OF TENSION AND COMPRESSION WALLS WITH THE RELEVANT LOAD MOMENT HISTORY

Fig. 3.22.b shows the various neutral axis depths considered according to the above condition when the maximum stipulated strain in the concrete is e_c and the maximum stipulated strain in the steel is e_{st}.

First the steel strain e_{st} was chosen as a fixed value. The strain in the concrete was varied. This concrete strain was less than or equal to the limiting strain, e_c. For each neutral axis position associated with steel strain, e_{st}, and concrete strain, $\leq e_c$, the axial load, P, the moment, M, and the curvature, φ, were computed. For computing the curvatures the following relationship was used. (See Fig. 3.22.b).

$$\varphi = \frac{e_{st}}{d_s - c} \qquad \ldots (3.28)$$

Next, the concrete strain, e_c, was chosen as a fixed value. The strain in the steel was varied. This steel strain was less than or equal to the limiting strain, e_{st}. As before, for each neutral axis position associated with the concrete strain, e_c, and steel strain, $\leq e_{st}$, the axial load, P, the moment, M, about the force centroid, and the curvature, φ, were computed. For computing the curvatures, the following relationship was used.

$$\varphi = \frac{e_c}{c} \qquad \ldots (3.29)$$

Thus for a set of stipulated limiting steel strains, e_{st}, and limiting concrete strains, e_c, one axial load-moment interaction curve was plotted using the axial loads and moments computed above. (See the curves (b) in the axial load-moment plane in Fig. 3.21). A particular point on this curve represents the axial load-moment combination when the steel strain is e_{st} and concrete strain is e_c. This point is usually considered as the "balanced" condition. Above this point the limiting concrete strain, e_c, controls. Steel strains are less than or equal to e_{st}.

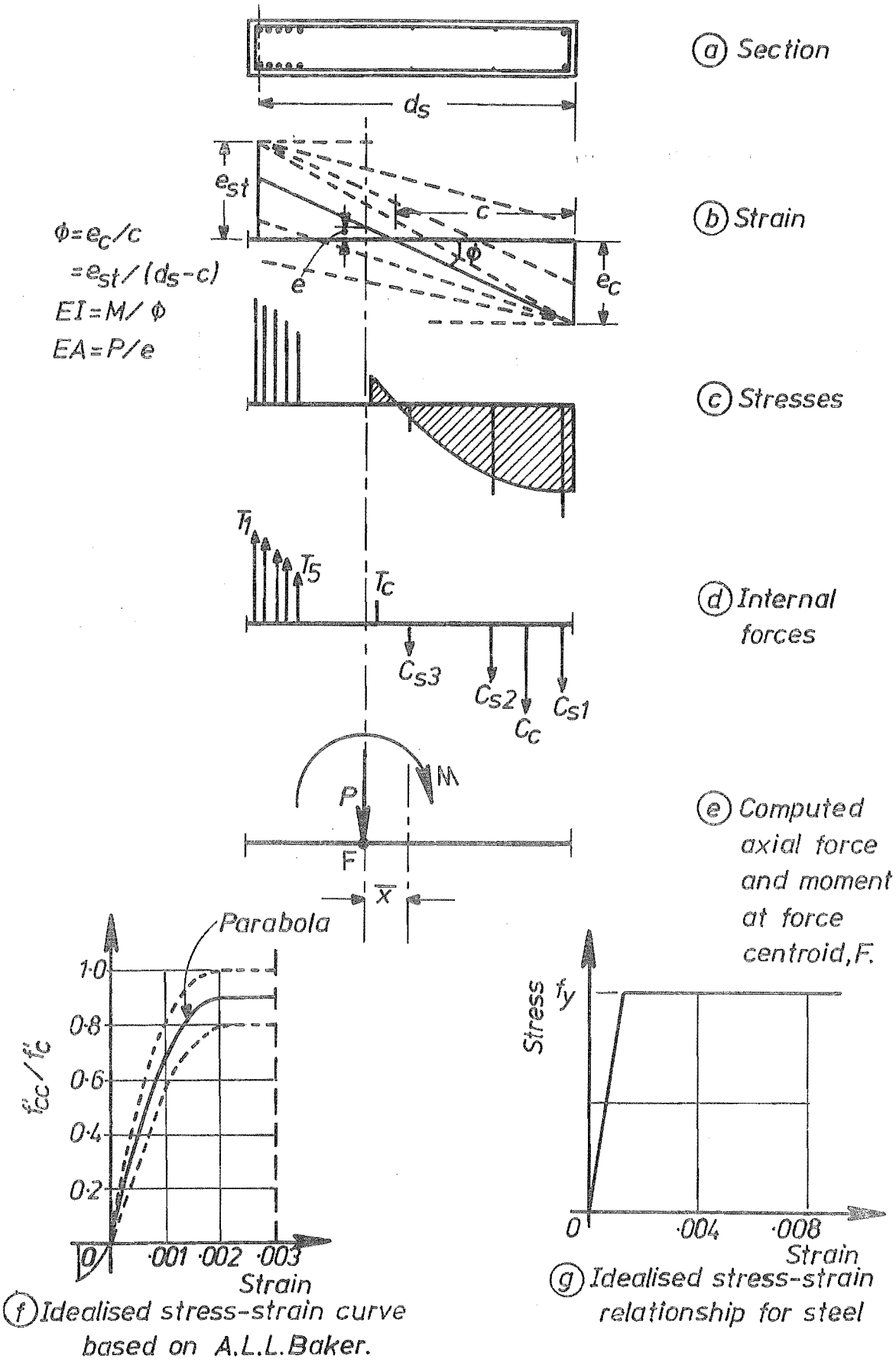

FIG. 3.22 COMPUTATION OF LOAD-MOMENT-CURVATURE RELATIONSHIP

For each neutral axis position, the curvature, φ , was plotted as vertical ordinates at the corresponding load-moment combinations. These ordinates are joined by a curve. Such a curve (c) shows the load-moment-curvature variation for the section (see Fig. 3.21). Such axial load-moment-curvature relationships were plotted for the following set of stipulated maximum strain limits at the base section of the shear wall models.

(1) The maximum concrete strain, $e_c = 0.003$. This corresponds to the theoretical ultimate axial load-moment curve. The curvature obtained using this maximum stipulated strain, $e_c = 0.003$, is the upper bound of the curvatures computed in this theoretical study. Hence the curve (c) so obtained is the outermost curve in Fig. 3.21. When the depth of neutral axis is very small, the values of curvatures are large since the steel strain, e_{st} , is large. The region "A_f" (See the outermost axial load-moment curve(b)for the tension wall) represents the combinations of ultimate axial load and ultimate moment for which there is the risk of tension steel fracturing before the theoretical maximum curvature predicted by the curvature curve (c) could be realised.

(2) The maximum concrete strain is $e_c = 0.002$. The maximum steel strain is $e_{st} = 0.0018$. A limiting strain of 0.0018 was chosen as this strain in the farthest steel from the neutral axis would cause yielding in approximately 90% of the tension steel provided for the base sections of the model walls. A maximum strain of 0.002 for concrete is arbitrarily chosen as the strain at the commencement of plasticity for concrete. It is seen that the loads and moments so computed are very close to the loads and moments computed for the ultimate condition. The curvature curve for this case, shown by a broken line, represents the theoretical yield curvatures. The deformations produced beyond this stage could be considered as entirely plastic deformations with very little increase in loads and moments.

(3) The maximum concrete strain is $e_c = 0.0011$. The maximum steel strain is $e_{st} = 0.0012$. The interaction curve represents the "elastic limit" condition. The concrete strain of 0.0011 is regarded as the strain at which the non-linear range of concrete strain commences. For the steel used in the model walls, 0.0012 is the strain at the end of linear stress-strain behaviour. This is based on the stress-strain curves for the reinforcement used in the shear wall models. When the farthest steel fibre reaches a strain of 0.0012, the non-linearity of the load-deformation relationship is expected to commence. The curvature curve for this case represents the theoretical "elastic limit" curvature.

(4) The following three strain limits, which represent the elastic cases, were also considered. This was to enable a continuous plot of the load-moment-curvature relationship to be made

(i) $e_c = 0.0009$ and $e_{st} = 0.0009$

(ii) $e_c = 0.0006$ and $e_{st} = 0.0006$

(iii) $e_c = 0.0003$ and $e_{st} = 0.0003$

The curvature curves for these cases represent "elastic curvatures".

(5) The origin, O , represents the interaction relationship when $e_c = 0$ and $e_{st} = 0$, i.e. when the specimen is in the unloaded condition.

Figs. 3.22.c and 3.22.f show the compressive stress block and the assumed stress-strain relationship for concrete used in the above analyses. These are based on Baker's[90,91] recommendations. The concrete stress-strain curve is a parabola up to a maximum stress of f'_{cc} at a strain of 0.002 where

$$f'_{cc} = \left(0.8 + \frac{0.1d}{c}\right) f'_c \leq f'_c \qquad \ldots (3.30)$$

The recommended range for $\frac{f'_{cc}}{f'_c}$ is 0.8 to 1.0 . After a strain of 0.002, the concrete stress remains constant at f'_{cc} until the theoretical maximum strain of 0.003 is reached.

For plotting these axial load-moment curves (Fig. 3.21), the moments were computed about the "force centroid" rather than the "geometric centroid" as shown in Fig. 3.22.e. When the loads and moments are related to the curvatures, it is necessary to compute all moments about the "force centroid" to avoid a positive moment being associated with a negative curvature. The tensile strength of concrete was also considered in the analysis as shown in Fig. 3.22.c.

Thus an estimate of the curvatures of the critical sections, subject to any load-moment combination, can be made from Fig. 3.21. On the same diagram, the load-moment histories of the critical section for the tension wall, represented by curve (e), and the compression wall, represented by curve (d), obtained from the elasto-plastic analysis,are plotted in the load-moment (P-M) plane. When plotting this load-moment history, due allowance was made to convert the values of the moments predicted by the elasto-plastic analysis to the corresponding values with respect to the "force centroid". The curvatures at the point of intersection of the load-moment interaction curve (b) and the load-moment history curve (e)or(d) for the section are the vertical ordinates from the point of intersection of these curves to the curvature curves, (c). These vertical ordinates are joined to get the theoretical load-moment-curvature variation for the tension wall, curve (g),and compression wall, curve (f).

The load-moment-curvature histories shown in Fig. 3.21 were used to determine the section ductilities of the critical section of the tension and compression walls of the models.

3.5.4 The Section Ductility

The curvature variation is not large till the limiting steel strain, e_{st}, reaches a value of 0.0018 or the limiting concrete strain, e_c, reaches a value of 0.002 as shown in Fig. 3.21. For the purpose of ductility studies this limit is taken as the yield condition for the section. Thus the curvatures computed, using the maximum stipulated strains indicated in case(2)in the previous section, are the yield curvatures. The curvature computed, when the concrete strain in the extreme fibre is $e_c = 0.003$ (case(1)) is the theoretical maximum curvature, φ_u. The section ductility, μ_s, is computed as the ratio of the theoretical maximum curvature, φ_u, to the theoretical yield curvature, φ_y, i.e.

$$\mu_s = \frac{\varphi_u}{\varphi_y} \qquad \ldots (3.31)$$

3.5.5 A Comparison of the Critical Section Ductility for the Tension and Compression Walls

As pointed out earlier, the shaded area in Fig. 3.21 shows the curvature variation with axial load and moment for the base sections of the tension and compression walls of the shear wall models. In Table 3.1, a comparison of the theoretical maximum section ductility for the critical sections of the tension and compression walls, is made.

TABLE 3.1 COMPARISON OF SECTION DUCTILITY FOR THE BASE SECTION OF THE WALLS OF THE MODELS

	Yield curvature	Theoretical maximum curvature	Theoretical maximum section ductility
	φ_y	φ_u	μ_s
Compression wall	$.12 \times 10^{-3}$	$.52 \times 10^{-3}$	4.33
Tension wall	$.10 \times 10^{-3}$	1.40×10^{-3}	14.00

The slopes of the compression and tension walls at any stage of loading must be nearly the same. A region with curvatures greater than yield curvature, φ_y, does not occur just at the critical section. The inelastic deformations are spread out over a finite length. When these factors are considered the curvature sustained by the compression wall, when the shear wall reaches ultimate condition, is always more than the curvature for the tension wall*. Thus the overall ductility attainable in a coupled shear wall will depend on maximum curvature at the base of the compression wall.

The section ductilities in Table 3.1 are based on a maximum concrete strain, $e_c = 0.003$. After the concrete cover spalled off, the area of the compressed concrete reduces to that inside the transverse reinforcement. If the concrete in the compression zone of the wall is confined by closely spaced stirrups, the ductility of the concrete may be greatly enhanced and large ultimate concrete strains may be reached. The limit of useful strain in this case could be 0.01 or even more[92]. Thus the ductility shown in Table 3.1 for the compression wall, may be regarded as the lower limit that could be achieved for the base section of the shear wall.

3.5.6. Analytical Assessment of the Flexural Rigidity, EI, and the Extensional Rigidity, EA, for the Walls in the Cracked State

It is necessary to assess, at least in an approximate way, the properties of the cracked walls in order to have an estimate of the overall deformations of the shear wall. An underestimate of the stiffness properties would lead to an overestimate of deflections and of ductilities which may not be realised in practice. As at present, there seems to be no reliable method of assessing the flexural rigidity,

---

* This is discussed in Chapter 4 (see Eq. 4.27).

EI, and the extensional rigidity, EA , in the cracked state by specified reduction factors applicable to the appropriate gross values of the tension and compression walls.

For ordinary reinforced concrete members, the axial deformation and the loss in stiffness due to reduction in EA, as a result of cracking, is not significant. For such members Kordina[85] has proposed certain global reduction factors. These are shown in Table 3.2. Such reduction factors make it unnecessary to integrate over the full height or length of the structural member, taking into account the variability of rigidities and stresses. However, in coupled shear walls axial deformation of the walls cannot be ignored. The elongation of the tension wall and the contraction of the compression wall introduces beam rotations which are opposite to the rotations caused by the flexural deformations of the walls. Thus an underestimate of the extension rigidity EA would lead to an overestimate of the beam rotations and beam ductilities. An estimate of extension rigidity and flexural rigidity is necessary to predict the post cracking behaviour of the shear wall. Paulay[74] suggested a value of $0.5EI_{gross}$ for the flexural rigidity, and a value of $0.7EA_{gross}$ for the extensional rigidity for the tension wall and allowed no reduction for the compression wall. While examining the effects of EI variation on the stability of frames, MacGregor[93] recommends that EI_{gross} could be used for columns. These suggestions are assembled in Table 3.2.

Fig. 3.23 shows the variation of the flexural rigidity for the critical sections of the tension and the compression walls of the models for various load-moment combinations. These load-moment combinations are given by curves marked (b). The variation of extension rigidity, EA (see curves marked (c))for the critical sections for the various load-moment combinations, represented by the curves marked (b) is shown in Fig. 3.24. The interaction curves marked (b) were obtained for the

TABLE 3.2 GLOBAL REDUCTION FACTORS FOR STIFFNESSES OF MEMBERS IN A CRACKED STATE

Reduction factor for EI = $\frac{\text{Effective stiffness } (EI)_{eff}}{\text{Stiffness based on gross concrete section-} (EI)_{gross}}$

Reduction factor for EA = $\frac{\text{Effective stiffness } (EA)_{eff}}{\text{Stiffness based on gross concrete section-} (EA)_{gross}}$

	Type of loading	Stage considered	Reduction factor for EI	Reduction factor for EA
Kordina [85]	Bending and axial compression (Compression Wall)	high overloads	$0.2 + 15(\rho+\rho')$	-
		service loads	$0.6 + 15(\rho+\rho')$	-
	Bending and axial tension (Tension Wall)	high overloads	$15\ (\rho+\rho')$	-
		service loads	$15\ (\rho+\rho')$	-
Paulay [74]	Compression Wall	Post cracking	1.00	1.00
	Tension Wall	Post cracking	0.50	0.70
MacGregor [93]	Bending and axial compression (Compression Wall)	Post cracking	1.00	-

previously defined (see Section 3.5.3) maximum stipulated strain limits. Reference may be made to Fig. 3.22.b where the strain variations for the various neutral axis depths considered are shown. The effective flexural rigidity, EI , and the extension rigidity, EA, were computed from the following relationships:

$$EI_{eff} = \frac{M}{\varphi} \qquad \ldots (3.32)$$

$$EA_{eff} = \frac{P}{e} \qquad \ldots (3.33)$$

where M = moment of all forces about the force centroid, F , shown in Fig. 3.22.e.

φ = curvature shown in Fig. 3.22.b.

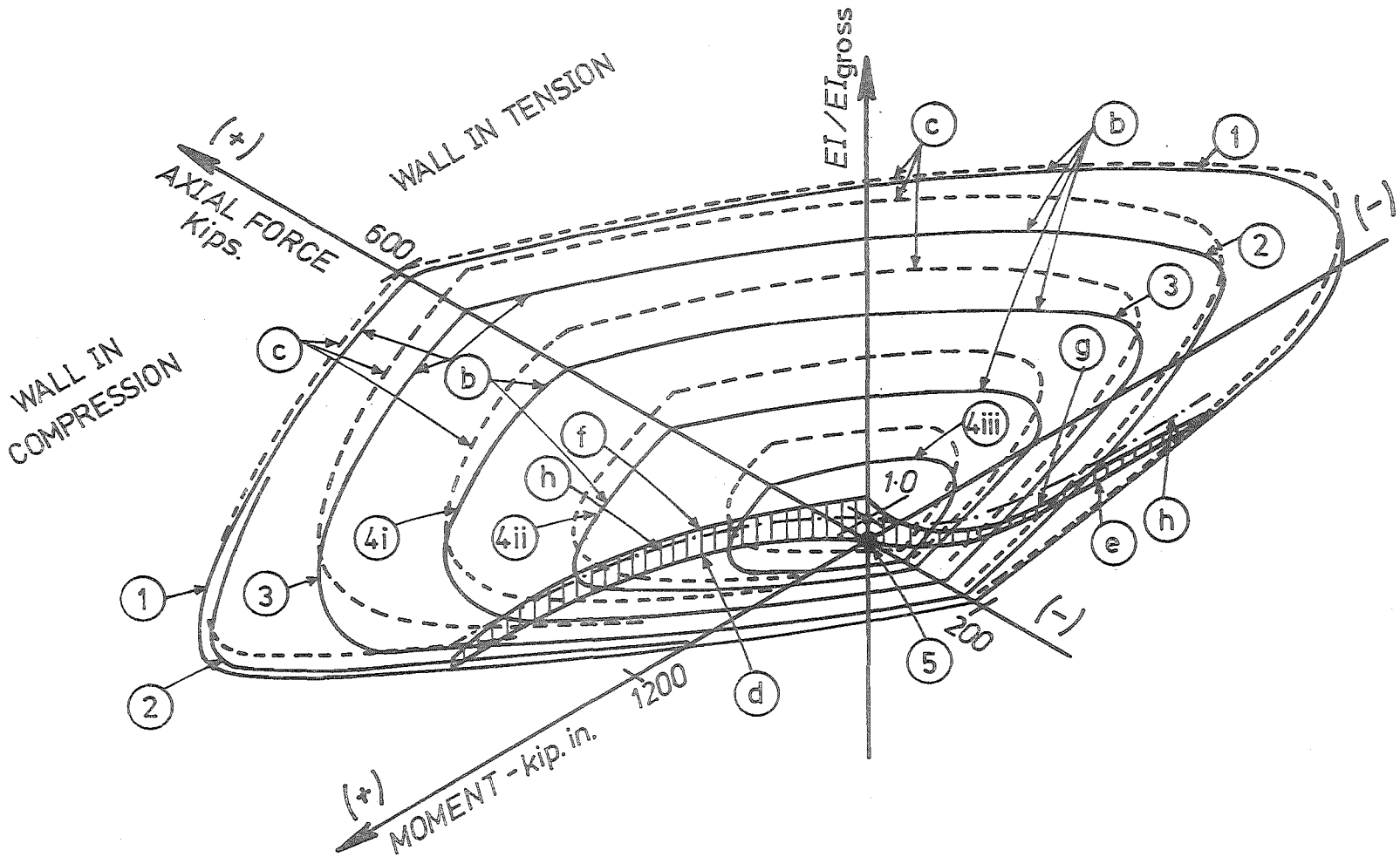

FIG. 3.23 VARIATION OF THE FLEXURAL RIGIDITY FOR THE CRITICAL SECTIONS OF THE TENSION AND COMPRESSION WALLS WITH THE RELEVANT LOAD-MOMENT HISTORY

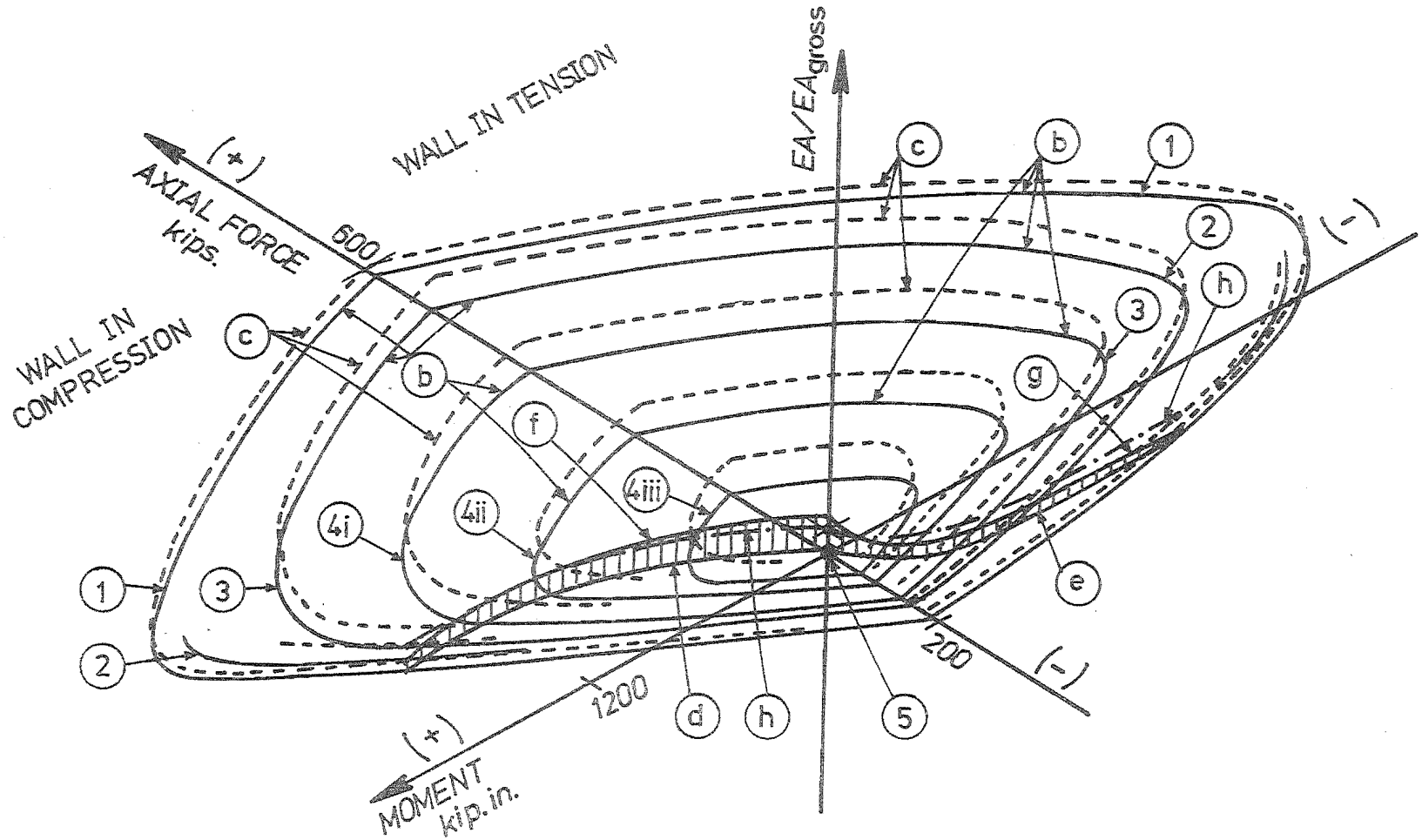

FIG. 3.24 VARIATION OF THE EXTENSION RIGIDITY FOR THE CRITICAL SECTION OF THE COMPRESSION AND TENSION WALLS WITH THE RELEVANT LOAD-MOMENT HISTORY

P = net axial force computed using the internal forces shown in Fig. 3.22.d.

e = strain at the force centroid F , shown in Fig. 3.22.b.

In the Figs. 3.23 and 3.24, the load-moment histories of the critical section for the tension wall (e) and the compression wall (d) obtained from the elasto-plastic analysis were also plotted. The properties EA and EI at the points of intersection of the load-moment interaction curve (b), and the load-moment history (e)or(d) curve, are the vertical ordinates to the curves marked (c) from the point of intersection. These ordinates when joined by a curve give the continuous variation of properties (EI and EA) for the section of the tension wall (g) and of the compression wall (f). Ordinates of curve(h) represent gross properties.

The reinforcement in the bottom three floors of the walls of the shear wall models were not varied with height. Adopting the same procedure as given in the preceding paragraph, the variation of properties at the level of these three floors for the corresponding load-moment history was also obtained. These are not shown in Figs. 3.23 and 3.24.

In the shear wall model,4 different sections, shown in Fig. 3.19, were used. For these sections similar interaction relationships as for the critical section shown in Fig. 3.23 and 3.24 were constructed. These are not shown.

The loads and moments at the sections at intervals of one storey were obtained from the elasto-plastic analysis for a particular stage of loading considered, for example, when the steel in the critical coupling beam reaches yield. For these loads and moments the values of EI and EA were found from the relevant load-moment EI or EA relationship. These were then plotted to obtain the variation of properties of the wall with height at the stage considered. The variation of EI and EA for the tension and compression wall when the steel in the critical

coupling beam reaches yield, are shown in Fig. 3.25.c,d,g,h. The variation of axial force and moments at this stage,as found from the elasto-plastic analysis, are also shown. In Figs. 3.25.c and g, the following values of EI are plotted:

(1) Flexural rigidity based on gross concrete area - $(EI)_{gross}$ - upper limit of Eq. (3.12).

(2) Flexural rigidity based on the uncracked section considering both steel and concrete.

(3) Flexural rigidity obtained from the interaction diagrams as explained earlier in this section.

(4) Flexural rigidity of the cracked transformed critical section - $(EI)_{cr}$ - lower limit of Eq. (3.12).

(5) Flexural rigidity computed using Eq. (3.12).

(6) Flexural rigidity computed using Paulay's suggestion - $0.5EI_{gross}$ for the tension wall and EI_{gross} for compression wall.

(7) Flexural rigidity computed using Kordina's equation for high overloads.

(8) Flexural rigidity computed using Kordina's equation for service loads.

In Figs. 3.25.d and 3.25.h, the following values of EA are plotted:

(1) Extensional rigidity based on gross concrete area.

(2) Extensional rigidity based on uncracked section considering both steel and concrete.

(3) Extensional rigidity obtained from the interaction diagrams as explained earlier in this section.

(4) Extensional rigidity computed using Paulay's suggestion - $0.7EA_{gross}$ for tension wall and EA_{gross} for compression wall.

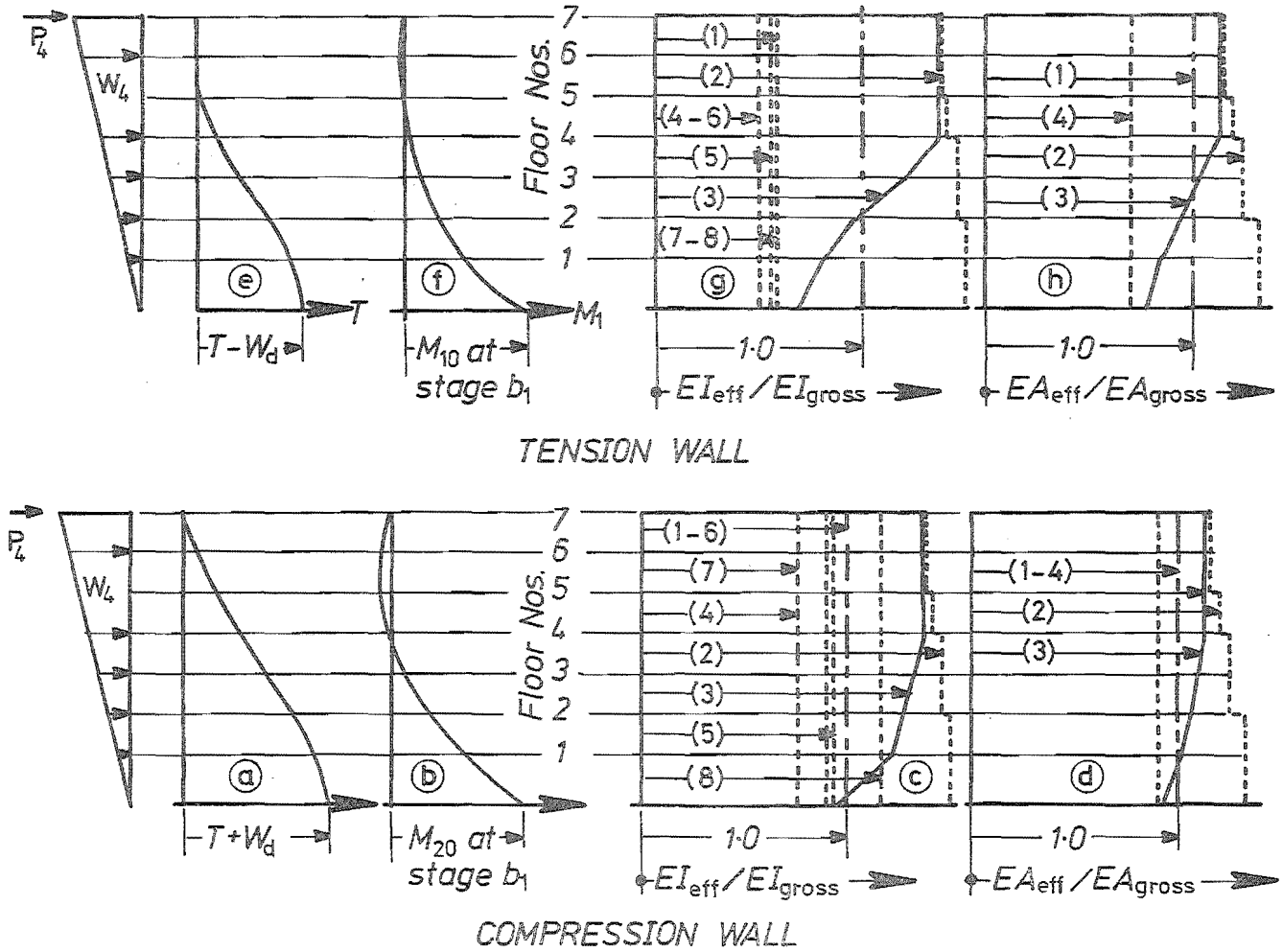

T = axial force at the base of the walls because of laminar shear

W_d = dead load on shear wall

M_{10} = moment at the base of wall 1

M_{20} = moment at the base of wall 2

b_1 = stage at which critical coupling reaches yield

P_4, W_4 = equivalent lateral seismic loads on the model at stage b_1

FIG. 3.25 COMPARISON OF EFFECTIVE FLEXURAL RIGIDITY, $(EI)_{eff}$, AND THE EFFECTIVE EXTENSION RIGIDITY, $(EA)_{eff}$, OBTAINED FROM THE APPROXIMATE METHODS WITH THAT COMPUTED USING INTERACTION DIAGRAMS TAKING INTO ACCOUNT THE VARIABILITY OF STIFFNESSES AND STRESSES ALONG THE HEIGHT OF THE MODEL SHEAR WALLS WHEN THE STEEL IN THE CRITICAL COUPLING BEAM REACHES YIELD (STAGE b_1)

In Fig. 3.25 the flexural and extensional rigidities are plotted in terms of their gross values. Thus, from the axial load-moment-rigidity (EI or EA) diagrams, and the loads and moments computed from the elasto-plastic analysis, the variation of properties with height at any stage of loading could be obtained. In Chapter 4, an incremental elasto-plastic analysis is proposed which uses this information. In Chapter 6 and Chapter 7, the deformations computed, using the relevant properties from Fig. 3.24 and Fig. 3.25 in the elasto-plastic analysis, are compared with the deformations measured during cyclic loading of the models.

The comparison of sectional properties in the cracked state, obtained from the three dimensional plots and those predicted by the suggested overall approximate reduction factors (see Table 3.2), indicate that these factors underestimate the stiffness of the walls. This is due to the large steel content (3.8%) used in these walls compared with ordinary beams or columns. In the test models, a constant force of 25 Kips was applied at the centreline of the walls by the prestressed cables, to simulate the dead load on the walls. This ensured that the base of the walls of the model and a comparable prototype shear wall were subjected to the same order of gravity stresses. However, in the upper floors the stresses produced by the gravity loads in the prototype shear wall are much less when compared with those produced in the model. This would influence the rigidity values. Fig. 3.25 indicates that the gross EI and the gross EA curves are the closest to the curves obtained taking into account the variability of stiffnesses and stresses. In the case of the prototype shear walls the variation of effective flexural rigidity, EI, and the effective extension rigidity, EA, may be more sensitive due to variation of dead load with height and lesser steel content in the walls.

For the nonlinear, incremental elasto-plastic analysis, proposed in Chapter 4, the properties of the walls were varied at each incremental load. This was done using the load-moment-property curves shown in Figs. 3.23 and 3.24.

3.6 CONCLUSIONS

(a) Conventionally Reinforced Coupling Beams

1. Paulay's analytical assessment of deformations of these beams has been reviewed and modified. The equations for the computation of rotations now proposed include the rotation of the coupling beam associated with the deformation of steel in the anchorages. The stiffnesses predicted by these equations and those observed by Paulay show reasonable agreement with the stiffnesses observed for coupling beams of Shear Wall A. Theoretical stiffnesses based on methods which do not make allowances for shear deformations lead to significant errors.

2. For the aspect ratio of the beam examined ($l_s/D = 1.00$), the rotations associated with the deformation of the stirrups and diagonal concrete struts (shear deformation) are larger than the flexural deformation when the steel content $\rho \geq 0.0075$. The stirrup steel content, ρ_w, required to prevent a diagonal tension failure when the flexural strength is fully developed, can be shown to be

$$\rho_w \geq \frac{2\rho\,(d-d')\,f_{ym}}{\varphi\, l_s\, f_{yst}}$$

This equation shows that excessive web reinforcement would be required when $l_s/D = 1$, $\rho_w \approx 2$.

3. Previous tests have shown that ductilities that could be attained during post-elastic high intensity loading of these beams are limited due to the ineffectiveness of the compression reinforcement and the imminent danger of sliding shear failure.

(b) Diagonally Reinforced Coupling Beams

1. Equations have been proposed for the determination of rotations of these beams based on theoretical considerations. The stiffnesses predicted by these equations and those witnessed during tests show reasonable correlation.

2. The rotation, θ_C, associated with the contraction of the compression strut is dependent on the diagonal steel content. This rotation is small compared with the total yield rotation, θ_y. Hence the errors introduced by arbitrary assumption regarding the depth of concrete resisting compression is not significant.

3. The rotation, θ_T, associated with the elongation of the tension chord, and the rotation θ_E associated with the elongation of steel in the anchorages, are independent of the diagonal steel content. Together these constitute the major portion of the total yield rotation.

4. For the same steel content, the diagonally reinforced beams are 1.40 to 2.00 times as stiff as a conventionally reinforced beam of the same aspect ratio ($\frac{l_s}{D} = 1.00$).

5. The studies of Paulay and Binney have revealed that these beams have better ductility and energy absorption characteristics. This will be further illustrated when Shear Wall B model is examined in Chapter 7.

(c) The Tension and Compression Walls

1. It was shown that the flexural capacity of the walls could be larger than those predicted using nominal strengths for steel and concrete. To avoid a shear failure, the shear capacity of the walls need to be increased according to Eq. (3.26) and Eq. (3.27) to account for the increased flexural capacity associated mainly with strain hardening.

2. The section ductility at the development of full strength of the base section in the tension wall is significantly larger than that of the compression wall, in the shear wall models studied. Thus the maximum ductility of the shear wall is limited by the maximum section ductility of the compression wall. This will be examined further in Chapter 4.

3. For the shear wall structures, the three-dimensional plots suggested may be used to evaluate the flexural and extensional rigidities of the wall sections at any stage of loading. These plots are used in Chapter 4 for the incremental nonlinear elasto-plastic analysis of the shear wall. It is not suggested that they be part of routine design.

4. The comparison of the sectional properties in the cracked state obtained using the three-dimensional plots, and those predicted using suggested overall approximate reduction factors, indicate that these factors underestimate the stiffnesses of the model walls. This will be examined further in Chapters 6 and 7.

CHAPTER FOUR

AN ELASTO-PLASTIC ANALYSIS OF COUPLED SHEAR WALLS

4.1 INTRODUCTION

The performance of coupled shear walls in high rise buildings has been the subject of study of a number of researchers during the last decade. Most of these focussed attention on the elastic behaviour of these major lateral load resisting structures.

In countries prone to earthquakes, the ability of the ductile structure to absorb energy by post-elastic deformation, assisted by such other factors as a reduced response due to damping, soil structure interaction and the change in the period of vibration due to reduction in stiffness caused by cracking, make it possible to design structures to resist lateral loads recommended by the design standards even though these loads are significantly less when compared with the theoretical elastic response inertia loads obtained from the analysis of records of severe ground motions [2,3]. Of the factors mentioned above, the absorption of energy by post-elastic deformations is by far the most important and hence the use of equivalent lateral loads for seismic design presumes the structure to have sufficient ductility [89].

To evaluate the full response of shear wall structures, it is necessary to examine their post-elastic behaviour. During severe ground motions the attainment of the ultimate load and subsequent elasto-plastic energy absorbing deformations are reality. It is necessary to quantify the magnitudes of the post-elastic deformations in the components of the structure during the various stages of their reaching ultimate capacities, and to estimate the total ductility demand on them in order to compare these with the ductilities that have been observed to be available in experimental specimens. It is not

suggested that the evaluation of various aspects of the elasto-plastic response of the structure to any given lateral load be part of a routine design procedure.

The elasto-plastic examination, presented here, attempts to quantify the ductility demand on the coupling beams and the walls. The history of the shear wall's behaviour is followed through stages of incremental loading till the ultimate load is reached and the required overall ductility is attained. Such a study will show the order of ductilities which are desirable if survival of a major earthquake is to be assured. It may then be seen that these theoretical ductilities can be met by various components of a shear wall structure provided it is designed and detailed accordingly.

4.2 COLLAPSE MECHANISM

The ultimate strength of the coupled shear wall subjected to seismic type of lateral load is obtained when a "collapse mechanism" is formed due to the development of "plastic hinges". These plastic hinges should possess the required rotation capacity to sustain large local increases in curvatures without significant loss in the moments carried. Reports on structural damage caused by earthquakes[94,95] indicate that the column sidesway mechanism, shown in Fig. 4.1.a, is unlikely to develop in coupled shear walls except in cases where the wall dimensions were drastically reduced at the foundation level, or where columns were used to support the walls. In fact, the behaviour of some shear walls show that most of the coupling beams failed before the ultimate strength of the walls was attained. Thus the beam-hinge mechanism, shown in Fig. 4.1.b, represents the most likely ultimate condition of the coupled shear wall.

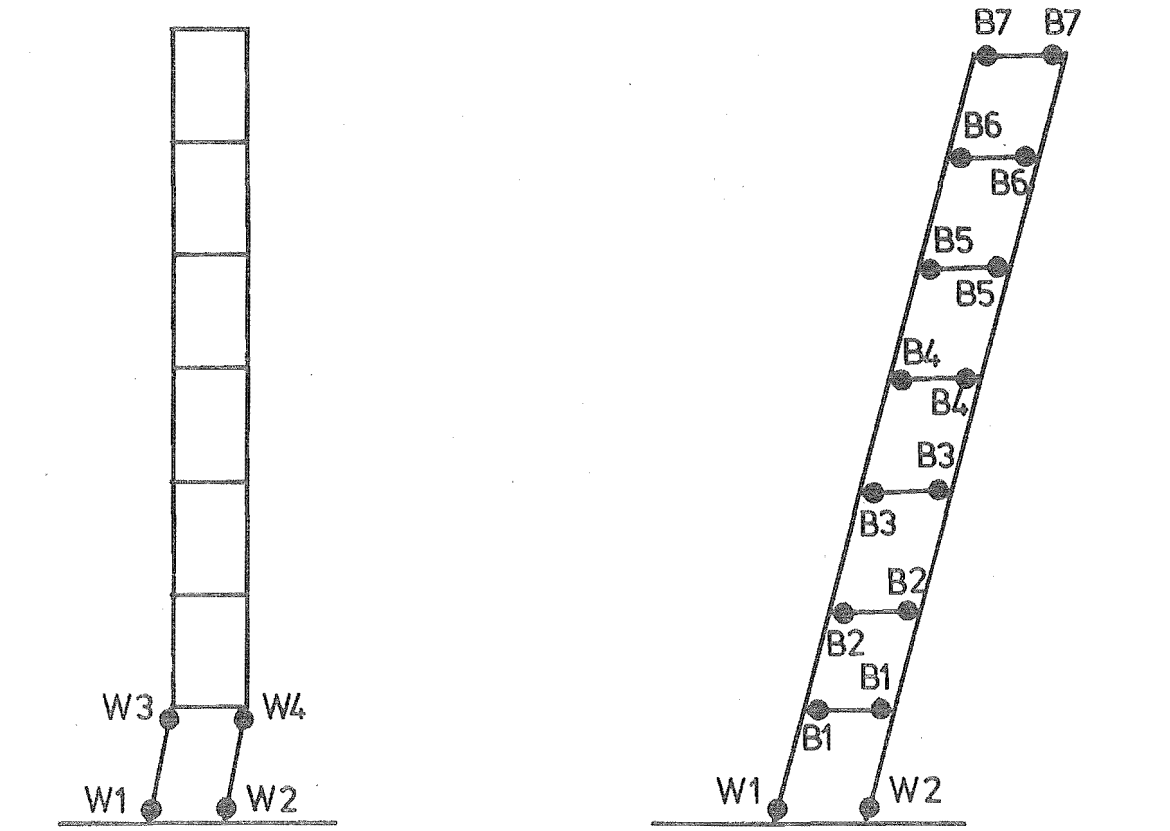

FIG. 4.1 COLLAPSE MECHANISMS OF COUPLED SHEAR WALLS

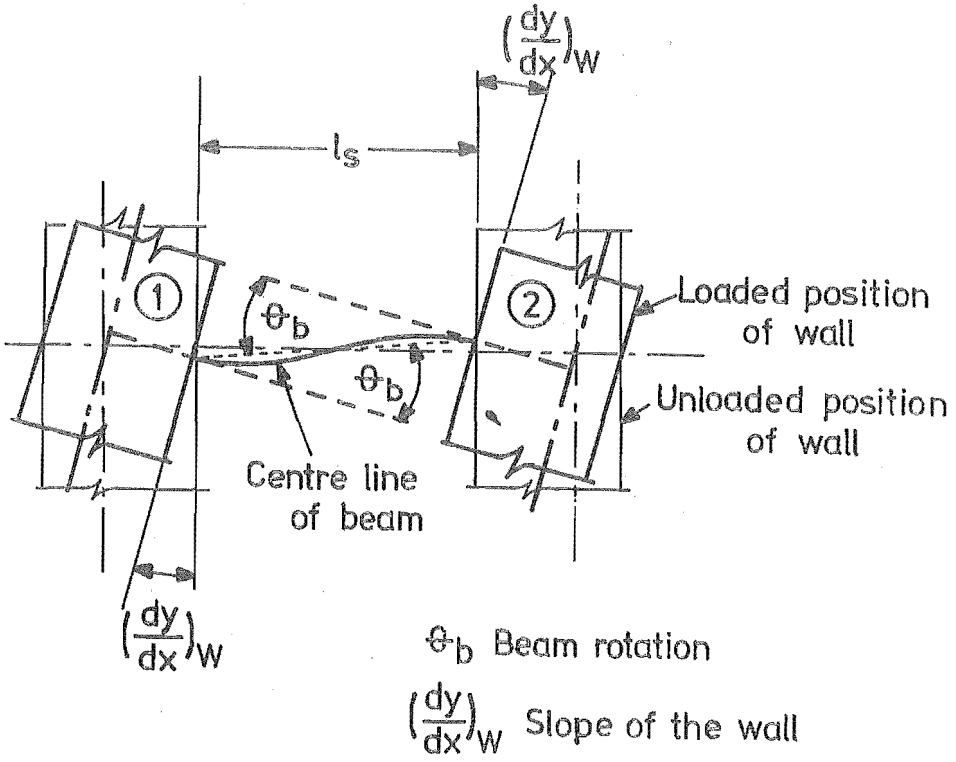

FIG. 4.2 ROTATIONS OF A COUPLING BEAM

For multistorey structures, the number of plastic hinges required for this type of failure mechanism to form depends on the number of storeys. Two hinges are required in each coupling beam to terminate its ability to accept further shear. In addition one plastic hinge needs to be developed in each of the cantilever walls, normally at the base, to complete the collapse mechanism. By means of a step by step procedure, Paulay[7] traced the post-elastic performance of the shear wall through the following six stages of loading.

(1) Design load entirely within elastic range.

(2) Onset of yielding in the critical lamina.

(3) Full plastification of the laminae.

(4) Capacity of wall 1 attained.

(5) Capacity of wall 2 attained.

(6) Overall ductility requirement for fully plastic deformations at constant load.

If yielding has commenced at the critical sections of all the beams before the walls reach yield curvature, further deformations in the beams will take place at constant beam shears due to plastic rotations occurring in the beam hinges. This would contribute to the major part of the lateral deformation at the top floor. The elasto-plastic analysis proposed by Paulay[7] assumes such a behaviour. It has been assumed that the plastic hinges form in all the coupling beams before plastic deformation of any kind would occur in the walls. This in fact is desirable, and it should be encouraged. It is advantageous to design the coupling beams so that they become the major energy dissipating devices. It is desirable that as much of the total energy be dissipated by the coupling system as possible before hinging of the walls commences because this will ensure that the walls remain in the elastic range of behaviour till a very late stage of a major disturbance and thus enjoy a high degree of protection against permanent damage. Yielding in the walls means permanent misalignment of a building which

will be next to impossible to repair. It is considerably easier to repair damaged coupling beams.

However, the sequence of hinge formation depends on the behaviour of the cracked components of the shear wall. If the shear wall is provided with stiff coupling beams, the plastic hinges at the ends of these may develop only over part of the height when the critical wall section reaches the yield curvature. It is also necessary to study the compatibility of rotations in the plastic hinges that form in the walls.

Paulay's[7] approximate analysis does not consider the slope compatibility at the base of the wall after the formation of plastic hinges at the base of the tension wall. The increase in base moment is assumed to be resisted by increase in wall moment, M_2, alone when the base of wall 1 undergoes plastic rotation at constant maximum ultimate moment, M_{1u}. This results in considerable plastic rotation at the base of wall 1 when the base of wall 2 is assumed to be elastic. During all the stages of incremental loading the slopes of wall 1 and wall 2 should be the same, i.e. $\frac{dy}{dx} = \frac{dy_1}{dx} = \frac{dy_2}{dx}$.

4.3 THE ELASTO-PLASTIC ANALYSIS

In shear walls resisting seismic forces, the magnitude and behaviour of post-elastic deformation of the structure and its components are of particular interest. These determine the energy absorption capacity of the structure. Paulay's[7] analysis, as pointed out earlier, assumes the sequence of hinge formation and hence cannot be applied to the shear walls in which the critical wall sections may yield before the capacity of the coupling system is exhausted. Gluck[62] has obtained expressions for the elasto-plastic deformations of the coupling beam when the plastic hinges in them develop only over part of the height. At ultimate load the coupled shear wall is assumed to form a mechanism as shown in Fig. 4.1.b. The increase in the rotations of

the beam hinges due to the plastic rotations of the wall hinges, the contribution of the rotations of the coupling beams which yield after the walls reach yield curvature and the contribution of wall rotations to the overall ductility need to be considered in order to have an estimate of the components' ability to supply the required ductilities. Thus, the expressions derived by Gluck[62] are useful to predict the deformations of the shear wall at the stage when part of the coupling beams have yielded but both walls remain elastic. If the analysis indicates that only a partial failure mechanism occurs or wall hinges tend to form prematurely, it might be necessary to redesign the structure so as to ensure a better and more desirable distribution of plastic hinges.

Herein, a step by step procedure, using a finite difference method, is suggested for the elasto-plastic analysis of the coupled shear wall. Using this analysis, the post-elastic behaviour of the two coupled walls and the coupling beams are traced. The sequence in which the plastic hinges are formed is detected using this incremental analysis and by a systematic search for the critical hinge location. The analysis is based on cracked sections of the beams and the walls.

This is followed by an example to illustrate the proposed analysis.

4.3.1 Definition of Rotations and Ductilities

The load-deformation relationship for the reinforced concrete structure is far from being bilinear elastic-perfectly plastic. Considerable degradation in stiffness usually occurs. From the load-deformation curve it is also difficult to define a particular limit at which plastic deformation commences. The overall ductility of a structure or a member is dependent on this definition of yield limit. The difficulties encountered in defining this yield limit have been pointed out by Bertero[96].

For the purpose of this elasto-plastic analysis the rotations and the associated ductilities for the components of the shear wall and the overall displacement ductility for the structure will be defined below.

(a) Coupling Beams

The meaning of the coupling beam rotation, θ_b, is defined in Fig. 4.2. It may be noted that the angle between the axis of the beam and the axis of the wall does not remain a right angle after loading.

It is assumed that the beams possess bilinear elasto-plastic load-rotation characteristics, shown in Fig. 4.3. θ_b is the beam rotation at any stage of loading. Prior to yielding θ_b represents the elastic rotation occuring in the beam. At yield, $\theta_b = \theta_{by}$, the elastic-limit rotation for the coupling beam. After yielding θ_b represents the yield rotation θ_{by} and the plastic rotation, θ_{bp}. (i.e. $\theta_b = \theta_{by} + \theta_{bp}$).

In the laminar analysis the compatibility condition for the vertical displacement at the mid-point of the laminae was shown to be satisfied[74] when

$$d_m = d_b + d_a \qquad \ldots (4.1)$$

where d_m = displacement at the midpoint of the lamina due to flexural deformations in the wall

d_b = displacement at the mid-point of the lamina due to the laminar deflection

d_a = differential displacement due to axial forces in the walls

The displacement at the mid-point of the lamina due to flexural deformation of the wall is

$$d_m = \frac{l dy_1}{dx} = \frac{l dy_2}{dx} = l\left(\frac{dy}{dx}\right)_w \qquad \ldots (4.2)$$

in accordance with the assumption that the mid-points of the laminae

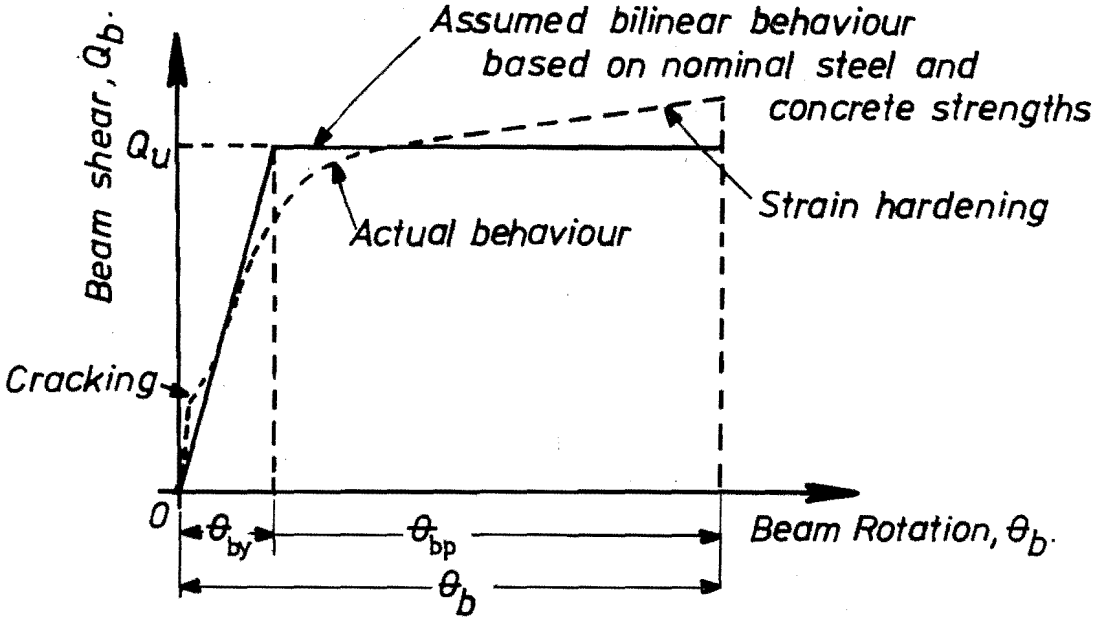

FIG. 4.3 ASSUMED BILINEAR RESPONSE FOR THE COUPLING BEAMS

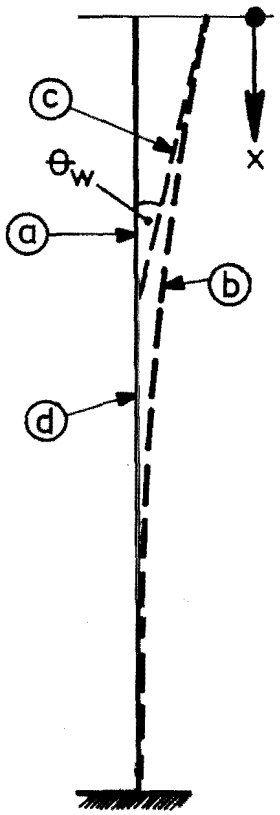

(a) Unloaded initial position of the wall

(b) Loaded position of the wall

(c) Tangent to the loaded position at the top

(d) Tangent to the loaded position at the base

θ_w is the wall rotation measured between (c) and (a)

Note: (a) and (d) are same when the wall is elastic.
Angle between (a) and (d) gives the plastic rotation at the base after the onset of yield in the wall.

FIG. 4.4 ROTATIONS OCCURRING IN THE WALL

are points of contraflexure. $\frac{dy}{dx}$ represents the slope of the wall.

The beam displacement, d_b, is expressed in terms of the beam rotation, θ_b, as

$$d_b = l_s \theta_b \qquad \ldots (4.3)$$

Substituting Eqs. (4.2) and (4.3) in Eq. (4.1) the beam rotation at any stage of loading is

$$\theta_b = \frac{1}{l_s}\left(\frac{dy}{dx}\right)_w - \frac{d_a}{l_s} \qquad \ldots (4.4)$$

The ductility of the coupling beam, μ_b is defined as the ratio of the rotation of the coupling beam, θ_b, at the stage for which the ductility is computed, to the yield rotation of the coupling beam, θ_{by}.

$$\text{i.e.} \quad \mu_b = \frac{\theta_b}{\theta_{by}}$$

An estimate of θ_{by} can be made using the analysis presented in Chapter 3.

(b) Tension and Compression Walls

The meaning of the wall rotation, θ_w, is defined in Fig. 4.4. It is given by

$$\theta_w = \int_0^H \varphi ds \qquad \ldots (4.6)$$

where φ = curvature

θ_w is the wall rotation at any stage of loading relative to the original vertical axis.

The plastic hinges in the walls are likely to develop at the base. It was shown in Chapter 3 that the strain limit $e_c = 0.002$ and $e_{st} = 0.0018$ could be taken as the elastic limit strain for the walls. Up to this limit the curvatures do not vary significantly for

a small increase in either axial load or moment. The rotation, θ_w, of the wall at this elastic limit stage is θ_{wy}. Beyond this limit the increase in loads and moments for an increase in the rotation of a wall section is negligible. Thus the assumed load-moment-rotation interaction for a wall section is as shown in Fig. 4.5.

The flexural rigidity, EI, of the cracked section is used to evaluate the elastic limit rotation

$$\theta_{wy} = \int_0^H \frac{M_x}{(EI)_{eff}} dx \qquad \ldots (4.7)$$

where M_x is the moment at any level when the critical wall section at the base reaches yield. Thus M_x, when $x = H$ is the yield moment, M_y.

The elastic limit rotation, θ_{wy}, is shown in Fig. 4.6.a. Δ_{wy} is the deflection at the top of the wall when the critical section reaches yield curvature. Till the yield curvature is reached, the slope of the wall at the base is assumed to be zero (full fixity). The elastic limit rotation, θ_{wy}, is measured as the angle between the tangent (c) drawn to the loaded deformed position of the wall (b) at the top at the instance of critical section reaching yield curvature and the unloaded position (a) of the wall.

Fig. 4.6.b shows the position of the wall at a stage when the plastic hinge formed at the base of the wall has rotated by an angle, θ_{wp}. Beyond the elastic limit, the entire rotation is assumed to take place at the hinge at the base of the wall. This assumption is critically examined in Section 4.4. θ_{wp} is the plastic rotation and Δ_{wp} is the deflection at the top floor due to this plastic hinge rotation. The plastic rotation, θ_{wp}, is measured as the angle between the tangent (d) for the loaded position of the wall at the base and the unloaded position of the wall (a).

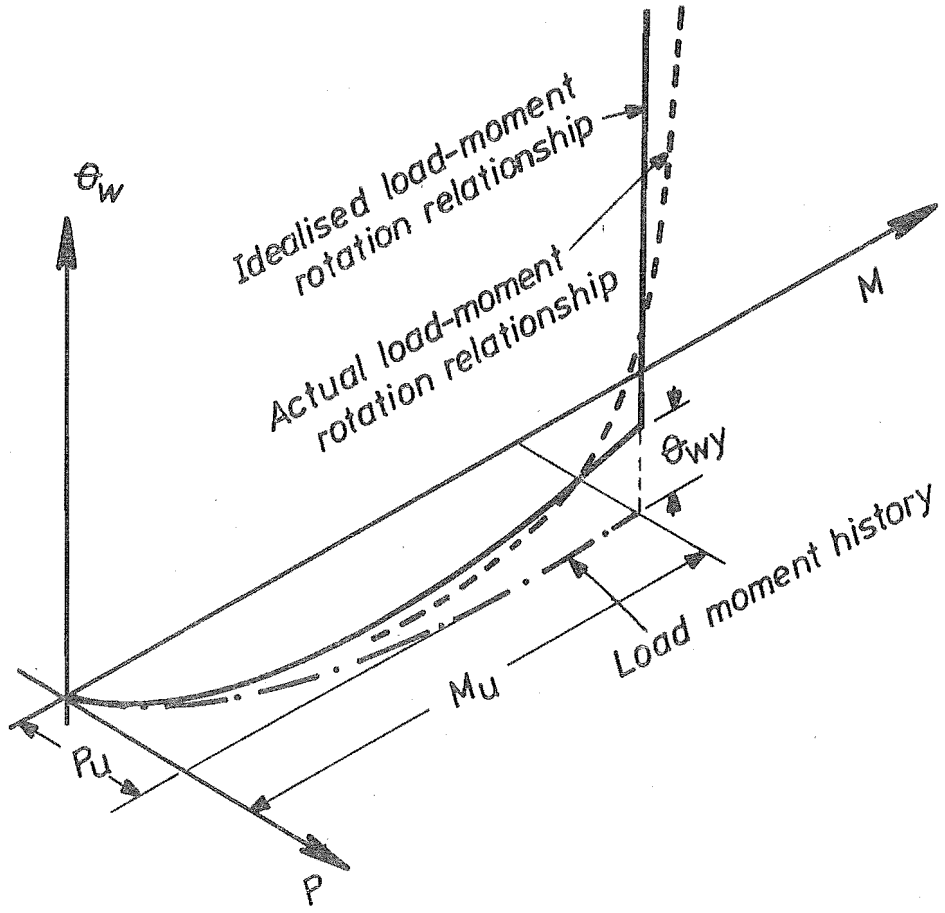

FIG. 4.5 ASSUMED LOAD-MOMENT-ROTATION RELATIONSHIP FOR THE WALLS

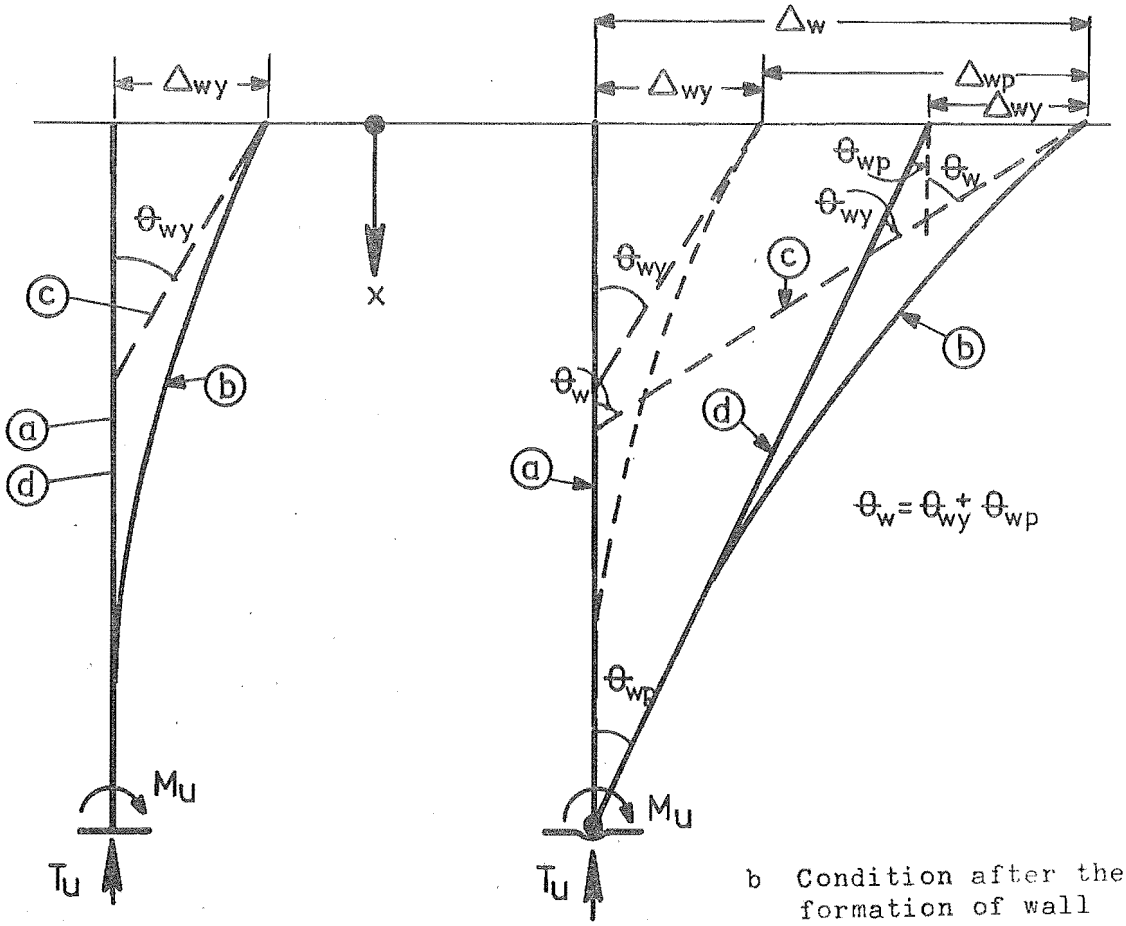

a Elastic limit condition just before formation of wall hinge - base fully rigid

b Condition after the formation of wall hinge. A certain plastic rotation, θ_{wp}, has occurred at the base

FIG. 4.6 GEOMETRY OF ELASTIC LIMIT AND PLASTIC WALL ROTATIONS

From the geometry of Fig. 4.6.b. it is seen that

$$\theta_w = \theta_{wy} + \theta_{wp} \qquad \ldots (4.8)$$

where θ_w = total wall rotation as defined in Fig. 4.4

θ_{wy} = elastic limit rotation of the wall

θ_{wp} = plastic hinge rotation which occurs after the onset of yielding at the base.

The ductility of the wall, μ_w, is defined as the ratio of the rotation of the wall, θ_w, at the stage considered, to its yield rotation, θ_{wy}, i.e.

$$\mu_w = \frac{\theta_w}{\theta_{wy}} \qquad \ldots (4.9)$$

The rotation of the topmost section of the wall is used to compute the member ductility of the tension and compression walls instead of the top floor displacement in order to differentiate between the ductility demands of tension and compression walls.

(c) Displacement Ductility of the Shear Wall

For the purpose of ductility studies it is assumed that the top floor displacement, when the critical coupling beam reaches yield, defines the yield displacement, Δ_y shown in Fig. 4.7. The dotted line is the idealised theoretical bilinear behaviour. Δ'_y is the yield displacement of the idealised bilinear curve.

The overall displacement ductility for the shear wall, μ_o, is defined as the ratio of the top floor displacement at the stage considered, to the theoretical yield displacement of the top floor, Δ'_y, for the idealised bilinear behaviour, i.e.

$$\mu_o = \frac{\Delta_s}{\Delta'_y} \qquad \ldots (4.10)$$

where Δ_s is the top floor deflection of the shear wall.

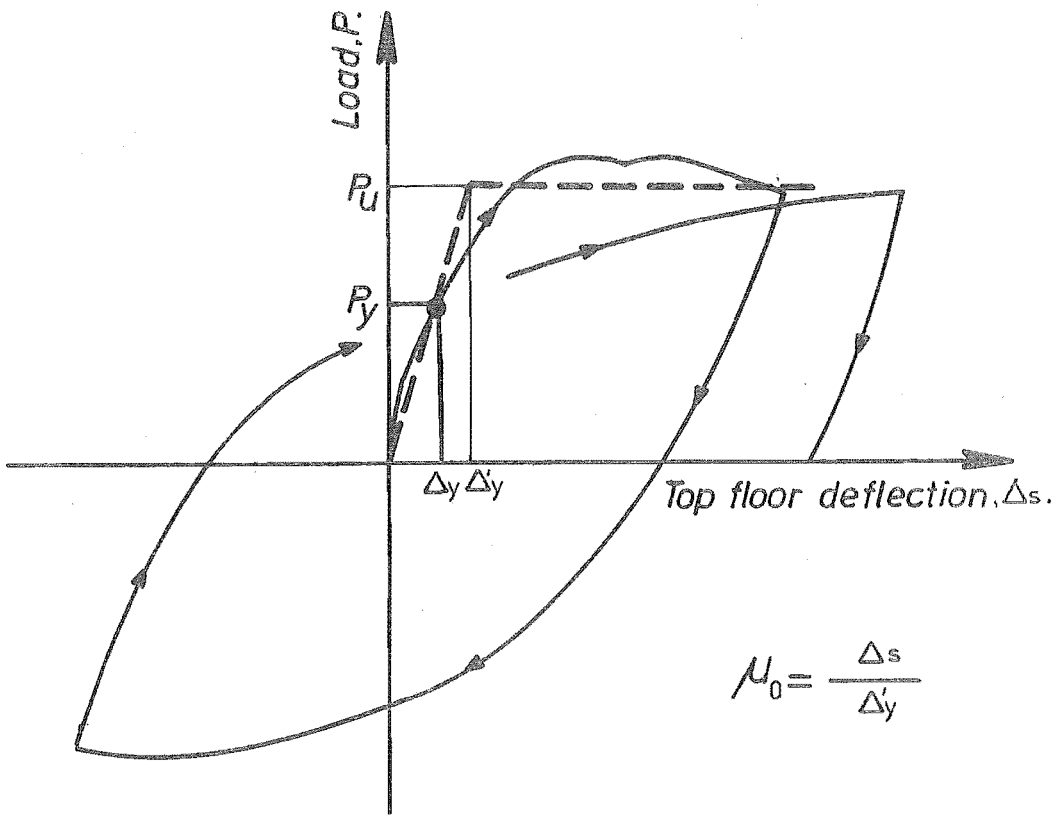

FIG. 4.7 DEFINITION OF OVERALL DISPLACEMENT DUCTILITY

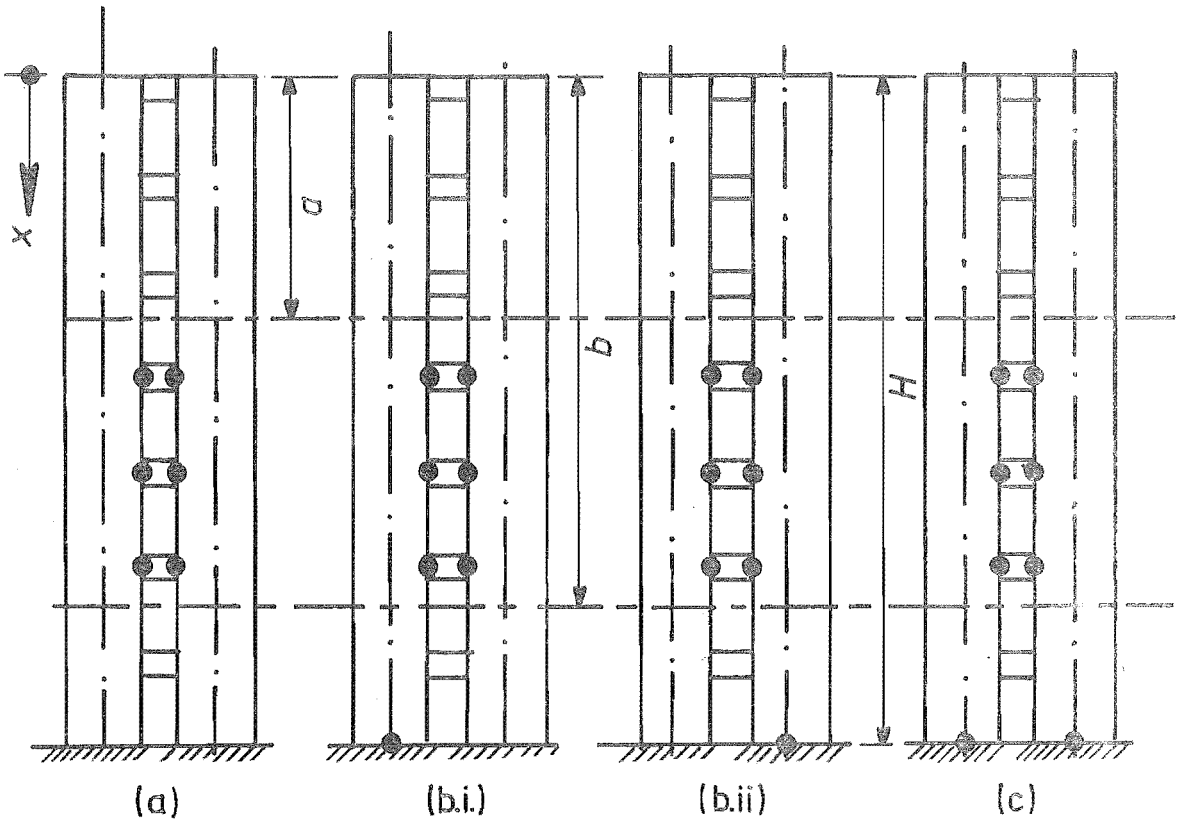

FIG. 4.8 TYPICAL CASES OF HINGE FORMATION

4.3.2 The Stages of the Elasto-plastic Analysis

The elasto-plastic examination is intended to expose the ductility demand of the coupling beams and the walls. The history of the structural behaviour is followed through stages of incremental loading till the mechanism has formed and the required overall ductility has been obtained. The various stages of analysis are designated by the letters as shown below:

a - Design load corresponding with code requirements

b_1 - Critical coupling beam reaching yield

b_j - jth coupling beam reaching yield

b_n - Last coupling beam reaching yield

c - Capacity of tension wall attained

d - Capacity of compression wall attained

e - The specified overall ductility is attained

a Design load: The structure carries a code prescribed equivalent static design load. All parts of the structure are "elastic". The stresses and deformations in the various components are obtained from the elastic laminar analysis described in Chapter 2.

b_1 Critical coupling beam reaching yield: Up to this stage the linear load-deformation relationship is applied to the coupling beams. This stage occurs before the capacities of the walls are attained.

b_j jth coupling beam reaching yield: This is an intermediate stage in the plastification of the coupling system. Some of the beams in the critical region have already exhausted their ability to accept further shear. The coupling beams at the top and/or at the bottom may still be elastic.

b_n Last coupling beam reaching yield: At this stage the laminar plastification is assumed to have spread over the height of the structure while each beam sustains its yield capacity. Beyond this stage any

further increase is possible only by increases in wall moments M_1 and M_2. If wall 1 and wall 2 had already yielded, this stage represents the attainment of ultimate load of the shear wall.

If the plastic hinges at the base of compression and tension walls had developed before stage b_n, it is possible to increase the load on the structure till the stage b_n is reached provided the hinges formed at the base of the walls are capable of maintaining the loads and moments on them. The increase in loads causes larger axial force to be transmitted till the stage b_n is reached. Under this axial force the moment capacity of the tension wall is likely to be reduced and that of the compression wall is likely to be increased (assuming that yielding of tension steel governs the failure). This effect on the wall hinges is neglected. The wall hinges are assumed to rotate at the constant ultimate moment M_{1u} and M_{2u} and the increase in load is assumed to be resisted by the increase in the 1T component after the formation of wall hinges.

c Ultimate load on wall 1: The load at which the tension wall critical section reaches yield curvature is designated as stage c. If the capacity of some or all the coupling beams have already been exhausted, it is assumed that the plastified beams maintain the ultimate shear during subsequent rotation in accordance with the assumed bilinear elasto-plastic behaviour.

d Ultimate load on wall 2: The load at which the compression wall critical section reaches yield curvature is designated as stage d. This usually occurs simultaneously with the formation of hinge at the base of the tension wall. The reasons for this are discussed in Section 4.3.3.

e Overall displacement ductility requirement: After all the plastic hinges develop, any further rotations which may occur at the base of the wall will induce proportional rotations in each coupling beam and increase the displacement at the top floor.

4.3.3 The Finite Difference Formulation of the Problem

For computing the rotations at various stages of incremental loading, the finite-difference approximation to laminar analysis is used. When the structure carries the code prescribed equivalent static design load, in accordance with elastic behaviour, rotations of the laminae, at the stage a , are proportional to the laminar shear, q .

The next incremental loading brings the critically situated coupling beam b_1 to its elastic limit. The rotations of the beams and the walls, just prior to the onset of yielding, are computed based on the elastic behaviour of the shear wall. This load stage terminates the "linear elastic" behaviour of the shear wall.

In general, the additional load, ΔP , required at any stage of loading for the next set of hinges to form in the coupling beams or the hinge to form at the base of the walls, depends on the hinge or hinges formed previously. Three cases shown in Fig. 4.8 may arise. The distances a and b are varied between the limits 0 and H depending on the height over which the laminae have reached their capacity.

Case (a): The laminae in the region $b > x > a$ (see Fig. 4.8.a) have reached their ultimate capacity. Their ability to accept further shear is terminated by substituting for further increments $I_x = 0$ for the laminae in this region in Eq. (2.27).

Case (b): Either the tension wall or the compression wall may reach its flexural capacity first (see Fig. 4.8.b). The difference equations for the various laminae are similar to those used in Case (a). The formation of hinges at the base of the walls introduces new boundary conditions at the base.

The differences in lateral deflections of wall 1 and wall 2 are due to different elongations of the coupling beams. These elongations are small compared to the deflections of the walls. Thus the slopes of wall 1 and wall 2 are approximately the same at any level. When one wall has yielded and the other wall is "elastic", further increase in moments at the base of the structure has to be resisted by the "elastic" wall. However, the consequent increase in rotations for both the walls is the same. This rotation causes the "elastic" wall to yield soon after the yielding of the other wall. Therefore, the stages c and d can be expected to occur very close to one another.

The boundary conditions at the base of the wall, when plastic hinge has formed only at the base of one wall, does not alter the slope compatibility of the two walls. Thus the step by step analysis itself leads to the formation of these wall hinges either simultaneously or very close to one another. Two boundary conditions arise under this category.

(i) Plastic hinge at the base of wall 1 forms first (Fig. 4.8.b.i) The boundary condition for the flexible foundation derived in Eq. (2.44) was used. Reference may be made to the notations with respect to the definition of terms. The mathematical model which includes the equivalent springs that represent the axial and rotational stiffness of the base of wall 1 and wall 2 can be seen in Fig. 2.22. Since the bases of both walls are assumed to remain at the same level the axial stiffnesses, $k_{\delta 1} = k_{\delta 2} = \infty$. The base section of wall 1 has lost its ability to accept further moments. Therefore, the rotational stiffness of the equivalent spring, $k_{\theta 1} = 0$. Thus the boundary condition reduces to

$$T_{z+1} = T_{z-1} - 2h_o \left(\frac{l^2}{\varphi k_{\theta 2}}\right) T_z + 2h_o \left(\frac{l}{\varphi k_{\theta 2}}\right) M_o \qquad \ldots (4.11)$$

where φ is defined by Eq. (2.25a).

(ii) Plastic hinge at the base of wall 2 (Fig. 4.8.b.ii)

As in the previous case $k_{\delta 1} = k_{\delta 2} = \infty$. The base section of wall 2 has lost its ability to accept further moments. Therefore, the rotational stiffness of the equivalent spring, $k_{\theta 2} = 0$. Thus, Eq. (2.44) reduces to

$$T_{z+1} = T_{z-1} - 2h_o \left(\frac{l^2}{\varphi k_{\theta 1}}\right) T_z + 2h_o \left(\frac{l}{\varphi k_{\theta 1}}\right) M_o \qquad \ldots (4.12)$$

(Case (c): When both the wall hinges have formed (see Fig. 4.8.c), the additional base moment, ΔM_o, is assumed to be resisted by the increase in the component lT_z at the base.

For this case Eq. (2.47), derived in Chapter 2, gives the boundary condition.

4.3.4 The Full Range Analysis

The analytical model described in the previous section enables an incremental approach to be used for the analysis of coupled shear walls. At each load level the structure is redefined with hinges at the locations where the capacity had already been exhausted. The analytical model is used to illustrate successive hinge formation, moment redistribution and eventual collapse. The finite difference approximation of the laminar analysis, explained in Chapter 2, is used to obtain a numerical solution at each stage of incremental loading.

The flow chart, shown in Fig. 4.9, represents the various operations performed to obtain the loads and deformations at various stages of loading. The first part of the flow chart records the computation of the effective properties of the beams and the walls and solves the simultaneous equations resulting from the application of finite-difference approximation to the laminar analysis, to obtain the force resultants and deformations. The second part is concerned with the determination of hinge location and the incremental load required to form the next plastic hinge with the associated deformations. The

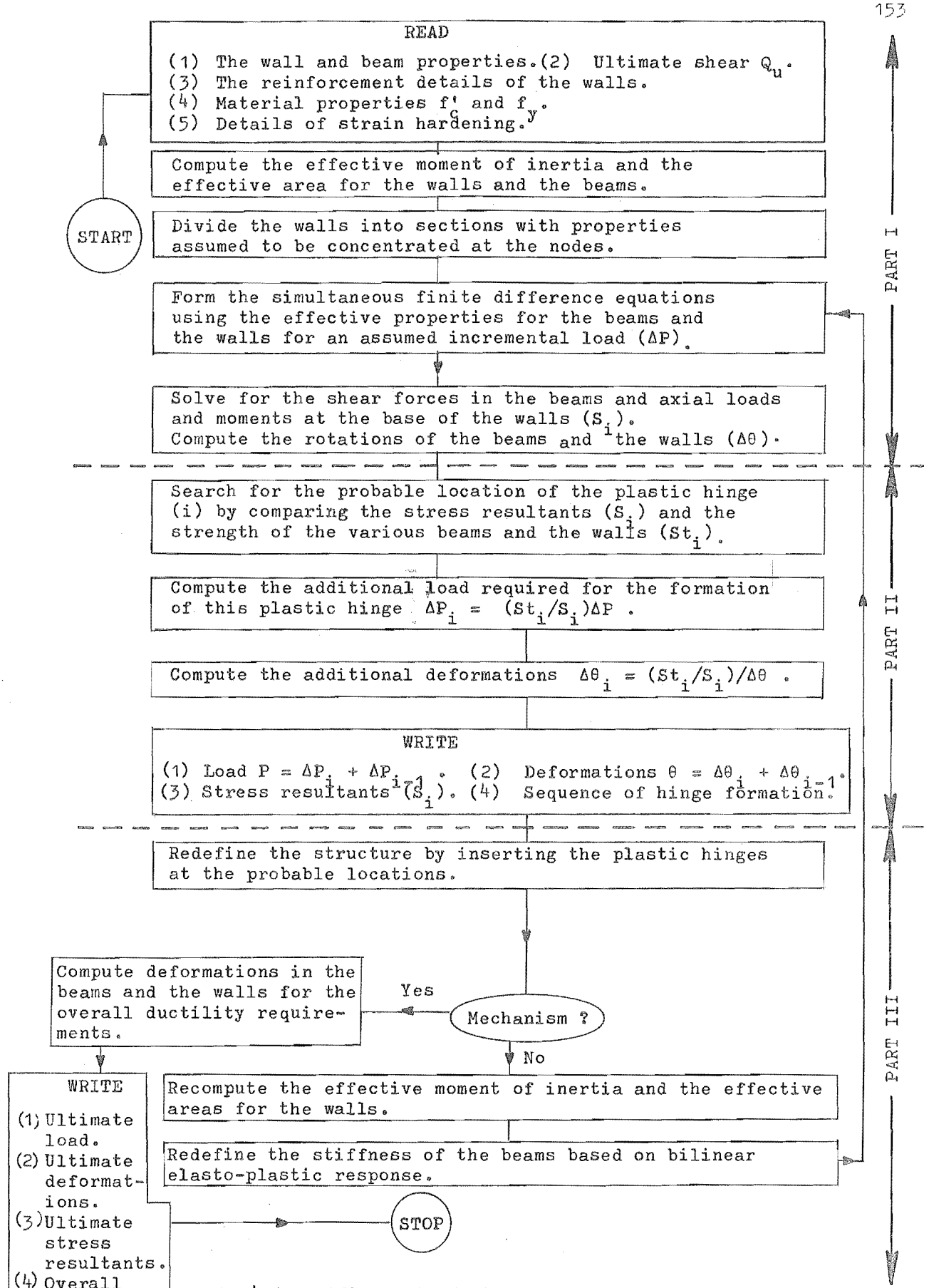

FIG. 4.9 FLOW CHART FOR THE FULL RANGE INCREMENTAL ELASTO-PLASTIC ANALYSIS FOR THE COUPLED SHEAR WALL STRUCTURES.

third part redefines the structure with hinges at the probable locations and recomputes the effective properties for the next stage of loading. A computer programme was written to perform these operations. The input necessary for the programme is

1. The wall and beam properties.
2. Ultimate shear, Qu, of the beam.
3. The reinforcement details of the walls.
4. Material properties, f'_c and f_y.

The output from the programme for each incremental load is:

1. Load and stage.
2. Rotations of coupling beams and walls.
3. Bending moment, shear and axial force variation with height for the walls.
4. Beam shear variation with height.
5. Location and sequence of hinge formation.
6. The top floor displacement.

In addition to homogeneous and isotropic material behaviour, the following assumptions are made.

1. A parabolic concrete stress-strain curve.
2. A bilinear stress-strain relationship for steel.

For computing the deformations, the load-moment-curvature relationship based on the method suggested in Chapter 3 was made use of.

In particular, the following two cases of steel behaviour were studied.

(a) A perfectly elastic-plastic steel behaviour.

(b) A perfectly elastic behaviour up to yield limit. A 15% increase in yield strength at a strain of 15 times yield strain. This increase was assumed to be linear commencing from yield point.

The numerical examples in Section 4.5 demonstrate the application of the full range elasto-plastic analysis of a coupled shear wall structure.

4.4 DEFORMATION ALONG THE HEIGHT OF THE TENSION AND COMPRESSION WALLS

Fig. 4.10 shows the typical moments and curvatures along the height of tension and compression walls at ultimate load. In the elasto-plastic analysis it was assumed that the entire plastic rotation of the walls takes place at the hinge at the base of the walls. The region with the curvatures greater than yield curvature, φ_y , does not occur just at the critical section. The inelastic deformation is spread out over a finite length. The rotation θ along the height of the member is given by

$$\theta = \int \varphi \, dx \qquad \ldots \quad (4.13)$$

where φ is the curvature of the section. Therefore, the area of the curvature diagram gives the rotation occuring between the ends of the member. The curvature distribution is divided into elastic and plastic regions as shown in Fig. 4.10.e and f. The idealised curvature at the elastic limit assumes cracked sections along the height of the member.

The yield rotations at the base of the tension wall and compression wall could be calculated as

$$\theta_{wyt} = \int \frac{(M_1)_x}{(EI_1)_{eff}} \, dx \qquad \ldots \quad (4.14)$$

and

$$\theta_{wyc} = \int \frac{(M_2)_x}{(EI_2)_{eff}} \, dx \qquad \ldots \quad (4.15)$$

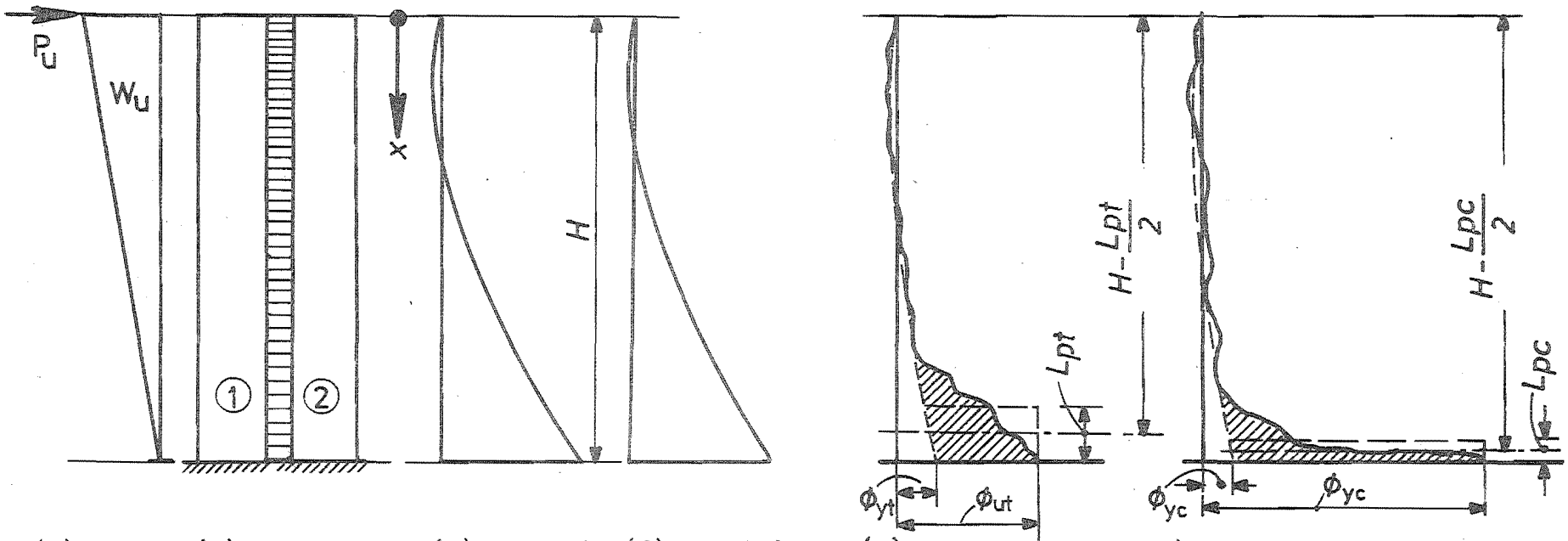

(a) Load (b) Shear wall (c) Moment in wall 1 (d) Moment in wall 2 (e) Curvature in wall 1 (f) Curvature in wall 2

FIG. 4.10 CURVATURE DISTRIBUTION ALONG THE HEIGHT FOR THE TENSION AND COMPRESSION WALLS

where $(M_1)_x$ and $(M_2)_x$ = moment at any level in the tension and compression walls when their bases attain yield curvature respectively.

θ_{wyt} = the tension wall rotation when the critical section at the base of wall 1 reaches yield curvature.

θ_{wyc} = the compression wall rotation when the critical section at the base of wall 2 reaches yield curvature.

The shaded area of Figs. 4.10.e and f show the extent of inelastic rotations which occur at the plastic hinges in the tension and compression walls. φ_{uc} and φ_{yc} represent the ultimate and yield curvatures for the critical section of the compression wall. φ_{ut} and φ_{yt} represent the corresponding curvatures for the tension wall. The shaded area for the compression wall is replaced by an equivalent rectangle of width $\varphi_{uc} - \varphi_{yc}$ and height Lp_c. The shaded area for the tension wall is replaced by an equivalent rectangle of width $\varphi_{ut} - \varphi_{yt}$ and height Lp_t. The heights Lp_c and Lp_t are the equivalent lengths of plastic hinges over which the plastic curvatures are assumed to be constant for the compression and tension walls respectively. Hence the plastic rotations for the compression and tension walls are

$$\theta_{pc} = \left(\varphi_{uc} - \varphi_{yc}\right) Lp_c \qquad \ldots (4.16)$$

and

$$\theta_{pt} = \left(\varphi_{ut} - \varphi_{yt}\right) L_{pc} \qquad \ldots (4.17)$$

The compatibility condition requires that the deflection, Δ, at the top of wall 1 and wall 2 are sensibly equal. The top floor deflection can be expressed in terms of the curvature of the wall as

$$\Delta = \int_0^h \frac{(M_1)_x}{(EI_1)_{eff}} \, x \, dx + \left(\varphi_{ut} - \varphi_{yt}\right) Lp_t \left(H - 0.5\, Lp_t\right) \qquad \ldots\ldots (4.18a)$$

$$\Delta = \int_{o}^{h} \frac{(M_2)_x}{(EI_2)_{eff}} \, x \, dx + \left(\varphi_{uc} - \varphi_{yc}\right) Lp_c \left(H - 0.5\, Lp_c\right) \quad \ldots (4.18b)$$

Since the plastic rotations are large compared to the elastic wall rotations, the elastic rotations are neglected. Thus the compatibility equation reduces to

$$\left(\varphi_{ut} - \varphi_{yt}\right)Lp_t \left(H - 0.5\, Lp_t\right) = \left(\varphi_{uc} - \varphi_{yc}\right)Lp_c \left(H - 0.5\, Lp_c\right) \quad \ldots . (4.18)$$

The length of the plastic hinge is small compared to the height of the structure. Therefore

$$H - 0.5Lp_t \approx H - 0.5Lp_c \quad \ldots (4.19)$$

Thus,

$$\left(\varphi_{ut} - \varphi_{yt}\right)Lp_t \approx \left(\varphi_{uc} - \varphi_{yc}\right)L_{pc} = \theta_{wp} \quad \ldots (4.20)$$

where θ_{wp} represents the rotation occurring at the plastic hinge.

Fig. 4.11 shows the plastic deformations occurring in the compression and tension walls after the formation of the plastic hinges. θ_{wp} is the plastic rotation at the base. The elastic deformations of the walls are not shown. Lp_c and Lp_t are the lengths of plastic hinges for the compression and tension walls respectively, and l is the distance between the centre lines of the walls.

From the geometry of this figure it is seen that

$$Lp_t = Lp_c + l\theta_{wp} \quad \ldots (4.21)$$

This shows that the length of the plastic hinge for tension wall is more than that of the compression wall by an amount $l\theta_{wp}$.

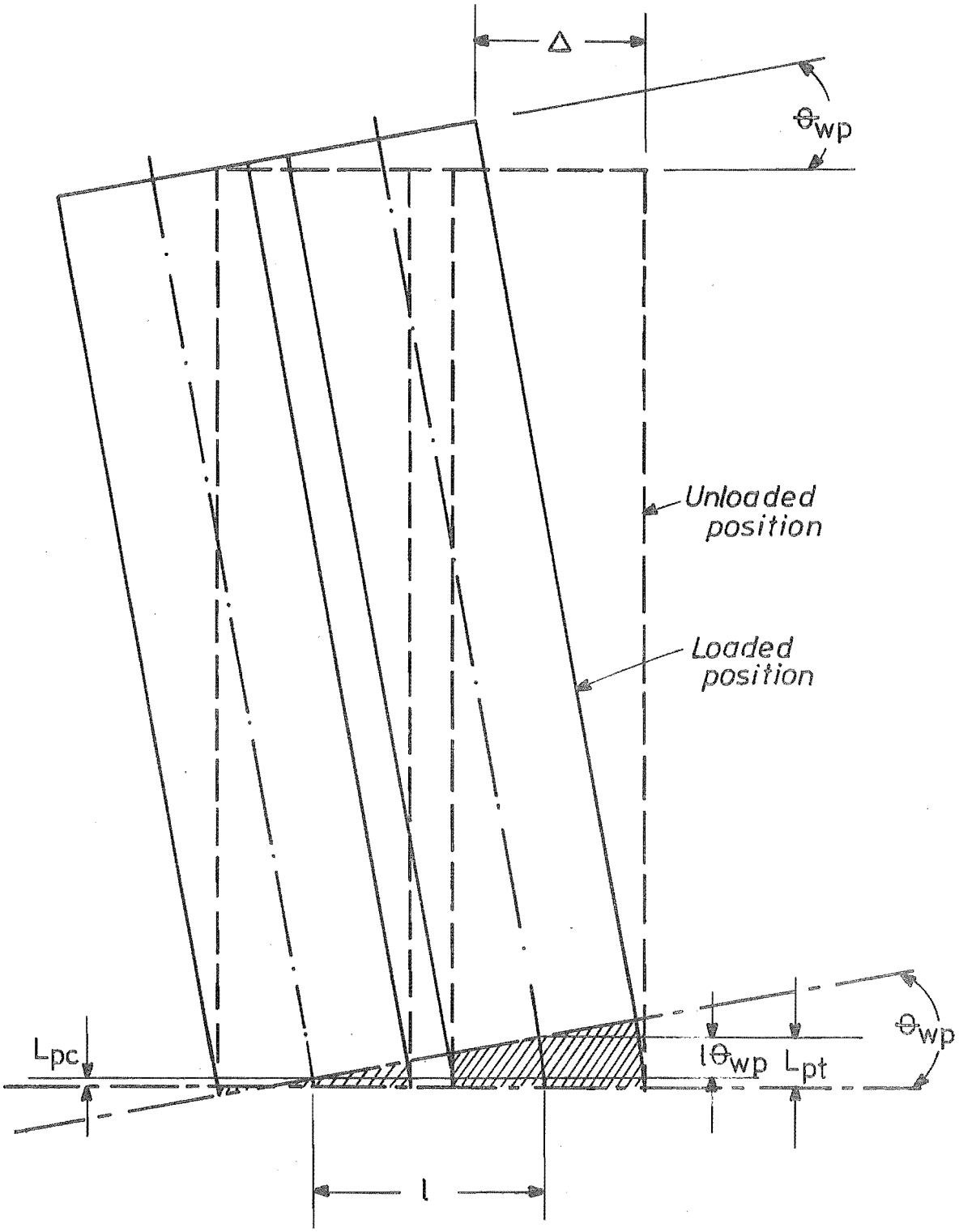

FIG. 4.11 PLASTIC DEFORMATIONS OCCURRING IN THE WALLS

Substituting this in Eq. 4.20 the following relationship between the curvatures of tension and compression walls is obtained

$$\left(\varphi_{uc} - \varphi_{yc}\right) = \left(\varphi_{ut} - \varphi_{yt}\right) \left(1 + \frac{l\,\theta_{wp}}{L_{pc}}\right) \qquad \ldots (4.22)$$

This shows that the post-elastic curvature for the compression wall is always larger than that of the tension wall.

In Chapters 6 and 7, the curvatures and the length of plastic hinges, observed during test for the shear wall models A and B, are used in Eq. (4.20) to compute the plastic rotation at the base of walls 1 and 2. In these chapters it will also be shown that the relationship between observed length of plastic hinges (L_{pt} and L_{pc}), the yield curvatures (φ_{yt} and φ_{yc}), ultimate curvatures (φ_{ut} and φ_{uc}) for the tension and compression walls and the plastic rotation, θ_{wp}, at the base of the walls are in accordance with Eq. (4.22).

4.5 NUMERICAL EXAMPLE

To illustrate the application of the proposed elasto-plastic analysis, a 10 storey shear wall is considered. The dimensions of the shear wall can be seen in Fig. 4.12.a. The period, T , of the building for which this shear wall was intended, was estimated to be 1.15 secs. The building was to be built in Wellington, New Zealand. For this period, and for this location, the New Zealand Standard Model Building Bylaw[75] (NZSS 1900 Chapter 8:1965) recommends an equivalent lateral static force corresponding with 0.072 g . The coupled shear wall was subjected to this base shear and the distribution of loading is as shown in Fig. 4.13.b. The coupling beams were provided with principal diagonal reinforcement. The dimensions of the coupling beams,and the reinforcement provided in them, varied along

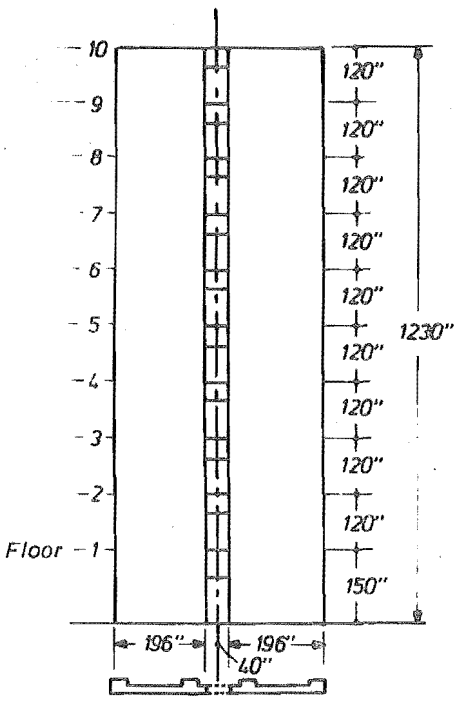

(a) Dimensions of the shear wall

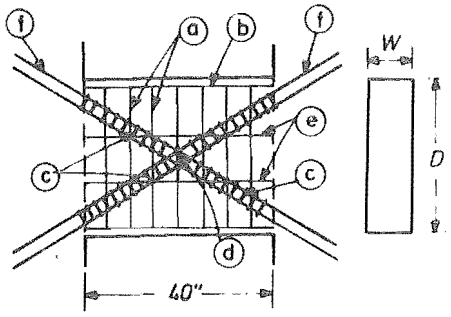

(b) Typical coupling beam

NOTES:

(a) # 3 closed stirrups at 6" crs.
(b) 2 - # 6 bars - 3'-6" long ($1\frac{1}{2}$" cover)
(c) Prefabricated # 2 helix (4 units) 4" pitch
(d) # 2 tie
(e) 2 - # 4 bars (nominal)

width W, the depth, D, of the beam and the diameter of principal diagonal reinforcement (f) varied along the height as given in the table below.

Table 4.1 Particulars of the coupling beams

Floor	Width W	Depth D	Details of diagonal reinforcement (f)	Nominal ultimate shear Q_u (Kips) provided	Nominal ultimate laminar shear q_u (Kip/in) provided
9th and 10th	10"	33"	4 - # 8 bars	120.00	1.000
7th and 8th	12"	33"	4 - # 9 bars	151.60	1.260
2nd to 6th	14"	33"	4 - # 10 bars	187.50	1.560
1st	14"	60"	4 - # 8 bars	184.00	1.530

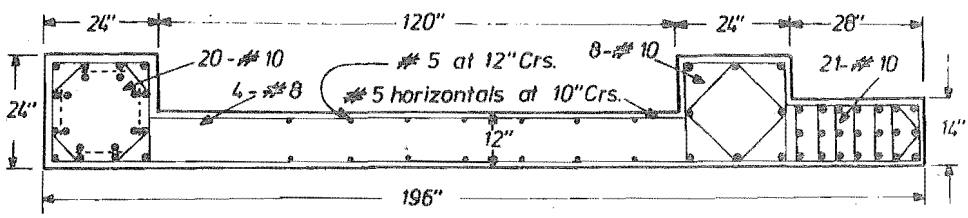

(c) Cross-section at the base of the left wall showing the reinforcements provided

FIG. 4.12 DETAILS OF THE EXAMPLE STRUCTURE

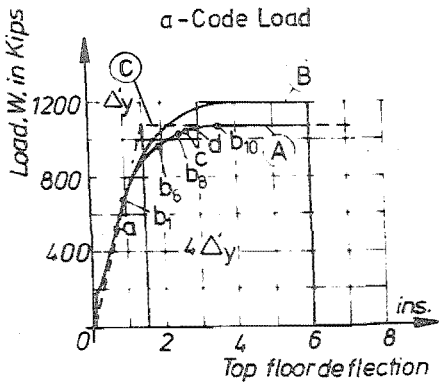

(a) Load-top floor displacement curves

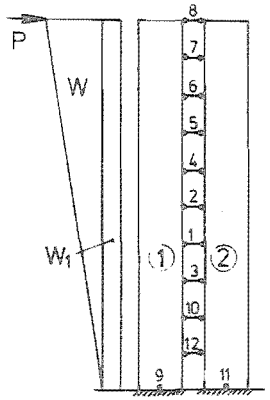

(b) Sequence of hinge formation

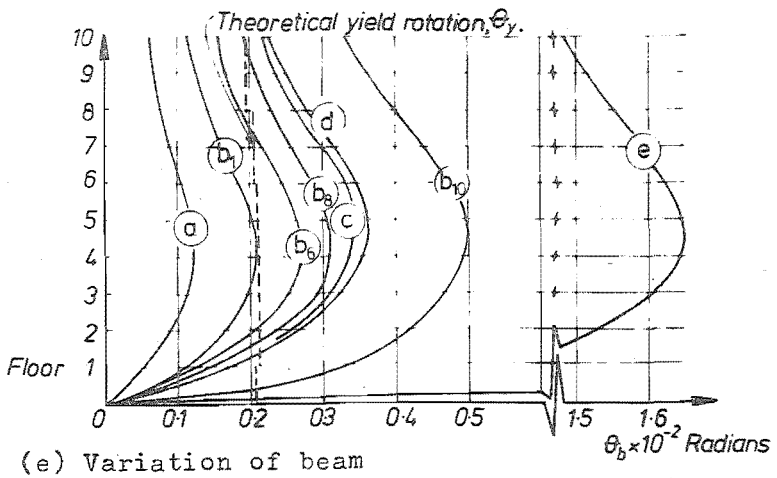

(e) Variation of beam rotations during different stages of loading

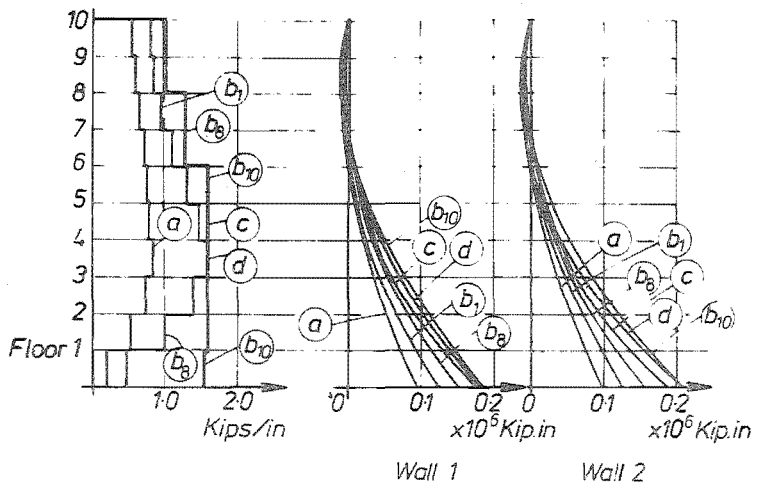

(c) Variation of laminar shear during different stages of loading

(d) Variation of moments in the walls

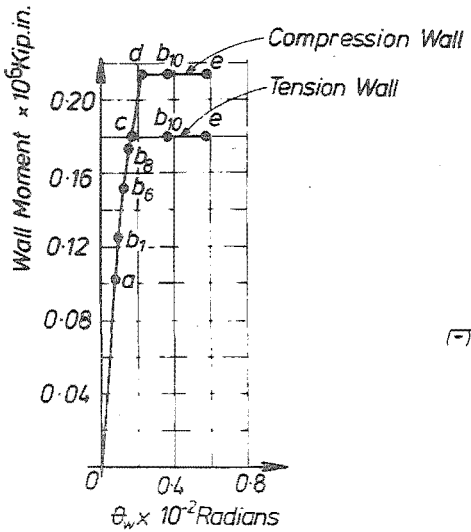

(f) Moment-rotation curves for the tension and compression walls

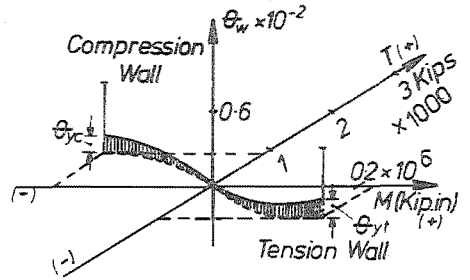

(g) Axial force-moment rotation relationship

FIG. 4.13 RESULTS OF THE ELASTO-PLASTIC ANALYSIS OF A TYPICAL COUPLED SHEAR WALL STRUCTURE

the height of the shear wall to approximately correspond with elastic laminar shear variation. A load factor of 1.25 was used while designing these beams. Fig. 4.12.b. shows a typical coupling beam. The reinforcement details and the shear strength of these beams are summarised in Table 4.1. The reinforcement provided in the bottom floor of the walls is shown in Fig. 4.12.c. A load factor of 1.69 was used for the design of the walls.

The elasto-plastic analysis proposed in Section 4.3.5 was used to predict the behaviour of this coupled shear wall. The results of this analysis are shown in Fig. 4.13.

Fig. 4.13.a shows the load-top floor displacement curves for the shear wall. Curve A represents the load-displacement curve for the shear wall in which the beams are assumed to have linearly elastic perfectly plastic bilinear relationship. Curve B represents the load-displacement curve for the shear wall in which the beam steel is assumed to have a strain hardening of 15% at a strain of 15 times the yield strain of steel. It is seen that this assumption increases the ultimate load of the shear wall by approximately 11%. The broken curve C represents idealised bilinear behaviour of the shear wall. On the curve A, different stages of attainment of ultimate capacity are also shown. It is seen that stages c and d occur close to each other.* Stage b_{10}, which is the full plastification of the laminar system, occurs after stages c and d. Thus at stage b_{10} the shear wall attains its full load capacity.

Fig. 4.13.b shows the sequence of hinge formation. The strengths of the beams were varied to correspond approximately with the elastic laminar shear distribution. It was pointed out in Chapter 3 that that portion of yield rotation which is dependent on the steel content in diagonally reinforced beams is insignificant. Therefore, the

---

* For definition of load stages see page 148.

yield rotation of all the coupling beams is almost the same. The critically situated coupling beam (fourth floor beam) reaches yield first. The tension wall hinge develops after 8 beams (from the 2nd to top floors) have yielded. The formation of 9th, 10th and 11th hinges are almost simultaneous. The first floor coupling beam was the last to reach ultimate capacity.

The laminar shear variation during different stages of loading is plotted in Fig. 4.13.c. The thick line shows the strengths of the coupling beams provided.

Fig. 4.13.d shows the variation of bending moments along the height of the structure during different stages of loading. After stage c, there is a small increase in moments of wall 1 along the height of the structure. However, there is no increase in moment at the base. Similarly, after stage d there is a small increase in moments of wall 2 along the height of the structure. The increase in moments at the base is zero.

Fig. 4.13.e shows the variation of beam rotations along the height of the structure during different stages of loading. Stages c and d occur very close to one another. Stage e represents the total beam rotations when the top floor displacement is $4\Delta y'$ (see Fig. 4.13.a). The broken line curve indicates the yield rotations of the various coupling beams. It is seen that the ductility demand for the critical coupling beam is

$$\mu_b \text{ (max)} = \frac{1.65 \times 10^{-2}}{0.2 \times 10^{-2}} = 8.25$$

Fig. 4.13.f shows the moment-rotation curves for the tension and compression walls. θ_{yt} and θ_{yc} represent the yield rotations for the tension and compression walls respectively. The maximum member ductility for the tension wall is

$$\mu_{wt} = \frac{0.58 \times 10^{-2}}{0.17 \times 10^{-2}} = 3.40$$

The maximum member ductility for the compression wall is

$$\mu_{wc} = \frac{0.58 \times 10^{-2}}{0.22 \times 10^{-2}} = 2.64$$

Fig. 4.13.g shows the load-moment-rotation relationship for the tension and compression wall. This figure shows that the increase in axial load sustained by the wall after the walls reach yield is negligible.

This shear wall was designed with the approximate method of Paulay[5]. In this it was assumed that all the coupling beams would yield before the capacity of the walls is attained. It can be seen from Fig. 4.13a that the walls begin to yield only at a high load of 97% of theoretical ultimate after all but the bottom coupling beams have attained their capacity. This shows that a considerable amount of total energy can be dissipated by the plastification of the coupling system while the walls are still "elastic".

Fig. 4.13.b shows that the coupling beams in the bottom two floors are elastic when the walls reach ultimate load. By either increasing the capacity of the walls or decreasing the capacity of the coupling system this shear wall could be redesigned so that all but the bottom floor coupling beam may yield before the walls attain their capacity. The actual failure load of the shear wall, when the strain hardening of the steel is considered, is of the order of $1.12V_p^*$. By redesigning the shear wall, the stages c and d may be made to approach this ultimate load. This would give further protection for the walls against the irrepairable permanent misalignment during moderate earthquakes. However, it is to be noted that it might not be possible to design so as to make the bottom floor coupling beam yield before the walls reach their capacities. Unlimited rotation in the

in the lamina close to the base of the walls cannot be expected to occur when the walls are elastic. V_p^* is the theoretical ultimate base shear on the prototype structure chosen in this example.

The broken line curve in Fig. 4.13.a shows the approximate theoretical bilinear elasto-plastic behaviour of the coupled shear wall. This assumes that the shear wall is elastic till the theoretical ultimate load V_p^* is attained. The stiffness of the shear wall in the "elastic" range is assumed to be constant till the ultimate load is attained. This constant stiffness is computed in terms of the top floor deflection of the shear wall when the critical lamina reaches yield ($\Delta = 1.00"$). Thus the deflection at the onset of yield for the assumed bilinear behaviour (broken line curve) at $V_p^* = 1.00$ is $\Delta_y' = 1.5"$. The evaluation of the overall displacement ductility for the shear wall was based on this theoretical yield deflection. However, the inelastic deflections commence when the critical lamina reaches yield. If this deflection ($\Delta_y = 1.00$) is taken as the basis instead of Δ_y' for the ductility studies, the maximum deflection computed for stage e would correspond to a ductility factor of $1.5 \times 4 = 6$ at ultimate load, $V_p^* = 1.00$. For the example this ultimate load is 1.5 times the load at which the critical lamina reaches yield. If it is desired, the shear wall could be redesigned with smaller overload factors for the beams and walls so that the ultimate load is of the order of say 1.25 times the load at which critical lamina reaches yield. At this load the ability of the beams and walls of the shear wall to sustain the required post-elastic deformation for an overall ductility factor of 4 can then be ascertained.

CHAPTER FIVE

TEST SPECIMENS, MATERIALS, LOADING SYSTEM AND TESTING PROCEDURE

5.1 THE TEST SPECIMENS

The dimensions of the coupled shear wall test specimens are shown in Fig. 5.1. The thickness of the walls was 4 in. and that of the coupling beams 3 in. The reaction was supplied by a 6 in. thick base block.

The base block was reinforced in such a manner that steel stresses were of the order of 15000 psi when the ultimate strength of the shear wall was attained. It performed satisfactorily during the test. At high load intensities a few diagonal cracks did appear.

Fig. A.1 in Appendix A shows a typical bay of a prototype seven storey shear wall structure. In Section A.2 of this Appendix the equivalent lateral seismic load for this prototype wall is compared with the theoretical ultimate loads on the models. The specimens represent a quarter scale model of this prototype shear wall. The prototype shear wall structure is designed to resist the lateral load corresponding with the mass of 5 bays, each 20'-0" wide

The load pattern on the shear wall was chosen so as to simulate, as nearly as possible, the code load distribution as required by the New Zealand Standard Model Building Bylaw[75]. Details of the moment and shear force patterns are recorded in Fig. 5.5.

The dead load on the shear wall was simulated by forces applied by two prestressed cables, one at the centroid of each wall. A force of 25 Kips was applied by these cables. A comparison of the stresses produced by the dead load in the prototype structure at the base of the walls and that produced by the prestressed cables in the bottom

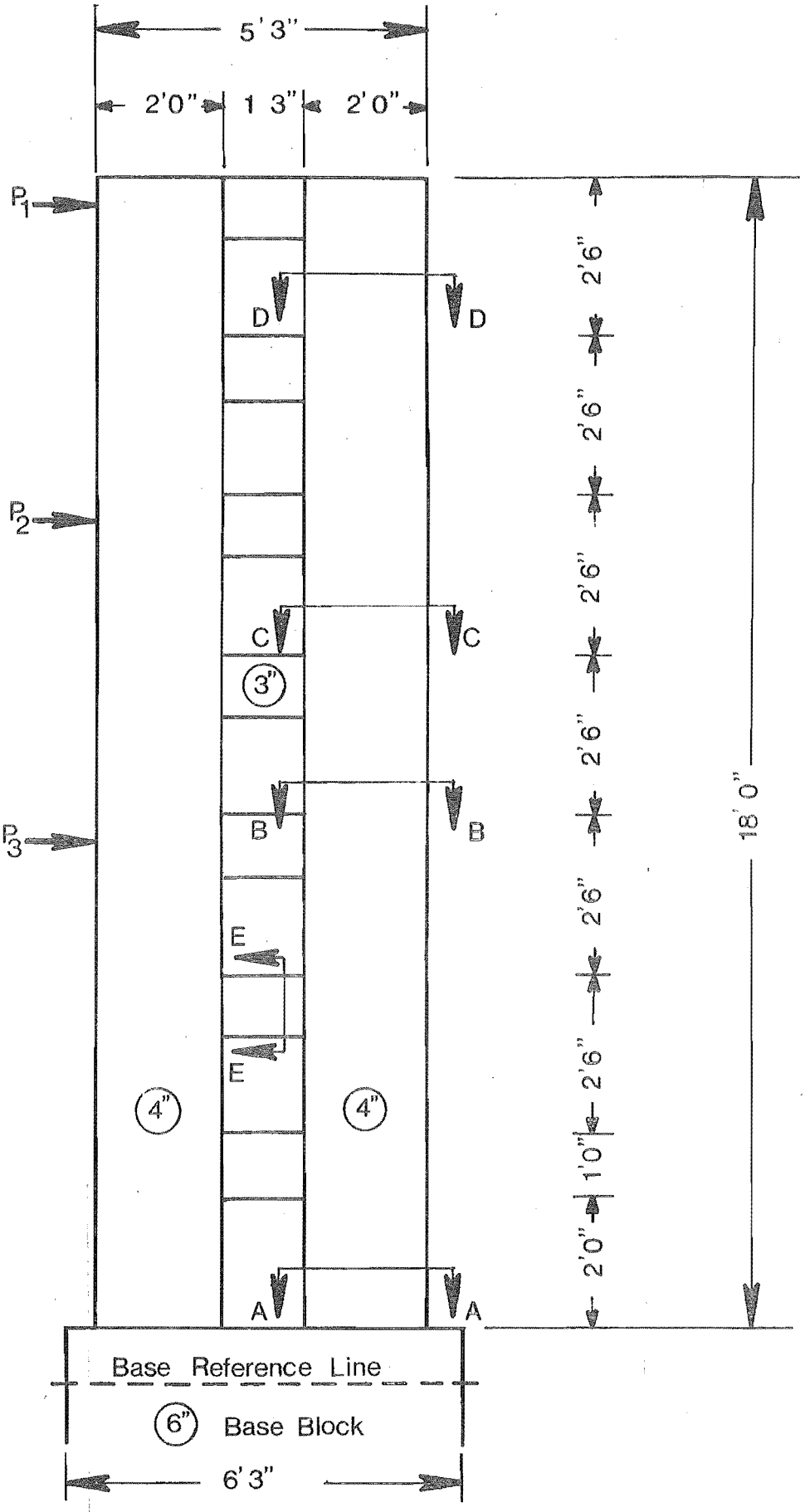

NOTE: Details of sections at A-A, B-B, C-C, D-D and E-E are shown in Figs. 5.2 to 5.4

FIG. 5.1 DIMENSIONS OF THE MODELS.

floor walls of the models is made in Section A.1., Appendix A.

5.2 THE CONCRETE

The concrete was obtained from a "ready mix" plant in Christchurch. The concrete mix proportions are given in Table 5.1. While placing, the concrete was compacted by an immersion type vibrator. After screeding and floating the specimen, the test cylinders, cubes and the temperature blocks were cured for seven days under a layer of wet sack covered with a polythene sheet to minimise evaporation losses. The relevant concrete strengths and other properties are assembled in Table 5.2.

5.3 THE REINFORCEMENT

The disposition of the reinforcement used in the models can be seen in Figs. 5.2 to 5.4, and in the photographs reproduced in Figs. 5.6 and 5.7. Typical stress-strain curves for the bars used in these shear walls are assembled in Fig. 5.8. Their properties are summarised in Tables 5.3 to 5.5.

Both the models, Shear Wall A and Shear Wall B, had similar reinforcement in the two walls. The beams of Shear Wall A had conventional reinforcement for shear and flexure (see Fig. 5.3). The coupling beams of Shear Wall B contained diagonal bars together with nominal secondary reinforcement. The diagonal bars were tied and the concrete in the diagonal was confined by a 12 gauge wire spiral at $\frac{3}{4}$ in. pitch (see Fig. 5.4).

The main bars of the walls were taken right through the base block (see Fig. 5.6). There they were welded to a rolled steel channel EC. To sustain the larger moment at the centre of the base block additional bars were provided. To ensure continuity these bars were welded to the channel and to the shear reinforcement in the block at the other end. To relieve the stress concentration at the central

TABLE 5.1 CONCRETE MIX PROPORTIONS

1	Water-cement ratio	0.576
2	Cement content	430 lbs/cub. yd.
3	Aggregate-cement ratio	15.3
4	Fines modulus of sand	2.635
5	Fines modulus of aggregate	6.523
6	Date of casting:	
	Shear Wall A	7-8-72
	Shear Wall B	20-11-72
7	Date of testing:	
	Shear Wall A	19-12-72
	Shear Wall B	1-6-73

TABLE 5.2 CONCRETE PROPERTIES

	Symbol	Units	Shear Wall A	Shear Wall B
Age when tested	-	days	135	225
Cube strength(1)	f'_{cu}	psi	5280	5536
Cylinder strength(2)	f'_c	psi	4576	4352
Strength ratio	f'_c/f'_{cu}	-	0.865	0.788
Modulus of rupture(3)	f'_t	psi	758	778
Density	γ	lbs/ft^3	143	144

Notes: (1) 6" x 6" x 6" Standard cubes.

(2) 12" x 6" Standard cylinders.

(3) 3" x 3" x 12" Standard prisms.

TABLE 5.3 THE POSITION AND PROPERTIES OF REINFORCEMENT USED IN THE WALLS OF BOTH SHEAR WALLS A AND B

		FLEXURAL REINFORCEMENT(4)						STIRRUP REINFORCEMENT(3)				SECONDARY REINFORCEMENT(3)			PRESTRESSING TENDONS	
POSITION (FLOOR)	EFFECTIVE DEPTH	NUMBER OF #5 BARS		STEEL(1) CONTENT		YIELD STRENGTH(2)	ULTIMATE(2) STRENGTH	$\frac{1}{4}$" ø 2-LEGGED STIRRUP(3) AT A SPACING OF	STEEL CONTENT	YIELD (2) STRENGTH	ULTIMATE(2) STRENGTH	STEEL CONTENT(1) OF 2 - $\frac{1}{4}$"ø BARS	YIELD STRENGTH(2)	ULTIMATE(2) STRENGTH	NUMBER AND SIZE OF TENDONS	ULTIMATE(2) STRENGTH
		OUTER FACE	INNER FACE	OUTER FACE	INNER FACE											
-	d	-	-	$\rho = \frac{A_s}{bd}$	$\rho' = \frac{A_s}{bd}$	f_y	f_u	-	$\rho_v = \frac{A_v}{bs}$	f_y	f_u	A''_s/bd	f_y	f_u	-	f_u
-	in.	-	-	%	%	ksi	ksi	in.	%	ksi	ksi	%	ksi	ksi	-	ksi
1st	20.41	10	2	3.49	0.70	44.2	68.4	3	0.88	51.0	72.2	0.26	49.8	70.7	FOUR 0.276" DIAMETER PRESTRESSING TENDONS	240
2nd	20.41	10	2	3.49	0.70	44.2	68.4	3	0.88	51.0	72.2	0.26	49.8	70.7		240
3rd	20.41	10	2	3.49	0.70	44.2	68.4	3	0.88	51.0	72.2	0.26	49.8	70.7		240
4th	21.10	8	2	2.79	0.70	44.2	68.4	4	0.67	51.0	72.2	0.25	49.8	70.7		240
5th	21.78	6	2	2.09	0.70	44.2	68.4	4	0.67	51.0	72.2	0.24	49.8	70.7		240
6th	22.47	4	2	1.39	0.70	44.2	68.4	6	0.44	51.0	72.2	0.23	49.8	70.7		240
7th	22.47	4	2	1.39	0.70	44.2	68.4	6	0.44	51.0	72.2	0.23	49.8	70.7		240

NOTES:
(1) Based on actual area of # 5 bars
(2) Average of six representative specimens tested
(3) Plain Bars
(4) Deformed Bars
# Indicates nominal diameter of deformed bar in multiples of $\frac{1}{8}$ inch.

TABLE 5.4 THE PROPERTIES OF REINFORCEMENT USED IN CONVENTIONALLY REINFORCED COUPLING BEAMS OF SHEAR WALL A

SHEAR WALL DESIGNATION	EFFECTIVE DEPTH	FLEXURAL REINFORCEMENT				STIRRUP REINFORCEMENT					SECONDARY REINFORCEMENT			
		NUMBER[1] AND SIZE[2] OF BARS	STEEL[3] CONTENT	YIELD STRENGTH[5]	ULTIMATE STRENGTH[5]	STIRRUP DETAILS	SPACING	STEEL[3] CONTENT	YIELD STRENGTH[5]	ULTIMATE STRENGTH[5]	NUMBER AND SIZE OF BAR[4]	STEEL[3] CONTENT	YIELD STRENGTH[5]	ULTIMATE STRENGTH[5]
-	d	-	$\frac{A_s}{bd}$	f_y	f_u	-	s	$\frac{A_v}{bs}$	f_y	f_u	-	A_h/bd	f_y	f_u
-	in.	-	%	ksi	ksi	-	in.	%	ksi	ksi	-	%	ksi	ksi
SHEAR WALL A	11.31	2 - # 3	0.62	45.65	62.57	$\frac{1}{4}$" Ø - 2 LEGGED STIRRUP	2.0	1.76	50.20	70.62	2 - 3/16" Ø BARS, ONE ON EACH FACE, AT THE CENTRE OF THE BEAM	0.14	33.30	49.20

NOTES:
(1) Refers to steel in one face of doubly reinforced beam.
(2) Deformed bars.
(3) Based on actual area of steel.
(4) Plain bars.
(5) Average of six representative specimens tested.
# Indicates nominal diameter of deformed bar in multiples of $\frac{1}{8}$ inch.

TABLE 5.5 THE PROPERTIES OF REINFORCEMENT USED IN DIAGONALLY REINFORCED COUPLING BEAMS OF SHEAR WALL B

SHEAR WALL DESIGNATION	EFFECTIVE(7) DEPTH	MAIN REINFORCEMENT				SECONDARY REINFORCEMENT						CONFINING SQUARE SPIRALS				
		NUMBER AND SIZE OF(1) BARS	STEEL(4) CONTENT	YIELD STRENGTH(6)	ULTIMATE(6) STRENGTH	NUMBER AND SIZE OF(3) BARS	STEEL(4) CONTENT	STIRRUPS	STEEL(4) CONTENT	YIELD STRENGTH(6)	ULTIMATE(6) STRENGTH	SIZE OF BAR	PITCH	STEEL(4) & (5) CONTENT	YIELD STRENGTH(6)	ULTIMATE(6) STRENGTH
-	d	-	A_s/bd	f_y	f_u	-	A_h/bd	-	A_v/bs	f_y	f_u	-	p	ρ_s	f_y	f_u
-	in.	-	%	ksi	ksi	-	%	-	%	ksi	ksi	-	in.	%	ksi	ksi
SHEAR WALL B	9.675	2 - #3(2) 2 - 4" ø(3)	1.12	45.65 AND 50.20	62.57 AND 70.62	3/16" ø BAR, 2 IN EACH FACE	0.16	3/16" ø 2 LEGGED STIRRUPS AT 4.5" SPACING	0.35	33.3	49.2	12 GAUGE WIRE	0.75	4.00	55.28	69.29

NOTES:
(1) Refers to steel in one diagonal of the coupling beam
(2) Deformed bars
(3) Plain bars
(4) Based on actual area of steel
(5) Approximate volume of binding steel, V_s , divided by volume of concrete bound, V_c
(6) Average of six representative specimens tested
(7) At the junction of coupling beam and wall

(7) # Indicates diameter of bars in multiples of $\frac{1}{8}$ inch.

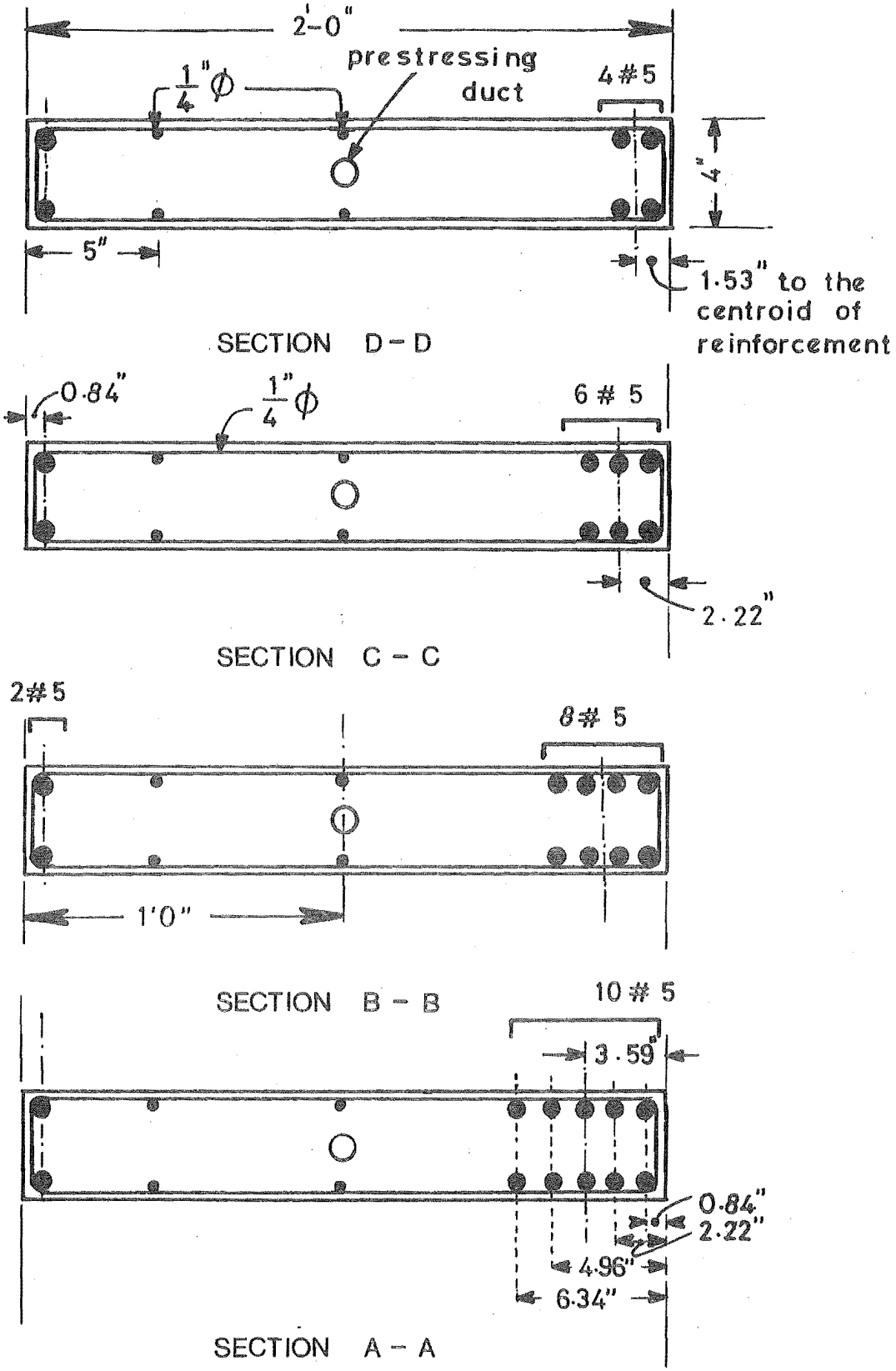

NOTE: φ denotes plain round bars
# denotes deformed bars
For levels of sections see Fig. 5.1

FIG. 5.2 DETAILS OF REINFORCEMENT IN THE WALLS.

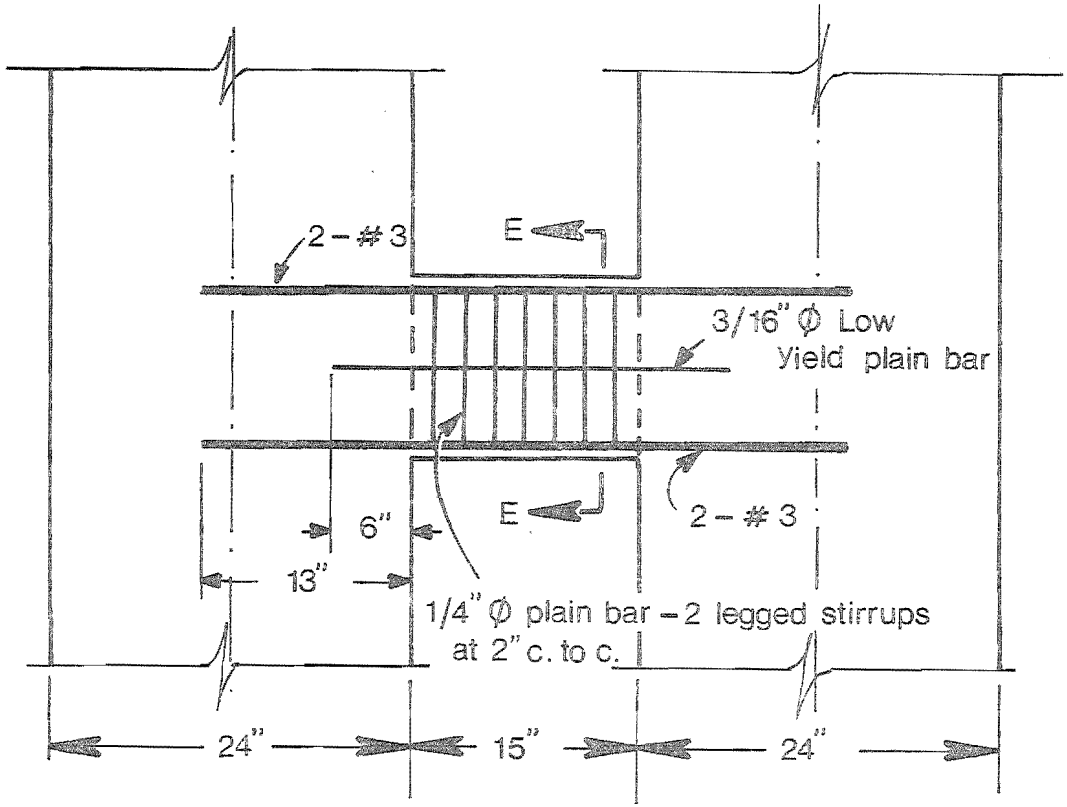

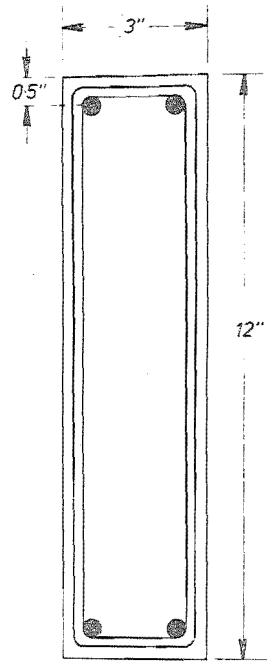

SECTION - EE

FIG. 5.3 COUPLING BEAM REINFORCEMENT IN SHEAR WALL A

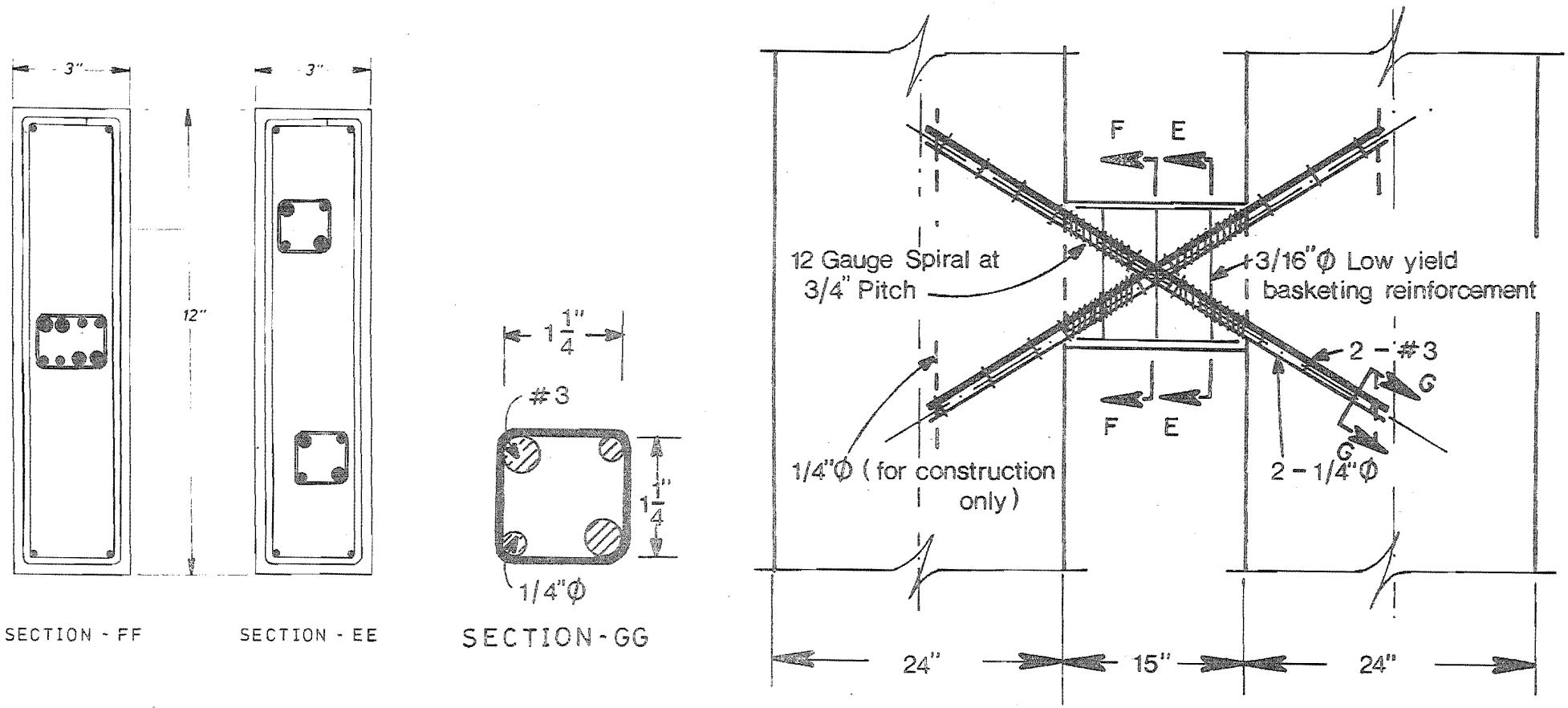

FIG. 5.4 COUPLING BEAM REINFORCEMENT IN SHEAR WALL B

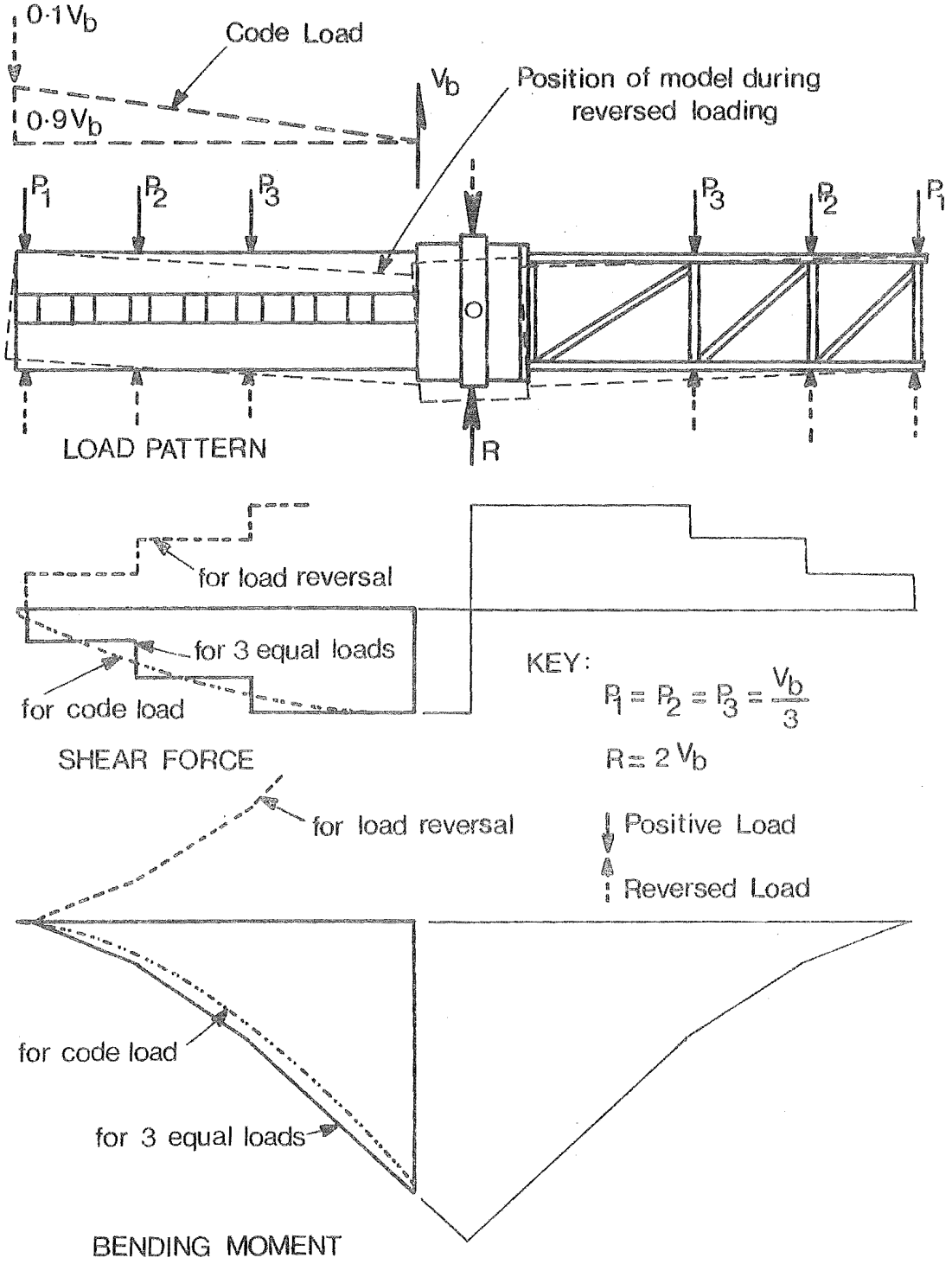

FIG. 5.5 LOAD PATTERN FOR THE MODELS

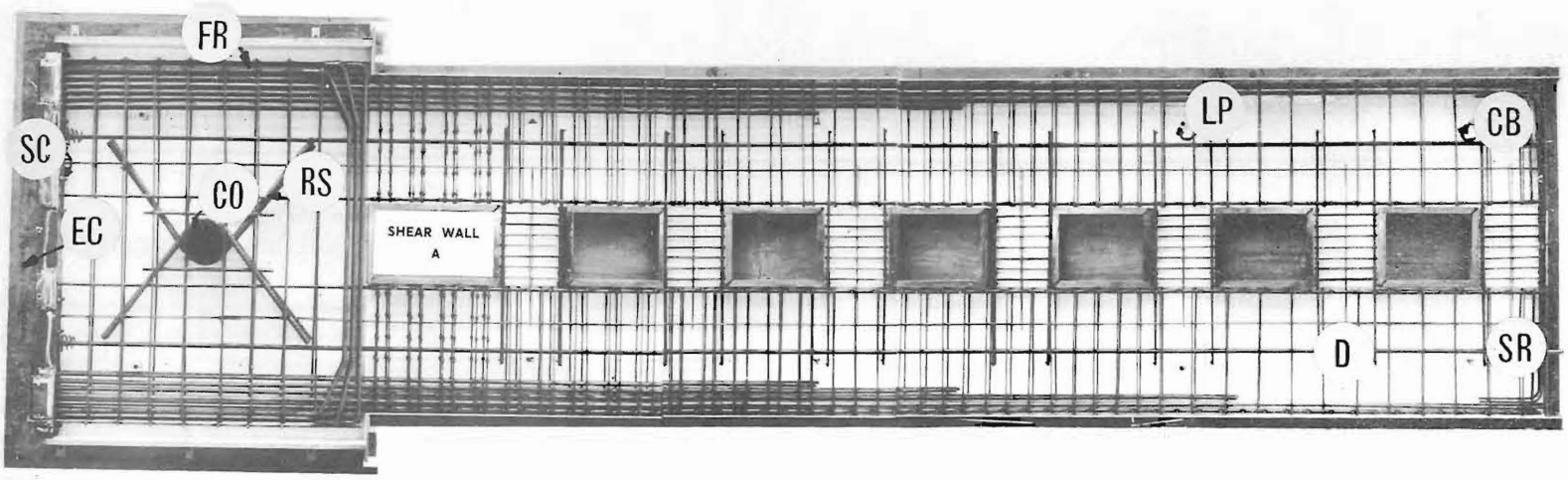

FIG. 5.6 DISPOSITION OF REINFORCEMENT IN SHEAR WALL A

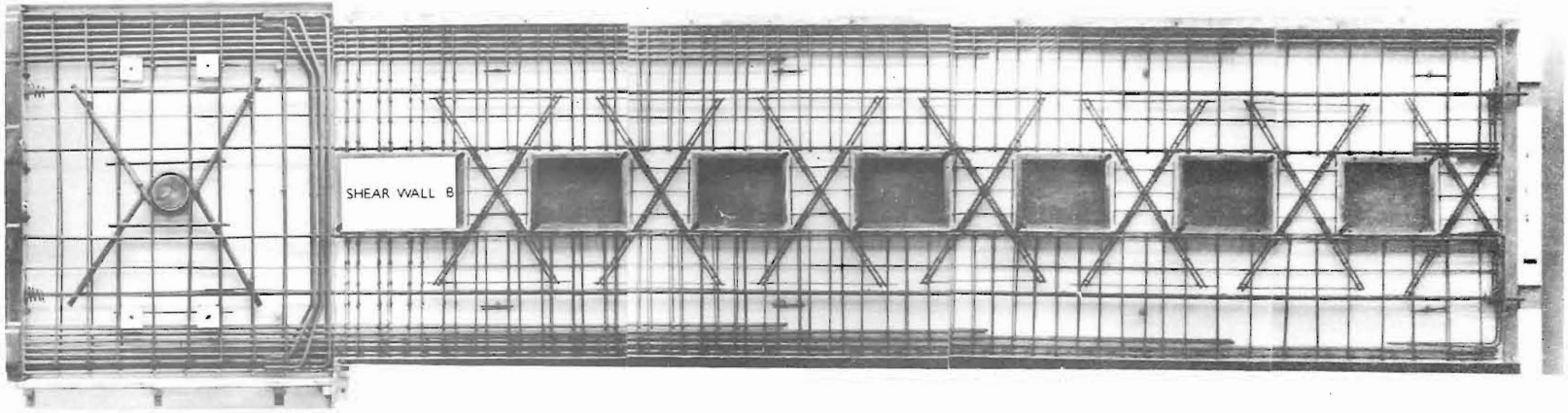

FIG. 5.7 DISPOSITION OF REINFORCEMENT IN SHEAR WALL B

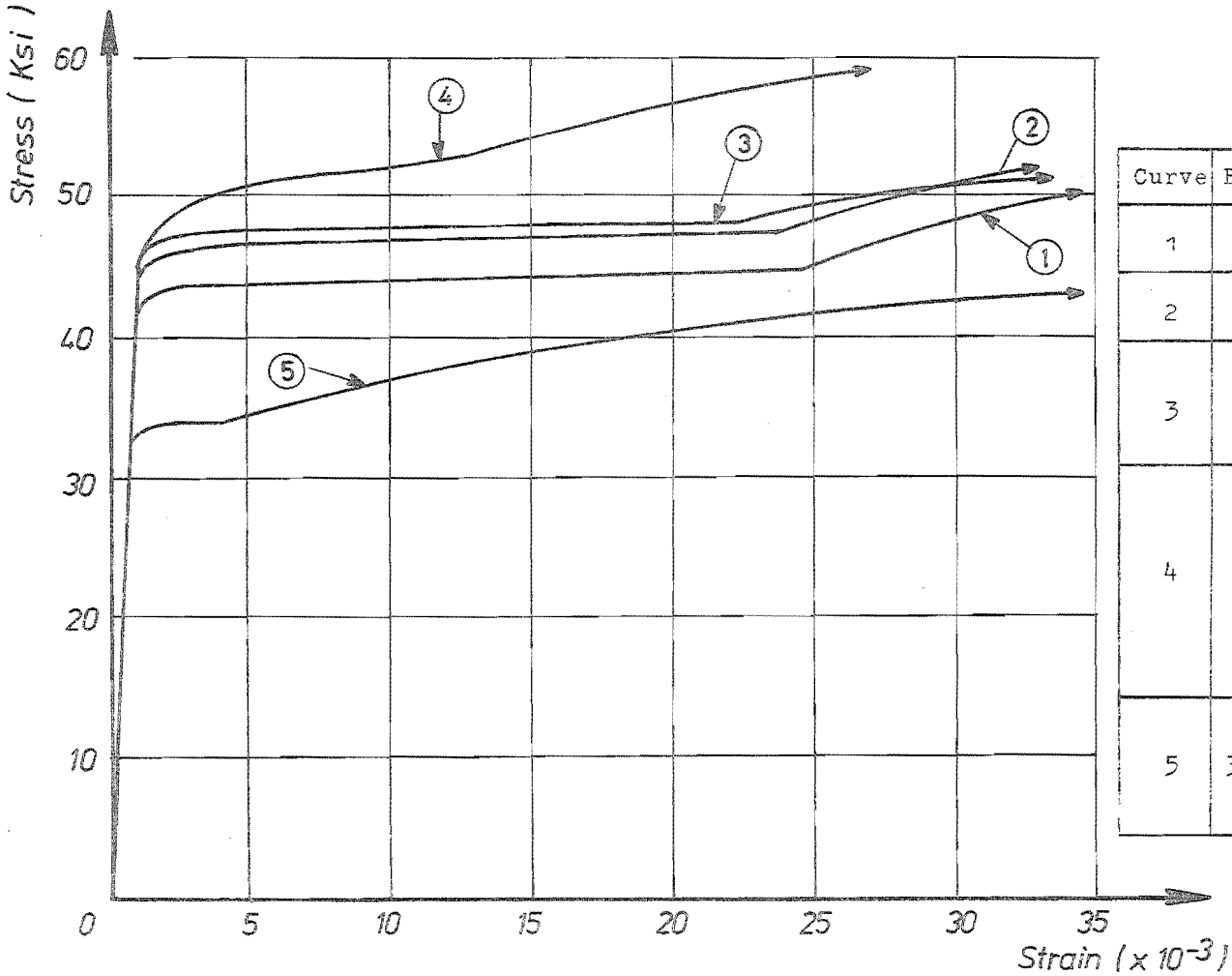

Curve	Bar Size	Used In
1	# 5	Flexural steel in the walls of Shear Wall A and Shear Wall B
2	# 5	Flexural steel in the walls of Shear Wall A and Shear Wall B
3	# 3	Flexural steel in the beams of Shear Wall A Diagonal steel in the beams of Shear Wall B
4	1/4" ø	Stirrup steel in the walls of Shear Wall A and Shear Wall B Stirrup steel in the beams of Shear Wall A Diagonal steel in the beams of Shear Wall B Secondary steel in the walls of Shear Wall A and Shear Wall B
5	3/16" ø	Secondary steel in the beams of Shear Wall A and Shear Wall B Nominal stirrup steel in the beams of Shear Wall B

FIG. 5.8 STEEL STRAIN RELATIONSHIPS

loading pin, No. 8 bars were welded to the collar, CO. Sufficient shear connectors, SC, were provided on the channel face to avoid sliding shear failure.

5.4 THE LOADING SYSTEM

The photograph reproduced in Fig. 5.9a shows the loading system consisting of seven frames with all attachments. A schematic diagram of loading and load measuring devices can be seen in Fig. 5.9b. The working of the double cantilever loading system is summarised below:

(a) The loads $P_2 = \frac{V_b}{3}$ and $P_3 = \frac{V_b}{3}$ (See Figs. 5.9b and 5.5) were applied by four 10 ton capacity jacks connected to a common pressure source. V_b is the base shear across the shear wall model. The reaction $R = 2V_b$ was supplied by a 60 ton capacity jack, from a separate pressure source. For static equilibrium of the desired forces acting on the shear wall and steel frame(see Fig. 5.5).

$$R = 2P_1 + 2P_2 + 2P_3 = 2V_b \qquad \ldots (5.1)$$

and

$$P_1 = \frac{V_b}{3} \qquad \ldots (5.2)$$

(b) The base block, B, was restrained by the steel truss, T, so that the moment produced by the loading on the shear wall could be balanced by an equal opposing moment (see Figs. 5.5 and 5.9).

(c) The truss , T , was designed to remain elastic when the shear wall was subjected to plastic deformations. The deflections of the shear wall were found relative to the position of the base block, as indicated in Fig. 5.10. The maximum end deflection, Δ_A , anticipated during loading, was of the order of 20 in. The rotation of the truss enabled the shear wall to have an end deflection of about 30 in. when the deflection at the base block, Δ, was 12 in.

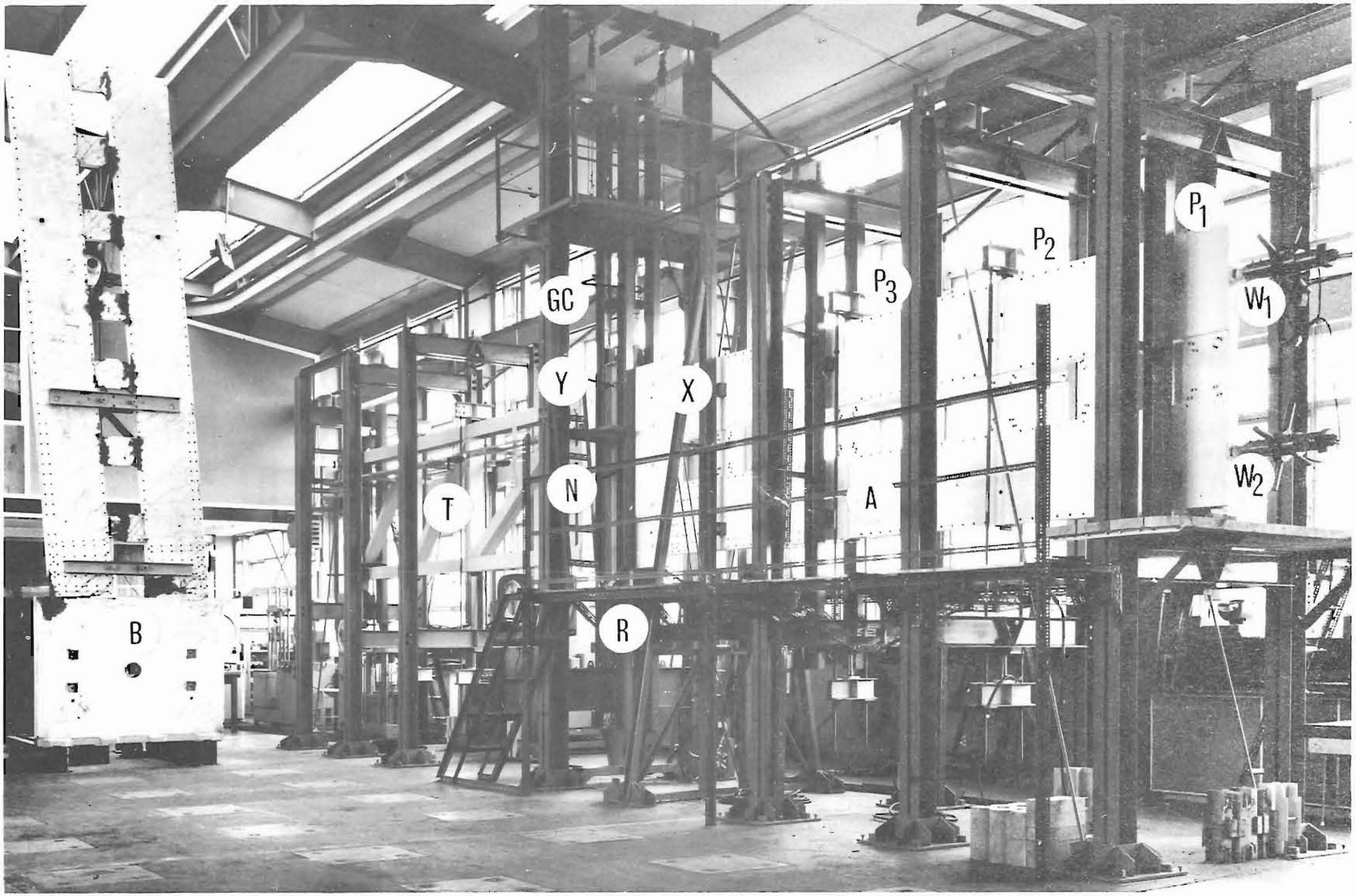

Reference may be made to page 182 with respect to notations used to represent the various components of the loading system

FIG. 5.9.(a) DOUBLE CANTILEVER LOADING SYSTEM, SHEAR WALL A AFTER FAILURE AND SHEAR WALL B LINED UP FOR TESTING

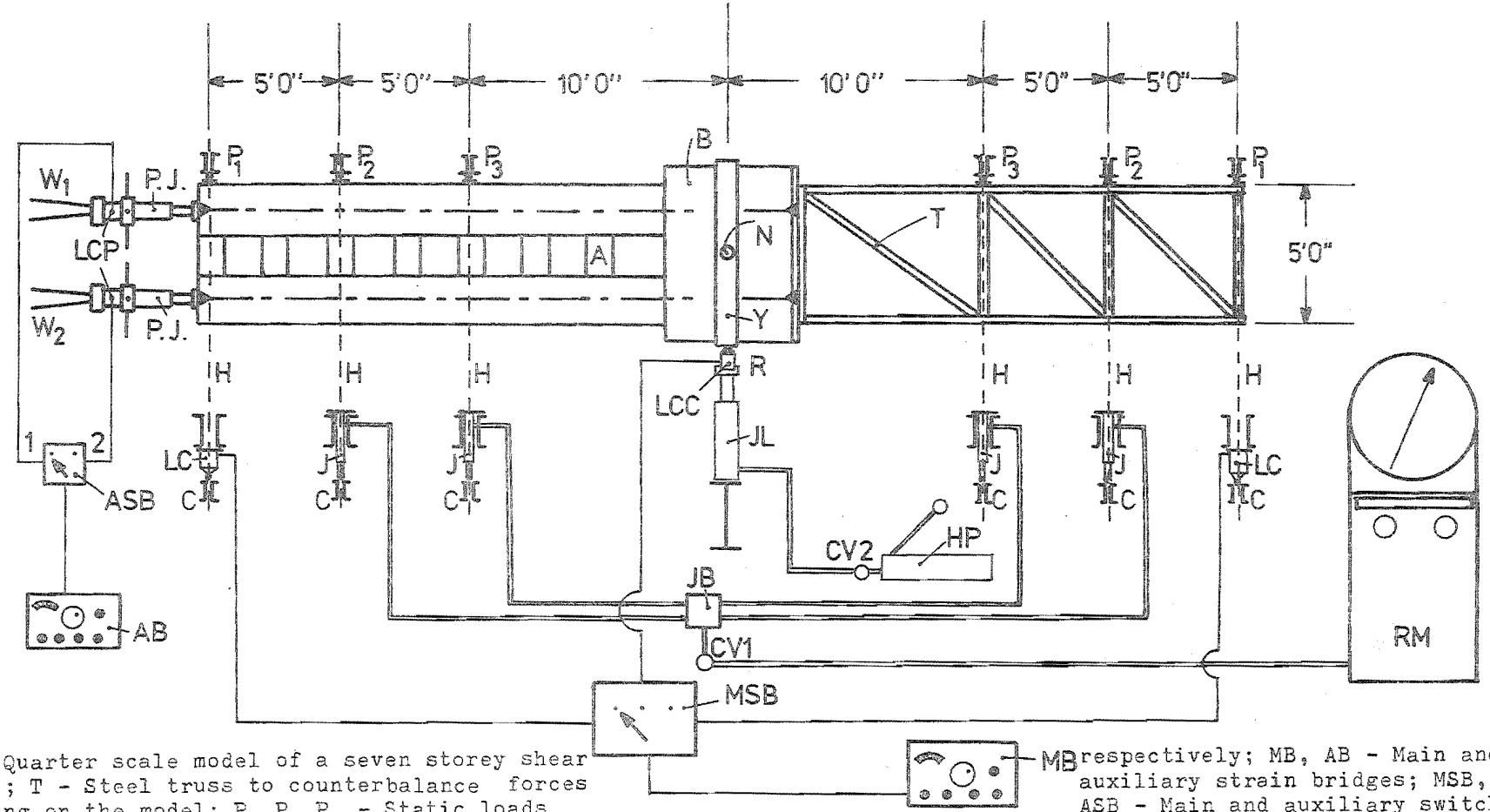

A - Quarter scale model of a seven storey shear wall; T - Steel truss to counterbalance forces acting on the model; P_1, P_2, P_3 - Static loads applied to the model; W_1, W_2 - Forces applied to the centre of the walls; R - The central reaction; N - The central pin facilitates the base block to rotate freely; H - Hanger rods allow the specimen to move horizontally; X - Roller support to prevent buckling; B - Base Block; Y - Yoke to transmit the reaction, R, to the pin, N; GC - Guiding channels ensure the reaction, R, to be vertical; JL, J, P.J. - 60 ton, 10 ton and Prestressing Jacks respectively; LCC, LC, LCP - 60 ton, 10 ton and 12 ton load cells respectively; MB, AB - Main and auxiliary strain bridges; MSB, ASB - Main and auxiliary switch boxes; HP - Hand Pump; RM - Riehle machine; CV1,CV2 - Control Valves to Riehle machine and hand pump; ——— Electrical leads; ═══ Oil pressure leads. C - Cross beams.

FIG. 5.9.b. A SCHEMATIC DIAGRAM OF LOADING & LOAD MEASURING DEVICES.

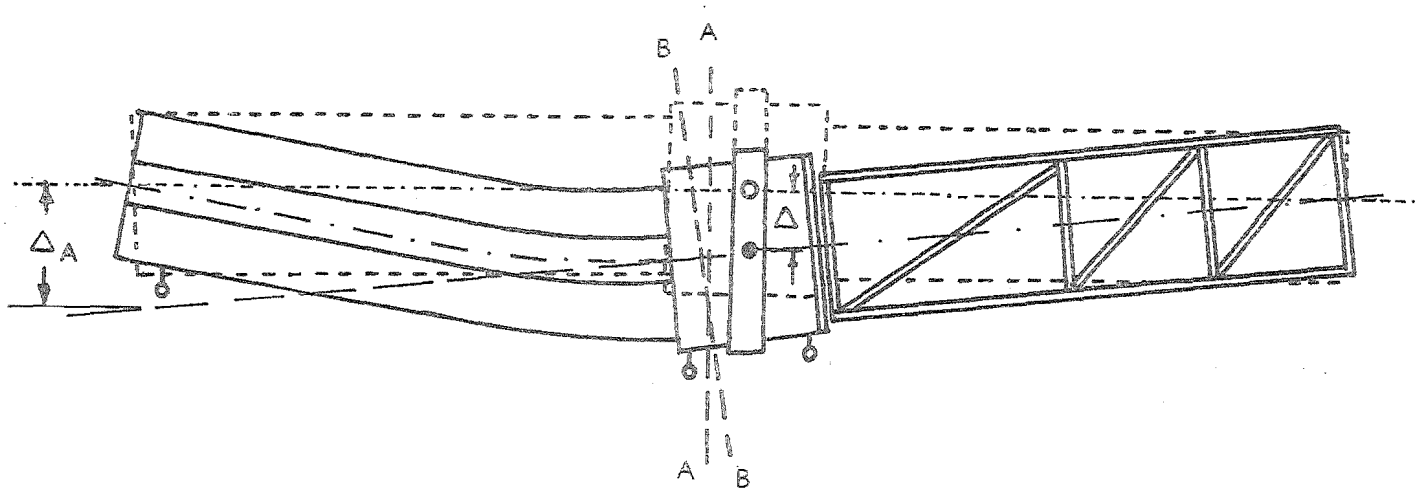

ELEVATION

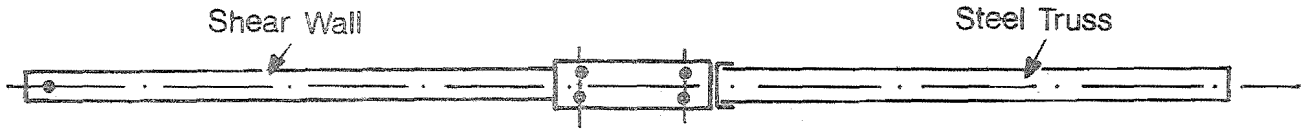

PLAN

NOTES:
- AA - Initial position of reference line.
- BB - Position of reference line during test.
- Δ - Deflection at the pin.
- Δ_A - End deflection of shear wall.
- δ^A - Dial gauge location in elevation.
- o - Dial gauge location in plan.

FIG. 5.10 DEFLECTION OF SHEAR WALL.

(d) An end deflection of 20 in. imposed horizontal movement of 2.5 in. at the extreme fibre of the model. The jacks, J, and the load cells, LC, were placed at the bottom of the cross beam, C, and the loads were applied by pairs of hanger bars, H . The hanger bars allow rotation about the hinge at the load point and the lateral movement of the model (see Fig. 5.9).

(e) The reaction, R, was applied through a 6 in. diameter steel pin, N, which rotates in a collar, CO, (Fig. 5.6) cast in the base block. This enabled the free rotation of the base block. The pin was connected to a yoke, Y . The lateral movement of the yoke was prevented by two pairs of guiding channels, GC, within which the yoke would freely move, up or down. This ensured that the reaction R was vertical. (See Fig. 5.9).

(f) The shear wall model was restrained against buckling by a system of rollers, X . These rollers slide over the steel channels connected between the top and bottom cross steel beams. (See Fig. 5.9).

(g) Prestressing to the walls was applied using screw jacks (see Fig. 5.11). This enabled the adjustment of the force during testing. This force was checked by the load cell readings and adjusted when necessary. The stresses produced by the gravity loads in the prototype wall varies along the height of the structure. In the models, a constant force of 25 Kips was applied at the centre line of the walls by the prestressed cables. This ensured that the base of the walls of both the model and the prototype shear wall were subjected to the same order of stresses. However, in the upper floors the stresses produced by the gravity loads in the prototype shear wall are less when compared with those produced by the constant prestress in the model. The stresses produced by the gravity loads are small when compared with those produced by the equivalent seismic lateral load. Thus, the above limitation is not likely toalter the overall behaviour of the model.

NOTES:

1. $\frac{7}{8}$" Ø steel duct.
2. Screw jack.
3. Turning handle.
4. S.K.F. bearing.
5. Load cell.
6. Freysnet anchor grip.
7. Prestressing strand 4 - 0.272 in.

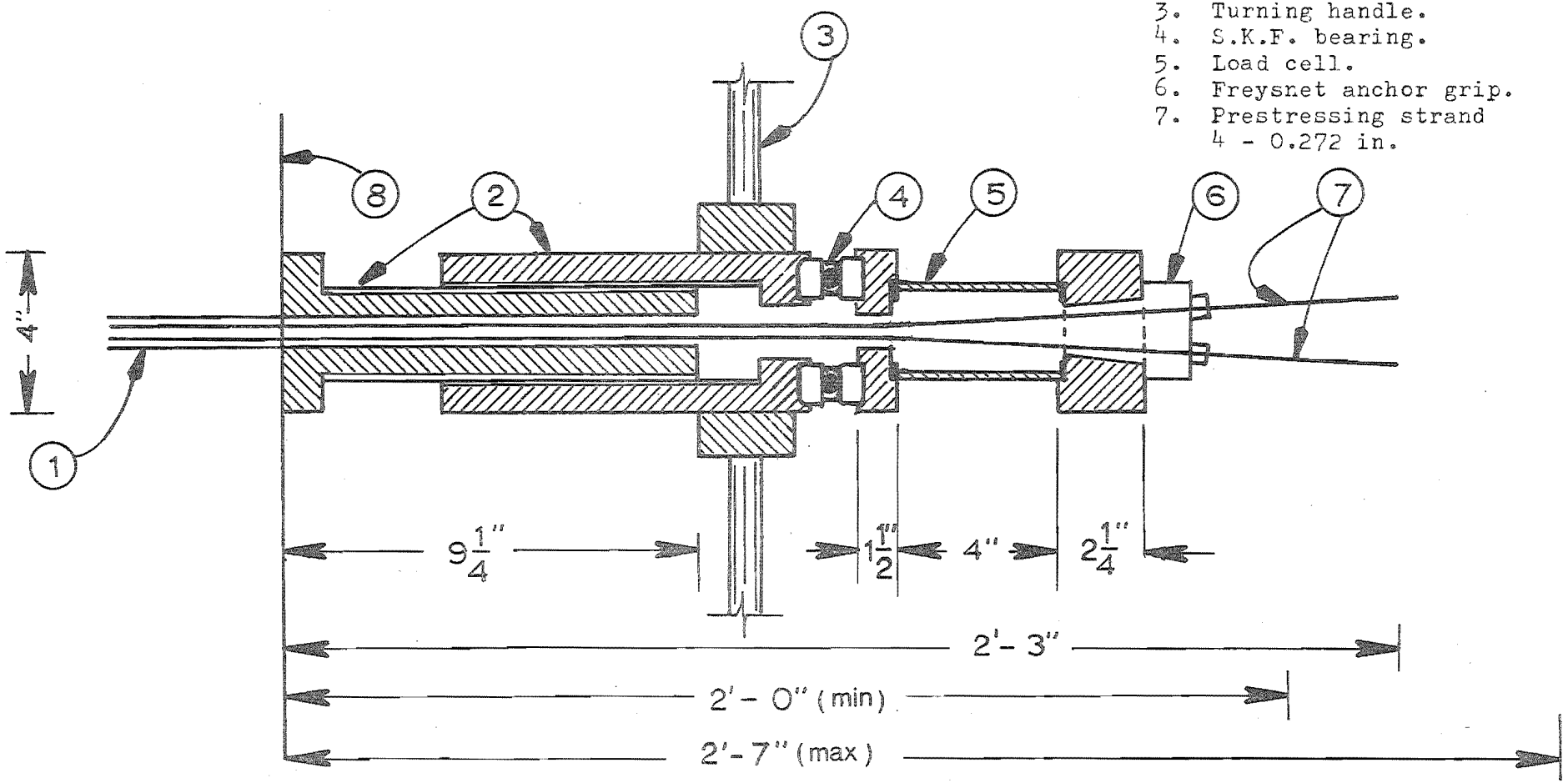

FIG. 5.11 DETAILS OF PRESTRESSING JACK

5.5 INSTRUMENTATION

5.5.1 Steel Strain Measurements

Demec mechanical strain gauges were used to measure the elongation of the reinforcing bars over 4 in. base lengths in the walls and over 2 in. base lengths in the coupling beams. Steel studs were welded on the reinforcement at the desired base lengths. A plastic tube was placed over each stud and the base of this was sealed with bituminous compound against entry of fluids. A few days after the test specimen was lifted from its form work, the plastic tube was removed so that an approximately $\frac{1}{8}$"gap was left between the surrounding concrete and the steel stud. This arrangement ensured free movement of the stud during test. Drilled stainless steel plates were attached to the ends of these studs to receive the points of the Demac gauge.

5.5.2 Rotation and Deflection Measurements

Five dial gauges were used to measure the free end deflection of the shear wall relative to the base block. Details of these may be seen in Fig. 5.10. In the interpretation of the results due allowance was made for the rigid body movements of the specimen.

The movements of the centre line of the walls and the reference line on the base block (see Fig. 5.10) were observed by two single-second theodolites during testing. Using these observations the following deformations were computed:

1. Transverse (vertical) deflection of the centre line of the walls.

2. The rotation, θ_b, of the coupling beam. Reference may be made to Section 4.3.1, Chapter 4, for the definition of the coupling beam rotation, θ_b.

3. The elongation of the coupling beam along the beam axis between the wall centre lines.

4. The elongation of the walls at any chosen point on the centre line of the walls relative to the base reference line (see Fig. 5.10).

Details of the computation of these deformations are summarised in Appendix B.

5.5.3 Load Application

The 60 ton capacity hydraulic jack was fed by a hand pump. The load was measured by a load cell placed on the jack as shown in Fig. 5.9b. The 10 ton jacks were fed by a 10,000 psi capacity Riehle testing machine, which maintained constant oil pressure over 2.07 sq. in. of ram area. Prior to testing, the Riehle pressure was also checked. At each increment the load was gradually applied in the following sequence:

1. Increasing the Riehle pressure to apply the desired loads P_2 and P_3.

2. While maintaining the loads at P_2 and P_3 applying the reaction R by the separate hand pump.

3. Checking the load cell readings to ensure the desired load P_1 had also developed.

4. Adjusting the prestress, simulating gravity load, if necessary.

5. Making finer adjustments to the load distribution by tightening or loosening the bolts on the hanger bars manually, to eliminate the errors introduced by friction within the hydraulic jacks.

6. Repeating step 3.

7. Closing all oil valves and thereby cutting off the pumps from the circuit.

The model was loaded in several cycles to destruction. In these cycles, the load was increased by predetermined increments from zero load to its maximum and then reduced to zero. A new cycle commenced when a similar sequence was followed with the load in the reversed direction. Fig. 5.12 illustrates the positive and negative directions with regard to the load application.

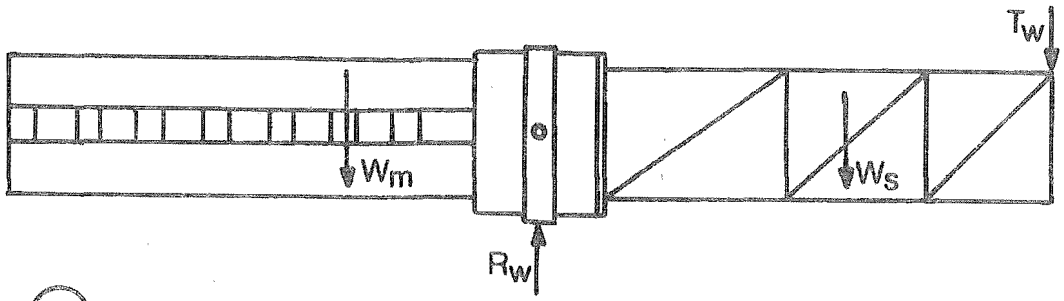

(i) Zero external load on Shear Wall – Base Shear = V_g

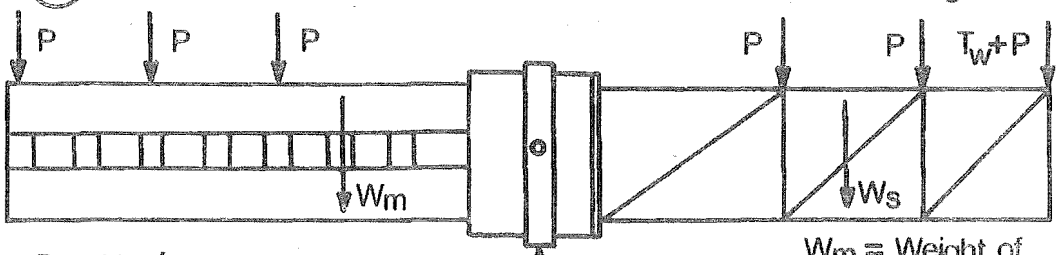

$P = V_b/3$

$R_w - T_w$ = Weight of model + truss

$R_w + 2V_b$

W_m = Weight of model

W_s = Weight of steel truss

(ii) Positive load on Shear Wall – Base Shear = $V_g + V_b$

(a) LOADS ON SHEAR WALL DURING POSITIVE INCREMENTS

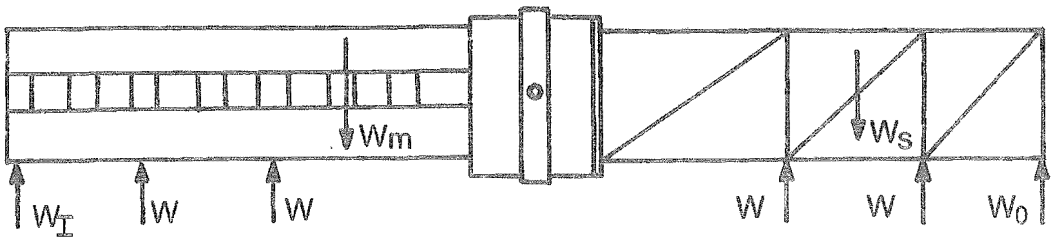

$W_I + 2W$ = Weight of model

$W_I + 4W + W_0$ = Weight of model + truss

(ii) Zero load on Shear Wall – Base Shear = Zero

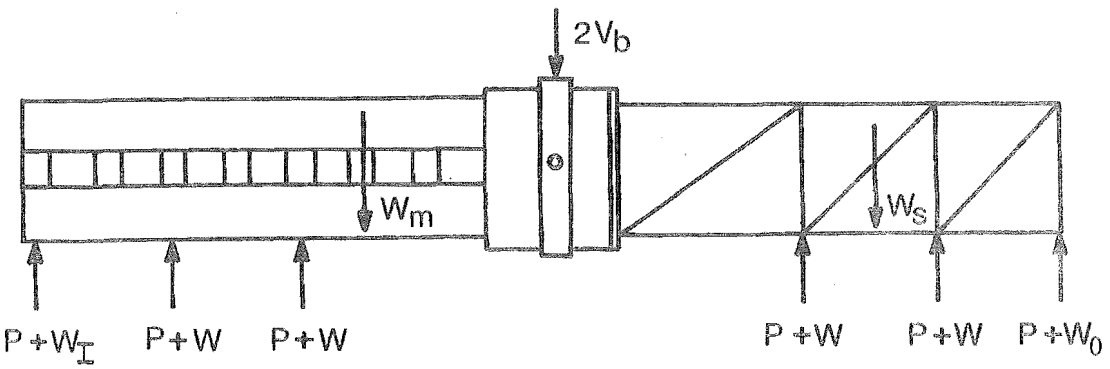

(ii) Negative load on Shear Wal – Base Shear = V_b

(b) LOADS ON SHEAR WALL DURING NEGATIVE INCREMENTS

FIG. 5.12 LOAD DISTRIBUTION DURING POSITIVE AND NEGATIVE INCREMENTS

During positive loading, the model was supported as shown in Fig. 5.12a(i). The reaction, R_W, at the centre and the force, T_W, at the right end balanced the weight of the shear wall and of the steel truss. In this position the base shear, V_g, on the model was estimated based on the self weight of the model. This position was assumed to be the zero load position for positive loading. Fig. 5.12a(ii) shows the load distribution on the model at any load increment. The total base shear is the sum of the base shear due to applied loads, V_b, and self weight, V_g, of the model. The base shear which is associated with the deformations relative to the zero load position is V_b.

During negative loading, the model was supported as shown in Fig. 5.12b(i). The forces W_I and W were such as to balance closely the self weight of the model ($W_I + 2W \approx$ self weight of the model). Thus the base shear in this position is zero. This position was assumed to be the zero load position for the reversed loading. Fig. 5.12b(ii) shows the load distribution on the model at any load increment. The base shear which is associated with the deformations relative to the zero load position is V_b.

5.5.4 Crack Observations

The cracks were located and their development followed after each load increment, with the aid of magnifying glasses. The propagation of cracks was marked. When a significant change occurred in the crack pattern a photograph was taken. A few of these are reproduced in this report. On the surface of the specimens, the width of some typical cracks was followed with a microscope.

5.5.5 Temperature Control

One 6 in. x 6 in. x 18 in. concrete temperature control block was provided with six 4 in. and six 2 in. gauge lengths. Measurements on these gauge points were made before and after taking a set of readings on the shear wall. At the particular load level, the mean

of these measurements was applied as the temperature correction to the steel strain readings.

In the case of deformation measurements either with the theodolites or with the dial gauges, the net movements of the specimen were calculated relative to the base block. Deformations due to temperature changes were considered to have had insignificant effect on the final results.

A few distance measurements were made under "no load" condition to establish the relative positions of the theodolite stations and the plane of the wall. These measurements were made with a survey steel band in accordance with standard procedures to ensure the necessary accuracy.

5.6 THE TESTING PROCEDURE

Initially, several readings were made to determine the "no load" values for the steel strain, dial gauge and theodolite readings. After the load was applied to the model the measurements were generally taken in the following sequence:

1. Checking the load distribution.
2. Checking the prestressing force.
3. Riehle Pressure and load cell readings (P_1, P_2 and P_3).
4. Central load cell reading (R).
5. Prestressing force W_1 and W_2.
6. Time.
7. Dial gauge readings.

When necessary:

8. Demac gauge readings on the standard bar and temperature control block over 2" gauge lengths.
9. Coupling beam main steel strains.
10. Repeated readings for temperature correction as in 8.
11. Demac gauge readings on the standard bar and temperature control block over 4" gauge lengths.

12. Wall flexural steel strains.

13. Wall stirrup steel strains.

14. Repeated readings for temperature correction as in 11.

15. Altitudes and bearing of the permanent fixed targets from the main theodolite. These targets are not on the specimen.

16. Altitudes and bearings of the targets on the specimen from the main theodolite.

17. Repeated readings as in 15.

18. Bearings of the permanent targets from the auxiliary theodolite.

19. Bearing of 6 targets on the specimen from the auxiliary theodolite.

20. Repeated readings as in 18.

21. Locating and marking the cracks on both sides of the model.

22. Crack widths measured.

23. Photographs taken.

24. Repeated dial gauge readings as in 7 to show possible deformations under "constant" displacement.

Finally, at each increment:

25. Prestressing force W_1 and W_2.

26. Load cell readings (P_1).

27. Central load cell reading (R).

28. Time.

The readings were recorded manually on standard data sheets and processed by a computer.

CHAPTER SIX

RESULTS OBTAINED DURING CYCLIC LOADING OF SHEAR WALL A

6.1 GENERAL

The results obtained during the cyclic loading of shear wall A are presented. The coupling beams of shear wall A were conventionally reinforced. The primary object of testing shear wall A was to compare its behaviour with that of shear wall B. The coupling beams of shear wall B were diagonally reinforced. The dimensions of the specimen, the details of the reinforcement and the properties of materials were included in Chapter 5.

6.2 ANALYTICAL ASSESSMENT OF FORCES AND MOMENTS IN THE COUPLING BEAMS AND WALLS

Shear wall A was a quarter scale model of a prototype shear wall. All the coupling beams of the shear wall possessed equal nominal strength both in flexure and shear. The estimated forces and moments on the model at ultimate load, corresponding with the pattern defined in Chapter 5, are shown in Fig. 6.1. These forces and moments were computed using the elasto-plastic analysis described in Chapter 4. Most of the coupling beams were expected to yield before the base of the walls reached yield curvature. The theoretical variation of laminar shear, during different stages of loading is shown in Fig. 6.1.a. The distribution after yielding is based on the assumption of bilinear load-deformation relationship for the beams. The symbols used to represent the different stages in these curves are the same as those defined in Chapter 4.

Figs. 6.1.b and c show the variation of axial force along the height of the model for the tension and compression wall at theoretical ultimate load. The ordinates represented by (1) indicate

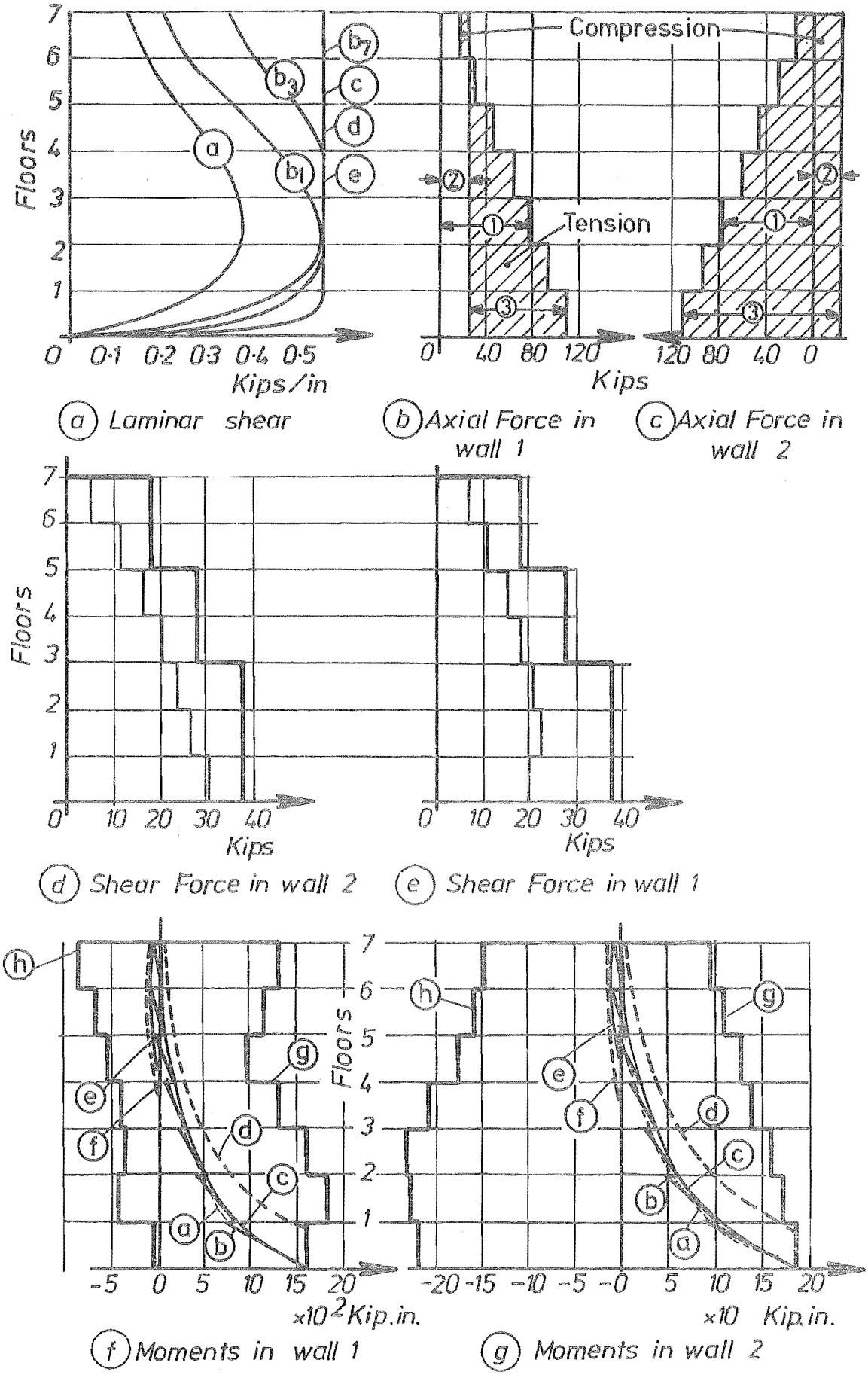

FIG. 6.1 ANALYTICAL ASSESSMENT OF FORCES AND MOMENTS IN THE COUPLING BEAMS AND WALLS OF SHEAR WALL A AND A COMPARISON OF STRENGTHS PROVIDED IN THE WALLS WITH MOMENTS AND FORCES DEVELOPED AT ULTIMATE LOAD

the force generated in the walls due to the accumulation of laminar shear. The ordinates (2) show the uniform compressive force in the walls due to the prestressing force of 25K, which was applied to simulate the dead load on the structure. The shaded area, whose ordinates are represented by (3), indicates the net axial force in the walls.

Figs. 6.1.d and e show the variation of shear force in the compression and tension walls. The stepped thin line variation indicates the maximum theoretical shear. The stepped thick line shows the variation of the reliable shear capacity provided by web reinforcement only. (The contribution of the concrete to shear strength has been neglected).

Figs. 6.1.f and g show the variation of moments in the tension and compression walls. The curves are designated as follows:

(a) Ultimate moment variation for the laminar model

(b) Moment variation taking into account the discrete location of beams

(c) Approximate envelope for positive moments

(d) Displaced positive moment envelope for cut-off of steel

(e) Design envelope for negative moment

(f) Displaced negative moment envelope for cut-off of steel

(g) Positive moment capacity provided

(h) Negative moment capacity provided.

The wall moment capacities shown (curves (g) and (h)) are based on the reinforcement as provided taking into account the variation of estimated maximum axial forces in the walls (Fig. 6.1.b and c). The moment capacity of wall 1 in the second floor is more than its capacity in the first floor (see Fig. 6.1.f and g, stepped lines (g) and (h)) eventhough the same amount of reinforcement was provided at both floors. This is due to a smaller axial tension in the second floor. (See Fig. 6.1.b). For the same reason the moment capacity

provided increases in the top two floors.

The moment capacity of the tension wall is sensitive to the amount of reinforcement provided at the outer face (tension face) of the wall. Necessarily the same amount of reinforcement at the compression face of the compression wall was provided to supply the required tension force when the load was reversed.

The simulation of dead load by a constant prestressing force has resulted in a smaller axial tension at the top of the model walls compared to a prototype wall. The flexural reinforcement in the model was curtailed along the height of the structure as shown in Fig. 5.6, the same way as it would have been done in the prototype wall. The excess strength in the top floor, exhibited by the moment capacity curves, is due to excess axial compression in both walls. (See Fig. 6.1.b and c). In a prototype shear wall the strength envelope for the tension wall would be closer to the demand at the top of the structure due to smaller compressive stresses associated with dead load. However, this would not significantly affect the behaviour of the shear wall.

The reinforcement on the outer face of each wall was provided to resist tension when the wall is in tension and compression when the wall is in compression. When the moment is reversed on the compression wall, the steel on the outer face is subjected to tension. Under this loading condition the moment capacity of the section is very large. The moment capacity of the compression wall with reversed moment (stepped line(h)in Fig. 6.1.g) shows this excess strength. It will be noted that a load-moment combination utilising this strength does not occur during loading.

6.3 THE LOADING

The shear wall model was subjected to static reversed cyclic loading. The load sequence is shown in Fig. 6.2. The load acting from left to right, as shown in Fig. 6.2, is considered positive. Unfortunately, while the hydraulic loading system described in Chapter 5 was being tested, inadvertently a considerable load was applied to the specimen. The cracks which formed as a consequence were marked '0'. These cracks can be seen in the photograph reproduced in Figs. 6.24 to 6.32. (See the cracks during cycle 1). From the crack widths measured, (w = 0.060") it was evident that the flexural steel in the critical coupling beam had yielded. However, the steel stresses induced in the walls remained below yield level.

Readings taken in the "zero load" position after the accident were termed "no load" readings. In each cycle the load was increased by predetermined increments from zero load to its maximum and then reduced to zero. A new cycle commenced when a similar sequence was followed with the load being applied in the other direction. The odd numbered cycles (see Fig. 6.2) refer to the positive direction of loading.

The loading in the first cycle was in the same direction as the accidental load. During the first two cycles of moderate loading, the maximum load caused yielding of flexural steel in the 1st, 2nd, 3rd and 4th floor coupling beams. It was less than the load required to yield the flexural steel in the walls. These load cycles were followed by two "elastic" cycles in which the maximum load was of the order of $0.35\ P_u^*$, where the theoretical ultimate base shear was $P_u^* = 51.6$ Kips. The two elastic cycles were then followed by 7 cycles of high intensity loading. During each of these cycles the model was loaded past the yield of the flexural steel in the walls till the ultimate load was reached or the required overall displacement attained. This displacement was such that the

P = Load Applied ; P_u^* = Theoretical Ultimate Load

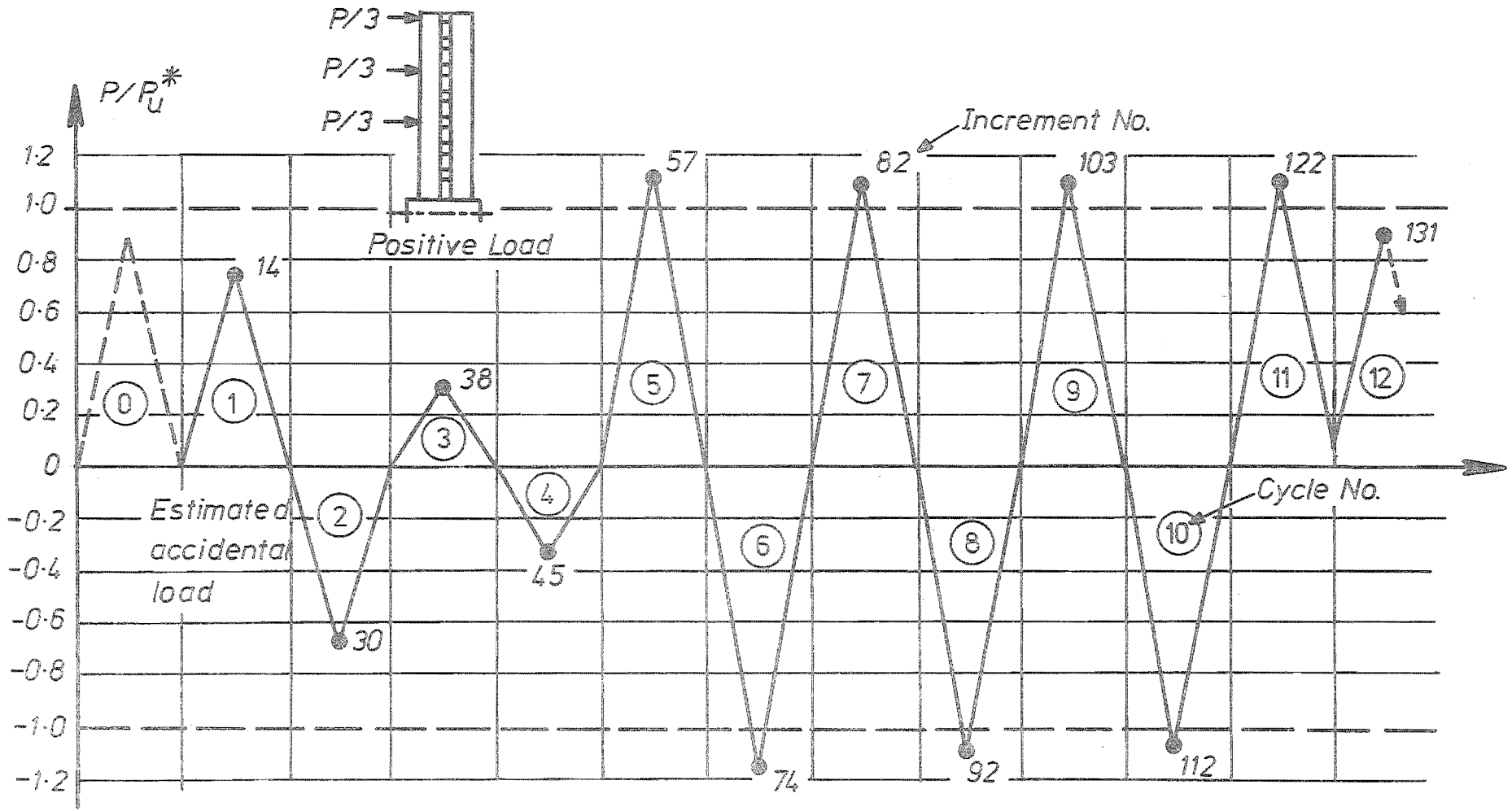

FIG. 6.2 LOAD SEQUENCE FOR SHEAR WALL A

overall displacement ductility factor attained during each of these cycles was approximately 3 or more. (See Chapter 4, Section 4.3.1.(c), for the definition of overall displacement ductility of the shear wall.) During cycle 11, which was intended to be the last one, the load had to be brought down to zero as the jacks had run out of travel. This resulted in the load for cycle 12 being applied in the same direction as cycle 11. During this last cycle the shear wall could resist a maximum load of $0.92\ P_u^*$.

6.4 BEHAVIOUR OF FLEXURAL REINFORCEMENT IN THE COUPLING BEAMS OF SHEAR WALL A

Each coupling beam was provided with four 2" demac gauge points on each face. The locations of these gauges can be seen in the photograph reproduced in Figs. 6.25 to 6.31, and in the key diagrams of Fig. 6.4.

The strains measured during positive and negative loading of a typical coupling beam (6th floor beam) is shown in Fig. 6.3. In this figure the measured strains are plotted as ordinates at the corresponding gauge locations. As expected, the strains are large at the tension corners of the beam. During the first and second cycle a small compression strain was observed at the compression corners of the beam. However, during 5th and 6th cycle, when ultimate load on the shear wall was attained, the gauge near the compression corner also recorded tensile strains. Thus, at this stage, both the top and the bottom reinforcement was subjected to tensile strains over its full length. This corresponds with the observations made by Paulay[74] during the cyclic loading of conventionally reinforced coupling beams.

In Fig. 6.4, the average strain measured at the tension corners (see key diagrams) of each beam is plotted at each floor. The average of strains was measured at locations 2 and 3 for the positive

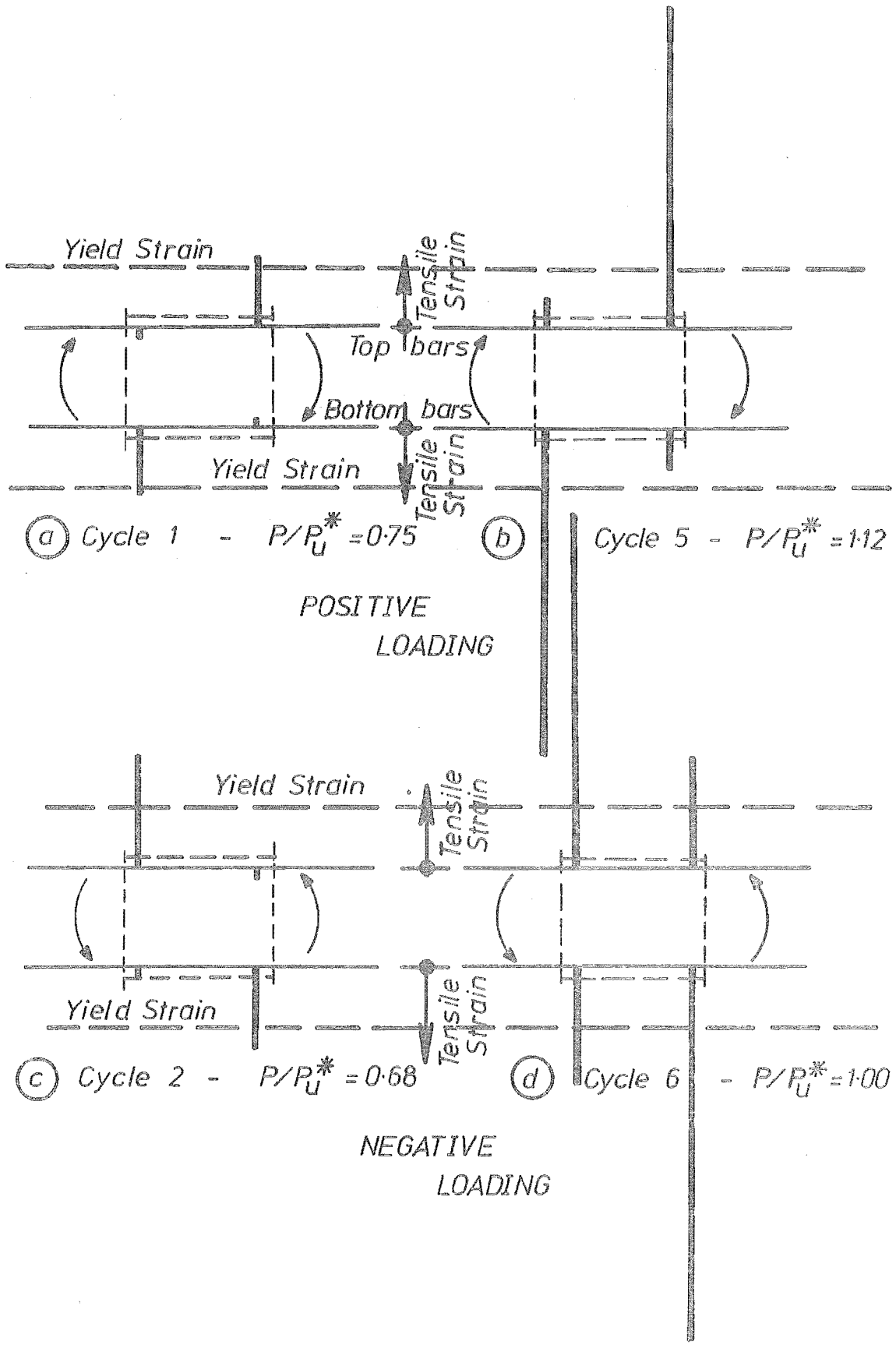

FIG. 6.3 MEASURED STRAINS IN THE 6TH FLOOR COUPLING BEAM DURING POSITIVE AND NEGATIVE LOADING

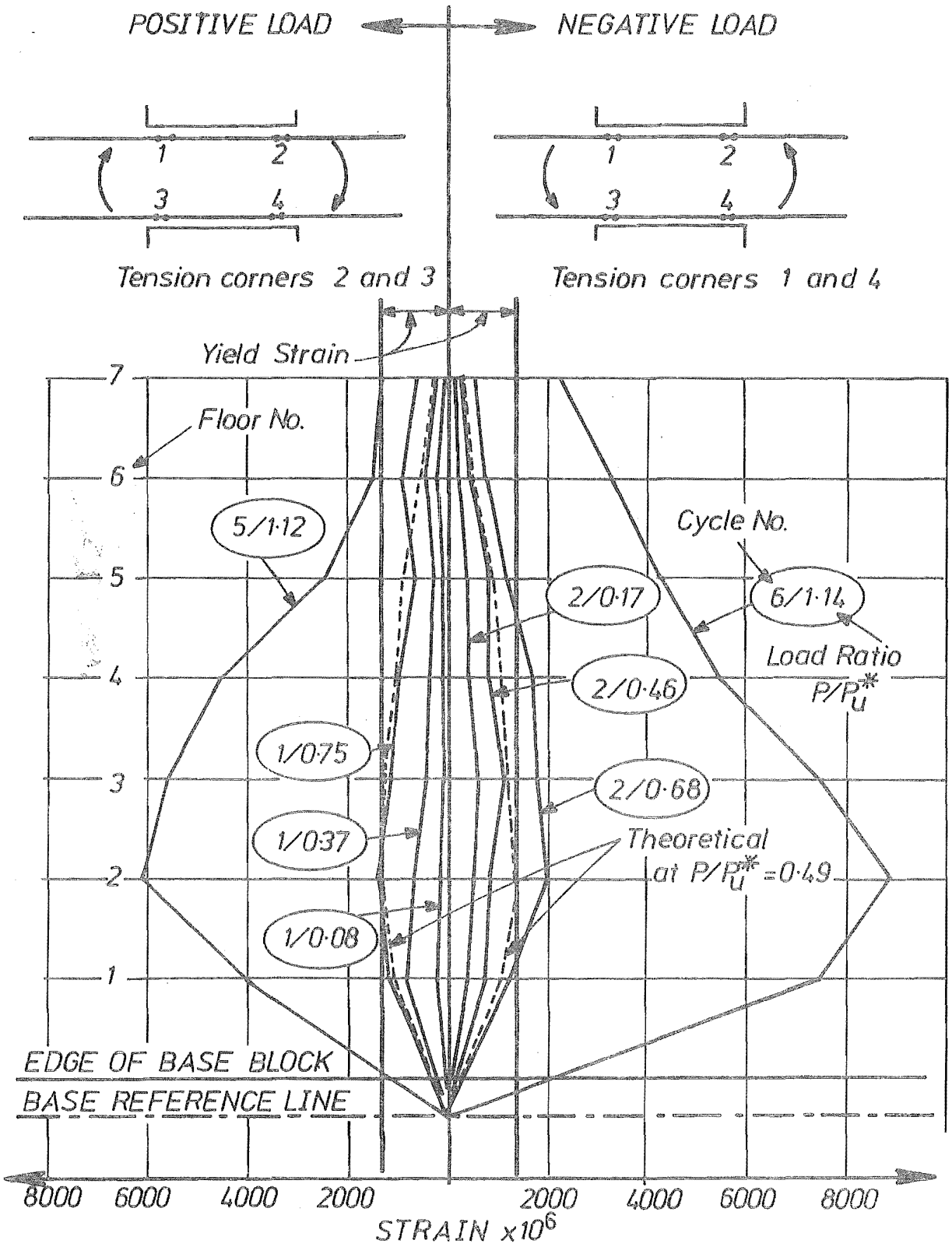

FIG. 6.4 AVERAGE STRAIN AT THE TENSION CORNERS OF COUPLING BEAMS DURING POSITIVE AND NEGATIVE CYCLES

loading and at locations 1 and 4 for negative loading. In the same figure the theoretical strain variation, at the onset of yield in the critical coupling beam, is shown with broken lines. The pattern of observed and computed strains are similar. However, during cycle 1 the measured strains are less than the strains predicted. The crack width measurements showed that the cracks which appeared in this cycle and the cracks which had already formed due to accidental loading did not cross the gauges provided. The crack which formed near the edge of the beam passed through the hole provided to house the demac stud. During further loading this crack propagated into the wall and crossed the holes over the flexural steel of the wall. (See Fig. 6.28 to 6.31). An examination of the crack patterns of 4th, 3rd, 2nd and 1st floor coupling beams shows this. This will be discussed in Section 6.8 with respect to crack formation and crack width measurements. However, the theoretical maximum strain was computed at the junction of the wall and the coupling beam. The measured strain corresponds to a point 2 in. from the face of the wall. Hence the measured strain is less than that predicted. During cycle 2 the values of predicted strain and measured strain have good correlation in the coupling beams in the upper storeys. The deterioration of the bond between the reinforcement and the surrounding concrete and the formation of new cracks across the instrumented gauges have contributed to better correlation.

6.5 BEHAVIOUR OF FLEXURAL REINFORCEMENT IN THE WALLS

6.5.1 Strain Variation of Flexural Steel Along the Height

The generous provision of gauge points enabled the strains to be assessed over the entire height of the walls. Figs. 6.5. a to d show the strain variation of the flexural reinforcement in the walls during cyclic loading. The insert in each figure shows the

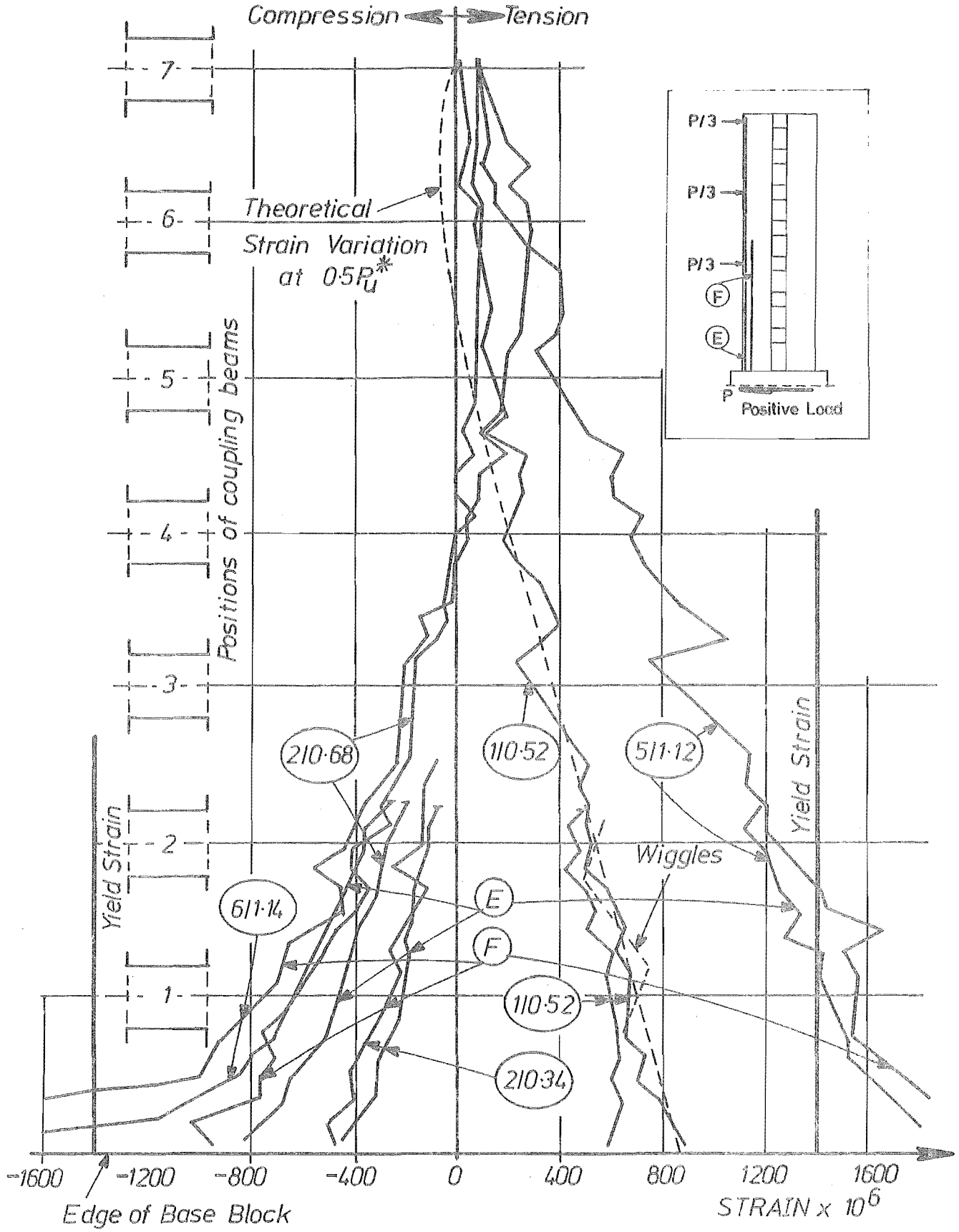

FIG. 6.5.(a) STRAIN VARIATION FOR THE FLEXURAL STEEL E AND F IN THE LEFT WALL

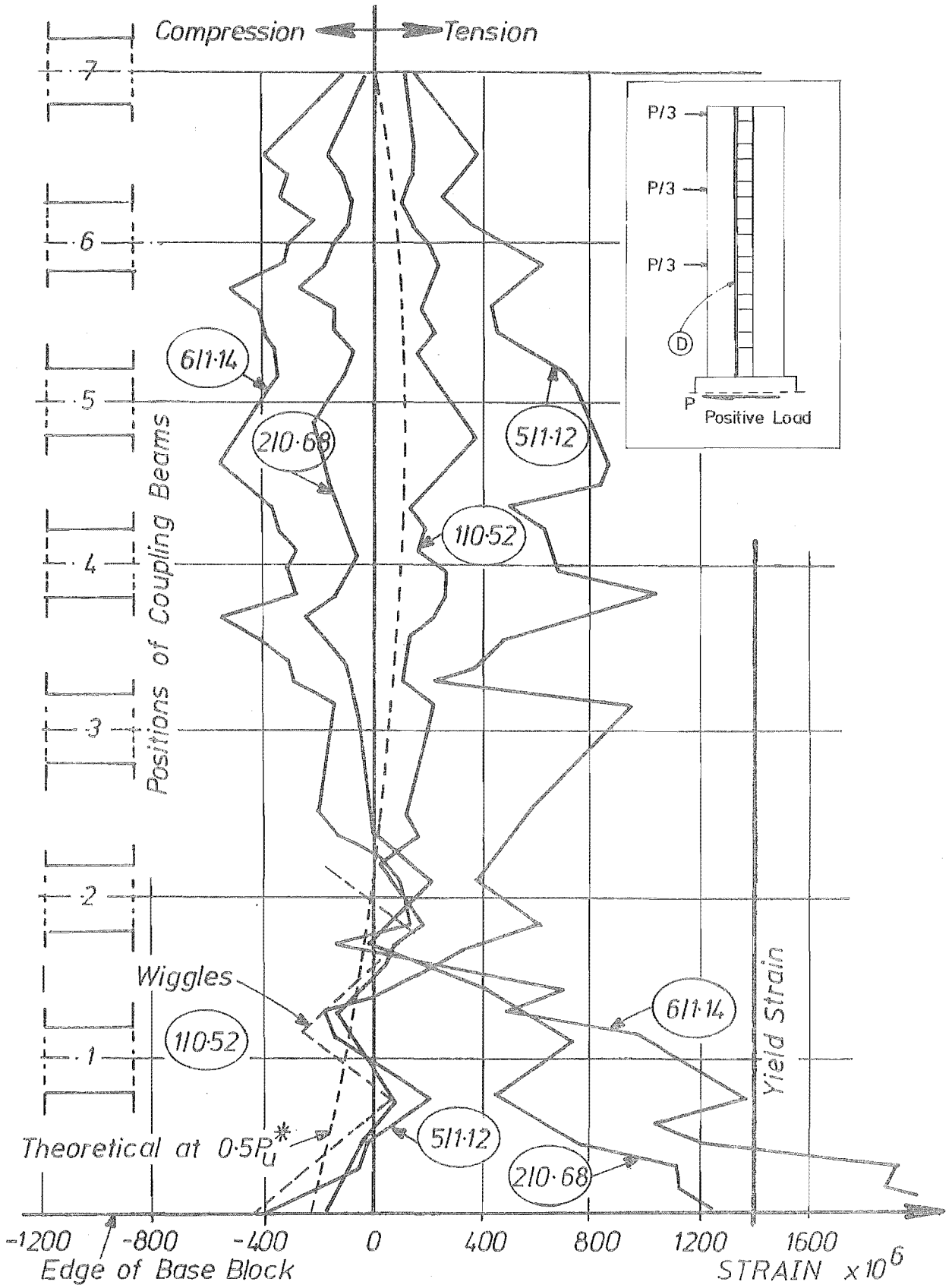

FIG. 6.5.(b) STRAIN VARIATION FOR THE FLEXURAL STEEL D IN THE LEFT WALL

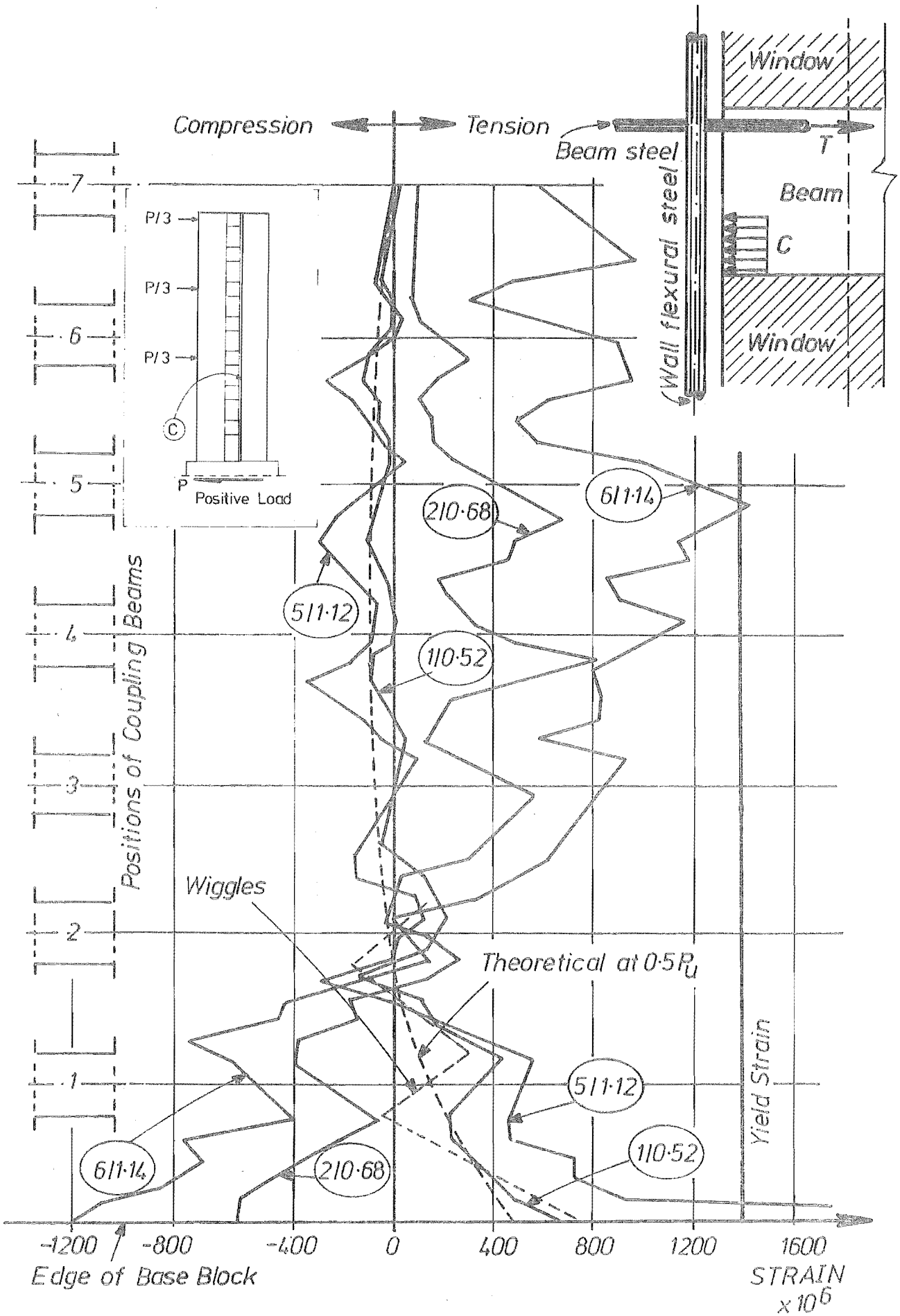

FIG. 6.5.(c) STRAIN VARIATION FOR THE FLEXURAL STEEL C IN THE RIGHT WALL

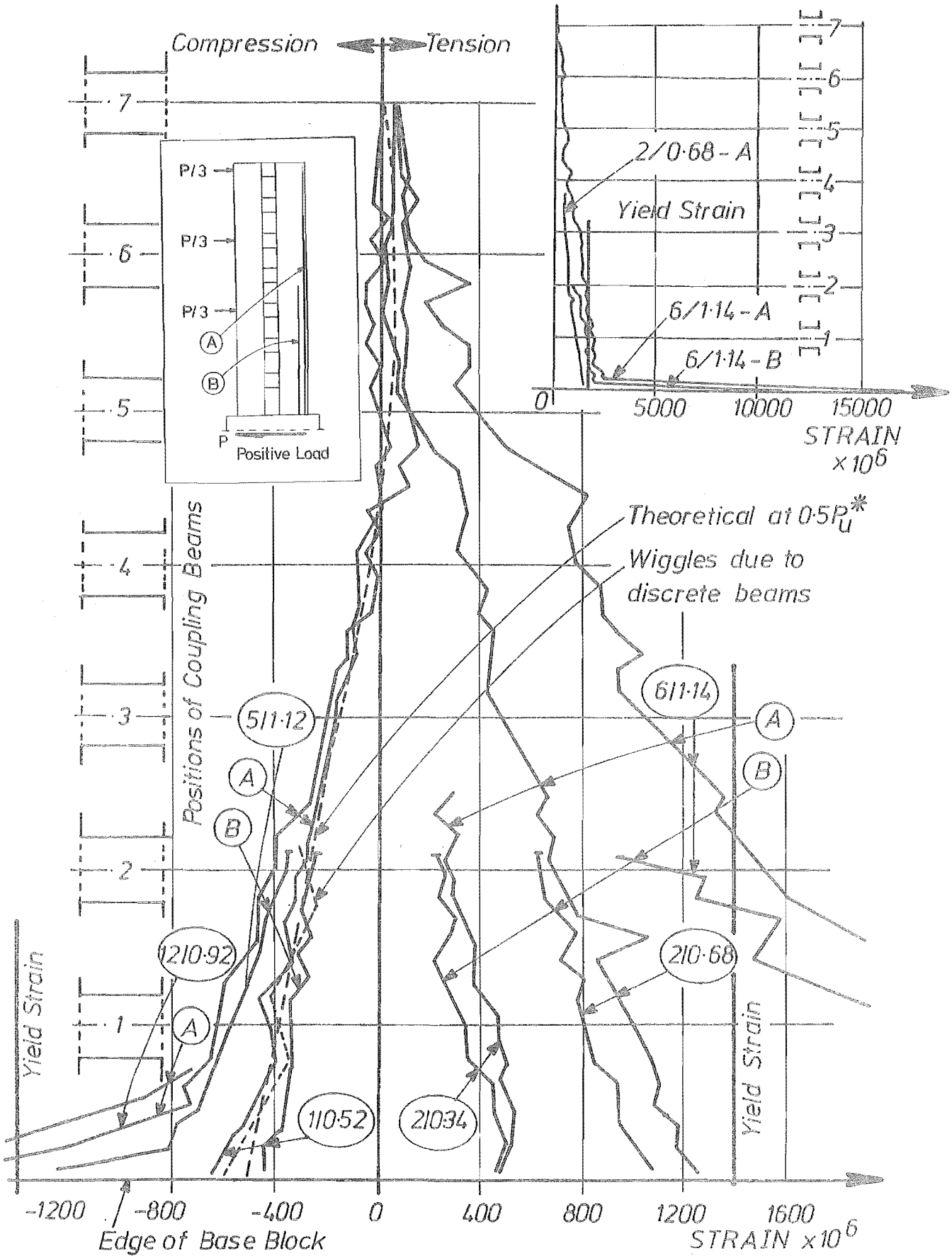

FIG. 6.5.(d) STRAIN VARIATION FOR THE FLEXURAL STEEL A AND B IN THE RIGHT WALL

location of the bar for which the strains have been plotted and the letter used to denote the particular bar. On each curve the cycle number and the load intensity, expressed as a fraction of the theoretical ultimate load, P_u^*, are shown. In each of these figures the theoretical strain variation at a load intensity of $0.5\ P_u^*$ is plotted for comparison. The elasto-plastic analysis proposed in Chapter 4 was used to compute the axial loads and moments along the height of the structure. For these axial load-moment combinations curvatures were found, using the load-moment-curvature relationship (see Section 3.5.3) for the section considered. Using these curvatures the theoretical strain in the reinforcement was estimated assuming linear strain variation across the section. This theoretical strain variation corresponds to the laminar model. The wiggles in the strain variation introduced by discrete beams were also estimated. These wiggles are shown for the bottom two beams only.

An examination of the strain distribution curves in Fig. 6.5.a to d shows that:

(a) Strains in the two layers of reinforcement, plotted for the bottom two storeys, are very similar. (See Fig. 6.5.a and d). The strains in the outer bars are larger, as one would expect from a linear distribution of strains across the section.

(b) The strains are maximum at the base of the wall. During the first two cycles of loading of moderate intensity the strains in the flexural steel in the walls were below yield level. During cycle 5, the first high intensity load cycle, the tension steel (outer bars F and E) in the tension wall and the compression steel in the right wall (outer bar A) yielded. Bar F yielded first at $0.88\ P_u^*$. The outer layer of compression steel, Bar A, yielded next at $1.03\ P_u^*$ which was followed by yielding of all bars in the tension zone of the tension wall at $1.04\ P_u^*$. The sequence of formation of plastic hinges is discussed in Section 6.7.1.

(c) For the outer bars E, F, B and A, the strain distribution follows the same pattern as the theoretical strain variation in the laminar model. A comparison of the broken line curve, which corresponds to the theoretical strain variation at $0.5\ P_u^*$, with the observed strain during cycle 1 at $0.52\ P_u^*$ shows this. Along this theoretical strain variation, the theoretical wiggles due to discrete moment transfer from the beams is shown at the level of the bottom two coupling beams. The theoretical strains in the inner bars are more sensitive to changes in moments compared to those at the outer edge. The theoretical wiggles introduced by the discrete beams are considerably smaller for the outer bars than for the reinforcement near the windows. For a change in the moment of resistance to occur, in the presence of the axial force, the disturbance in the strain could be expected to be more when the reinforcement is in a single layer.

(d) As expected the tensile strains are larger than the compressive strains (see Fig. 6.5.a and Fig. 6.5.d). The length over which the outer bar has yielded in tension is more than twice the corresponding length for the outer bar in compression. This is in accordance with the theoretical study made in Section 4.4 which shows that the length of plastic hinge for the tension wall is larger than that for the compression wall. (Eq. (4.22)).

(e) In Fig. 6.5.b and c, the strain variation for the inner bars D and C are plotted. Again the tensile strains are significantly larger. During cycle 5 and the reversed cycle 6, the tensile strains in bar C and bar D were more than the yield limit at $1.12\ P_u^*$ and $1.14\ P_u^*$ respectively. However, during the first high intensity loading (cycle 5), bar D did not yield in compression.

(f) For the inner bars C and D the strain variation computed at $0.5\ P_u^*$, using the laminar model, corresponds with the approximate measured mean strain in the bar (see the observed strain variation at

0.52 P_u^* during cycle 1). On the computed strain variation the wiggles, due to coupling beams, are superimposed for the bottom two beams. At this stage, the second floor coupling beam, for which the wiggle is shown, had yielded. The wiggles that occur during cycle 5 at 1.12 P_u^* are considerably larger than the "theoretical maximum" disturbance. An examination of the strain variation of bar D in the 5th cycle reveals this. This is due to nearness of the bars C and D to the internal tension, T , and compression, C , introduced by the coupling beams (see insert in Fig. 6.5.c). The beam forces introduced at right angles to the vertical wall bars cause local bending in the wall bars. The phenomenon affects strain measurements in these localities.

6.5.2 Strain History of the Flexural Reinforcement at the Base of the Walls

Strain measurements were made on four gauge points near the base block at frequent load intervals with the intention of obtaining the strain history of the flexural bars at the base section of the walls during cyclic loading. Fig. 6.6.a to d show the strains at these locations plotted against the lateral load. The location of the gauge for which the strain history was plotted is also shown in these figures. An examination of these figures reveals that:

(a) During cycle 5, at a maximum lateral load of 1.12 P_u^*, tension steel in both the tension and compression walls yielded. (See the strain in bars E and C in Figs. 6.6.a and 6.6.b). However, the compression steel D in the tension wall did not yield (see Fig. 6.6.b). The outer bar A in the compression face of the compression wall yielded in compression (see Fig. 6.6.c). At the end of cycle 5 there was a large permanent tensile strain in bar C (insert in Fig. 6.6.d).

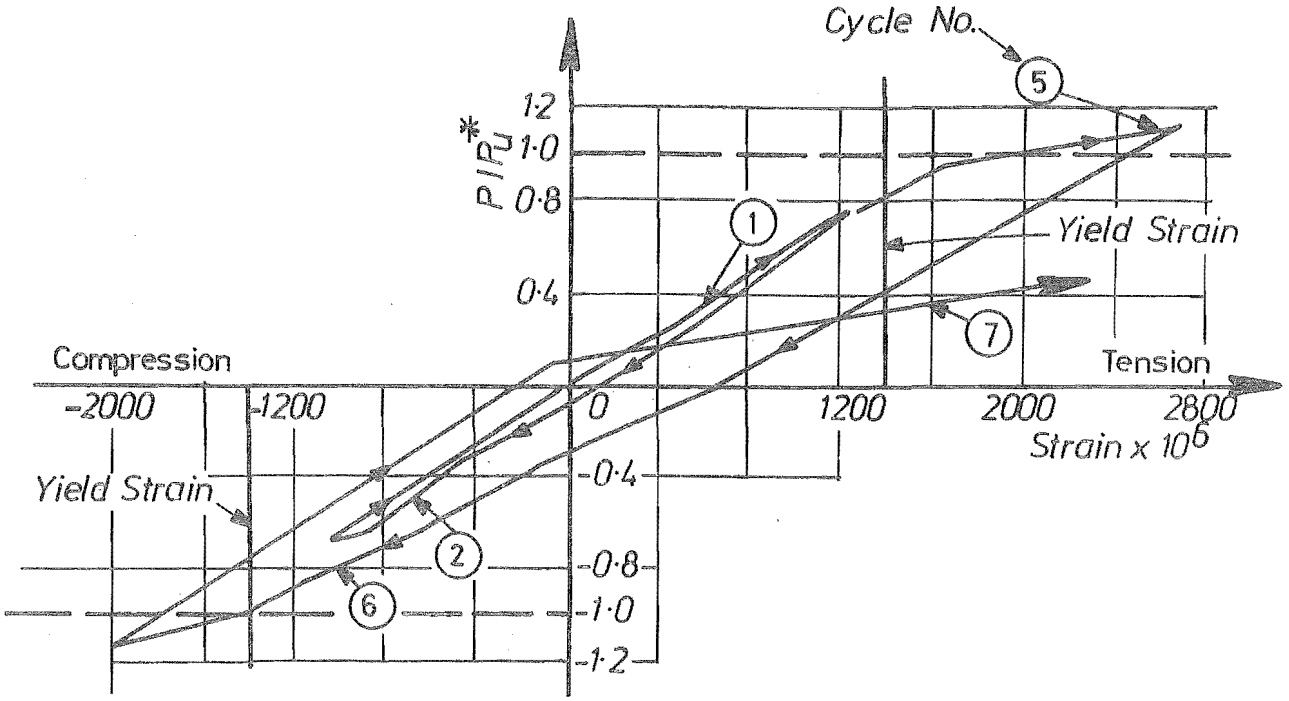

FIG. 6.6.(a) STRAIN HISTORY AT LOCATION W_4 FOR BAR F

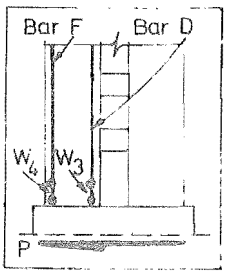

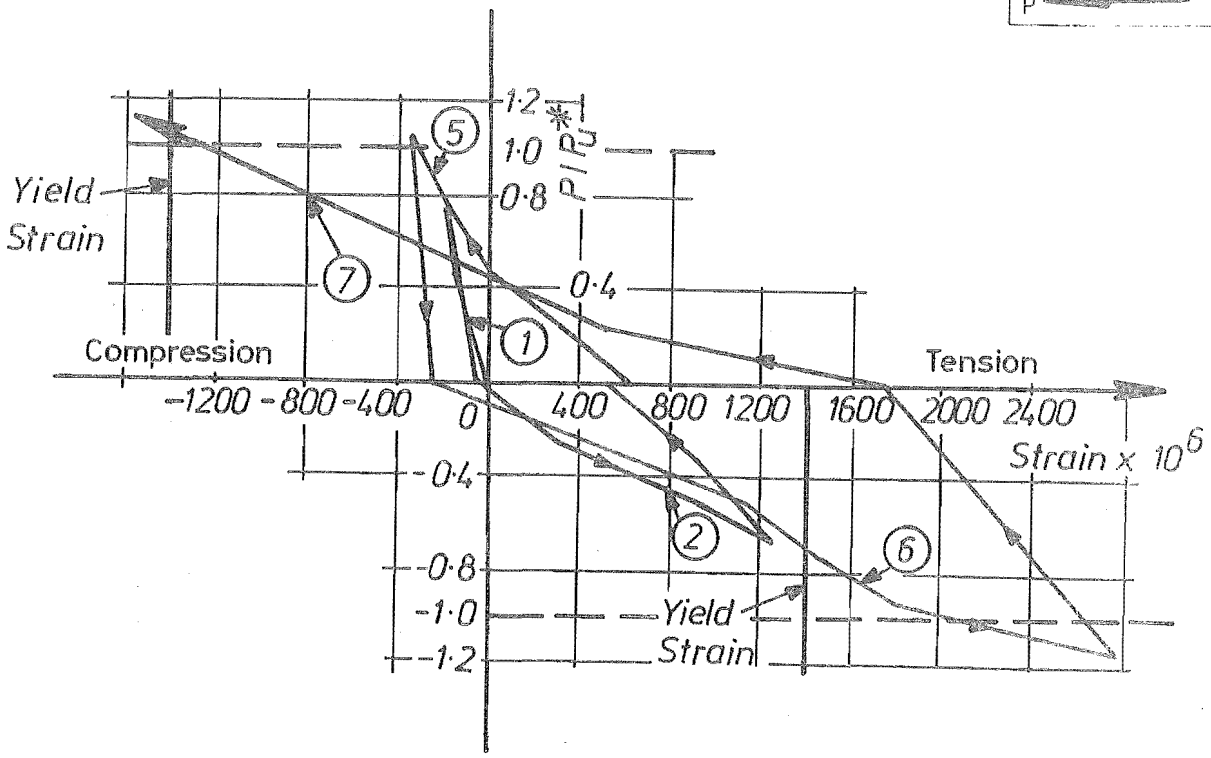

FIG. 6.6.(b) STRAIN HISTORY AT LOCATION W_3 FOR BAR D

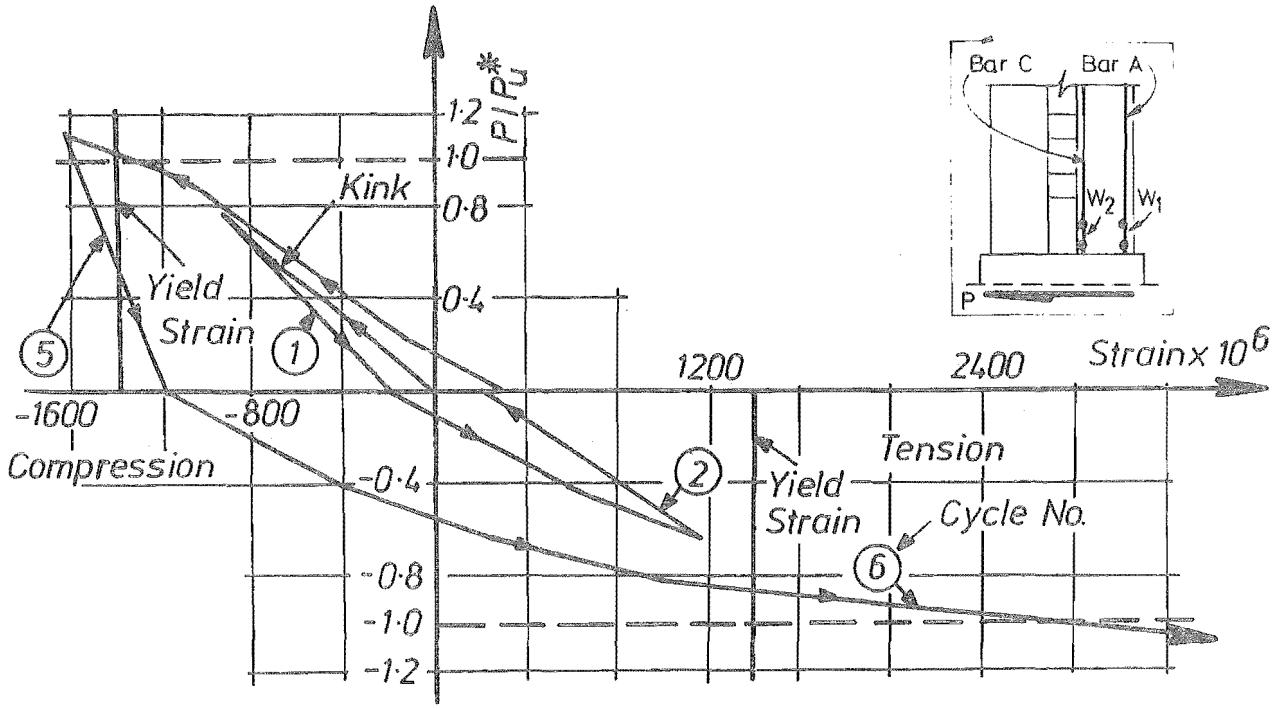

FIG. 6.6.(c) STRAIN HISTORY AT LOCATION W_1 FOR BAR A

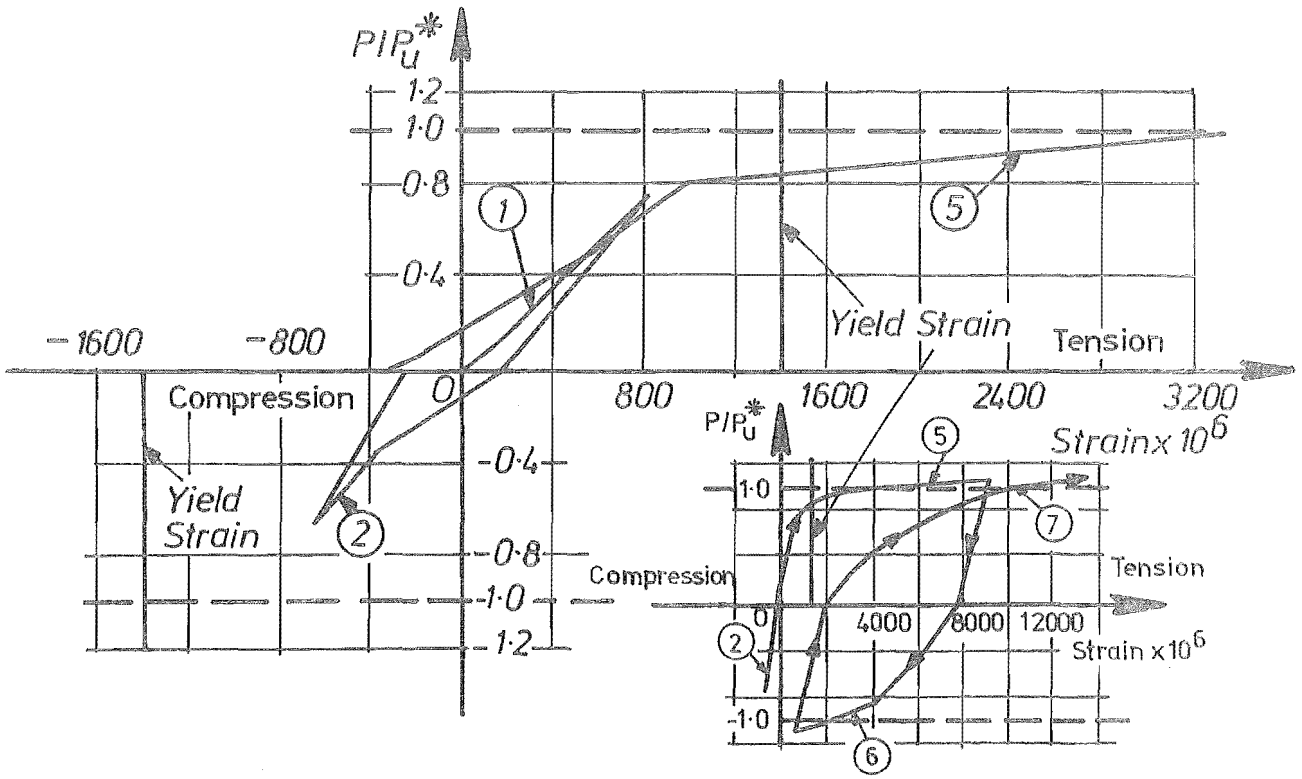

FIG. 6.6.(d) STRAIN HISTORY AT LOCATION W_2 FOR BAR C

(b) During cycle 6, at a load of 1.14 P_u^* , the tension steel in both the walls (bars A and D in Figs. 6.6.b and c) yielded. The compression steel in the compression wall (left wall), bar F, yielded in compression (see Fig. 6.6.a). The residual permanent strain at the end of 5th cycle in bar C was 8000 microstrains. During cycle 6 , a total compressive strain of approximately 7000 microstrains (see Fig. 6.6.d) was imposed on this bar. Hence compression yielding did occur in this bar.

(c) The increase in stiffness (Fig. 6.6.d) which can be seen in the strain history curve for cycle 2 for bar C at location W_2 is due to closing of the cracks which had formed during the positive loading (cycle 1). After closing of the cracks concrete also contributes in resisting the external action. Therefore, the stiffness indicated by the load-strain history curve is more than that observed at low loads.

(d) The large tensile strains in bars A and C (see Figs. 6.6.c and 6.6.d) have contributed to the lengthening of the right wall.

(e) At location W_3, bar D in the left wall is subjected to compressive strains during cycle 5 (positive loading). The increase in stiffness (Fig. 6.6.b) which can be seen during this cycle is due to closing of the cracks that had formed during the previous reversed loading. As expected the tensile strains induced during cycle 6 are far in excess of the compressive strains induced during cycle 5.

(f) Both bars A and C (locations W_1 and W_2) were in tension during the accidental load and the cracks had already crossed the gauges at W_1 and W_2. Hence the curves in Fig. 6.6.c and d do not show the behaviour of the reinforcement when the section was in the uncracked state. (The widths of the cracks that crossed the instrumented gauge lengths nearest to the foundation block were 0.001".)

6.6 BEHAVIOUR OF STIRRUPS

The key diagrams in Fig. 6.7 and 6.8 indicate the five gauge positions (numbered 1 to 5) for the eight instrumented stirrups (numbered 1 to 8) in each wall. The photographs of the walls, reproduced in Fig. 6.3.2 show the diagonal cracks formed in the bottom storey of the two walls. These photographs were taken from the northern side. The crack pattern is also shown in the key diagrams in Figs. 6.7 and 6.8. In these diagrams the cracks formed during positive loading are shown in thick lines. In the following section the behaviour of stirrups is discussed.

6.6.1 Load-Stress Relationships

The heavy lines along a stirrup in the key diagrams of Figs. 6.7 and 6.8 indicate the length of each stirrup over which the stresses are reproduced in the major portion of these figures. These lengths are the most highly stressed locations for the eight instrumented stirrups in the left and right walls. The continuous lines indicate the stresses during positive loading and the thin broken lines indicate negative loadings.

In general stresses are low until the stirrup is crossed by a crack. The stirrups which had already been crossed by cracks, due to the accidental load, indicated significantly larger stresses (see stirrup 7, gauge 3 and stirrup 3, gauge 4, in the left wall shown in Fig. 6.7, and stirrup 4, gauge 1 and stirrup 3, gauge 2 in the right wall shown in Fig. 6.8).

The continuity of the curves between the readings for the first and fifth cycles indicate very little strength degradation with cyclic loading up to the first high intensity loading during which flexural steel in the walls yielded. Indeed the stirrup stresses are well below yield even at ultimate load. In cycle 5, at a maximum load of $1.12\ P_u^*$ the maximum stresses recorded in most of the stirrups were of the order of 50 to 75% of their yield stress.

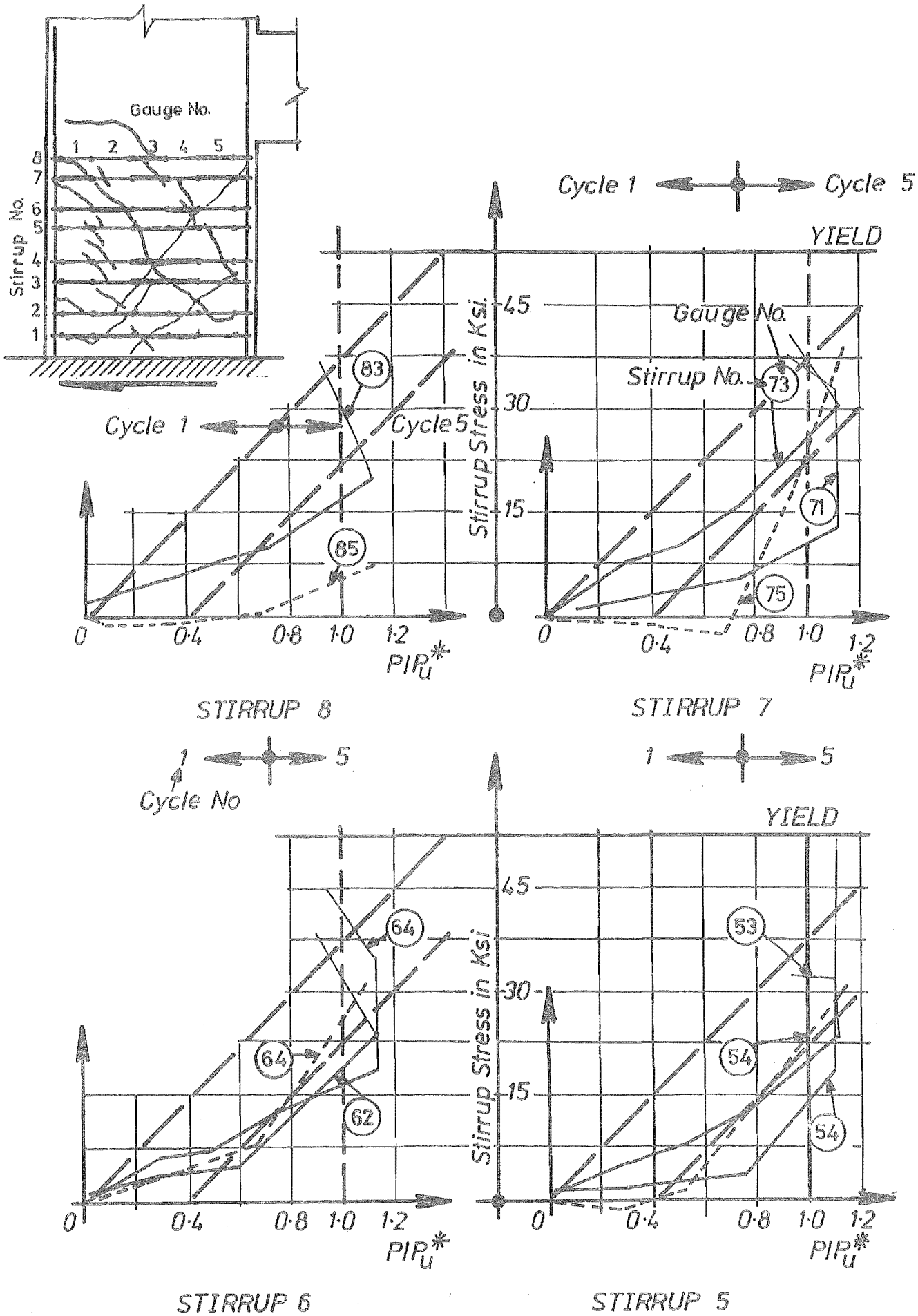

Fig.6.7 (Contd on next page)

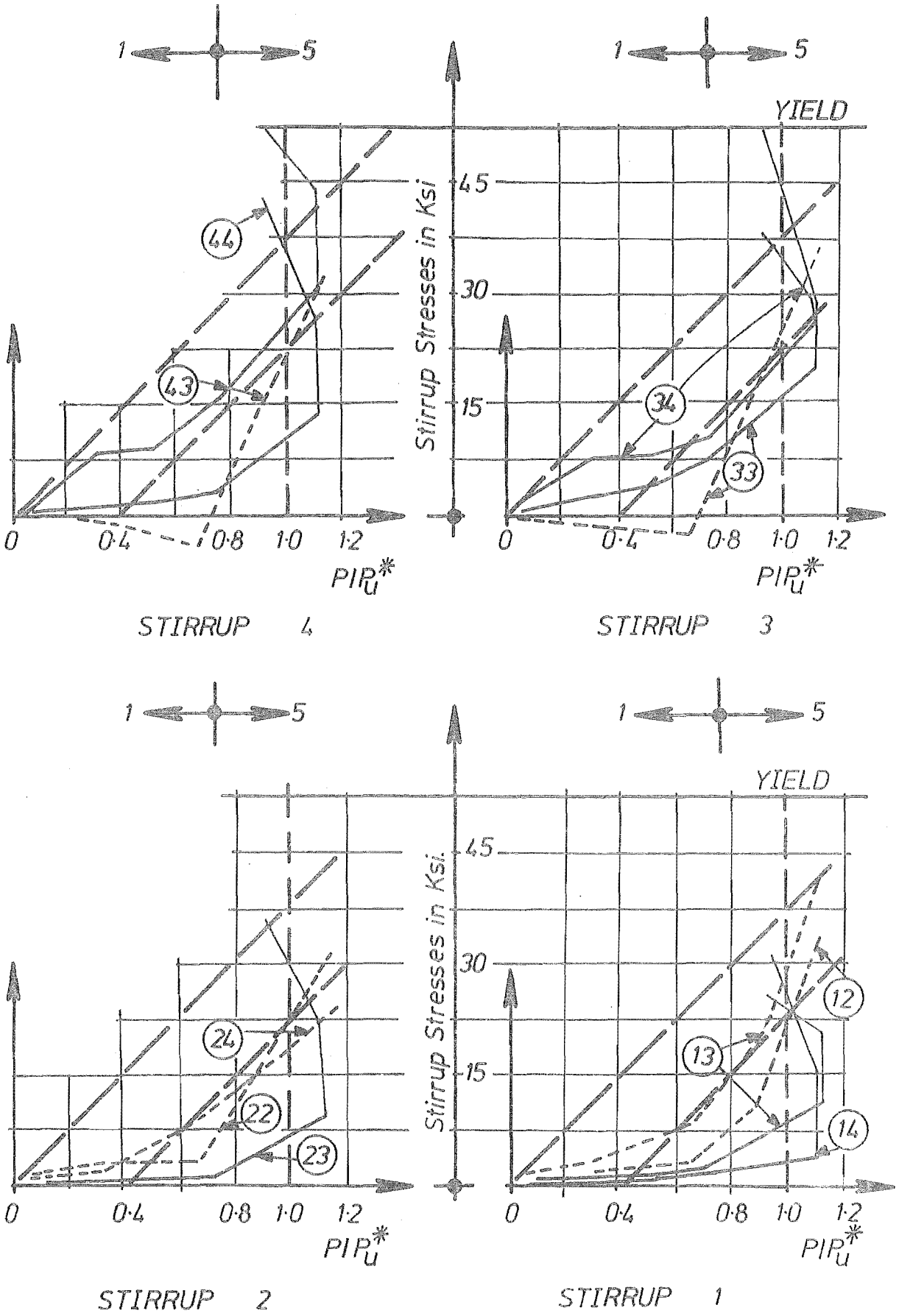

FIG. 6.7 A COMPARISON OF MEASURED STIRRUP STRESSES IN THE LEFT WALL WITH THOSE PREDICTED BY ACI EQUATIONS

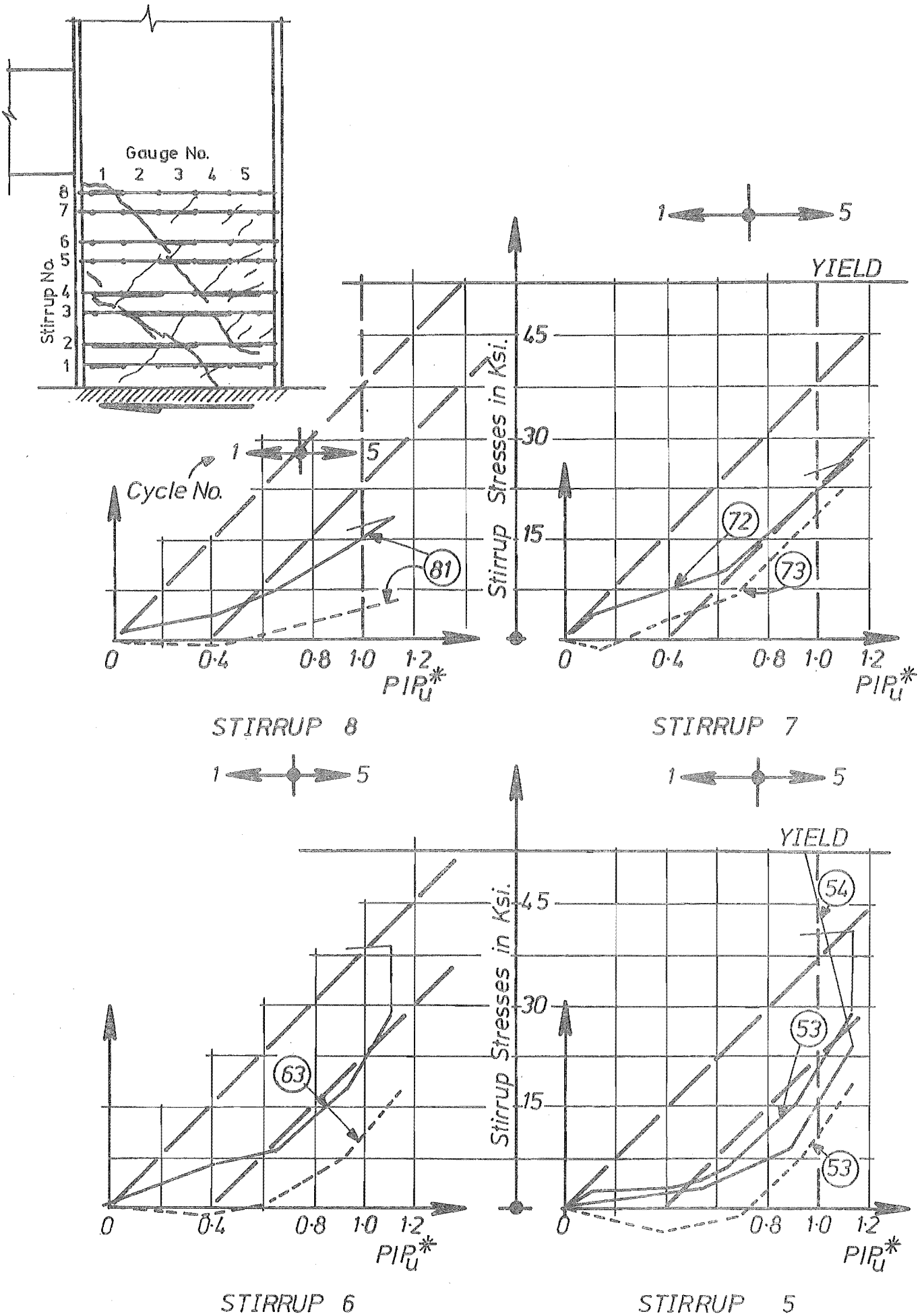

Fig. 6.8 (Contd on next page)

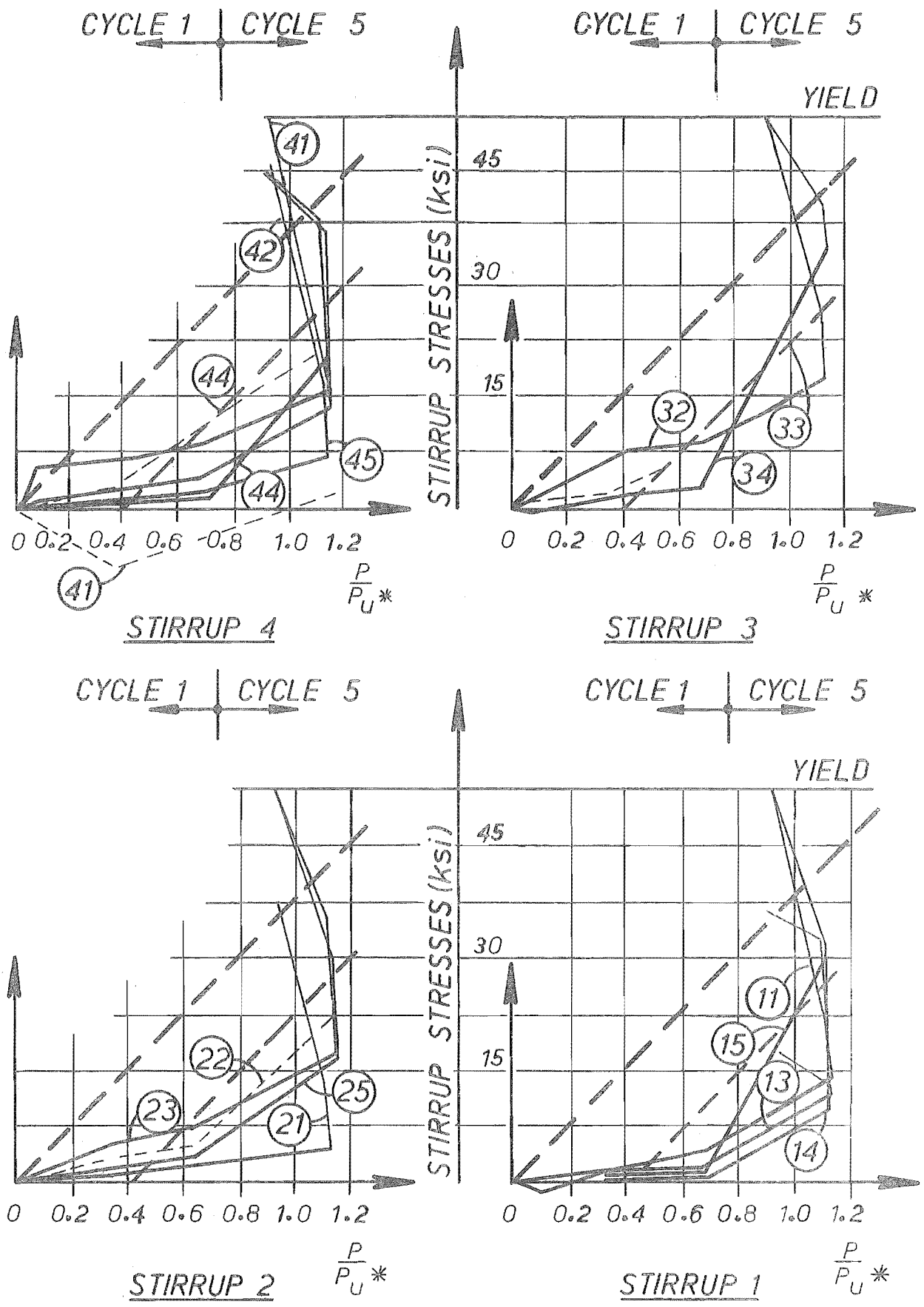

FIG. 6.8 A COMPARISON OF MEASURED STIRRUP STRESSES IN THE RIGHT WALL WITH THOSE PREDICTED BY ACI EQUATIONS

The stirrup stress during cycle 7, for the same gauge locations, at 1.11 P_u^* was considerably larger than those recorded for cycle 5. This is indicated by thin lines. These vertical rises indicate the discontinuity of the curves. They do not represent the stirrup stress variation between cycles 6 and 7. They show the shear strength degradation that occured between cycles 6 and 7. (See stirrup 6, gauge 4 and stirrup 5, gauge 4 for the left wall in Fig. 6.7 and stirrup 5, gauge 3 and stirrup 1, gauge 4 for the right wall in Fig. 6.8).

During cycle 12, when large post-elastic deformations were imposed and a mechanism of failure had formed, the stirrup stresses increased across the potential diagonal cracks with decreasing loads and increasing deformations. This is indicated in these diagrams by thin straight lines which show increase in stresses as load drops off. (See stirrup 7, gauge 1 and stirrup 3, gauge 3 for the left wall and stirrup 2, gauge 5 for the right wall). This indicates that failure is imminent.

The end stirrup stresses (stirrups 1 and 2) in both the walls are low when compared with the stresses in the remaining 6 stirrups. However, the end stirrup stresses also rise up sharply during the final cycle.

The observed stirrup stresses are compared with those predicted by the ACI code[82]. This code recommends the following equation for the shear that can be resisted by a section subjected to both moment and axial force.

$$V_u = \left(V_c + V_s\right) \varphi \qquad \ldots\ (6.1)$$

where $V_s = \dfrac{A_w f_y d}{s}$, the force resisted by stirrups

$V_c = bd\left(1.9\sqrt{f_c'} + 2500\, \rho_w \dfrac{Vd}{M'}\right)$, the shear resisted by concrete

Here V = applied shear

s = stirrup spacing

$M' = M - N\left(\frac{4D - d}{8}\right)$

D = total depth of the section

d = effective depth of the section

N = axial force positive when compressive

V_c = 0 if tensile stress induced by the axial force is more than 500 psi.

φ = the capacity reduction factor.

Substituting the relevant properties of materials and theoretical forces developed at ultimate load with $\varphi = 1.0$ in the above equation,

V_c = 10.5 Kips, for the compression wall

V_c = 0 , for the tension wall

V_s = 37.5 Kips, for the tension or compression wall.

The axial stress in the tension wall is more than 500 psi at ultimate load. At low loads, when the axial stress in the tension wall is considerably less, the concrete is assumed to contribute to the shear resistance. The shear capacity, V_c' , with no tensile stress applied is $V_c' = 9.8$ Kips. Thus the upper limit of shear assumed to be resisted by both the walls is

$$V_u = 10.5 + 9.8 + 37.5 + 37.5 = 95.3 \text{ Kips} \approx 1.8\ P_u^*$$

By neglecting the contribution of concrete in both walls, the lower limit of the shear resistance of both walls may be assessed at

$$V_u = 37.5 + 37.5 = 75.0 \text{ Kips} \approx 1.4\ P_u^*$$

When it is assumed that the contribution of the concrete remains constant at all stages , the two limits are represented by inclined straight lines, shown in Figs. 6.7 and 6.8 . In general it is seen that the observed stresses follow the lower limit curve, based

on the assumption that the concrete is effective in resisting shear. In later cycles the strength degradation of concrete makes the stirrups accept larger portions of the external shear. Hence the curves rise up to the upper limit. When large deformations are imposed during the final cycle the stirrup stresses exceed those predicted by the upper limit line. By then the potential diagonal crack had formed and the failure conditions were imminent. The potential crack crossed only 6 stirrups in the left wall and 7 stirrups in the right wall. The ACI equation, based on the classical truss analogy, assumes the diagonal crack to form at 45^{o}. Such a crack would have crossed 8 stirrups. Added to this, due to the displacements occurring between the faces of the crack, the stirrups were bent giving rise to transmission of forces by dowel action. At this stage the stirrup strain readings were no longer meaningful.

6.6.2 Stirrup Force Distribution Along Diagonal Cracks

The forces in stirrups at points where they were crossed by the major diagonal crack have been plotted in Fig. 6.9.a. for the right wall and Fig. 6.9.b. for the left wall. As expected, during cycle 1 stirrup forces are low and are more for the tension wall (left wall). During cycle 5, at a maximum load of $1.12\ P_u^*$ the stirrup forces across the major diagonal cracks are well below yield. The forces are higher in the middle stirrup than in the stirrups at the edge of the crack. During the last cycle the stirrup stresses increased considerably. The stirrups at the lower edge of the compression wall yielded. This is associated with the failure mechanism and is discussed in Section 6.8.

Fig. 6.10 shows the total shear applied and proportions of shear resisted by the stirrups of the left and right wall across the potential diagonal crack for cycles 1, 5 and 11. The shaded area represents the shear resisted by stirrups. The ordinates measured

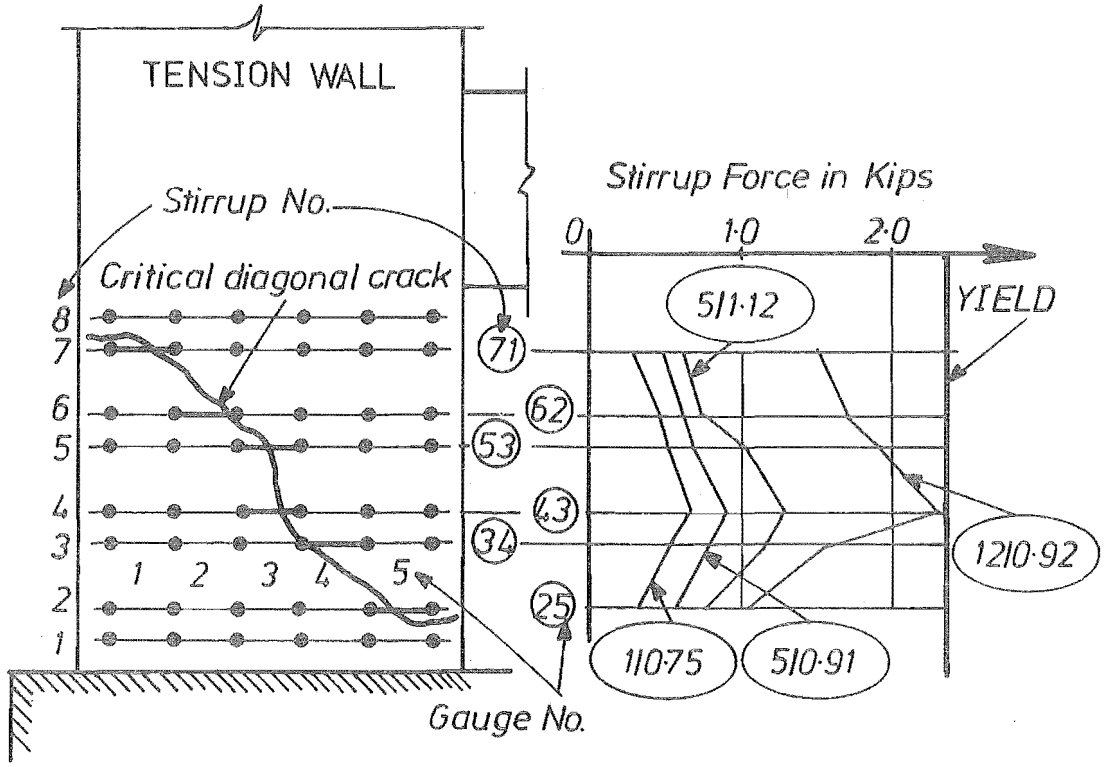

FIG. 6.9.(a) STIRRUP FORCE VARIATION ACROSS THE POTENTIAL CRACK IN THE LEFT WALL

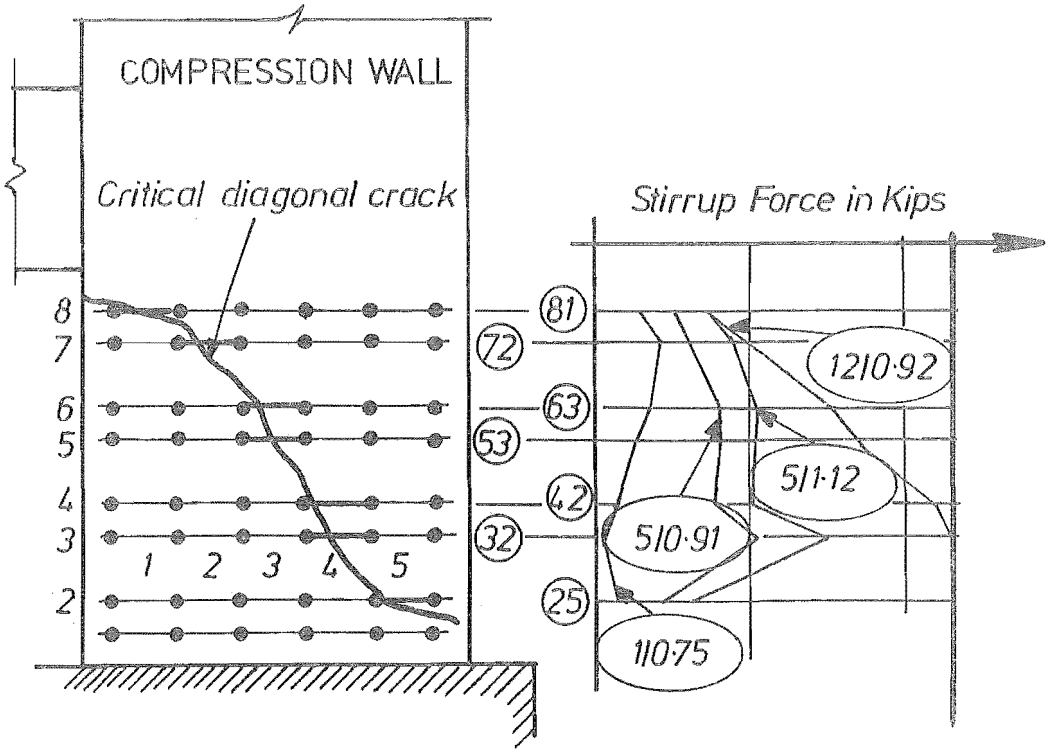

FIG. 6.9.(b) STIRRUP FORCE VARIATION ACROSS THE POTENTIAL CRACK IN THE RIGHT WALL

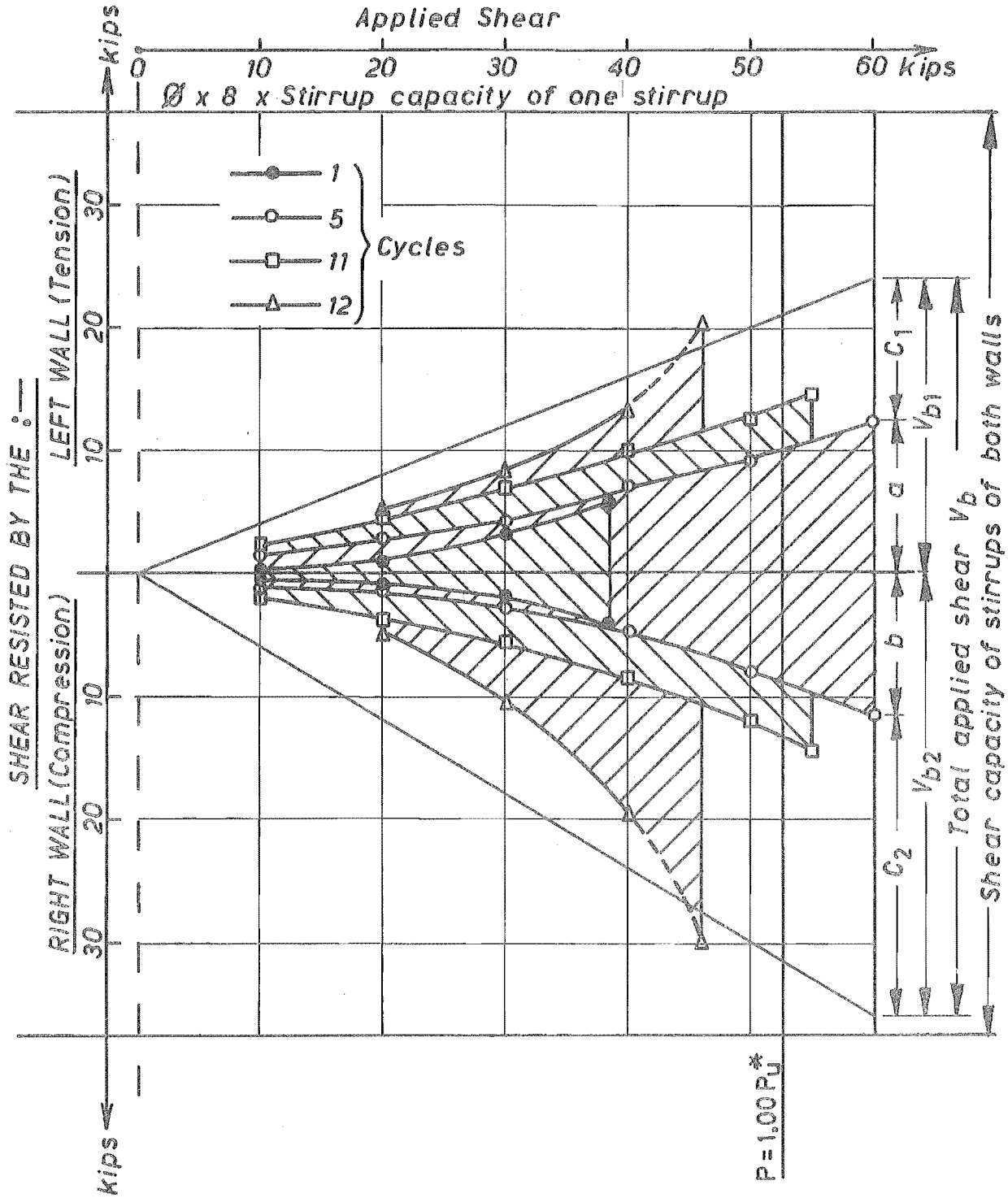

FIG. 6.10 THE TOTAL SHEAR FORCE RESISTED BY THE STIRRUPS ACROSS THE POTENTIAL DIAGONAL FAILURE CRACKS OF THE WALLS DURING CYCLES 1, 5 AND 11

between the straight outer lines represent the total shear applied. The unshaded areas represent the shear resisted by other mechanisms such as aggregate interlock action and the dowel action of the reinforcement. For example, at a maximum load of 60 Kips, during cycle 5, the ordinate 'a' represents the shear resisted by the stirrups across the potential crack in the left wall. The ordinates V_{b1} and V_{b2} represent the theoretical shear to be resisted by wall 1 and wall 2 respectively. Thus the ordinates C_1 and C_2 show the shear resisted by other mechanisms for the tension and compression walls. As expected, the shear resisted by other mechanisms is considerably larger for the compression wall. During cycle 1 the shaded area is small. At a load of $0.70\ P_u^*$ only 25% of the applied shear is resisted by the stirrups. During cycle 5 the initial portion of the curve is similar to that obtained during cycle 1. This shows that the strength degradation with cyclic loading up until cycle 5 is small. The continuity of the curve between the first and the fifth cycle also indicates this.

At ultimate load the computed contribution of the stirrups to the applied shear was 40% during cycle 5 and 53% during cycle 11. These contributions are low. The stirrup contributions were underestimated because the residual strains caused by the accidental preload could not be accounted for.

During cycle 12, when large deformations were imposed on the model, the stirrup contribution increased sharply. At $0.9\ P_u^*$ the load resisted by stirrups appears to be more than the total applied shear. By then the mechanism of failure, initiated by yielding of the flexural bars, had formed. Failure was imminent and there were large displacements along the faces of diagonal cracks resulting in bending of stirrups. Hence, the strain readings on the stirrups were no longer meaningful. The forces computed at this stage are shown by broken lines in Fig. 6.10.

The increase of the shaded area in Fig. 6.10 with cyclic loading shows the progressive deterioration of the shear capacity of the walls and the consequent reduction of the shear resisted by concrete.

6.6.3 The Strain Distribution Along Stirrups

Figs. 6.11.a and 6.11.b show the strain distribution for four typical stirrups in the left wall and right wall. The chosen stirrups are shown in thick lines in the key diagram. The positions of cracks are indicated in the key diagram as well as in each of the diagrams which show the stirrup strains. During the first two cycles the strains have been plotted for two typical increments. The strain variation at maximum load levels reached are shown for cycles 5, 6, and 7. Finally, for cycle 12 the strain variation is plotted for a load ratio of $0.92\ P_u^*$. This was after the formation of failure mechanism. From an observation of the strain distribution curves in Fig. 6.11.a and 6.11.b it is seen that:

(a) The strains are higher in stirrups at the middle of the diagonal cracks than those at the ends. Comparison of strains in stirrup 8 with other stirrups in both the walls show this.

(b) The stirrup strains are large at the locations crossed by diagonal cracks.

(c) At locations crossed by the diagonal cracks, the stirrup strains at ultimate load during cycle 7 is significantly more than the stirrup strains observed at ultimate load during cycle 5. This shows the shear strength degradation of the wall. As the shear carried by the concrete is reduced, the stirrup strains increase.

(d) During the entire cyclic loading the strains are well below yield. However, the stirrups did yield during the final cycle when large deformations were imposed on the shear wall.

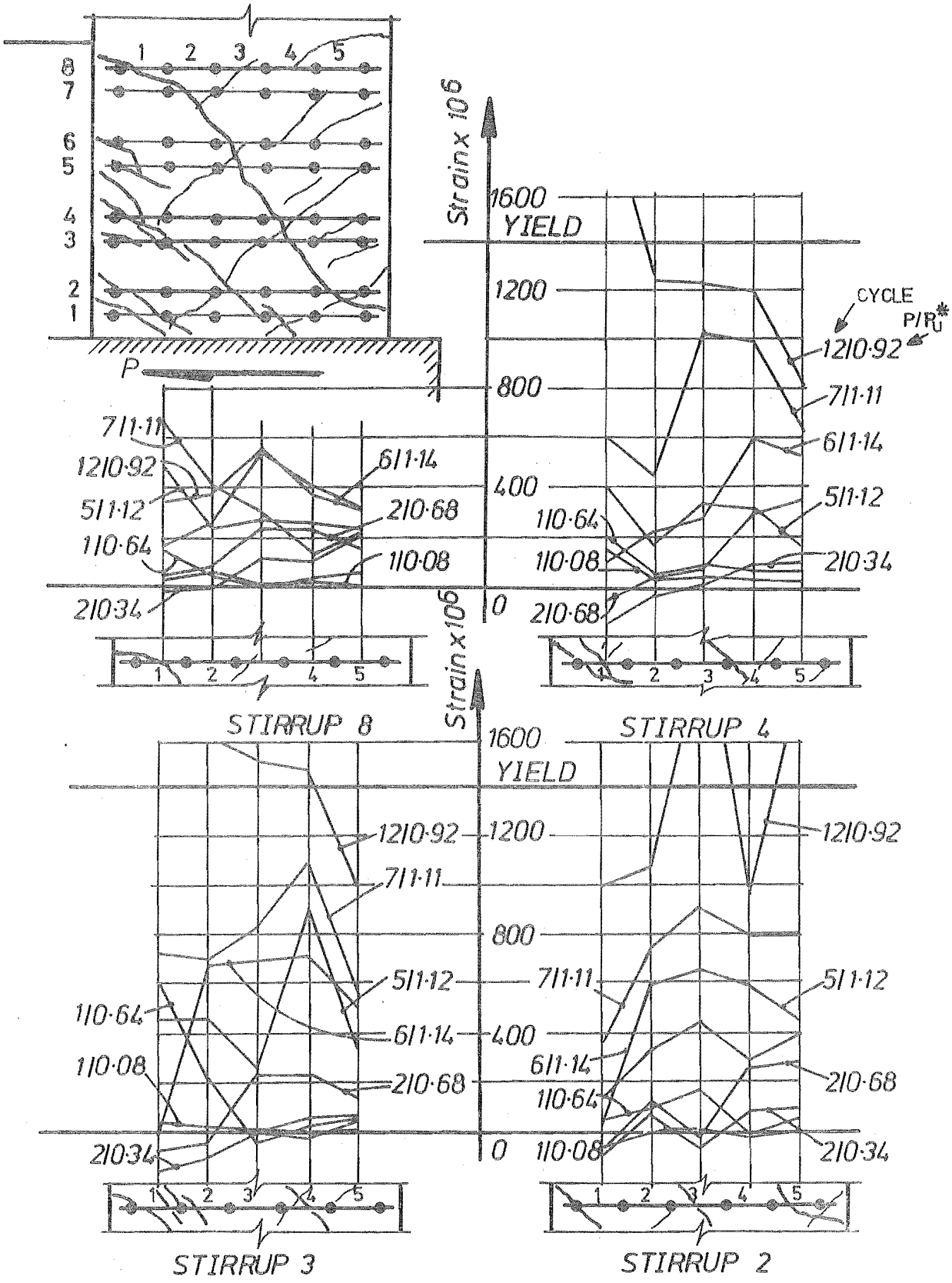

FIG. 6.11.(a) DISTRIBUTION OF STRAINS ALONG 4 TYPICAL STIRRUPS IN THE RIGHT WALL

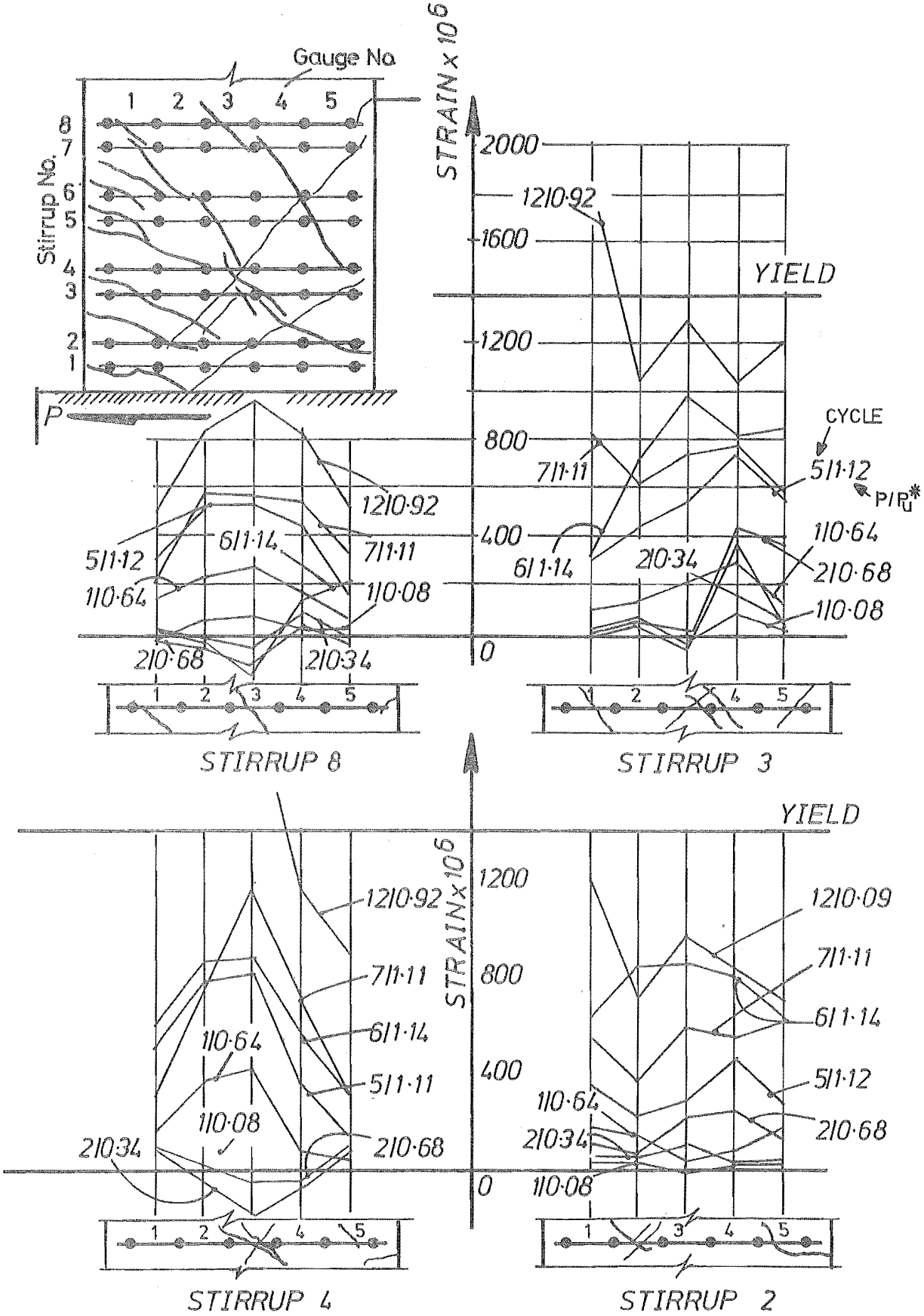

FIG. 6.11.(b) DISTRIBUTION OF STRAINS ALONG 4 TYPICAL STIRRUPS IN THE LEFT WALL

The contribution of concrete to shear strength was ignored and excess stirrups were provided in order to suppress a premature shear failure. To this end, the stirrups performed satisfactorily. When large deformations were imposed, involving yielding of the flexural steel, the stirrups across the potential crack were also subjected to shear displacements. The potential crack did not form at 45^{o} as assumed by the classical truss analogy owing to the presence of large axial forces. When failure was imminent the forces in the stirrups were considerably more than those predicted by the ACI equations.

The compression forces in both the tension and compression walls have to be transmitted across the compression zone into the foundation. These compression zones in both walls have been associated with the alternate opening and closing of cracks. The provision of excess stirrups helps in

(a) maintaining the integrity of concrete in compression zones due to confining action of stirrups around the flexural bars.

(b) reducing shear displacements and assisting in the transmission of forces across the potential crack by dowel action. This allows the flexural bars to yield considerably more before sliding along the potential crack reduces the load carrying capacity of the shear wall.

6.7 DEFORMATIONS

6.7.1 Top Floor Deflections

Using theodolite and dial gauge measurements the top floor deflection relative to the base reference line was computed. Reference may be made to Chapter 5, Section 5.5.2 and Appendix B, wherein the details of the various measurements made and the computation of the top floor deflection are reported. The load-

top-floor deflection relationship is shown for all the 12 cycles in Fig. 6.12.

During cycles 1 and 2 the maximum load on the shear wall ($0.7\ P_u^*$) caused a top floor deflection of 0.75". The corresponding deflection at the onset of yield in the critical beam could not be assessed exactly because of the following two reasons.

(a) The permanent deformations suffered by the critical beam during the accidental preload was uncertain.

(b) As pointed out in Section 6.4., the cracks formed at the junction of the wall and the beam bypassed the instrumented gauge. Therefore the steel in the critical beam must have yielded earlier than when observed at the instrumented length of the bar.

The top floor deflection at which yielding was observed in one of the instrumented gauges of the critical beam is shown in Fig. 6.12 for cycles 1 and 2.

Cycles 3 and 4 were "elastic" cycles. The stiffness of the shear wall during the first four cycles remained approximately the same.

During cycles 5 and 6 the shear wall was loaded till yielding occurred also in the flexural reinforcement of both walls and thus distinct plastic hinges were observed. During cycle 5 the middle layer of tension steel and the single layer of compression steel in the tension wall yielded simultaneously. During the reversed cycle 6, the single layer of tension steel in the compression wall yielded. The top floor deflections at which the yielding was observed are shown as the first wall yield for cycles 5 and 6 respectively. A maximum top floor deflection of 1.4" during cycle 5 and 2.1" during cycle 6 were attained.

During each of the following four cycles the deflection attained at ultimate load was more than 2.3". Cycle 11 was intended to be the last one. During this cycle large plastic

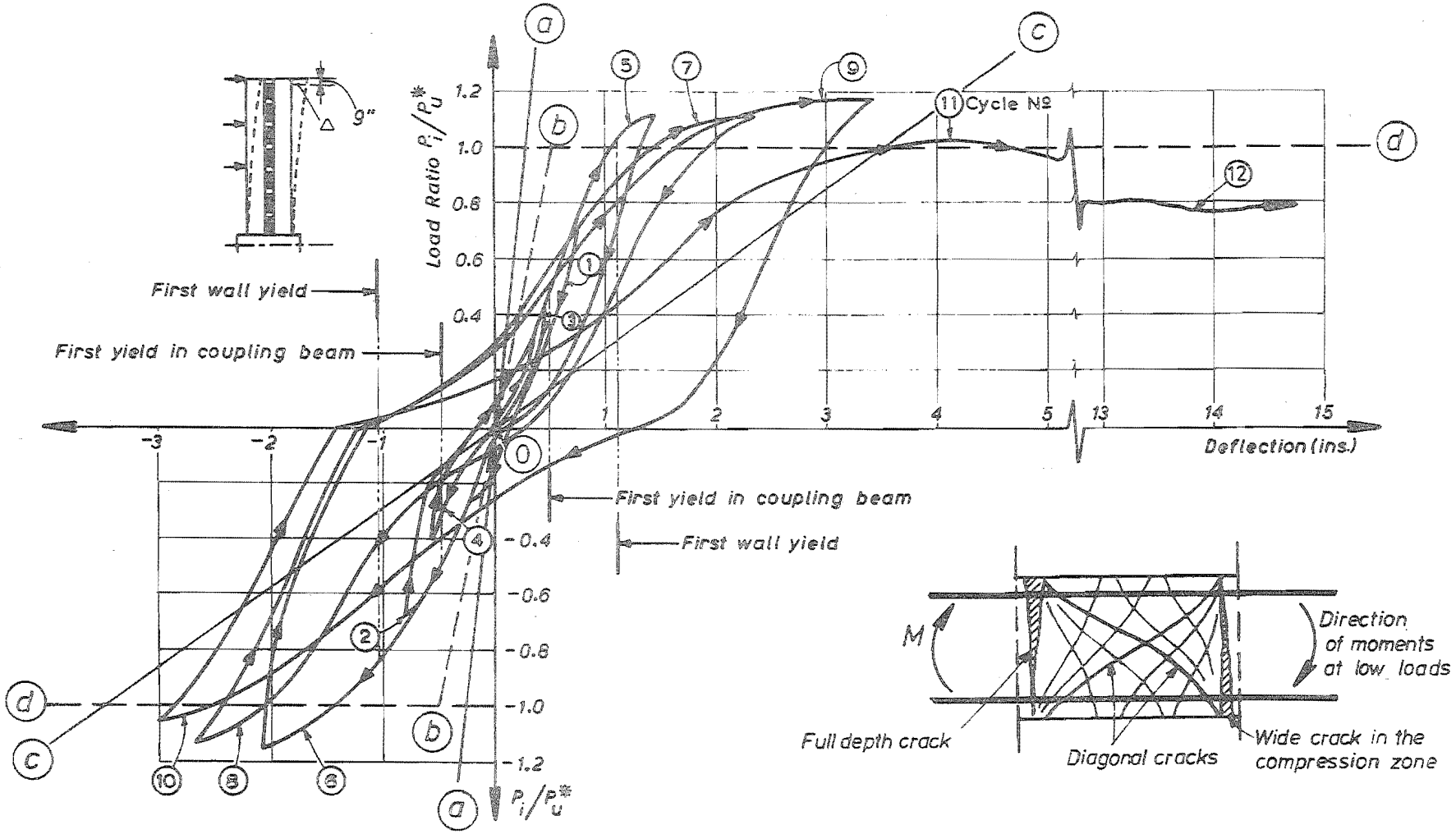

FIG. 6.12 LOAD-TOP FLOOR DEFLECTION CURVE FOR SHEAR WALL A

deflections were imposed on the model. The shear wall attained a top floor deflection of 4.5" at the theoretical ultimate load and after this the load on the structure gradually decreased. The portion of the load deflection curve during which the load was reduced to zero (cycle 11) and increased again in the positive direction (cycle 12) is not shown.

Three theoretical stiffnesses (oa),(ob) and (oc), based on the following considerations, are also shown in Fig. 6.12.

(oa) Properties of the beams and walls based on uncracked sections (I_g and A_g)

(ob) Properties of beams and walls based on cracked section, using the load-moment property curves included in Chapter 3, at the instance of the critical coupling beam reaching yield.

(oc) Zero efficiency of coupling ($I^* \approx 0$), i.e. two cantilevers only are assumed to resist the external action with the coupling beams transmitting horizontal axial forces only. Properties of walls based on cracked sections.

At the start, as expected, the stiffness of the shear wall is less than the theoretical stiffnesses indicated by the lines oa and ob. Cycle 1 indicates the stiffness of the model when all the beams and both the walls had cracked and the steel in at least three coupling beams had attained yield strain owing to accidental load. The broken line obd represents the assumed theoretical elasto-plastic bilinear relationship for the shear wall model. From cycle 7 onwards, at low load ($< 0.2\ P_u^*$), the stiffness of the model is approximately equal to the stiffness indicated by (oc). Note the pinching in the shape of the load-deflection curves at these loads.

The insert in Fig. 6.12 shows the cracked coupling beam at the beginning of a cycle after it had been subjected to a few cycles of

high intensity loading. Eventually, the compression force in the beams has to be transmitted across the crack at the junction of the wall and the beam. By then the crack runs along the full depth of the beam. Until the crack is closed only the steel is effective in resisting compression. However, this steel is soft due to the Bauschinger effect associated with tensile yielding which occurred during the previous high intensity cycles. Moreover the compression zones of the walls have also been penetrated by large cracks and the steel across these cracks is also soft due to Bauschinger effect. The low stiffness of the coupling beams at low loads due to full depth cracking, shear deformation and bond deterioration in the beams and the softness of steel due to the Bauschinger effect in the compression zones of the beams and the walls have resulted in the pinching shape of the load-deflection curves. At these loads the stiffness of the shear wall is approximately equal to the stiffness of the equivalent "elastic" structure in which the external action is resisted by moments developed at the base of two cantilevers with the coupling beams transmitting horizontal axial forces only. When the cracks closed an increase in stiffness was observed. ($0.8\ P_u^* > P > 0.4\ P_u^*$). The observed stiffness of the shear wall lies between the stiffnesses indicated by (ob) and (oc).

The most important function of the load-top floor deformation diagram is the information that it provides with respect to ductility of the shear wall. Reference may be made to Section 4.3.1 regarding the definition of overall ductility. For computing the ductility factor the deflection at the top floor at the onset of yield (b) for the theoretical bilinear behaviour (obd), is assumed as the yield deflection of the shear wall. For the model this is 0.5". The top floor deflection of 4.5" at $1.00\ P_u^*$ during cycle 11 resulted in a ductility factor of 9 . If the permanent

deformation of 1", which was present at the end of cycle 10, is taken into account the ductility factor attained is 11. The ductilities attained during each cycle and the energy absorption properties of this shear wall are discussed in Chapter 8.

In Fig. 6.13 a comparison of the load-top floor deformation curve observed during the cyclic loading with that predicted using the elasto-plastic analysis, as presented in Chapter 4, is made. The broken lines OX , OY and OZ indicate the approximate stiffnesses computed from properties based on different conditions in the walls and beams as detailed and discussed on page 229. The load deformation curves obtained during cycles 5 and 7 are also shown in Fig. 6.13. On the load-top floor deflection curve for cycle 5 the different stages ,at which the steel in the coupling beams and the walls reached yield strain,are indicated. The plastification of the beams and the walls took place at various increments of loading rather than at a particular load. The observed ranges of plastification are indicated at the left hand of Fig. 6.13 by the following notation: I - yielding of the critical beam; J - yielding of beams; K - yielding of tension wall; L - yielding of compression wall. On the same figure the load-top floor deflection, computed with the analysis presented in Chapter 4, is indicated. Curve 1 shows the results obtained with the use of the bilinear stress-strain curve for steel, shown in Fig. 6.13.a. The sequence of hinge formation is shown in Fig. 6.13.c. The different stages of plastification of the components, in accordance with the notations used in Chapter 4,are indicated on the curve(1). When curve(1) is compared with the load-top floor deflection curve during cycle 5, two significant discrepancies are noticed. They are:

(i) The stiffness indicated by the experimental curve during cycle 5 is less than the stiffness predicted by curve (1).

(ii) The ultimate load observed is almost 15% more than that predicted.

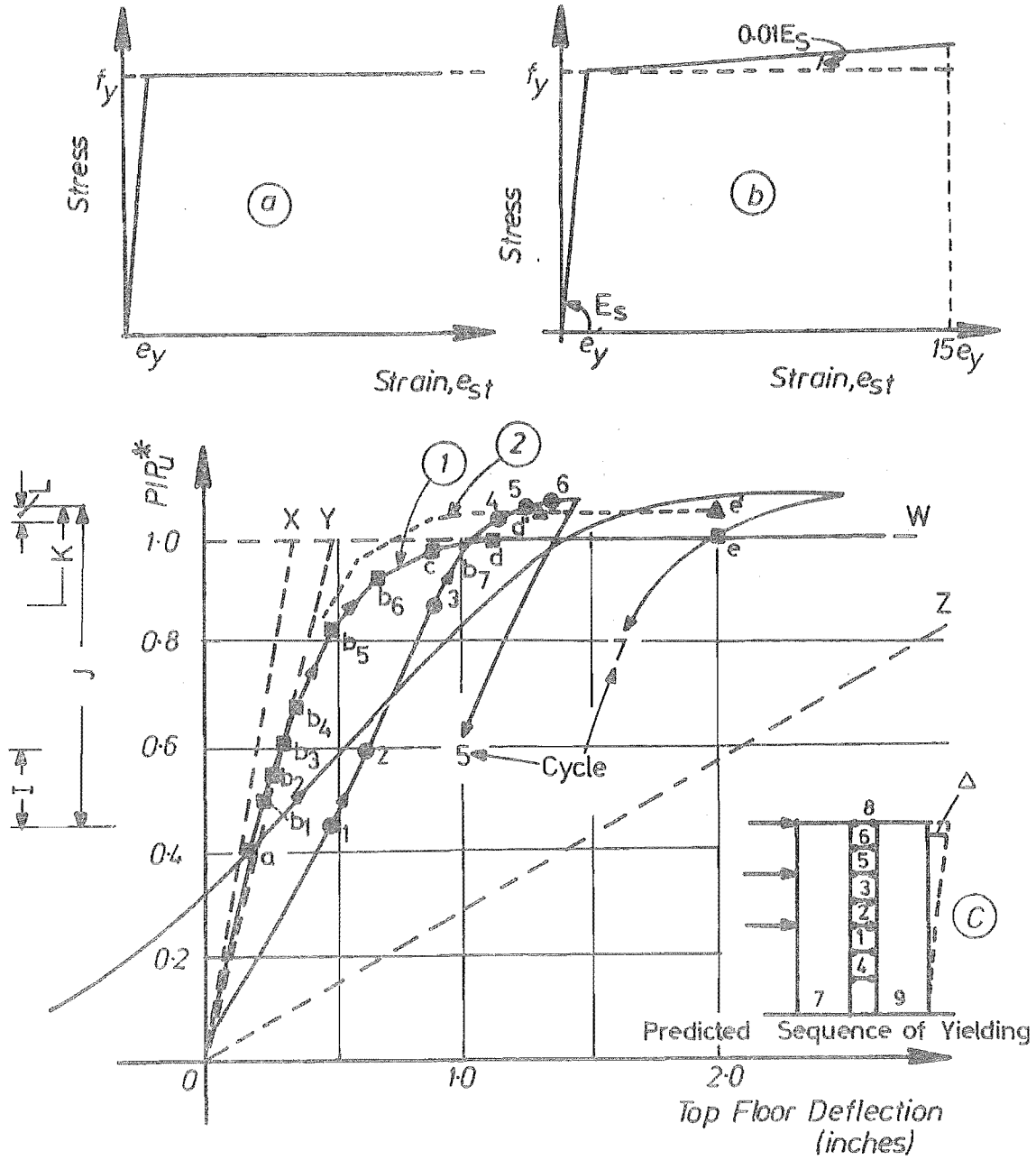

a Code design load

b_1 Onset of yield in critical beam

b_n Onset of yield in the nth beam

b_7 Full plastification of laminar system

c Tension wall reaching yield

d Compression wall reaching yield

e Overall ductility requirement

(1) Flexural steel on one side of the 6th floor beam yielded

(2) Flexural steel in both faces at both the tension corners of the 6th floor beam yielded

(3) Outer layer of tension steel in the tension wall yielded

(4) One layer of tension steel in the compression wall yielded

(5) Outer layer of compression steel in compression wall yielded

(6) Middle layer of tension steel in tension wall yielded.

FIG. 6.13 A COMPARISON OF THE MEASURED LOAD-TOP FLOOR DEFORMATION RELATIONSHIP WITH THOSE PREDICTED USING THE ELASTO-PLASTIC ANALYSIS PROPOSED IN CHAPTER 3

It is reasonable to expect a lower stiffness during cycle 5. The theoretical curve assumes monotonic loading. Thus it does not allow for the stiffness degradation that would have occurred due to the accidental preload and due to the previous cyclic loading.

It was pointed out in Chapter 3 that the strain hardening of steel in the coupling beams and the walls increases the ultimate load capacity of the shear wall. To quantify this increase the stress-strain curve for steel was assumed to have a strain hardening range as shown in Fig. 6.13.b. The broken curve(2)in Fig. 6.13 shows the load-top floor deflection based on this stress-strain relationship for the steel used in the beams and the walls. When the strain hardening of steel is considered, it is seen that there is a better agreement between the predicted and observed ultimate loads.

6.7.2 The Variation of Stiffness

Using the load-top floor deflection curve shown in Fig. 6.12, the stiffness of the model at various load levels during the various cycles was computed as the slope of the tangent to the load-deflection curve at the load level considered. The stiffness so obtained is plotted against the load ratio in Fig. 6.14. On the same figure the theoretical stiffnesses have also been indicated for comparison. The broken horizontal lines show the theoretical stiffnesses at the following stages of behaviour.

(a) Both walls and the beams in the uncracked state - the stiffness is indicated by the line(X).

(b) Both walls and the beams in the cracked state at the onset of yield in the critical lamina. The stiffness is indicated by the line(Y).

(c) Both walls and the beams are in the cracked state and the bottom four coupling beams have yielded. The top three beams and both walls elastic. The stiffness at this stage is indicated by line (Y4).

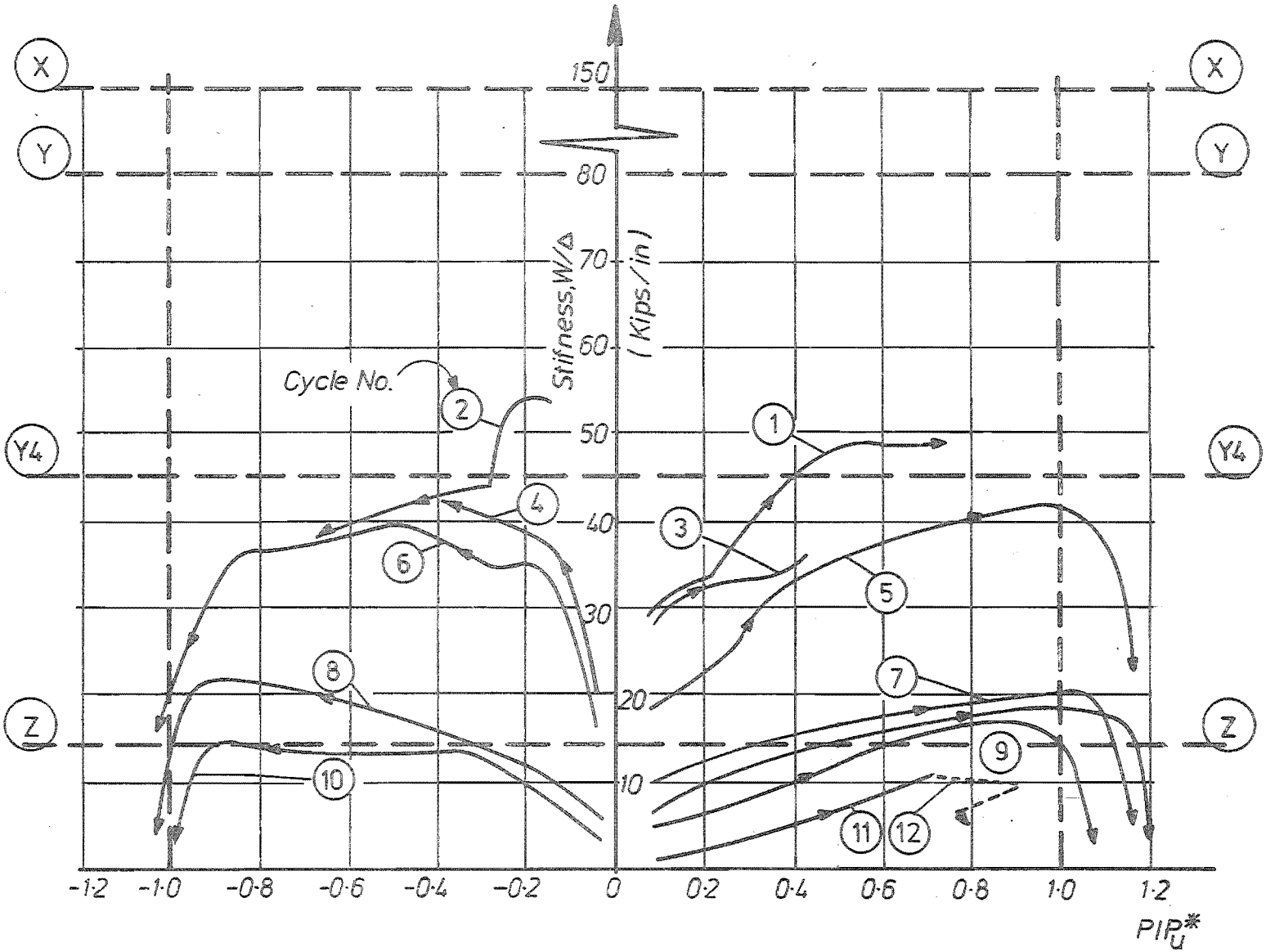

FIG. 6.14 VARIATION OF STIFFNESS OF SHEAR WALL A WITH CYCLIC LOADING

(d) Both walls in the cracked state with zero stiffness of the coupling. The walls act as two cantilevers with coupling beams transmitting horizontal axial forces only. The stiffness is indicated by the line(Z).

It is unfortunate that the information regarding the stiffnesses of the shear wall in the uncracked state and in the cracked state with beams still "elastic" was lost due to the accidental load. The theoretical stiffnesses indicate a loss of approximately 45% due to cracking when compared with the stiffness of the shear wall in the uncracked state. The stiffness of the shear wall in cycles 7 to 10 is approximately one half of its stiffness in cycles 1 to 6. After one high intensity loading in either direction, causing yielding, the stiffness reduced to nearly that of two connected cantilevers. (See the stiffness during cycles 7 to 12 in Fig. 6.12).

In general, the later cycles commence with a low stiffness. Gradually the stiffness increases as the cracks are closed. It is seen that the curves generally exhibit three ranges of behaviour after the structure is subjected to a few high intensity load reversals. These ranges are:

(a) A "soft range" at very low loads ($< 0.2\ P_u^*$).

(b) A "steady range" at medium loads ($0.4\ P_u^* \leq P \leq 0.8\ P_u^*$)

(c) A "plastic range" at near ultimate load resulting from yielding of flexural reinforcement in the beams as well as in both the walls ($P > P_u^*$) .

These three ranges are similar to those observed by Paulay[74] during the experimental investigation of conventionally reinforced beams. The type of reinforcement in the beams has a considerable influence on the overall behaviour of the shear wall after it has been subjected to a few cycles of high intensity loading. It was pointed out in Chapter 2 that the total external moment is resisted by the wall moments M_1 and M_2 together with the moments generated by

the axial force, $1T_u$. For shear wall A the $1T_u$ component is approximately 70% of the total resisting moment, M_o, at ultimate load. The axial force, T_u, is developed by the accumulation of beam shears, Q_b. After a few high intensity cyclic loads, at low loads, the conventionally reinforced coupling beams are known to become "soft" due to the presence of open cracks in the compression zone and the deformations caused by shear. Because of these, the coupling efficiency at low loads tends to be negligible. At these low loads the stiffness of the walls are also low due to open cracks formed near the base during the previous cycles. The combined effects of the stiffness degradation of the walls and the coupling beams have resulted in a coupled shear wall whose stiffness is less than that of an equivalent "elastic" structure which resists the external action by moments developed at the base of the two cantilevers with coupling beams transmitting horizontal axial forces only. The stiffness of the model increases during subsequent loading, with the closing of cracks in the compression zones of the beams and the walls, to a value above that based on the stiffness of "two cantilevers".

6.7.3 Rotations of Coupling Beams

Using the measurements made with the theodolite at the centre line of the walls, rotations of the coupling beams were computed as detailed in Appendix B. Reference may be made to Section 4.3.1 regarding the definition of beam rotation and beam ductility. The key diagram in Fig. 6.15 also shows the meaning of the beam rotation. In the main portion of this figure, rotations of the beams during the various cycles are plotted against the positions of the coupling beams. In the same figure, the approximate yield rotation at the instance of onset of yield in the critical beam is also shown. It is seen that the maximum beam ductility attained during negative loading

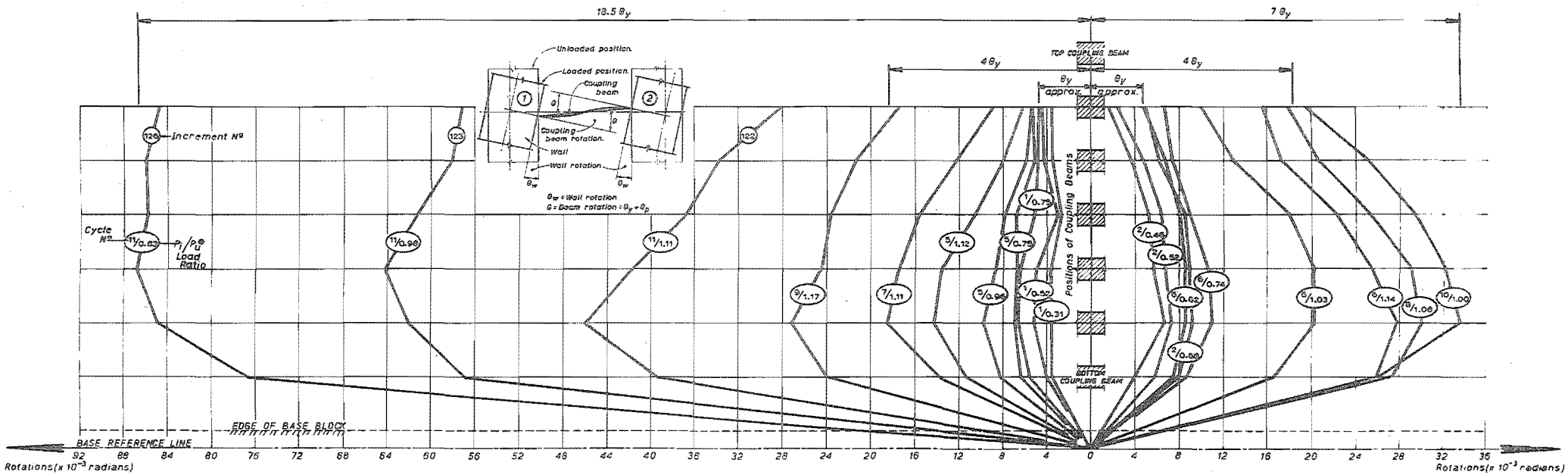

FIG. 6.15 ROTATIONS OF THE COUPLING BEAMS COMPUTED FROM THEODOLITE MEASUREMENTS MADE ON WALL CENTRE LINES

(cycle 10) is approximately 7 and the maximum ductility attained during positive loading (cycle 11) at a load of 1.11 P_u^* is approximately 12.

Fig. 6.16.a compares the theoretical rotations computed during different stages of loading (shown in broken lines), with those measured using theodolite observations as indicated in the previous paragraph. To examine the sensitivity of beam rotation to the assumed stiffness of the walls, the rotations at the theoretical ultimate load were computed based on the following assumptions:

(I) Stiffness of the walls based on Paulay's[5,74] approximate method (see Table 3.2, Chapter 3, Section 3.5.b).

(II) Stiffness of the walls computed from the load-moment-property curves presented in Chapter 3, Section 3.5.b.

(III) Stiffness of the walls computed from gross properties for the walls.

(IV) Observations made with the theodolite during experiments.

The block diagram in Fig. 6.16.b shows the theoretical rotations of the second floor coupling beam at stage(d)based on the above wall stiffnesses. In the same figure the measured rotation of this beam at ultimate load during cycle 5 is also shown. It is seen that the rotations based on methods(II)and(III)give results comparable with that observed during test. Paulay's approximate method overestimates the rotations by about 30% when compared with the experimental evidence. However in prototype shear walls the stiffness is likely to be closer to Paulay's approximate method due to dead load variation with height.

6.7.4 The Elongation of Coupling Beams

The coupling beams elongate owing to the accumulation of tensile strain in both the top and bottom reinforcement. In the model the elongation of the coupling beam was evaluated from theodolite measurements made at the centre line of each wall. The elongation of the beams was taken as the difference in the lateral deflection

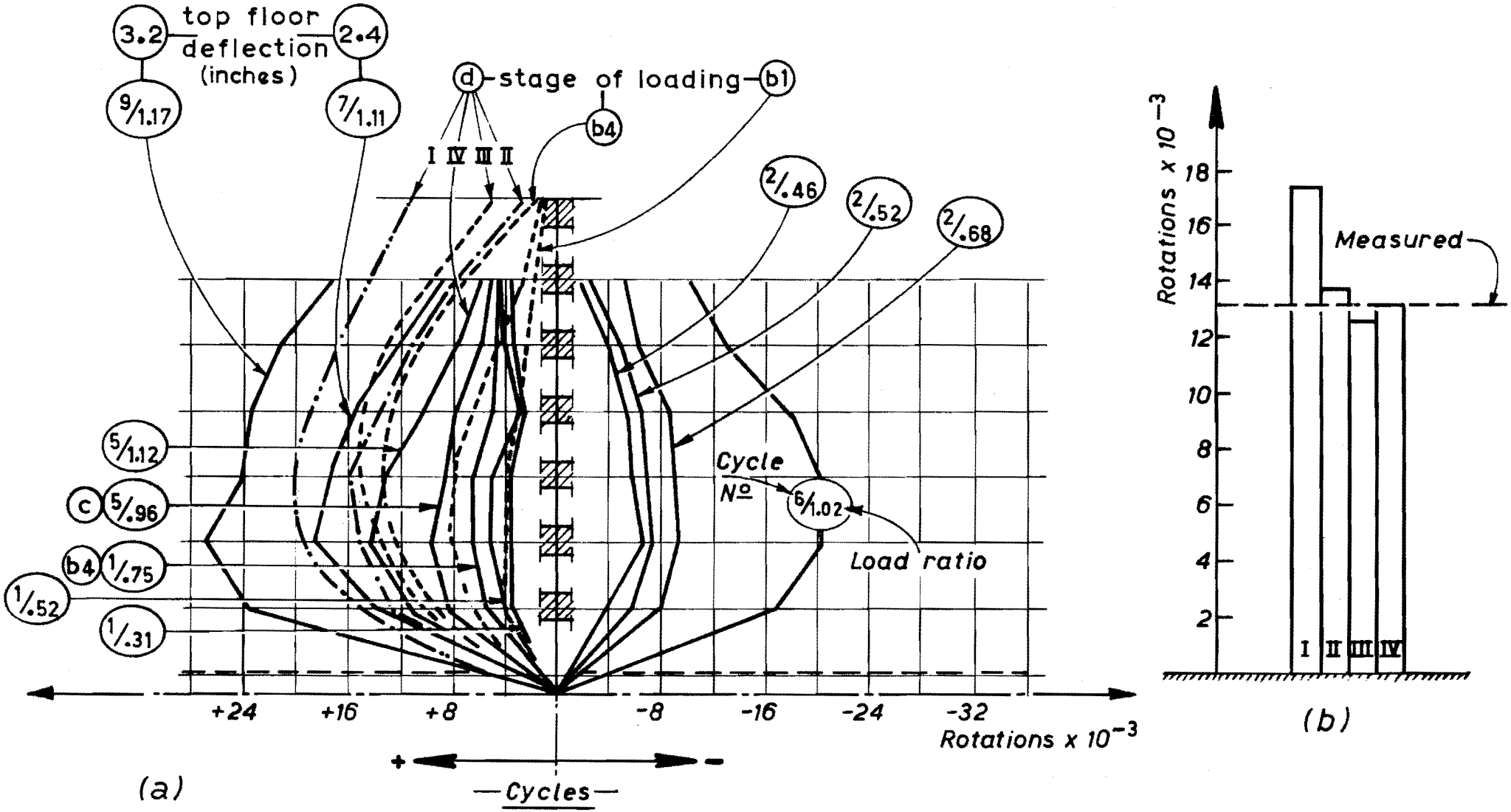

FIG. 6.16.(a) A COMPARISON OF THE OBSERVED BEAM ROTATIONS WITH THOSE PREDICTED BY ELASTO-PLASTIC ANALYSES BASED ON DIFFERENT ASSUMED PROPERTIES OF THE WALLS

at the centre lines of the walls. The elongation measurements had to be accurate as these were relatively small compared to the wall deflections. The theodolite measurements were made on all targets (see Appendix B for the location of the targets at the centre line of the wall) to assess the distribution of coupling beam elongations at maximum load levels. For these measurements only the main theodolite was used. The accuracy of the results obtained was of the order of 0.01". The elongations during cycles 1 to 4 were very small (of the order of 0.001"). Thus, no reliable results could be obtained for these cycles. The elongations obtained at maximum load levels during later load cycles are plotted against the position of the coupling beams in Fig. 6.17.a and Fig. 6.17.b.

The elasto-plastic analysis presented in Chapter 4 ignores beam elongations. While the critical lamina is "elastic" the beam elongations are proportional to beam shear. Based on this assumption, and using the equations derived in Section 3.2.2, the beam elongation for various coupling beams at the onset of yield of the critical lamina were computed. This is shown in broken line in Fig. 6.17.a. The curves of Fig. 6.17.a and 6.17.b show that:

(a) The coupling beams in the critical region are subjected to large plastic elongations.

(b) The observed and computed distributions of beam elongations in the various coupling beams have the same pattern.

(c) During the final cycle the coupling beams contract (see cycle 11 and cycle 12 in Fig. 6.17.b). This is associated with the failure mechanism. Due to large shear deformations the beams were distorted as shown in the photographs of Fig. 6.26 (cycle 12). This pulls the two walls together.

(d) A comparison of elongation curves of Fig. 6.17.a and the rotation curves of Fig. 6.15 shows that the patterns are similar. However, it is noted that the elongations are not so large at the top where the rotations are still large. (Compare the curves for cycle 7 at

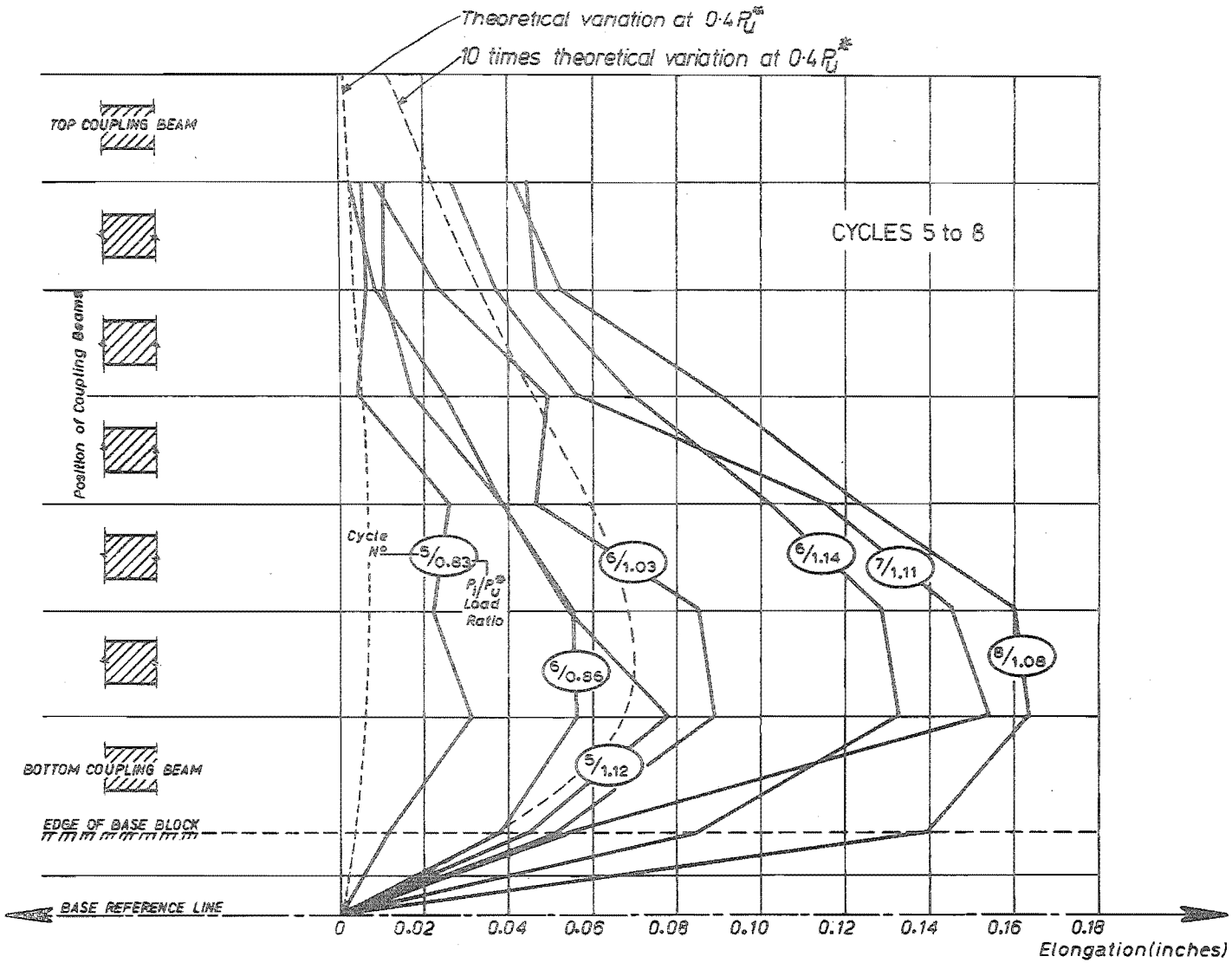

FIG. 6.17.(a) ELONGATION OF COUPLING BEAMS DURING CYCLIC LOADING DERIVED FROM THEODOLITE MEASUREMENTS

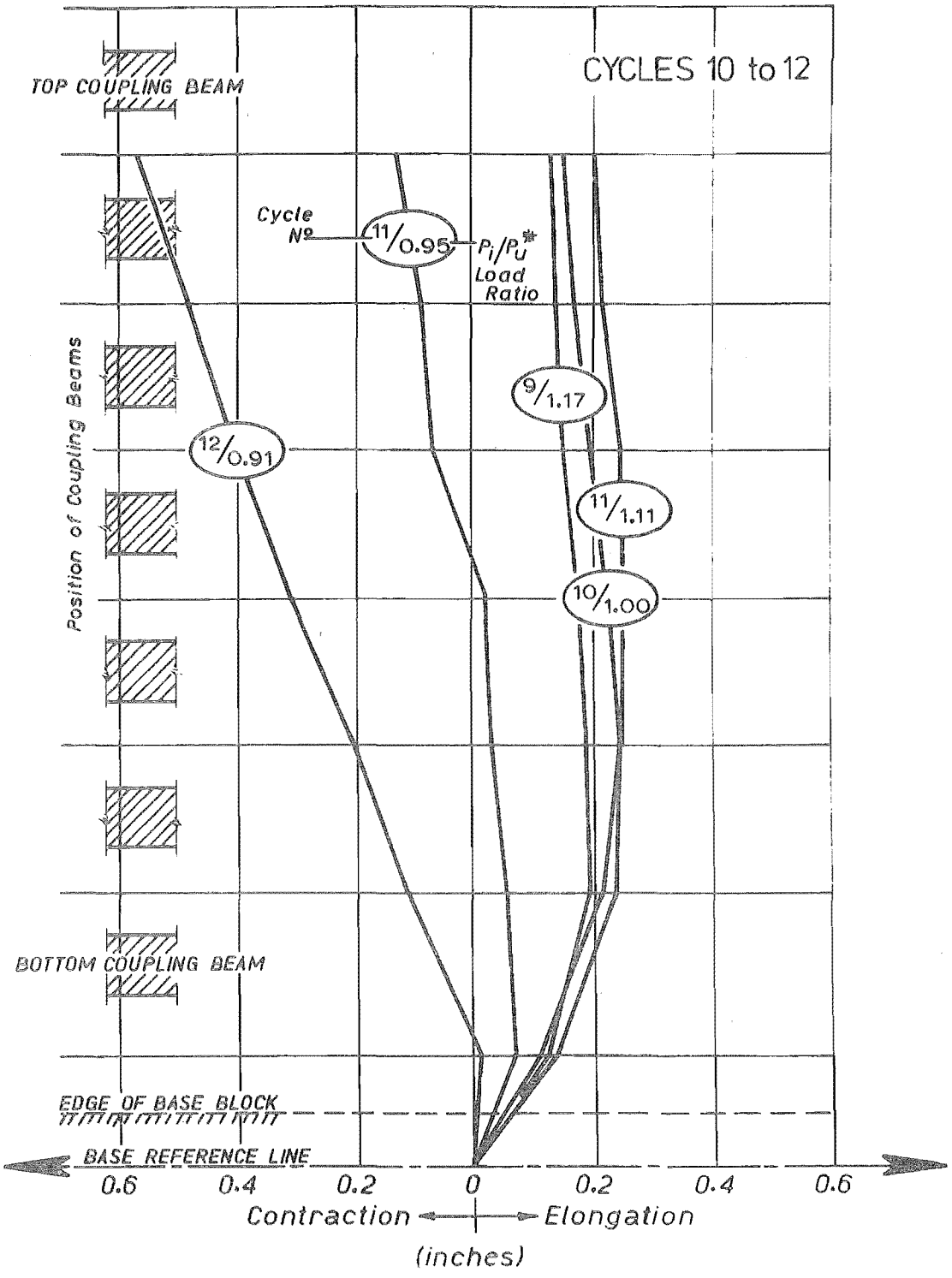

FIG. 6.17.(b) ELONGATION OF COUPLING BEAMS DURING THE LAST CYCLES OF LOADING. (NOTE DIFFERENT SCALE)

1.11 P_u^*). The deterioration of bond and the consequent spread of yielding length in the main flexural bars were considerably more for the beams situated near the critical region. This has resulted in large residual deformations and full depth wide cracks for the beams in the critical region compared to the beams at the top. This is revealed by an examination of the crack patterns of the top floor beam (Fig. 6.25) and 2nd floor beam (Fig. 6.30) at cycle 10. The phenomena contributed to the larger elongation increases for the beams in the critical region.

With the intention of recording the load-elongation history of the top floor coupling beams, measurements were made on two targets in the top floor using the two theodolites at regular intervals (0.2 P_u^*) of loading. The average of the deformations derived from the measurements made with two theodolites were used to compute the elongation of the top floor coupling beam. The two targets mentioned above were not situated at the point of intersection of the centre line of the coupling beam and the centre line of the walls. The position of these two targets can be seen in Fig. B.1 in Appendix B. Hence, the elongation obtained using the measurements made with the two theodolites is termed as "proportionate" elongation of the top coupling beam. Fig. 6.18 shows the "proportionate" elongation of the top floor coupling beam plotted against the load ratio for cycles 5 to 12. The elongations during the first four cycles were too small to be determined accurately enough and hence they are not shown.

The broken line (a) shows the theoretical stiffness of the beam with respect to elongation. The curves show the elongation response of the beam with cyclic loading. During the first high intensity loading (cycle 5) the beam elongates with increase in load. When the load is released the beam contracts. When the load is increased in the opposite direction (cycle 6), the beam first contracts. This is due to the closing of the cracks formed during the previous cycle. After this,

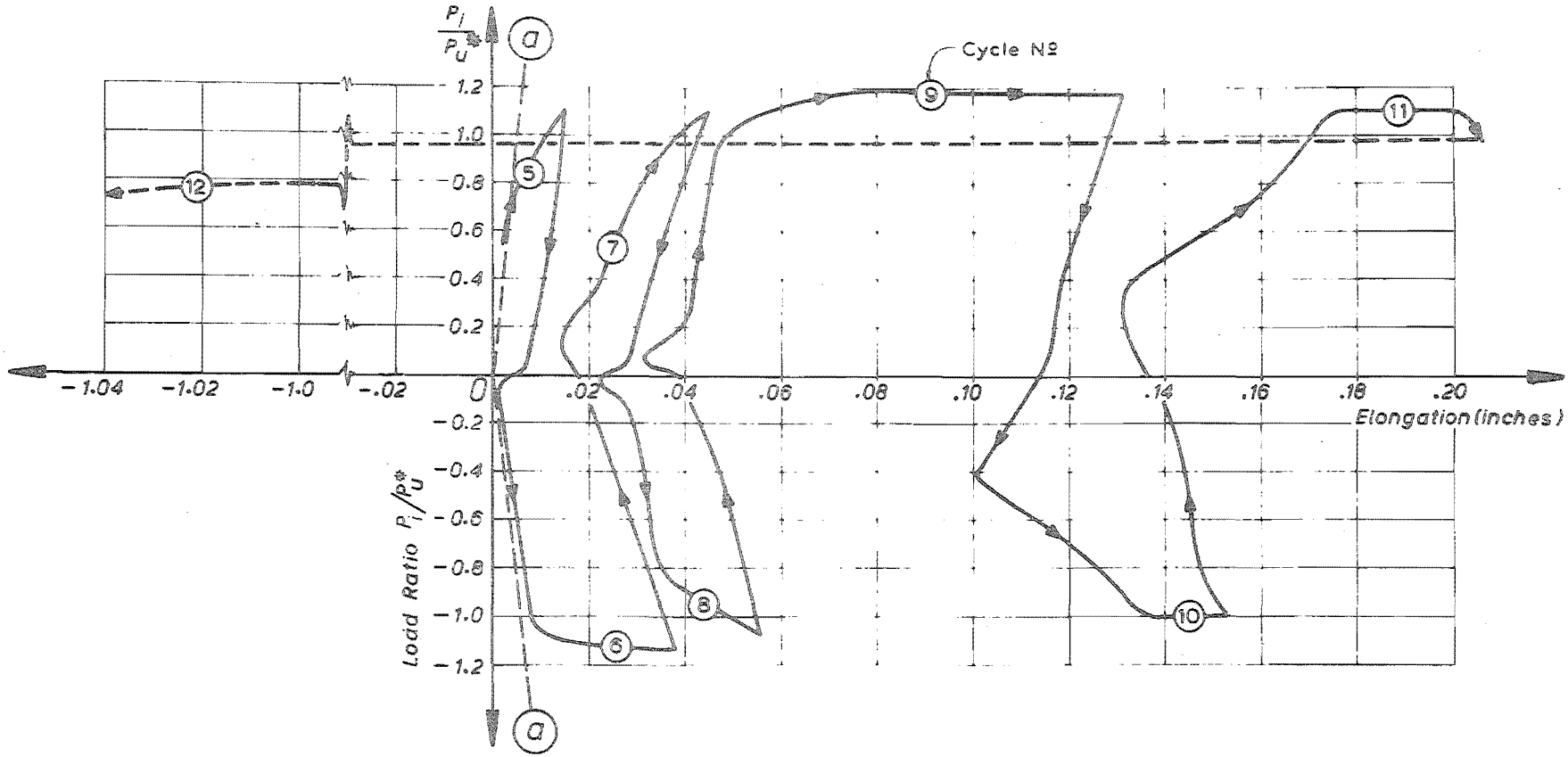

FIG. 6.18 PROPORTIONATE ELONGATION OF THE TOP FLOOR COUPLING BEAM DURING CYCLES 5 TO 12

the beam again elongates with increase in load. The contraction associated with the closing of the cracks at low loads is prominent in later cycles and this indicates wider cracks and increased bond deterioration.

During cycle 11, after the formation of failure mechanism, the beam starts contracting. This is shown in broken lines. As mentioned earlier this large contraction of the beam is due to sliding shear failure which can be seen in the photograph of Fig. 6.31 (cycle 12). The contraction occurs simultaneously with that in other beams.

6.7.5 The Deflection Profiles of the Walls

The wall deflections are much larger than the beam elongations and hence the difference in deflections of the two walls could not be plotted to sufficient accuracy. Hence, only overall deflections of both the walls were considered. Fig. 6.19.a and b show the deflection profiles of the walls during cycles 1, 2 and 5, 6 respectively. It is seen that the deflection at ultimate load during cycle 6 is larger than the deflection at ultimate load during cycle 5. Fig. 6.19.c shows the deflection profiles during the high intensity cycles 7 to 10. The permanent deformations at the beginning of cycle 7 and cycle 9 are also shown. (See cycle 7, $P/P_u^* = 0.08$ and cycle 9, $P/P_u^* = 0.02$). The maximum permanent deflection at the free end of the shear wall was about 1". Fig. 6.19.d shows the deflection profiles during the final cycles. At a load of 1.11 P_u^*, during cycle 11, the maximum top floor deflection was 4". At this stage the failure mechanism had not formed yet. A maximum free end deflection of 10" was attained during cycle 11 at a load ratio of 0.95. At this stage the load was brought down to enable the jacks being readjusted. The deflection profile during cycle 12 at a load ratio $P/P_u^* = 0.08$ indicates the permanent deformation at the end of cycle 11. The maximum deflection at the top of the shear wall was 8". During cycle 12 the maximum load reached was 0.91 P_u^*, at which load the maximum top floor deflection

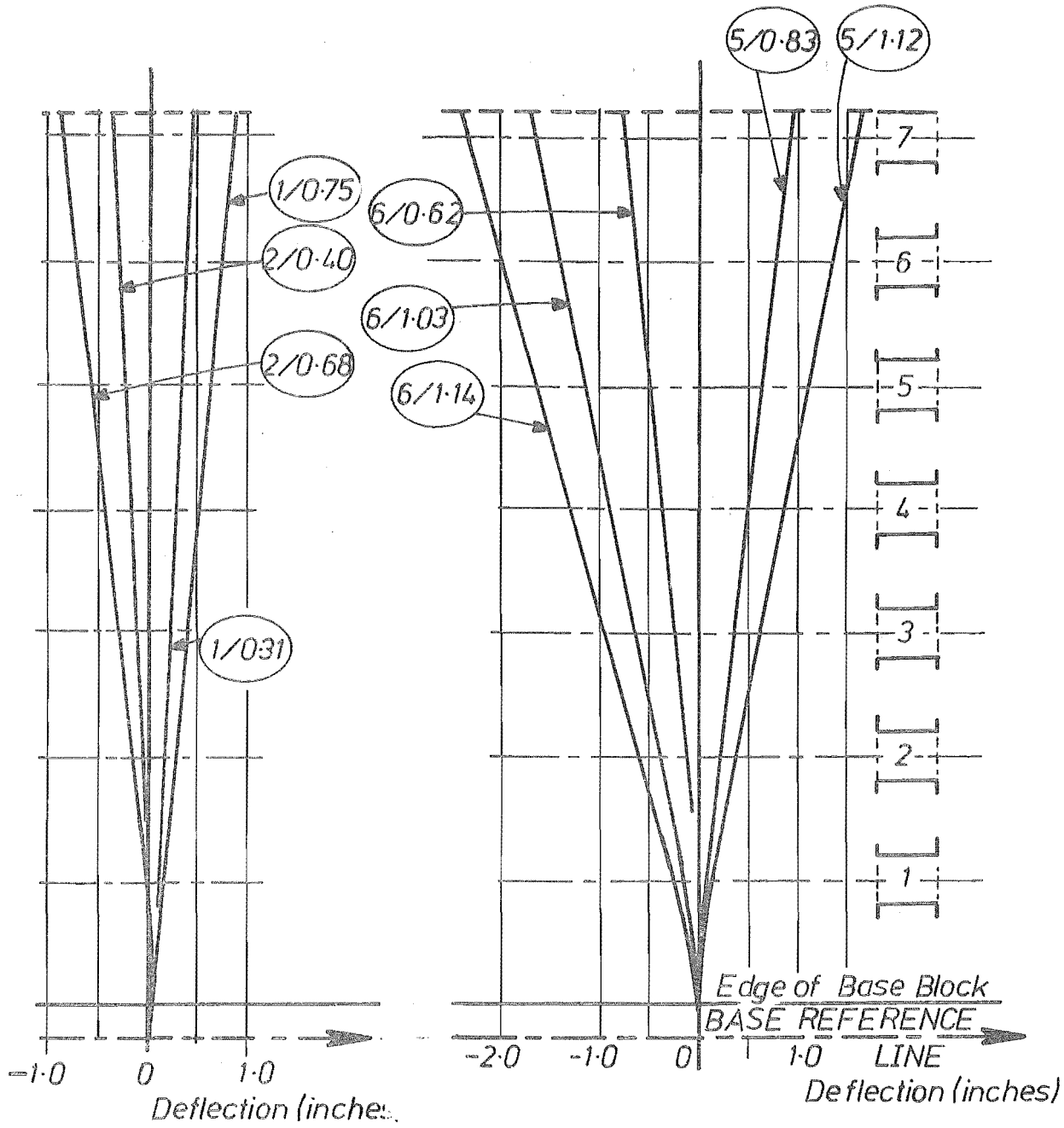

(a) Cycles 1 and 2

(b) Cycles 5 and 6

Fig. 6.19 (Contd on next page)

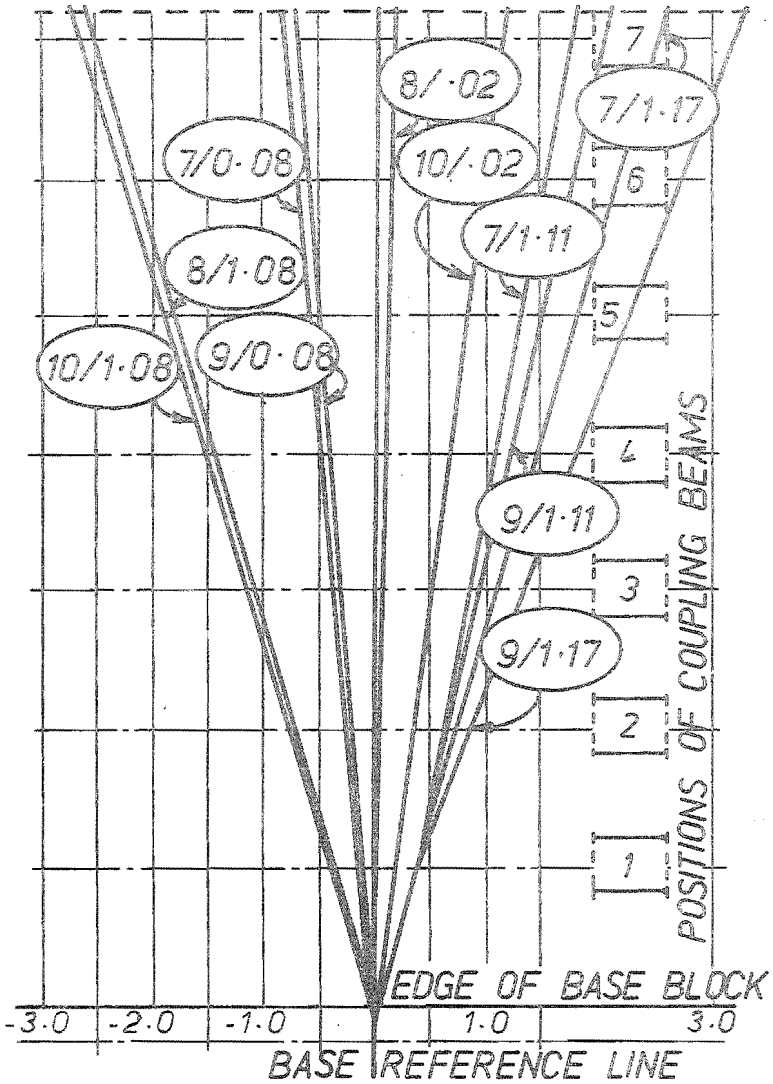

(c) Cycles 7 to 10

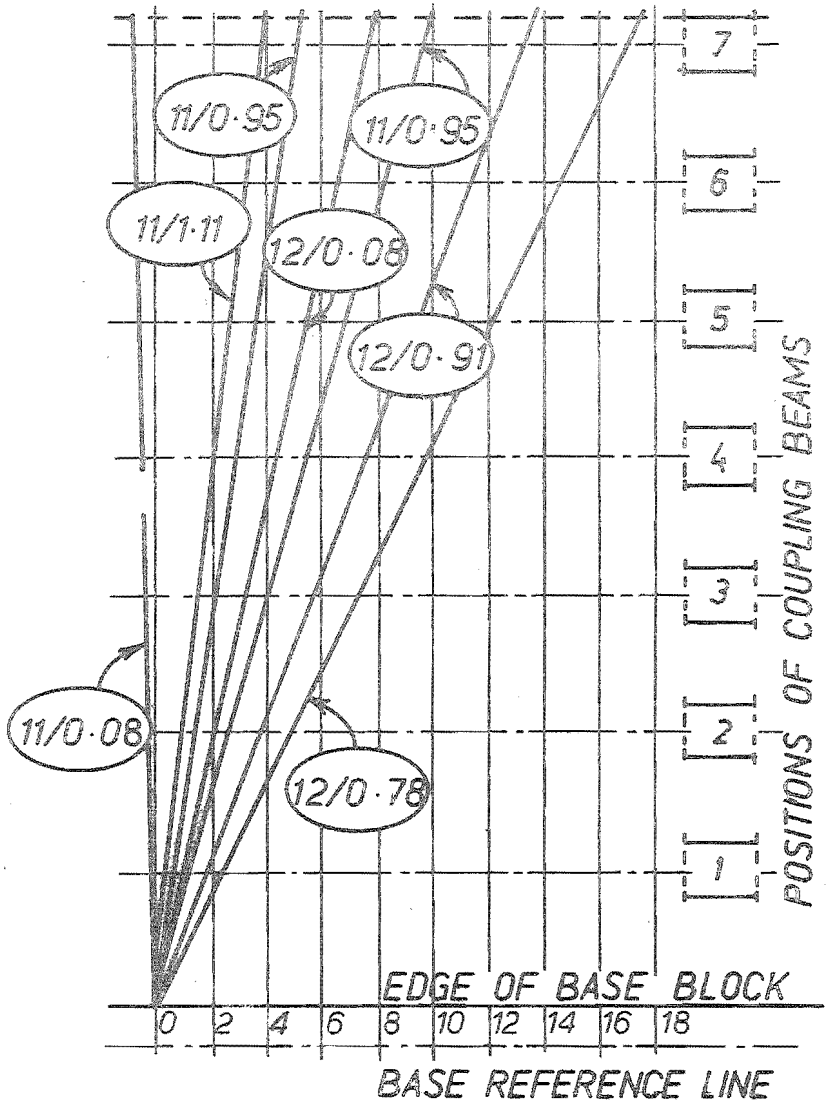

(d) Cycles 11 and 12
(Note different scale)

FIG. 6.19 DEFLECTIONS OF THE WALL DURING THE VARIOUS CYCLES

was 11.5" . The deflection profiles show that the walls are nearly straight above the bottom floor and that the major portion of the wall rotations occur at the base.

6.7.6 Elongation of the Walls

The accumulation of tensile strains of the reinforcement makes both the walls elongate during cyclic loading. Using the measurements made on the targets in the top floor the elongation of both walls relative to the base reference line was computed as outlined in Appendix B. In Fig. 6.20, the elongation of both walls during cyclic loading is plotted against the load ratio. The left wall is subjected to tension during odd numbered cycles and to compression during even numbered cycles. It is seen that the contraction during the cycles in which the wall is subjected to compression is much less than the elongation during the cycles in which the wall is subjected to tension. At the end of each cycle the residual elongation of the walls increases. This is due to open cracks consequent to yielding of the flexural reinforcement. Progressive elongation of the walls after each cycle shows that these cracks have widened. This is due to the deterioration of bond between concrete and the main flexural bars at the base of the walls and filling of cracks with debris. During the final cycle, the tension wall experienced a significant contraction. With the collapse and contraction of the coupling beams the tension wall was pulled towards the compression wall. Hence the sliding of the tension wall along the potential crack at the base has contributed to this shortening. (See Fig. 6.32).

6.7.7 Curvature Variation along the Height of the Wall

Using the strain measurements made on the flexural steel of the walls, the curvature was computed for the various cycles. Fig. 6.21 shows the curvature variation for cycles 1 and 5. The theoretical curvature was computed for the lateral load $0.5\ P_u^*$ based on the

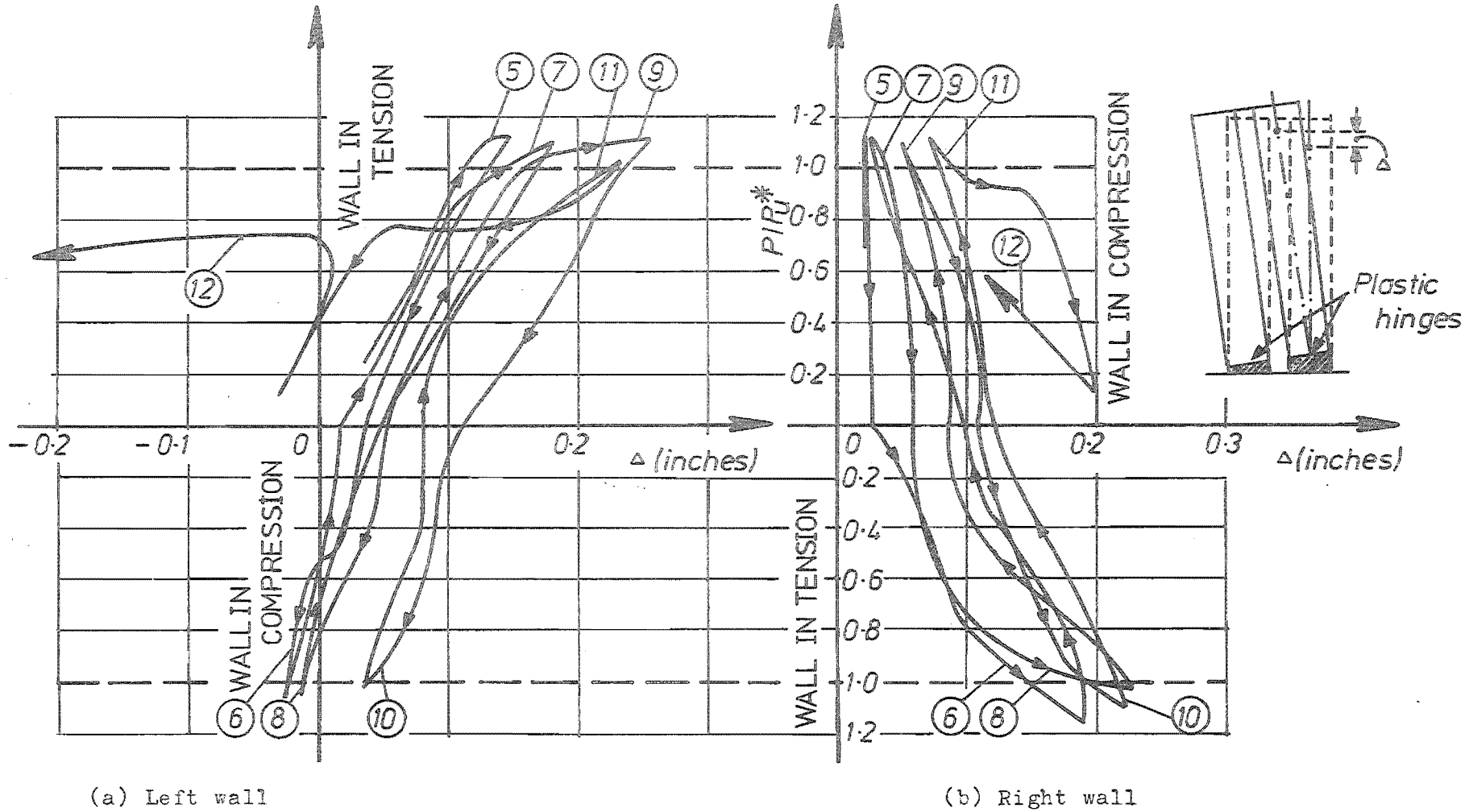

(a) Left wall

(b) Right wall

FIG. 6.20 THE ELONGATION OF WALL A AT THE TOP FLOOR RELATIVE TO THE BASE REFERENCE LINE

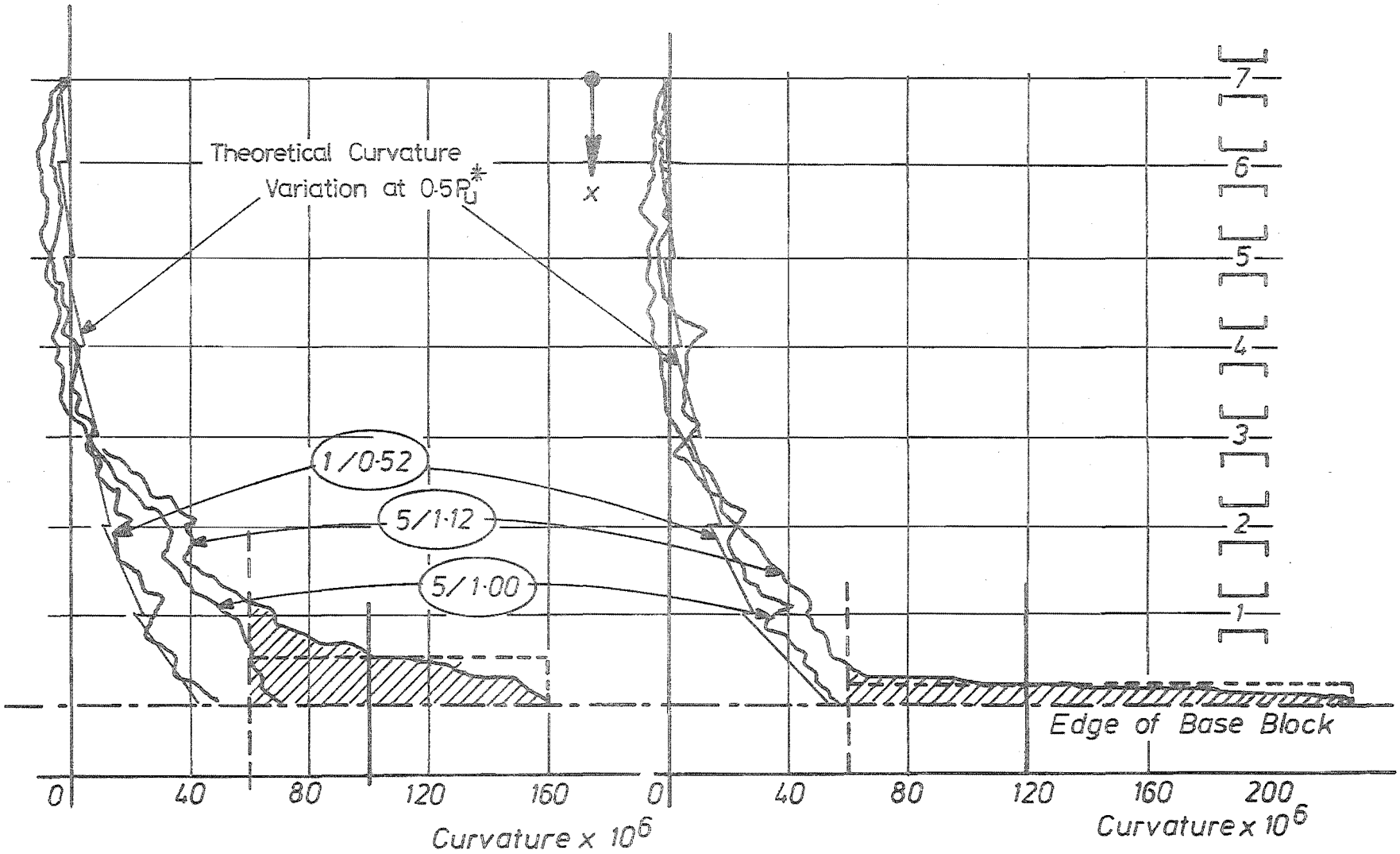

Left(Tension)Wall

Right (Compression) Wall

FIG. 6.21 COMPARISON OF CURVATURES OF TENSION AND COMPRESSION WALLS DURING CYCLES 1 AND 5

elasto-plastic analysis presented in Chapter 4, and the load-moment-property curves (see Chapter 3). This theoretical curvature variation is shown in stepped lines in Fig. 6.21. The figure shows that the theoretical and observed curvatures correlate well in the lower storeys. In the upper storeys the observed results, and those predicted, are significantly different. The curvatures in the upper storeys are very small. In the upper storeys the variations introduced by cracking and by the disturbance from the forces in the coupling beams are considerably larger than the strains due to wall moments.

Two theoretical limits of curvature are indicated in the plastic hinge region. For the tension wall the broken lines represent the onset of yield in the outermost bar on the tension side of the neutral axis. The full line represents the yield in the middle layer of reinforcement on the tension side , or the yield in the single layer of reinforcement on the compression side.

Fig. 6.22 shows the curvature variation in the bottom two floors in the left wall during the various cycles. This wall is subjected to axial tension during the odd numbered cycles. In the same figure the following theoretical curvatures based on the load-moment-curvature relationship are also shown:

(A) Onset of yield in the outermost bar in tension, or the concrete on the compression face reaching a strain of 0.001.

(B) Yielding of the middle layer of the bar in tension or concrete strain of 0.002 in the compression face.

(C) Theoretical maximum curvature based on a maximum concrete strain of 0.003.

It is seen that the theoretical maximum curvatures predicted by the analysis are exceeded in the compression wall. By the time the theoretical maximum curvature is attained in the tension wall the compression wall is subjected to nearly twice the maximum theoretical curvature predicted by the line(C). The estimated maximum concrete strain in the extreme fibre of the compression wall at this stage is

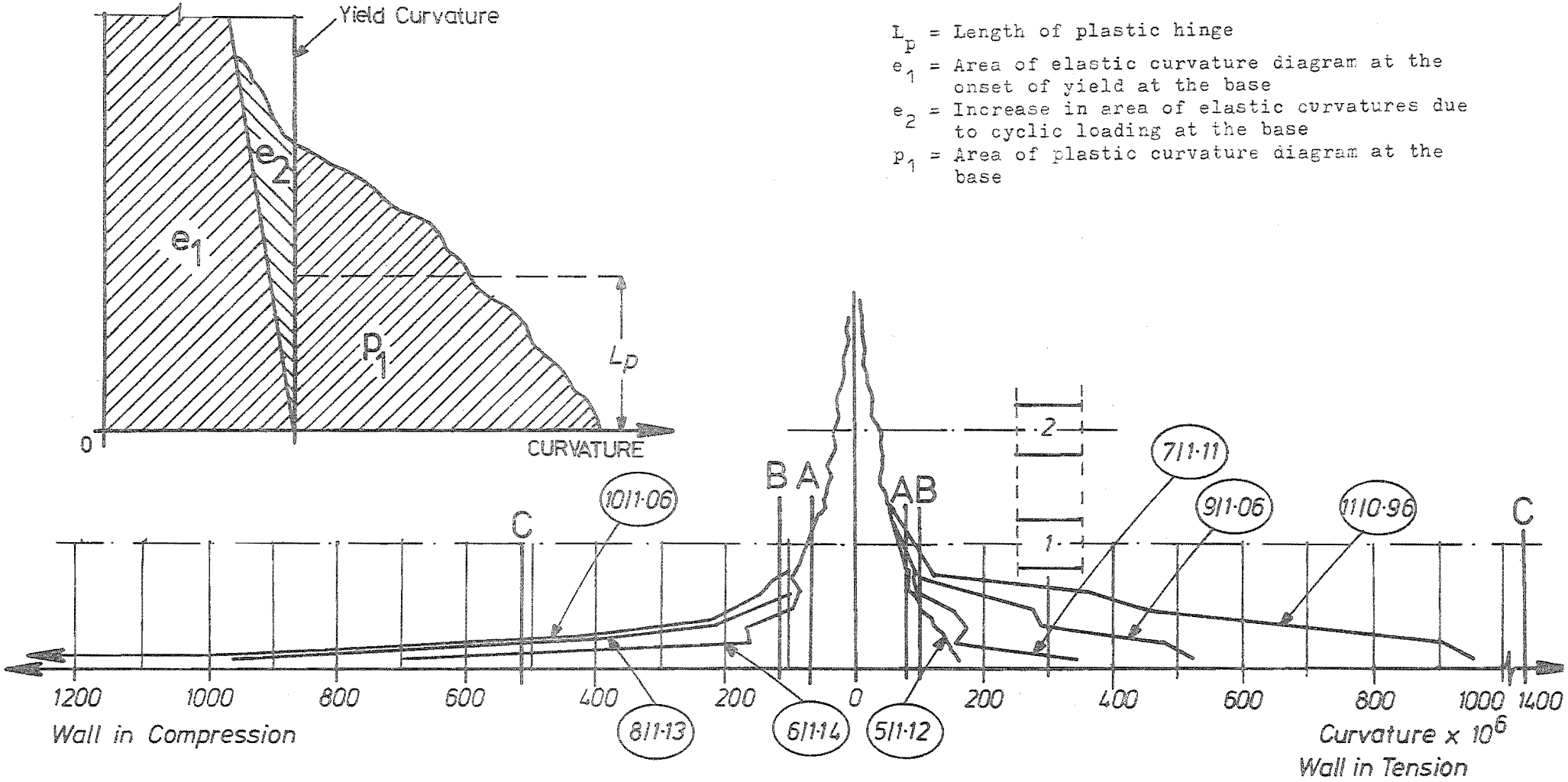

FIG. 6.22 CURVATURE VARIATION OF THE LEFT WALL IN THE PLASTIC HINGE REGION

approximately 0.009 . The figure shows that with cyclic loading the plastic hinge lengths and the maximum curvatures attained increased. Inclined diagonal cracking, deterioration of the bond between steel and the surrounding concrete and consequent spreading of yielding length of the tension steel have contributed to this increase. The area enclosed by the curvature curve and the vertical wall axis in the plastic hinge region is a measure of the total rotation which occurs at the base of the wall. The spreading of this area at approximately the same maximum load levels shows that more energy is absorbed by the plastic hinges at the base of the walls in the later cycles.

6.7.8 Relationship Between the Length of Plastic Hinge, Maximum Curvature, Wall Rotation and the Top Floor Displacement

The shaded area in Fig. 6.21 represents the plastic rotation that occurs at the plastic hinges in the tension and compression walls after the onset of yield in the walls. It is seen that the length of plastic hinge for the tension wall, Lp_t , is larger than that in the compression wall, Lp_c . The maximum curvature for the compression wall, φ_{uc} , is large compared with the maximum curvature for the tension wall, φ_{ut} . These are in accordance with Eq. (4.22) derived in Chapter 4. This equation gives the relationship between the length of plastic hinges, the maximum curvatures attained and the total base rotation for the two walls. Accordingly the shaded area of the tension wall, θ_{pt} should be equal to the shaded area of the compression wall, θ_{pc}. To make this comparison the shaded area is replaced by an approximate equivalent rectangle shown with broken lines. The plastic rotations based on these equivalent rectangles shown in Fig. 6.21 are:

$$\theta_{pt} = Lp_t \times \varphi_{ut} = 16 \times 100 \times 10^{-6} = 1600 \times 10^{-6}$$
$$= 0.0917^{o}$$

$$\theta_{pc} = Lp_c \times \varphi_{uc} = 8 \times 180 \times 10^{-6} = 1440 \times 10^{-6}$$
$$= 0.0825^{o}$$

The difference between θ_{pt} and θ_{pc} is due to the approximations involved and the different elongations in the coupling beam. The top floor deflection due to plastic rotation at the base of the walls at the end of the 5th cycle is

$$\Delta pw = \theta_p H = 1600 \times 10^{-6} \times 205 = 0.34" .$$

The top floor deflection due to elastic curvatures along the height, Δew, is

$$\Delta ew = \int_0^H \varphi dx$$

This elastic deflection, based on the curvature diagram for cycle 5 at $1.12\ P_u^*$ shown in Fig. 6.21, is $0.90"$. The total measured top floor deflection was $\Delta = 1.45"$ at this stage.

The top floor deflection due to shear, Δs, and due to rotation occurring in the foundation block, Δfb, could not be determined individually. The sum of these deflections were computed as

$$\Delta s + \Delta fb = \Delta - (\Delta ew + \Delta pw)$$

For cycle 5, this is $(\Delta s + \Delta fb)_{cycle\ 5} = 1.35 - (0.90 + 0.34)$

$$= 0.21".$$

Table 6.1 shows the contribution of different actions (elastic bending along the height, plastic rotation at the base, shear, rotation occurring in the end block) to the top floor deflection during the various high intensity cycles at the maximum deflections attained. An examination of the table shows that:

TABLE 6.1 A COMPARISON OF THE CONTRIBUTIONS OF DIFFERENT ACTIONS TO THE TOP FLOOR DEFLECTION FOR THE VARIOUS HIGH INTENSITY CYCLES AT MAXIMUM DEFLECTIONS ATTAINED

(Deflections are given in inches)

Cycle	Total Measured Top Floor Deflection Δ.	Contribution of					
		Elastic Curvature along the height of the wall, Δel		Plastic Curvature * in the plastic hinge region, Δpw		Shear Deformation and the deformation due to rotation occurrence in the foundation block, Δs + Δfb	
		Δel	% of Δ	Δpw	% of Δ	Δs + Δfb	% of Δ
5	1.45	0.90	62	0.33	23	0.22	15
6	2.11	0.95	45	0.80	38	0.36	17
7	2.39	0.97	40	0.97	45	0.45	19
8	2.66	0.99	37	1.14	43	0.53	20
9	3.39	1.00	29	1.73	51	0.66	20
10	3.01	1.01	34	1.44	48	0.57	18
11	4.15	1.10	26	2.14	52	0.91	22

* For cycles during which strain measurements were not taken when maximum deflection was attained, extrapolated strain readings based on measurements made at earlier increments were used to compute the curvatures along the height of the wall.

(a) During cycle 5, the contribution of plastic rotation at the base of the wall to the top floor deflection is small. With cyclic loading the contribution of plastic rotation at the bottom of the wall to the top floor deflection increases, reaching a maximum of 52% for the final cycle. This is due to an increase in the length of plastic hinge as well as the increase in curvatures attained.

(b) The elastic deflection increases with cyclic loading. This is due to an increase in area e_2 (see insert in Fig. 6.22) with increases in the plastic hinge length. This increase is small, however, compared with the increase in area of the plastic curvature, ρ_1. Hence the deflections caused by elastic curvatures along the height remain sensibly constant.

(c) This total elastic deflection of approximately 1", which has been evaluated from curvature measurements, agrees well with the observed deflection at the top floor at the onset of yield in the walls. (1.15" for cycle 5 shown in Fig. 6.12). The observed deflection includes the elastic rotation occurring in the foundation block and shear deformation in the walls.

(d) During cycle 5, 62% of the top floor deflection results from the elastic curvatures. The deflection profile of the walls (see Fig. 6.19.b) is practically straight above the first floor level. This shows that the major portion of elastic rotation occurs also at first floor level. An examination of the curvature diagram (Fig. 6.21) at 1.12 P_u^* during cycle 5 confirms that the major portion of elastic rotations occurs at the first floor level.

(e) The contribution of end block rotation and shear to the top floor deflection is 15% during cycle 5 and in the final cycle this increases to 22% .

6.8 CRACK FORMATION, CRACK WIDTH MEASUREMENTS AND FAILURE MECHANISM

During the accidental load, diagonal cracks had formed in all the coupling beams and in the bottom storey of the walls. Before the start of the test these cracks were marked O-O at both ends. These cracks can be seen in the photographs taken during cycle 1 which are presented in Fig. 6.24 to Fig. 6.31. There were only a few cracks at the base of the compression wall (see Fig. 6.32.a). The cracks which formed at the junction of the coupling beams and the walls were wider than the diagonal cracks in the coupling beams, indicating that the flexural steel in the coupling beams situated near the critical region (2nd, 3rd and 4th floor beams) had yielded. A comparison of crack widths at no load before the start of the test at locations 2B, 3B, 4B and 5B with the widths at 2A, 3A, 4A, 5A in Fig. 6.23 shows this. As pointed out in Section 6.4 the diagonal cracks, as well as those that formed at the junction of the beam and the wall did not cross the gauge lengths provided. The close-up photographs of the coupling beams taken during cycle 1, reproduced in Figs.6.25 to 6.30,show this. The maximum load during the first cycle was less than the estimated maximum load during the accident. Only a few new flexural cracks in the bottom floor of the compression wall formed across the single layer of tension reinforcement.

During the second cycle, the first significant cracks near the tension corners of the second floor coupling beam developed at a load of 0.15 P_u^* . These were accompanied by cracks along the diagonal across the cracks formed during the accidental loading. This can be seen in the photographs taken at the beginning of cycle 3, reproduced in Figs. 6.25 to 6.30. The first significant crack in the tension wall appeared at a load of 0.2 P_u^* . These formed across the tension reinforcement approximately at right angles to the line of the reinforcement. These were accompanied by diagonal cracks which can be seen in Fig. 6.32.b.

The maximum load during cycle 3 and cycle 4 were of the order of

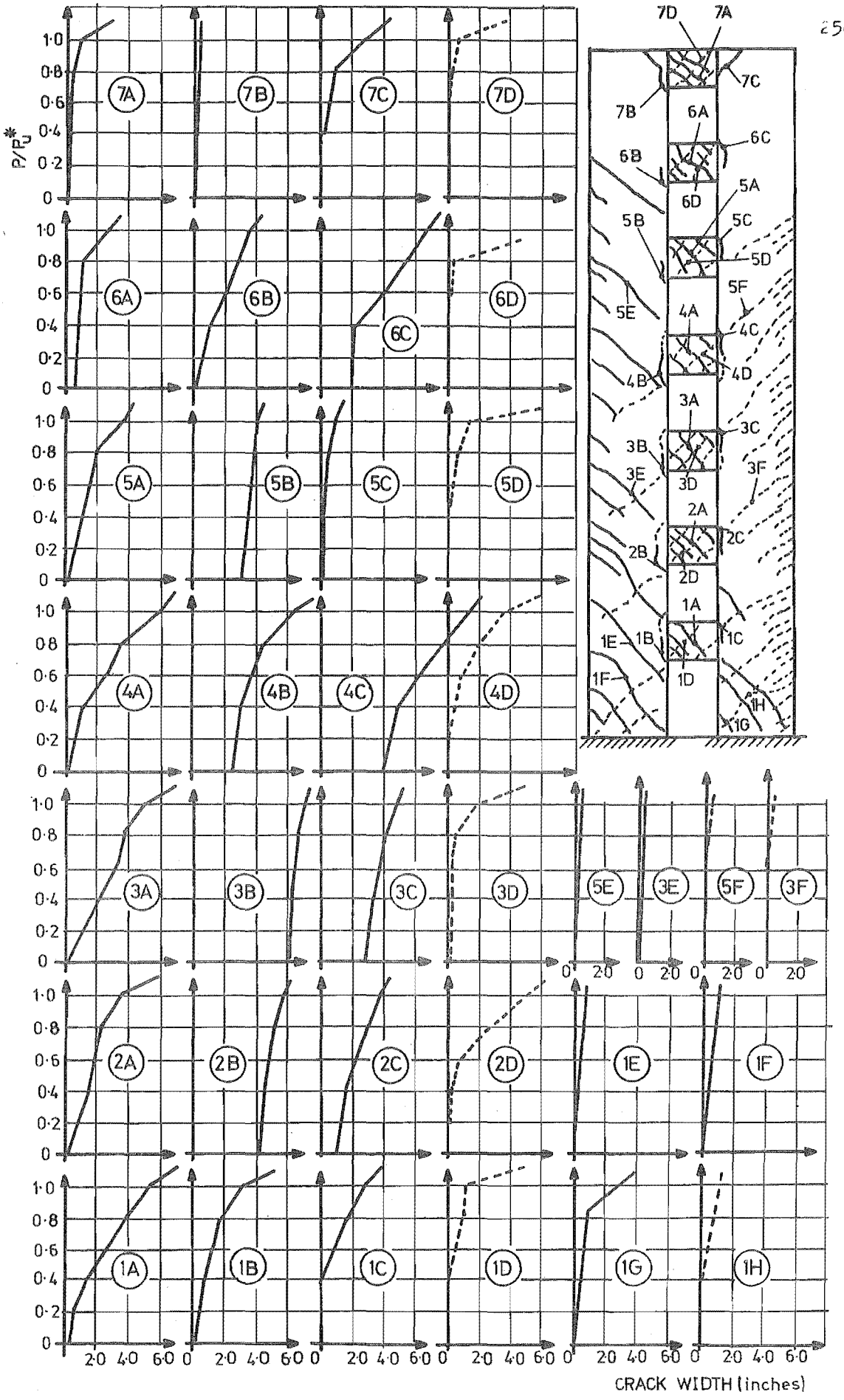

FIG. 6.23 CRACK WIDTHS MEASURED DURING POSITIVE AND NEGATIVE LOADING

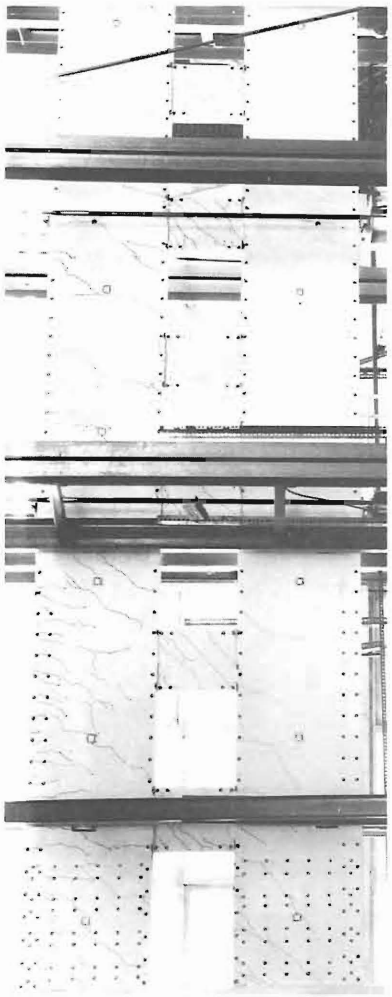

(a) First load cycle

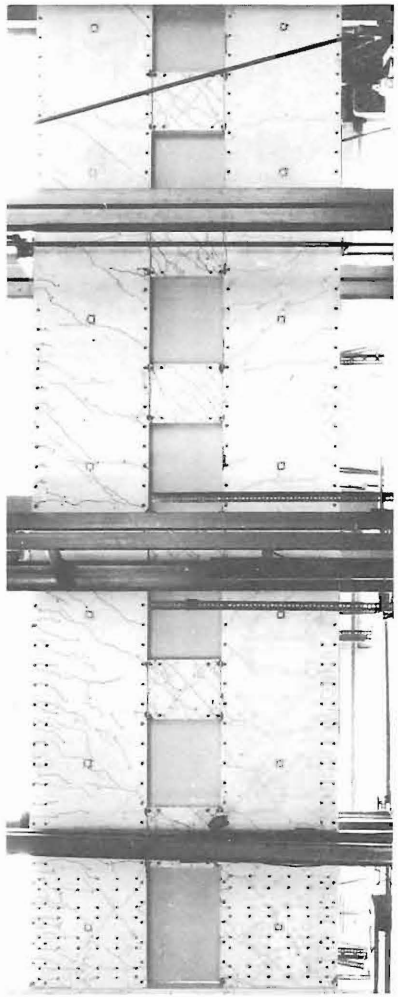

(b) Seventh load cycle

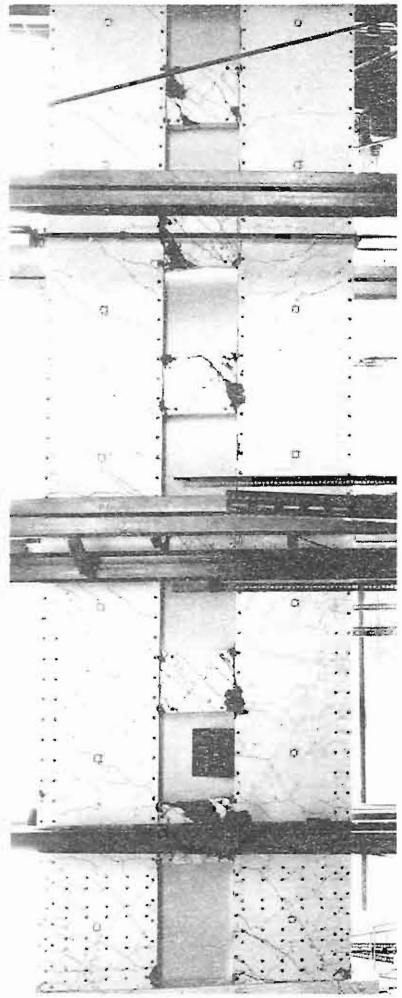

(c) Eleventh load cycle

FIG. 6.24 CRACK PATTERNS OF SHEAR WALL A

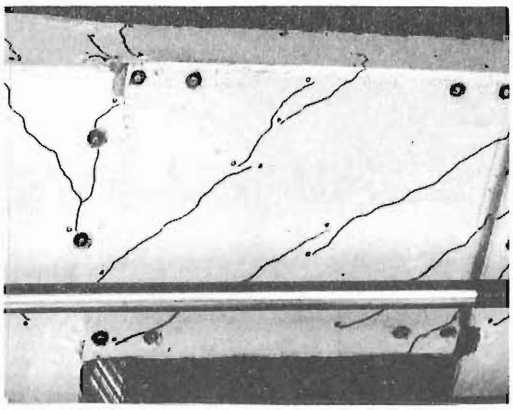

Cycle 1

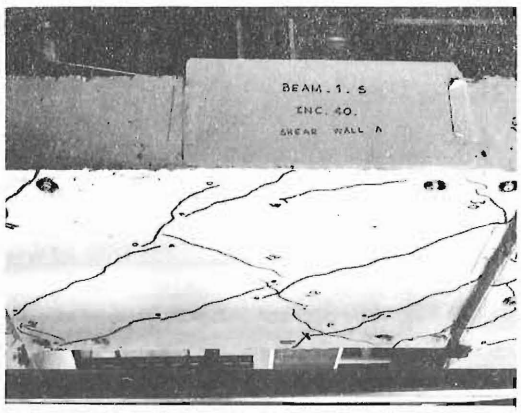

Cycle 3

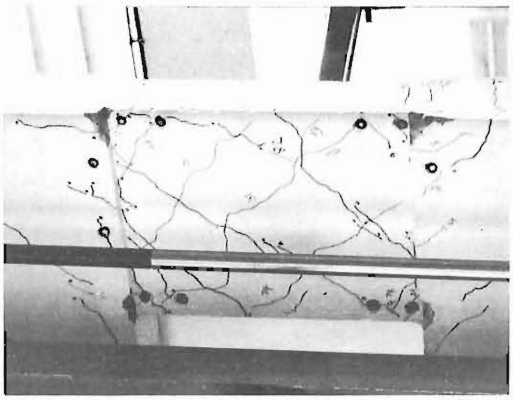

Cycle 6*

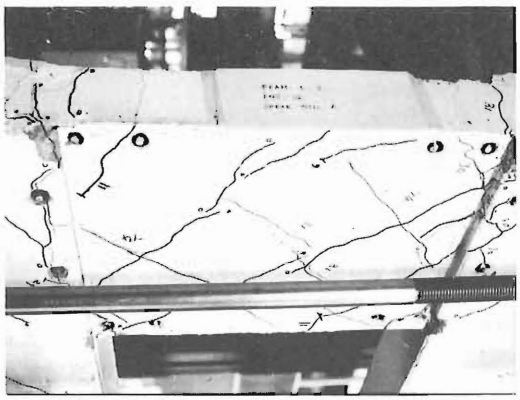

Cycle 10

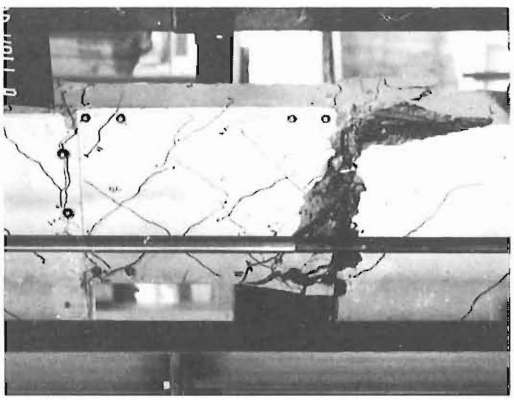

Cycle 11

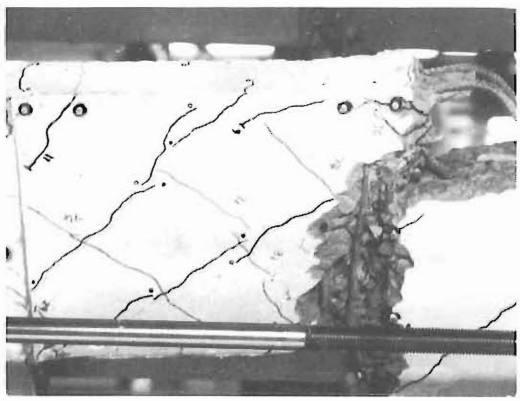

Cycle 12

* photograph taken from the North side

FIG. 6.25 TOP FLOOR BEAM DURING CYCLIC LOADING

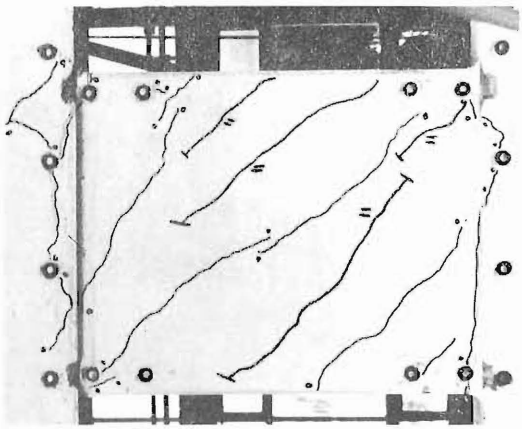

Cycle 1

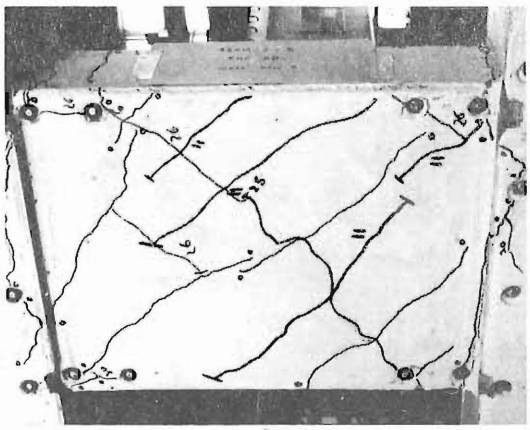

Cycle 3

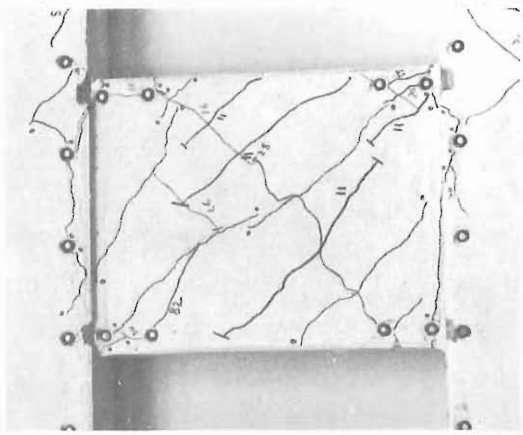

Cycle 5

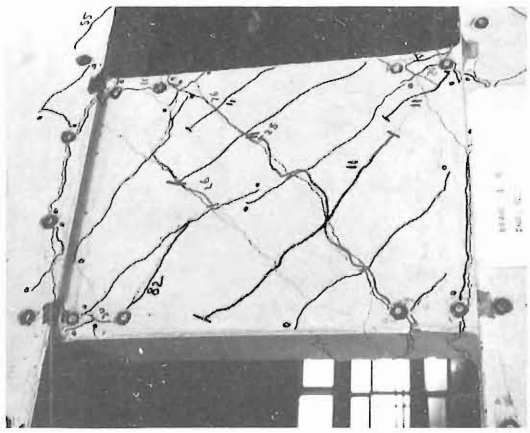

Cycle 10

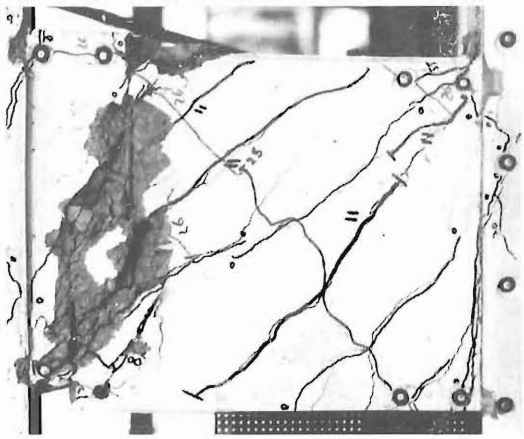

Cycle 11

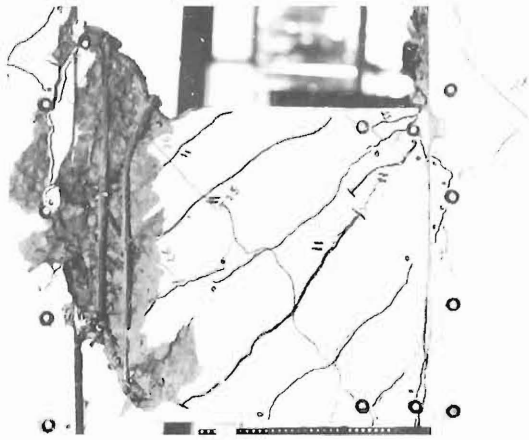

Cycle 12

FIG. 6.26 6TH FLOOR BEAM DURING CYCLIC LOADING

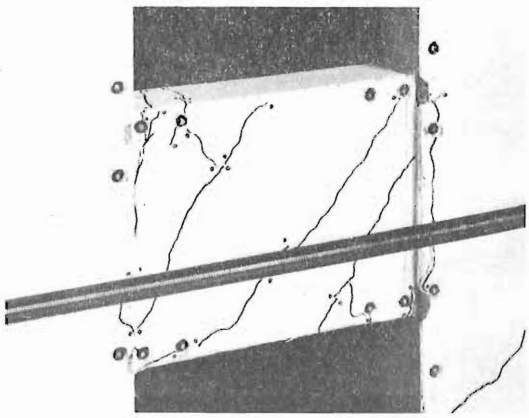

Cycle 1

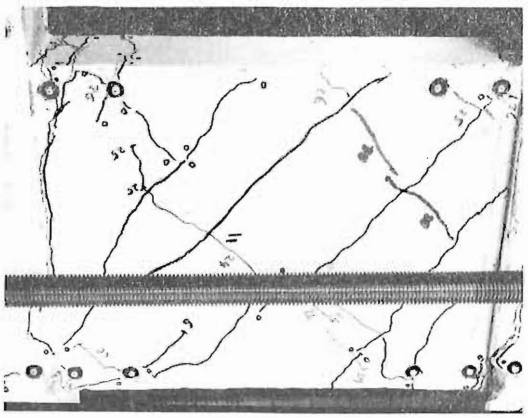

Cycle 3

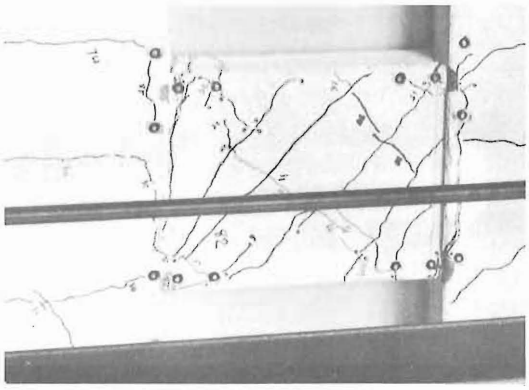

Cycle 6

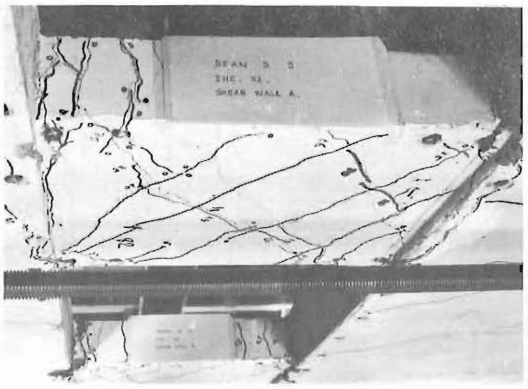

Cycle 10

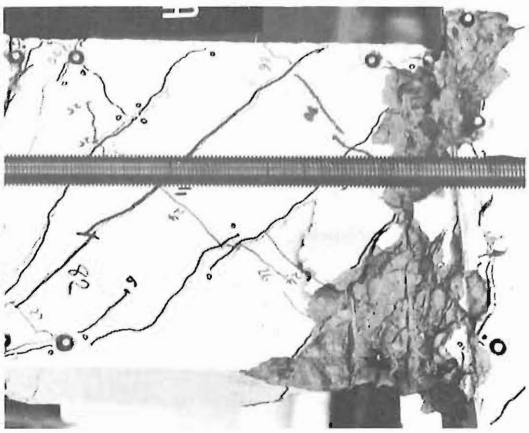

Cycle 11

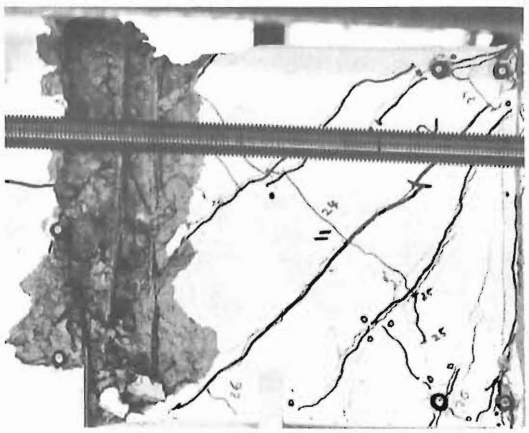

Cycle 12

FIG. 6.27 5TH FLOOR BEAM DURING CYCLIC LOADING

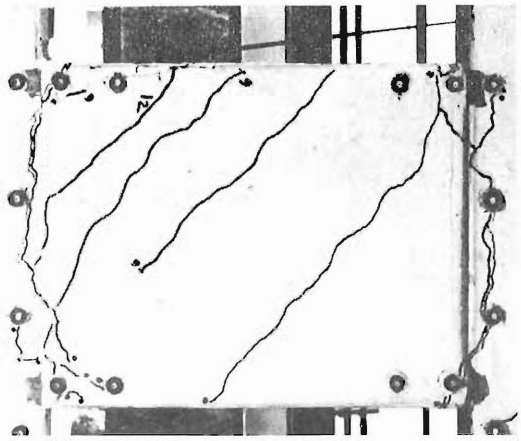

Cycle 1

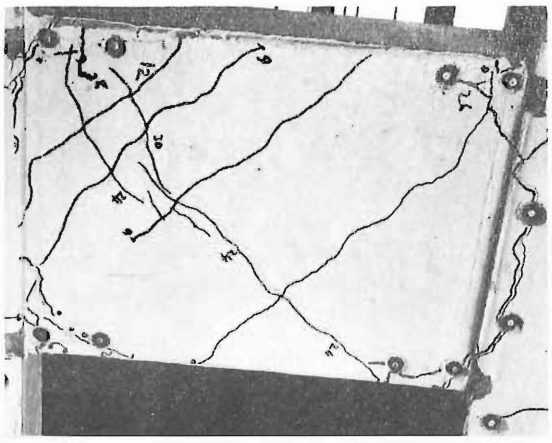

Cycle 3

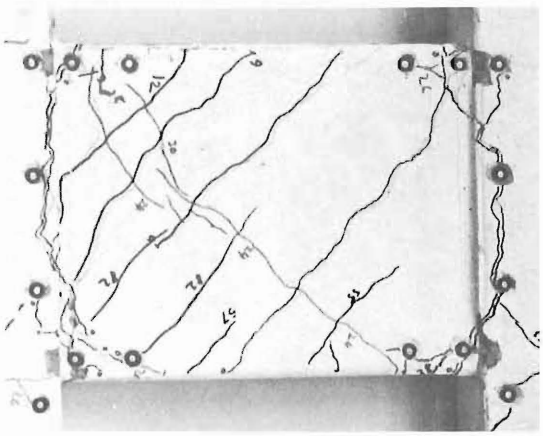

Cycle 6

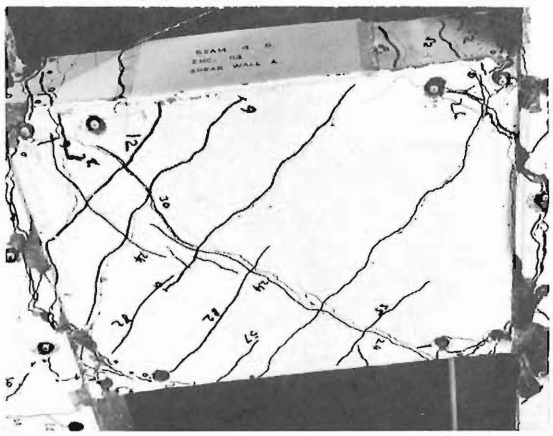

Cycle 10

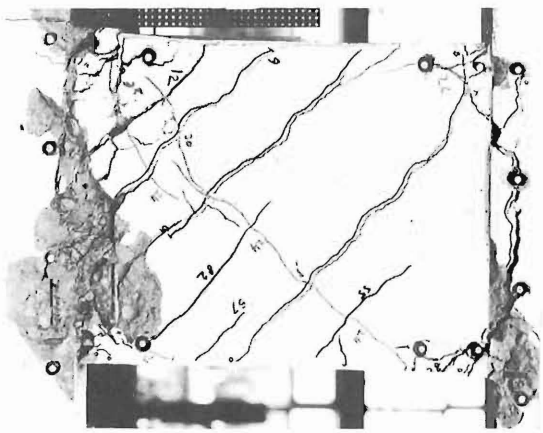

Cycle 11

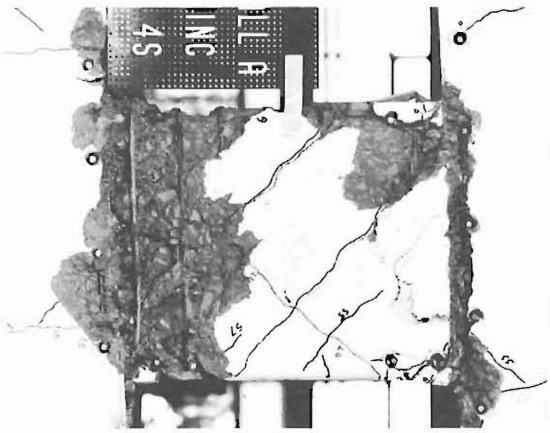

Cycle 12

FIG. 6.28 4TH FLOOR BEAM DURING CYCLIC LOADING

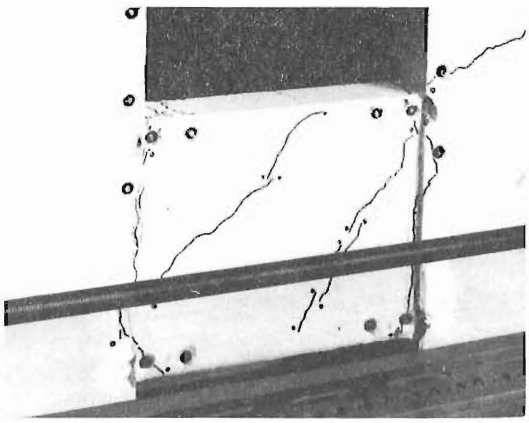

Cycle 1

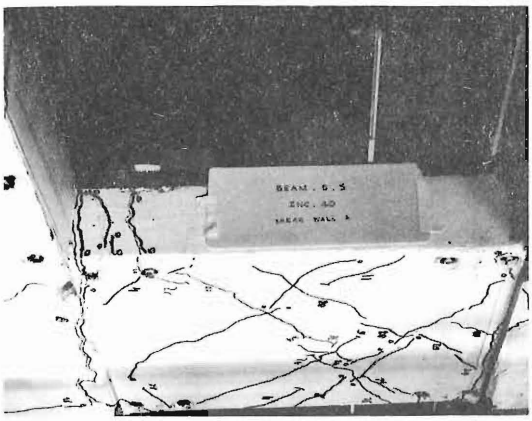

Cycle 3

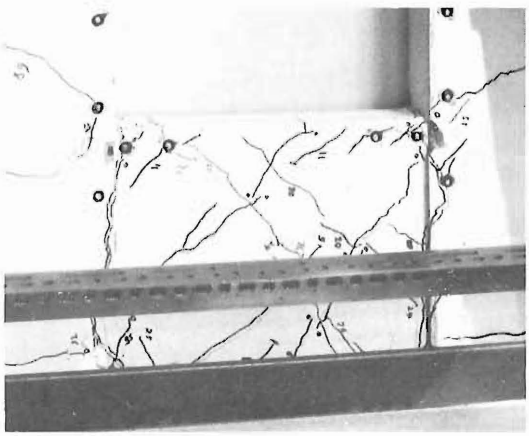

Cycle 6

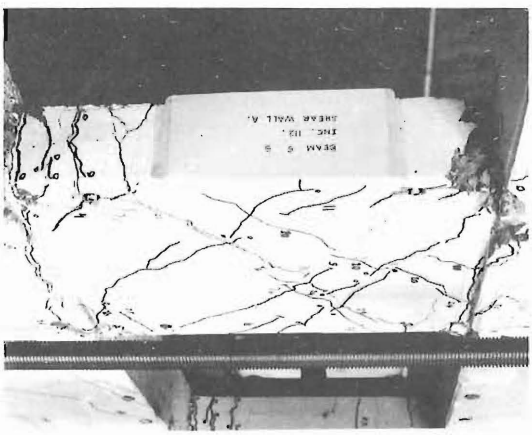

Cycle 10

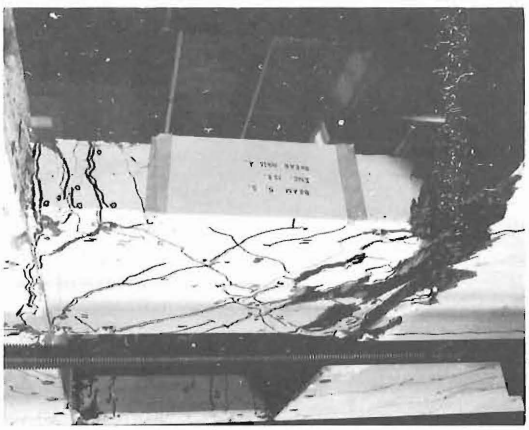

Cycle 11

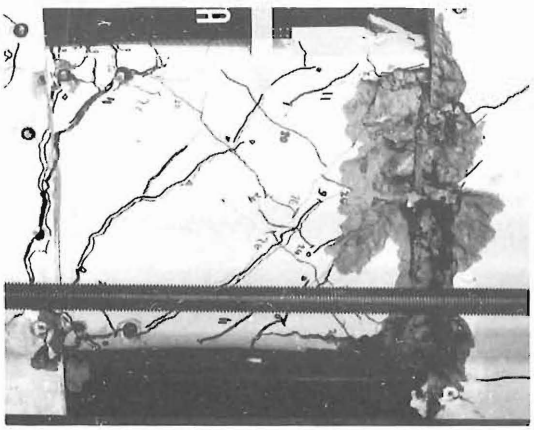

Cycle 12

FIG. 6.29 3RD FLOOR BEAM DURING CYCLIC LOADING

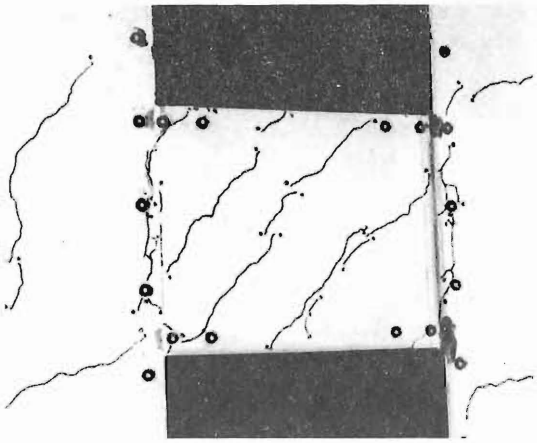

Cycle 1

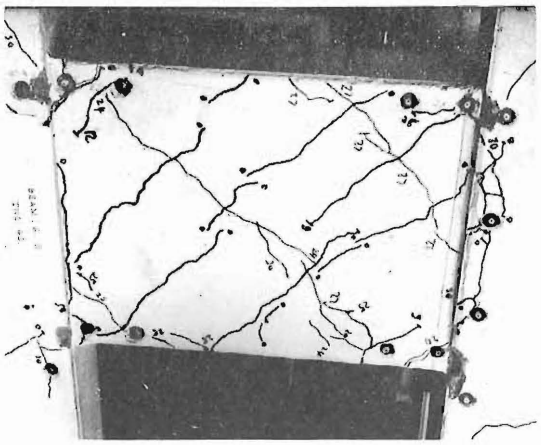

Cycle 3

Cycle 6

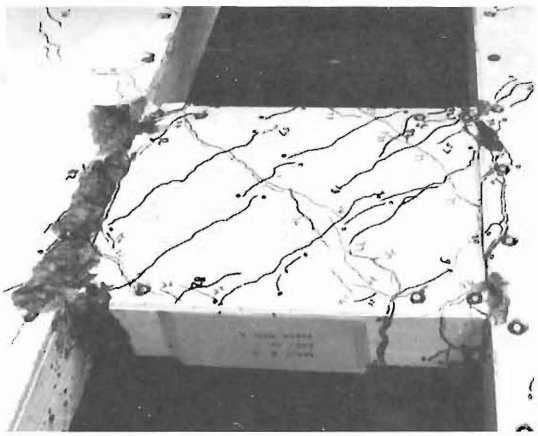

Cycle 10

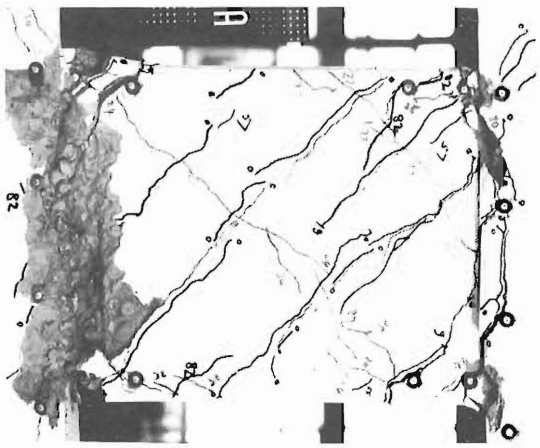

Cycle 11

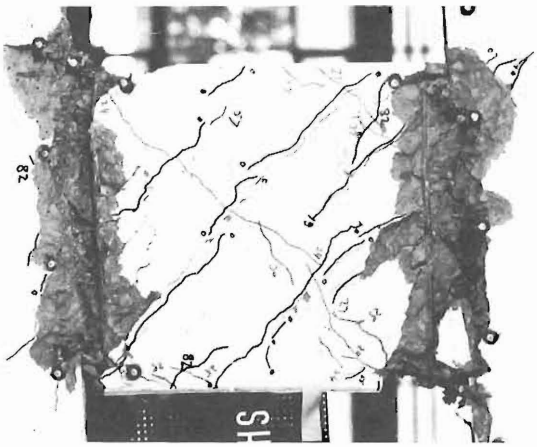

Cycle 12

FIG. 6.30 2ND FLOOR BEAM DURING CYCLIC LOADING

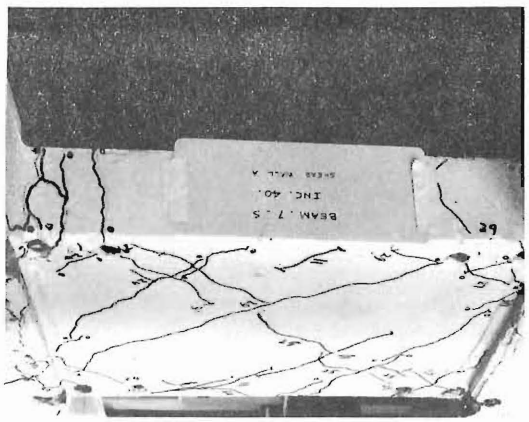

Cycle 3

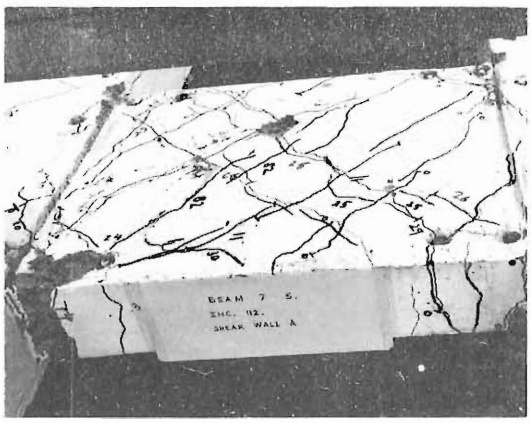

Cycle 10

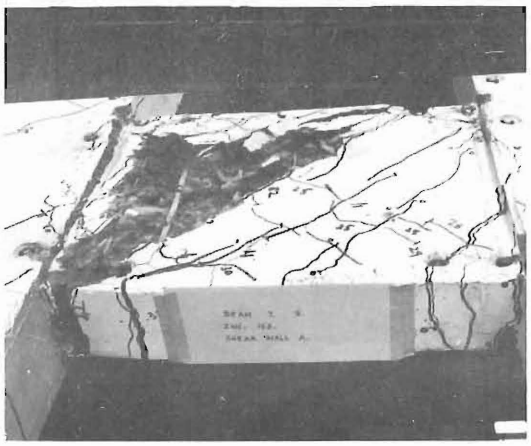

Cycle 11

Cycle 12

FIG. 6.31 BOTTOM FLOOR BEAM DURING CYCLIC LOADING

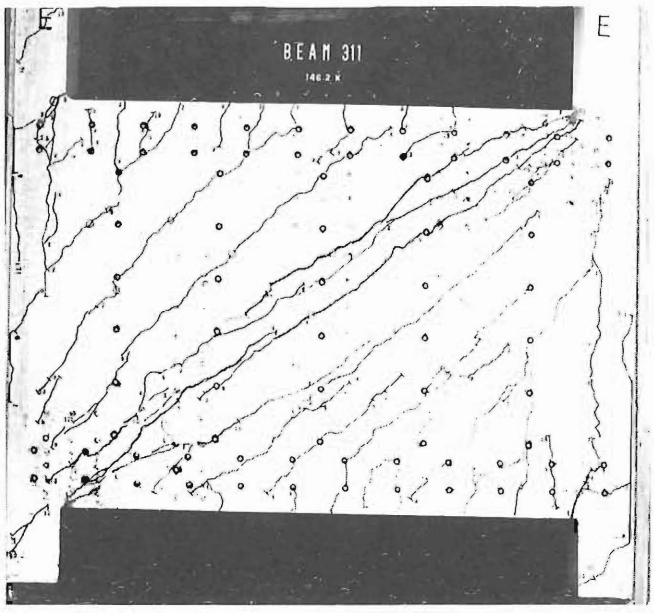

FIG. 3.1.h. CRACK PATTERN IN A TYPICAL CONVENTIONALLY REINFORCED BEAM

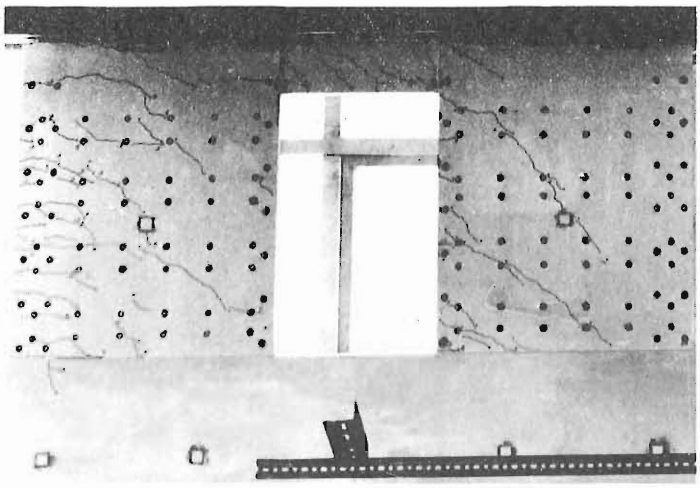

(a) Cycle 1

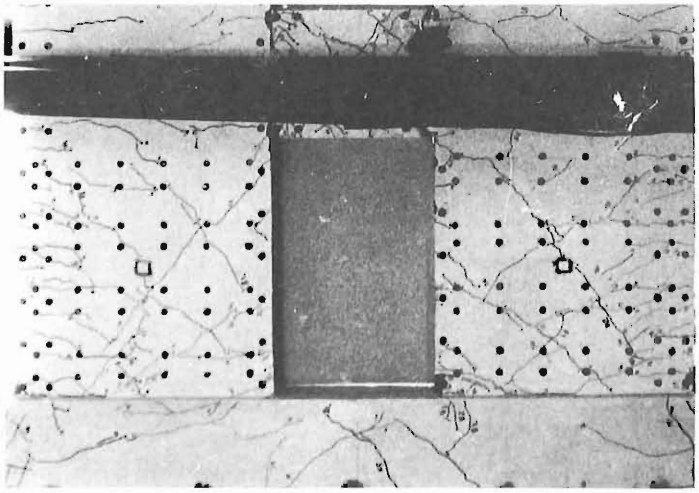

(b) Cycle 7

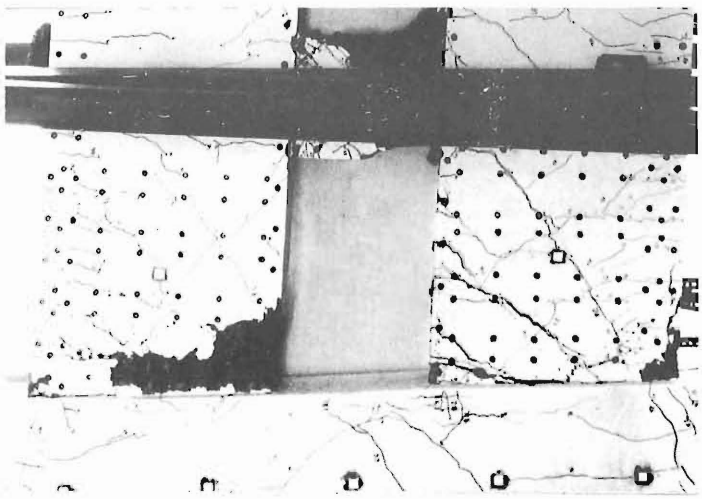

(c) Cycle 12

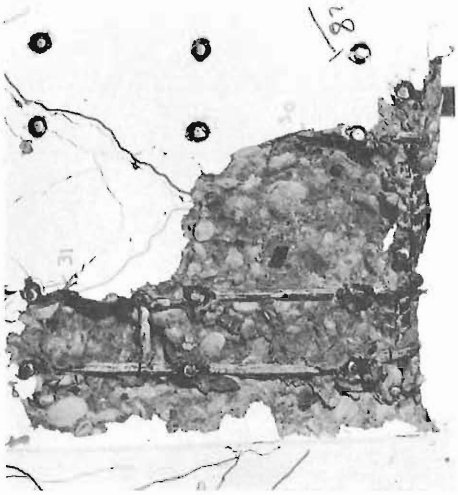

(d) Enlargement showing the buckling of single layer of reinforcement in the left wall

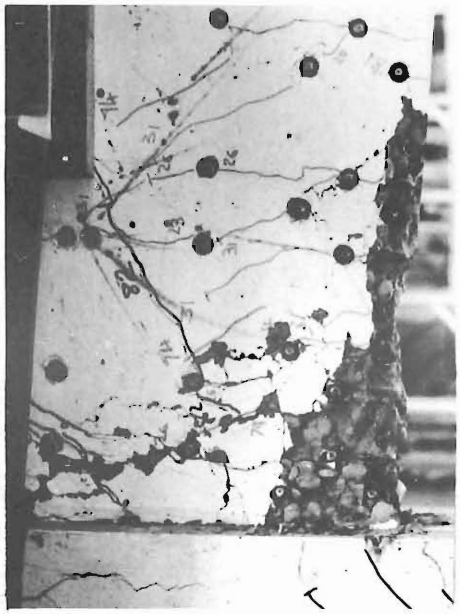

(e) Enlargement showing the destructed compression corner of the right wall

FIG. 6.32 CRACKS FORMED IN THE WALLS IN THE BOTTOM FLOOR

$0.4\ P_u^*$. Very few new cracks developed during these "elastic" cycles.

Cycle 5 and cycle 6 were high intensity load cycles. During each of these cycles the shear wall was loaded past the yield level. At the end of cycle 6 severe cracking developed in both walls in the bottom storey and also in all the coupling beams. Fig. 6.24.b shows the cracks that had developed during the first six cycles. This photograph was taken at the beginning of the seventh load cycle. The cracks in the bottom storey of the shear wall can be seen in Fig. 6.32.b. The photographs taken at ultimate load during cycle 6, reproduced in Figs. 6.25 to 6.32, show the cracks formed in the coupling beams.

During the subsequent high intensity cycles (cycles 7 to 10) the opening and closing of the cracks at the corners of the beam caused deterioration of the concrete. At the end of cycle 10, there were full depth cracks at the junctions of the beams and the walls in all except across the top coupling beam. This can be seen in Figs. 6.25 to 6.31. The concrete in the region of the full depth cracks had spalled off for the beams at the 2nd and 3rd floors. (See Fig. 6.29 and Fig. 6.30). At this stage both the walls were severly cracked in the bottom storey. However, the spalling of cover concrete had not yet occurred.

Cycle 11 caused rapid deterioration of all the beams with extensive spalling of concrete. The photographs taken during cycle 11 (Fig. 6. 25 to 6.31) shows this. Also the cover concrete spalled near the compression corner of both walls. However, in comparison to the beams the damage to the base of the walls was much less. Fig. 6.24.c shows this. This photograph was taken at maximum load during cycle 11. At this stage the shear displacement along the full depth cracks in the beams was noticeable (see Figs. 6.25, 6.26 and 6.30). The beams in the critical region were subjected to a shear displacement of the order of 1 to $1\frac{1}{2}$ inches.

The crack widths measured during cycles 1 to 6 are shown in Fig. 6.23. The key diagram gives the locations at which these crack width measurements were made. In this diagram the cracks formed during positive loading are shown in full lines. The crack widths at zero load at locations 5B, 4B, 3B, 2B, 4C, 3C and 2C refer to the start of the test. The crack widths in the coupling beams situated near the critical region are larger than at the top of the shear wall. A comparison of crack width at 1.00 P_u^* for the locations 2A, 3A and 4A with the crack width for location 7A shows this. The deterioration of bond and the consequent spread of yield length were more for the beams in the critical region. This resulted in full depth wide cracks for beams in the critical region (see Figs. 6.25 and 6.30 - cycle 10). As pointed out in Section 6.7.4 this has contributed to larger elongation increases for the beams in this critical region. During cycles 5 and 6 the increase in the width of the major diagonal crack across the beams is more than the corresponding increase at the junction of the wall and the beams. A comparison of the width of the cracks measured at 3B, 3C, with those measured at 3A, shows this. Measurements at 1D to 7D show that at ultimate load the width of the cracks is larger during the reversed loading than during positive loading,

The crack widths measured in the bottom storey of the walls are significantly larger than those measured at the top of the structure. A comparison of crack widths at locations 5E, 3E, 5F, 3F, with those measured at 1G, 1F, 1H and 1E, shows this. A comparison of crack widths measured at 1F with those at 3A or 4A indicates that the beams in the critical region have undergone a larger extent of damage than the bottom storey of the walls.

The failure was initiated in the tension wall during cycle 11. The compression face of the tension wallwas provided with only one layer of No. 5 bars. During the previous loadings this area was subjected to alternate opening and closing of the cracks. During cycle 11, the cover concrete at the junction of this wall and the base block spalled off.

Since the concrete in the narrow compression region of the tension wall had deteriorated, the single layer of steel had to transmit the major portion of the compression force. The stirrup spacing at the base of the walls was alternating between 2" and 4" to give an effective spacing of 3". Due to the compression force in the flexural steel and due to the ineffectiveness of the deteriorated concrete, the single layer of steel buckled outward between the two stirrups where the spacing was 4". This can be seen in Fig. 6.32.d.

The compression corner of the compression wall (Fig. 6.32.e) suffered comparitively minor damage. This compression zone had 5 layers of # 5 bars. Hence, even after the failure of tension wall, it could resist axial compression and the moment M_2 .

At this stage the coupling beams have seriously deteriorated. There were also large shear displacements in all the beams. The photographs taken during cycle 12 and presented in Figs. 6.25 to 6.31 show this.

During cycle 12, when the displacements were increased further, the left wall slid along the potential diagonal crack and along the weakest sections in the coupling beams forming sliding failure mechanism. Fig. 8.10.a. shows the model at the end of the test. The shear displacement of the beams and the destroyed compression corner of the tension wall can be seen in this photograph.

At the end of the test, when the top floor displacement was 14", the shear wall could hold a load of 0.75 P_u^* in a stable manner. This strength was derived from the forces transmitted across the failure cracks in the beams and base of the left wall by the dowel action and kink effect of the flexural reinforcement.

CHAPTER SEVEN

RESULTS OBTAINED DURING CYCLIC LOADING OF SHEAR WALL B

7.1 GENERAL

The results obtained during the cyclic loading of Shear Wall B are presented. The coupling beams of this specimen were diagonally reinforced. The reinforcement provided in the walls of both test structures was the same. The dimensions, details of reinforcment and the properties of materials for these models were included in Chapter 5.

7.2 ANALYTICAL ASSESSMENT OF FORCES AND MOMENTS IN THE COUPLING BEAMS AND WALLS

All coupling beams of this model possessed equal nominal strength both in flexure and shear. The strength of the walls of specimen A and B were approximately the same. However, the strength of the beams of Shear Wall B was 1.10 times those of Shear Wall A. Thus, the theoretical ultimate base shear of Shear Wall B (56.60 kips) was more than the theoretical ultimate load of Shear Wall A (51.6 kips). These theoretical loads were computed from mean steel and concrete strengths.

The estimated forces and moments on the model at ultimate load, as per the pattern defined in Chapter 5, are shown in Fig. 7.1. These forces and moments were computed using the elasto-plastic analysis described in Chapter 4 . The theoretical variations of laminar shear during different stages of loading are shown in Fig. 7.1.a. Figs. 7.1.b and c show the variation of axial force along the height of the model for the tension and compression walls

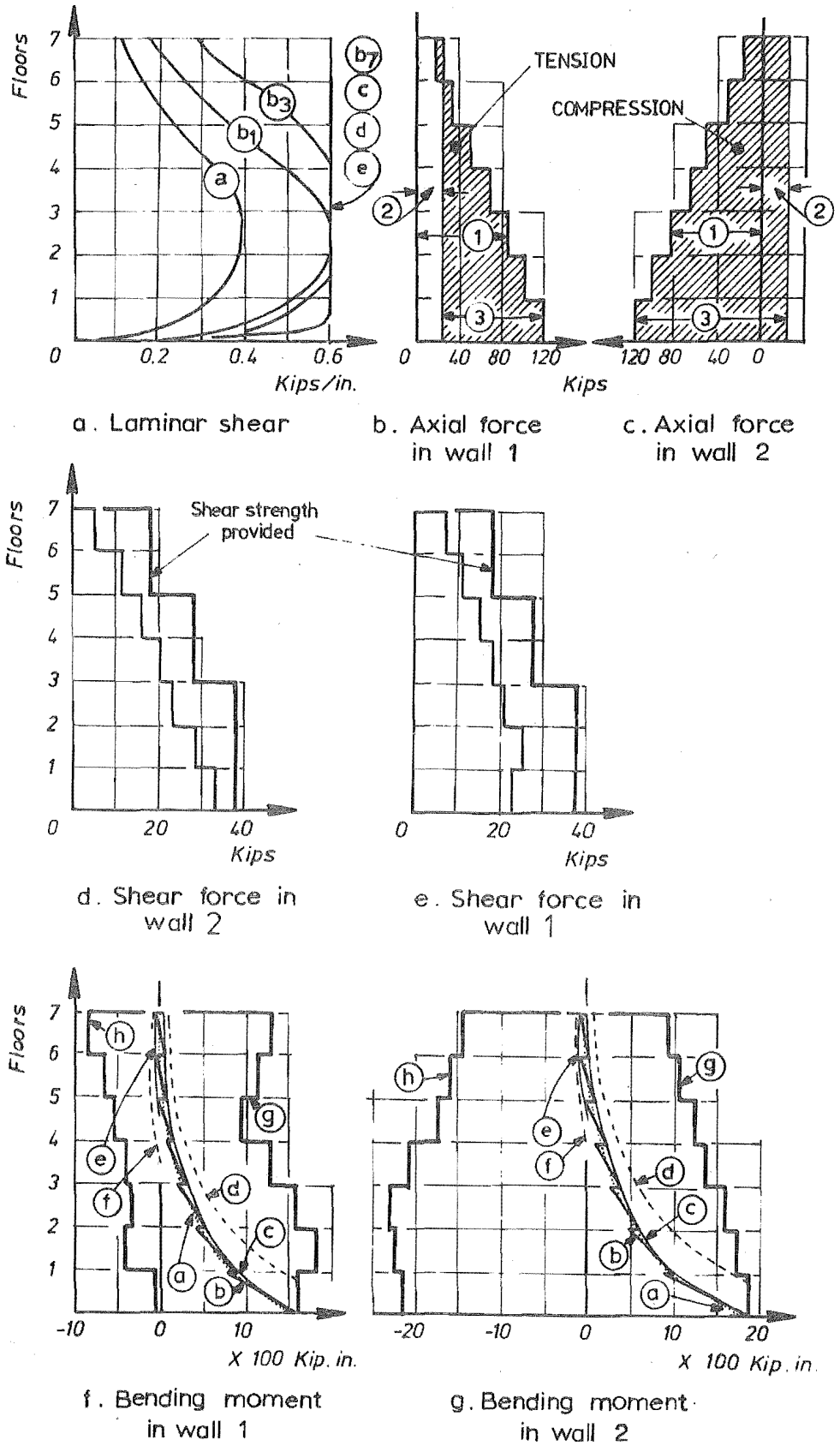

FIG. 7.1 ANALYTICAL ASSESSMENT OF FORCES AND MOMENTS IN THE COUPLING BEAMS AND WALLS OF SHEAR WALL B AND A COMPARISON OF THE STRENGTHS PROVIDED IN THE WALLS WITH THE MOMENTS AND FORCES DEVELOPED AT ULTIMATE LOAD

at ultimate load. The ordinates represented by (1) indicate the forces generated in the walls due to the accumulation of laminar shear. The ordinate (2), shows the uniform compressive force due to prestress. The shaded diagram, whose ordinates are represented by (3), indicates the net axial force in the walls.

Figs. 7.1.d and e show the variation of shear force in the compression and tension walls. The stepped thin line indicates the maximum external shear when the ultimate capacity of the wall is attained whereas the stepped thick line shows the reliable shear capacity provided, ignoring the contribution of concrete to shear strength.

Figs. 7.1.f and g show the variation of moments in the tension and compression walls where the curves are designated as follows:

(a) Moment variation for the laminar model at ultimate (Pointed line)

(b) Moment variation at ultimate taking into account the discrete nature of beams.

(c) Design envelope for positive moment.

(d) Displaced positive moment envelope for cut off of steel.

(e) Design envelope for negative moment.

(f) Displaced negative moment envelope for cut off of steel.

(g) Positive moment capacity provided.

(h) Negative moment capacity provided.

The moment capacities of the walls (curves (g) and (h)) were based on the reinforcement provided and the variation of estimated axial forces present at ultimate load. (Figs. 7.1.b and c). As in the case of Shear Warr A, the moment capacities provided at the base of the tension and compression walls were equal to the estimated maximum moments at ultimate load. The reason for the excess strengths of the walls in the top floor and for the reversed moments were discussed in Section 6.2.

7.3 LOADING

The load sequence is shown in Fig. 7.2. The loads acting from left to right, as shown in the insert, are considered positive when the model is viewed from the north side. The maximum load during the first two cycles was of the order of 0.15 P_u^* . This was less than the estimated cracking load.

During cycles 3 and 4 the maximum load was increased to approximately 0.4 P_u^* , and this was less than the estimated load required to yield the steel in the critical beam.

These load cycles were then followed by two cycles of moderate loading (cycles 5 and 6), during which yielding of the diagonal bars in the 1st, 2nd and 3rd floor coupling beams occurred. The load was less than that required to yield the flexural steel in the walls. Two elastic cycles followed with a maximum load intensity of 0.4 P_u^* .

Finally, 8 cycles of high intensity loading were applied. During each of these cycles the model was loaded so that the diagonal steel in all the beams and the flexural steel in both the walls yielded. After attaining the ultimate load, the model was subjected to increasing deformations till the predetermined top floor displacement was attained. This displacement was such that the overall ductility of the model attained during each of these cycles was at least 4 . During cycle 16, which was intended to be the last one, large plastic deformations were imposed till the model failed by buckling.

7.4 BEHAVIOUR OF DIAGONAL REINFORCEMENT IN THE COUPLING BEAMS

Each coupling beam was provided with eight 2 in demac gauge points on each face as shown in the key diagrams of Fig. 7.3.a. Figs. 7.3.a and b show the strain variation in the tension diagonal of all coupling beams. For positive loading the average of the

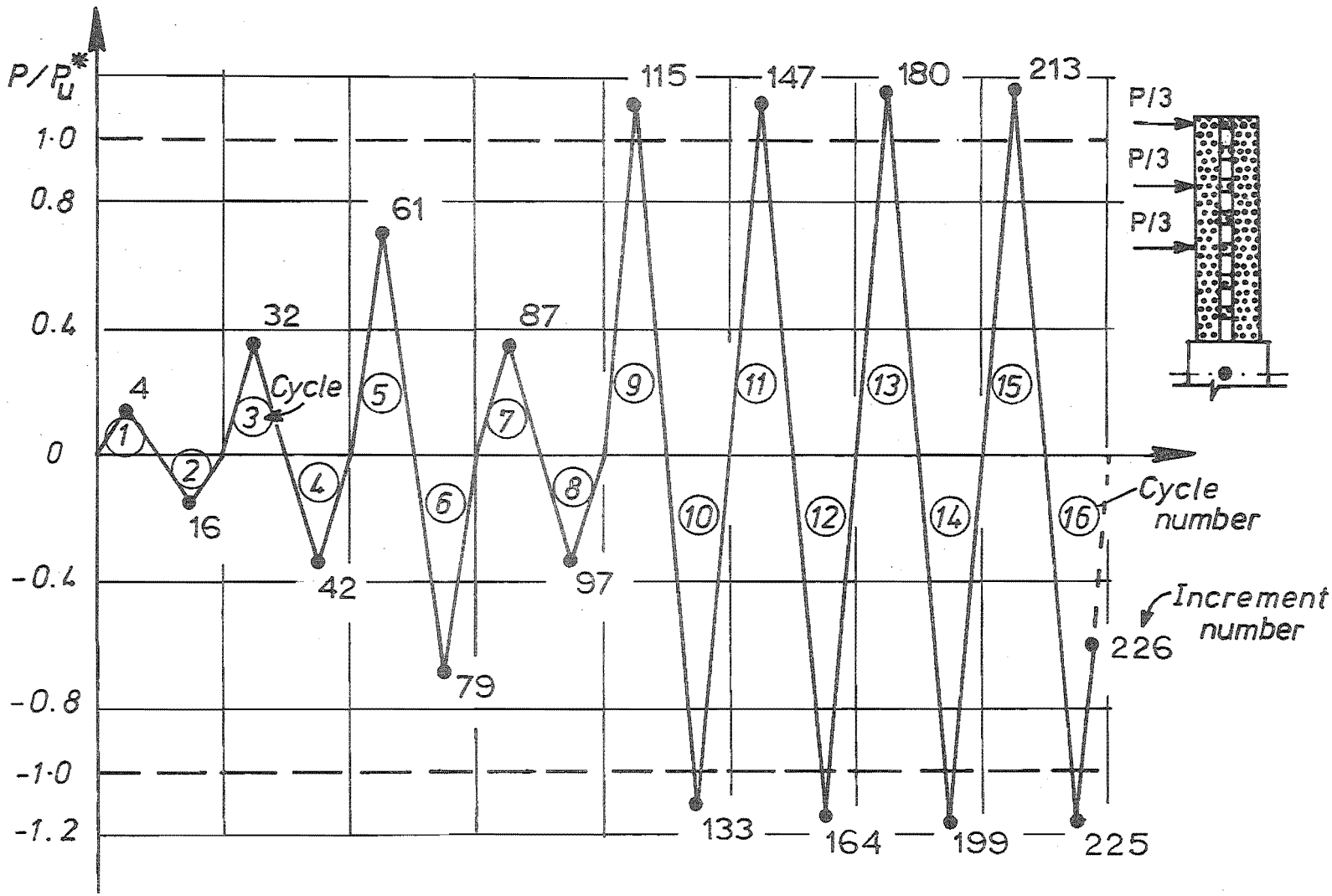

FIG. 7.2 LOAD SEQUENCE FOR SHEAR WALL B

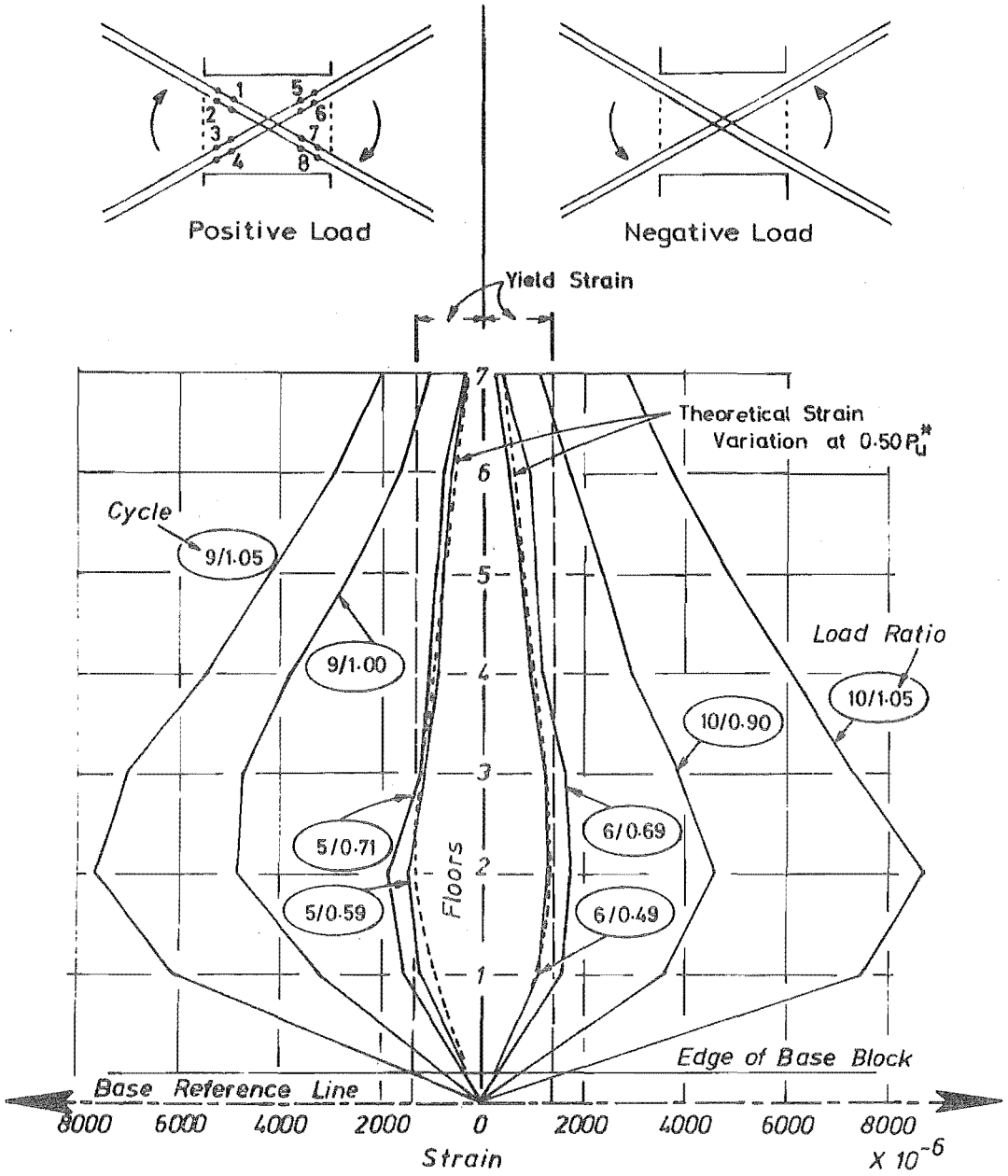

FIG. 7.3.(a) AVERAGE STRAIN ALONG TENSION CHORD IN THE COUPLING BEAMS FOR CYCLES 5 TO 10

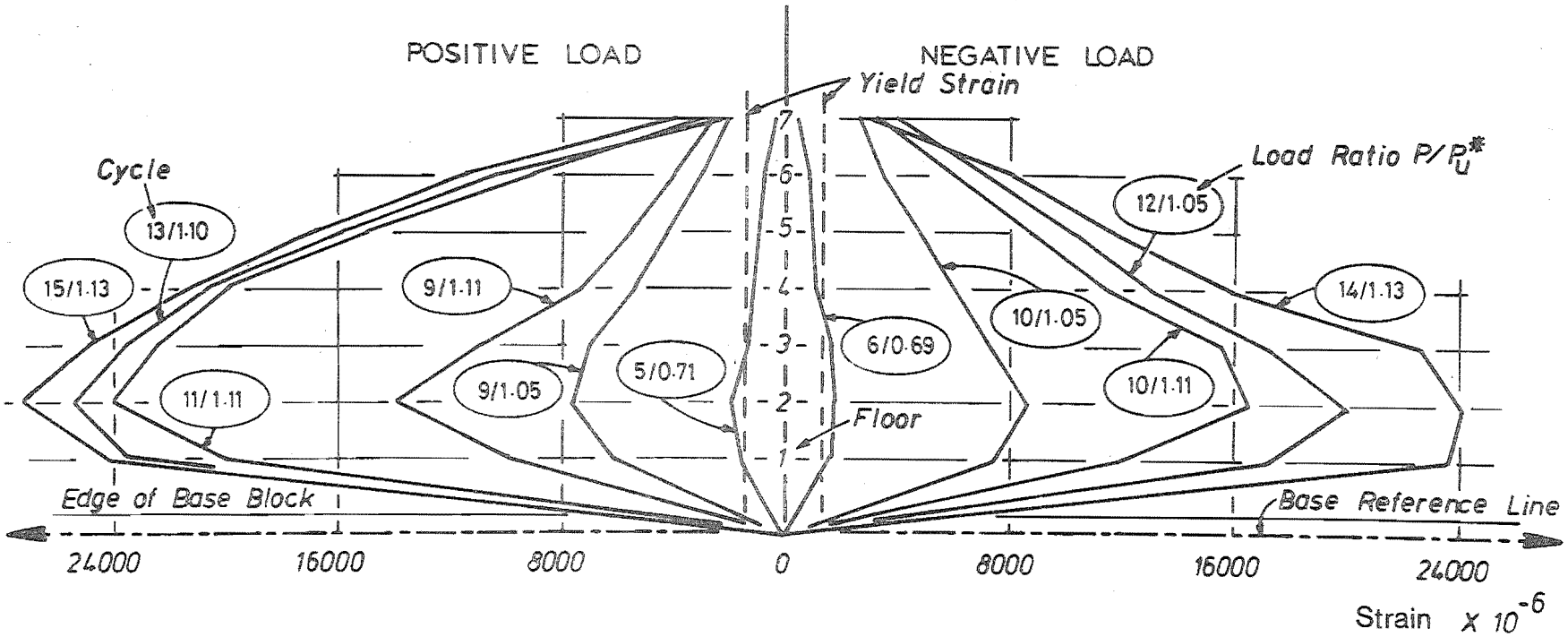

FIG. 7.3.(b) AVERAGE STRAIN ALONG TENSION CHORD IN THE COUPLING BEAMS FOR HIGH INTENSITY CYCLES AT MAXIMUM LOAD LEVELS

strains measured at gauge locations 3, 4, 5 and 6 are plotted against the height of the structure. For negative loading the average strain is based on the measurements made at gauge locations 1, 2, 7 and 8. In Fig. 7.3.a the theoretical strain variation at the onset of yield in the critical beam at $P = 0.5\ P_u^*$ is shown with broken lines. The observed strains and the measured strains are seen to be similar. In Fig. 7.3.b the maximum strains attained during high intensity cycles 9 to 15 are shown. It is seen that the beams in the critical region have been subjected to nearly 20 times the yield strain of steel.

Fig. 7.4 shows the typical strain history of the diagonal reinforcement at the instrumented location in the 2nd floor coupling beam. Fig. 7.4.a shows variation of strain at this location during moderate loading up to cycle 9. The broken line shows the approximate theoretical strain variation up to the onset of yield of the reinforcement. For drawing this theoretical strain variation, it has been assumed that steel strain in the tension chord of the coupling beam varies linearly with the increase in load on the shear wall. The yield strain of steel, based on uniaxial steel stress-strain relationship, was 1400 microstrains. At $0.6\ P_u^*$ the steel at the instrumented location attained this yield strain. This steel was expected to yield at a load of $0.5\ P_u^*$. The initial cracks which formed during cycle 3 and cycle 5 did not cross the instrumented gauge. An examination of the photograph of this beam, reproduced in Fig. 7.23.e, shows this.

Fig. 7.4.b shows the strain history during the high intensity cycles. The "Bauschinger effect" associated with cyclic loading of steel members is noticeable. During the negative cycles at high load intensities ($> 0.8\ P_u^*$), for cycles 12 and 14 the strain history curve indicates stiffening of the member. This is associated with the closing of the cracks. The diagonal cracks formed in

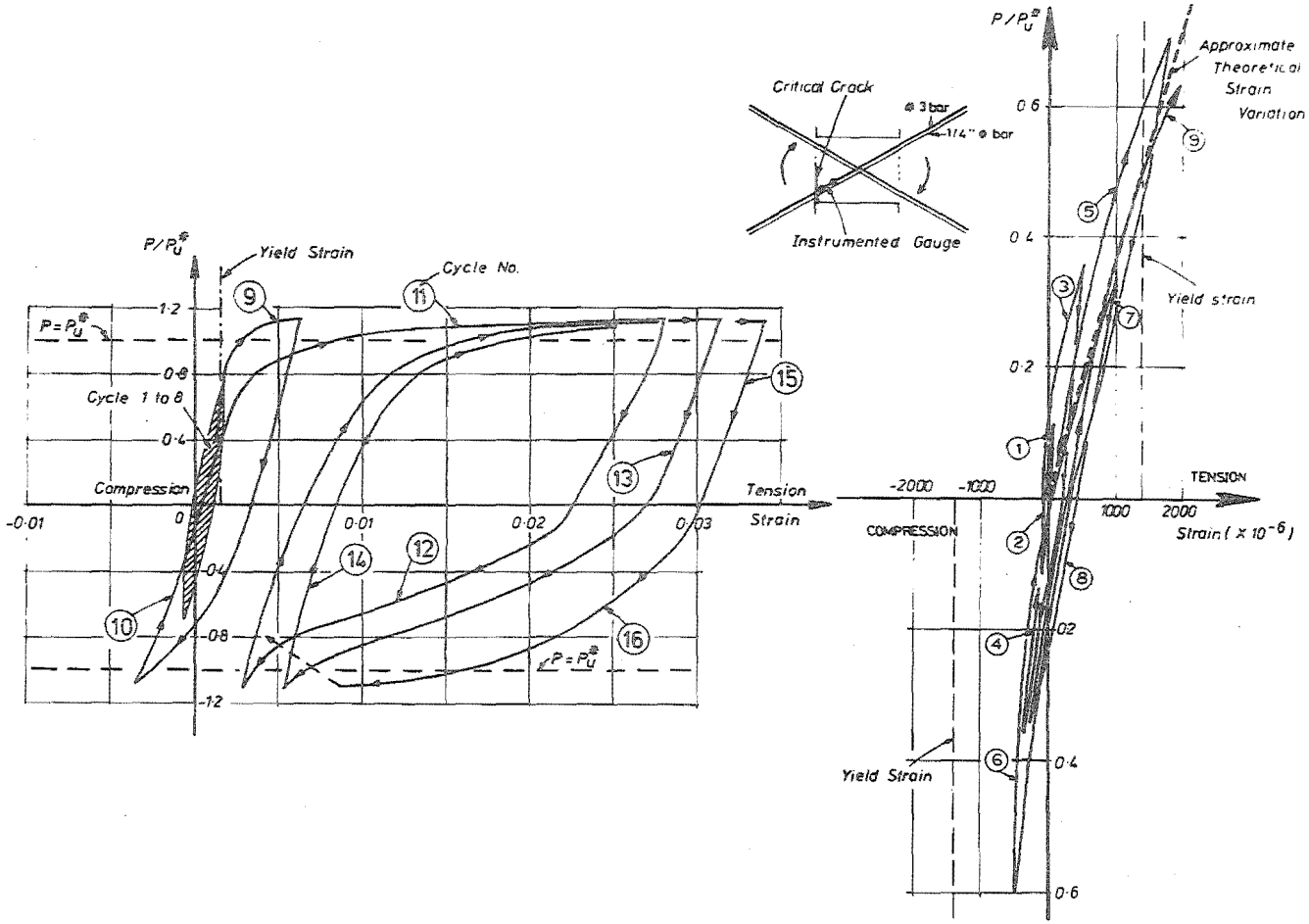

(a) Cycles 1 to 8

(b) Cycles 9 to 16

FIG. 7.4 THE STRAIN HISTORY OF A TYPICAL DIAGONAL REINFORCEMENT IN THE 6TH FLOOR COUPLING BEAM AT THE INSTRUMENTED LOCATION

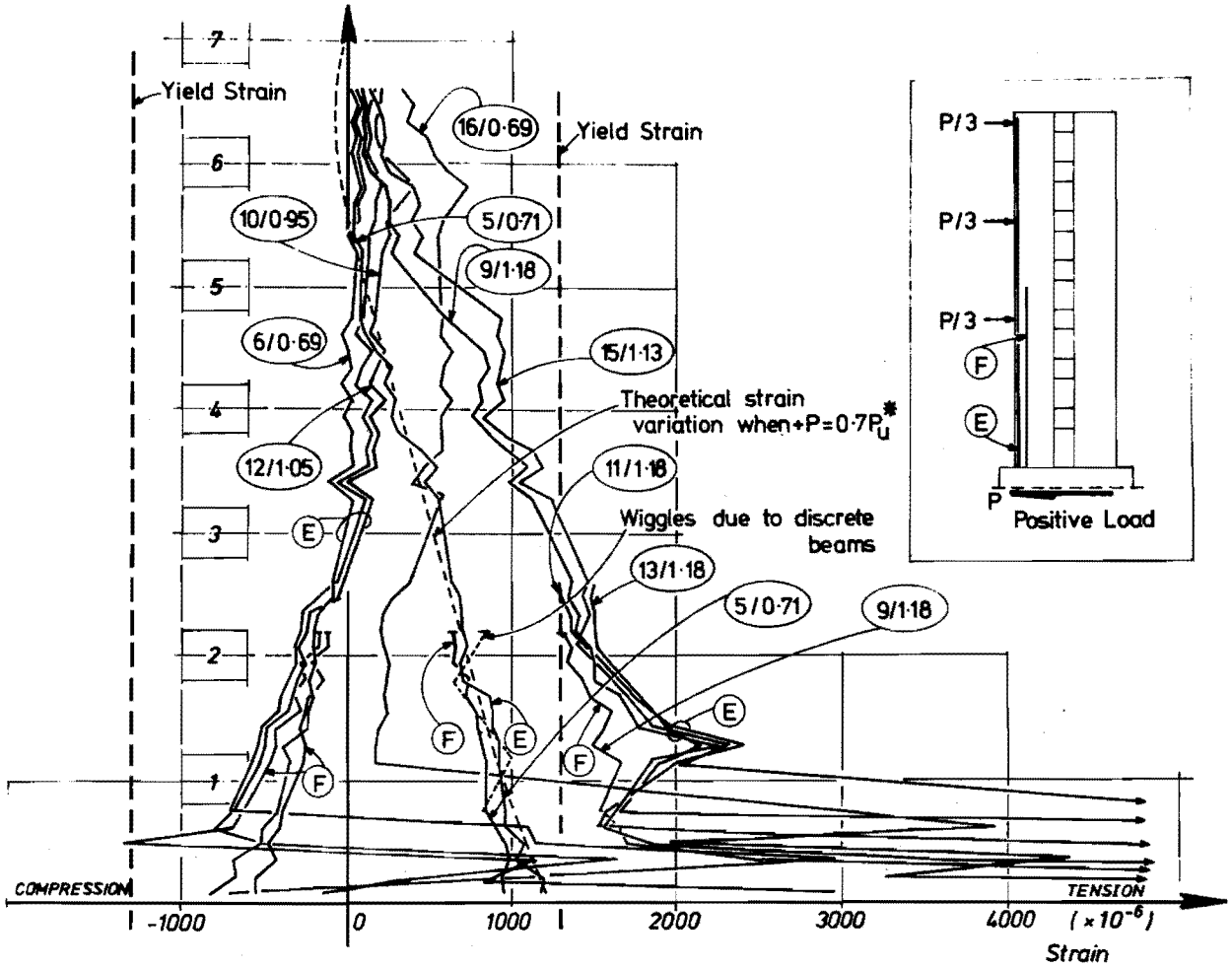

FIG. 7.5.(a) STRAIN VARIATION FOR THE FLEXURAL STEEL E AND F IN THE LEFT WALL

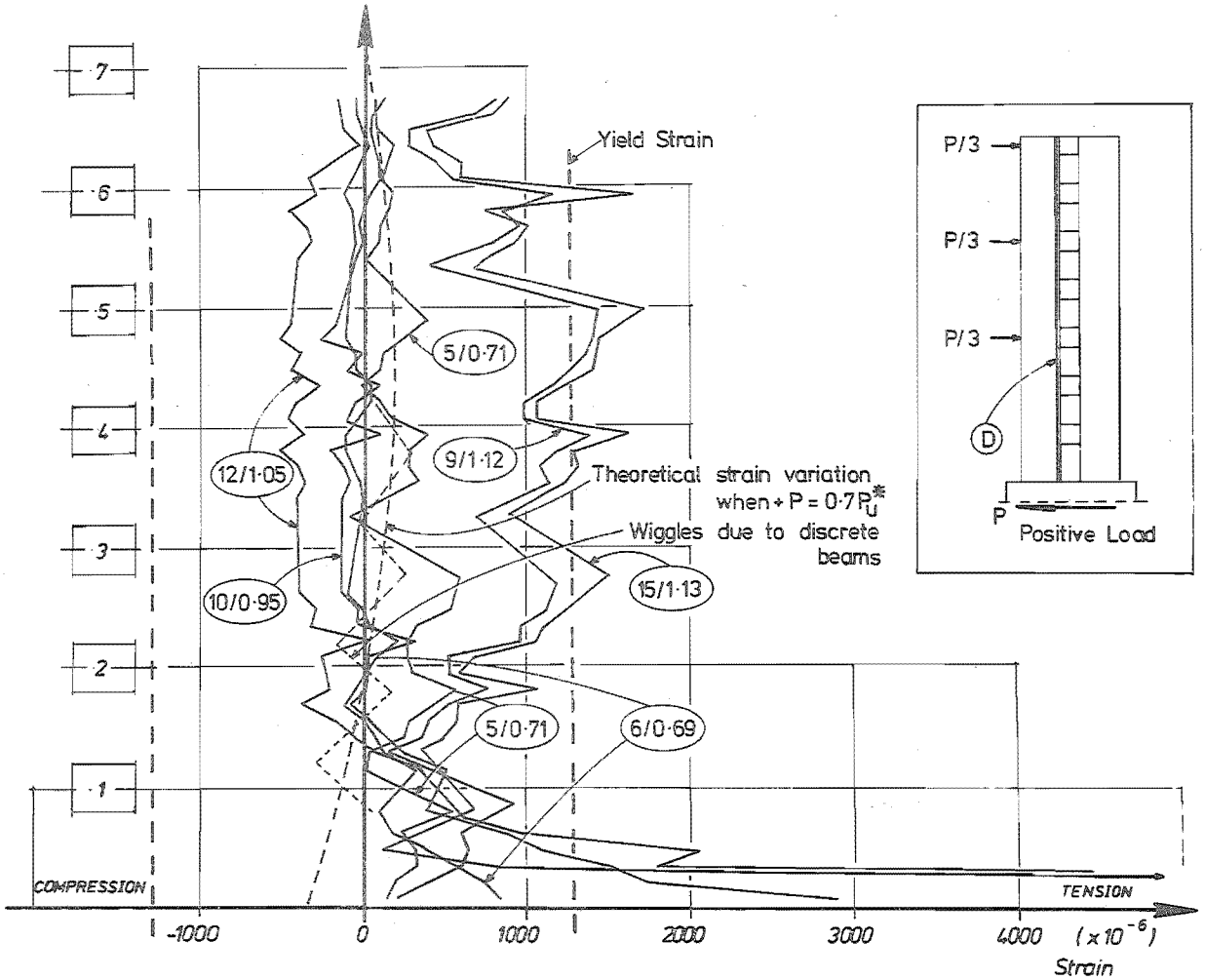

FIG. 7.5.(b) STRAIN VARIATION FOR THE FLEXURAL STEEL D IN THE LEFT WALL

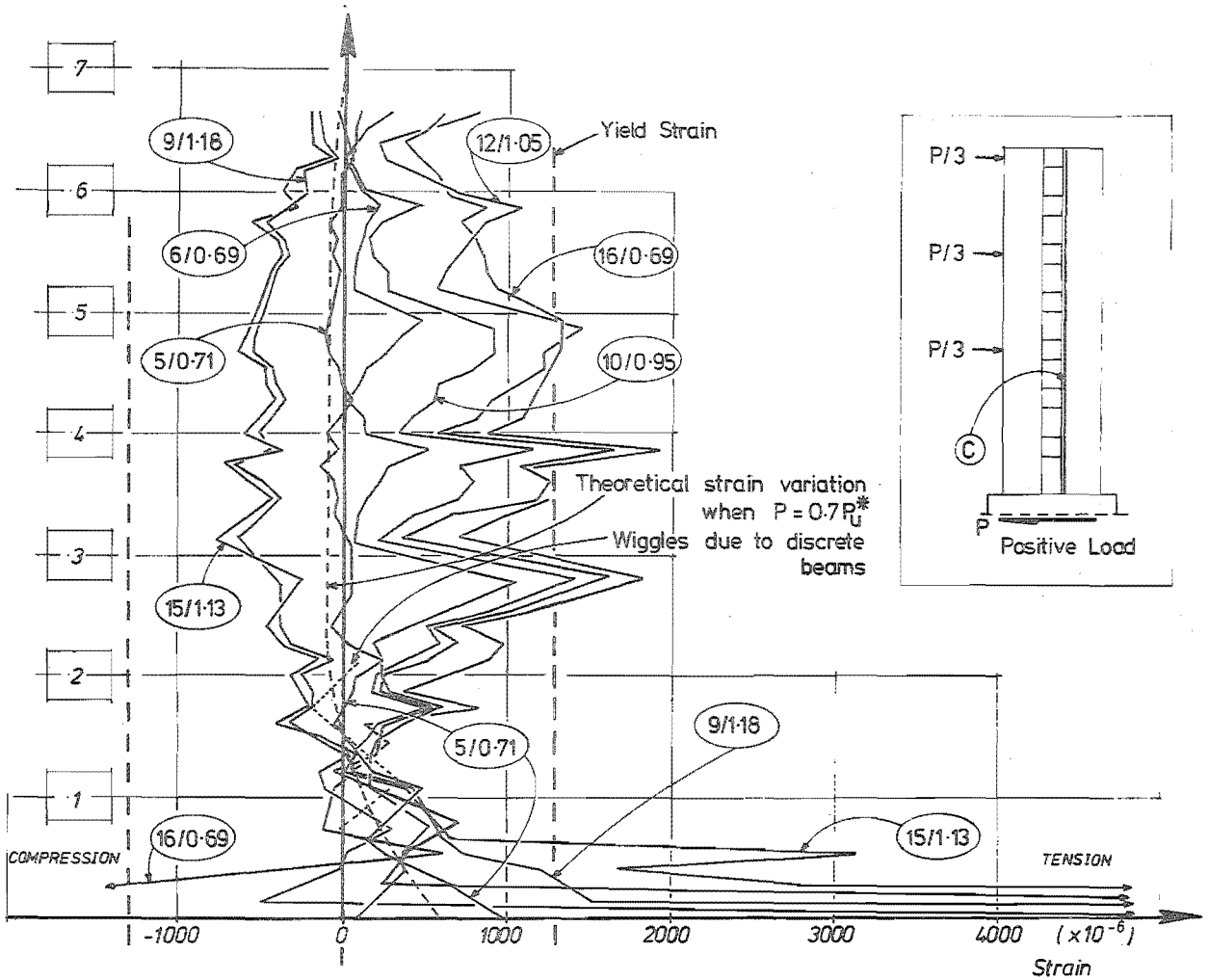

FIG. 7.5.(c) STRAIN VARIATION FOR THE FLEXURAL STEEL C IN THE RIGHT WALL

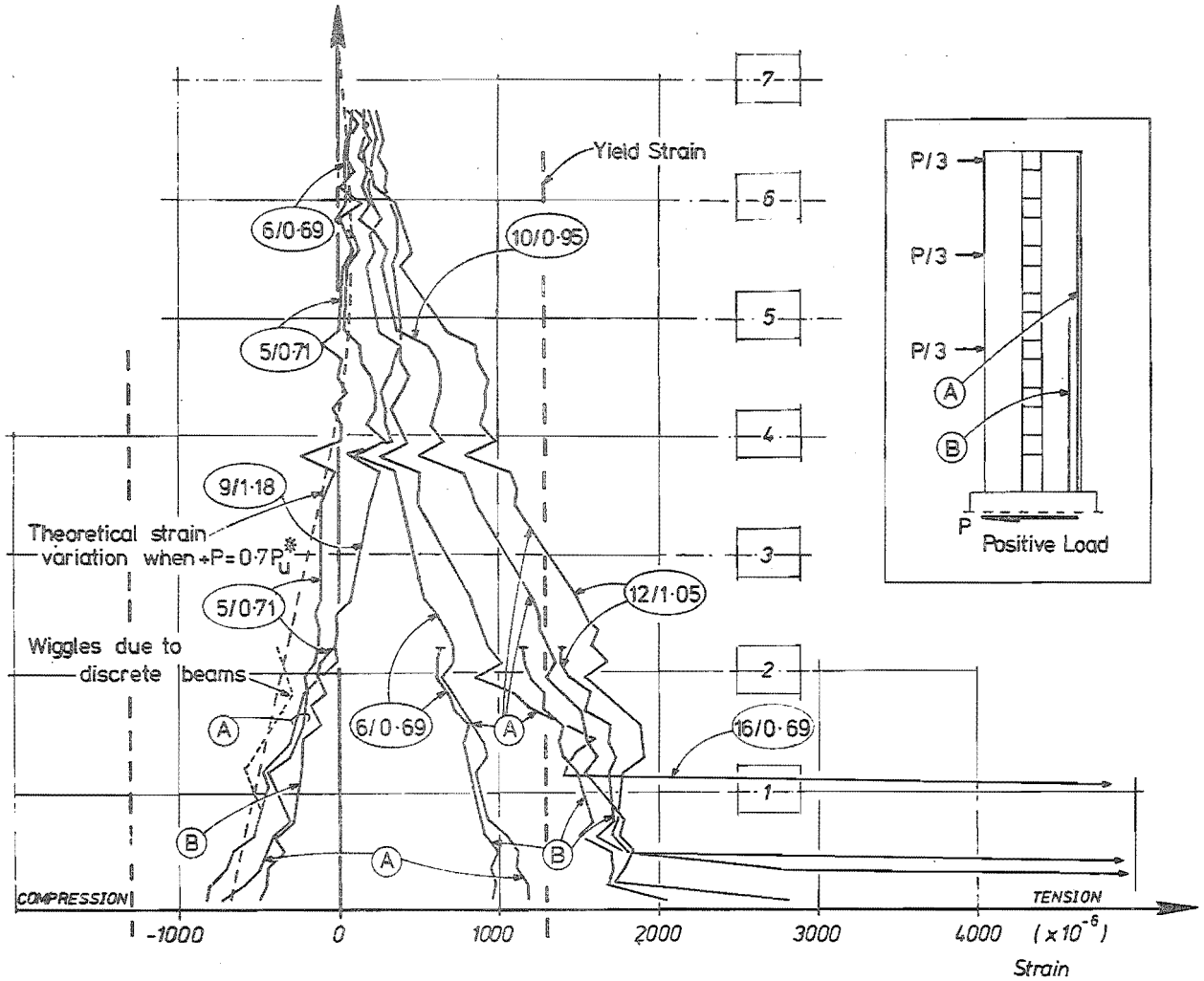

FIG. 7.5.(d) STRAIN VARIATION FOR THE FLEXURAL STEEL A AND B IN THE RIGHT WALL

cycles 11 and 13 are closing because of compression across the cracks during cycles 12 and 14. After the closure of the cracks the concrete also contributes in resisting compression. During cycle 15, at a load of 1.12 P_u^* , the instrumented bar was capable of sustaining a maximum strain of 34,000 x 10^{-6} . This is approximately 23 times the yield strain of steel. The hysteresis loops indicate that a diagonally reinforced beam is capable of dissipating large amounts of energy by yielding of the diagonal bars. The energy absorption properties of these beams are discussed in Chapter 8.

7.5 BEHAVIOUR OF THE FLEXURAL REINFORCEMENT IN THE WALLS

Figs. 7.5.a to d show the strain variation of the flexural wall reinforcement with height during cyclic loading. The insert in each figure shows the designation and the location of the reinforcement for which the strains have been plotted. On each curve the cycle number and the load intensity expressed as a ratio to the theoretical ultimate load, P_u^* , are shown. In each of these figures the theoretical strain variation at a load of 0.70 P_u^* is plotted for comparison. (See the broken line curves). This theoretical strain variation was based on considerations of the laminar model as explained in Section 6.5.

In Fig. 7.5.a the strain variations for the outer bar (F) and the middle bar (E) for the left wall are shown. In Fig. 7.5.d the strain variation for the outer bar(A)and the middle bar (B) for the right wall are shown. As in Shear Wall A, the strains in the two layers of reinforcement which were plotted for the bottom two storeys are very similar. The strains in the outer bars are larger, as one would expect from a linear distribution of strains across the section.

The strains are maximum at the base of the walls. (See Figs. 7.5. a to d.) During cycles 1 to 8 the strains in the flexural steel in the walls were below yield level. During cycle 9, which was the first high intensity cycle, the outer and middle layer of tension steel (bars (F) and (E)) in tension wall (see Fig. 7.5.a) and the single layer of tension steel (bar (C)) in the compression wall (see Fig. 7.5.c) yielded. The sequence of plastification in these flexural bars is discussed in Section 7.7.1.

For the outer bars (E) (F) (B) and (A) the strain distribution follows the same pattern as the theoretical strain variation for the laminar model. A comparison of the broken line curve, which corresponds to the theoretical strain variation for a load intensity of $0.7\ P_u^*$, with the observed strain during cycle 5 at $0.71\ P_u^*$, shows this. (See Figs. 7.5. a and d.) For bar (E) the theoretical and observed strain variation (see Fig. 7.5.a) show a fair agreement at approximately $0.7\ P_u^*$. However, the theoretical and observed strain variations for the bars (A) (C) and (D) (see Figs. 7.5. b, c and d) are significantly different due to slip at cracks and lack of closure of cracks formed in previous cycles. On the theoretical strain variation for the laminar model the wiggles due to the discrete nature of beams is shown for the bottom two beams. Similar to the observations made in Shear Wall A, the discrete nature of the beams does not significantly alter the strain distribution in outer bars (A) and (E). The strain variation for the inner bars (C) and (D) shows that the wiggles introduced by discrete beams are considerably larger. This is due to the beam forces introduced by diagonal bars which affects the strain measurements along the inner faces of the model.

As expected the tensile strains are larger than compressive strains (see Figs. 7.5. a and d). The length over which the tension steel yielded in tension wall was considerably larger than the

corresponding length of yield for the tension steel in the compression wall. For example, compare the strain variation during cycle 9 at 1.18 P_u^* in the bottom floors for bar(E)in tension wall and bar(C)in the compression wall. The differences in the lengths of yielding of the tension steel in the walls leads to different lengths of plastic hinges. This is in accordance with the theoretical study made in Section 4.4. Based on these strain variations a quantitative assessment of rotations occurring in the plastic hinge for the two walls is made in Section 7.7.7.

Figs.7.6. a to d shows the strain at the instrumented locations nearest to the base block plotted against the lateral load. The location of the gauge for which the strain history has been plotted is shown in the key diagram. During cycles 1 to 4 and cycles 7 and 8, the strains were low and hence the strain variation during these cycles is not shown. A study of these figures shows that:

(a) During cycle 9, at ultimate load, tension steel in both the tension and compression wall yielded. The compression steel (D) in the tension wall (see Fig.7.6.b) and the compression steel (A) in the right wall (see Fig. 7.6.c) did not yield. At the end of cycle 9 there were large permanent strains in the bars (F) and (C). The permanent strains in the bars (D) and (A) were at this stage insignificant.

(b) During the reversed cycle 10, bars(F)and (C) were in compression. Figs.7.6. a and d indicate that these bars have yielded in compression. Bars (D) and (A)were subjected to tensile strains beyond yield. At the end of cycle 10 large permanent tensile strains remained in all bars

(c) The hysteresis loops for the outer bars F and A are similar. They indicate that the cracks formed across these outer bars close when the wall is in compression. At W_4 the strains return to compression during even numbered cycles near ultimate

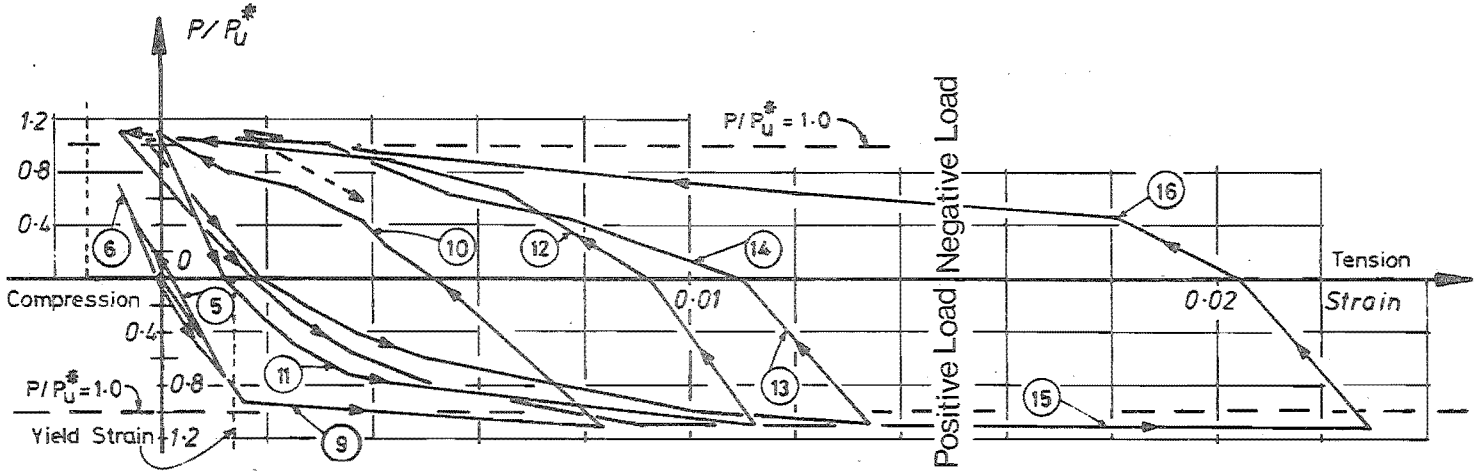

FIG. 7.6.(a) STRAIN HISTORY FOR BAR F AT LOCATION W_4

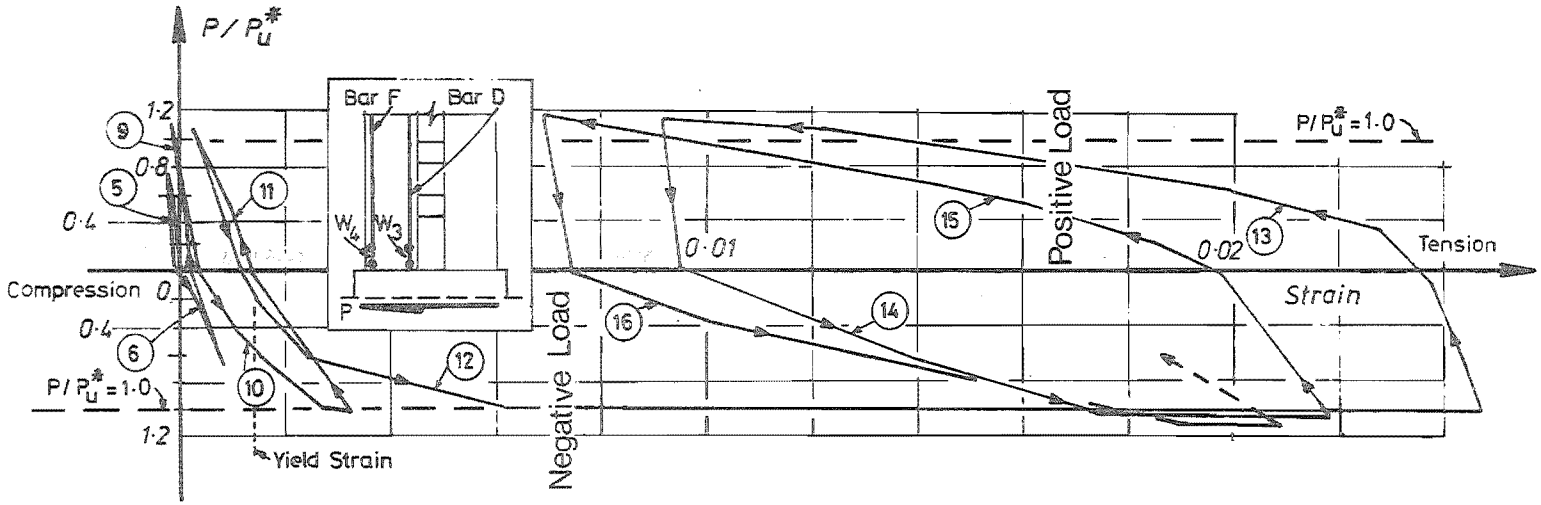

FIG. 7.6.(b) STRAIN HISTORY FOR BAR D AT LOCATION W_3

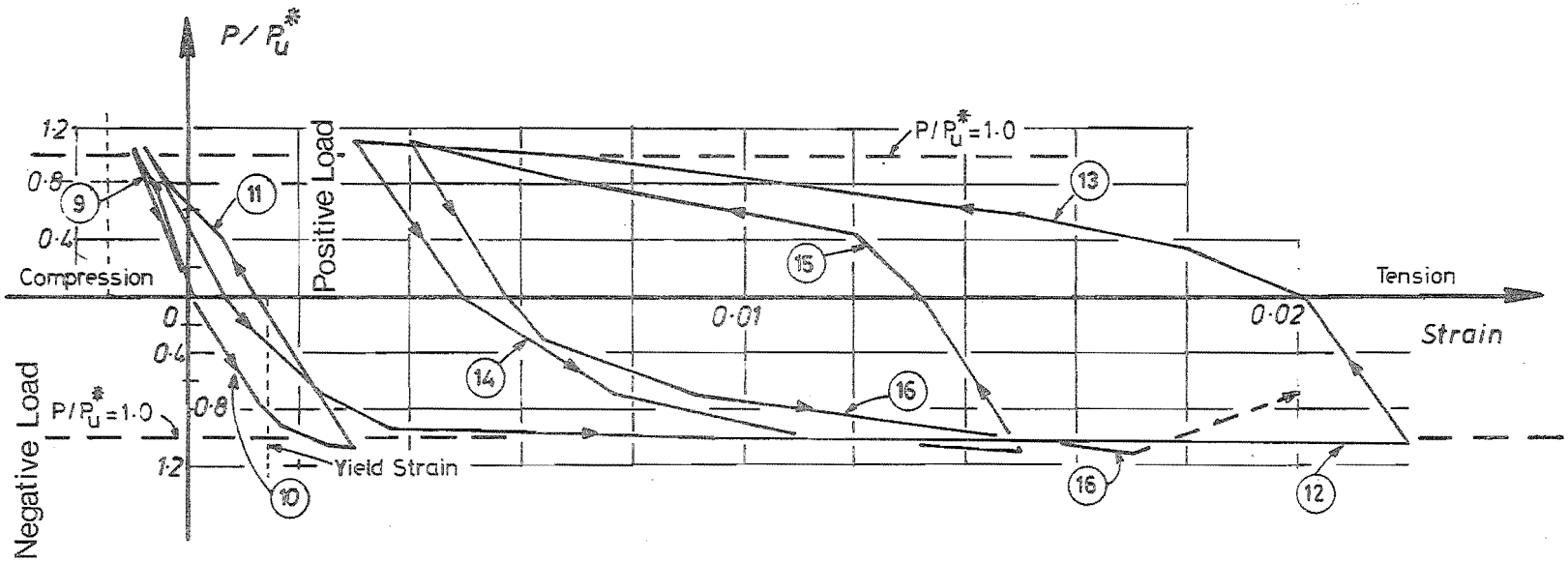

FIG. 7.6.(c) STRAIN HISTORY FOR BAR (A) AT LOCATION W_1

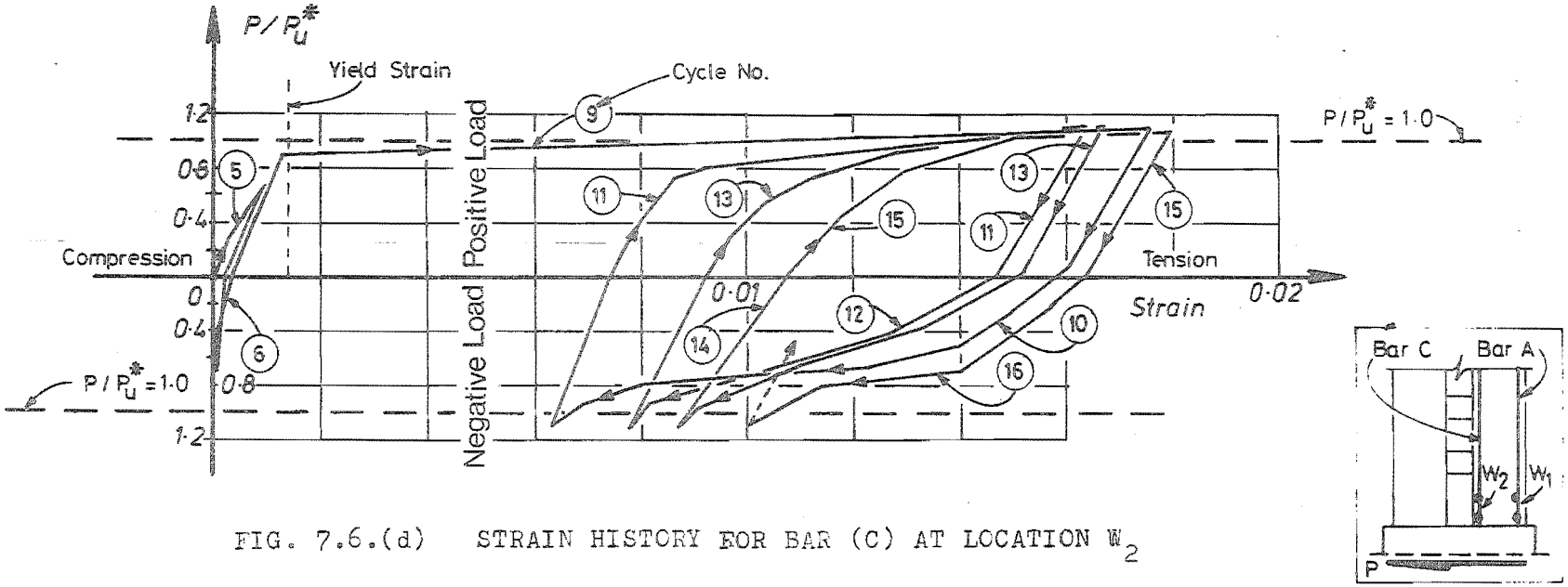

FIG. 7.6.(d) STRAIN HISTORY FOR BAR (C) AT LOCATION W_2

loads whereas at these loads the strains measured at W_1 during odd numbered cycles indicate a net residual tension of approximately 2800×10^{-6}. The closure of crack at W_1 is less compared to that at W_4. This is caused by more extensive damage at W_1 (right hand bottom corner) than at W_4 (see Fig. 7.25.d). The wider cracks formed at W_1 has encouraged the accumulation of debris which has prevented the cracks from closing completely.

(d) The force resisted by the single layer of steel is less. During positive cycles maximum tensile strains at W_2 are considerably smaller than the maximum tensile strains at W_4, in accordance with the compatibility of rotations at the base of the walls. During the reversed cycles the closure of cracks is more effective at W_4 due to large compressive forces generated in the compression zone of the compression wall than at W_2 situated in the narrow compression zone of the tension wall. Hence the hysteresis loops for the inner bars (C and D) are smaller than those for the outer bars.

(e) In all the bars, the low stiffness associated with the Bauschinger effect during compression yielding is noticeable at loads less than $0.6\ P_u^*$ from cycle 12 onwards. Consider for example, the stiffness of bar(A)at W_1 during cycle 13. Near theoretical ultimate loads an improvement in stiffness is witnessed at W_2. This is due to the forces transmitted by the debris which had filled the cracks. It is to be noted that such an improvement in stiffness is not observed at W_3 or at W_1. The extent to which the concrete is effective in transmitting compressive forces across the cracks is dependent on the uncertain effects of filling of dislodged particles in the cracks in the later high intensity cycles.

(f) With progressive cyclic loading the permanent tensile strains increased in all bars. This has contributed to the lengthening of both the walls.

(g) It can be seen that the reinforcement has performed satisfactorily during test. At the critical location all the bars were subjected to tensile strains of the order of 16 times the yield strain.

7.6 THE BEHAVIOUR OF STIRRUPS IN THE WALLS

7.6.1 Load-Stress Relationships

Fig. 7.7 and Fig. 7.8 show the load-stress relationships for the eight instrumented stirrups at locations crossed by diagonal cracks in the left wall and right wall respectively. In general the stirrup stresses are low until the stirrup is crossed by a crack. Indeed some of the stirrups are in compression at low loads. The continuity of curves between the readings for the fifth and nineth cycles indicate very little strength degradation with cyclic loading up to cycle 9. During cycle 9, at ultimate load the stirrup stresses were 50 to 80% of yield stress level. Stirrup stresses during subsequent cyclic loading at ultimate load were considerably larger than those recorded for cycle 9. These are indicated by thin lines which do not represent the stress variation with load. These thin lines compare the shear resisted by stirrups near ultimate load for different high intensity cycles. The stirrup stresses in the later cycles are significantly larger, indicating progressive shear strength degradation.

In Figs. 7.7 and 7.8 the observed stirrup stresses are compared with those predicted based on the considerations outlined in Section 6.6. For each stirrup two theoretical limits, one considering the contribution of the concrete and the other that of the stirrups only, are shown. The upper limit line is based on the classical truss analogy which assumes that the critical diagonal crack will form at 45° crossing 8 stirrups. However, the critical diagonal crack crossed only 5 stirrups in the left wall and 6 stirrups

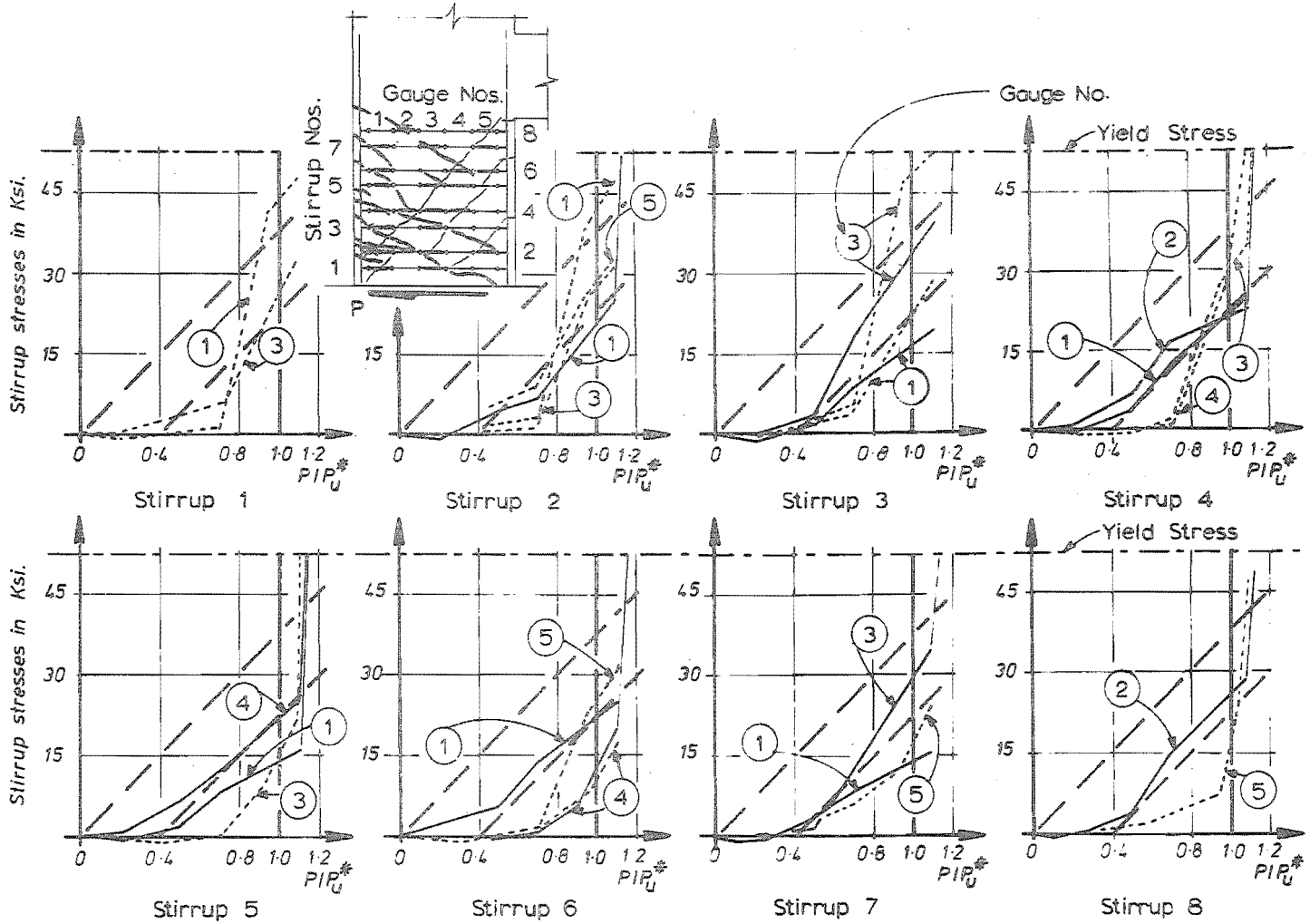

FIG. 7.7 LOAD STRESS RELATIONSHIP FOR THE STIRRUPS OF LEFT WALL

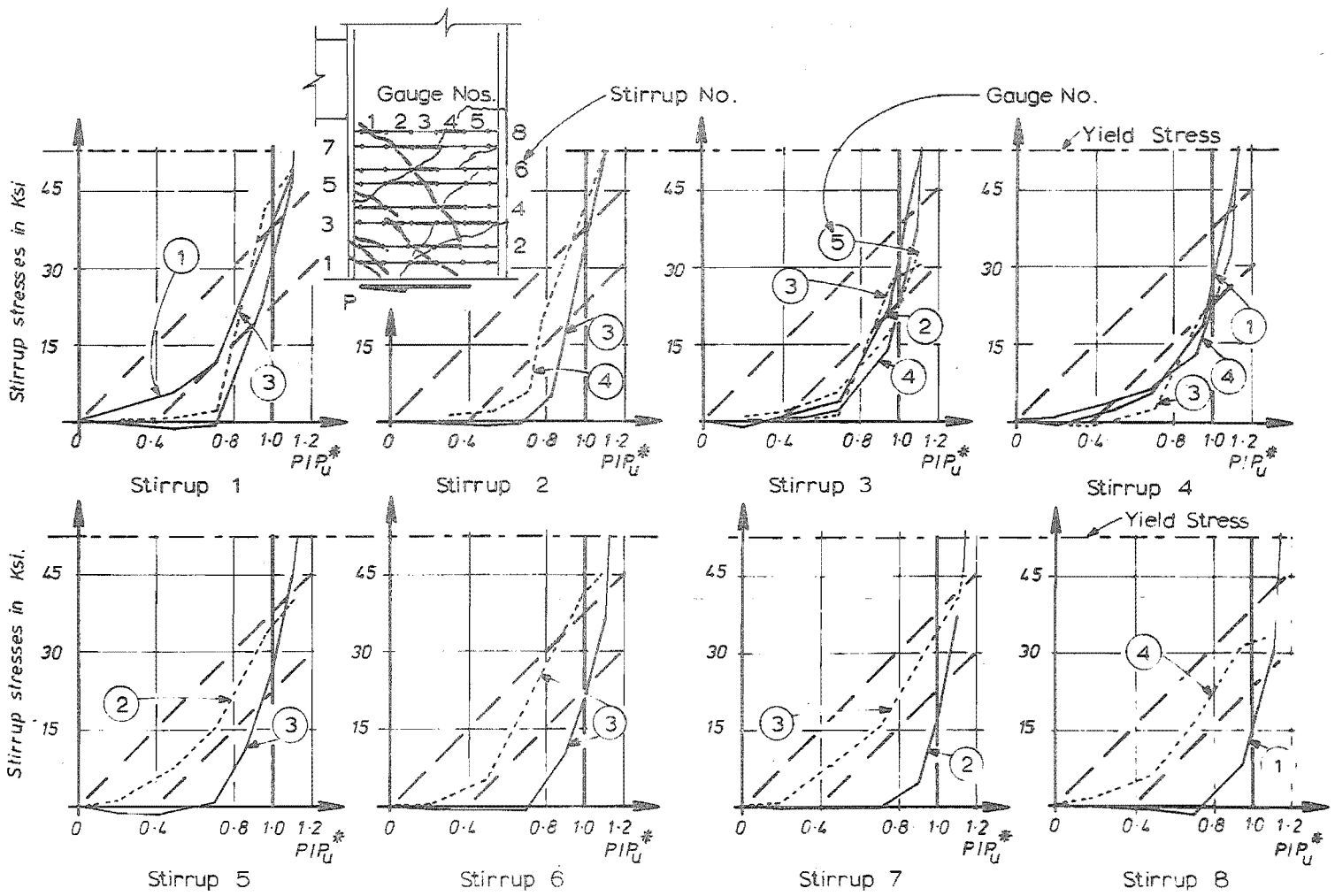

FIG. 7.8 LOAD-STRESS RELATIONSHIPS FOR THE STIRRUPS OF RIGHT WALL

in the right wall. It is seen that at 80% of theoretical ultimate load, the observed strain is close to the lower limit. As the loads in subsequent cycles increase, the strength of concrete degrades and hence the stirrups accept larger portions of the external shear. Hence, the curves rise up to and beyond the values predicted by the upper limit. With further cyclic loading the stirrups yielded.

7.6.2 Stirrup Force Distribution along Diagonal Cracks

The forces in stirrups, at points where they were crossed by the major diagonal cracks, have been plotted in Fig. 7.9.a for the left wall and in Fig. 7.9.b for the right wall. Up till cycle 5 the stirrup forces are low. During cycle 9, at a maximum load of 1.11 P_u^* , the stirrup forces across the major diagonal cracks in both walls are still well below yield. The forces are higher in the middle stirrups than in those at the edge of the diagonal cracks. However, during cycle 13, when large deformations were imposed, most stirrups yielded across the potential diagonal failure cracks.

It is noted that the critical diagonal crack in the tension wall does not form at 45° crossing 8 stirrups as assumed by the classical truss analogy. Due to the presence of large axial tension in the left wall, the crack forms crossing only 5 stirrups. In the right wall, although the diagonal crack crossing stirrups 3 to 7 forms approximately at 45°, the flexural cracks across the single layer of reinforcement in the inner face formed during the positive loading,and across the five layers of reinforcement at the base formed during reversed loading joins up with the diagonal cracks. Hence stirrups 1 and 2 do not effectively contribute to the shear resistance. However, large shear forces could be transmitted across the horizontal portion of the crack by the concrete because of the large compressive forces generated in this area.

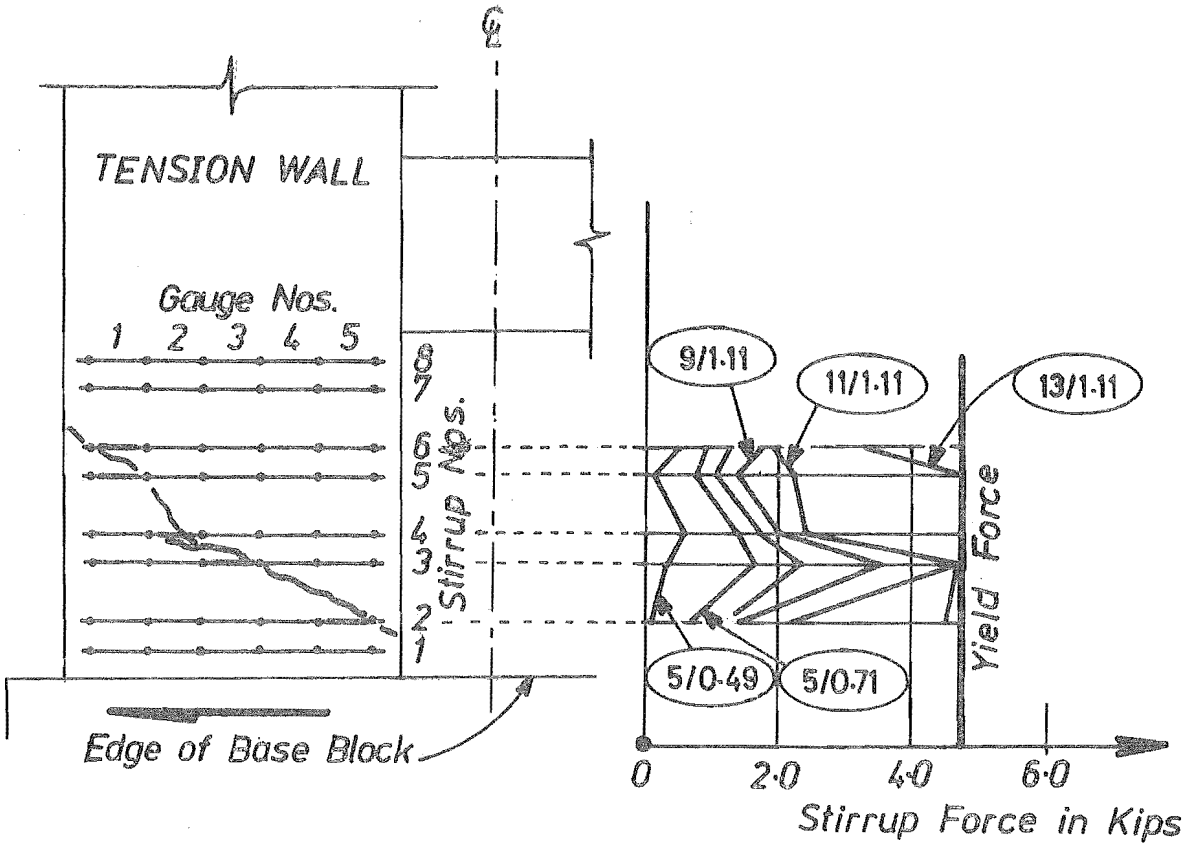

FIG. 7.9.(a) STIRRUP FORCE VARIATION ACROSS A TYPICAL DIAGONAL CRACK IN THE LEFT WALL

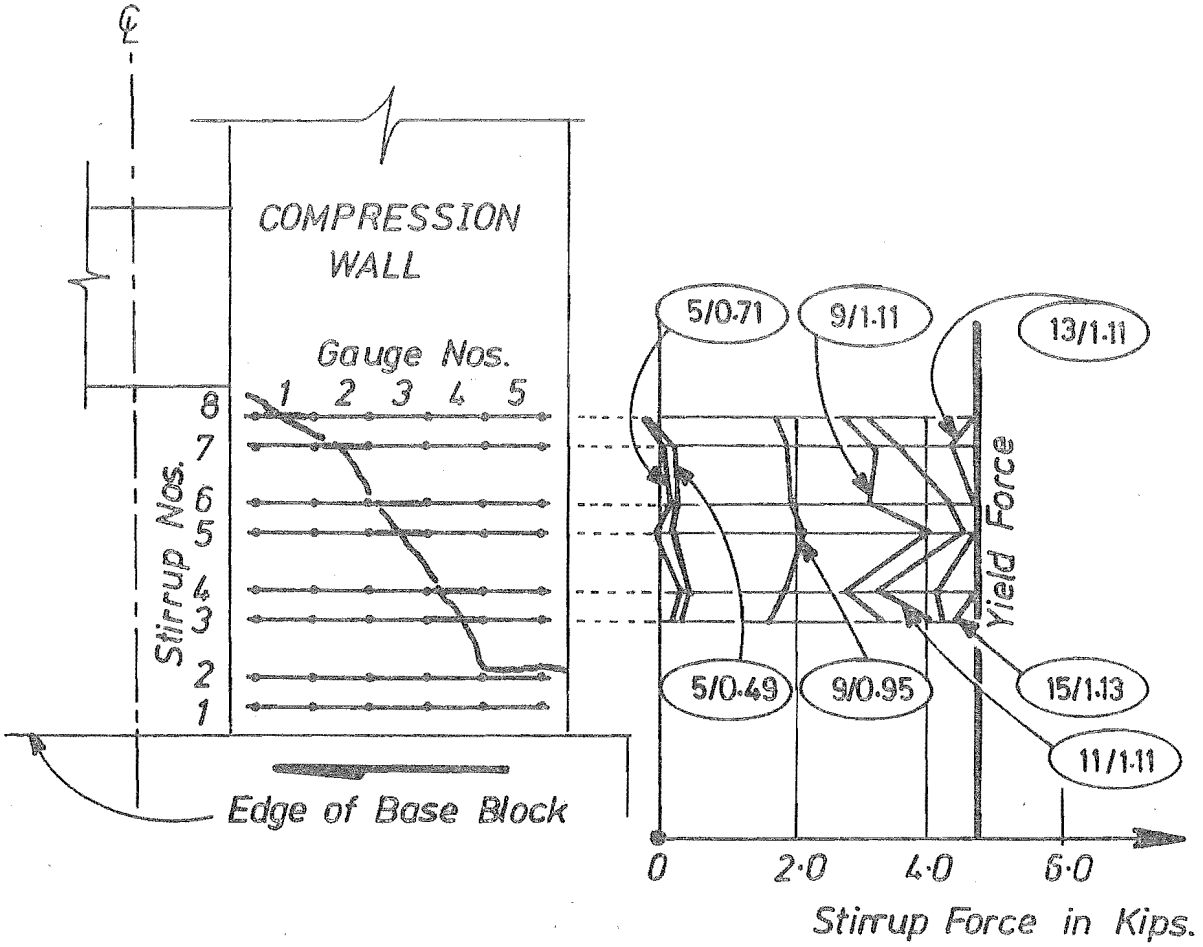

FIG. 7.9.(b) STIRRUP FORCE VARIATION ACROSS A TYPICAL DIAGONAL CRACK IN THE RIGHT WALL

During a positive cycle, near ultimate load, the strains in the outer layer of flexural reinforcement are of the order of $20{,}000 \times 10^{-6}$. The residual tensile strain in the inner bar is approximately 8000×10^{-6}. An examination of Fig. 7.6. a to d shows this. This indicates considerable lengthening and rotation of the tension wall plastic hinge. Under these circumstances the shear resistance offered by the concrete in the tension wall will be negligible. Stirrups 3 to 5 however, would still be effective. The resistance offered by the stirrups 2 and 6 at the end of the diagonal cracks to sliding shear is likely to be negligible owing to the presence of a number of flexural cracks parallel to the stirrups at the ends. At this stage the force resisted by three stirrups (3 to 5) in the tension wall could be no more than $0.26\ P_u^*$.

In the compression wall, the force resisted by 6 stirrups crossed by the potential diagonal crack is $0.53\ P_u^*$. Therefore the remaining shear, $0.31\ P_u^*$, $(1.10\ P_u^* - 0.26\ P_u^* - 0.53\ P_u^*)$ must be resisted by other mechanisms such as the concrete in the compression wall and dowel action of flexural reinforcement etc. The ultimate shear resisted by concrete in the compression wall based on the ACI shear equation was shown (see Section 6.6) to be $0.20\ P_u^*$. The foregoing discussion shows that nearly 75% of the total shear is resisted by the compression wall at ultimate load. This involves shear redistribution. Horizontal axial forces in the beams are required to transmit the shear to the compression wall's plastic hinge zone.

Fig. 7.10 shows the proportions of total shear resisted by the stirrups across the potential diagonal cracks of the left and right walls for the positive load cycles. The vertical ordinate between the relevant curve and the horizontal axis represents the shear resisted by stirrups. The ordinates measured between the inclined

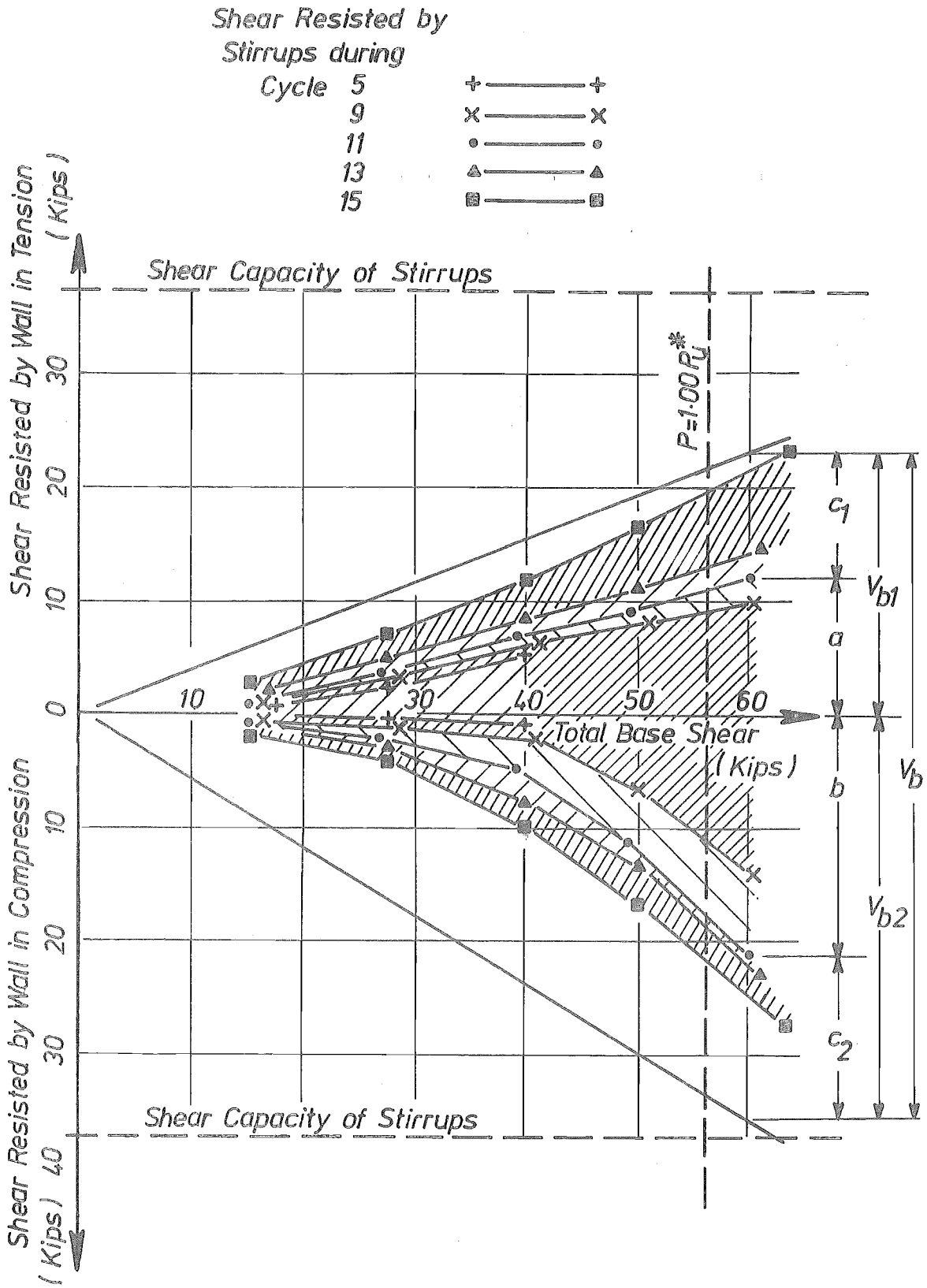

FIG. 7.10 THE SHEAR FORCE RESISTED BY STIRRUPS ACROSS CRITICAL DIAGONAL CRACK IN THE WALLS DURING POSITIVE CYCLES

straight lines represent the total base shear. The ordinate between the relevant curve and the inclined straight line represents the shear resisted by mechanisms other than the web reinforcement. For example, at a maximum load of 62.25 kips, during cycle 11, the ordinates 'a' and 'b' represent the shear resisted by the stirrups across the potential cracks, whereas V_{b1} and V_{b2} represent the total theoretical shear resisted by the left and right wall respectively. The ordinates 'a' and 'b' are based on measurements made on the stirrups. The ordinates V_{b1} and V_{b2} were computed using the elasto-plastic analysis described in Chapter 4. Thus, the ordinates 'c_1' and 'c_2' show the theoretical shear resisted by the 'concrete' in the left and right wall respectively. As expected the shear resisted by 'the concrete' is considerably larger for the compression wall than for the tension wall.

During cycle 5 the shear resisted by stirrups is small. At a load of 0.7 P_u^* less than 20% of the applied shear is resisted by stirrups. During cycle 11, at a load of 1.11 P_u^*, 60% of the applied shear is resisted by stirrups. The increase in the shear resisted by stirrups during the later cycles shows the progressive deterioration of the shear capacity of the walls consequent to the reduction in the shear resisted by the concrete. During the final cycle the stirrup contribution to the shear resistance is more than 80%.

7.6.3 Strain Distribution along Stirrups

Figs. 7.11. a and 7.11.b show the strain distribution for the eight instrumented stirrups in the left and right wall respectively. The positions of cracks are indicated in the key diagram as well as in each of the diagrams which show the stirrup strains. The cracks which may be considered as potential failure cracks during positive and negative load are underlined with thin broken lines in the key diagram. For cycle 5 the strains have been plotted for two typical

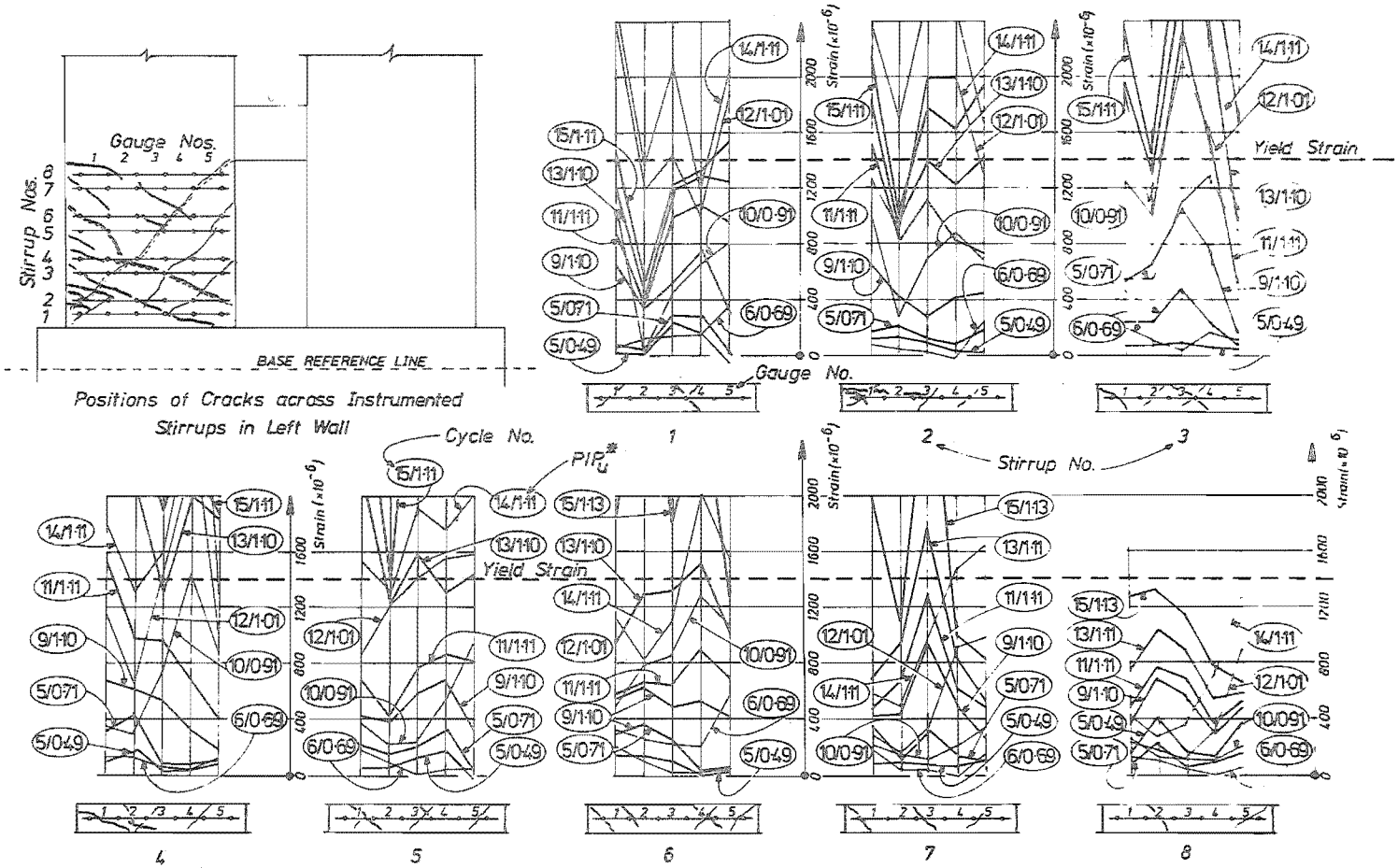

FIG. 7.11.(a) STRAIN DISTRIBUTION FOR THE EIGHT INSTRUMENTED STIRRUPS IN THE LEFT WALL

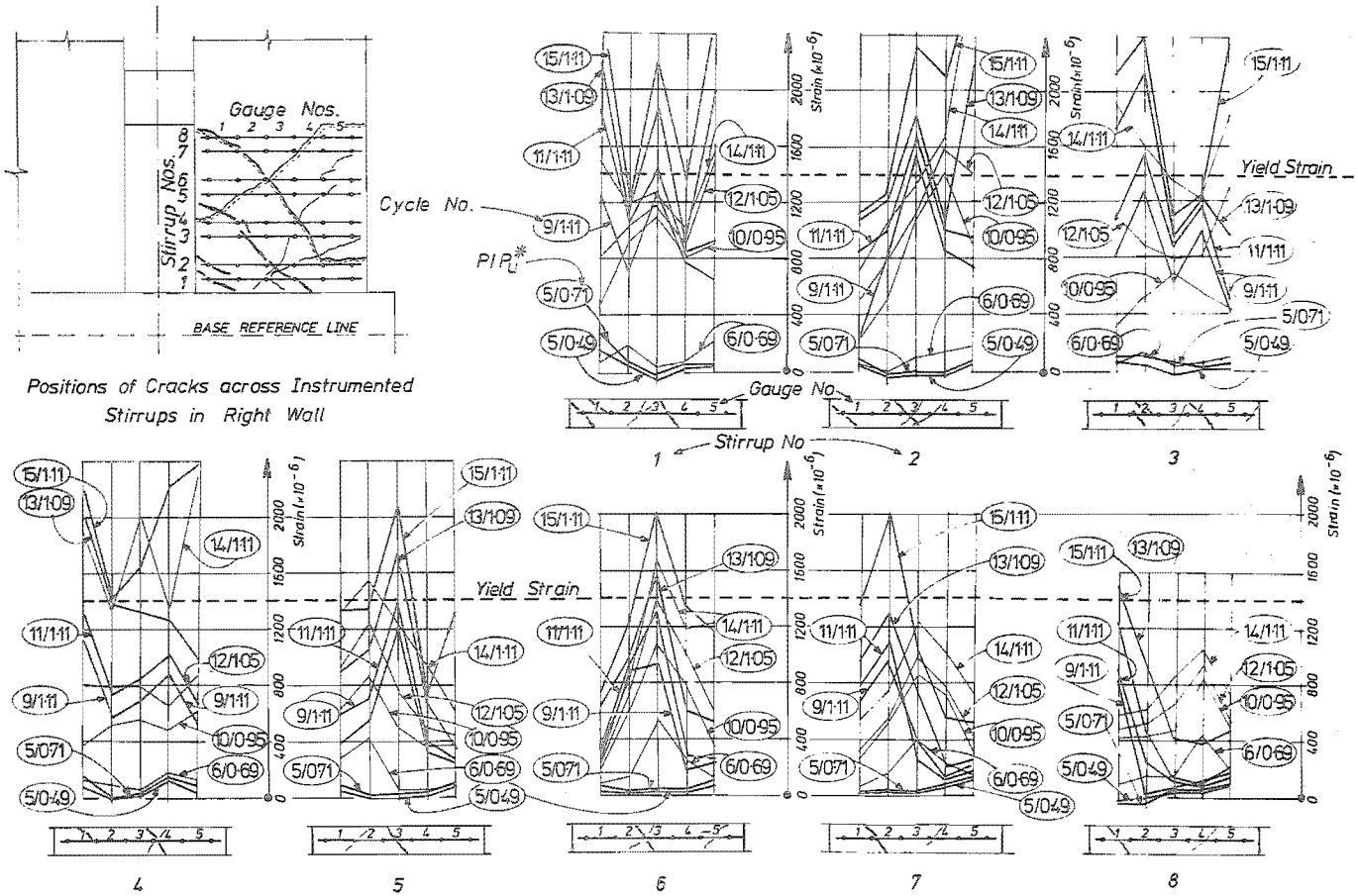

FIG. 7.11.(b) STRAIN DISTRIBUTION FOR THE EIGHT INSTRUMENTED STIRRUPS IN THE RIGHT WALL

increments. The strain distribution at maximum load levels attained are shown for cycles 6 and 9 to 15. These measurements show that:

(a) The stirrup strains are large at locations crossed by cracks.

(b) During cycle 9, the strains are more for the stirrups at the middle of the diagonal cracks than for those at the ends. Comparison of strain distribution in stirrup 8 and stirrup 1 with other stirrups in both of the walls show this.

(c) At locations crossed by diagonal cracks, the stirrup strains at ultimate load during cycle 11 are significantly more than those at ultimate load during cycle 9. This shows the deterioration of the shear strength of the wall.

(d) Up to cycle 10, the stirrup strains are less than yield strain. From cycle 11 onwards, large deformations were imposed on the shear wall. However, during the entire loading the maximum strain in the stirrups was less than twice the yield strain.

7.6.4 Strain History of a Typical Stirrup

Fig. 7.11.c shows the strain history of a typical stirrup during cyclic loading. The instrumented stirrup and the positions of cracks are also shown in this figure. During the first eight cycles the stirrup strains are low. During cycle 9 the stirrup strain increased in all the five gauges. The stirrup strains are less than yield strain until cycle 12. During cycle 13, at maximum loads, the stirrups yielded at locations crossed by diagonal cracks.

7.7 DEFORMATIONS

7.7.1 Load-Top Floor Deflection Relationship

The load-top floor deflection relationship for cycles 1 to 8 is shown in Fig. 7.12.a. During cycles 1 and 2 the maximum load on the shear wall ($0.12\ P_u^*$) was less than the estimated cracking load. During cycles 3 and 4 the maximum load was increased to

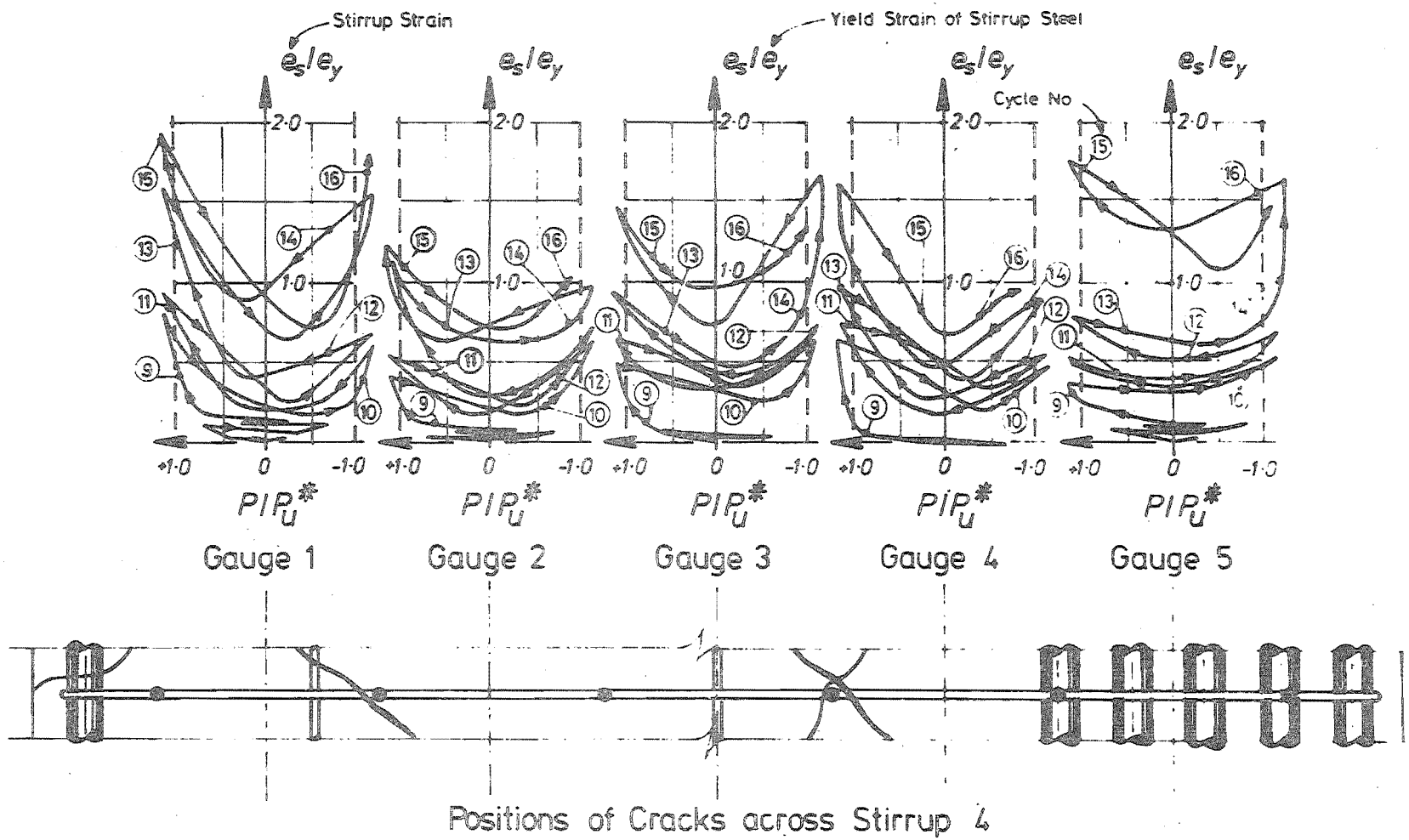

FIG. 7.11.(c) STRAIN HISTORY OF STIRRUP 4 IN THE RIGHT WALL

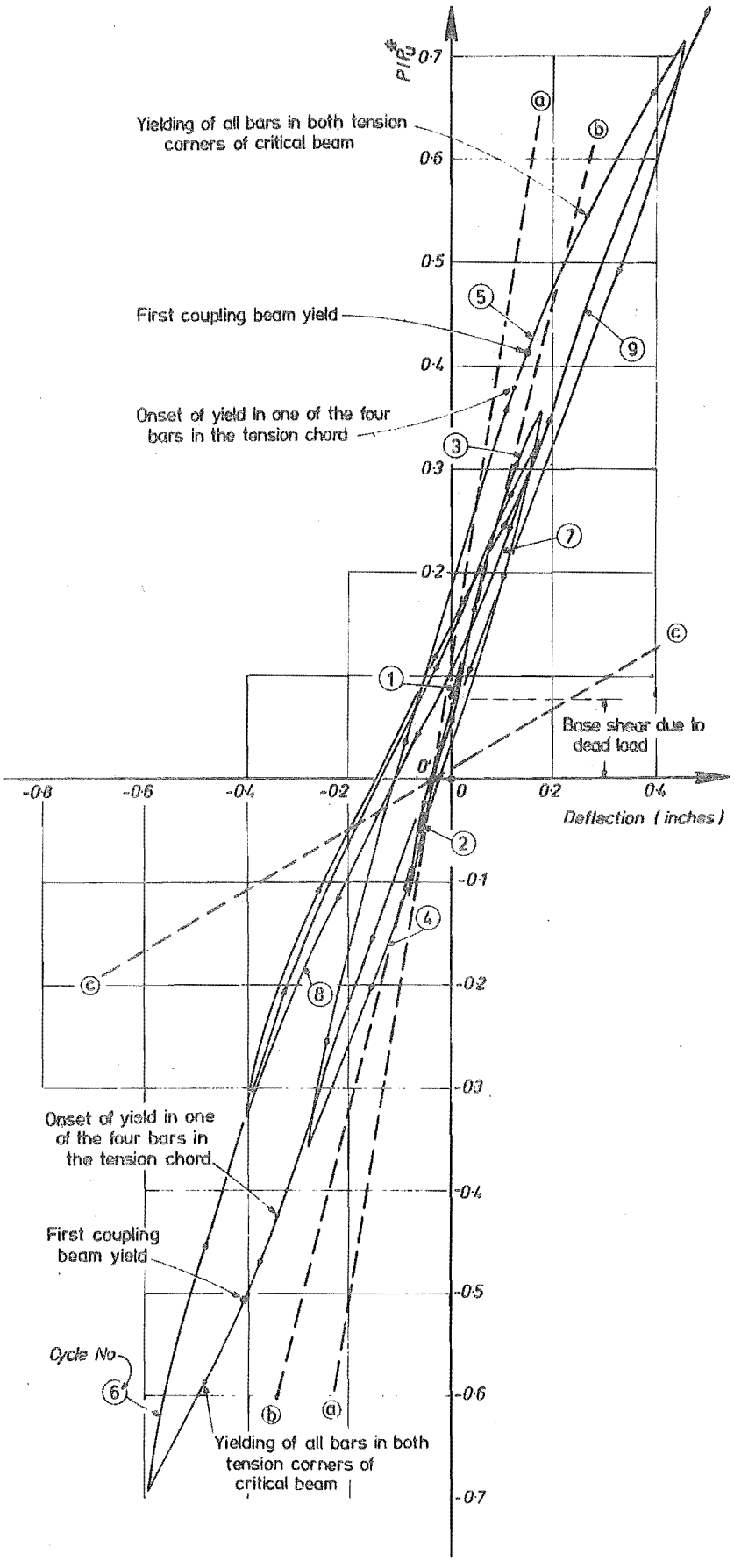

FIG. 7.12.(a) LOAD-TOP FLOOR DEFLECTION CURVE FOR THE FIRST EIGHT CYCLES OF MODERATE LOADING

0.36 P_u^* . This was less than the load required to yield the steel in the critical coupling beam. At this load, during cycle 4, the maximum top floor deflection was 0.24", i.e. H/875. Cracks were first observed in the 2nd floor coupling beam at loads of 0.15 P_u^* during cycle 3 and 0.18 P_u^* during cycle 4. During cycles 5 and 6 the maximum load (0.7 P_u^*) caused a top floor deflection of 0.43" (H/490) and 0.6" (H/350) respectively. Yielding of the tension chord steel in the critical (2nd floor) coupling beam was observed over a load range. This is indicated on the load-top floor deflection curves for cycles 5 and 6. The deflection at which all the four bars at either of the tension corners of the 2nd floor beam yielded is indicated as the first coupling beam yield. This deflection was 0.15" (H/1400) for the positive cycle and 0.4" (H/525) for the reversed cycle. This load was followed by "elastic" cycles 7 and 8 during which the deflections were less than 0.4" (H/525).

The load-top floor deflection relationship for the high intensity cycles 9 to 16 is shown in Fig. 7.12.b. During cycles 9 and 10 the shear wall was loaded past the yield. The maximum deflections attained during cycles 9 and 10 were 2.3" and 2.1" respectively. During cycle 9 the deflection, when the single layer of tension steel in the compression wall yielded, is indicated as the first wall yield. During the reversed cycle 10, yielding was first observed in the tension steel of the tension wall. The deflection when the middle layer of this tension steel attained yield level is indicated as the first wall yield.

During each of the subsequent cycles (11 to 16) the deflection at ultimate load was more than 2.5" (H/84). Cycle 16 was intended to be the last one. During this cycle large plastic deformations were imposed on the model. The shear wall attained a top floor deflection of 7.5" (H/28) at 1.10 P_u^* before failing.

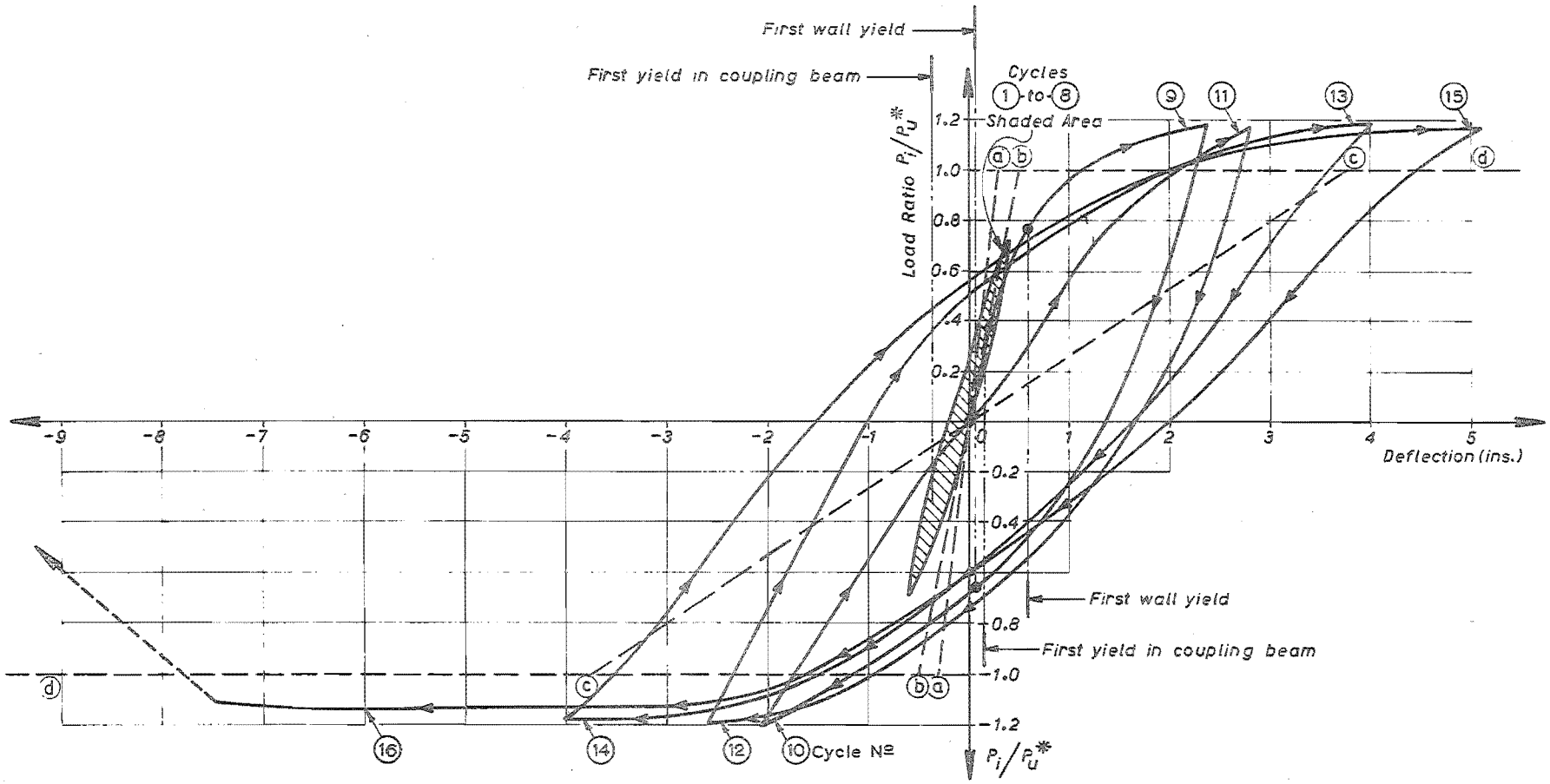

FIG. 7.12.(b) LOAD-TOP FLOOR DEFLECTION CURVES FOR CYCLES 9 TO 16

Three theoretical stiffnesses (oa)(ob)and(oc) are shown in Fig. 7.12.a and Fig. 7.12.b. These were based on the same considerations as described in Section 6.7.1.

In Fig. 7.12.a the origin is shifted to(O')to allow for the deflection of the model due to its own weight. During cycles 1 and 2 the stiffnesses predicted by line (O'a) and obtained experimentally agree well. During cycles 3 and 4 the predicted (O'b) and observed stiffnesses have good correlation up to a load of 0.25 P_u^* for cycle 3 and 0.2 P_u^* for cycle 4. Beyond this load the observed stiffness is less. As expected, after the onset of yield in the critical beam, the stiffness of the model lies between the values corresponding with lines (oc) and (ob).

The broken line (obd) in Fig. 7.12.b is the assumed theoretical bilinear relationship for the shear wall model. In all the high intensity cycles, the stiffness of the shear wall at low loads ($< 0.2\ P_u^*$) is considerably larger than that indicated by oc This is due to the superior performance of the diagonally reinforced beams.

For computing ductility, the deflection at the top floor at the onset of yield (b) for the theoretical bilinear behaviour (obd) is taken as reference yield deflection of the shear wall. For the model this is 0.5" . When the permanent deformation of 2", which was present at the end of cycle 15, is also considered, the ductility attained before failure in cycle 16 is 19. The ductility attained in each cycle and the energy absorption properties of the model are discussed in Chapter 8. The stable hysteresis loops resemble the shapes obtained for a steel member.

Fig. 7.13.e. presents a comparison of the load-top floor deflection curves observed during cyclic loading, shown in heavy full lines for cycles 5 and 9, with those predicted. Along the observed load-top floor deflection curve the observed sequence of

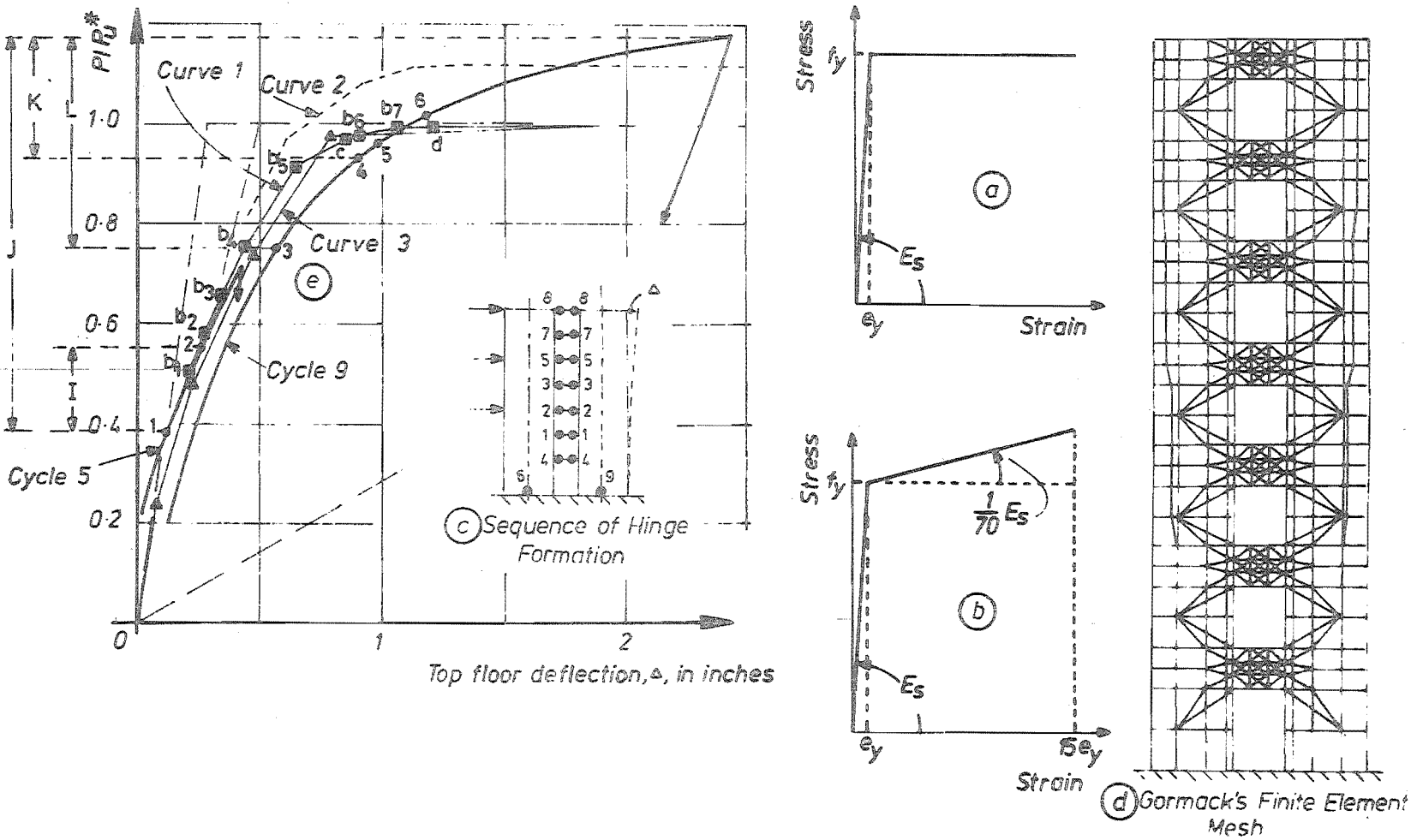

FIG. 7.13. A COMPARISON OF THE OBSERVED LOAD-TOP FLOOR DEFLECTION CURVES WITH THOSE PREDICTED BY THEORETICAL ANALYSES

yielding of diagonal reinforcement in the beams and flexural reinforcement in the walls is also shown with the following numbers at filled small circles:

1. One of the four bars in the tension chord of the second floor beam yields in cycle 5.

2. All bars in both tension corners of the second floor beam yields in cycle 5.

3. The single layer of tension steel in the compression wall yields in cycle 9.

4. Outer layer of tension steel in the tension wall yields.

5. Middle layer of tension steel in the tension wall yields.

6. The diagonal steel in all the beams and the flexural steel in the walls have all attained yield level.

The tension chords of the coupling beams were reinforced with 2 # 3 and 2 - $\frac{1}{4}$" diameter bars. The onset of yield at $P = 0.38\ P_u^*$ was first witnessed in the outer # 3 bar. The strains at the instrumented gauges of the other three bars were below yield level. The strains at all the four instrumented gauges were above yield level only after a load of $P = 0.54\ P_u^*$ was reached. Similar spread of yield was observed in the wall flexural steel. The ranges of load intensities at which yielding in various parts of the structure developed are indicated at the left hand of Fig. 7.13.e. using the following notation:

Range I - yielding of second floor beam.

Range J - yielding of all beams.

Range K - yielding of tension wall.

Range L - yielding of compression wall.

Curve 1 shows the computed load-top floor deflection relationship, based on the analysis presented in Chapter 4, for the model using a bilinear stress-strain curve for the steel with no strain hardening (see Fig. 7.13.a). The theoretical sequence of

hinge formation is shown in Fig. 7.13.c. The theoretical stages of plastification of the components, with the notation used in Section 4.3.2. are indicated on curve 1 (see the filled squares).

Considering the assumptions used in the derivation of the theoretical curve, it may be said that good agreement exists between the computed results and the relationship obtained during cycle 5. However, the theoretical curve overestimates the stiffness during cycle 9. This is to be expected. The theoretical curve implies monotonic loading. The stiffness during cycle 9 should be less than that based on monotonic loading, because considerable amount of stiffness degradation must have occurred, particularly during cycle 6. Also the ultimate load observed is about 17% more than that predicted. This is due to strain hardening of steel in the coupling beams as well as in the walls.

The dotted curve 2 in Fig. 7.13 was obtained with the use of the steel stress-strain relationship shown in Fig. 7.13.b. When strain hardening of the steel is considered there is a better correlation between the predicted and observed ultimate loads.

In another project at this University, Gormack[63] applied a nonlinear finite element analysis to predict the behaviour of Shear Wall B specimen. The finite element mesh used is shown in Fig. 7.13.d. An incremental iterative method was employed. In this, ultimate load was attained in four equal increments. The load-top floor deflection relationship predicted by this analysis is shown with triangles (curve 3). The deflections predicted by Gormack up to $0.9\ P_u^*$ are more than those obtained using the finite difference method.

Iterative finite element analyses recognise stiffness reduction due to stress concentrations in the wall elements adjacent to the beam wall junction. At approaching ultimate load, Gormack's analysis considers zero stiffness for yielding elements only, whereas the

finite difference solution assumes zero stiffness for the whole wall section. Hence the deformations predicted by the two analyses at these stages are slightly different.

7.7.2 The Variation of Stiffness

Using the load-top floor deflection relationship shown in Fig. 7.12.a and 7.12.b, the stiffnesses of the model was computed as the slope of the tangent to the load-deflection curve at the load levels considered. The stiffnesses so obtained are plotted against the load ratio in Fig. 7.14. The arrows indicate progressing loading (full lines) and unloading (broken lines). On the same figure the following theoretical stiffness levels have also been shown:

X - Both walls and beams are in the uncracked state.

Y - Both walls and beams are cracked at the onset of yield in the critical lamina. (Refer to Section 6.7.2.)

Z - Both walls in the cracked state and beams having zero stiffness ($I_x = 0$). For the purpose of stiffness study only, it is assumed that the two walls resist the external action and the beams transmit horizontal axial forces only.

As expected the stiffness of the shear wall during cycles 1 and 2 is close to the stiffness indicated by X . The reduction in stiffness due to cracking (cycles 3 and 4) is about 35%. After this the stiffness progressively reduces.

During cycles 5 and 6, the stiffness degradation due to yielding of the three coupling beams in the critical region, and owing to the formation of the diagonal cracks at the base of the walls, may be observed. The low stiffnesses at the commencement of cycles 7 and 8 are due to the open cracks formed during previous loading.

The low stiffness during the beginning of cycle 9 is due to open cracks in the coupling beams formed across the diagonal steel while yielding occurred during the reversed loading (cycle 6).

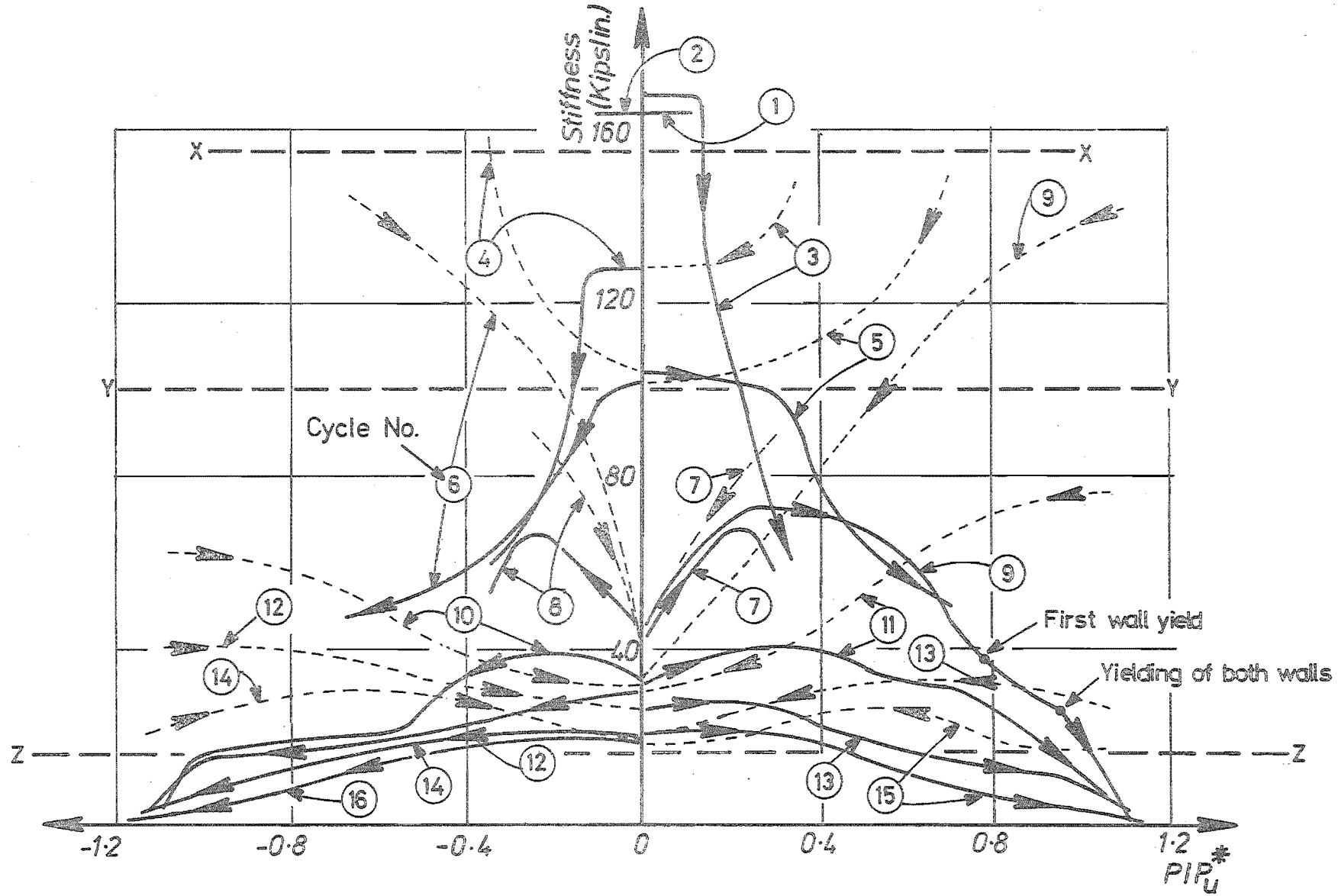

FIG. 7.14 THE VARIATION OF STIFFNESS WITH CYCLIC LOADING

When these cracks are closed an improvement in stiffness is observed due to the concrete also contributing to the load resistance. After reaching a maximum stiffness at $0.3\ P_u^*$ the stiffness begins to fall off due to the yielding of diagonal steel in the coupling beams. Yielding of steel in both the walls was observed at a load of $0.95\ P_u^*$. At $1.12\ P_u^*$ the stiffness of the shear wall was almost zero.

Curves for cycles 10 to 16 indicate the stiffness of the model when large plastic deformations are imposed. At low loads the stiffness is larger than the theoretical stiffness, indicated by broken line Z. The improvement in overall stiffness, compared with Shear Wall A, is due to the larger stiffness of the diagonally cracked diagonally reinforced beams. During each of these high intensity cycles the stiffness of the shear wall gradually reduces to zero at ultimate load. After cycle 12 no significant change of stiffness occurred. The stiffness characteristics of Shear Wall B are compared with those of Shear Wall A in Chapter 8.

7.7.3 Rotations of Coupling Beams

Using the measurements made with the theodolite at the centre line of the walls, rotations of the coupling beams, defined in Section 4.3.1, were computed as detailed in Appendix B. In Fig. 7.15.a, rotations of the coupling beams observed during various cycles are plotted against the positions of the coupling beams. In the same figure the approximate yield rotation of the identical beams is also shown. The maximum ductilities attained during cycle 15 and cycle 16 at ultimate load $(1.11\ P_u^*)$ by the 2nd floor beam is approximately 20. In the same figure the theoretical variation of beam rotation with height for a load of $0.5\ P_u^*$ is shown in thin broken lines for comparison.

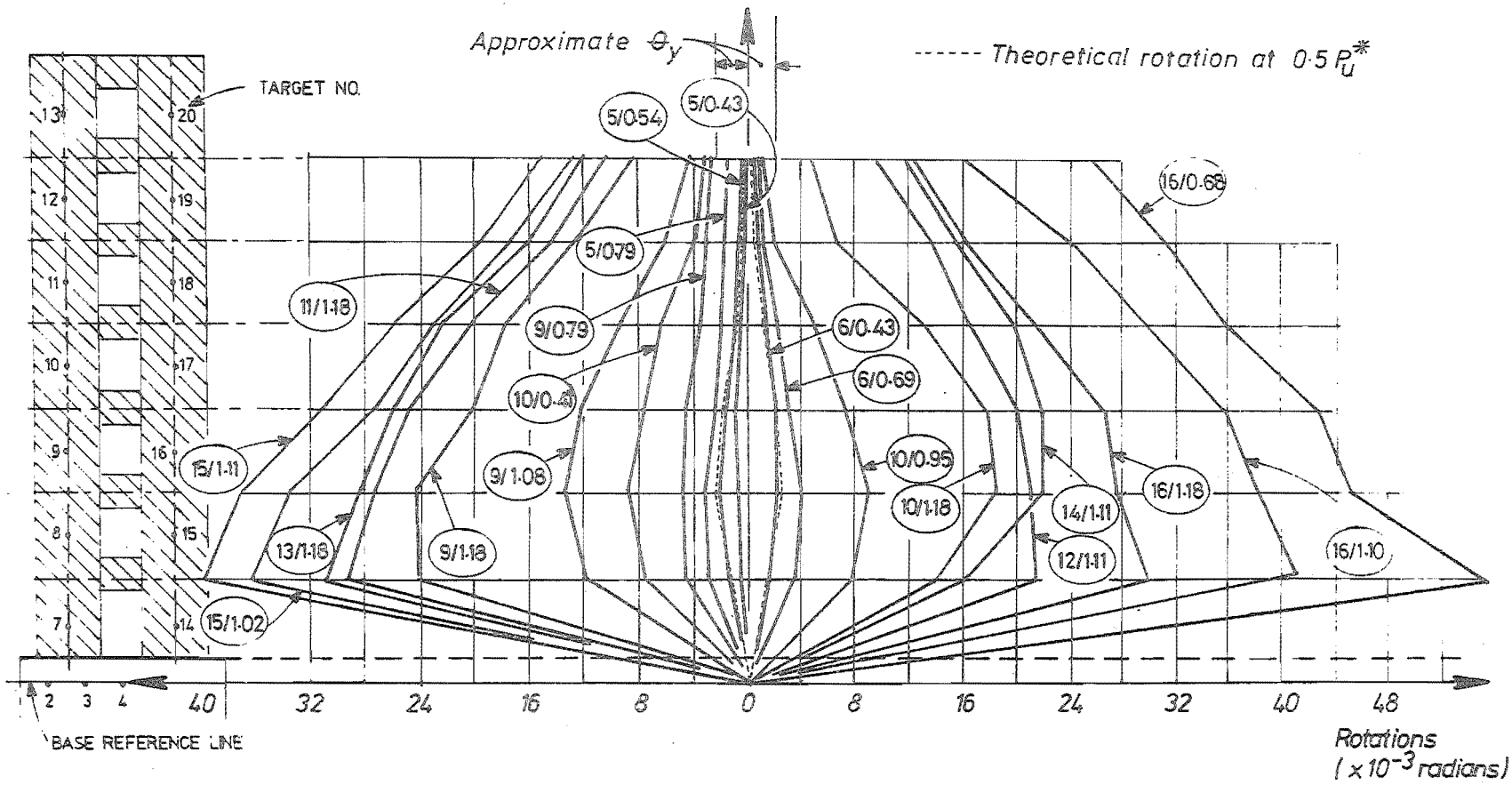

FIG. 7.15.(a) VARIATION OF ROTATIONS OF COUPLING BEAMS WITH HEIGHT DURING CYCLIC LOADING

The rotation computed from measurements made on the centre line of the wall includes the deformation of the portion of the wall between the face of the beam and the centre line of the wall, wherein the steel is anchored. To have an estimate of the rotations due to deformation of the steel anchored in the walls, rotations were also computed using the diagonal steel strain readings. The assumed development lengths for the compression strut, l'_{dc} , and tension member, l'_{dt} , respectively, are shown in Fig. 7.15.c.(i) and (ii). The strain, ϵ_t , along the tension chord was assumed to be constant as shown in Fig. 7.15.c.(i). The assumed variation of strain in the compression chord is as shown in Fig. 7.15.c.(ii). This variation results from the assumed effective area of concrete resisting compression, shown shaded in Fig. 7.15.c.(iii). ϵ_c represents the average strain measured at the instrumented location on steel in the compression strut. The elongation of tension chord, Δ_1 , and the contraction of compression chord, Δ_2 , were computed as the area of the strain diagram shown in Fig. 7.15.c.(i) and (ii). Using these deformations and the geometry of the distorted beams(see Fig. 3.10.c) the beam rotation, θ_b was computed as

$$\theta_b = \frac{\Delta_1 + \Delta_2}{2l_s \sin \alpha} \qquad \ldots (7.1)$$

where α is the inclination of the diagonal steel to the horizontal axis of the beam.

For each load increment the beam rotation was computed for the following set of assumed development lengths:

(a) $l'_{dc} = l'_{dt} = 0$. This gives the rotation of the beam between the faces of the walls.

(b) $l'_{dt} = 0.15l_s$ and $l'_{dc} = 0$.

(c) $l'_{dt} = 0.25l_s$ and $l'_{dc} = 0.15l_s$.

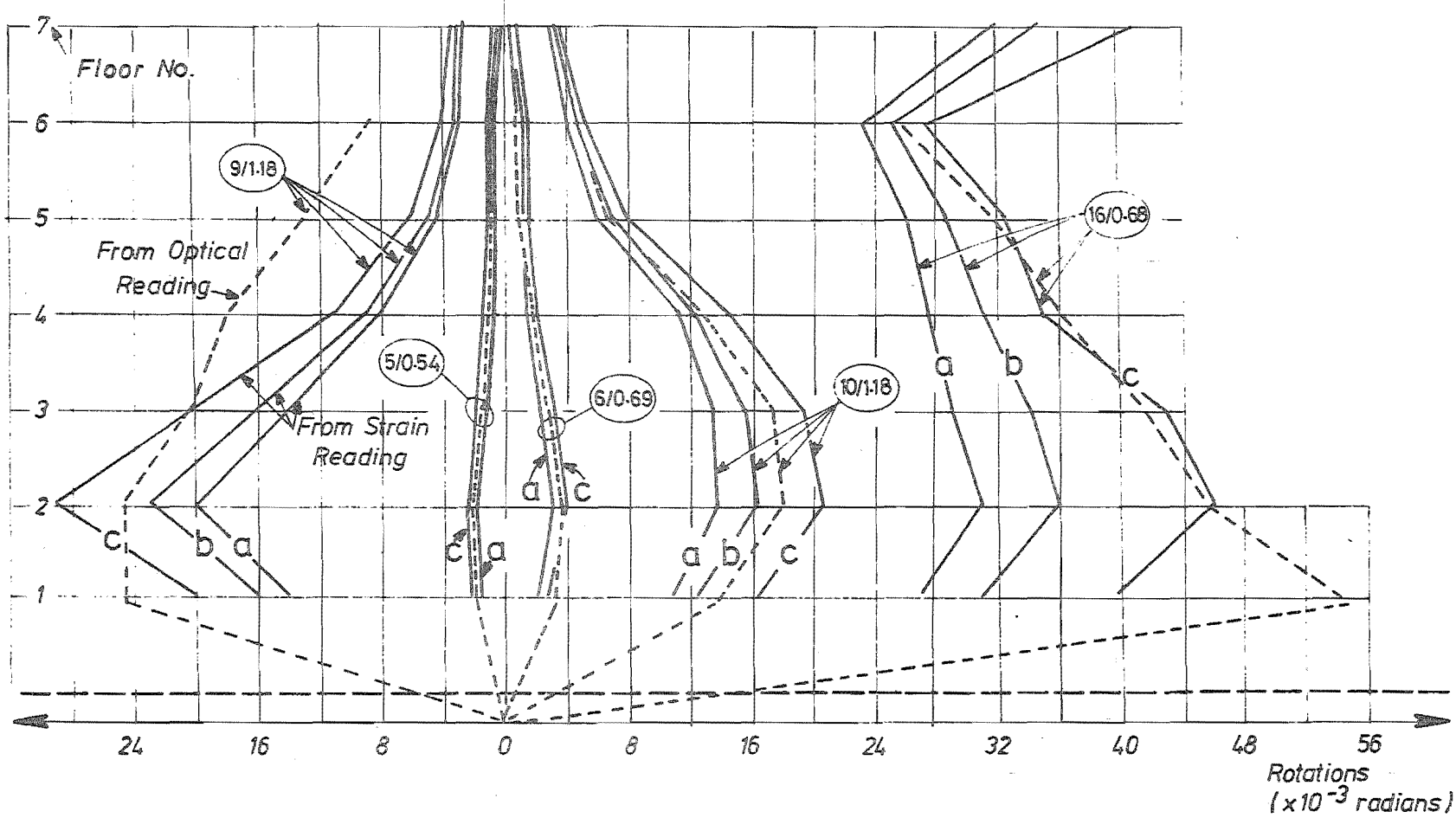

FIG. 7.15.(b) A COMPARISON OF ROTATIONS OBTAINED USING STRAIN MEASUREMENTS WITH THAT BASED ON THEODOLITE OBSERVATIONS

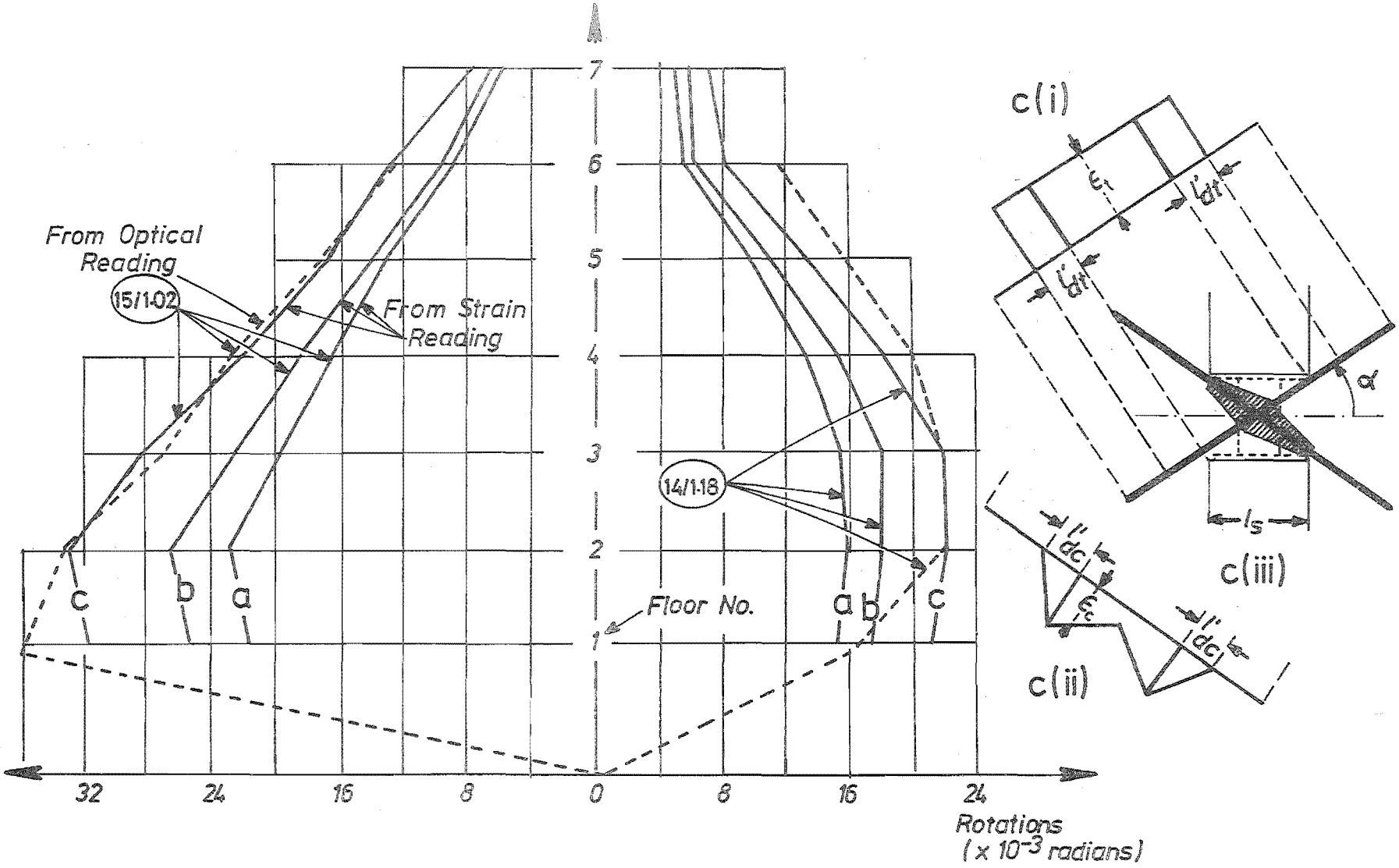

FIG. 7.15.(c) A COMPARISON OF ROTATIONS OBTAINED USING STRAIN MEASUREMENTS WITH THAT BASED ON THEODOLITE OBSERVATIONS

The rotations so derived are then compared with those obtained from theodolite measurements at the centre line of the wall. Fig. 7.15.b and c show this comparison for cycles 5, 6, 9, 10, 14 and 15 respectively. The broken lines show the rotations of the beams which include the deformations of the steel anchored in the end block. These were derived from the theodolite measurements. The full lines represent the rotations based on the strain readings with the assumed development lengths as defined in (a), (b) and (c) in the preceding paragraph.

As expected, during moderate loading, the contribution of the deformation of steel anchored in the wall to the beam rotation is small. (See cycles 5 and 6 in Fig. 7.15.b.) During cycle 9, for the bottom three coupling beams the rotations obtained from the optical measurements indicate that the values of l'_{dc} and l'_{dt} lie within the range (b) and (c). The rotations obtained from strain readings underestimate the overall deformation of the beams at the top of the structure. At this stage the cracks, which developed in the beams at the top, did not pass through the instrumented gauges (see Fig. 7.24.a and b, cycle 10). With progressive cyclic loading the contribution of deformation of steel anchored in the walls to the beam rotation increases. Comparison of the full line curve(a), which disregards this deformation and the broken line curve obtained by optical measurements, for different cycles, shows this. In later cycles (compare cycles 10, 14 and 15 with cycle 9) the patterns of variation of rotations obtained from strain measurements and optical measurements agree well. During the high intensity cycles at near ultimate loads, 20 to 30% of the beam rotation results from the deformation of steel anchored in the walls.

Fig. 7.16 shows the variation of beam rotation plotted against the load ratio P/P^*_u for all the sixteen cycles for the

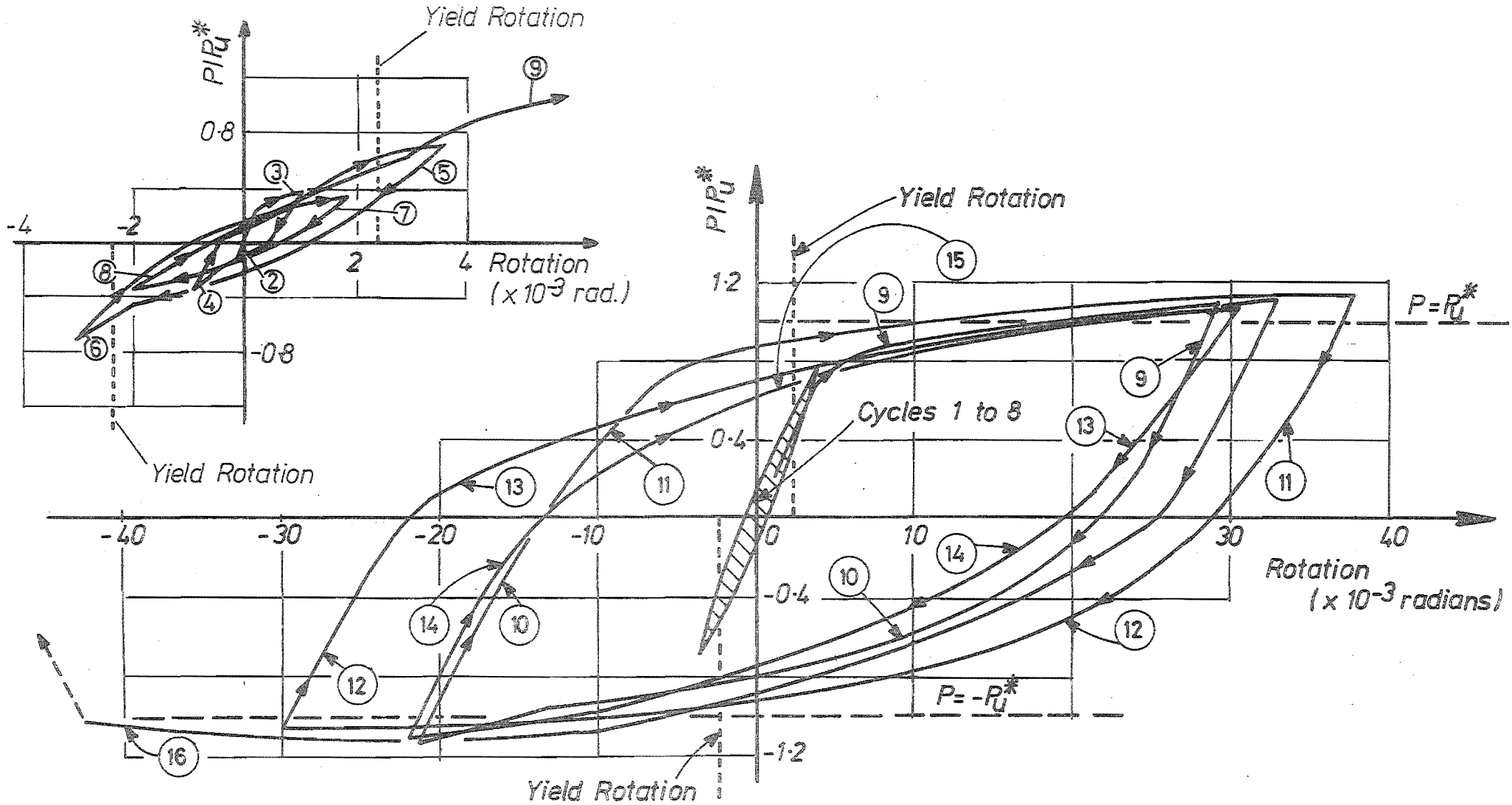

FIG. 7.16 VARIATION OF ROTATION OF THE SECOND FLOOR BEAM WITH CYCLIC LOADING

most severely affected beam at the second floor. These were computed using the strain measurements made on diagonal steel with the assumption $l'_{dt} = 0.25 l_s$ and $l'_{dc} = 0.15 l_s$. An enlarged rotation scale was used (at the top left hand corner of the diagram) to present the behaviour during the first eight cycles. This is included in the shaded area of the main part of Fig. 7.16. The stiffness degradation due to cracking can be seen during cycle 3. The stiffness degradation due to yield of the reinforcement in the tension chord is noticeable during cycle 5. Cycles 9 to 16 are high intensity cycles. The stable hysteresis loops during these cycles show the excellent behaviour of the diagonally reinforced beams. This will be compared with the behaviour of conventionally reinforced beams of Shear Wall A in Chapter 8.

7.7.4 Elongation of Coupling Beams

Using the theodolite measurements made at the centre line of the walls, the elongation of the coupling beams were estimated. These elongations, obtained during cycles 5 to 16, are plotted against the position of beams in Fig. 7.17.

The elasto-plastic analysis presented in Chapter 4 ignores beam elongations. Till the onset of yield in the critical lamina the structure is elastic. Up to this stage the theoretical beam elongations, ignoring the contribution of deformation of steel anchored in the end block, are assumed to be proportional to beam shears. Based on this assumption and defining elongation, Δ_H, (see Fig. 3.10) as

$$\Delta_H = (\Delta_1 - \Delta_2)/2 \cos \alpha$$

the beam elongations for the various coupling beams at the onset of yield of the critical lamina was computed. This is shown in Fig. 6.17 in broken lines. The pattern of observed elongation (see cycle 9 at 1.08 P_u^*) and that computed (see enlarged theoretical

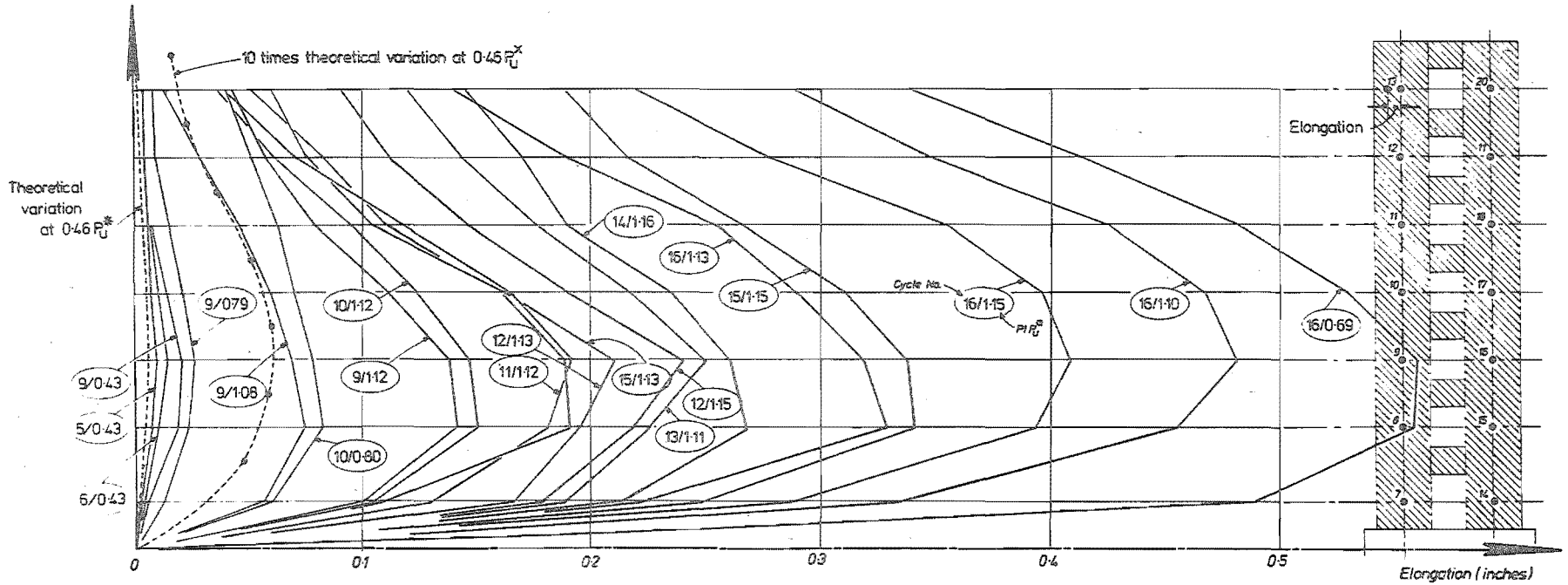

FIG. 7.17 ELONGATION OF COUPLING BEAMS DURING CYCLIC LOADING

variation at 0.46 P_u^*) are similar. Also the pattern of elongation variation and the pattern of rotation variation (see Fig. 7.15.a) for the coupling beams are similar. However, a comparison of theoretical beam elongations at 0.46 P_u^* (broken line curve) with those measured during cycle 5 at 0.43 P_u^* shows that the predicted value is less. This is to be expected as the observed values include elongations of the beam associated with the deformation of the steel anchored in the wall. The observations during cycle 9 at 1.08 P_u^* indicate that the elongation increases are more for the second floor beam than for the beams near the top of the structure. During cycle 9 at 1.08 P_u^* the second floor beam had suffered considerable yielding whereas the top floor beam had just attained yield level. In general, the figure shows that the coupling beams in the critical region are subjected to large plastic deformations.

In the model the two walls were free to move apart. These beam elongations, being rather small when compared with the top floor deflection, did not significantly affect the overall behaviour. In a prototype structure floor slabs will restrict the movement of the walls. This would prevent the beam elongating freely. Hence compressive and shear stresses will be generated at the slab wall junction. The floor slab could also increase the stiffness of the coupling system. The tensile cracks which will develop at the slab wall junction at the inner face of the walls will, however, reduce the beneficial effects of the floor slab in assisting the beams. The likely effects of the restraint by slabs against beam elongation on the overall behaviour needs further investigation.

In Fig. 7.18 the elongation history of the 2nd floor beam is shown. The full lines were based on the theodolite measurements made at targets 9 and 16 (Fig. 7.17) at regular load intervals. As can be seen these two targets were not situated at the intersections of the centre lines of the beams and the walls. Hence the

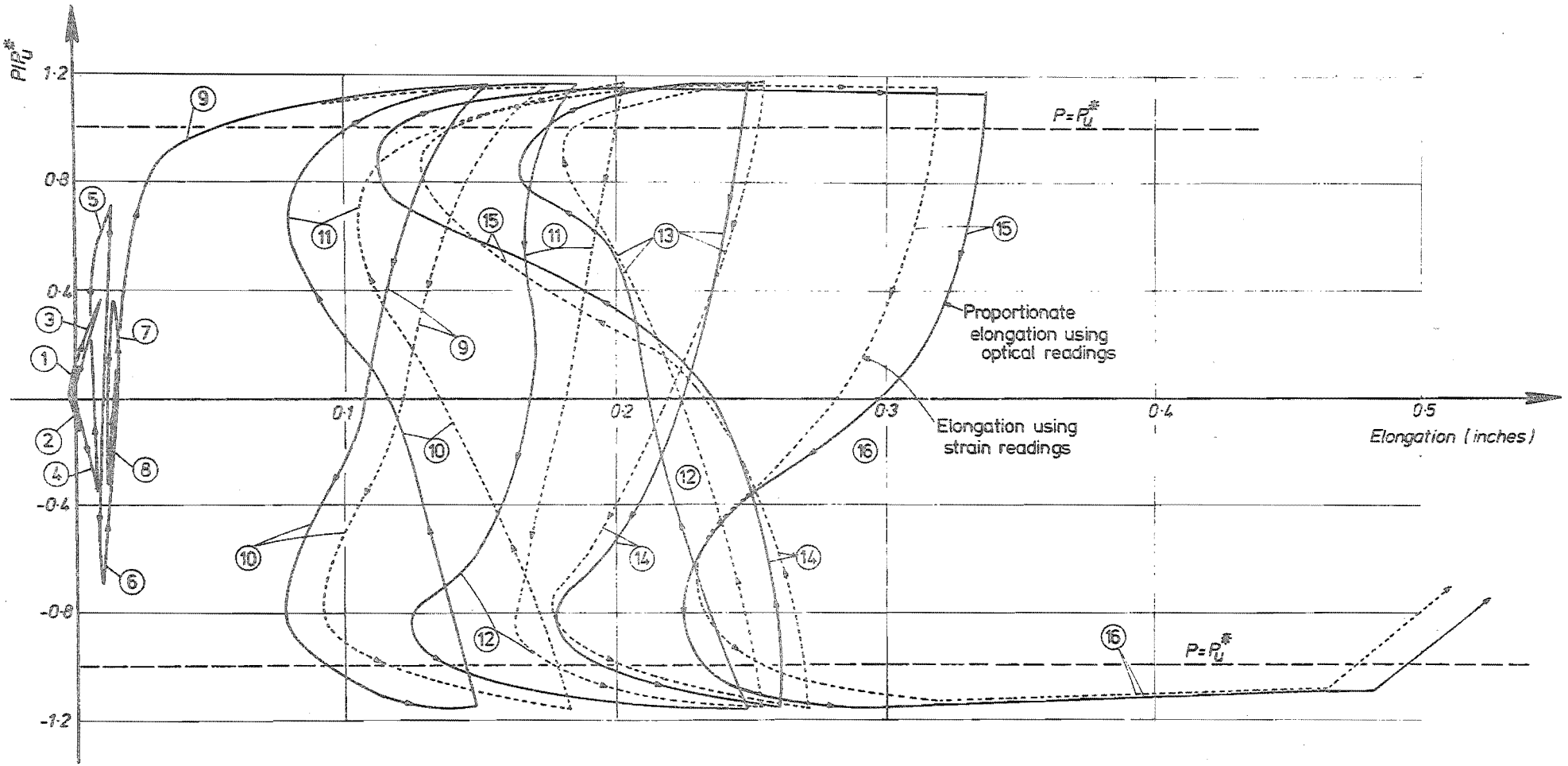

FIG. 7.18 ELONGATION HISTORY OF SECOND FLOOR COUPLING BEAM

elongation obtained using the measurements made at targets 9 and 16 are termed "the proportionate elongations" of the 2nd floor beam.

Elongations were also estimated from strain measurements made at the instrumented locations. For this the idealised strain variation as shown in Fig. 7.15.c.(i) and (ii) were used for the tension and compression chord respectively, and the net elongation of the beam was computed (Eq.(7.2)) at various load intervals with the assumed development lengths $l'_{dt} = 0.25l_s$ and $l'_{dc} = 0.15l_s$. These elongations are shown with dotted lines in Fig. 7.18. An observation of this figure shows that:

(a) There is good agreement between the "proportionate elongation" obtained using the theodolite measurements and the results obtained using the strain measurements as indicated above.

(b) During the first eight cycles the elongations are small compared with the high intensity cycles. In these first four cycles the coupling beam elongations varied proportionally with the load.

(c) During cycle 9 the beam drastically elongates with the load approaching ultimate. When the load is reduced, after reaching the ultimate load, the beam contracts. During reversed loading in cycle 10, the beam contracts up till a load of $0.8\ P^*_u$. With further increase in load the beam again elongates. This phenomenon is associated with the closing of cracks formed during cycle 9 at location where steel yielded extensively. Till these cracks are closed the contraction of the compression chord is more than the elongation of the tension chord. This is due to the Bauschinger effect of the steel in the compression chord. After closing of the cracks the concrete also contributes to the resistance of the external action in the compression chord, whereas steel alone is responsible for resisting tension in the tension chord. The latter dominates deformations from there on and hence the beam again elongates till the ultimate load is attained.

(d) With subsequent high intensity cyclic loading, the elongation of the beam near ultimate load, and the associated contraction of the beam due to Bauschinger effect at low loads, progressively increase. During each of these cycles the elongation at ultimate load is considerably larger than the contraction of the beam at low loads. Thus, at the end of each cycle the beam becomes longer. In the latter cycles (15 and 16) the elongation at ultimate load and the contraction at low loads are larger than they were during cycles 9 and 10. The larger contraction at low loads during the later cycles indicates the presence of wider cracks. This agrees with the crack width measurements made and which are discussed in Section 7.8.

(e) The elongations derived from strain measurements with allowance for the assumed development lengths (see Fig. 7.15.c.(i) to (iii)), $l'_{dt} = 0.25l_s$ and $l'_{dc} = 0.15l_s$ are more than those based on optical measurements during cycles 9 to 13. From cycle 14 the two elongations agree well.

7.7.5 Deflection Profiles of the Walls

Fig. 7.19 shows the deflection profiles of the left wall during cycles 5 and 6 and high intensity cycles 9 to 16. These deflections were computed from theodolite measurements made at targets 1 to 13. The deflection profiles show that the shear wall is practically straight above the first floor at all load levels. This indicates that the top floor deflection resulting from the contribution of flexural and shear deformation of the walls above the first floor level is small. A quantitative assessment of this is made in Section 7.7.7, based on the wall curvature variation with height derived from measured steel strains.

7.7.6 Elongation of the Walls

Using the measurements made at the targets in the top floor of the walls, the elongation of both walls relative to the base

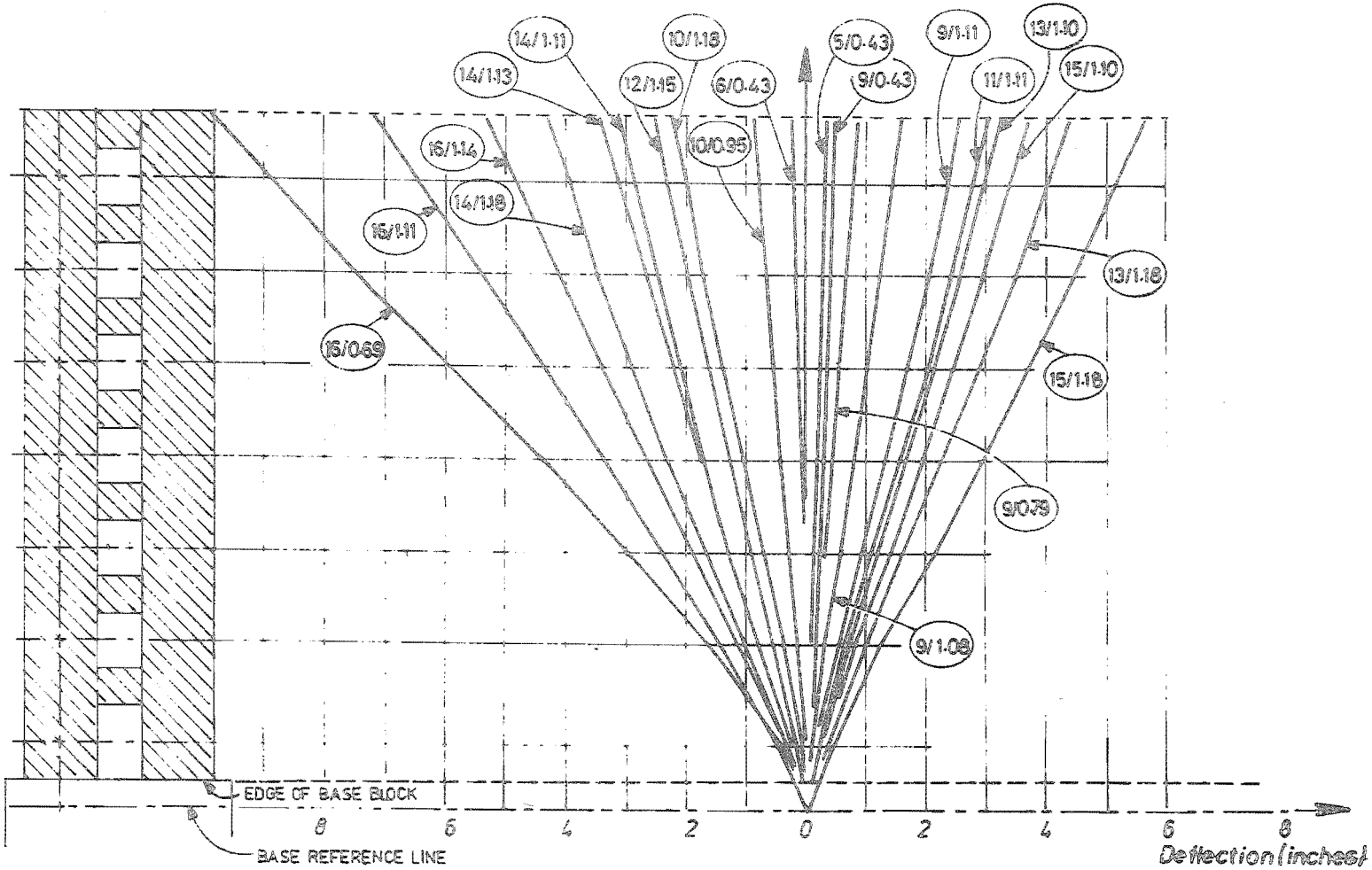

FIG. 7.19 THE DEFLECTION PROFILE OF THE LEFT WALL

reference line was also computed. In Fig. 7.20, the elongation of the left and right wall, during cyclic loading, is plotted against the lateral load. The left wall is subjected to tension during odd numbered cycles and to compression during even numbered cycles. The contraction during the even numbered cycles is less than the elongation during odd numbered cycles. Hence, with cyclic loading the wall progressively elongates. At the end of cycle 15 there is a permanent deformation of approximately 0.3" in both the walls. Significantly large permanent yield deformations of the reinforcement in the bottom floor of both walls have contributed to this elongation of the walls.

7.7.7 Curvature Variation along the Height of the Walls

The curvatures at various wall sections were estimated using the strain measurements made on the walls. The curvature was computed using the relationship

$$\varphi_n = \frac{e_{tn} - e_{cn}}{d_{fn}} \qquad \ldots (7.3)$$

where φ_n = curvature at the nth section

e_{tn} = strain in the tension reinforcement at the nth section

e_{cn} = strain in the compression reinforcement at the nth section

d_{fn} = the distance between the tension and compression reinforcement where the strain e_{tn} and e_{cn} were measured.

Fig. 7.21 shows the curvature variation for cycles 5 and 9. The theoretical curvature was computed at 0.65 P_u^* based on the elasto-plastic analysis presented in Chapter 4. This theoretical curvature is shown in thin stepped lines in Fig. 7.21. The figure shows that the theoretical and observed curvatures correlate well

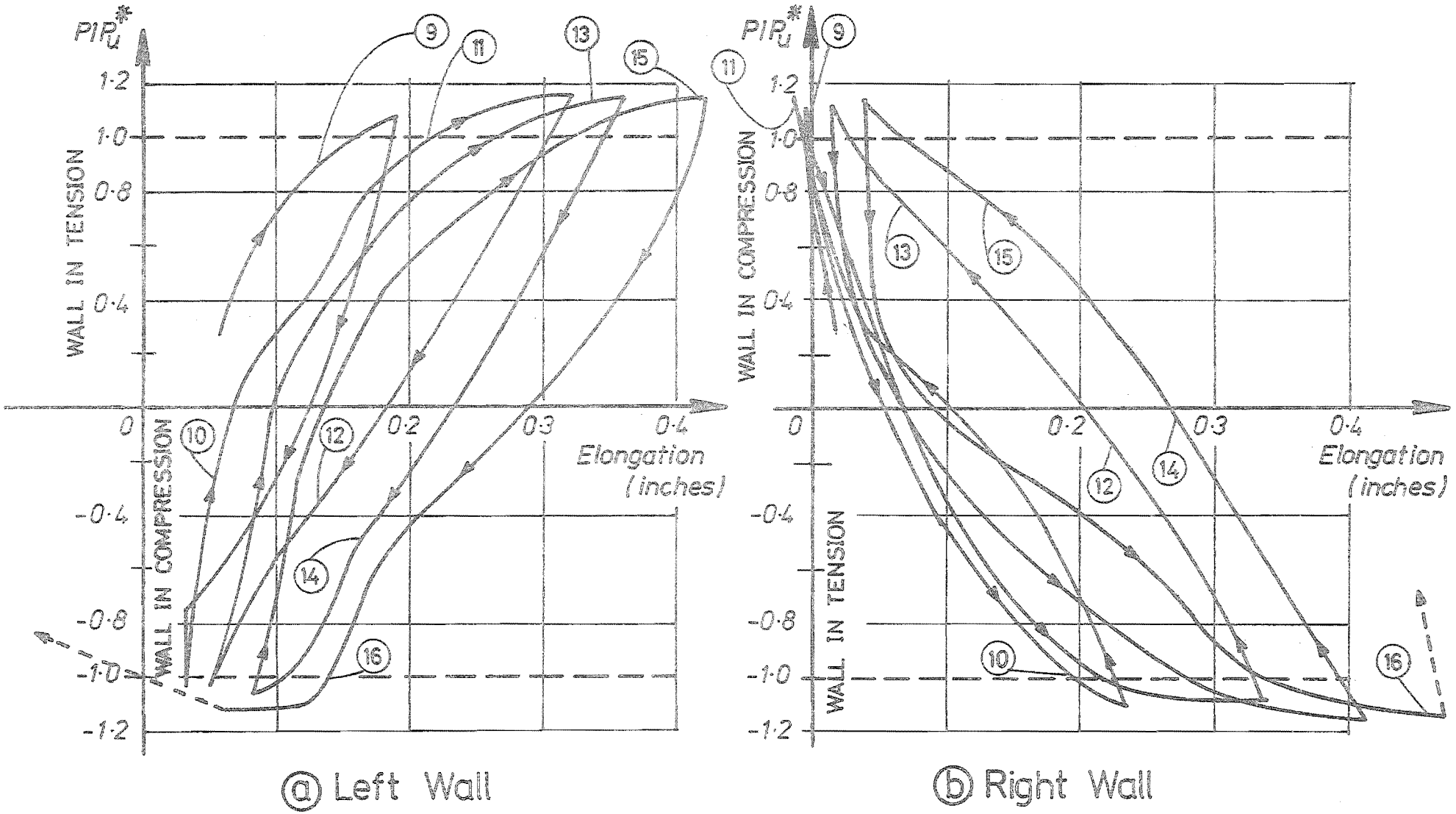

FIG. 7.20 ELONGATION OF THE WALLS RELATIVE TO BASE REFERENCE LINE

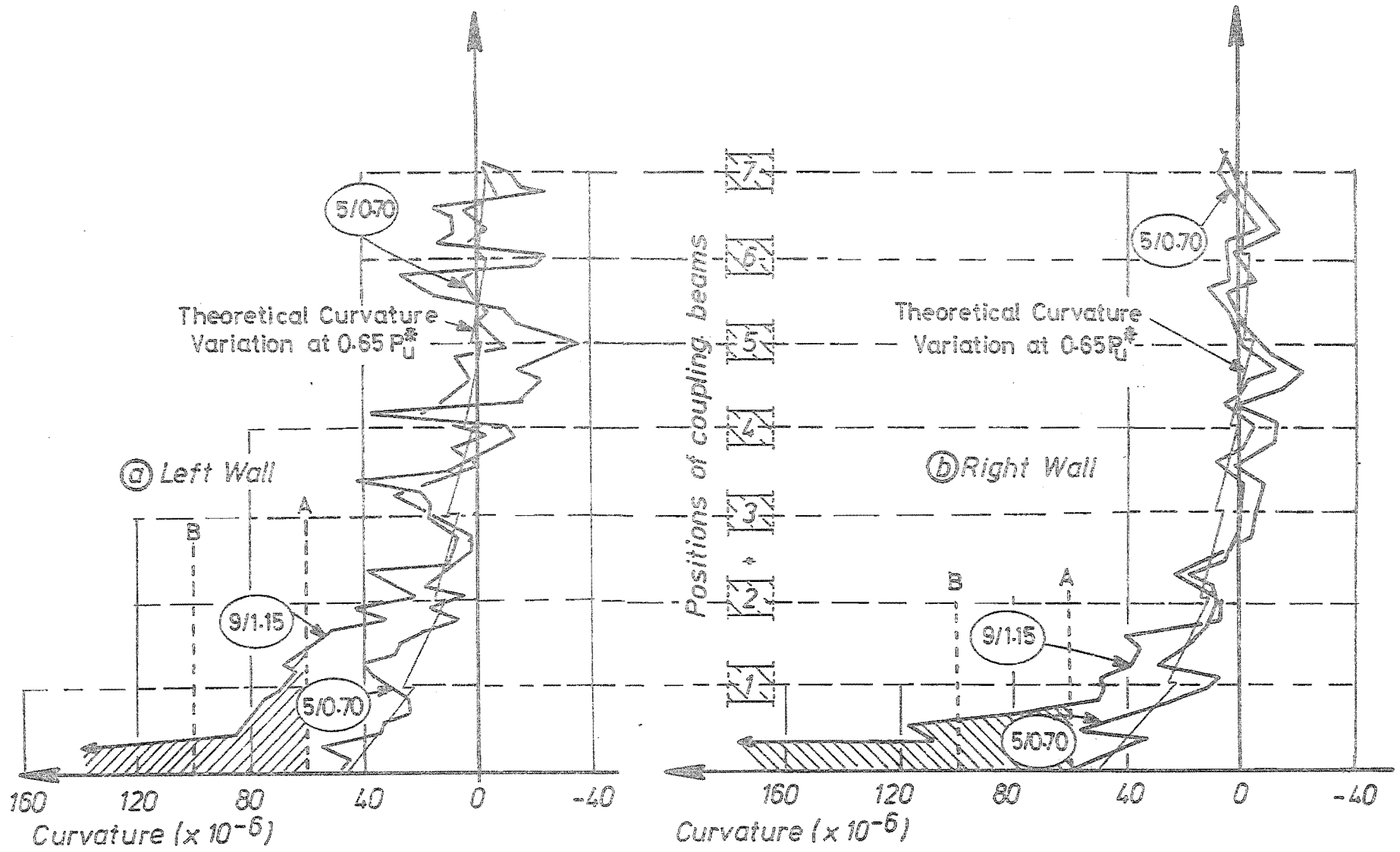

FIG. 7.21 COMPARISON OF CURVATURES OF TENSION AND COMPRESSION WALLS DURING CYCLES 5 AND 9

in the lower storeys. Two theoretical limits of curvature are indicated in the plastic hinge region. These theoretical limits were based on the stipulated strains for the onset of yield curvature (the broken line A) and full yield curvature (broken line B) for the critical section described in Section 3.5.3.

Fig. 7.22 shows the curvature variation in the bottom two floors of the left wall during various high intensity cycles. This wall is subjected to axial tension during odd numbered cycles. In the same figure three theoretical curvatures based on load-moment curvature relationship are also shown with the notation described in Section 6.7.7. It is seen that the theoretical maximum curvature predicted by the analysis (line C) is attainable for the compression wall. In accordance with the theoretical study made in Section 4.4, the curvatures attained by the compression wall are large. By the time the theoretical maximum curvature is attained in the tension wall, the compression wall is subjected to nearly twice the maximum curvature predicted by line C. This is as expected. The estimated maximum concrete strain in the extreme fibre of the compression wall at this stage is approximately 0.01.

7.7.8 Relationship between the Length of Plastic Hinge, Maximum Curvature, Wall Rotation and Top Floor Deflection

The shaded area in Fig. 7.21 represents the plastic rotation that occurs at the base of the walls. As described in Section 6.7.8, this area was replaced by an equivalent rectangle whose breadth and height are the length of plastic hinge and maximum ultimate curvature respectively. Based on this approximation the rotations and consequent top floor deformation were computed. The details of these calculations are similar to those described in Section 6.7.8 and hence they are not given here. This study revealed that:

(a) The length of plastic hinge for the tension wall is more than twice the length of plastic hinge for the compression wall during the various cycles.

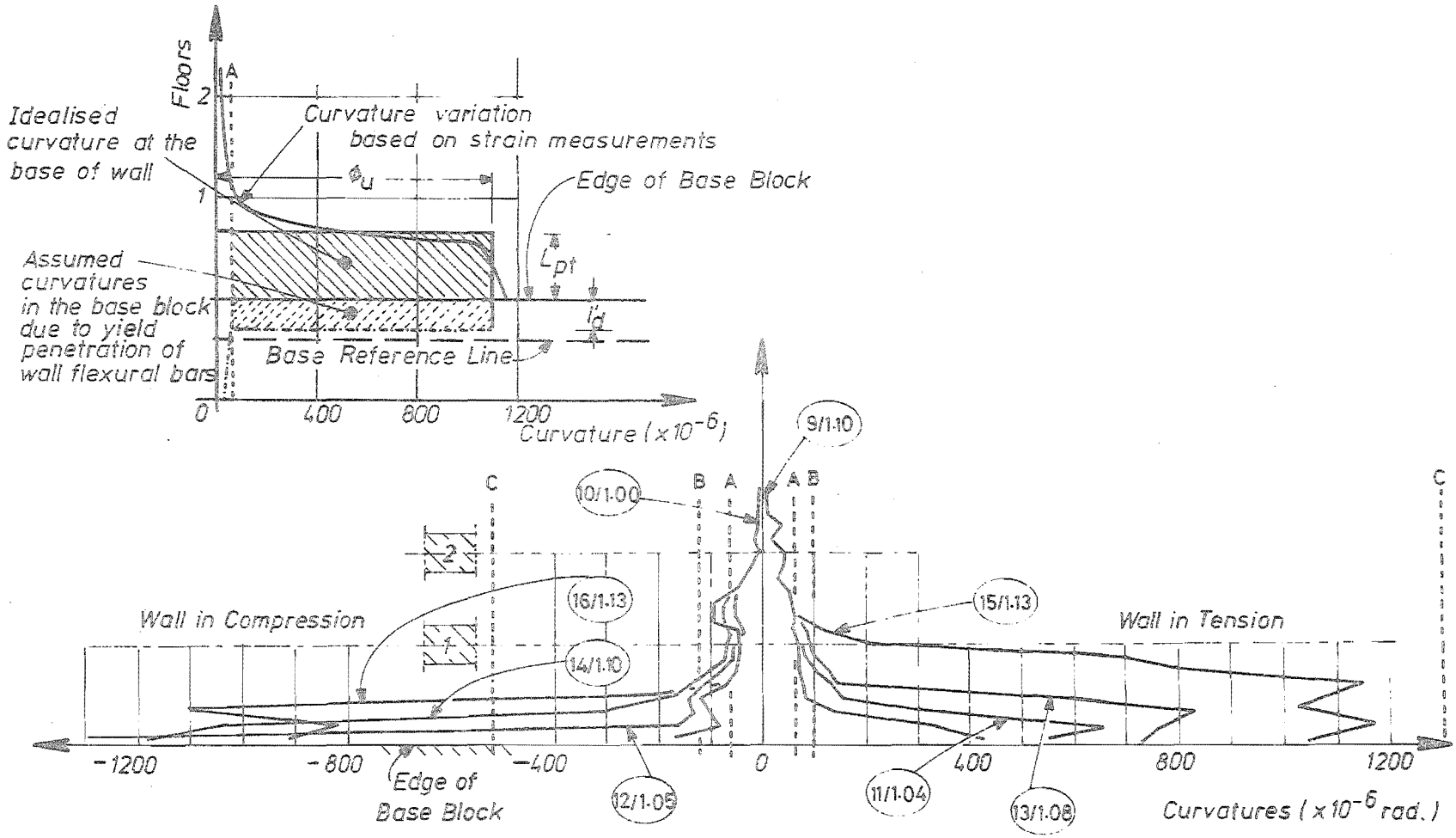

FIG. 7.22 CURVATURE VARIATION OF THE LEFT WALL IN THE PLASTIC HINGE REGION

(b) The maximum curvature for the compression wall is more than twice that of the tension wall during various cycles.

(c) The areas of the curvature diagrams at the base of the two walls are approximately equal in accordance with Eq. (4.22) derived in Chapter 4.

Table 7.1 shows the contribution of different causes, such as elastic bending along the height, plastic rotation at the base, shear deformations and rotation occurring in the end block, to the top floor deflection during the various high intensity cycles at the maximum deflections attained. The various contributions were computed using the same assumptions as those described in Section 6.7.8. An examination of this tables shows that:

(a) The increase in elastic deflection with cyclic loading from 0.85" to 1.11" is insignificant.

(b) The total elastic deflection of approximately 0.85" during cycle 9, which has been evaluated from curvature measurements, agrees well with the observed deflection at the onset of yield in the outer layer of tension steel in the tension wall (0.9" during cycle 9 shown in Fig. 7.13). The onset of yield in the compression wall occurred earlier, i.e. when the top floor deflection was 0.6".

(c) During cycles 9 and 10, 35 to 43% of the top floor deflection resulted from elastic curvatures. However, the deflection profiles of the walls (see Fig. 7.19) are practically straight above first floor level. An examination of the curvature diagram at 1.15 P_u^* (Fig. 7.21) during cycle 9 confirms that the major portion of elastic rotations occur between the ground and first floor levels. However, large wiggles in the curvature diagram at the top of the structure are noticeable. The forces introduced by the beam steel affected the strain measurements made on wall flexural steel near the windows. Therefore the curvatures based on these measurements show unrealistic large wiggles.

TABLE 7.1 A COMPARISON OF THE CONTRIBUTIONS OF DIFFERENT ACTIONS TO THE TOP FLOOR DEFLECTION FOR THE VARIOUS HIGH INTENSITY CYCLES AT MAXIMUM DEFLECTIONS ATTAINED*

CYCLE	Total Measured Top Floor Deflection	CONTRIBUTION OF:					
		Elastic Curvature along the height of the wall		Plastic Curvature in the plastic hinge region		Shear distortion and deformations occurring in the foundation block	
	Δ (in)	Δel (in)	% of Δ	Δpw (in)	% of Δ	Δs + Δfb (in)	% of Δ
9	2.4	0.85	35	1.19	50	0.36	15
10	2.1	0.90	43	0.90	43	0.30	14
11	2.8	0.92	33	1.40	50	0.48	17
12	2.6	0.88	34	1.23	47	0.49	19
13	4.0	1.00	25	2.20	55	0.80	20
14	4.0	1.03	26	2.09	52	0.88	22
15	5.0	1.05	21	2.70	54	1.25	25
16	7.5	1.11	15	4.29	57	2.10	28

* For cycles during which strain measurements were not taken when maximum deflection was attained, extrapolated strain readings, based on measurements made at earlier increments, were used to compute the curvatures along the height.

(d) The sum of the deflections resulting from shear distortions in the walls and anchorage deformations of the flexural steel in the foundation block, Δfb , are significant in cycles 15 and 16. During the final cycle the contribution of end block rotation (deformation of steel anchored in the block) to the top floor deflection was estimated. For this the development length, l'_d , for flexural steel in the walls was assumed to be $d/3$, as shown on the insert of Fig. 7.22. This corresponds to a yielding length of approximately ten times the diameter of No. 5 bar used in the walls. The curvature variation inside the end block was assumed to be constant over this length, l'_d , at φ_u , where φ_u is the average measured curvature in the wall near the end block. The contribution of elastic curvature inside the end block to the top floor deflection was neglected. With the above assumptions it was estimated that a top floor deflection of approximately 1.6" results from the deformation of steel anchored in the end block during the final cycle at near ultimate load. This indicates that the remaining 0.5" (i.e. 2.10" - 1.6") is due to shear deformation occurring in the walls at near ultimate load. Thus, the contribution of the anchorage deformation of the wall steel in the base block, Δfb , to the total deflection, Δ , is larger than that of the shear distortions, Δs . Shear deformation is likely to be maximum in the final cycle. Its contribution to the top floor deflection in this cycle is approximately 6% .

7.8 CRACK FORMATION, CRACK WIDTH MEASUREMENTS AND BUCKLING FAILURE

Figs. 7.23 to 7.25 show the crack patterns of the beams and walls at various stages of cyclic loading. The maximum load during the first two elastic cycles was less than the load required to crack the model. The first cracks were observed at the tension corners in the second floor coupling beam at a load of $0.15\ P^*_u$ during cycle 3

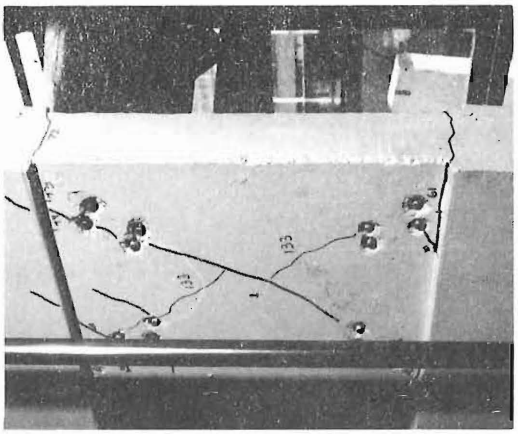

Cycle 10

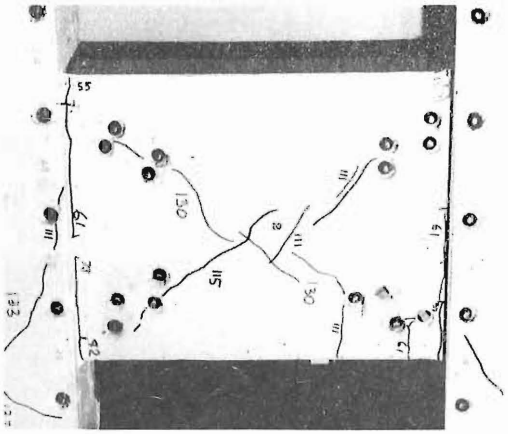

Cycle 10*

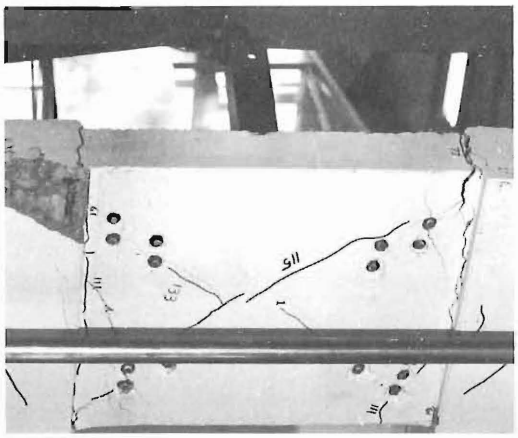

Cycle 16*

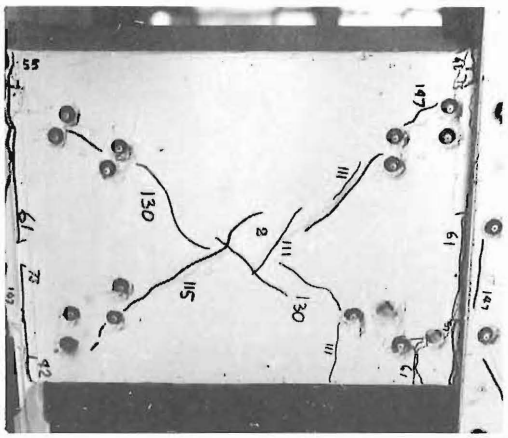

Cycle 15*

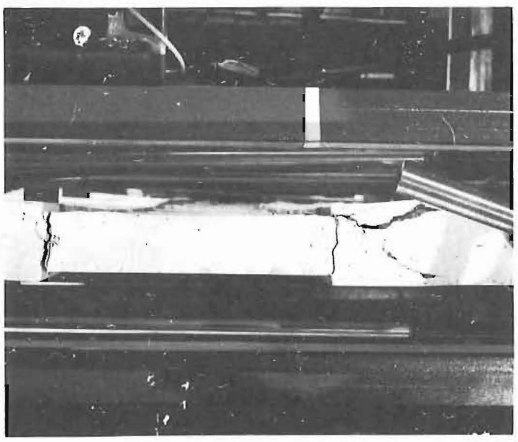

After buckling

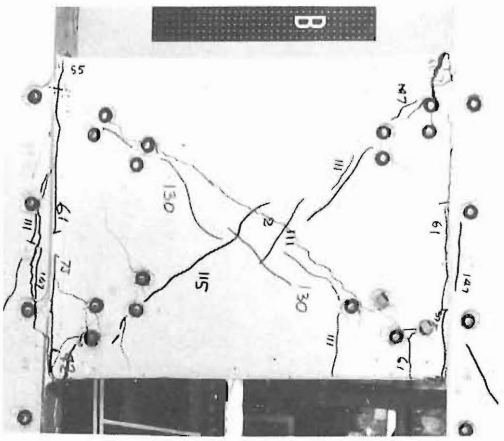

Cycle 16*

FIG. 7.23. (a) TOP FLOOR BEAM

FIG. 7.23. (b) 6TH FLOOR BEAM

* Photographs taken from South side

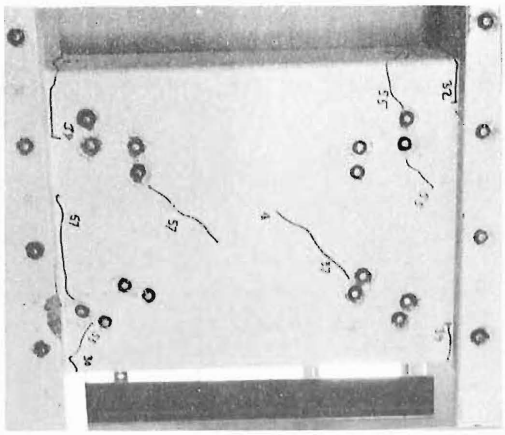

Cycle 5

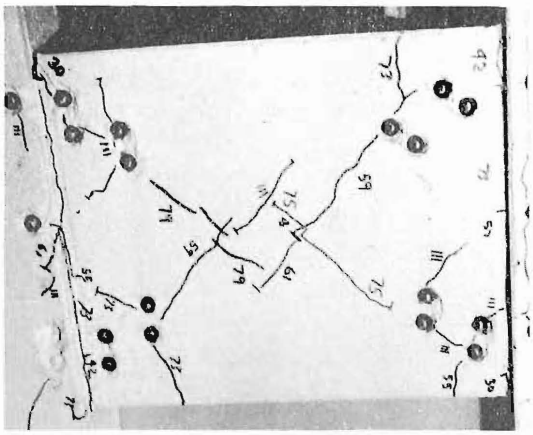

Cycle 10*

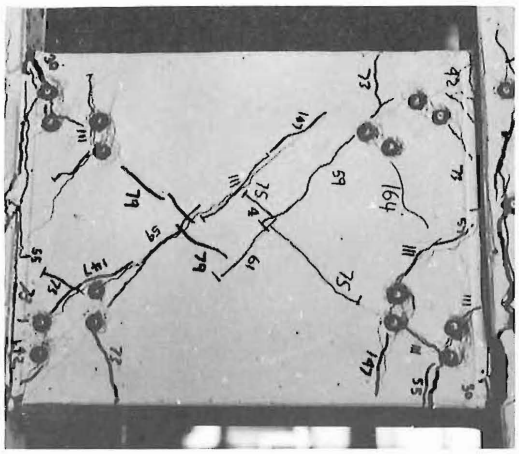

Cycle 15*

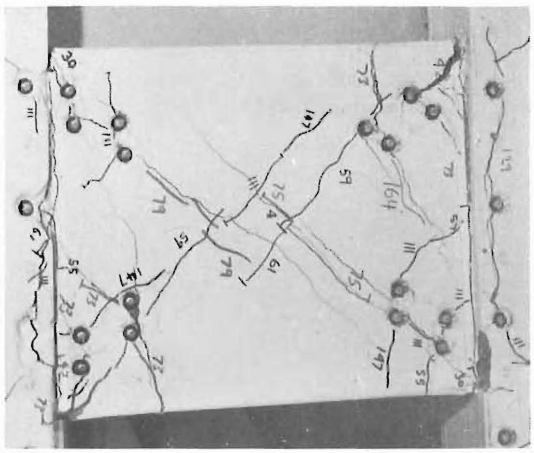

Final cycle*

FIG. 7.23. (c) 4TH FLOOR COUPLING BEAM

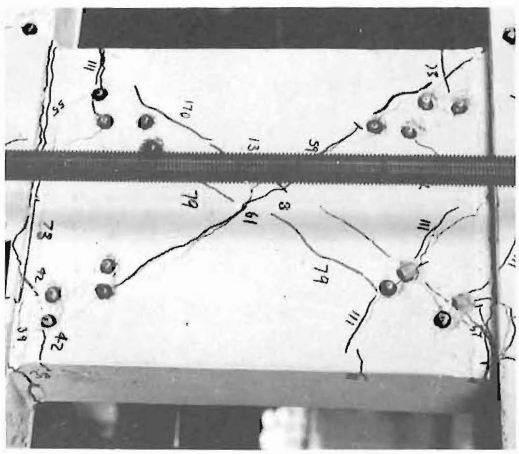

Cycle 15*

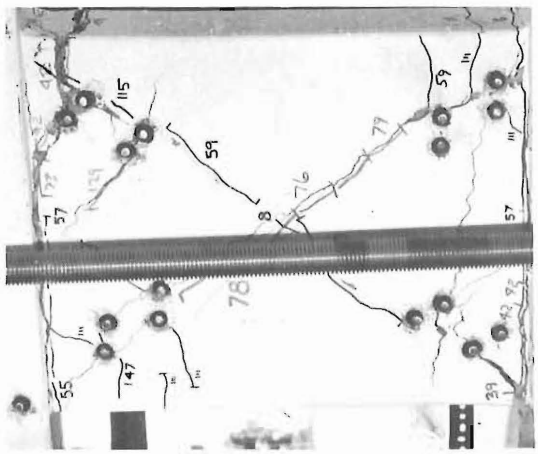

Final cycle*

FIG. 7.23. (d) 5TH FLOOR COUPLING BEAM

* Photographs taken from the South side

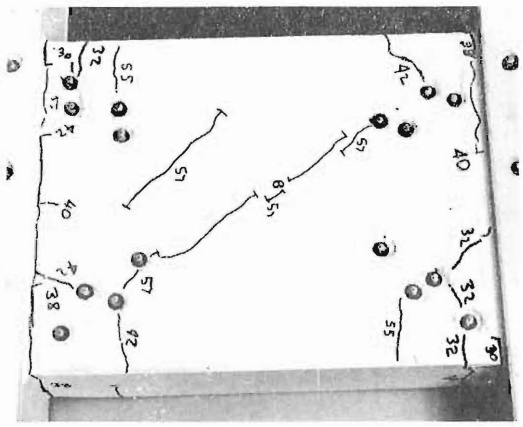

Cycle 5 *

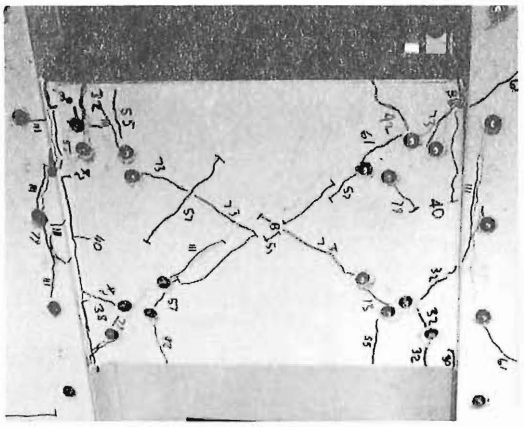

Cycle 10 *

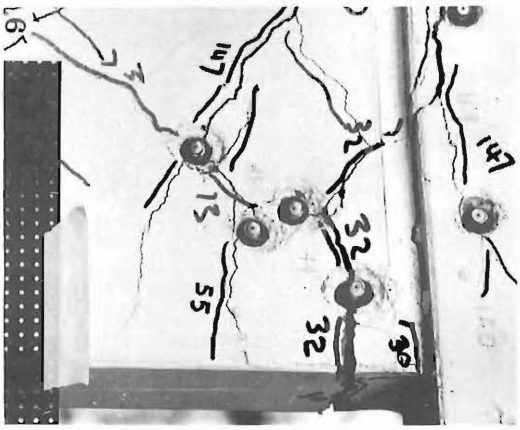

Cycle 15 *

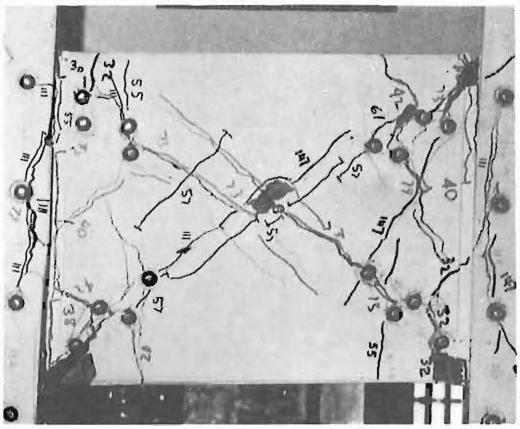

Cycle 16 *

FIG. 7.23. (e) 2ND FLOOR COUPLING BEAM

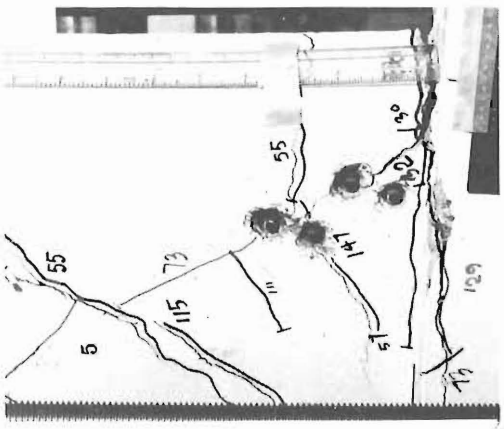

Cycle 15

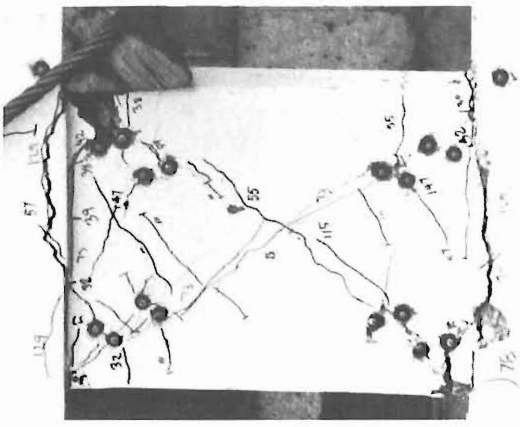

Cycle 16

FIG. 7.23. (f) 3RD FLOOR COUPLING BEAM

* Photographs taken from South side

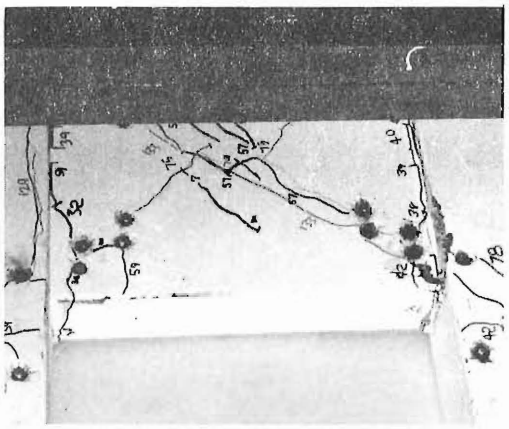

Cycle 10

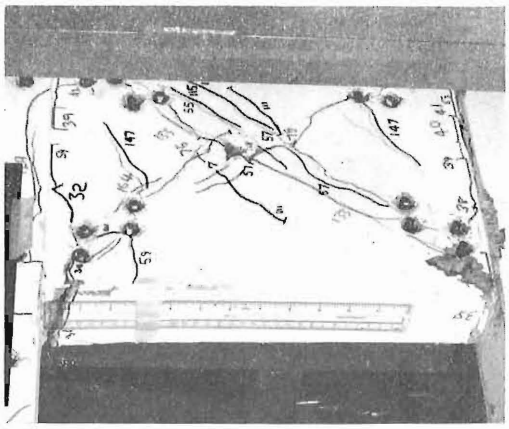

Cycle 15

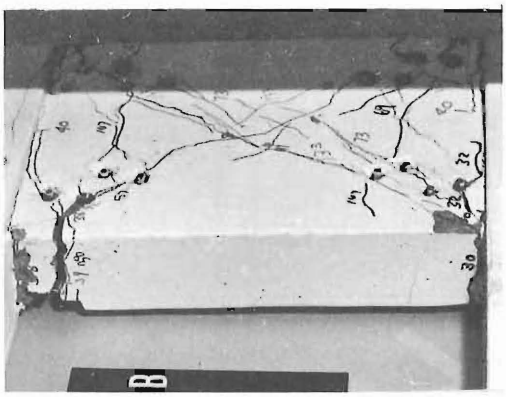

Cycle 14*

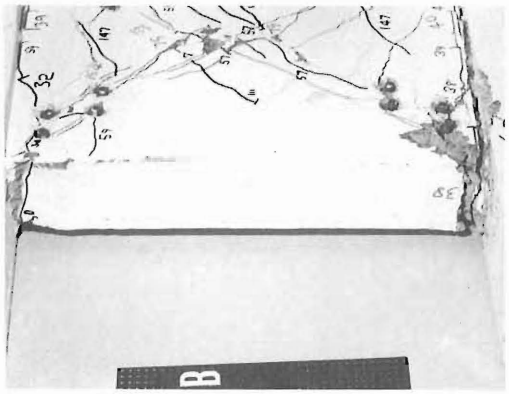

Final cycle

FIG. 7.23. (g) BOTTOM FLOOR COUPLING BEAM

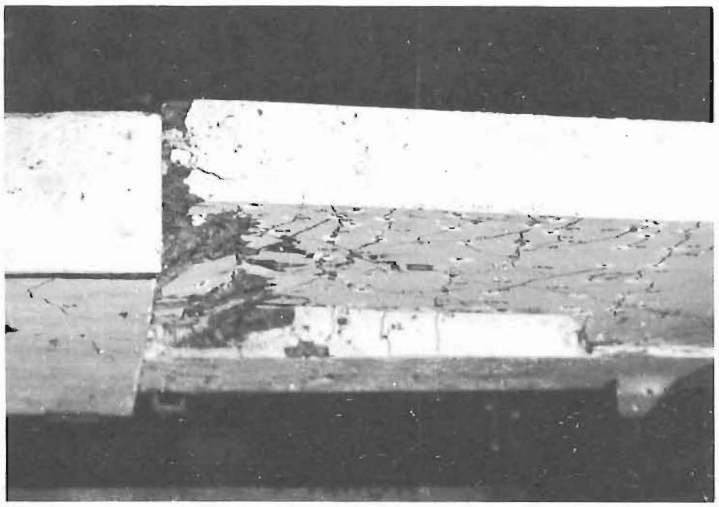

FIG. 7.24 THE BUCKLED COMPRESSION WALL

* Photograph taken from South side.

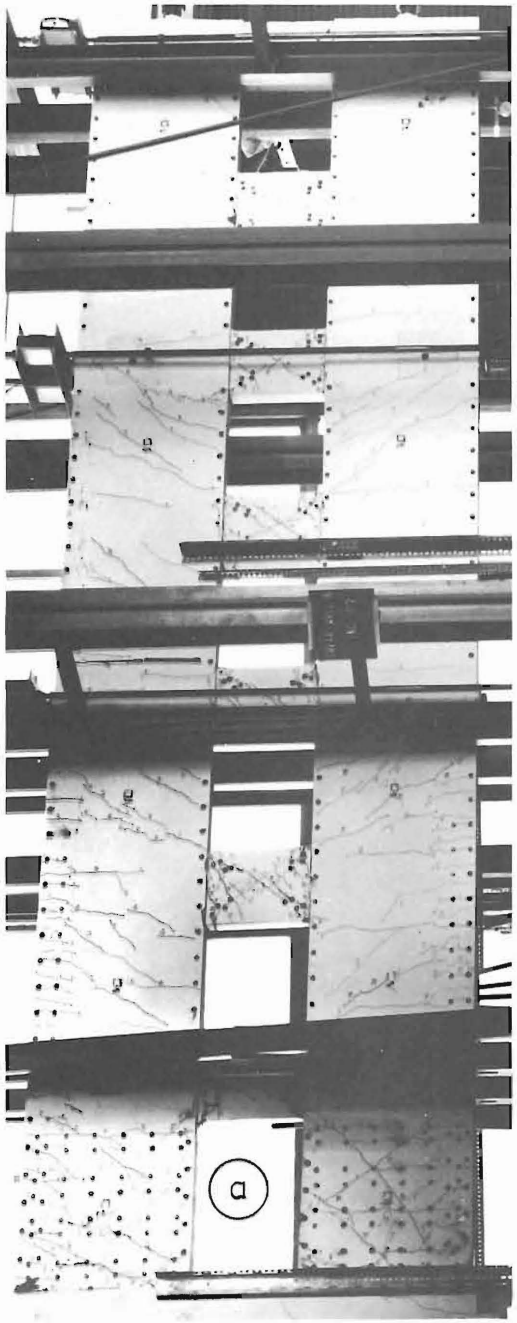

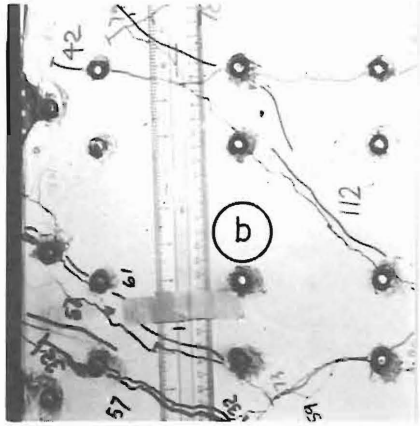

Tension corner of right wall

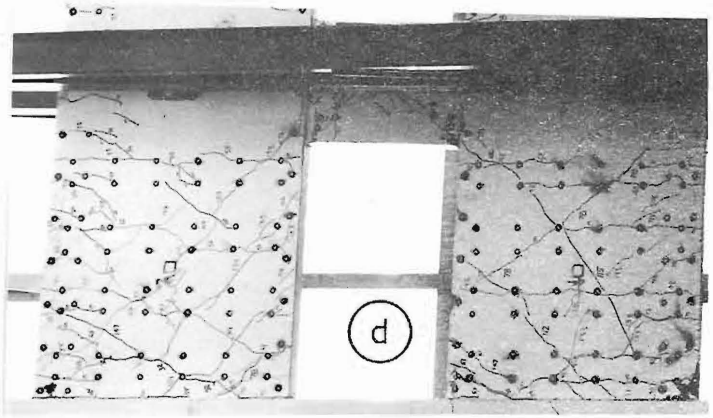

Diagonal cracks in the bottom floor of the walls (cycle 10)

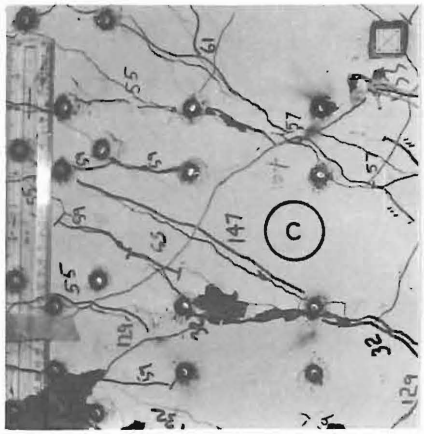

Tension corner of left wall (cycle 15)

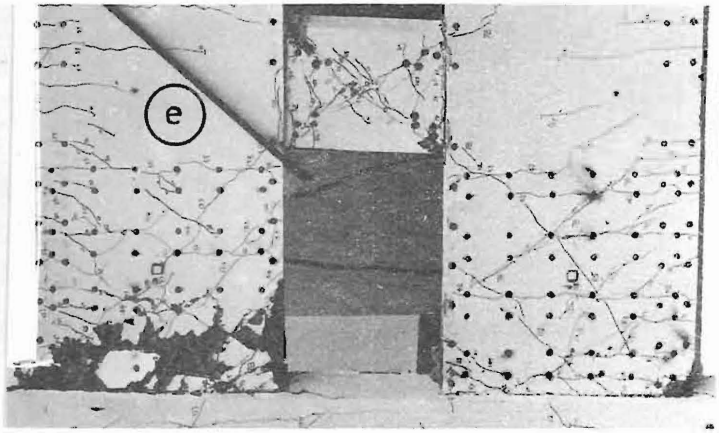

Buckling failure of left wall

FIG. 7.25 CRACKS FORMED IN THE LEFT AND RIGHT WALLS

and $0.18\ P_u^*$ during cycle 4. These cracks were vertical flexural type cracks which formed at the junction of the wall and the beam and propagated along the beam depth. These were then followed by the diagonal cracks in the beams. During subsequent loading similar cracks developed in the bottom four coupling beams (see Figs. 7.23. c to g).

During cycle 5 at $0.38\ P_u^*$ the first cracks developed at the base of the tension wall across the 5 layers of reinforcement. This was followed by cracks at the base of the compression wall across the single layer of tension steel near the windows. These flexural type cracks were then followed by diagonal cracks in both walls during the next incremental load ($0.40\ P_u^*$). They can be seen in Figs.7.25. a and d. During the reversed cycle 6 similar diagonal cracks formed in the coupling beams and at the base of the walls. The diagonal cracks formed during cycles 5 and 6 were approximately orthogonal (see Fig. 7.23. c to g). In the top floor beam the diagonal cracks formed only at $0.65\ P_u^*$ (see Fig. 7.23.a). The inclination of the cracks at the base of the wall in tension was less than 45°. This resulted in these cracks crossing fewer number of stirrups,as pointed out in Section 7.6.1.

The maximum loads during cycles 7 and 8 were of the order of $0.4\ P_u^*$. Very few new cracks developed during these elastic cycles.

Cycles 9 and 10 were high intensity load cycles. By the end of cycle 10 severe cracking had developed in both walls in the bottom storey and also in all the coupling beams (see Fig. 7.23. a to g and Fig. 7.25.d). The photograph reproduced in Fig. 7.25.d was taken at the beginning of the 11th cycle. There were very few cracks in the top floor walls. (See Fig. 7.25.a.)

During the subsequent high intensity cycles (11 to 14) the cracks alternately opened and closed at the corners of the beams and the walls. Cycle 15 caused rapid deterioration of the left (tension)

wall with spalling of the cover concrete. The damage suffered by this wall up to this stage can be seen in Fig. 7.25.c. The tension corner of the compression wall suffered relatively less damage (see Fig. 7.25.b). The damage suffered by the beams was less even though the cracks in the tension corners widened (0.3" to 0.4") considerably. (See Fig. 7.23. e to g.)

The crack widths measured during cycles 5 to 10 are shown in Fig. 7.26.a. The key diagram gives the location at which these crack width measurements were made. Here the cracks formed during positive loading are shown in thick lines and those opened during negative cycles are in thin lines. At low loads ($< 0.4\ P_u^*$), the width of cracks could not be estimated accurately due to the limitations of measuring equipment used. In the major portion of Fig. 7.23.a. crack widths are plotted against the lateral load from $0.4\ P_u^*$ onwards. The figure shows the following:

(a) As expected the width of cracks in the coupling beams near the critical region (locations 2A and 2B) are larger than at the top (locations 6A and 6B).

(b) The crack widths in the walls above first floor level are small (locations 2C, 4B, 2D and 4A).

(c) The cracks in the coupling beams near the critical region (locations 2A and 2B) are wider than those at the base of the walls (locations 1A, 1B, 1C and 1D).

In Fig. 7.26.b. the variation of average crack widths at the top right and bottom left corner (see insert) of the second floor beam is plotted against the load ratio. As expected, the load-crack width loops are similar to the diagonal steel load-deformation loops (see Fig. 7.4). During even cycles the load-crack width curve indicates softening of the member at low loads (Bauschinger effect).

The failure was initiated in the compression wall (left wall) during cycle 16. (See Fig. 7.25.a.) At the end of cycle 15, the left hand corner of this wall (Fig. 7.25.c) was damaged due to

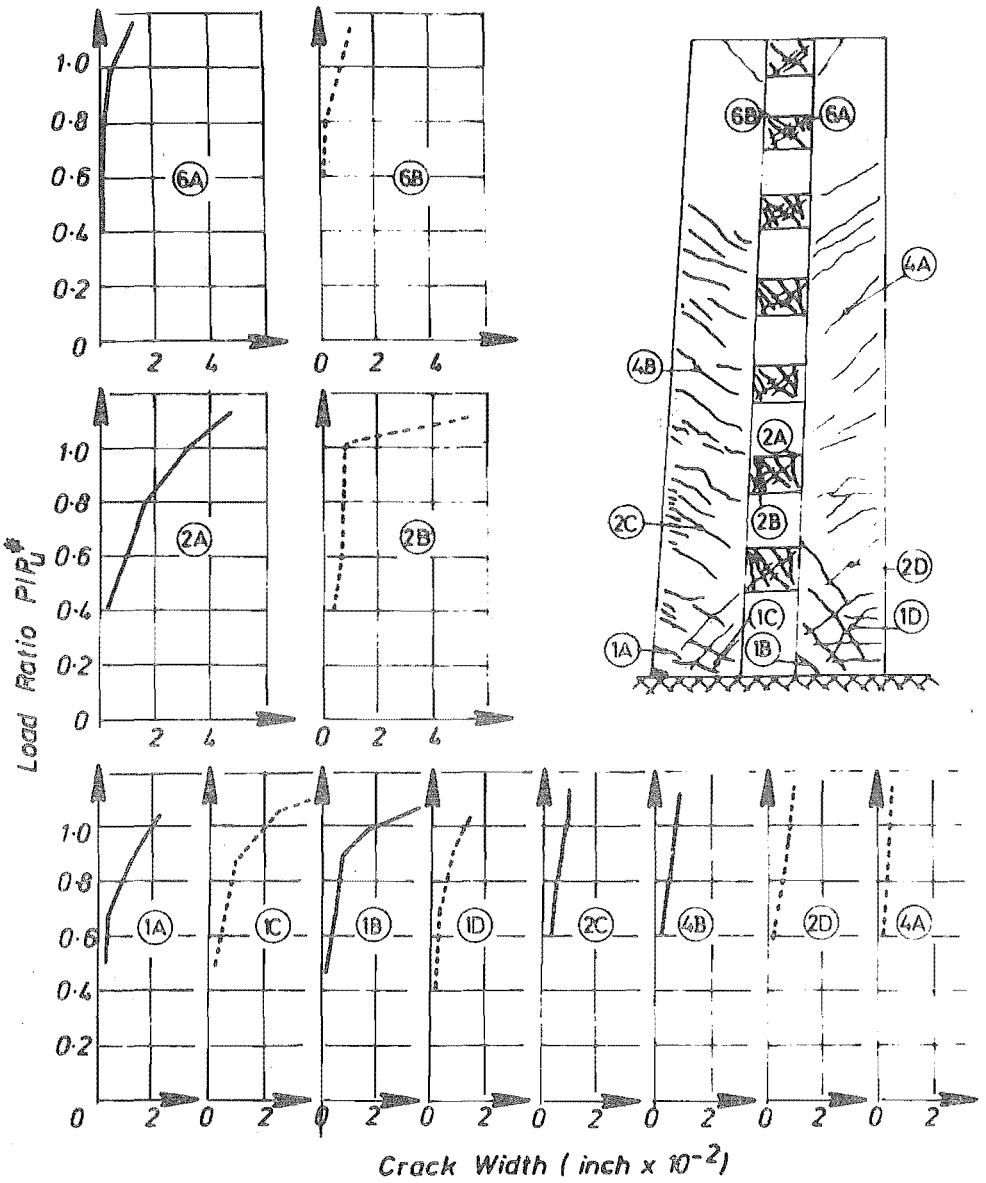

FIG. 7.26.(a) CRACK WIDTHS MEASURED DURING POSITIVE AND NEGATIVE LOADING

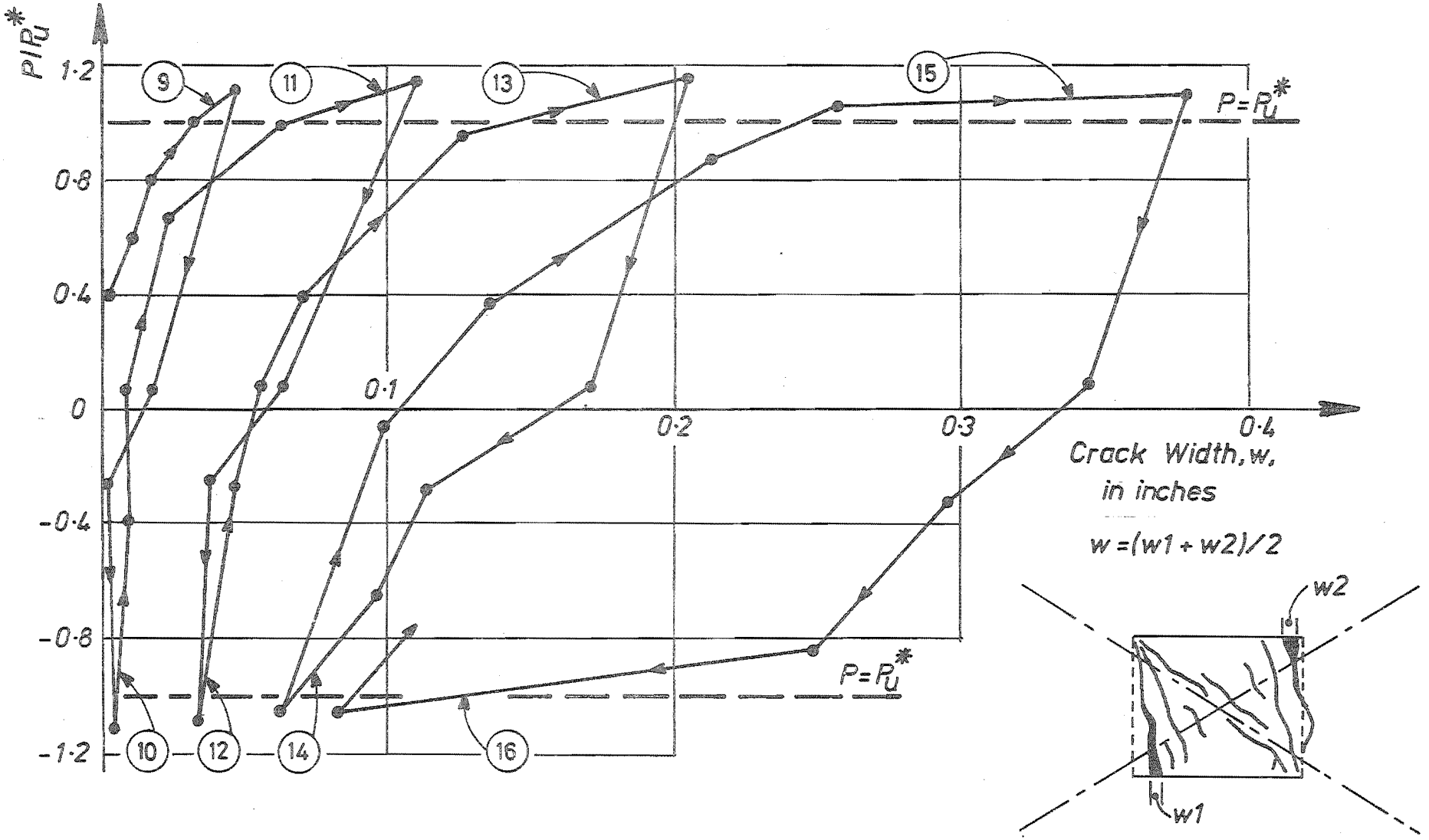

FIG. 7.26.(b) VARIATION OF THE AVERAGE CRACK WIDTH AT THE CORNERS OF THE SECOND FLOOR BEAM WITH CYCLIC LOADING

alternate opening and closing of cracks. At the end of cycle 16 there were 0.2" wide cracks in this area. Unfortunately an inadvertent misalignment in the formwork resulted in a kink at the junction of the wall and the base block. This is shown in Fig. 7.27.a. At the end of cycle 16 the compression wall had to transmit the force, C_h, into the base block. The compression force, C_h, which was inclined as shown, as a result of the kink, encouraged the deteriorated compression wall to buckle towards the southern side.

Fig. 7.27.b. shows the strains at ultimate load on the compression face of the reinforcement. The bars F_S and F_N are on the southern and northern side of the wall as shown. The strains in these two bars are plotted against the gauge locations separately at various top floor deflection levels during cycle 16. The strains plotted were computed ignoring the permanent deformation suffered by these bars up till cycle 15. The figure shows that the compression strain decreased on the southern bar, F_S, and increased on the northern bar, F_N, with increasing top floor deflections. This indicates that this portion of the wall buckled towards the south. Indeed at a top floor deflection of 7.5" the bar F_S experienced tensile strain. Fig. 7.25 shows the buckled compression wall. This wall twisted about its axis moving towards the south at the outer edge and towards the north at the inner edge. Fig. 7.24.a. shows the twisted wall at the top floor level.

After sudden buckling, the structure held a load of $0.5\ P_u^*$.

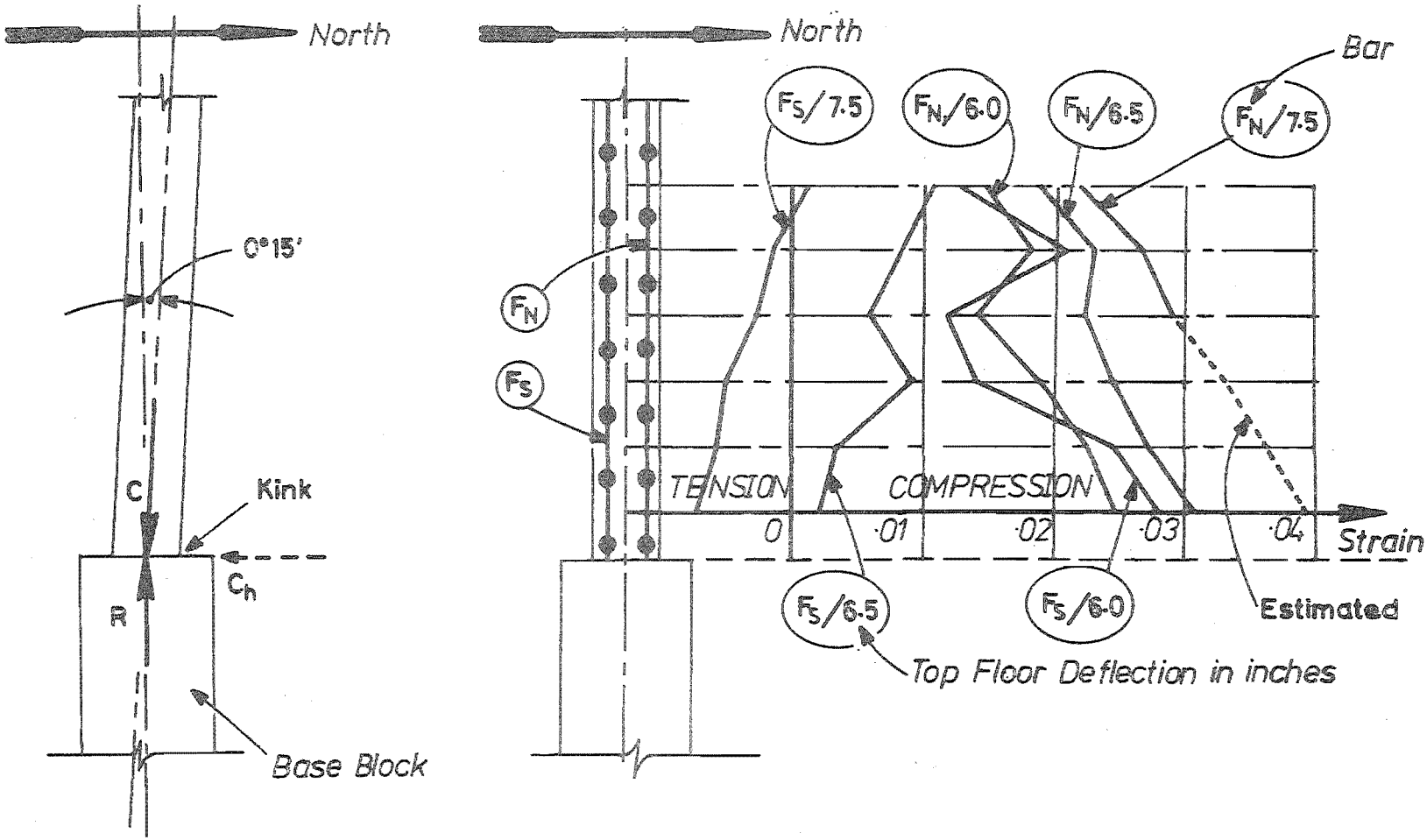

(a) The kink at the junction wall and base block

(b) Strain variation in the Southern and Northern face bars at the outer edge of compression wall during buckling failure

FIG. 7.27 BUCKLING FAILURE OF THE MODEL

CHAPTER EIGHT

COMPARISON OF THE BEHAVIOUR OF TWO MODELS

8.1 GENERAL

Both models were provided with the same quantity of flexural reinforcement and stirrups in the walls. The strength of the coupling beams of Shear Wall B was 10% more than those of Shear Wall A. This resulted in a larger ultimate load for Shear Wall B.

8.2 BEHAVIOUR OF REINFORCEMENT IN THE WALLS

8.2.1. Behaviour of Flexural Reinforcement

The two models show similar strain patterns in the wall flexural reinforcement (see Fig. 6.5.a to d and Fig. 7.5.a to d). In both the models the maximum strain at the base section of the instrumented flexural bars was approximately 20 to 25 times its yield strain. This resulted in large curvatures at the critical section of the walls (see Fig. 6.22 and Fig. 7.22) and confirms the satisfactory behaviour of flexural reinforcement in both the models.

8.2.2. Behaviour of Stirrups

As pointed out in Chapters 6 and 7, the contribution of concrete to shear resistance was ignored and excess stirrups were provided in both walls of Shear Wall A and B. The observed stirrup forces in Shear Wall B were larger than those of Shear Wall A (see Figs. 6.10 and 7.10), eventhough the same amount of stirrups was provided in both models. This is due to the following reasons:

(a) In wall A the measured stirrup forces were underestimated because the residual strains due to the accidental preload could not be estimated.

(b) The base shear of wall B at ultimate was approximately 10% larger.

(c) The axial force in wall B was larger by probably more than 10% because of the increased capacity of the beams. Consequently the inclination of the critical diagonal crack in the tension wall of wall B was less than 45°. This resulted in fewer number of stirrups resisting the shear force in the tension wall.

In both models the performance of stirrups was satisfactory. Even when large deformations were imposed, the maximum strain in the stirrups was less than twice the yield strain. The test has also shown, however,that the real weakness in the whole structure was in the shear carrying capacity of the plastic hinge zones. The stirrup strain increases show clearly that shear strength deterioration seems inevitable. Continued application of reversed cyclic loading, corresponding with an overall ductility of 4 or more would probably have resulted in shear failure near the base of the walls. The phenomenon, however, is no different from that encountered in any reinforced concrete beam subjected to alternating plasticity. In the tests, the excess stirrups have allowed very large yielding of flexural steel to take place. Thus they have contributed to the attainment of large overall ductilities in both models.

At ultimate load the shear capacity of tension wall drastically reduces because of the presence of large axial tension. At this stage the shear capacity of the compression wall is large due to large axial compression. This makes the compression wall to accept the major portion of the shear. Horizontal axial forces in the coupling beams at the bottom few floors assist in this redistribution of shear between the plastic hinge zones of the tension and compression walls. Indeed, for wall B it was shown that nearly 75% of the total applied shear near ultimate load was resisted by the compression wall. The provision of excess stirrups has also been helpful in resisting the increased shear due to redistribution in compression wall.

8.3 BEHAVIOUR OF COUPLING BEAMS

8.3.1 Behaviour of Flexural Reinforcement in the Beams of Shear Wall A and Diagonal Reinforcement of the Beams of Shear Wall B

Fig. 8.1 compares the strain history of the flexural reinforcement of coupling beams of Shear Wall A and of the diagonal reinforcement in the coupling beams of Shear Wall B during a typical high intensity load cycle at the instrumented location shown. For wall A the average strain, $(\epsilon_{CB1} + \epsilon_{CB2})/2$, during cycle 9 and for wall B the average strain $(\epsilon_{DB1} + \epsilon_{DB2})/2$ during cycle 13 for the most severely affected second floor beam is plotted against the load, P . Both cycles correspond with the third high intensity loading in the positive direction and hence the load to which the models had been subjected up until this stage is approximately the same. The origin of the strain history curves has been made to coincide for the purpose of this study. A comparison of the two curves indicates that the energy absorbed by the diagonal reinforcment is considerably larger at low levels. The shaded area shows the extra energy absorbed by the instrumented length of the diagonal reinforcment. This area is approximately 33% of the total area under the strain history curve for wall B.

The superior performance of the diagonal reinforcement has resulted in stable hysteresis loops for the beams of Shear Wall B. Fig. 8.2 shows the load-rotation curves for cycle 9 and cycle 13 for the second floor coupling beam of Shear Wall A and Shear Wall B respectively. The energy absorbed by the second floor coupling beam of Shear Wall B is approximately 30% more. The stiffness of the coupling beams of Shear Wall B at low loads is significantly larger.

8.3.2 Comparison of Deformation of the Second Floor Coupling Beams

The deformations, Δ_{V1} , of the second floor beams of the models, as defined in the insert of Fig. 8.3, were estimated using theodolite readings made at the centre line of the walls. In the major portion of this figure a comparison of these deformations for wall A and wall B

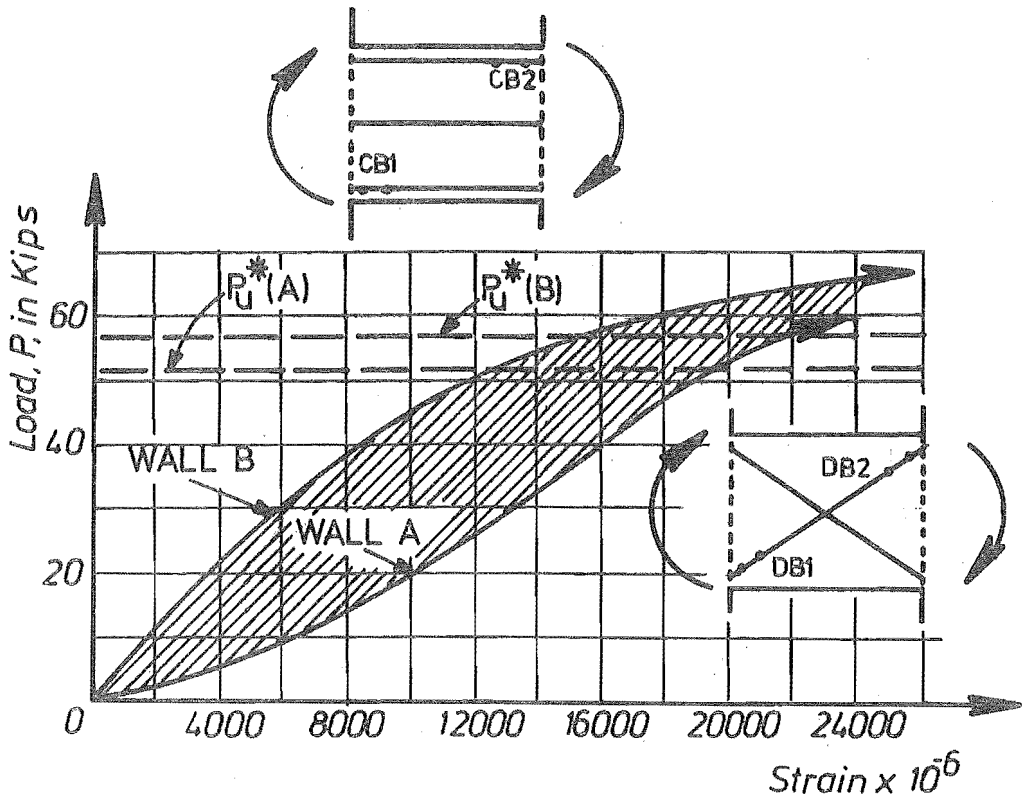

FIG. 8.1 COMPARISON OF THE STEEL STRAIN HISTORY OF THE SECOND FLOOR BEAMS OF THE MODELS

$P_u^*(A)$ - Theoretical ultimate load for Wall A

$P_u^*(B)$ - Theoretical ultimate load for Wall B

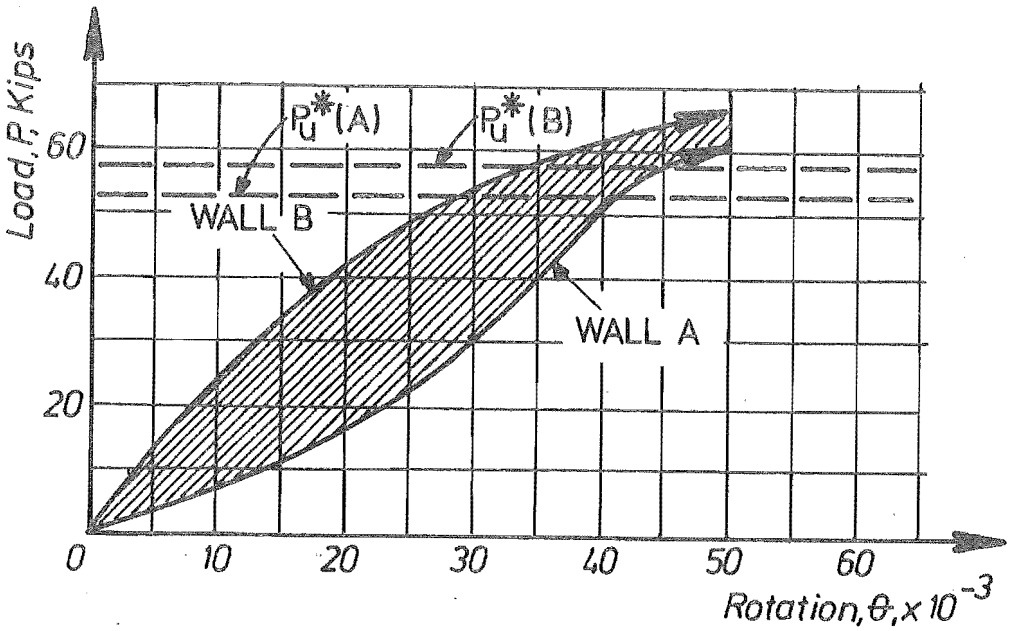

FIG. 8.2 COMPARISON OF THE VARIATION OF ROTATIONS OF THE SECOND FLOOR BEAMS FOR THE TWO MODELS

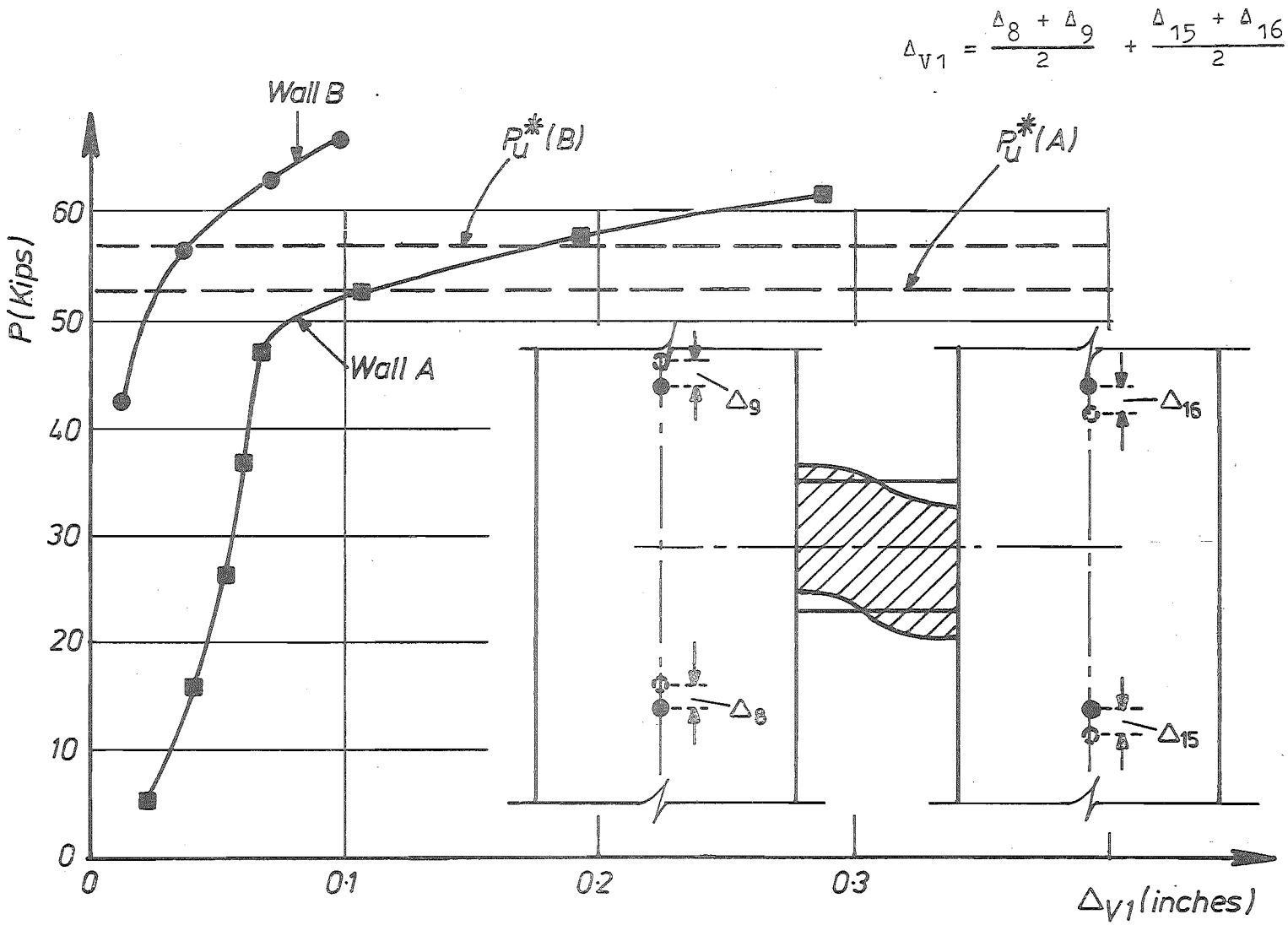

FIG. 8.3 COMPARISON OF DEFORMATION OF THE SECOND FLOOR BEAMS OF THE MODELS

during cycles 9 and 13 respectively, at approximately the same overall top floor displacements of the models, is made. Note that the displacement of the second floor beam of wall A is nearly $2\frac{1}{2}$ times that in wall B at ultimate load. The theoretical study made in Section 3.2 shows that the displacement, Δ_{V1}, for the conventional beams results from deformations due to truss action, Δ_V, flexural action, Δ_F, and beam elongation, Δ_E. Of these, the shear deformation associated with truss action overshadows the other two. For the diagonally reinforced beams, Δ_{V1} results from the deformations of the diagonal steel only.

The displacement in the coupling beams of wall A is larger at all load levels. In this wall, after a few load reversals, the full depth crack forming at the face of the wall encourages a sliding shear failure mechanism to form in the beams. The stirrups provided are ineffective in preventing this. At this stage the shear resistance is offered mainly by other mechanisms such as aggregate interlock action and dowel action of flexural reinforcement. In diagonally reinforced beams the full depth crack cannot form without crossing the diagonal bars. The vertical components of these bars supply the major portion of shear resistance and effectively minimise shear deformation. The difference in the behaviour of the two beams is due to the different role played by the main flexural bars and diagonal bars.

8.4 DEFORMATIONS

8.4.1 Load-Top Floor Displacement Relationship of the Models

The most effective comparison of the two structures can be made by studying the load-displacement relationship, obtained during the test for each specimen. Fig. 6.12, giving the results of wall A with conventional beams, shows that considerable ductility was attained with little loss of strength during cyclic loading. However, the pinching of the hysteresis loops, characteristic of the break down of shear resisting mechanism in reinforced concrete members, and the loss of overall stiffness is evident.

From Fig. 7.12, giving the load-roof deflection relationship for wall B with diagonally reinforced coupling beams, shows convincingly the superior performance of this structure. The hysteresis loops not only show large ductilities with no loss of strength but also indicate the stable characteristics of ductile steel structures.

When the difference in the behaviour is considered in the light of differently reinforced beams, it is evident that the pinching shape of the load-deflection curves of wall A is due to shear deformation and the low stiffness of conventionally reinforced coupling beams.

8.4.2 Stiffness of the Models

The stiffnesses of the models during two typical high intensity cycles are compared in Fig. 8.4.a. The stiffness of wall A is considerably lower at low loads compared with the stiffness of wall B. As pointed out earlier, the low stiffness of wall A at low loads is due to poor performance of the reinforcement in the conventional coupling beams. With loading the stiffness of wall A increases to a steady value. The stiffness of wall B, however, decreases, exhibiting Bauschinger effect. A comparison of the stiffnesses during cycle 10 for wall A, and cycle 14 for wall B at near ultimate loads, show that the stiffness of wall B is larger. During the positive cycle 13 the stiffness of wall B was less than that of wall A during cycle 9. These stiffness variations at near ultimate loads are small. At this stage the main reinforcement in the beams and the flexural reinforcement in the walls had started yielding.

In Fig. 8.4.b the load resisted by the models for a top floor deflection of 1" during various cycles is shown. The top floor deflection of 1" corresponds approximately to the deflection at the onset of yield in both walls of both models. The figure shows that the strength degradation for the same top floor deflection is considerably larger in wall A after one excursion into the ultimate range in both directions. This is again due to the poorer performance of the conventionally reinforced beams.

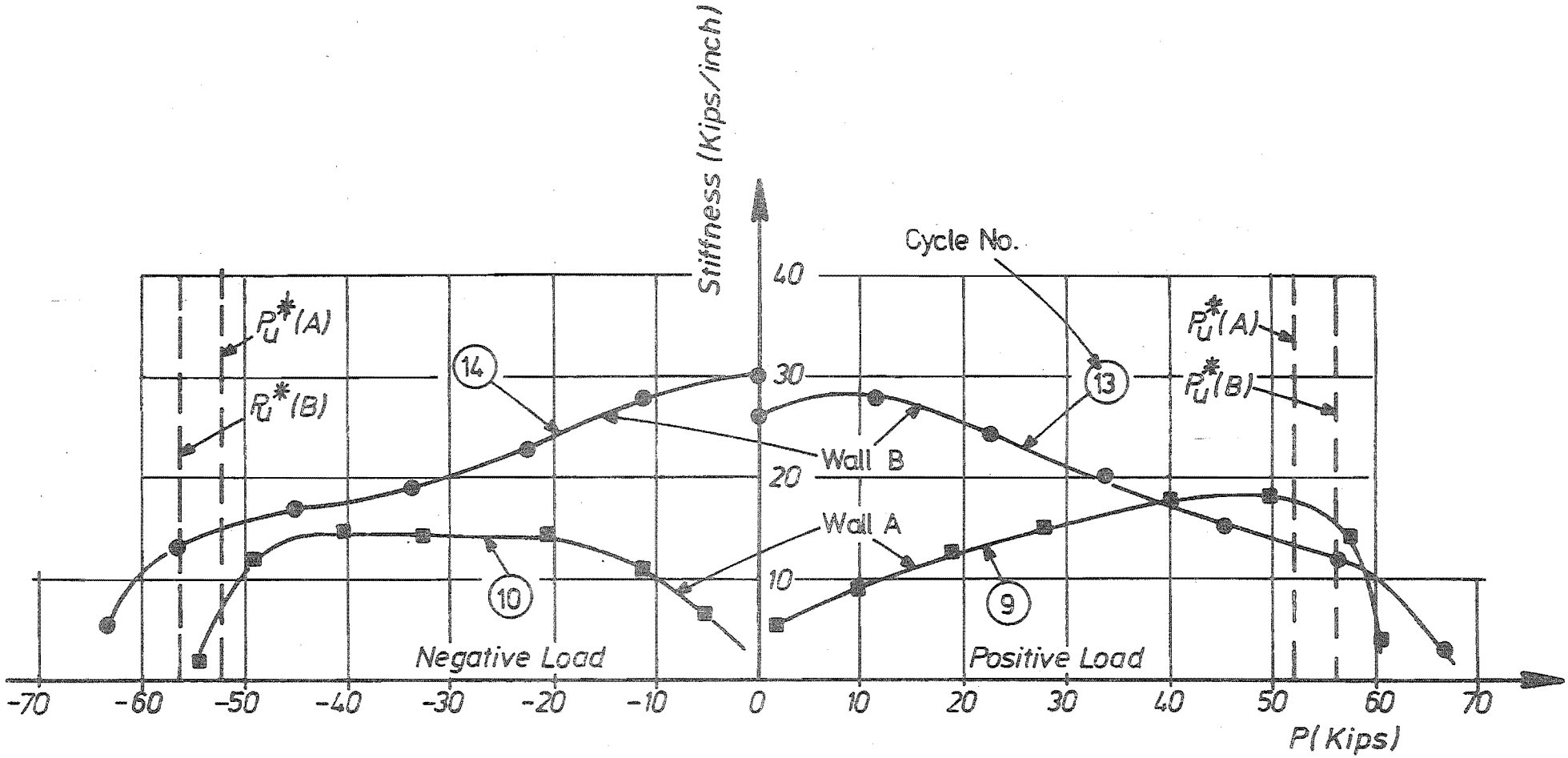

FIG. 8.4.(a) A COMPARISON OF THE STIFFNESS OF THE MODELS

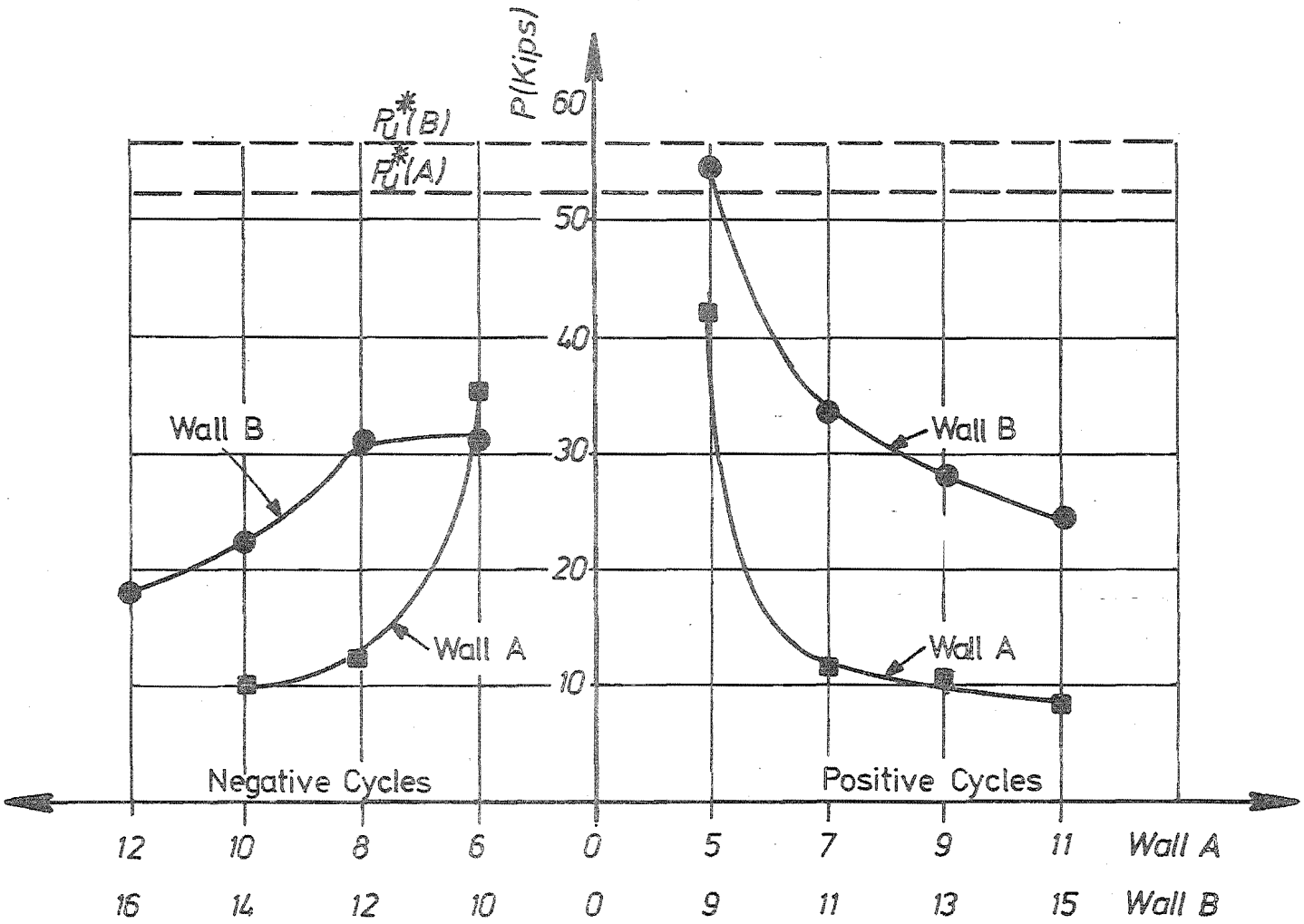

FIG. 8.4.(b) COMPARISON OF LOAD RESISTED BY THE MODELS WHEN THE TOP FLOOR DISPLACEMENT IS 1"

8.4.3 Ductilities Attained by the Models During the Cyclic Loading

Fig. 8.5 shows the ductilities, μ_N , attained by wall A and wall B during the various cycles at maximum load levels. Reference may be made to the insert in this figure for the definition of ductility. For the high intensity cycles, the maximum loads are also shown at maximum ductilities. Cycle 5 for wall A and cycle 9 for wall B were first high intensity cycles for the models. Cycles 5, 6, 7, 8, 9, 10, and 11 for wall A, and cycles 9, 10, 11, 12, 13, and 15 for wall B are corresponding cycles respectively. During the corresponding high intensity cycles the ductilities attained by the models are of the same order. Note that wall B was subjected to one additional large load cycle at the end. In both walls the overall ductilities during final cycles (cycle 15 and 16 for wall B, and cycles 10 and 11 for wall A) were of the order of 10 to 15. The ductility attained during cycle 16 for wall B was less than that attained during cycle 12 for wall A. This was due to buckling failure of wall B. This type of failure would not normally occur in prototype structures because of the resistance offered by the floor slabs at each floor level. The ductility attained in wall B at the end would have been much larger if the buckling failure had been effectively prevented.

In Fig. 8.6 the cumulative overall ductilities attained by the two models are plotted against the load. During the negative loading the ductilities attained for wall B are significantly larger than for wall A. During the positive loading the maximum cumulative ductility of wall A is large because of the gradual failure.The load attained several times in both models, P_u , exceeds the theoretical ultimate strength, P_u^* , because of the strain hardening effects of the mild steel used. The figure shows that at approximately the same cumulative ductilities wall A suffers larger strength degradation than wall B. This comparison indicates that carefully designed and detailed coupled shear walls can possess adequate ductilities to give the highest degree of protection to ensure survival during catastrophic ground shaking.

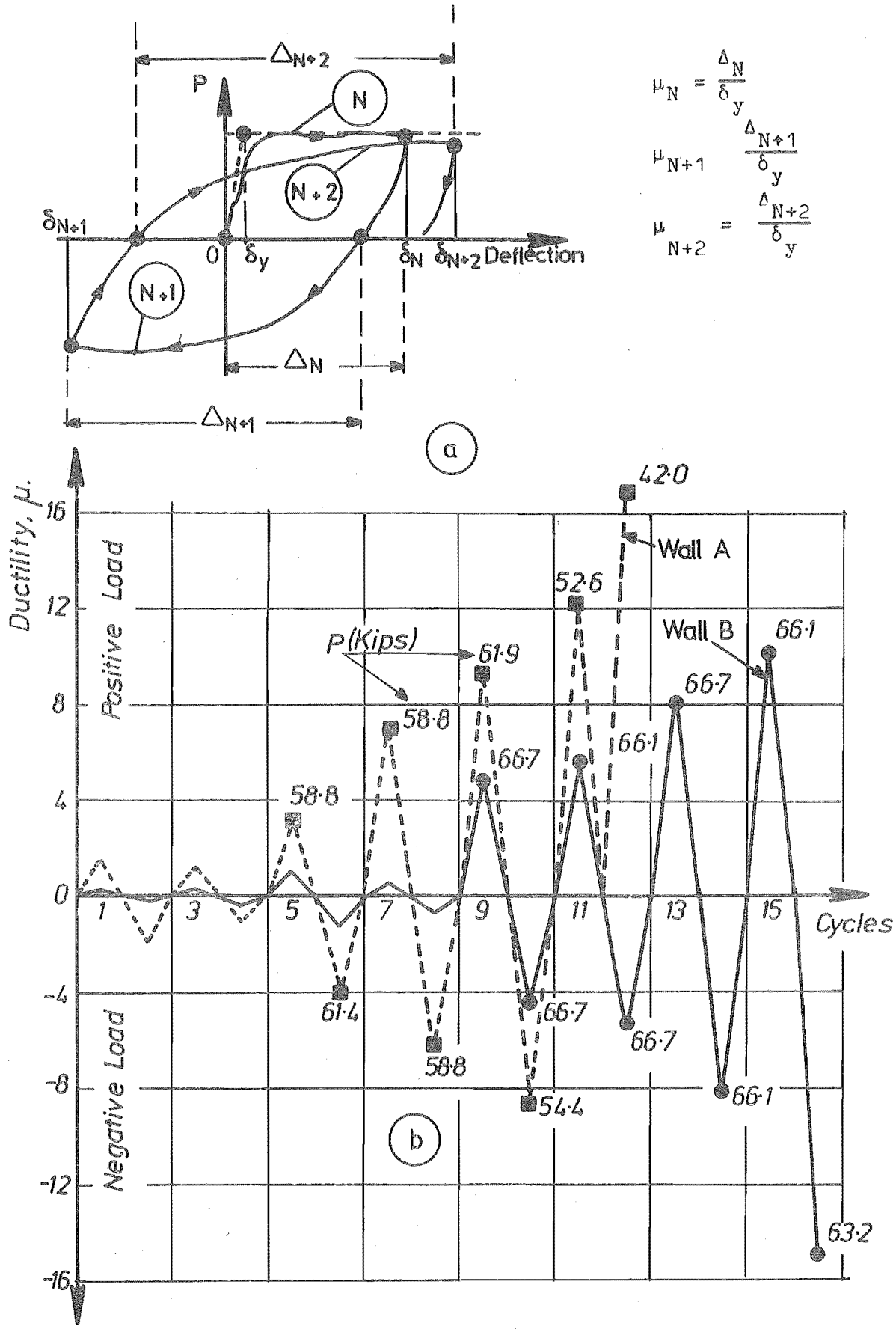

FIG. 8.5 OVERALL DUCTILITIES ATTAINED DURING EACH CYCLE FOR THE MODELS

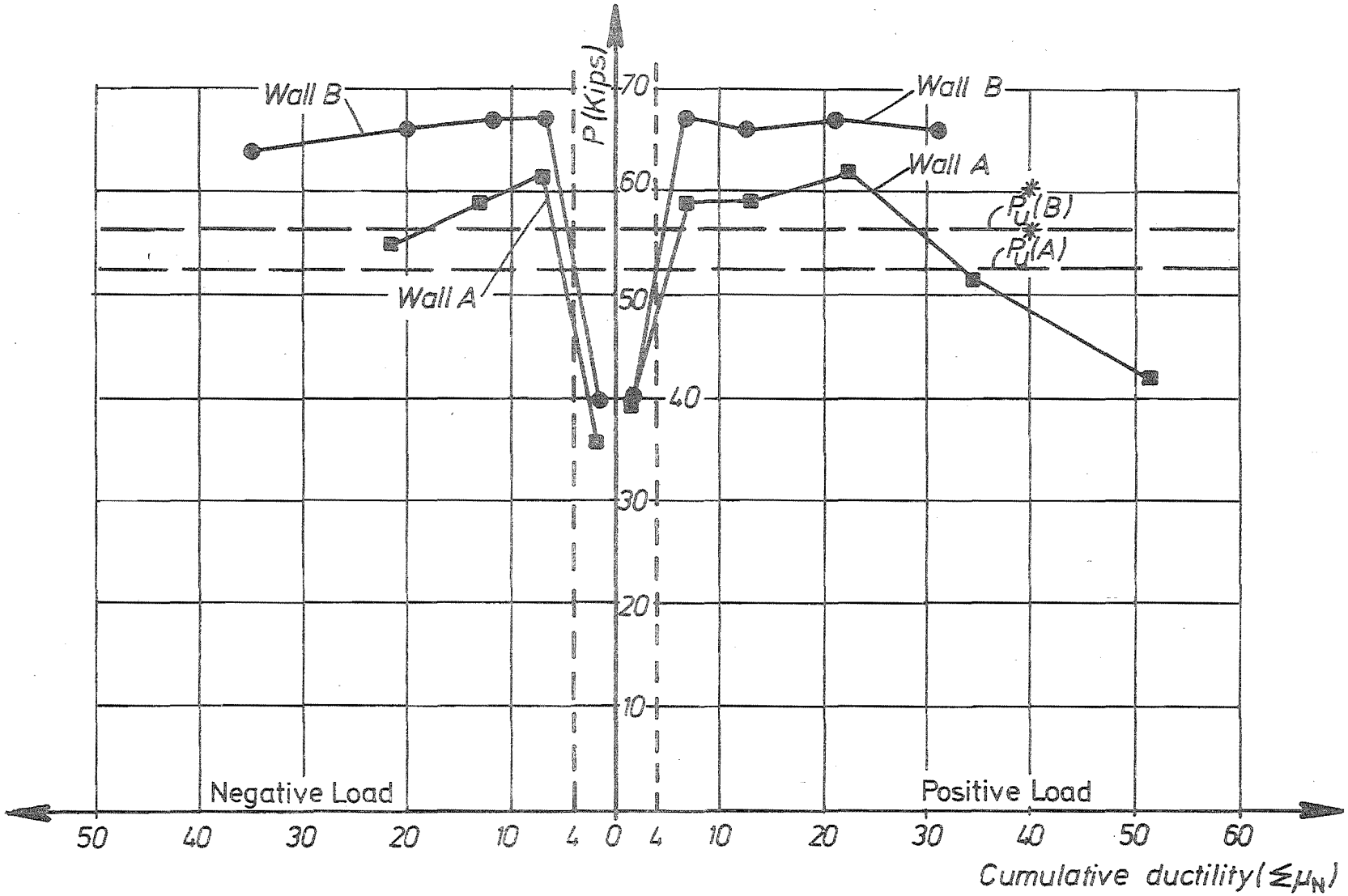

FIG. 8.6 COMPARISON OF CUMULATIVE DUCTILITIES ATTAINED AT MAXIMUM LOAD LEVELS FOR THE HIGH INTENSITY CYCLES OF THE MODELS

8.5 ENERGY ABSORPTION PROPERTIES

To quantify the energy absorption characteristics, the total energy absorbed by the models, E_A, was expressed in terms of the base shear, P, and the top floor displacement, Δ, based on the assumed linear deflection profile shown in the insert of Fig. 8.7.a. The energy absorbed by a model is

E_A = 0.70 x area enclosed by the hysteresis loops of Fig. 6.12 and Fig. 7.12 for wall A and B respectively.

The factor 0.70 has been introduced to take into account the work done by the resultant at the fifth floor level. To compare the energy absorption characteristics of the two models a nondimensional damping constant, h_e, is used. This constant is defined as

$$h_e = \frac{E_A}{E_o} \qquad \ldots (8.1)$$

where E_A = the energy absorbed by the model as defined

$E_o = 0.70 \times 0.5 \times P_u^* \times \Delta_e$, the energy absorbed by an equivalent elastic structure

Δ_e = 0.5", the top floor deflection of the equivalent elastic structure at theoretical ultimate load, P_u^*.

8.5.1 Total Energy Absorbed by the Models

Fig. 8.7.a shows the cumulative energy absorbed by the two models during the various cycles. The energy absorption during loading and energy recovery during unloading are included. The cumulative energy absorbed by wall B is approximately twice that absorbed by wall A at the theoretical ultimate load during the final cycles. The improvement in the energy absorption has resulted from the superior behaviour of diagonally reinforced beams.

In Fig. 8.7.b the energy absorbed during each complete cycle (one positive and one subsequent negative high intensity load cycle giving the area of one complete loop) is plotted against the cycles.

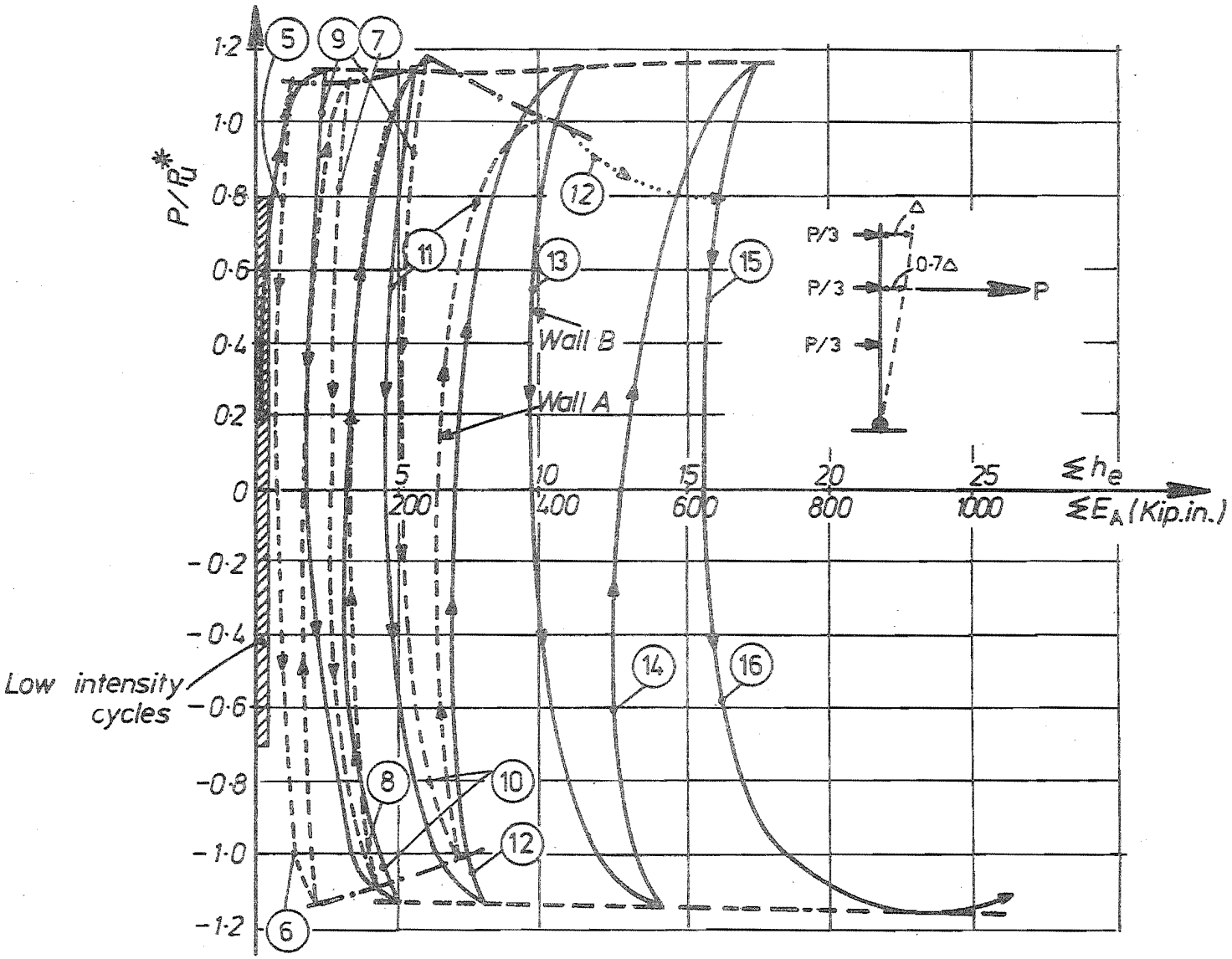

E_A = Energy absorbed

h_e = Damping constant

FIG. 8.7.(a) COMPARISON OF THE CUMULATIVE ENERGY ABSORBED DURING CYCLIC LOADING IN THE TWO MODELS

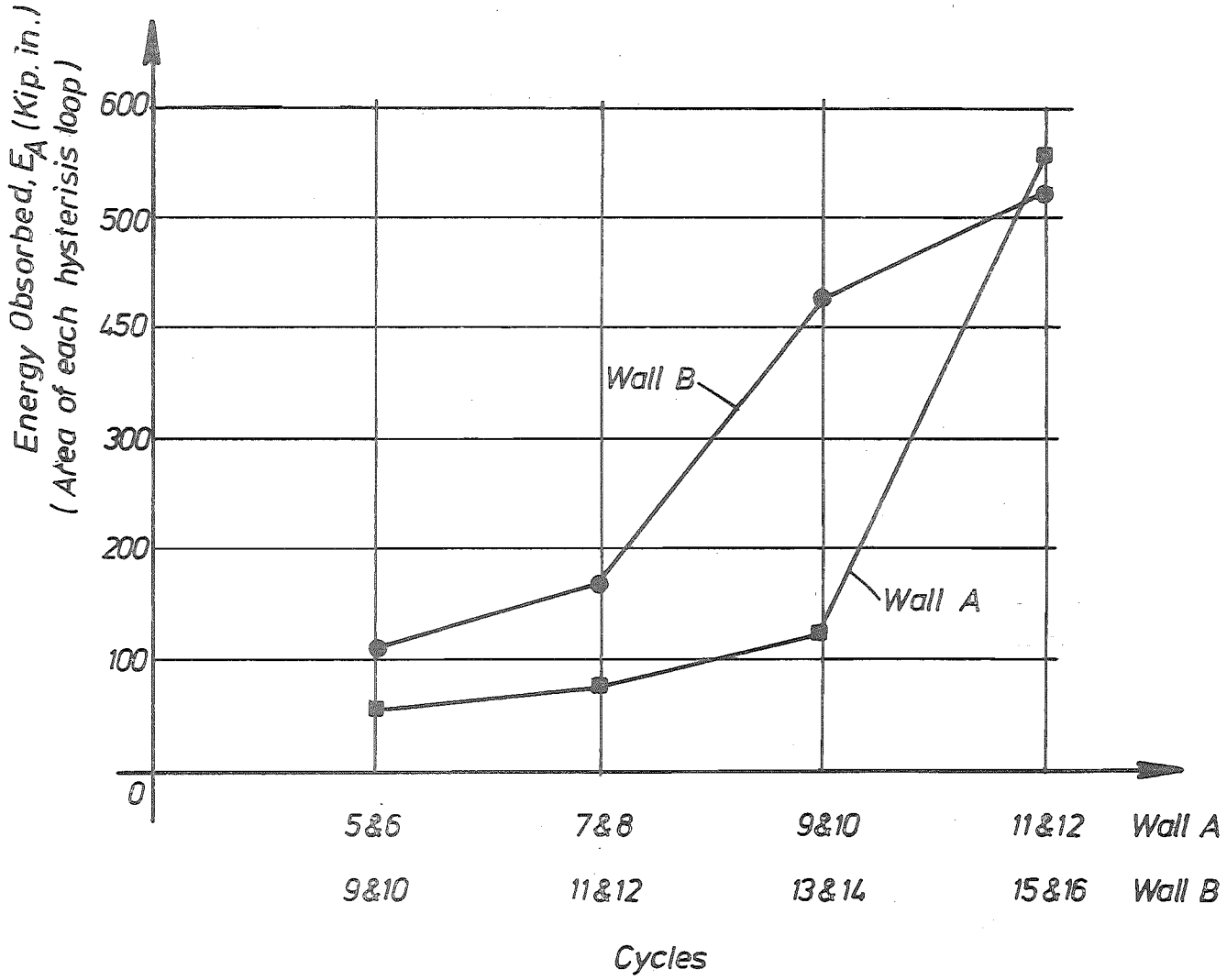

FIG. 8.7.(b) A COMPARISON OF THE ENERGY ABSORBED, E_A, DURING VARIOUS HIGH INTENSITY CYCLES

The energy absorbed by wall B is more during the entire cyclic loading with the exception of the final cycle. This was due to gradual failure of wall A compared with the buckling failure of wall B.

8.5.2 Relationship Between Cumulative Energy Absorbed and Cumulative Top Floor Displacement

Fig. 8.8 shows the relationship between cumulative energy absorbed and cumulative top floor displacement of the models. During the final cycle the energy absorbed up to the maximum loads attained in both the models was only considered. The descending load-deformation curves below P_u^* were not considered. Excepting points obtained during final half cycles the relationship between cumulative energy absorbed and cumulative top floor displacement is linear. The dotted curve for both models indicates the estimated relationship that would have resulted if the energy recovery during the final cycle was also considered. The figure shows that for the same cumulative top floor displacement the energy absorbed by wall B is considerably larger than that in wall A.

8.5.3 Energy Absorbed by the Walls and Beams of Shear Wall B

Using the strain measurements made on the reinforcement in the coupling beams and the previously assumed strain variation (see Fig. 7.15.c), the energy absorbed by each coupling beam, E_{Ab}, was estimated as

$$E_{Ab} = \int T_s \, d\Delta_1 + \int (C_c + C_s) \, d\Delta_2 \qquad \ldots (8.2)$$

where T_s = estimated force in tension diagonal

C_s = estimated force in compression steel

C_c = estimated force in the assumed concrete strut

$\Delta_1 = \epsilon_1 l'$, the total elongation of tension diagonal

l' = length of diagonal steel

ϵ_1 = average strain measured in the tension diagonal

Δ_2 = total contraction of compression diagonal based on the measured strain and the strain variation shown in Fig. 7.15.c

$d\Delta_1, d\Delta_2$ = differential elongation of tension chord and contraction of compression chord respectively.

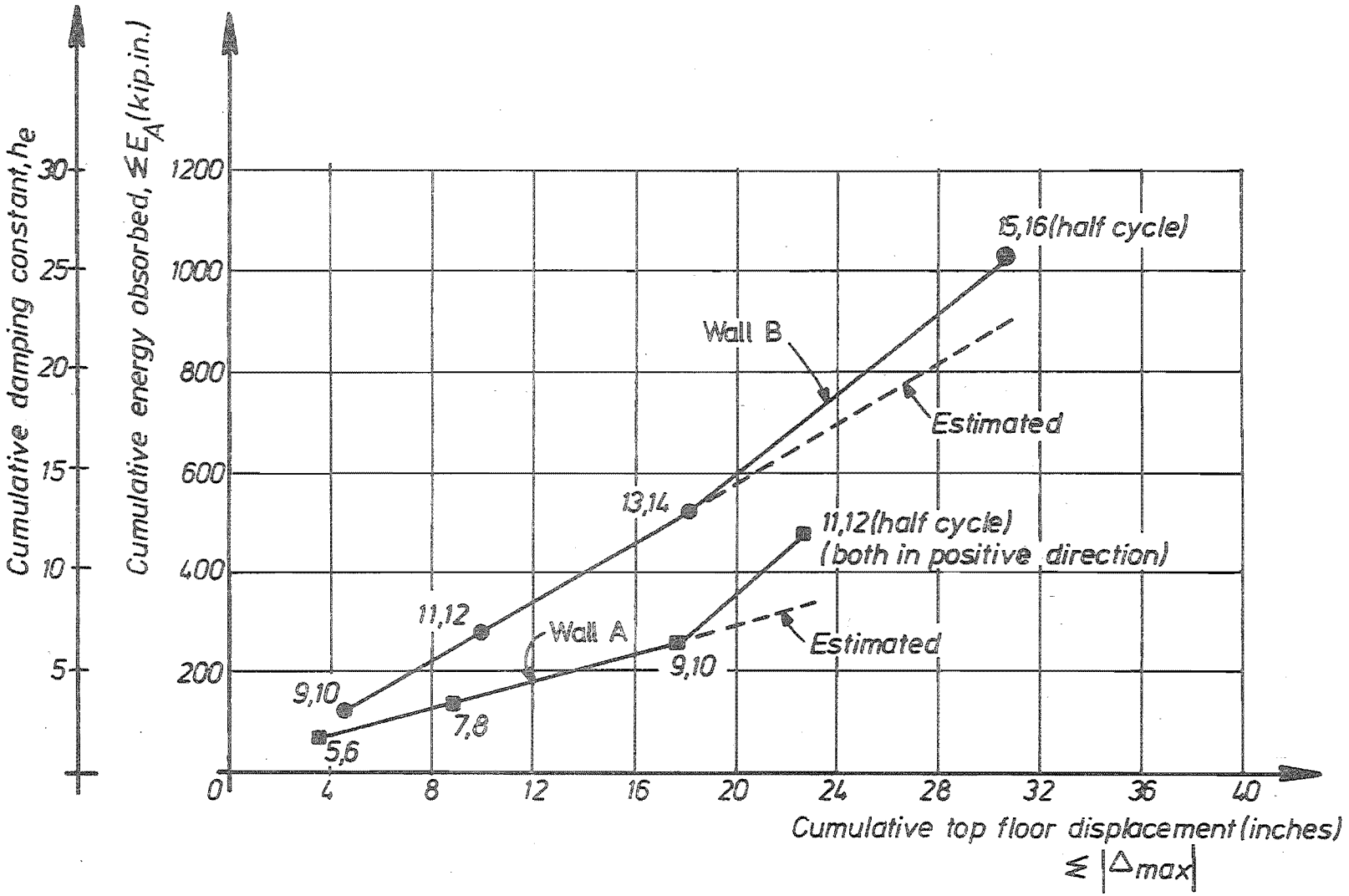

FIG. 8.8 RELATIONSHIP BETWEEN THE CUMULATIVE ENERGY ABSORBED AND THE CUMULATIVE TOP FLOOR DISPLACEMENT IN THE MODELS

The total energy absorbed by the coupling system is computed as the sum of the energy absorbed by the various coupling beams up until the stage considered.

The energy absorbed by the wall moments was found using the curvature variation (Fig. 7.21) and estimated moments in the walls. This for the tension and compression wall is

$$E_{Aw} = \int_0^H \int M_1 \, d\varphi_1 \, dx + \int_0^H \int M_2 \, d\varphi_2 \, dx \qquad \ldots \quad (8.3)$$

where M_1 = estimated moment at a section a distance x from top of wall 1

φ_1 = curvature of wall 1 at the above section

M_2 = estimated moment in wall 2 at level x

φ_2 = curvature of wall 2 at the above section

$d\varphi_1, d\varphi_2$ = differential curvature of wall 1 and wall 2 at the above section.

The proportions of energy absorbed by the beams and walls for wall B during cycle 9 are shown in Fig. 8.9. At $P = P_u^*$ nearly 50% of total energy is absorbed by the beams. The additional energy required to be dissipated above the theoretical ultimate load was absorbed mainly by walls so that at $P = 1.18\ P_u^*$ less than 30% of the total energy is absorbed by the beams. The reduction in the contribution of beams is due to large plastic rotations occurring at the base of the walls. The energy absorbed by other mechanisms (shear in the walls and axial forces in the walls and beams) was computed as the difference between the total input energy (derived from the top floor displacements) and the sum of the energies absorbed by diagonal steel in the beams (Eq. 8.2), and flexural steel in the walls (Eq. 8.3). This was found to be less than 10% of the total energy absorbed at all stages of loading.

Unfortunately such as estimate could not be made for wall A. The forces in the various components could not be estimated individually because of the residual strains caused by the accidental pre-load.

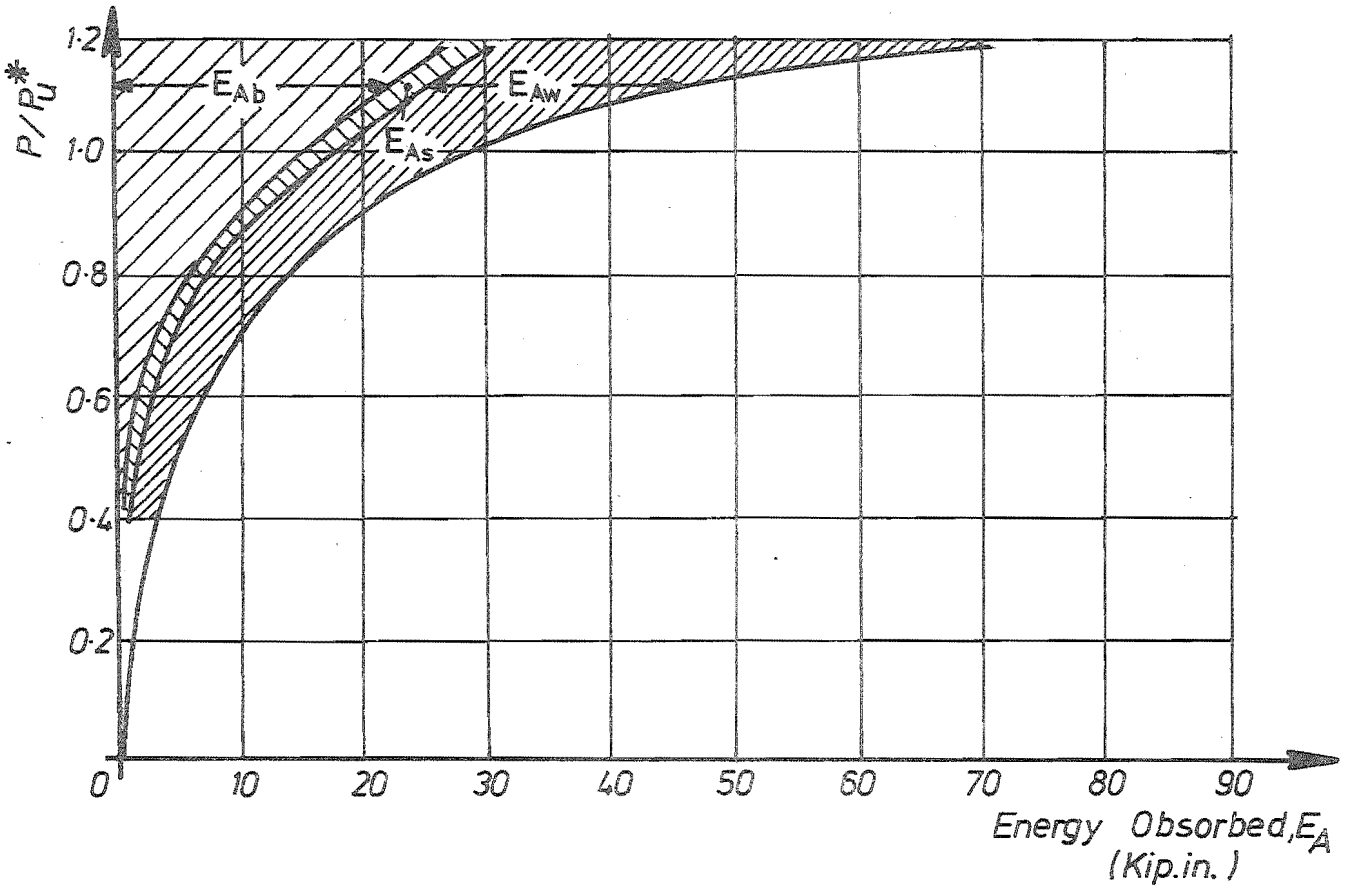

E_A = Total energy absorbed by the model

E_{Ab} = Energy absorbed by coupling system

E_{As} = Energy absorbed by shear, axial force in the beams and axial force in the walls

E_{Aw} = Energy absorbed by flexural steel in the walls

FIG. 8.9 PROPORTIONS OF ENERGY ABSORBED BY THE COUPLING SYSTEM AND WALLS OF SHEAR WALL B DURING CYCLE 9

8.6 FAILURE MECHANISMS

These have been fully discussed for each model in the previous chapters. In summarising:

Wall A: During cycles 11 and 12 the deterioration and the consequent spalling of concrete in the narrow compression zone was severe near the single layer of compression reinforcement in the tension wall. This reinforcement buckled outward and initiated failure. It is felt that larger ductilities could be attained by providing at least two layers of reinforcement in the inner face of the walls and effectively containing the concrete in this region by binding steel.

Wall B: The kink at the junction of the wall and the base block caused the compression wall to buckle. In prototype structures this type of failure cannot occur due to the restraint offered by the floor slabs. Hence this wall would have exhibited considerably more ductility.

Figs.8.10.a and b show the models after test. It is evident that in wall A eventually all the coupling beams failed by sliding shear. In spite of large yielding in the beams of wall B, the beam distortions were much smaller and the damage much less than in wall A.

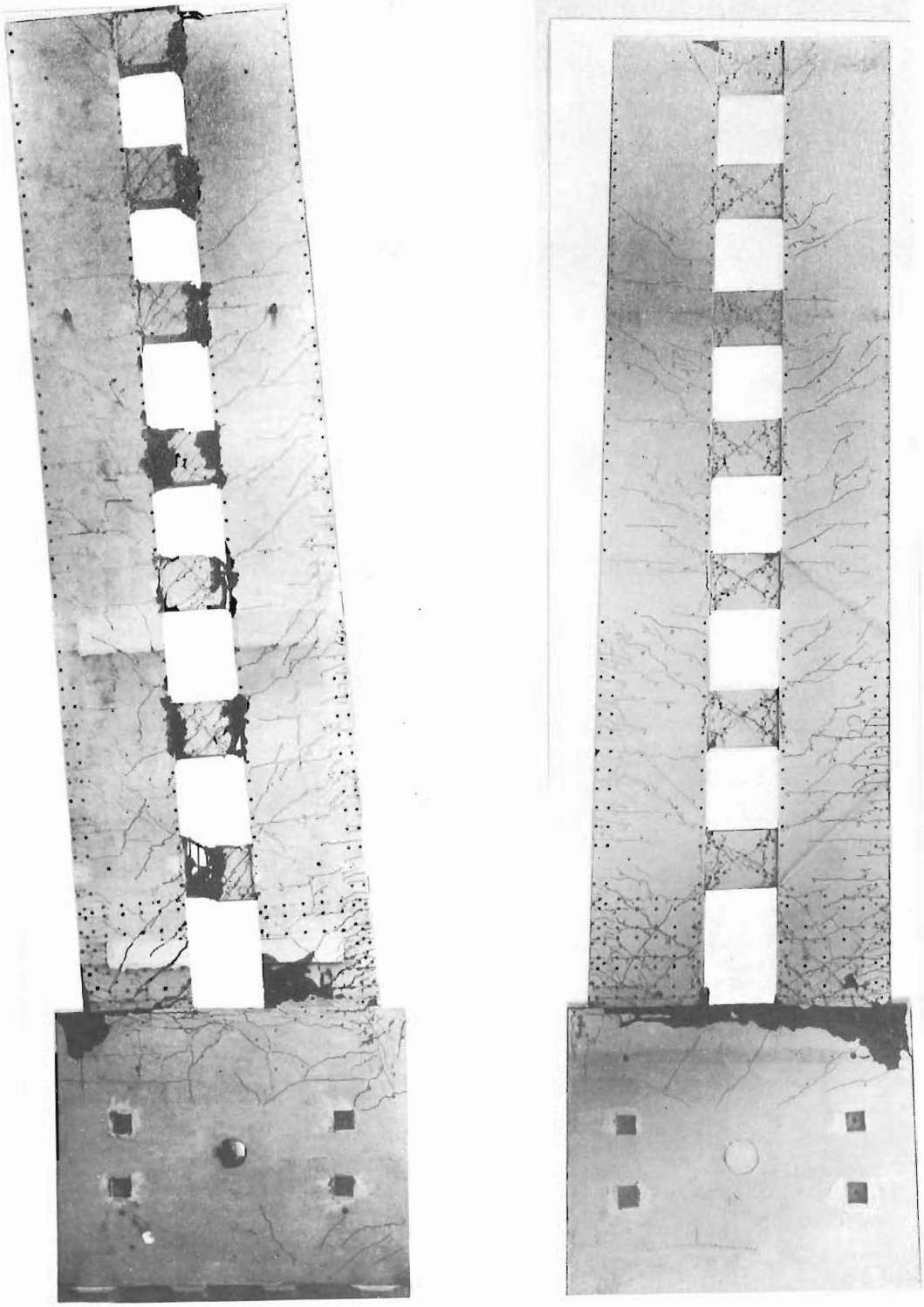

(a) Wall A

(b) Wall B

FIG. 8.10 MODELS AFTER TEST

CHAPTER NINE

CONCLUSIONS AND RECOMMENDATIONS

9.1 ELASTIC BEHAVIOUR

Based on the elastic laminar analysis, the sensitivity of shear wall response to changes in relative dimensions of the beams and walls and the effects of cracking were examined. This study showed that the provision of rigid diaphragm at the top, variation of total stiffness of the walls and variation of relative stiffness of walls do not significantly affect the laminar shear when the aspect ratio of rectangular beams $D/l_s > 0.33$ and $35 \times 10^6 > I_o > 50 \times 10^3$ in^4 units, the range within which this study was undertaken. For these shear walls, the reduction in laminar shear due to cracking was shown to be insignificant when the beam aspect ratio $D/l_s > 0.60$.

Using a finite difference approximation the application of the laminar analysis was extended to coupled walls with variation in properties of beams and/or walls with height, different boundary conditions, different pattern of external lateral load and two or more rows of openings.

9.2 ELASTO-PLASTIC ANALYSIS

The theoretical stiffness properties of the cracked coupling beams with conventional as well as diagonal reinforcement were examined and compared with available experimental evidence. The elastic and elasto-plastic responses of wall sections to static loading were evaluated using the load-moment-curvature and load-moment-property (EI and EA) relationships. These relationships, together with the finite difference approximation in the laminar analysis, formed the basis of the non-linear elasto-plastic analysis in which the history of the shear wall behaviour was followed through stages of incremental loading. An advantage of the analysis is that it yields information regarding the sequence of hinge

formation in the beams and walls. If the analysis indicates that only a partial failure mechanism occurs, or wall hinges tend to form prematurely, it might be necessary to redesign the structure so as to ensure a better and more desirable distribution of plastic hinges.

In the example of a 10-storey structure, it was shown that owing to strain hardening of the steel in the coupling beams and walls, the capacity of the shear wall can increase by 10% or more.

9.3 EXPERIMENTAL EVIDENCE

In two quarter full size seven storey reinforced concrete coupled shear wall models the various effects of differently reinforced coupling beams upon overall behaviour were studied.

9.3.1 Coupling Beams

Steel strain measurements made at the instrumented locations and optical deformation measurements showed that the stiffnesses of coupling beams of wall A were low after they had been subjected to a number of high intensity load reversals. This was due to full depth cracking and shear deformations. The stirrups provided were not effective in minimising the shear deformations at the critical sections after the formation of the full depth crack. Thus in wall A conditions of beam sliding shear failures prevailed, resulting eventually in severe damage to the coupling beams. In spite of this, considerable ductilities with little loss of strength were observed for all coupling beams during progressive reversed loading.

The hysteresis loops of the beams of wall B, however, exhibited the characteristics of a steel member. In these beams the entire shear and flexure could be resisted by steel alone. Optical deformation measurements revealed that the shear deformations of these beams were significantly less than those of the beams in wall A. Indeed the behaviour of the beams was dominated by the response of diagonal bars

only after a few cycles of high intensity loading. Crack width measurements indicated that the cracks across the diagonal bars became wider when the bar was in tension and effectively closed upon load reversal due to compression yielding. The compression yielding and the Bauschinger effect associated with it were evident in the load-rotation loops obtained for such a beam. The damage resulting from alternate opening and closing of cracks in these diagonally reinforced coupling beams was much less than that in the beams of wall A, where sliding shear failure occurred.

The tests demonstrated that large member ductilities were attainable in both types of coupling beams. However, the following superior characteristics of the diagonally reinforced beams were evident.

(a) higher stiffness of the whole structure at low loads

(b) stable non-degrading hysteresis loops

(c) larger energy absorption capacity

(d) significantly less shear deformation

(e) much less overall damage to the beams.

9.3.2 Walls

9.3.2.1 Flexural reinforcement: As expected, the behaviour of flexural reinforcement in the walls of both specimens was similar during the major portion of the cyclic loading. During the final cycle the behaviour was different owing to dissimilar failure conditions.

The steel strain measurements in both models showed that large ductilities were attainable in the wall plastic hinges. The length of the plastic hinge and hence the magnitude of the section curvature are significantly affected by the presence of the axial load. Axial tension was found to increase the length of the plastic hinge and consequently the section curvatures observed were relatively low. The opposite is true when compression acts across the plastic hinge.

In both walls only a single layer of reinforcement, consisting

of two # 5 deformed bars, was provided near the openings. Steel strain measurements at near ultimate load indicated that maximum concrete strains attained in the compression wall were approximately three times those present at the same instant in the tension wall. During cyclic loading the concrete in the vicinity of the single layer of compression reinforcement at the base of the walls deteriorated earlier because of poor confinement by the stirrups. This deteriorated zone was in compression at the base of the tension wall. On the other hand the compression zone of the compression wall suffered much less damage because of the beneficial effects of five layers of compression reinforcement and the binding action of stirrups around them. Indeed, in wall A the deterioration of the concrete in the compression zone of the tension wall at the base created the failure mechanism. It is likely that the failure could have been delayed by a concentration of stirrup reinforcement or by additional confining ties around a number of layers of compression reinforcement adjacent to the windows at the base, to maintain the integrity of concrete in this region, which thereby could transmit the shear forces into the base block.

Strain measurements made on flexural steel of both models indicated that approximately 80% of the top floor deflection resulted from the flexural deformation of the walls at near ultimate load.

9.3.2.2 Stirrups: In both models the contribution of concrete to shear strength was ignored and excess stirrups were provided in order to suppress a possible premature shear failure. To this end the performance of stirrups was satisfactory.

Due to the presence of large axial tension the critical diagonal crack did not form at 45°, as assumed by the classical truss analogy. Therefore, when failure was imminent, the stirrup strength was less than that predicted by ACI equations.

In wall A the failure was initiated in the tension wall. Since the concrete in the narrow compression region in the tension wall had deteriorated the major portion of the shear had to be transmitted across the single layer of flexural steel to the base by dowel action. This resulted in severe shear displacement and hence the single layer of steel buckled outward. In wall B, buckling of the compression wall occurred before this stage in the tension wall was reached. The provision of excess stirrups in the walls helped in:

(a) maintaining the integrity of concrete in the compression zone because of confining action around the main flexural bars.

(b) resisting shear resulting from increased flexural capacity because of strain hardening of the steel in the coupling beams and walls.

(c) the compression wall resisting the major portion of the external shear after the shear capacity of the tension wall had been drastically reduced by the narrowed compression zone.

9.3.3 Overall Deformations

9.3.3.1 Load-top floor deflection relationships: The load-top floor deflection relationship for wall A and wall B showed that considerable ductility was attained with little loss of strength during cyclic loading. However, the pinching of the hysteresis loops, characteristic of the breakdown of the shear resisting mechanism in conventional beams, which resulted in the loss of stiffness at low loads in the later high intensity cycles, was evident in wall A. The stable hysteresis loops of wall B showed convincingly the superior performance of a shear wall with coupling beams having diagonal reinforcement. The cumulative ductilities for wall B were much larger with no loss of strength. The displacement ductilities imposed in the 15th and 16th half cycles were of the order of 8 to 13.

9.3.3.2 Stiffness: Theoretical studies indicated that the loss of stiffness due to cracking in the models could be 50% or even more.

The measured stiffnesses of wall B before and after cracking verified this. This information could not be obtained for wall A because of the accidental overload at the start of the test.

As long as the beams behaved within the elastic range, a number of load reversals did not significantly alter the overall stiffness. However, a few excursions into the post-elastic range made wall A and wall B behave differently. Wall A exhibited the following three ranges of behaviour, common in conventionally reinforced deep coupling beams:

(a) A "soft range" at low loads when the stiffness of the shear wall was approximately equal to that of two equivalent elastic cantilevers in which the beams transmit horizontal axial forces only.

(b) A "steady range" at medium loads with improvement in stiffness similar to linear elastic behaviour.

(c) A "plastic range" near ultimate load resulting from yielding of flexural steel in both walls and beams.

On the other hand, the behaviour of wall B was dominated by the performance of diagonally reinforced beams. The compression yielding and the Bauschinger effect associated with it were evident. At low loads the stiffness of wall B was significantly larger than that of two connected cantilevers. The stiffness gradually decreased with increasing load reaching almost zero at near ultimate load resulting from yielding of diagonal bars in the beams and flexural bars in both walls.

9.3.4 Energy Absorption Characteristics

Energy absorbed by wall B was nearly twice that of wall A at the end of the test. Also during each comparable high intensity cycle the energy absorbed by wall B was larger. The superior performance of the structure which was demonstrated by the hysteresis loops has also resulted in a much greater energy absorption capacity.

The wall and beam reinforcement in both models was proportioned so that the coupling system was expected to yield before the full strength of the two walls was approached. It is desirable that as much energy be dissipated by the coupling system as possible before hinging of the walls commences because this will ensure that the walls remain in the elastic range of behaviour during disturbances generating forces comparable with the ultimate capacity of the structure and thus enjoy a high degree of protection against permanent damage. At the attainment of the theoretical ultimate load, during cycle 9, the energy absorbed by the coupling system of wall B was more than 50% of the total input energy. With hinging of the walls more energy is absorbed at the base of the walls. The contribution of the coupling system to the total energy absorbed reduces then to about 30%.

In conclusion, the two tests demonstrated that coupled shear walls containing apparently brittle elements can be made ductile to the extent that they could meet the most severe ductility demand likely to be imposed by a catastrophic earthquake. The tests have also revealed conclusively the superior performance of shear walls with diagonally reinforced coupling beams in the following respects:

(a) better stiffness characteristics at low loads so desirable in minimizing nonstructural damage during a moderate earthquake.

(b) less damage to the coupling beams.

(c) better energy absorption characteristics essential in ensuring survival during catastrophic ground shaking.

9.4 COMPARISON OF ANALYTICAL STUDIES WITH EXPERIMENTAL EVIDENCE

Wherever applicable the results obtained during the experiment were compared with those predicted by the theoretical study. The load-deformation curve obtained using the elasto-plastic analysis and that

derived from a nonlinear iterative finite-element analysis correlate well. However, both analytical studies underestimated the deformations because they did not recognise the stiffness loss associated with cyclic loading.

Within the limits of errors involved in the experiments and the assumptions made in the theoretical study, the measured stiffnesses of the beams of both models agree with the corresponding analytical assessments. For approximately the same steel content the diagonally reinforced beams were 1.4 to 2.00 times stiffer.

Attention was also drawn to the significance of stiffness reduction of the walls in the assessment of overall deformation properties of the coupled shear walls.

9.5 SUGGESTIONS FOR FUTURE RESEARCH

(a) The elasto-plastic analysis, and the nonlinear iterative finite-element analysis, ignore beam elongations associated with the yielding of diagonal bars. It would be useful to estimate the order of errors introduced in these analyses by neglecting beam elongations.

(b) Attempts may be made to extend the finite difference approximation of the laminar analysis to the solution of coupled walls with variable properties with height subjected to dynamic loading.

(c) Functional requirements often dictate the use of an irregular pattern of openings in reinforced concrete shear walls. Shear walls with two or more rows of openings, coupled by beams which are staggered, can be analysed using the finite difference approximation of the laminar technique. The development of a rational analysis leading to the assessment of approximate behaviour, the failure mechanism and ultimate strength for these shear walls would be useful.

(d) In shear walls coupled only by reinforced concrete floor

slabs, the extent of the connecting medium, effective in transmitting shear, and its influence on the overall behaviour of the wall system need to be developed. In the slab to wall connection the shear transfer mechanism and the effect of reversed cyclic loading need to be investigated.

(e) A different arrangement of the flexural wall reinforcement near the windows, together with the concentration of stirrups and binding steel adjacent to the foundation block, could be useful in assisting the shear transfer across the narrow compression region of the tension wall. The destructive action of the shear displacement across the narrow cracked compression zone is likely to be severe in flanged shear walls. Suitable tests could reveal whether the confinement of concrete, as mentioned above, would prevent or at least delay the shear displacement so as to allow a ductile type of failure to occur.

(f) The use of shear reinforcement bent at an angle to the main vertical flexural bars at the base of the walls and their influence on post-elastic performance of the wall hinges could be investigated within the limits of constructional possibilities.

(g) The possibility of placing the main flexural wall reinforcement near the two extremities of the wall section, at a slope, could also be studied. In this case actions, similar to those occurring in diagonally reinforced coupling beams, could be utilised to improve shear transfer across the plastic hinge zones of the walls.

9.6 DESIGN RECOMMENDATIONS

9.6.1 Coupling Beams

(1) When conventionally reinforced beams are used the ductility demand on the structure must be limited. The flexural steel content in both faces of such beams must be limited to ensure full protection against sliding shear failure which is an unsuitable energy

dissipating mechanism during cyclic loading. Additional stirrup reinforcement will not improve the behaviour of such beams. Satisfactory performance of these beams will be assured for wind loads in earthquake free areas.

(2) To ensure a satisfactory performance, when coupled shear walls are subjected to severe lateral reversed cyclic loading, such as result from seismic shocks, diagonal reinforcement should be provided in the coupling beams in order to supply the large ductility demands imposed. It is essential that the diagonal reinforcement is provided with adequate ties to enable the compression strut to sustain yield load without buckling.

9.6.2 Walls

(1) To avoid a shear failure the shear capacity of the walls needs to be increased according to Eq. (3.26) and Eq. (3.27) to account for the increased flexural capacity resulting from the strain hardening of the flexural steel in the beams and in the walls, and differences in the nominal and actual strengths of steel and concrete.

(2) Particular attention should be given to detailing potential plastic hinge zones to ensure full protection against early shear failure which can be a consequence of alternate reversed flexural yielding.

(3) Adequate stability for the yielding compression bars and confinement of compressed concrete need to be provided, especially in the narrow compression zone of the tension wall.

9.6.3 Coupled Shear Wall Structures

(1) The elastic behaviour of the two coupled shear walls with variable properties may be conveniently assessed by the finite difference approximation of the laminar analysis. With the use of the equations presented in Chapter 3, the loss of stiffness caused by cracking in beams and walls can be satisfactorily assessed. Because of cracking alone the reduction in the overall stiffness of a

coupled shear wall structure can be 50% or more.

(2) In seismic areas it is essential that the coupling beams rather than the walls form the weaker elements. With suitable detailing, coupled shear walls can be made both efficient in load resistance and sufficiently ductile for energy dissipation. The plastic hinges can be dispersed over the entire structure and thus, as opposed to single cantilever walls, several lines of defence may be mobilised when survival against catastrophic earthquakes is envisaged.

(3) While designing coupled walls with known static indeterminacy, it is desirable to proportion the reinforcement to result in an advantageous sequence of hinge formation. This may be determined so that damage occurs in repairable and less critical areas first. The principal gravity load carrying units (walls) need to be made to enjoy the highest degree of protection against permanent damage. Therefore, an intelligent hierarchy in the most probable strength levels that are to be provided for each shear wall component must be established. The non-linear elast-plastic analysis presented in Chapter 4 is useful in determining the sequence of hinge formation after the final choice of the strength levels is made.

(4) In many shear wall structures the overturning capacity at foundation level will limit the magnitude of the lateral forces that can be generated. In the process of evaluating the non-linear response of a coupled shear wall, the limits set by the capacity of the foundation must not be overlooked.

APPENDIX A

COMPARISON OF THE REAL STRUCTURE AND THE MODEL

A.1 Dead Load

A typical bay of a seven storied shear wall structure is shown in Fig. A.1. The approximate tributary floor area supported by the shear wall is assumed to extend half way between the shear wall and the adjoining frames. The dead load on the shear wall at the ground floor level is calculated as follows:

Weight of floor (5" thick slab)	:	60 lbs/sq. ft.
Partitions and floor finish	:	20 lbs/sq. ft.
Equivalent seismic live load	:	20 lbs/sq. ft.
Total	:	100 lbs/sq. ft.
Weight of seven floors (7 x 20'-0" x 41'-0" x 100 lbs/sq.ft.)	:	577 Kips
Weight of shear wall (2 x 70'-0" x 8'-0" x 1'-4" x 150 lbs/cu. ft.)	:	224 Kips
Weight of seven coupling beams (7 x 4'-0" x 5'-0" x 1'-0" x 150 lbs/cu. ft.)	:	21 Kips
Total gravity load on two walls at ground floor	:	822 Kips
Load on each wall	:	411 Kips
Simulating load applied to the quarter scale model $411/42$	:	25 Kips
Gravity stress due to dead load on the real structure	$\frac{411,000}{8 \times 12 \times 16}$	: 268 psi.
Stress due to prestress in the quarter scale model	$\frac{25,000}{24 \times 4}$	: 260 psi.

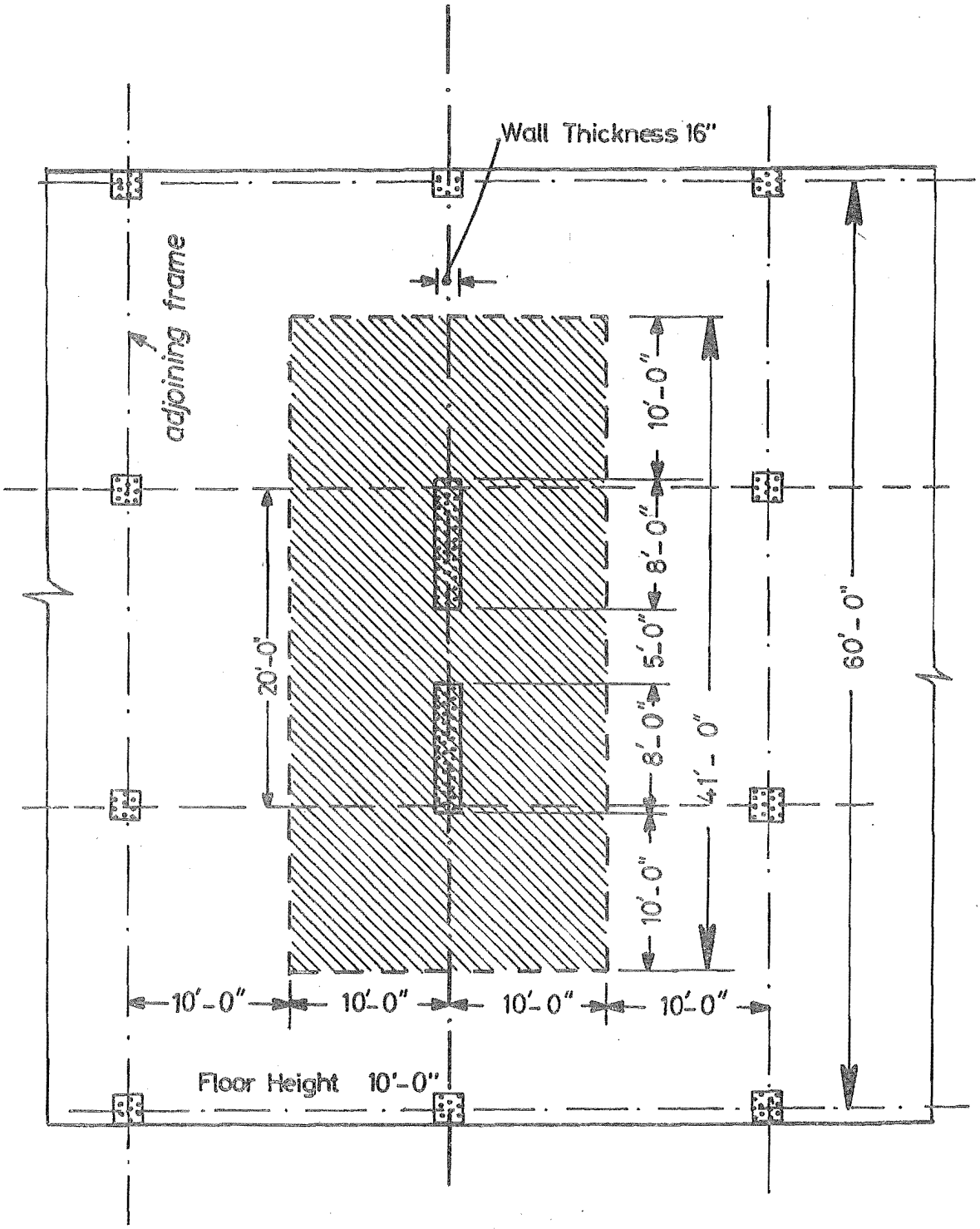

FIG. A.1 A TYPICAL BAY OF A SHEAR WALL STRUCTURE

A.2 Equivalent Lateral Seismic Load

(a) Weight of a typical 20'-0" Shear Wall Bay

Weight of shear wall (see Section A.1)	:	224 Kips
Weight of seven coupling beams	:	21 Kips
Weight of seven floors per bay (7 x 20'-0" x 60'-0" x 100 lbs/sq.ft.)	:	840 Kips
Weight of beams per bay across 7 x 2 x 20'-0" x 250 lbs/ft.	:	70 Kips
along 7 x 2 x 20'-0" x 250 lbs/ft.	:	70 Kips
Weight of columns per bay 7 x 2 x 10'-0" x 300 lbs/ft.	:	42 Kips
Weight of exterior beams per bay along 7 x 2 x 20'-0" x 200 lbs/ft.	:	56 Kips
Total		1323 Kips

(b) Weight of a typical 20'-0" Frame Bay

Weight of seven floors per bay (same as for the shear wall bay)	:	840 Kips
Weight of beams per bay across 7 x 60'-0" x 250 lbs/ft.	:	105 Kips
along 7 x 2 x 20'-0" x 250 lbs/ft.	:	70 Kips
Weight of columns per bay 7 x 4 x 10'-0" x 300 lbs/ft.	:	84 Kips
Weight of exterior cladding per bay (same as for the shear wall bay)	:	56 Kips
Total	:	1155 Kips

The structure was assumed to be situated in Zone A as defined by the New Zealand Standard Model Building Bylaw[75] Thus the equivalent base shear for the structure at working stress level is approximately $0.10\ W_t$, where W_t is the gravity load. It is assumed that the shear wall is designed to resist the lateral load for 5 bays.

Thus the base shear for the prototype shear wall,

$$V_p = 0.10 \times W_t = 0.10 \times (1323 + 4 \times 1155) = 594 \text{ Kips.}$$

Ultimate base shear for the prototype wall, allowing also for the flexural capacity reduction factor, φ

$$V_{up} = \frac{1.25V_p}{\varphi} = \frac{1.25 \times 594}{0.9} = 825 \text{ Kips.}$$

Approximate base shear for the model,

$$V_{um} = \frac{825}{4^2} = 51.5 \text{ Kips.}$$

Theoretical base shears, V_{um}, computed using the elasto-plastic analysis for the model shear walls A and B are 52.5 Kips and 57.0 Kips respectively.

A.3 Equivalent Wind Load on 5 Bays

The wind load for 5 bays required by the New Zealand Standard Model Building Bylaw[75] is approximately 20% of the equivalent lateral seismic base shear.

APPENDIX B

THE DETERMINATION OF DEFORMATIONS FROM THEODOLITE MEASUREMENTS

B.1 General

The relative positions of the theodolites and the model are shown in Fig. B.1. The positions of the instruments were established by bearings and altitudes to three permanent stations A , B and C. Measurements made under "no load" condition was used to establish the plane of the wall. During loading, the planar movements of the model was computed using the bearings measured at R . The horizontal and vertical movements of the targets,attached to the model, were computed using bearings and altitudes measured at O' .

B.2 Displacements of the Targets

Fig. B.2 and Fig. B.3 show the effect of the movement of the base block. At no load, OX and OY are the reference axes. The coordinates of any target I are x_{io} and y_{io} . At any subsequent load increment J , the model, as well as the reference axes OX and OY , move. The axes OX and OY move to O'X' and O'Y' and the target I moves to I' . The coordinates of I' are x_{jo} and y_{jo} with respect to the axes at O and x'_{jo} and y'_{jo} with respect to the axes at O' , i.e, O'X' and O'Y' .

The axes OX and OY move by δx and δy in the respective directions and rotate by an angle θ . The point I moves by Δx and Δy in the OX and OY directions.

From the geometry of Fig. B.3.

$$x_{jo} = x_{io} + \Delta x \qquad \ldots \quad (B.1)$$

$$y_{jo} = y_{io} + \Delta y \qquad \ldots \quad (B.2)$$

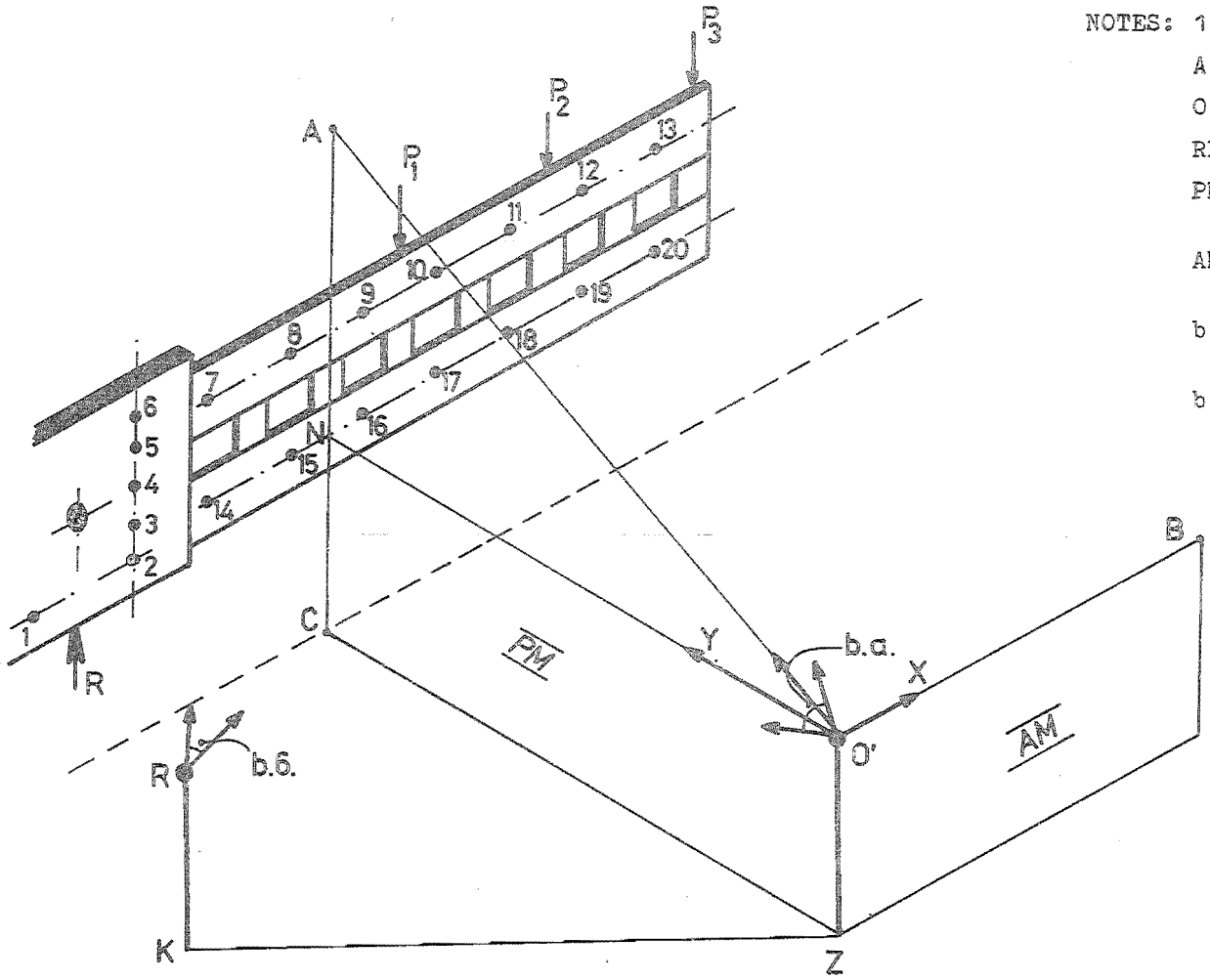

NOTES:

1 TO 20	TARGETS ON THE MODEL
A,B,C	PERMANENT TARGETS
O'Z	MAIN THEODOLITE
RK	AUXILIARY THEODOLITE
PM	PLANE PERPENDICULAR TO THE SURFACE OF THE MODEL
AM	PLANE PARALLEL TO THE SURFACE OF THE MODEL
b.a.	BEARINGS AND ALTITUDES FOR ALL THE TARGETS
b.6.	BEARINGS FOR 6 TARGETS ON THE MODEL

FIG. B.1 DISPOSITION OF THE THEODOLITES, THE SHEAR WALL AND THE TARGETS

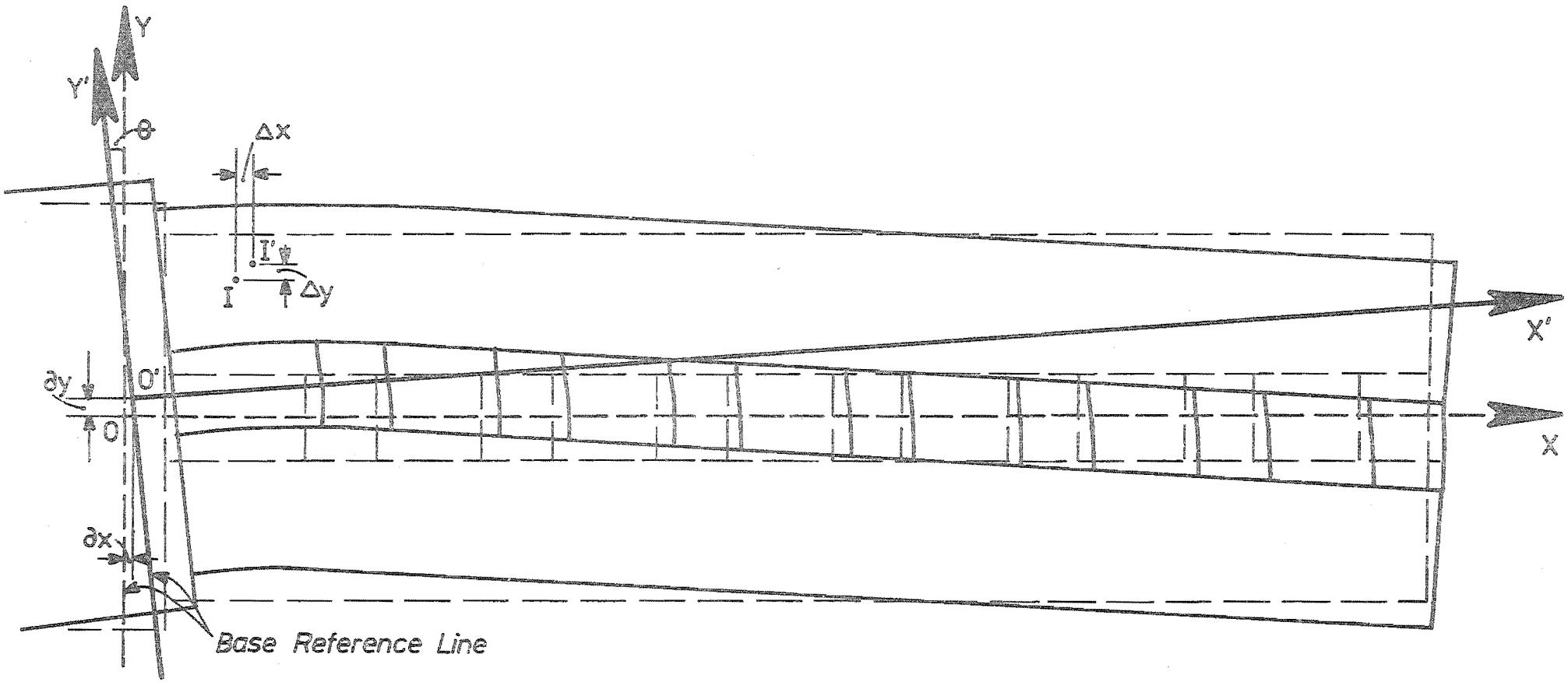

FIG. B.2 DEFORMATIONS OF THE SHEAR WALL

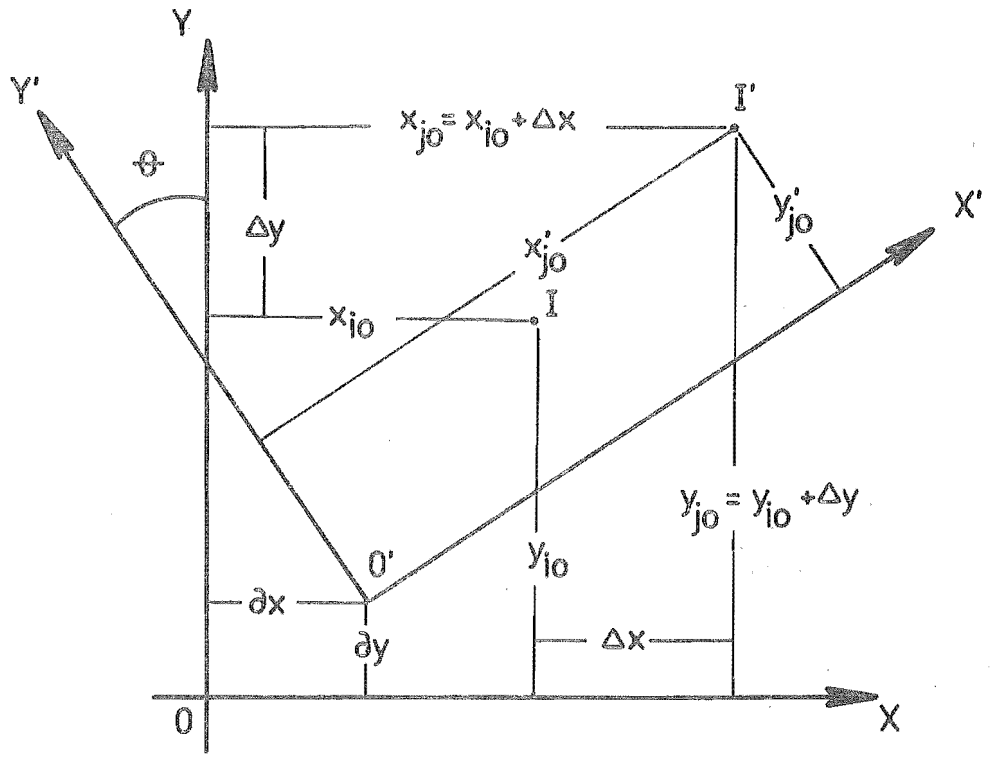

FIG. B.3 MOVEMENTS OF THE TARGET AND THE BASE REFERENCE LINE

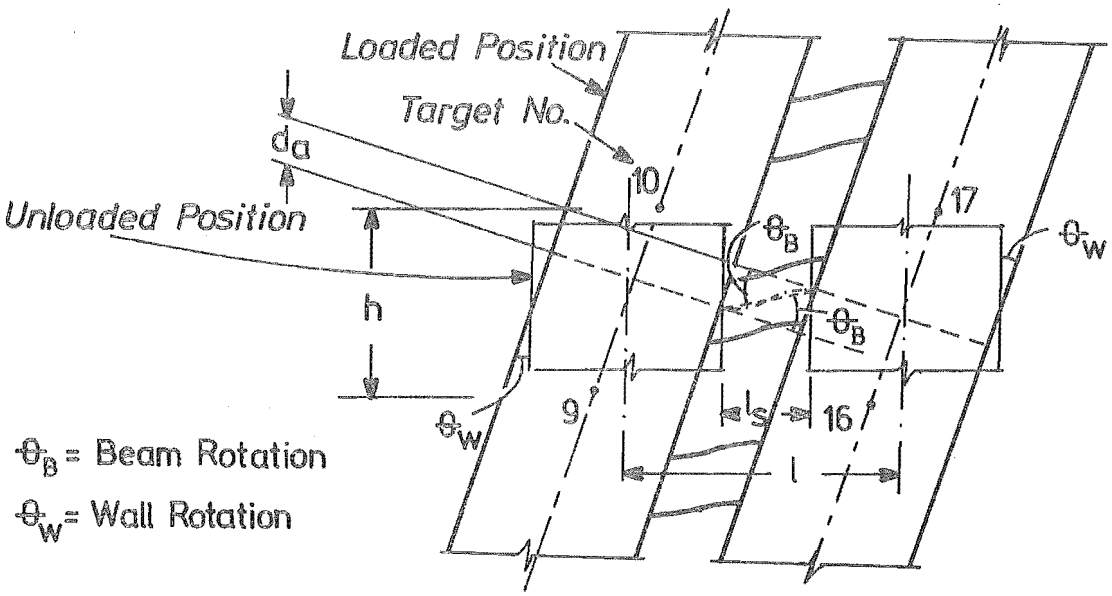

FIG. B.4 DEFORMATIONS OF A TYPICAL SHEAR WALL SECTION

$$x'_{jo} = \left(y_{io} + \Delta y - \delta y\right) \sin\theta + \left(x_{io} + \Delta x - \delta x\right) \cos\theta \quad \ldots (B.3)$$

$$y'_{jo} = \left(y_{io} + \Delta y - \delta y\right) \cos\theta + \left(x_{io} + \Delta x - \delta x\right) \sin\theta \quad \ldots (B.4)$$

Hence
$$\Delta x_I^{Rel} = x'_{jo} - x_{io} \quad \ldots (B.5)$$

$$\Delta y_I^{Rel} = y'_{jo} - y_{io} \quad \ldots (B.6)$$

where Δx_I^{Rel} and Δy_I^{Rel} are the displacements of the point I relative to the base reference line.

B.3 The Deformations of Shear Wall

The deformations of a typical shear wall section can be seen in Fig. B.4. It may be noted that:

(a) The average slope of the walls between any two floors is

$$\theta_w = \left(\Delta y_{10}^{Rel} + \Delta y_{17}^{Rel} - \Delta y_9^{Rel} - \Delta y_{16}^{Rel}\right)/2h \quad \ldots (B.7)$$

(b) The differential displacement between the walls relative to the base reference line along the axis of the walls is

$$d_a = \left(\Delta x_{10}^{Rel} + \Delta x_9^{Rel} - \Delta x_{17}^{Rel} - \Delta x_{16}^{Rel}\right)/2 \quad \ldots (B.8)$$

(c) The rotation of the coupling beam is

$$\theta_b = \frac{l}{l_s} - \frac{\Delta a}{l_s} \quad \ldots (B.9)$$

(d) The elongation of the coupling beam between wall centre lines is

$$\Delta H = \left(\Delta y_{17}^{Rel} + \Delta y_{16}^{Rel} - \Delta y_{10}^{Rel} - \Delta y_9^{Rel}\right)/2 \quad \ldots (B.10)$$

(e) The deflection of the centre line of the walls is

$$y_9 = \Delta y_9^{Rel}, \; y_{10} = \Delta y_{10}^{Rel}, \; y_{16} = \Delta y_{16}^{Rel}, \; y_{17} = \Delta y_{17}^{Rel} \quad \ldots (B.11)$$

(f) The elongations of the walls are

$$x_9 = \Delta x_9^{Rel} \quad , \quad x_{10} = \Delta x_{10}^{Rel} \, , \; x_{16} = \Delta x_{16}^{Rel} \quad , \; x_{17} = \Delta x_{17}^{Rel} \qquad \ldots \text{(B.12)}$$

The deformations (a) to (d) were computed at the intersection of wall and beam centre lines. The deformations (e) and (f) were computed at the targets.

The above computations have been performed by an electronic computer.